CONSTITUTIVE MODELLING OF CYCLICALLY LOADED SOILS FOR APPLICATION IN OFFSHORE ENGINEERING

by

DAVID ABADIAS GOMEZ

Department of Civil and Environmental Engineering

Imperial College London

FEBRUARY 2019

A thesis submitted to Imperial College London in partial fulfilment of the requirements for the degree of Doctor of Philosophy and for the Diploma of Imperial College London in the Faculty of Engineering

Declaration

The research presented in this Thesis was carried out in the Geotechnics Section of the Department of Civil and Environmental Engineering at Imperial College London. The thesis and work presented here are my own research. Any description or quotation of the work of others, published or unpublished, is appropriately referenced.

The copyright of this thesis rests with the author and is made available under a Creative Commons Attribution Non-Commercial No Derivatives licence. Researchers are free to copy, distribute or transmit the thesis on the condition that they attribute it, that they do not use it for commercial purposes and that they do not alter, transform or build upon it. For any reuse or redistribution, researchers must make clear to others the licence terms of this work.

Abstract

The increasing demand of energy combined with the aim for reduction of carbon emissions has driven the development of alternative energy sources such as offshore wind. In this sense, significant research efforts have focused and focus today in the reduction of the installation costs of these super-structures. The research presented in this thesis, carried out under the umbrella of the PISA (PIle Soil Analysis) research project, focuses on the development of constitutive models capable of reproducing soil behaviour subjected to cyclic conditions as those encountered in offshore wind turbines. This thesis presents a comprenhensive study on the applicability of non-linear kinematic hardening rules to soils under cyclic conditions.

While non-linear kinematic hardening rules are widely used to describe ratchetting and cyclic behaviour of rubbers and metals, they are less popular in the field of geomaterials. In this sense the work included in this thesis is novel as it presents a new framework for soil modelling covering the theory, its implementation and also application to real engineering problems. The presented constitutive models uses the lessons learned from the endochronic theory from the 70-80's, combined with the mathematical structure of hypoplasticity and finally, uses several acknowledged modelling strategies from cyclic plasticity used in metals. The framework is presented as general as possible as a unified framework capable of reproducing both sand and clay with simple modifications.

The thesis also studies comprehensively the computational performance of various numerical integration strategies for the rate form equations comprising the framework. Two models are tested under a wide range of directions where a semi-implicit discretisation using an augmented variational form of the closest return method showed excellent capabilities in terms of precision, global convergence and performance.

Extensions to the basic models for sand and clay are presented using the principle of backstress superposition with the objective of enhancing their response under cyclic conditions. The proposed extensions are tested for the basic sand version with real laboratory data from the Karlsruhe soil database, where the predicitons of 82 laboratory tests are presented. Other type of possible extensions are also presented through the use of "numerical artifices" to include perturbation of other history variables, in particular, a method for introducing a jump-in-cycles

method as a backstress perturbation is presented in order to include the modelling of large batches of cycles.

The last part of the thesis focuses on the application of the previous proposed extensions to different boundary value problems, where all the capabilities of the model are tested and discussed at a global and local level. Finally, the sand model with various superimposed hardening rules is applied to reproduce the monotonic and cyclic large scale field tests carried out in Durkirk sand during the PISA research project, where the response of the pile is described in detail, covering both: the soil response arround the pile and its structural response.

Acknowledgements

The research work presented in this thesis has been carried out in the Geotechnical Section of the Civil and Environmental Department, Imperial College London and was motivated as part of the PISA (Pile Soil Analysis) project, focused on cyclic loading of monopiles. Firstly, I want to express my gratitude to my supervisors Lidija Zdravkovic and David Taborda for the great opportunity of being part of such an important research project for the offshore wind industry. Apart from the great opportunity I want to acknowledge my gratitude to both supervisors for the independence, encouragement, good advices and positive discussions through all the PhD.

I also want to thank the Geotechnics Section at Imperial College and the PISA Project Industry Partners comprising Ørsted (formerly DONG Energy), Alstom Wind, E.ON, EDF, Iberdrola, Innogy, SSE, Statkraft, Statoil, Van Oord and Vattenfall for funding my PhD research. I also want to express my gratitude to prof. Potts for his patience, time and tolerance with the "wild" formulations during model implementation, where I could find his door always open for discussion despite his busy agenda.

I want to express my gratitude to all the colleges in the department for the nice environment and frequent group activities organized, in particular to the student reps for their personal time and efforts for the benefit of the research group. In particular, I want to thank all the members, which with more or less frequency, joined the unofficial *"muffin-coffee club".* Thanks for the company, discussions and natural curiosity, always open for scientific discussion and *"intellectual contamination"* on a wide range of topics that could range stochastically from thermal to discrete element analysis, from tensor algebra to politics.

Aside from the academic group, I do not have words to describe my gratitude towards Biliana. Firstly, for embarking with me in this "adventure", or in perhaps better words "this chapter in my life" despite all the challenges to overcome. Not only I admire your strength against adversity but also your sweetness and support during all this period. In addtion, I want to thank my parents Jose Maria and Elvira, for their proximity, love and unconditional support. Finally, I want to dedicate this thesis to the memory of my grandma who left us during the completion of this thesis.

CHAPTER 1: Introduction 34
1.1. General 34
1.2. Aims of research 35
1.3. Outline of the thesis 36
1.4. Modelling strategies for cyclic loading 37
1.5. Modelling strategies for high number of cycles 42
1.5.1. NGI methodology 42
1.5.2. The high-cycle accumulation (HCA) model 46
1.6. Relevant FE Analysis of laterally loaded piles for offshore wind 51
CHAPTER 2: Development of Non-linear Kinematic hardening rules for soils 58
2.1. Governing equations 58
2.2. Geometric implications of the yield surface shape 59
2.2.1. DeFinition of "Encapsulation" 61
2.2.2. Example: encapsulated endochronic model 61
2.2.3. Example: encapsulated Hypoplasticity 66
2.2.4. Asymptotic properties 68
2.3. Fundamental components of models 70
2.3.1. Definition of Limit surface and goal function 71
2.3.2. Implications of the recall term: Stable attractors 75
2.3.3. Implications of the recall term: Asymptotic states 79
2.3.4. Mapping tensor 84
2.3.5. Influence of model Parameters 88
2.3.6. Inversion of the NLKH – Pseudo flow rule 92
2.3.7. Reduction of NLKH rule to a differential Equation 99
2.3.8. Response under stress cycles 103

2.3.9. Response under strain cycles 105
2.3.10. Superposition of backstresses 107
2.4. Thermodynamic admisibility 109
2.5. Application of non-linear kinematic hardening rules to soils 115
2.5.1. Non-Linear Kinematic Hardening rule for Sand 116
2.5.2. Comparison of basic sand model with von Wolffersdorff (1996) model 125
2.5.3. Non-Linear Kinematic Hardening rules for Clays 132
2.5.4. Comparison of basic clay model with Masin (2013) model 138
2.6. Summary of chapter 146
CHAPTER 3: Numerical integration 148
3.1. Object oriented local integration driver 148
3.2. Local integration 151
3.2.1. Context 151
3.2.2. Explicit methods: Substepping solver 153
3.2.3. Implicit integration 156
3.2.4. Constrained Substepping solver 170
3.2.5. Constrained implicit solver 173
3.3. Numerical study: Wu encapsulated model (Wu, 1992) 174
3.3.1. Model Performance in triaxial conditions 175
3.3.2. Analytical derivatives 177
3.3.3. Isoerror maps 178
3.3.4. Precisison for Zig-Zag strain path 189
3.3.5. Convergence rate 191
3.3.6. Global Convergence 194
3.4. Numerical study: Basic Sand Model 198

3.4.1. Model response in triaxial conditions 198
3.4.2. Analytical derivatives 199
3.4.3. Isoerror maps 204
3.4.4. Convergence rate 211
3.4.5. Global Convergence 213
3.4.6. Computational cost of the substeppinG algorithm 216
3.5. Algorithm Performance 217
3.5.1. Triaxial tests cases and methodology 218
3.5.2. Numerical derivatives or analytical? 225
3.5.3. Computational efficiency 228
3.6. Sumary of chapter 229
CHAPTER 4: Model extensions, evaluation, and implementation 232
4.1. Specialised hardening rules 232
4.1.1. Densification hardening rule 233
4.1.2. Enforced ratcheting 240
4.1.3. Strain history surface – Intergranular strain 248
4.2. Karlsruhe sand calibration benchmark 256
4.2.1. Calibratrion procedure 258
4.2.2. Benchmark of model predictions for all tests 263
4.3. Advanced FE Implementation features 296
4.3.1. Modifications for the tensile region 296
4.3.2. Backstress perturbations: Safety factor 297
4.3.3. Backstress perturbation: Jump-in-cycles method 301
4.4. Sumary of chapter 313
CHAPTER 5: Model application 314

5.1. Verification of implementation: Rigid Footing 314
5.1.1. Mesh, boundary and initial conditions 315
5.1.2. Description of 2D analysis 317
5.1.3. Monotonic loading in dense, medium dense and loose sand 319
5.1.4. Backstress perturbation analysis 327
5.1.5. Cyclic loading cases 336
5.2. Application to monopile foundations for offshore wind turbines 344
5.2.1. Dunkirk field testing programme 344
5.2.2. Soil characterisation and modelling 347
5.3. Results of 3D analyses 359
5.3.1. Load-displacement curves 359
5.3.2. Verification of automatic calibration and predicted response 362
5.3.3. Large diameter pile (DL1, DL2) 363
5.3.4. Medium size piles (DM3, DM4, DM7) 382
5.3.5. Large diameter pile (DL1) under cyclic loading 389
5.4. Summary of chapter 407
CHAPTER 6: Conclusions and discussion 410
6.1. On NLKH models for soils 411
6.1.1. Early development 411
6.1.2. On the general mathematical form 412
6.1.3. Constitutive model “constructors” 413
6.1.4. Comparison with current Hypoplastic models 415
6.1.5. On the bipotential 416
6.2. On Model evaluation and extensions 417
6.2.1. On the specialiSed hardening rules 417

6.2.2. On the calibration for Karlsruhe sand 418
6.3. On the numerical integration and Implementation 420
6.3.1. On the constitutive driver 420
6.3.2. On the Numerical integration 421
6.3.3. On the implementation in a FE code 423
6.3.4. On Backstress perturbations 424
6.4. On the application of the model 424
6.4.1. On the verification of the constitutive model 425
6.4.2. On the calibration for Dunkirk sand 425
6.4.3. On THE 3D modelling of the PISA piles 426
6.4.4. On the structural response of short laterally-loaded piles 427
6.4.5. On The cyclic response 427
CHAPTER 7: References 430
Appendix I Aplication of non-smooth mechanics to plasticity theory 438
a. Subgradient 438
b. Polar function 439
c. Extremal couples 439
d. Bipotential 440
Appendix II Other responses of calibration sets for karlsruhe sand: Pitfalls 442
a. Monotonic response for cyclic set 443
b. Cyclic response – large amplitudes for monotonic set 445

List of symbols

ε_{ij}	Total strain
ε_{ij}^{e}	Elastic strain
ε_{ij}^{p}	Plastic strain
σ_{ij}	Effective stress
D_{ijkl}^{e}	Elasticity tensor
α_{ij}^{T}	Total backstress
α_{ij}	First backstress
$\alpha_{ij}^{(n)}$	Nth backstress
λ	Plastic multiplier
$\vec{n}_{ij}$	Normal of yield surface
M_{f}	Model parameter for encapsulated endochronic model
M_{c}	Model parameter for encapsulated endochronic model
G	Shear modulus
K	Bulk modulus
m	Yield surface size
e	Void ratio
e_{i0}	Maximum void ratio parameter
e_{d0}	Minimum void ratio parameter
e_{c0}	Critical state void ratio parameter
h_{s}	Parameter 1 for CSL slope
n	Parameter 2 for CSL slope
f_{d}	Function for CSL conditions
f_{e}	Void ratio stiffness function

f_p	Mean stress stiffness function
f_s	Mean stress stiffness function for clay version
α	Peak strength parameter for f_d
β	Void ratio stiffness parameter for f_e
φ_{cr}	Critical state friction angle in TXC conditions
N	Compression line parameter
λ^*	Slope of compression line
κ^*	Slope of unloading compression line
r	Hypoplastic clay parameter
σ_{ij}^{assimp}	Asymptotic stress state
L_{ijkl}	Mapping tensor
Y	Limit surface
$\tilde{Y}$	Backstress part of limit surface
$\vec{\Upsilon}_{kl}$	Goal function independent of f_d
$\vec{\Upsilon}_{ij}^{f_d}$	Goal function dependent of f_d
z	Plastic endochronic time
k	Parameter for endochronic time metric
$g(\theta)$	Van Eekelen deviatoric shape function
XF	Van Eekelen parameter
YF	Van Eekelen parameter
ZF	Van Eekelen parameter
ϑ	Curvature of the limit surface
$ob_{\max}$	Maximum obliquity of goal function
$ob_{\min}$	Minimum obliquity of goal function
δ	Parameter for goal function
$p_\alpha = \alpha_{kk}/3$	Invariant of the backstress
$J_\alpha = \sqrt{1/2\alpha_{ij}^*\alpha_{ij}^*}$	Second invariant of the backstress

$\eta = J_\alpha / p_\alpha$	Ratio of second and first invariant
η^{Assimp}, η^{A}	Assymptotic state
$ob = \dot{\varepsilon}_{kk} / \left\| \dot{\varepsilon}_{ij} \right\|$	Plastic strain obliquity
$\tilde{\varepsilon}_{ij}^{p}$	Pseudo-plastic strain
Σ_{ijmn}	Plastic metric tensor
$C^{(n)}$	Weights on hardening rules
$\dot{\kappa}$	Thermomechanical flows
π	Thermomechanical forces
$b(\dot{\kappa}, \pi)$	Bipotential function
λ	Plastic multiplier
λ^{vol}	Eigenvalues of the mapping tensor
λ^{dev}	Eigenvalues of the mapping tensor
$S_f = \lambda^{vol} / \lambda^{dev}$	Shape factor of the mapping tensor
f_p^{VF}	Stiffness function from Von Volferndorf (1996)
L_{ijkl}^{VF}	Mapping tensor from Von Volferndorf (1996)
N_{ij}^{VF}	Non-linear tensor from Von Volferndorf (1996)
p_e^*	Equivalent Hvorslev pressure
$\hat{\alpha}_{ij}^{e} = \alpha_{ij} / p_e^*$	Normalised backstress tensor
θ_n	Discretisation parameter for normal of yield surface
θ_α	Discretisation parameter for backstress
c	Penalty term for local solver
η^{LS}	Line search parameter
β^{LS}	Line search parameter
P_{ijkl}^{V}	Volumetric projector of mapping tensor
S_d	Weight on deviatoric projector
a	Parameter for densification rule
H	Parameter for densification rule

R_{UR}	Parameter for densification rule
$\vartheta^{(2)}$	Parameter for densification rule
$\beta^{(2)}$	Parameter for densification rule
$ob_e^{(3)}$	Parameter for enforced obliquity
$\beta^{(3)}$	Parameter for enforced ratchetting rule
H	Parameter for enforced ratchetting rule
$\vartheta^{(3)}$	Parameter for enforced ratchetting rule
$X^{(3)}$	Parameter for enforced ratchetting rule
$C^{(3)}$	Weigth of enforced ratchetting rule
Σ_{ij}	Intergranular backstrain
R	Parameter for intergranular strain
β	Parameter for intergranular strain
X	Parameter for intergranular strain
M_d	Parameter for intergranular strain
M_v	Parameter for intergranular strain
SF	Safety factory internal variable
$S_v^{(k)}$	Volumetric projector weight in the mapping tensor for k^{th} rule
$S_d^{(k)}$	Deviatoric projector weight in the mapping tensor for k^{th} rule
$C^{(k)}$	Weight in the mapping tensor for k^{th} rule

List of figures

Figure 1: simplified load conditions assumed for the potential failure surface. (Andersen and Lauritzsen, 1988) 42

Figure 2: Number of cycles to failure for various combinations of average shear (τ_a) and cyclic shear (τ_{cy}) in triaxial tests on normally consolidated Drammen Clay. (Andersen and Lauritzsen, 1988) 43

Figure 3: Contours of cyclic shear strain γ_{cy} and normalized permanent pore pressure $\mathbf{u_p/\sigma_{oct'c}}$ as a function of normalised shear stress τ_{cy}/σ_{oct} and number of cycles. Cross section at $\tau_a = \tau_0$. Baskarp sand with Dr 95%, vertical consolidation stress σ_{vc} = 250. (Jostad et al., 2015) 44

Figure 4: (a) cyclic load history applied in the undrained DSS test on Baskarp sand, (b) Measured and calculated pore pressure versus number of cycles (c) Calculated pore pressure accumulation and equivalent number of cycles, (d) Measured stress path at the end of parcel 3 and during first cycle in Parcel 4. (Jostad et al., 2015) 45

Figure 5: Idea of explicit calculation strategy of the accumulative deformation. (Niemunis et al., 2005) 47

Figure 6; Scheme of the construction of the strain amplitude tensor. Direction r(i) and size R(i) of the strain loop.(Niemunis et al., 2005) 48

Figure 7:Soil domain and mesh discretization (Corciulo et al., 2017) 52

Figure 8: Displacement response at mudline at varying soil permeability (Corciulo et al., 2017) 53

Figure 9:Comparison of measured and predicted responses. (a) centrifuge measurents (b) Undrained trixial tests and clay hypopastictic prediction. (c) Measured versus calculated normalized pile displacement versus number of cycles (Hong et al., 2017) 54

Figure 10: Computed lateral capacity factors along the pile: (a) flexible pile; (b) semi-rigid pile; (c) rigid pile(Hong et al., 2017) 55

Figure 11: Detail of the 3D mesh used in the analysis (Machacek et al., 2018)..... 56

Figure 12: Deatil of the 3D mesh used in the analysis (Machacek et al., 2018)..... 57

Figure 13: Simple encapsulated-endochronic model stress controlled tests for $M_c = 0.2/3\sqrt{1.5}; M_f = 1/3\sqrt{1.5}$ 63

Figure 14: Small strain probes for the “encapsulated” endochronic model..... 65

Figure 15:Drained triaxial test of “encapsulated” Von Wolfendorff model 67
Figure 16:Undrained triaxial test of “encapsulated” Clay Hypoplastic model 67
Figure 17: Graphical representation of the Limit surface for $f_d = 1$ and $\vartheta = 1$ 73
Figure 18: Graphical representation of the Goal Funtions $f_d = 1$ and $\vartheta = 1$ 73
Figure 19: Parametric study of the Goal Function 74
Figure 20: Stable attractors for goal function dependent of f_d $\vec{\Upsilon}_{ij}^{f_d}$ 77
Figure 21: Stable attractors for goal function independent of f_d $\vec{\Upsilon}_{ij}$ 77
Figure 22: Parametric study of asymptotic attractors. Goal Function dependent on f_d 80
Figure 23: Parametric study of asymptotic attractors Goal Function independent of f_d 81
Figure 24: Asymptotic probes for $f_d = 1.5$ 82
Figure 25: Envelope of asymptotic strain paths for both goal functions 83
Figure 26: Comparison of mapping tensors 87
Figure 27: Strain perturbations mapping for $\tilde{Y} = [0.0, 0.5, 0.75]$: (a) Case 1, (b) Case 2, (c) Case 3, (d) Case 4 and (e) Case 5. 91
Figure 28: Graphical interpretation of the metric of plastic strain 92
Figure 29: Stress probe for Case 1 96
Figure 30: Stress probe for Case 2 97
Figure 31: Stress probe for Case 3 98
Figure 32: Phase portraits of J/p – p for equations (2.73) and (2.74) $\lambda^{dev} = 4000$ $\lambda^{vol} = 200$ 102
Figure 33: Ratcheting accumulation over 2 cycles for Case 1a 104
Figure 34: Ratcheting accumulation over 2 cycles for Case 1b 104
Figure 35: Stable cycles for equation (2.73) for different combinations of f_d and ob 107
Figure 36: Response of a TXC with extra backstress 108
Figure 37: Detail of First and Second backstress (grey) and total stress black 108
Figure 38: Strain-Backstress paths for pure deviatoric strain conditions (ob=0) 121
Figure 39: Strain-Backstress paths for isotropic conditions ($ob = -\sqrt{3}$) 122
Figure 40: Strain-Backstress path for oedometric conditions (ob=-1) 123
Figure 41; Liquefaction backstreess paths for positive obquiquity: (a) ob = 0.1, (b) ob = 0.5 124
Figure 42: Comparison of equivalent goal function for basic sand and Von Wolffersdorff . 126

Figure 43: Finite perturbation for VW (black) and Basic Sand (grey), initial void ratio e = 0.8 127
Figure 44: Comparison triaxial compression response of Basic Sand model and Von Wolffersforff for various initial void ratios 128
Figure 45: Comparison of undrained triaxial response of Basic Sand model and Von Wolffersforff for various initial void ratios 129
Figure 46: Comparison oedometric response of Basic Sand model and Von Wolffersforff exporession for loose state 130
Figure 47: Comparison oedometric response of Basic Sand model and Von Wolffersforff exporession for dense state 131
Figure 48: Critical state framework (Schofield and Wroth, 1968) 132
Figure 49: Definition of N, λ^*, κ^* and p_e,from Masin (2005) 133
Figure 50: Undrained triaxial tests for various OCRs 136
Figure 51: Drained triaxial tests for various OCRs 137
Figure 52: Compression tests. (a) isotropic, (b) oedometric 137
Figure 53: Comparison of equivalent goal function (a), limit surfaces (b) and f_d functions (c) for Basic Clay and Masin (2013) models 141
Figure 54:Mapping of a finite perturbation of the Basic clay model and hypoplasticity clay with explicitly defined asymptotic states 142
Figure 55: Drained triaxial tests for various initial OCRs 143
Figure 56: Undrained triaxial tests for various initial OCRs 144
Figure 57: Comparison of models under isotropic conditions 145
Figure 58: Comparison of models under oedometric conditions 145
Figure 59: General structure of the object-oriented solver 150
Figure 60: Integration in a Finite Element Program 150
Figure 61: Biaxial loading for Non-linear kinematic hardening model. All equations solved at the mid of the step (left). Mixed discretisation, hardening rule solved in the mid step and consistency condition at the end of the step (right). (Chaboche and Cailletaud, 1996) 157
Figure 62: Illustration of trust-region method 168
Figure 63: Evaluation of Wu (1992) “encapsulated” model in Triaxial conditions (TXC)... 176
Figure 64: Numerical triaxial tests detailed from Wu (1992) 177
Figure 65: Backward Euler (BE) 182

Figure 66: Mid-Point (MID05) 182
Figure 67: Half Mid-Point (MID1) 183
Figure 68: Half Trapezoidal (TZ1) 183
Figure 69: Backward-Euler (BE) in Plane Strain Conditions for non-diagonal excursions .. 185
Figure 70: Backward Euler (BE) in Plane Strain Conditions for diagonal excursions 185
Figure 71: Mid-Point (MID05) in Plane Strain Conditions for non-diagonal excursions 186
Figure 72: Mid-Point (MID05) in Plane Strain Conditions for diagonal excursions 186
Figure 73: Half-Mid-Point (MID1) in Plane Strain Conditions for non-diagonal excursions 187
Figure 74: Half Mid-Point (MID1) in Plane Strain Conditions 187
Figure 75: Half trapezoidal (TZ1) in Plane Strain Conditions for non-diagonal excursions. 188
Figure 76: Half trapezoidal (TZ1) in Plane Strain Conditions for diagonal excursions 188
Figure 77: Zig-Zag strain test exact solution versus Backward-Euler discretisation. 190
Figure 78: Zig-Zag strain test exact solution versus Mid-Point and Half-Mid-Point discretisations 190
Figure 79: Rate of converge of each of the algorithms for pure deviatoric strain(a), oedometric compresion strain path(b), isotropic compresion strain path(c) and oedometric swelling strain path (d) 192
Figure 80: Rate of converge for aug-CPPM for various penalty terms 1E-2 to 1E-6 for oedometric swelling strain path 193
Figure 81: Isoerrors for global convergence test. (a) non-diagonal excursions, (b) diagonal excursions 195
Figure 82: Iterations map for closest-Projection-Point Method (CPPM), non-diagonal excursions (a), diagonal excursions (b) 196
Figure 83: Iterations map for constrained-Closest-Projection-Point Method (primal-CPPM), non-diagonal excursions (a), diagonal excursions (b) 196
Figure 84: Iterations map for augmented-Closest-Projection-Point Method (augmented-CPPM), non-diagonal excursions (a), diagonal excursions (b) 197
Figure 85: Dogleg-Trust-Region method (DTM), non-diagonal excursions (a), diagonal excursions (b) 197
Figure 86: Model response in triaxial conditions 199
Figure 87: Backward Euler (BE) 205
Figure 88: Half-Mid-Point (MID1) 205

Figure 89: Mid-Point (MID05) 206
Figure 90: Trapezoidal discretisation (TZ1) 206
Figure 91: BackWard-Euler (BE) in Plane Strain Conditions for non-diagonal excursions . 207
Figure 92: BackWard-Euler (BE) in Plane Strain Conditions for diagonal excursions 208
Figure 93: Half Mid-Point (MID1) in Plane Strain Conditions for non-diagonal excursions 208
Figure 94: Half Mid-Point (MID1) in Plane Strain Conditions for diagonal excursions 209
Figure 95: Mid-Point (MID05) in Plane Strain Conditions for non-diagonal excursions 209
Figure 96: Mid-Point (MID05) in Plane Strain Conditions for diagonal excursions 210
Figure 97: Trapezoidal (TZ) in Plane Strain Conditions for non-diagonal excursions 210
Figure 98: Trapezoidal (TZ) in Plane Strain Conditions for diagonal excursions..... 211
Figure 99: Rate of converge of each of the algorithms for pure deviatoric strain(a), oedometric compresion strain path(b), isotropic compresion strain path(c) and oedometric swelling strain path (d) 212
Figure 100: Convergence mapping of CPPM for half-Mid-Point discretisation..... 214
Figure 101: Convergence mapping of primal-CPPM for half-Mid-Point discretisation 214
Figure 102: Convergence mapping of augmented-CPPM for half-Mid-Point discretisation 215
Figure 103: Convergence mapping of Trust-Dogleg-Method (DTM) for half-Mid-Point discretisation 215
Figure 104: Substepping mapping in the rendulic plane 216
Figure 105: Substepping mapping in plane strain conditions..... 217
Figure 106: Undrained triaxial case for performance benchmark TXU1: small increments. 219
Figure 107: Undrained triaxial case for performance benchmark TXU2: Large increments 219
Figure 108: Drained triaxial case for performance benchmark TXD1 220
Figure 109: Convergence study for TXU1 (small increments) for basic sand 221
Figure 110: Convergence study for TXU2 (large increments) for basic sand..... 222
Figure 111: Convergence study for TXD1 for basic sand 223
Figure 112: Comparison of “exact” solution with Backward-Euler discretisation for TXU cyclic conditions 224
Figure 113: Comparison of “exact” solution with Half-Mid-Point discretisation for TXU cyclic conditions..... 224
Figure 114: Benchmark of analytical and numerical derivatives for encapsulated Wu model 226

Figure 115: Benchmark of analytical and numerical derivatives for basic sand rule 227
Figure 116: Same quality of integration for MID1 in one step and SS under SSTOL = 10-3. Relative average error of exact solution SS = 6.1E-3 MID1 = 6.8E-3 228
Figure 117: Effect of the specialised densification rule under isotropic conditions: (a) no specialised rule, (b) constant ratcheting, (c) constant ratcheting with smaller concavity, (d) residual ratcheting and (e) full shakedown. 237
Figure 118: Effect of the specialized densification rule under oedometric conditions: (a) no specialized rule.....238
Figure 119: Effect of the specialized densification rule under oedometric conditions: (b) constant ratcheting 238
Figure 120: Effect of the specialized densification rule under oedometric conditions (c) constant ratcheting less concavity.....238
Figure 121: Effect of the specialized densification rule under oedometric conditions (d) residual ratcheting.....239
Figure 122: Effect of the specialized densification rule under oedometric conditions (e) full shakedown.....239
Figure 123: Case (a), basic sand model with no specialized rules, excessive ratchetting 243
Figure 124: Case (b), simple contribution of the specialised rule, reduction of ratcheting for low amplitudes and no significant change in ratcheting direction.....244
Figure 125: Case (c), reduction of ratcheting and change in ratcheting direction depending on the amplitude of the cycle 245
Figure 126: Case (d), smaller reduction of ratcheting but higher influence on the ratcheting direction 246
Figure 127: Case (e), residual ratcheting 247
Figure 128: Numerical prediction of cyclic undrained test with and without intergranular “backstrain”.....250
Figure 129:Case (a) No Intergranular strain 251
Figure 130:Case (b).....252
Figure 131:Case (c).....252
Figure 132:Case (d).....253
Figure 133:Case (e).....254
Figure 134:Case (f) 254

Figure 135: Step 1, adjust of the CSL slope with isotropic compression tests or oedometers. $\mathbf{e_{d0}}$, $\mathbf{e_{c0}}$, $\mathbf{h_s}$ and $\mathbf{n}$ 259
Figure 136: Step 2. Position the CSL slope for loose and dense states. Parameters adjusted $\mathbf{e_{c0}}$ 260
Figure 137: Step 3. Use shear tests (TXD, TXU, SS) to characterize the deviatoric shape. Parameters adjusted XF, YF, ZF....260
Figure 138: Step 4. Normalise drained shear tests (SS, TXD) to characterize the goal function distribution and the curvature of the limit surface with J/p. Parameters adjusted $\mathbf{ob_{min}}$, $\mathbf{ob_{max}}$, δ and ϑ 261
Figure 139: Example of calibration, final result 262
Figure 140: Example of use of specialised hardenign rules to improve cyclic predictions...263
Figure 141: Calibration versus Test for non-constant amplitude....265
Figure 142: Calibration versus loose sand - isotropic cyclic test....266
Figure 143: Calibration versus dense sand - isotropic cyclic test....266
Figure 144: Calibration versus very dense sand - isotropic cyclic test....267
Figure 145: Karlsruhe sand drained triaxial compression tests 268
Figure 146: Normalized paths for Karlsruhe Drained triaxial test 269
Figure 147: Triaxial test for very dense sand....270
Figure 148: Triaxial test for dense sand....270
Figure 149: Traiaxila test for medium sand....271
Figure 150: Triaxial test for medium dense sand....271
Figure 151: Triaxial test for loose sand 272
Figure 152: Karlsruhe sand undrained triaxial tests 273
Figure 153: Undrained triaxial compression tests in dense sand versus numerical prediction (1) 274
Figure 154: Undrained triaxial compression tests in dense sand versus numerical prediction (2) 274
Figure 155: Undrained triaxial compression tests in loose and very dense sand versus numerical prediction (3)....274
Figure 156: Undrained triaxial extension tests in dense sand versus numerical prediction (1) 275
Figure 157: Undrained triaxial extension tests in dense sand versus numerical prediction (2) 275

Figure 158: Undrained triaxial extension tests in dense sand versus numerical prediction (3) 275
Figure 159: Load-unload oedometer tests for loose-dense versus numerical prediction.....276
Figure 160: Load-unload oedometer tests for dense-very dense sand versus numerical prediction 277
Figure 161: Cyclic oedometer tests versus numerical prediction 277
Figure 162: Large amplitude undrained strain controlled triaxial tests 279
Figure 163: Large amplitude undrained strain controlled triaxial test 15 against numerical prediction 280
Figure 164: Large amplitude undrained strain controlled triaxial test 16 against numerical prediction 280
Figure 165: Large amplitude undrained strain controlled triaxial test 17 against numerical prediction 280
Figure 166: Large amplitude undrained strain controlled triaxial test 18 against numerical prediction 281
Figure 167: Large amplitude undrained strain controlled triaxial test 19 against numerical prediction 281
Figure 168: Large amplitude undrained strain controlled triaxial test 20 against numerical prediction 281
Figure 169: Large amplitude undrained strain controlled triaxial test 21 against numerical prediction 282
Figure 170: Large amplitude undrained strain controlled triaxial test 22 against numerical prediction 282
Figure 171: Large amplitude undrained strain controlled triaxial test 23 against numerical prediction 282
Figure 172: Small amplitude undrained strain controlled triaxial tests 284
Figure 173: Stress relaxation over number of cycles for cyclic undrained strain controlled test 285
Figure 174: Small amplitude undrained strain controlled triaxial test 1 against numerical prediction 286
Figure 175: Small amplitude undrained strain controlled triaxial test 2 against numerical prediction 287

Figure 176: Small amplitude undrained strain controlled triaxial test 3 against numerical prediction 287
Figure 177: Small amplitude undrained strain controlled triaxial test 4 against numerical prediction 288
Figure 178: Small amplitude undrained strain controlled triaxial test 5 against numerical prediction 289
Figure 179: Small amplitude undrained strain controlled triaxial test 6 against numerical prediction 289
Figure 180: Small amplitude undrained strain controlled triaxial test 7 against numerical prediction 290
Figure 181: Small amplitude undrained strain controlled triaxial test 8 against numerical prediction 291
Figure 182: Small amplitude undrained strain controlled triaxial test 9 against numerical prediction 291
Figure 183: Small amplitude undrained strain controlled triaxial test 10 against numerical prediction 292
Figure 184: Small amplitude undrained strain controlled triaxial test 11 against numerical prediction 293
Figure 185: Small amplitude undrained strain controlled triaxial test 12 against numerical prediction 293
Figure 186: Small amplitude undrained strain controlled triaxial test 13 against numerical prediction 294
Figure 187: Small amplitude undrained strain controlled triaxial test 14 against numerical prediction 295
Figure 188: Graphical description of Jump-in-cycles method for one cycle. 302
Figure 189: Benchmark of four proposed Jump-in-Cycles methods for mid size strain excursions, undrained strain controlled triaxial test 307
Figure 190: Illustration of benchmark analysis: cyclic strain controlled probes for N = 5 ... 310
Figure 191: Cyclic strain probes for strain amplitude 1E-4 311
Figure 192: Cyclic strain probes for strain amplitude 1E-4 312
Figure 193: Detail of mesh used in footing analyses 315
Figure 194: Simulated triaxial compression tests at initial void ratio (0.75, 1.0 and 1.2) with model parameters given in Table 28 317

Figure 195: Reaction – displacement curves for three initial void ratios 319
Figure 196: Incremental displacements at failure for very dense case (multiplied by a factor of 150) 320
Figure 197: Incremental displacement at failure for medium dense case (multiplied by a factor of 150).....321
Figure 198: Incremental displacement at failure for very loose case (multiplied by a factor of 150) 321
Figure 199: Several of the elements investigated for local integration 322
Figure 200: Stress paths for the elements investigated in the mesh, dense case, $ein = 0.75$323
Figure 201: Stress paths for 25 elements in the mesh, slightly dense case.....324
Figure 202: Stress paths for 25 elements in the mesh, loose sand case 325
Figure 203: Stress-Strain curves at el. 132 and 188 for dense, medium dense and loose cases (x/R = [0.0 , 1.3], z/R = 1).....326
Figure 204: Load-displacement curve for monotonic analysis and backstress perturbation analysis and detail of incremental displacements below the footing.....329
Figure 205: Vertical displacement contours at points D and D' for monotonic and backstress perturbation simulations.....331
Figure 206: Mean effective stress at points D-D' for monotonic and backstress perturbation simulations 332
Figure 207: Void ratios at points D and D' for monotonic and backstress perturbation simulations 333
Figure 208: Vertical stress under the footing for monotonic and backstress perturbation analysis 334
Figure 209: Stress-Strain curves at element 132 and 188(x/R =[0.0 1.0], z/R = 1).....335
Figure 210: Displacement - Reaction at centre for three cases.....337
Figure 211: Displacement - Reaction at centre for backstress superposition cases (detail Figure 210). 338
Figure 212: Stress-Strain curves at element 132 (x/R = 1.3, z/R = 1) 339
Figure 213: Stress-Strain curves at element 188 (x/R = 0.0, z/R = 1) 340
Figure 214: Detail of load-displacement curve for one backstress (a) five backstresses (b).341
Figure 215: Stress-Strain curves at element 188 (x/R = 0.0, z/R = 1) 342
Figure 216: Detail of gap and vertical slope during test loading (AWG, 2015).....345
Figure 217: Pile layout at Dunkirk (McAdam, 2018).....346

Figure 218: Test configuration for lateral loading for each pile diameter (McAdam, 2018) 346
Figure 219: Mesh used for 2m. diameter pile DL2 348
Figure 220: Pore water pressure profile at Dunkirk from CPTu tests (AWG, 2015) 350
Figure 221: New CPT profiles for Dunkirk site (AWG, 2015) 351
Figure 222: Triaxial tests in Dunkirk sand used for calibration. (Liu et al, 2017) 352
Figure 223: Calibration of strategy 1 354
Figure 224: Calibration of strategy 2 354
Figure 225: Diagram for calibration class 356
Figure 226: Asymptotic strain tests for GA1 and GA2 calibration 358
Figure 227: Numerical triaxial tests for GA1 and GA2 calibration 358
Figure 228: Comparison at ultimate conditions: mudline displacement ~ 0.1D, between measured load – displacement curves, 3D FE analyses and API/DNV methodology, from (McAdam, 2018) 360
Figure 229: Comparison at operational conditions: mudline displacement ~ 0.01D, between measured load – displacement curves, 3D FE analyses and API/DNV methodology, from (McAdam, 2018) 361
Figure 230: Load – displacement prediction of sets of parameters, manual versus numerical calibration 362
Figure 231: Accumulated deviatoric strain at various simulation stages 366
Figure 232: Accumulated mean effective stress 369
Figure 233: Lode's angle 372
Figure 234: Incremental displacement vectors 374
Figure 235: Void ratio 377
Figure 236: Deflected shape at 30, 60, 79, 91 and 100% of the maximum lateral load 378
Figure 237: Bending moment distribution at 30, 60, 79, 91 and 100% of the maximum lateral load 378
Figure 238: Normalized deflection versus normalized pile length at 30, 60, 79, 91 and 100% of the maximum lateral load 379
Figure 239: Detail of point A and B for field test comparison – DL1-DL2 load displacement curves, from (McAdam, 2018) 380
Figure 240: Embedded responses of pile DL2: at point A (a) ground-level displacement of 10.1 mm and (b) ground level-moment of 10.8 MNm; and at point B loading (c) ground-level

displacement of 110 mm and (d) ground-level moment of 34.1 MNm, from (McAdam et al, 2018) 381
Figure 241: Failure mechanism of medium diameter piles (a) DM3, (b) DM7 and (c) DM4 384
Figure 242: Typical failure mechanism for rigid piles 385
Figure 243: Deflected shape and bending moment distribution of DM3, DM4 and DM7 medium diameter piles 386
Figure 244: Normalized deflection versus normalized depth of: (a) DM3, (b) DM4 and (c) DM7 387
Figure 245: Shear force versus depth of: (a) DM3, (b) DM4 and (c) DM7 388
Figure 246: Equivalent pressure versus depth of: (a) DM3, (b) DM4 and (c) DM7 388
Figure 247: p-y curves DM7 389
Figure 248: Monotonic and cyclic loading stages for DL1 390
Figure 249: Detail of cyclic tests (a) full test, (b) detail, batches at 10% and 20% of pile capacity, stable cycles 391
Figure 250: Load displacement curves at mudline for Set1: Comparison with DL1-2 393
Figure 251:Comparison of load displacement curves at mudline for Set1 and Set4 and field data: (a) One Backstress, (b) Two backstresses; field test – dotted light line, simulation – dark grey line 394
Figure 252: Comparison for N=20 840 KN cycles and cyclic field tests (a) One Backstress, (b) Two backstress 395
Figure 253: Points of study 396
Figure 254: Stress paths for point A2 397
Figure 255: Stress paths for point D1 398
Figure 256: Stress paths for point B2 399
Figure 257: Stress paths for point B1 400
Figure 258: Stress paths for point D2 401
Figure 259: Comparison of deflected shape of Set1 and Set2 predictions at beginning and end of cycle batch 403
Figure 260: Comparison of bending moments of Set1 and Set2 bending moment predictions at beginning and end of cycle batch 403
Figure 261: Comparison of equivalent p-y curves for Set1 and Set 2 under operational conditions 404

Figure 262: Load displacement curves of parametric 3D FEA analysis, load displacement curve at mudline. (a) Set1, (b) Set 2, (c) Set 3, (d) Set 4, (e) Set 5. 407
Figure 263: Triaxial test for very dense sand.....443
Figure 264: Triaxial test for dense sand.....443
Figure 265: Traiaxila test for medium sand.....444
Figure 266: Triaxial test for loose sand 444
Figure 267: Large amplitude undrained strain controlled triaxial test 16 against numerical prediction: (a) monotonic set (b) cylic set 445

List of tables

Table 1: Input parameters for encapsulated hypoplastic sand model 66
Table 2: Input parameters for encapsulated hypoplastic clay model 66
Table 3: Parametric inputs for asymptotic probes 82
Table 4: Parametric inputs 88
Table 5: Parametric inputs 95
Table 6: Input values for sand model 120
Table 7: Input parameters of Sand model and VW model used for comparison 125
Table 8: Input parameters for Clay study 136
Table 9: Input parameters for Basic Clay model comparison 140
Table 10: Cases of time step discretisations for implicit integration 158
Table 11: initial conditions for Iso-Error maps Wu encapsulated model 179
Table 12: Cases of time step discretisation for implicit integration 179
Table 13: Zig-Zag strain test 189
Table 14: Inputs of Basic Sand Model used in this numerical study 198
Table 15: Characteristics of the tests for numerical benchmarking 218
Table 16: Numerical output of cyclic TXU 229
Table 17: Parametric study of specialized densification rule 235
Table 18: Inputs for parametric study of enforced ratchetting hardening rule 241
Table 19: Parameters used parametric study for intergranular backstrain rule 250
Table 20: Summary table of all tests used for benchmarking 256
Table 21: Parameters determined with cyclic isotropic tests 265
Table 22: Parameters determined with ISO, TXD and TXU tests 269
Table 23: Parameters determined with cyclic undrained triaxial test 278
Table 24: Input parameters for benchmark tests, same inputs as Chapter: Numerical Integration 306
Table 25: Absolute and relative error for three large cycles 306
Table 26: Absolute and relative errors of cyclic strain probe 1 (5E-4) 310
Table 27: Absolute and relative errors of cyclic strain probe (2) (1E-4) 311
Table 28: Input parameters for benchmark tests, same inputs as Chapter: Numerical Integration 316
Table 29: Input parameters for cyclic benchmark tests 337

Table 30: Input parameters for five backstress case 340
Table 31: Test pile geometries and loading at Dunkirk site 345
Table 32: Stratigraphy at Dunkirk and CPT measurements 351
Table 33: Manual versus genetic algorithm calibration..... 357
Table 34: Cyclic loading stages for DL1 DL2..... 390
Table 35: Set of input parameters for cyclic simulations 392
Table 36: Set of input parameters for parametric study of cyclic simulations 405
Table 37: Parameter sets for static and cyclic tests for Karlsruhe sand calibration..... 442

CHAPTER 1: INTRODUCTION

1.1. GENERAL

Design of monopiles for offshore wind turbine (OWT) foundations began in earnest some 20 years ago. It was soon realised that the available design methods had significant shortcomings when applied to this task. The existing methodologies were developed for Oil & Gas type sub-structures, usually with different design criteria and loading conditions compared to the current OWT monopiles. Their inadequacy results primarily from the limitations of the experimental database for laterally loaded piles, in particular with respect to the range of cyclic loading, dimensions and slenderness ratios.

Amongst different efforts in recent years to improve design methodologies, the most ambitious project, initiated in 2013, has been the PISA (PIle-Soil Analysis) project, which involved medium-scale field tests of laterally loaded piles, numerical analysis and laboratory and field testing, integrated together to develop future design methodologies for OWT monopiles. The PISA project is a collaborative research effort involving Imperial College London (ICL), University of Oxford (UO) and University College Dublin (UCD) on the academic side, together with Ørsted (formerly DONG Energy), and ten offshore industry partners whose commercial activities involve the design, construction and operation of several wind farms in Europe.

ICL was responsible for soil characterisation at two monopile test sites and for numerical modelling of monopile foundations under the PISA project, utilising the bespoke finite element software ICFEP (Potts and Zdravkovic, 1999), which is the computational platform of the Geotechnics research group. This PhD thesis has been developed under the umbrella of the PISA project, focusing on the numerical modelling of laterally loaded piles for offshore wind applications under cyclic conditions.

1.2. AIMS OF RESEARCH

The main aim of the research was the development and application of the non-linear kinematic hardening framework (NLKH) for soils in the context of cyclic loading. This framework has proven superior to others in the context of metals and rubbers under cyclic conditions, which are the materials with at least 50 extra years of "experience" in terms of material modelling, compared to soils. For example, in metals, the NLKH framework progressively substituted Mroz family kinematic rules and multi-surface plasticity models and is at the moment the most popular framework to model this types of material under cyclic conditions (Chaboche, 2008). However, few to none experiences in the context of modelling of geomaterials exist with respect to this type of strategy. Nevertheless in the recent years new theories sharing features with the NLKH approach, such as generalised plasticity (Pastor et al., 1990) or rate-form theories such as hypoplasticity (Kolymbas, 1991b) have proven to have excellent applicability in the context of soils. In this sense, exploring the possibilities of NLKH rules to capture the general aspects of soil behaviour, given its favourable mathematical form, its simple implementation and its cyclic capabilities, is a topic worthy of further research.

In addition to the theoretical aspects of the problem, the second main aim of the research was the FE modelling of offshore wind monopiles. Offshore wind monopiles are typically short and stubby, with low length to diameter, L/D, ratios and are subjected to a large number of cycles during their design lives. In this sense, the developed constitutive model needed, firstly, to capture the main aspects of soil behaviour, secondly, to exhibit good capabilities for cyclic conditions, thirdly, to incorporate strategies to account for large numbers of cycles and finally to prove its applicability to the real engineering problem of laterally loaded monopiles, such as the field testing carried out during the PISA project.

1.3. OUTLINE OF THE THESIS

The current thesis presents the formulation of a framework based on NLKH rules extended for soils, which is developed in a sufficiently general form to include the behaviour of both sands and clays. Its numerical integration and FE implementation is studied in depth, outlining the challenges and performance issues that several integration strategies and algorithms may experience when using this family of models. Specific aspects and extensions of the framework are also detailed, enriching the basic modelling framework in order to capture further complex cyclic aspects of soil behaviour, providing it with the ability to model large numbers of cycles. All the extensions are detailed and are benchmarked against laboratory data, providing a good response and illustrating the wide range of capabilities of the adopted modelling framework. Finally, the basic sand version of the model is implemented in ICFEP and applied to real boundary value problems. The outline of the thesis is given below in more detail:

Chapter 1 contextualises the engineering challenges of offshore wind and introduces the background to the two most widely used modelling strategies for a large number of cycles. It also illustrates a selection of relevant FE modelling examples of laterally loaded piles described in the literature, to put into context the need for modelling large number of cycles.

Chapter 2 starts by illustrating the geometrical implications of the yield surface and shows how the rate form models can be wrapped by NLKH rules. The next part describes systematically one by one the backbone components of the hardening rule, providing examples of their implications. Finally, the chapter provides examples of how to account for sand and clay behaviour using the proposed general form and compares the response with popular hypoplastic models.

Chapter 3 carries out a systematic numerical study of this type of rate equations. Implicit and explicit strategies for local integration are studied and benchmarked regarding the accuracy and the performance of the two models: (i) an encapsulated version of a basic hypoplastic model and (ii) the basic sand model proposed in the previous chapter.

Chapter 4 is the most heterogeneous, where the limitations of the basic models are outlined and extra specialised hardening rules are proposed to improve the capabilities of the basic versions.

Numerical tests are tested with real soil behaviour for an advanced version of the model, using the large Karlsruhe database of laboratory experiments on sand. Finally, the possibility of including numerical artifices is detailed, where a jump-in-cycles method is proposed, using a favourable implicit integration scheme from the previous chapter.

Chapter 5 applies the model to real boundary value problems, where firstly a 2D footing is analysed using ICFEP to verify all the implemented model capabilities. Once all features are verified, the laterally loaded piles tested at the Dunkirk site for the PISA project are modelled under monotonic and cyclic conditions.

Chapter 6 includes the conclusions and discussion, and future possibilities of the modelling framework are outlined.

1.4. MODELLING STRATEGIES FOR CYCLIC LOADING

This section aims to provide a brief introduction on the constitutive modelling strategies for cyclic soil behaviour but also to describe the motivation of adapting NLKH rules for soils. In general, non-linearity, shear-volumetric coupling and irreversibility are typical features of soil behaviour and in order to reproduce such features advanced models are required. In this sense from a modelling viewpoint the proposed strategies to model cyclic soil behaviour can be summarized as:

- Classic hardening plasticity with strain-dependent elastic moduli (small strains, non-linear elastic or variable moduli). Examples of this approach are Jardine et al. (1986), Pyke (1986), or Taborda and Zdravkovic (2012), to cite various examples.
- Generalised, or bounding surface plasticity (Dafalias, 1976) originally for metals later adapted to soils (Dafalias and Manzari, 2004), (Taborda et al., 2014) to mention some.
- Multi-surface, nested or continuous yield surface theories (Mroz, 1967), where some adaptations for soils are detailed in Puzrin and Kirschenboim (2001) and Einav et al. (2003a).
- Non-linear incremental theories for soils, endochronic theory (Valanis and Peters, 1991, Bažant et al., 1985) or the recent hypoplasticity framework (Kolymbas, 1991b), (von Wolffersdorff, 1996), (Masin, 2012b) to mention some.

- Non-linear kinematic hardening rules (Armstrong and Frederick, 1966), which are widely used in the field of metals but have not been adapted for soils.

All these theories can capture the incremental non-linear behaviour in 1D conditions showing the so called Bauschinguer effect. However, their formulations differ significantly from one another, having advantages or limitations wih respect to each another. The aim of this section is to cover briefly why the NLKH framework has been chosen to be developed in this thesis and why no other strategies have been used.

The first strategy to discard is the use of strain-dependent elastic moduli with reversals, although this startegy is easy to implement it can never capture shear volumetric coupling under cyclic conditions, being unable to produce densification or pore water pressure generation. Secondly, its formulation is based on direct measurements combined with empirical curve fitting. Finally, its formulation requires the use of internal variables within elasticity.

On the other hand, the differences between Bounding surface plasticity (Dafalias and Popov, 1976), multi-surface plasticity (Mroz, 1967) and non-linear kinematic hardening rules (Amstrong and Frederick, 1966) are more subtle. Their similarities and differences are elegantly described in Chaboche (1986) using the concept of number of surfaces. Which can be summarised as:

- Multi-surface theory: a family of surfaces, succesively attained during loading, where the last one activated is the loading surface.
- Bounding surface plasticity theroy: only two surfaces, yield surface and bounding surface, attained assymptotically.
- Non-linear kinematic hardening rules: only two surfaces, yield and assymptotic surface. The assymptotic surface is governed by the differential equations imposed by the hardening rule, which implicitly define a boundary surface.

Of these three, the least attractive when applied to soils, is the multi-layer strategy, which is characterised to exhibit the correct non-linearity under alternating tension compression cycles but tends to stabilize (no-ratchetting) after the first cycle leading to rapid shakedown. Secondly, its implementation into a FE code involves a large number of internal variables which is not computationally efficient and requires the yield surfaces not to intersect. A study on the

numerical integration of an advanced soil model using this framework is described in Einav et al. (2003b) concluding that for appropiate precisions, over 10 yield surfaces need to be used in combination with small strain step. In this sense such computational cost is not attractive for boundary value problems.

Between bounding surface plasticity and non-linear kinematic hardening rules, the advantages and disadvantages are not that clear when applying the modelling framework to soil behaviour. Firstly, it must be noted that both strategies include a boundary or limit surface. However, it is in its definition where the major differences exist: in bounding surface plasticity a general translation rule applies defining a continuisly varying hardening modulus to an scaled bounding surface. In this sense the yield surface and the bounding surface need to be defined with similar shape and cannot intersect. On the other hand non-linear kinematic hardening rules are not bounded by a definition of a metric between its boundary surface and the yield surface, and indeed the limit surface is a consequence of the definition of the hardenign rule.

A priori, non-linear kinematic hardening rules seem more flexible from a formualtion viewpoint, however, Chaboche (1986) carries out an exercise comparing the three backbone frameworks in the context of cyclic loading with the original models of each framework, namely: Mroz (1967) for multi-surface, Dafalias and Popov (1976) for bounding surface plasticity and Armstrong and Frederick (1966) for NLKH. The conclusions the study are:

- Each of them can describe reversed loading conditions;
- Bounding surface plasticity and non-linear kinematic hardenign rules can describe ratchetting effects, but the non-linear kinematic hardening rule overestimates this effect;
- Bounding surface is better for random loading conditions, due to the updating procedure, but plastic flow must be sufficiently reversed in each stress-strain loop;
- None of the simple models is able to describe the anisotropy and the over hardening effect induced by out-of phase loadings

The study ends sugesting some future areas to develop (in 1986), in particular it suggests the use of specific rules and specific coefficients to improve ratchetting and stress relaxation, and secondly other internal variables to improve the out-of-phase loading response.

Based on the conclusion of the previous study in 1986, it can be expected that the bounding surface plasticity provides a better response under random loading and does not exhibit as much excessive ratchetting as NLKH. However the paradigm comes during the historical development of these two frameworks in the field of metals in the 90's (where they were competing). Over the years, the use of non-linear kinematic hardening rules (Armstrong and Frederick, 1966) with their extensions (Chaboche, 1991), (Ohno and Wang, 1993a, Ohno and Wang, 1993b) imposed over bounding surface plasticity theory as the new constitutive models developed in complexity proving to describe accurately advanced features of the cyclic behaviour of metals, becoming the most used framework under cyclic conditions. A detailed revisit and comparison of both theories is described again in Chaboche (2008), also comparing rate effects during cyclic loading, where non-linear kinematic rules with extended specialised hardening rules provided a better response over advanced bounding surface models. In summary, the advantage of non-linear kinametic rules over bounding surface plasticity relies in its adaptability in terms of formulation and implementation, where advanced features can be included easyly via strain memory variables or via backstress superposition.

Contrary to the field of metals if we turn our sight to the last 30 years of soil mechanics it can be seen how bounding surface plasticity has been widely used for both clay and sand, and non-linear kinematic hardenign rules have not even attempted to be used for to soils. Bounding surface plasticity requires the yield surface and bounding surface to have the same shape, which can be limiting from a formulation point of view as soils are not confined in the mean stress space, this limitation does not occur for NLKH rules opening future possibilities.

The paradox in the field of soil mechanics is that, contrary to the field of metals, the theory that has appeared to compete with bounding surface plasticity is hypoplasticity which is a non-linear incremental theory, similar to the endochronic theory (Valanis, 1971). The irony is that hypoplasticity theory shares the main elements of non linear kinematic hardening rules, where an assymtotic limit surface is defined by its rate form.

The paradox that occurs when comparing metals and soils in terms of framework development is that, it is known that non-linear kinematic hardening rules share the same formulation of non-linear incremental theories, however they have never been used for soils. Conversely, many examples in metals show that rate form theories are equivalent to NLKH (Watanabe and

Atluri, 1986b), (Ohno and Wang, 1991). An interesting example is the original endochronic theory, which was revisited through a redefinition of the intrinsic time scale, concluding that the Armstrong-Frederick model was indeed an asymptotic case of the endochronic theory (Valanis, 1980), which then was revisited by Wu and Komarakulnanakorn (1992). More recently, Erlicher and Point (2006) also found similarities with another rate form theory: Lubliner's generalised plasticity (Lubliner et al., 1993) with endochronic and non-linear kinematic rules. Finally, only in the field of geomaterials, Einav (2012) stablished a unification of concepts between the hypoplasticity and the plasticity theories, where the plasticity was found to be a limit case of hypoplasticity theory, akin to the equivalence between plasticity and the "second" endochronic theory.

Based on the previous evidences and historical development this thesis proposes the development of the non-linear kinematic hardening framework using the lessons learned from hypoplasticity and from 30 years of non-linear kinematic hardenign rules in the field of metals. Secondly, a particular effort is placed in its application into FE boundary value problems covering not only the theoretical aspects but the numerical FE implementation ones. The backbone of hypoplasticity theory already supposes an advanced starting point for the development of non-linear kinematic hardening rules for soils.

1.5. MODELLING STRATEGIES FOR HIGH NUMBER OF CYCLES

Marine structures, and particularly offshore wind turbines, are subjected to a wide range of cyclic loading conditions, induced by the operation of the turbine and the hydrodynamic effects, which mobilise the highly non-linear soil behaviour. In this sense modelling large number of cycles in a traditional way (e.g. simulating each cycle) is a cumbersome task and not practical from an engineering point of view. In this sense the model has to be capable of including numerical artifices capable of capturing the effect of cyclic loading as packages of cycles. This section describes some existing methodologies in the soil mechanics literature which account for the modelling of large number of cycles. Two methodologies that treat the cycles as packages are described: the NGI (Norwegian Geotechnical Institute) methodology and the High Cycle Accumulation (HCA) model.

1.5.1. NGI METHODOLOGY

The NGI methodology was initially developed as a semi-empirical method to predict the bearing capacity of offshore shallow foundations under cyclic loads (Andersen and Lauritzsen, 1988). The main idea for the estimation of the bearing capacity relies in the assumption that the failure mechanism can be characterised by laboratory testing as shown in Figure 1. Under that assumption, the resistance under cyclic loading, and therefore the bearing capacity, can be obtained from standard laboratory tests and can be summarised in charts that describe the capacity of the soil versus the number of cycles. An example of this idea is shown in Figure 2.

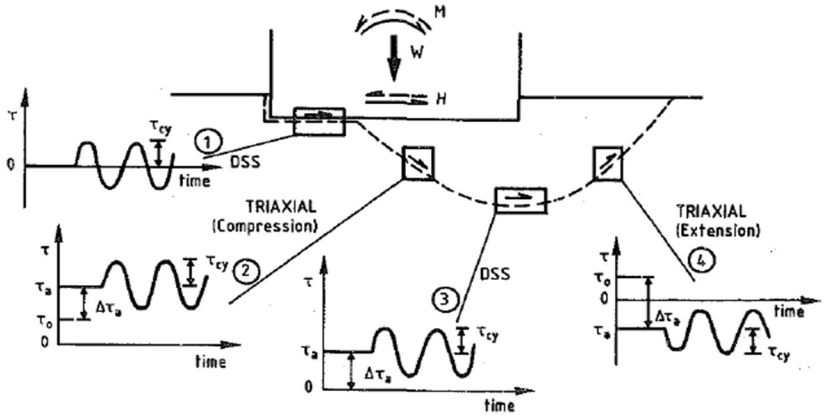


Figure 1: simplified load conditions assumed for the potential failure surface. (Andersen and Lauritzsen, 1988)

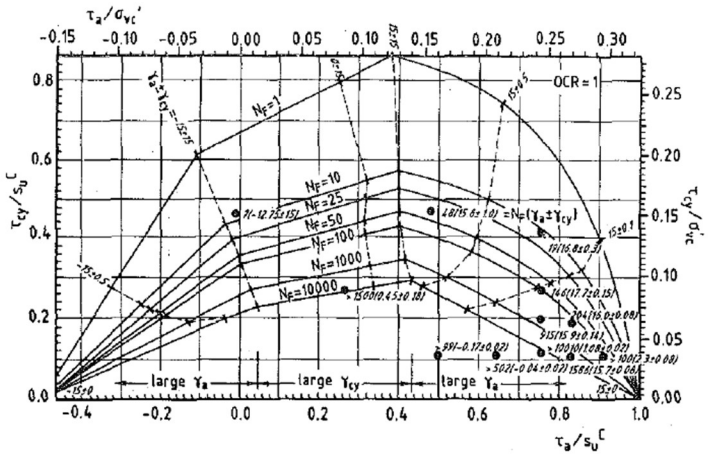


Figure 2: Number of cycles to failure for various combinations of average shear (τ_a) and cyclic shear (τ_{cy}) in triaxial tests on normally consolidated Drammen Clay. (Andersen and Lauritzsen, 1988)

The concept has been further extended to include not only the ultimate capacity but also the accumulation of strains during cyclic loading. To do so, a pseudo-constitutive relation between accumulated strain and accumulated stress has been extracted from extensive soil testing data, using data interpolation between the types of tests. The obtained "constitutive-charts" were then summarised in tables and can be interrogated numerically through interpolation. In this sense, given an accumulated total strain, it is possible to obtain an absolute final stress using assumptions of coaxiality between the current strain and current stress (not between the incremental stress and strain values). This idea of stress-strain relationship can be included in a conventional FE analysis through the balance of momentum equation. However, in order to generalise the laboratory tests charts into a multiaxial stress-strain space the following assumptions are required:

- Coaxiality between stress and strain tensors
- Behaviour in the deviator plane obtained through interpolation between triaxial extension and triaxial compression as a function of the intermediate principal strain ε_2.
- Stress ratios τ_{cy} / σ_{oct}, τ_a / σ_{oct} interpolated from charts, no constitutive relationship, not even incremental.

The methodology has been implemented in PLAXIS as a UMAT (User-Defined Model). For each packet of cycles, the average and cyclic stresses or average and cyclic strains are

calculated at the integration (Gauss) points and through an interpolation process their counterparts are obtained. The whole process for undrained or drained conditions is described in detail in Jostad et al. (2014) and Jostad et al. (2015).

Figure 3 shows a sketch of the interpolation process for an undrained cyclic test. The specimen is firstly consolidated to an effective vertical stress of σ_{vc} = 250 kPa and an effective horizontal stress of σ_{hc} = 112.5 kPa. The average stresses are then kept constant during simulation of the undrained cyclic test. The effective octahedral stress is σ_{oct} =158.3 kPa, and the average shear stress τ_a = (250-112.5)/2 kPa=68.75 kPa. After static equilibrium, a packet of 100 cycles with a cyclic shear stress of τ_{cy} = 125 kPa. As a result, the normalised cyclic shear stress becomes τ_{cy}/σ_{oct}=0.79. The condition of constant average stress of 0.434 corresponds to the charts below. Then, through interpolation, the strain amplitude during the first cycle is γ_{cy} = 0.34% and 1.7% after cycle 100 (Figure 3 left).

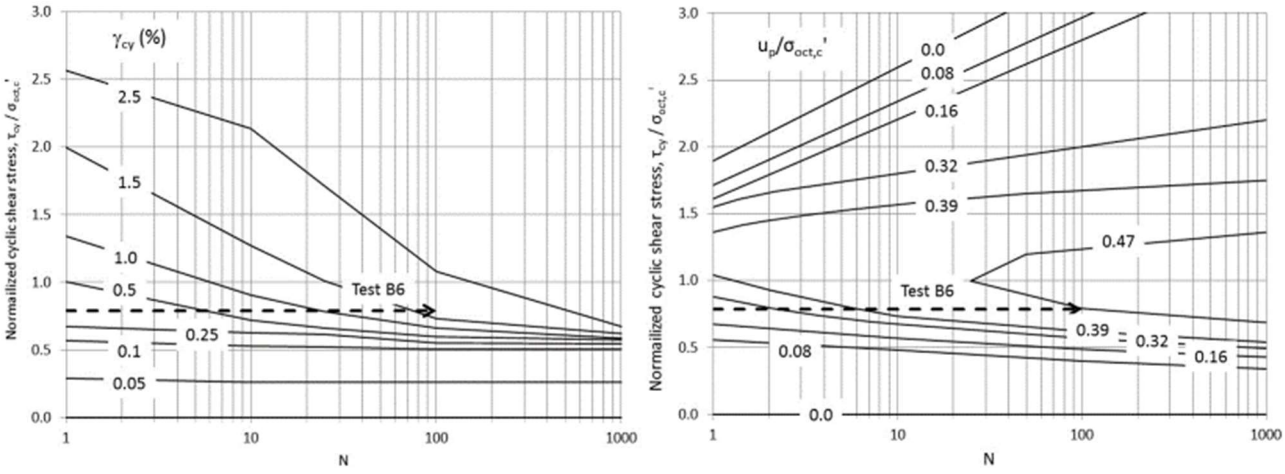
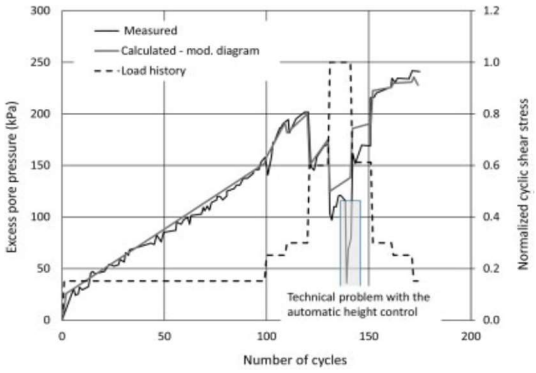


Figure 3: Contours of cyclic shear strain γ_{cy} and normalized permanent pore pressure $u_p/\sigma_{oct'c}$ as a function of normalised shear stress τ_{cy}/σ_{oct} and number of cycles. Cross section at $\tau_a = \tau_0$. Baskarp sand with Dr 95%, vertical consolidation stress σ_{vc} = 250. (Jostad et al., 2015)

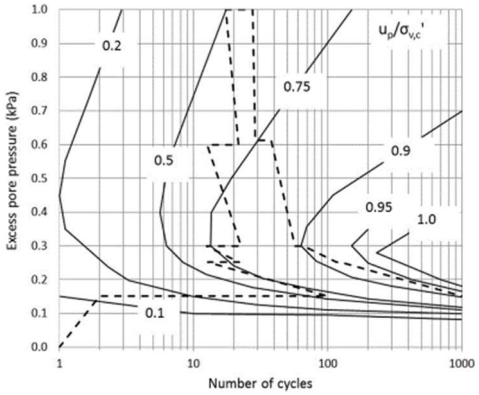
A second example is described for different parcels of cycles as shown in Figure 4. In this case, the simulation corresponds to a two-way direct simple shear (DSS) involving Baskarp sand. Figure 4b shows the calculated accumulated pore pressure with the FE method and the laboratory test result. Figure 4c shows the equivalent number of cycles within the pore pressure contour diagram at the beginning and at the end of each parcel, while Figure 4d shows the stress path at the end of parcel 3 and during the first cycle in parcel 4.

Parcel	No. of cycles	τ_{cy} (kPa)	τ_{cy}/σ'_{vc}
1	100	38	0.15
2	10	62	0.25
3	11	75	0.30
4	10	151	0.60
5	11	250	1.00
6	10	152	0.60
7	10	76	0.30
8	10	62	0.25
9	355	37.5	0.15

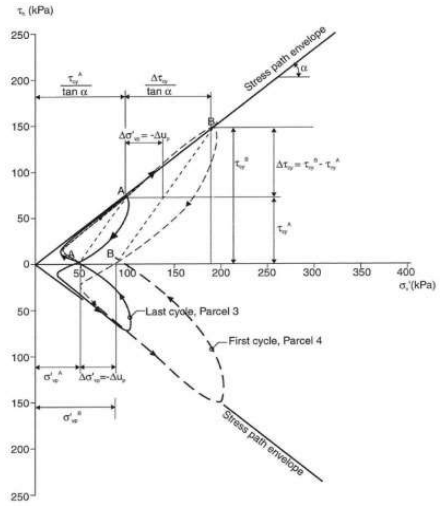
(a)



(b)



(c)



(d)

Figure 4: (a) cyclic load history applied in the undrained DSS test on Baskarp sand, (b) Measured and calculated pore pressure versus number of cycles (c) Calculated pore pressure accumulation and equivalent number of cycles, (d) Measured stress path at the end of parcel 3 and during first cycle in Parcel 4. (Jostad et al., 2015)

11

In summary, the method is an adaptation of an interpolation process in a Gauss point that can be included in a FE domain. Although it solves the balance of momentum or imposes equilibrium in the boundary value problem, it is not a standard incremental finite element based procedure. The inputs of the model are tables characterising the cyclic and average stress and strain from soil tests including its pore pressure generation.

1.5.2. THE HIGH-CYCLE ACCUMULATION (HCA) MODEL

The high cycle accumulation model (Niemunis et al., 2005) is a hypoplastic model that includes an extra nonlinear term which is dependent on the number of cycles. The model has been calibrated for sands under various cyclic conditions (Wichtmann et al., 2009), (Wichtmann et al., 2010), (Wichtmann et al., 2015). However, the idea can be extended to other types of soil such as clay without difficulty (Wichtmann et al., 2013). The model deals with cycles as a time-like continuous variable N and establishes a dependence of the accumulated strains caused by cyclic loading ($\dot{\varepsilon}_{ij}^{acc}$). A good analogy of the HCA model can be established with the endochronic theory (Niemunis and Wichtmann, 2014), where the endochronic time includes an extra term depending on the arbitrary history variable N (number of cycles), which, as a result of an additional non-linear contribution, produces extra accumulated strain over a closed stress cycle. The model is a standard incremental model and has three very interesting characteristics:

1. It uses a hypoplastic model, which exhibits natural asymptotic properties.
2. Can include jump-in-cycles based on pasty stress hystory of the hypoplastic model. The history of a cycle can be stored in a very elegantly formulated fourth order tensor history variable named “amplitude tensor” which is used to produce the jump-in-cycle strain.
3. The fourth order amplitude tensor corresponds to a measure of the cyclic characteristics of the past stress history, where the eigenvalues and eigenprojections give a measure of the amplitudes and the orientation of the characteristics of the cycle.

Finally, to characterise the magnitude of a batch of cycles, the model defines an irreversible rate of strain $\dot{\varepsilon}_{ij}^{acc}$ dependent on scalar functions, which are functions of the amplitude of the strain tensor and the stress in the centre of the cycle, as:

$$\dot{\varepsilon}_{ij}^{acc} = f_{ampl} \frac{\partial f_N}{\partial N} f_p f_Y f_e f_\pi \vec{m}_{ij} \tag{1.1}$$

The functions $f_{ampl}, f_p, f_Y, f_N, f_e$ and f_π are independent from each other and include, respectively, the influence of the strain amplitude (f_{ampl}), the number of cycles (f_N), the

average mean pressure (f_p), the average stress ratio(f_Y), the void ratio (f_e) and the change of polarisation π (orientation) of the strain loop (f_π). The direction of the accumulated strain rate is governed only by the unitary vector $\hat{m}_{ij}(\sigma_{ij}^{av})$ depending only on the average stress of the strain loop. The model assumes that the direction of accumulation follows a Cam-Clay flow rule (Wichtmann et al., 2014), based on the findings by Chang and Whitman (1988), expressed as

$$m_{ij} \sim -\frac{1}{3}\left(p - \frac{q^2}{M^2 p}\right)\delta_{ij} + \frac{3}{M^2}\left(\sigma_{ij} - p\delta_{ij}\right) \tag{1.2}$$

where *M* is the slope of the critical state line, and p and q are the first and second stress invariants. Once the flow direction is obtained it can be made unitary and used into (1.1) to compute the extra non-linear contribution induced by the package of cycles. Figure 5 shows a sketch of how the model uses the normal and cyclic accumulation operation modes, which shares the same idea with the visco-hypoplastic model of Niemunis (2002). However, rather than including a contribution function of the time it uses the number of cycles as time like variable.

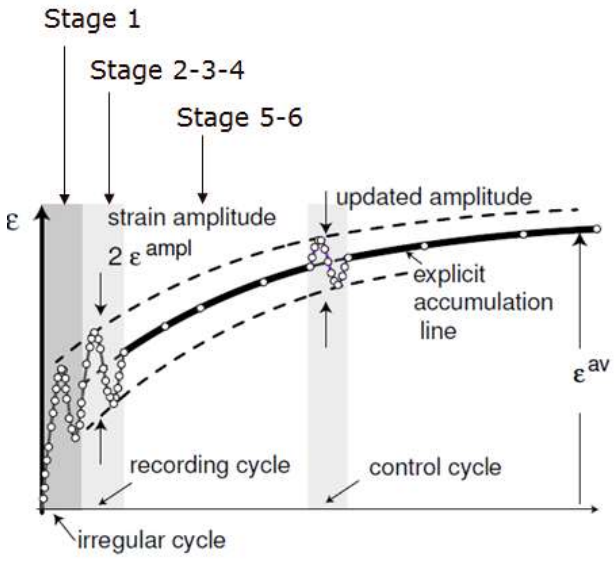


Figure 5: Idea of explicit calculation strategy of the accumulative deformation. (Niemunis et al., 2005)

The stages to integrate a batch of cycles are :

1. Calculate initial stress (self-weight & monotonic loads)
2. Calculate the last two first load cycles
3. Record the strain path during the second cycle at each integration point
4. Calculate the tensorial strain amplitude A_{ijkl}.
5. Find the rate of accumulated cyclic strain using (1.1)
6. Find the rate stress $\dot{\sigma}_{ij}$
7. Update the stress as $\sigma_{ij} = \dot{\sigma}_{ij} \Delta N$

During stage 3 a set of accumulated strains, normally calculated using a conventional FE analysis, are stored and used to calculate the amplitude tensor. Figure 6 shows at the top a sketch of the process of recording the strains, while at the bottom, it shows how to obtain the amplitude tensor for an arbitrary strain cycle.

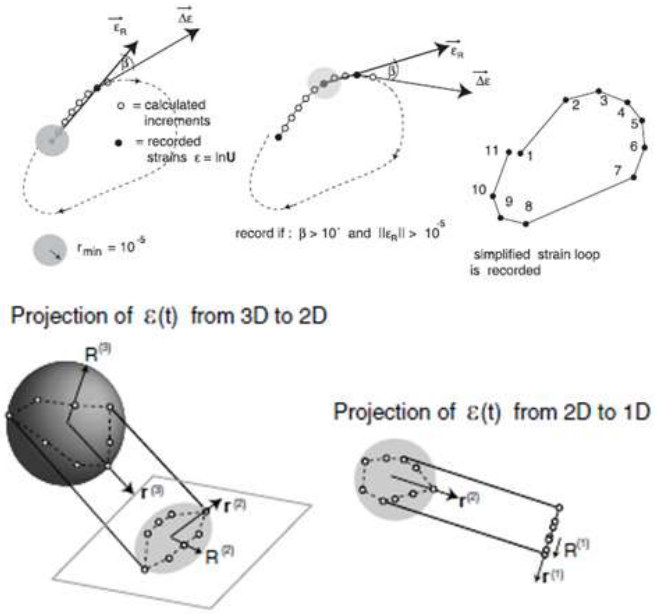


Figure 6; Scheme of the construction of the strain amplitude tensor. Direction r(i) and size R(i) of the strain loop.(Niemunis et al., 2005)

Stage 4 (calculation of tensor amplitude) can be repeated as many times as desired, preferably as the system is being drifted from its asymptotic state in each jump. In this sense the model recommends to use intermediate cycles under normal operation to better characterise the

amplitude tensor. This section describes in detail how to obtain this tensor from a given history of strains $\varepsilon_{ij}(t_k)$ as:

$$\begin{aligned} 2R^{(6)} &= \left\| \varepsilon_{ij}(t_a) - \varepsilon_{ij}(t_b) \right\| \\ \vec{r}_{ij}^{(6)} &= r_{ij}^{(6)} / \left\| r_{ij}^{(6)} \right\| = \left(\varepsilon_{ij}(t_a) - \varepsilon_{ij}(t_b) \right) / \left\| \varepsilon_{ij}(t_a) - \varepsilon_{ij}(t_b) \right\| \end{aligned} \tag{1.3}$$

where $\varepsilon_{ij}(t_a)$ and $\varepsilon_{ij}(t_b)$ correspond to the strain tensors whose difference norm is maximum for the whole set of strains $\varepsilon_{ij}(t_k)$. The maximum distance between strains in the loop is $R^{(6)}$, corresponding to the half distance between $\varepsilon_{ij}(t_a)$ and $\varepsilon_{ij}(t_b)$. Once the first set is determined, a new set of strains $\varepsilon_{ij}^{(5)}(t_k)$ is obtained projecting the strain set $\varepsilon_{ij}(t_k)$ on the hyperplane perpendicular to $\vec{r}_{ij}^{(6)}$. This results in a "flattened" strain history $\varepsilon_{ij}^{(5)}(t_k)$ in the plane defined by $\vec{r}_{ij}^{(6)}$. The new set of strains is determined as:

$$\varepsilon_{ij}^{(5)}(t_k) = \varepsilon_{ij}^{(6)}(t_k) - \vec{r}_{ij}^{(6)} \vec{r}_{kl}^{(6)} \varepsilon_{kl}^{(6)}(t_k) \tag{1.4}$$

The process of projecting the strain history on successive hyperplanes continues until the six eigenprojections are obtained, or the trivial solution is obtained. Note that it is possible to describe a whole cycle with one eigenprojection and one amplitude. The result of this process are 6 orthogonal projectors that are the bases of the strain loop $\varepsilon_{ij}(t_k)$, where $R^{(i)}$ is a measure of the cycle amplitude in that hyperplane:

$$A_{ijkl} = \sum_{i=1}^{6} R^{(i)} \vec{r}_{ij}^{(i)} \vec{r}_{kl}^{(i)} \tag{1.5}$$

The former tensor captures the characteristics (amplitude and direction) of any strain loop history in the 6D strain space. It must be noted that the tensor A_{ijkl} is a linear mapping function as the stress tensor is independent of the reference system. The amplitude tensor will provide the magnitude of accumulated strain through the scalar function f_{ampl}

$$f_{ampl} = (\varepsilon^{amp} / \varepsilon_{ref}^{amp}) \qquad \varepsilon^{amp} = \left\| A_{ijkl}^{amp} \right\| \tag{1.6}$$

Another aspect that governs the amount of accumulated cyclic strain is the polarisation function f_π. Polarisation is defined as the rotation or misalignment of the bases $\vec{r}_{ij}^{(i)}$ of the amplitude tensor as cycles evolve. In this sense, to account for polarisation, a history variable will be required that will evolve according to the directions of the eigenprojections of the successive amplitude tensors. A unitary polarisation tensor π_{ijkl} is defined to take into account the change in polarisation of the amplitude packets. The angle of misalignment α establishes the amount of misalignment between the history variable and the current or recalculated amplitude tensor:

$$\cos\alpha = \vec{\pi}_{ijkl} A_{ijkl} / \varepsilon^{amp} = \vec{\pi}_{ijkl} \vec{A}_{ijkl} \tag{1.7}$$

Notice that when $\vec{\pi}_{ijkl} = \vec{A}_{ijkl}$, $\cos\alpha = 1$ and no polarisation takes places. Therefore, the polarisation tensor must asymptotically approach the current $\vec{A}_{ijkl}$ with the number of cycles. If a new packet with another orientation is obtained from the simulation, the cross product $\vec{A}^{(2)}_{ijkl}\vec{\pi}_{ijkl}$ will change producing misalignment and will trigger the polarisation function. The rate at which the angle of misalignment changes and the effect it produces in the accumulated strains is controlled by two scalar inputs: $C_{\pi 1}$ and $C_{\pi 2}$.

$$\begin{aligned} f_\pi &= 1 + C_{\pi 1}(1 - \cos\alpha) \\ \dot{\alpha} &= -C_{\pi 2}\alpha(\varepsilon^{amp})^2 \\ \Delta\alpha &= \dot{\alpha}\Delta N \end{aligned} \tag{1.8}$$

The tensor $\vec{\pi}_{ijkl}$ will "rotate" its eigenprojections towards the new $\vec{A}_{ijkl}$ asymptotically with the number of cycles (N). The rotation of π_{ijkl} towards $\vec{A}_{ijkl}$ is obtained through an eight-order tensor using the Euler-Rodrigues formula as:

$$\begin{aligned} &\Delta\pi_{ijkl} = \mathbb{R}_{ijklmnop}\pi_{mnop} - \pi_{ijkl} \\ &\mathbb{R}_{ijklmnop} = (\cos\Delta\alpha - 1)(\mu_{ijkl}\mu_{mnop} + v_{ijkl}v_{mnop}) + \sin\Delta\alpha(v_{ijkl}\mu_{mnop} - \mu_{ijkl}v_{mnop}) + \delta_{ijklmnop} \\ &\mu_{ijkl} = \vec{A}_{ijkl} + \pi_{ijkl} \\ &v_{ijkl} = \vec{A}_{ijkl} - \pi_{ijkl} \end{aligned} \tag{1.9}$$

where $\delta_{ijklmnop}$ is the eight order identity tensor (note that when $\vec{A}_{ijkl} = \vec{\pi}_{ijkl}$ $\mathbb{R}$ becomes the identity and $\Delta\pi_{ijkl} = 0$). Although the mathematical expression is cumbersome, the interpretation is simple: the tensor $\vec{\pi}_{ijkl}$ is a history variable representing the former characteristics of the cycles. As an incresing number of cycles take place $\vec{\pi}_{ijkl}$ with different orientation, they will produce more strain accumulation as the magnitude of the polarization function will be $f_\pi > 1$. In this sense it is possible to account for the effect where random vibrations produce more accumulated strains that uniform loading. However, while the mathematical gateway to include this effects is included and formulated very elegantly, calibration of the polarization function values in (1.8) is not straightforward.

1.6. RELEVANT FE ANALYSIS OF LATERALLY LOADED PILES FOR OFFSHORE WIND

This section describes analyses of boundary value problems reported in the literature that are relevant for this thesis. A large number of papers exist covering large diameter monopiles, in particular in the recent years due to the growth of offshore wind, but only a few using advanced constitutive models. The objective of this section is not to cover the state of the art in laterally loaded pile modelling, but describe a selection of relevant papers for contextualisation. Examples of laterally loaded monopiles include the use of bounding surface plasticity (Corciulo et al., 2017), hypoplasticity (Hong et al., 2017) and the high-cycle accumulation model (Machacek et al., 2018).

An interesting analysis of laterally loaded monopiles under transient conditions is described in Corciulo et al. (2017). A dynamic u-p formulation is used in combination with a bounding surface model capable of producing a pore pressure build up upon cyclic loading. The analyses are carried out in OpenSees simulation platform where H1-P1ssp stabilised elements are used to avoid spurious pore pressure oscillations during transient analysis. The objective of the analysis is to assess the damping in offshore turbines, and also to investigate the effects of pore pressure build up and its effect on the natural frequency of the wind turbine.

The loading effects of a 5 MW realistic turbine are included in a simple structural model to represent the superstructure, while the soil and pile are modelled using standard 3D elements. A detail of the problem geometry is included in Figure 7. The constitutive model can account for advanced soil aspects such as: non-linear hypoelasticity, shear strength anisotropy, non-linear shear stress-strain curves and a phase transformation line, capable of distinguishing between dilatant and contractant soil responses. The model however does not account for void ratio dependency, nevertheless due to the duration of the transient simulations (30 secs) this limitation is negligible as the void ratio is not prone to drastic changes.

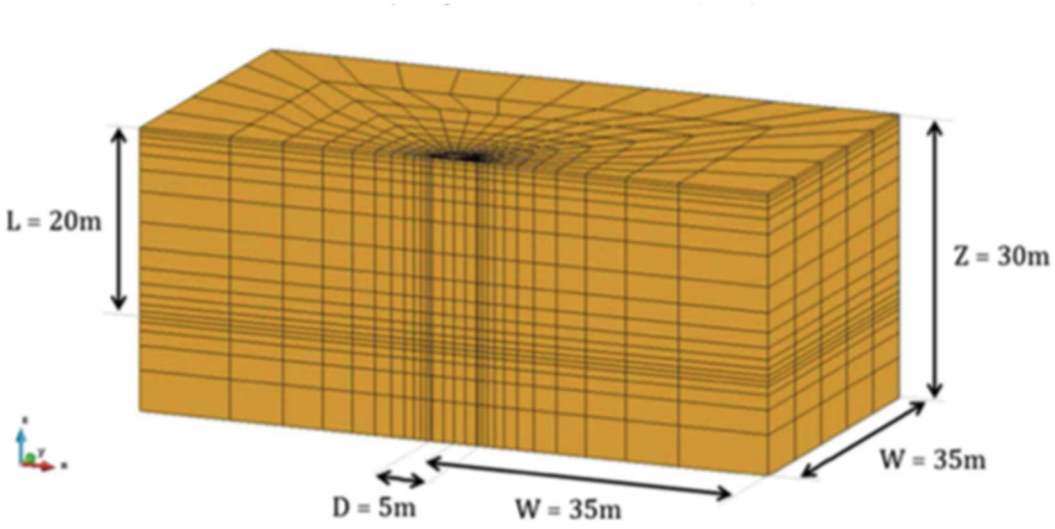


Figure 7:Soil domain and mesh discretization (Corciulo et al., 2017)

The conclusions of the study show that soil non-linearities play a significant role above a wind speed above 10 m/s, which is a relatively low threshold as a normal wind turbine's range of operation is between 8 to 25 m/s. A second conclusions from the study is that at medium to large mobilisation levels the pore pressure regime has an influence on the pile displacements, but negligibly affects the OWT response at the hub in terms of natural frequency degradation, Figure 8 shows the displacements at the mudline for all simulations at various load levels under different permeabilities illustrating the effect of pore pressure generation.

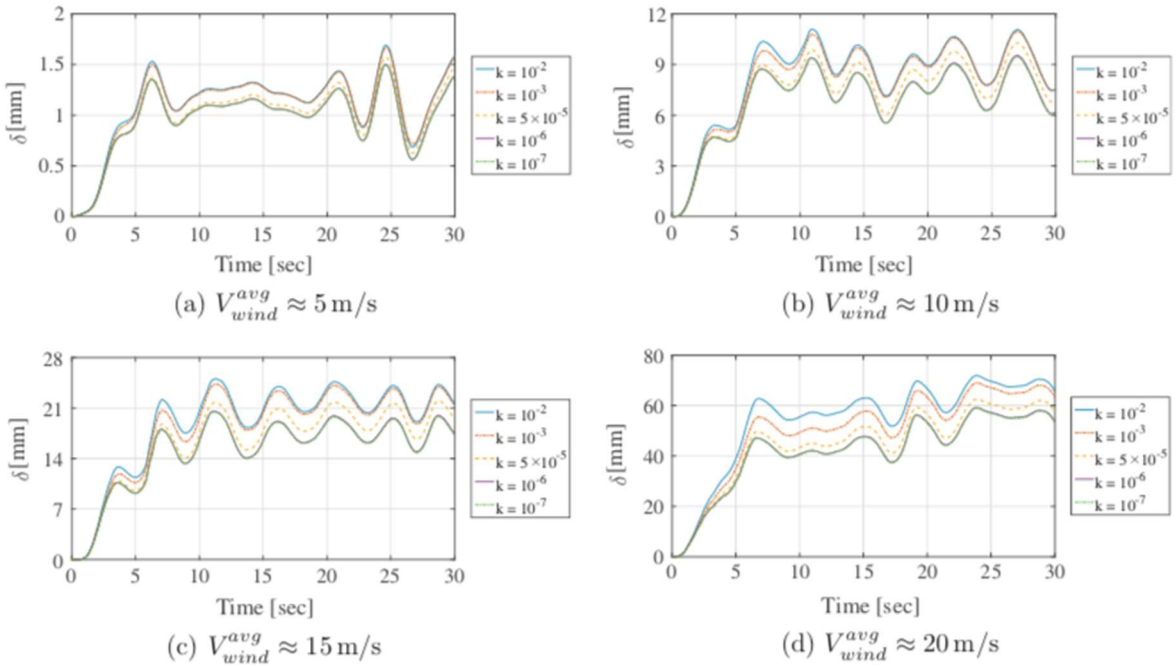


Figure 8: Displacement response at mudline at varying soil permeability (Corciulo et al., 2017)

A second relevant study using an advanced constitutive model in the contexts of laterally loaded piles is described in Hong et al. (2017), where the centrifuge tests of various laterally loaded piles are modelled using a hypoplastic model with intergranular strains. The paper focuses on centrifuge testing, though it includes a section where the plastic flows around the pile are assessed. The paper also includes a study of the ultimate capacity of the piles for the three different L/D ratios. Additionally, the numerical modelling of the three piles under cyclic conditions is also included. All the numerical simulations are carried out using the commercial FE software ABAQUS and a user-defined hypoplastic model.

In general, the paper shows that the hypoplastic model predicts adequately the static and cyclic behaviour of the piles. In particular, under cyclic conditions the intergranular strain seems to reach near shakedown conditions while for medium and large amplitudes it captures the rate at which ratchetting progresses. Figure 9b includes a detail of the calibration of the constitutive model with an undrained triaxial cyclic test, while Figure 9a and c show the FE predictions.

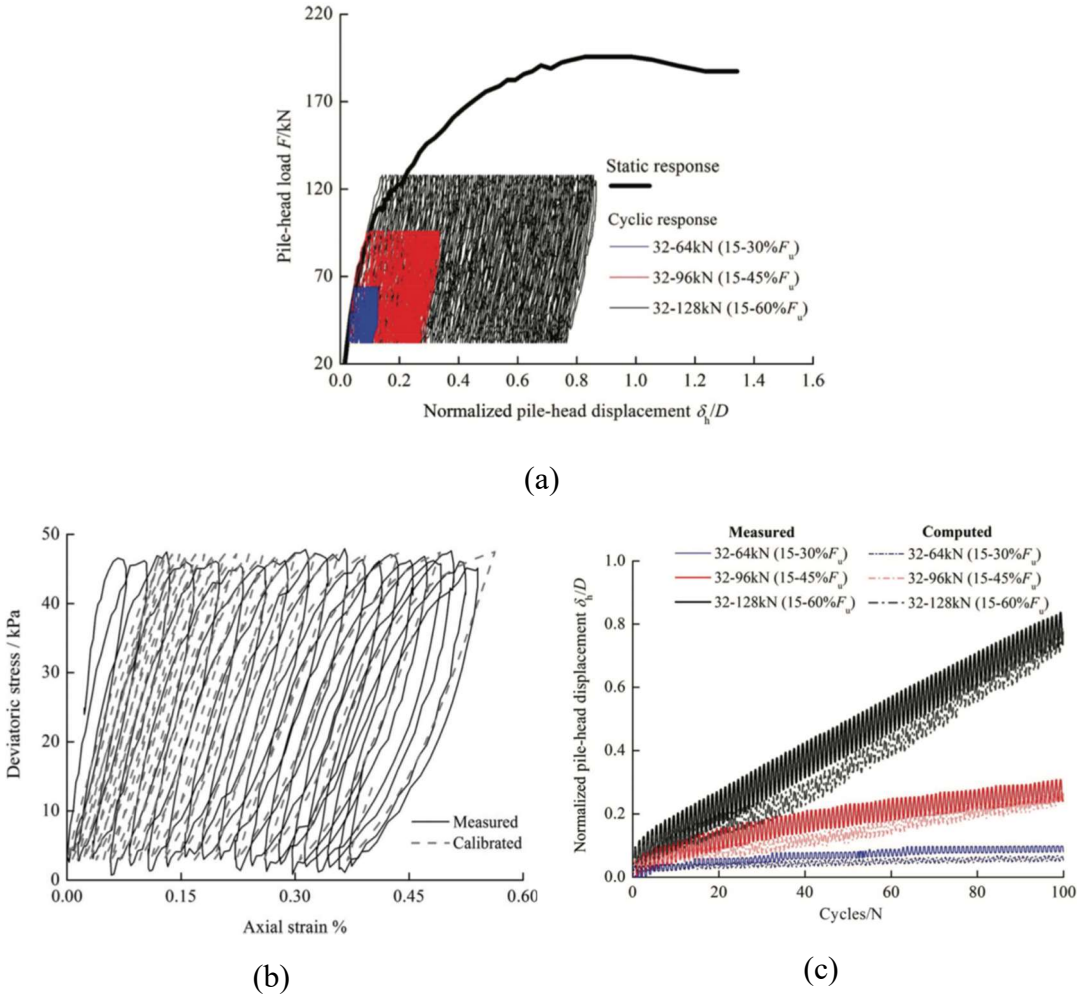


Figure 9:Comparison of measured and predicted responses. (a) centrifuge measurents (b) Undrained trixial tests and clay hypopasticticy prediction. (c) Measured versus calculated normalized pile displacement versus number of cycles (Hong et al., 2017)

With respect to capacity, the hypoplastic clay model seems to predict the plastic flows of the piles, the lateral capacity and the rotation points in monotonic conditions, as observed in the field tests. Figure 10 presents results from the paper, where the plastic flows and predicted lateral pile capacity for the three studied geometries are shown and compared with the API lateral capacity solutions.

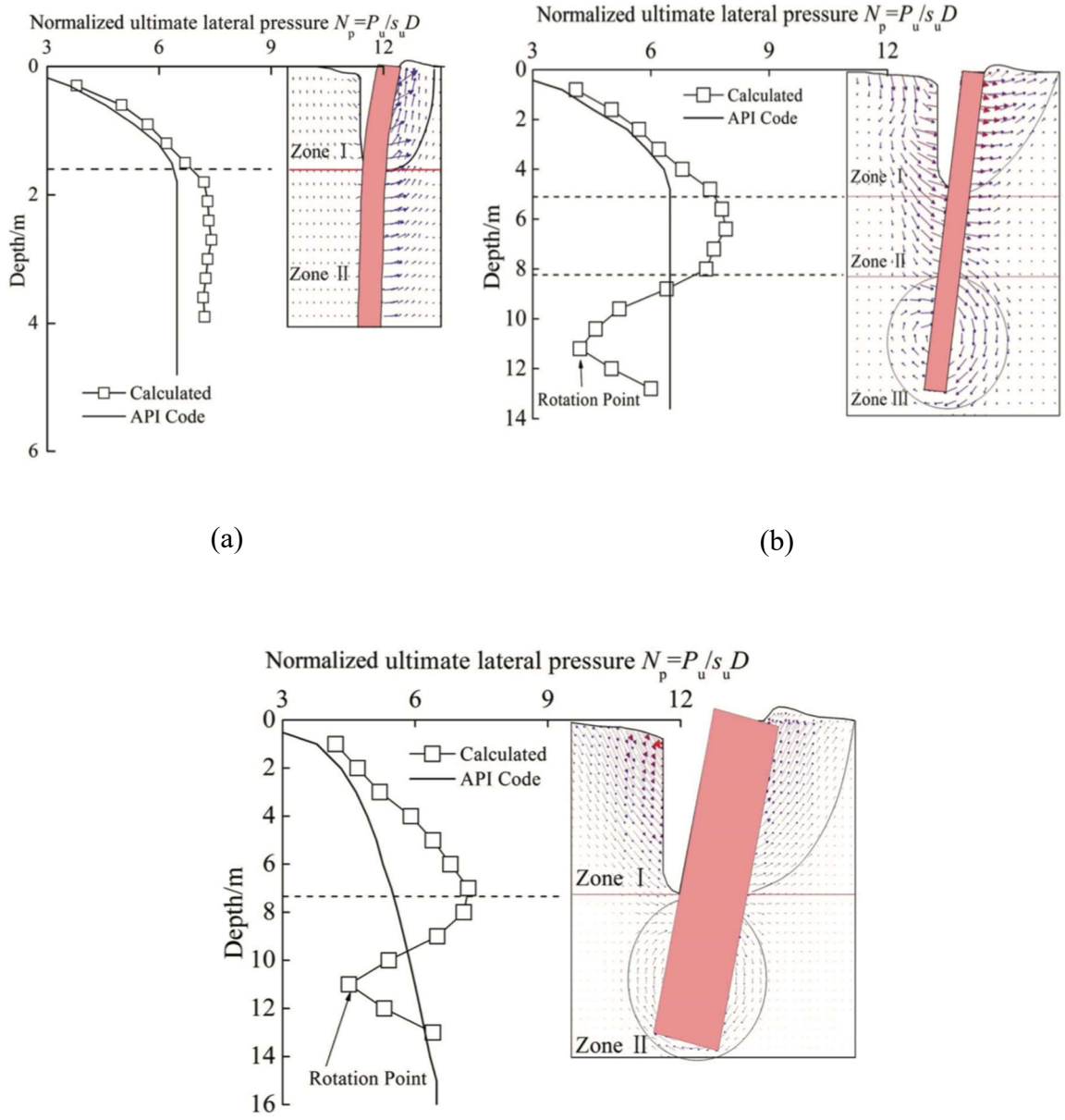


Figure 10: Computed lateral capacity factors along the pile: (a) flexible pile; (b) semi-rigid pile; (c) rigid pile(Hong et al., 2017)

The final paper of this section, does not focus on laterally loaded piles, but applies the high-cycle accumulation model to a boundary value problem involving a large number of cycles. The paper describes the modelling of a ship lock subjected to around 90.000 cycles due to the filling-emptying of the water lock over decades. The settlements in the lock are obtained from long-term monitoring and are used to benchmark the predictions of the high cycle accumulation

model. The FE software used to carry out the simulation is ABAQUS, with the model implemented in a user-defined subroutine. The lock is simulated as a 3D slice and the lateral strains are set to zero to enforce plane strain conditions. The type of elements used in the mesh are solid brick elements (C3D8R) with linear shape functions and reduced integration. A detail of the mesh is shown in Figure 11.

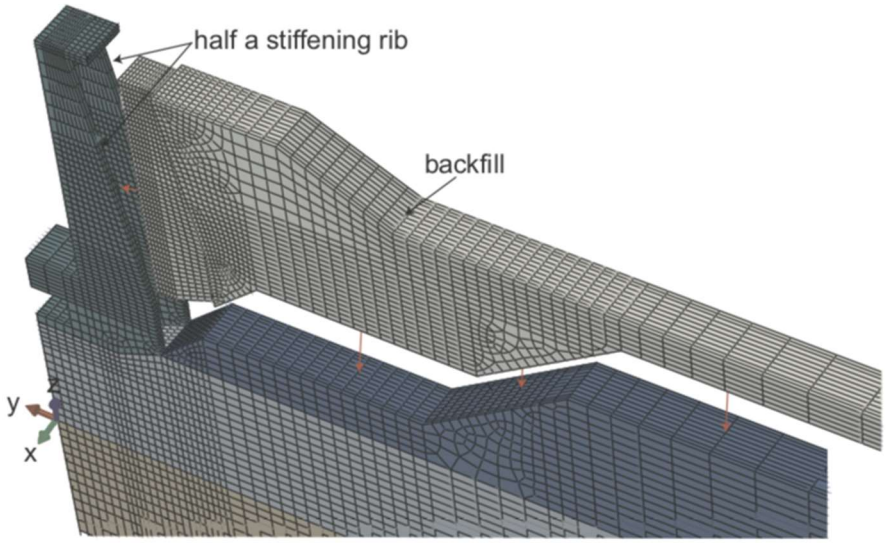


Figure 11: Detail of the 3D mesh used in the analysis (Machacek et al., 2018)

The model seems to predict the measured settlements over the years, however the calibration of the real sand is not carried out as there is no available data. The parameters used are inferred from other sands with similar granulometric distributions and properties. A parametric study is carried out where two different initial density profiles are studied. In general, the predictions of the model are good when compared with the measurements. Nevertheless, the important aspect for this thesis is that the high-cycle accumulation model seems to provide the expected behaviour in terms of accumulating strains through a jump-in-cycles method.

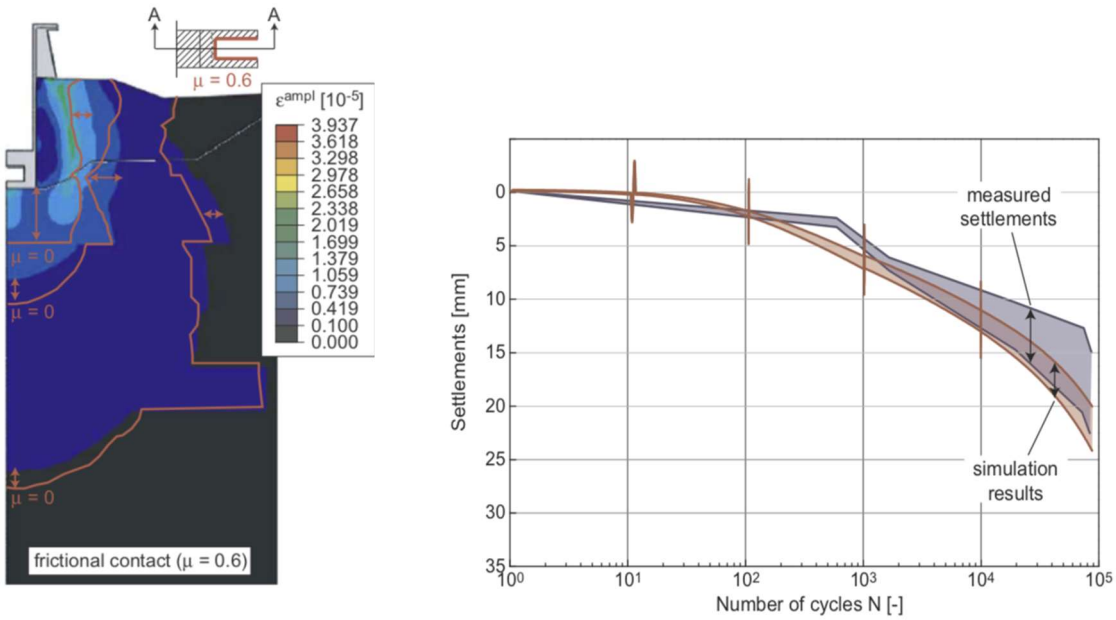


Figure 12: Deatil of the 3D mesh used in the analysis (Machacek et al., 2018)

CHAPTER 2: DEVELOPMENT OF NON-LINEAR KINEMATIC HARDENING RULES FOR SOILS

This chapter describes a general formulation for non-linear kinematic hardening rules adapted for soils. The methodology to define the hardening rules borrows concepts from hypoplasticity, endochronic theory and the cyclic plasticity framework. The chapter is structured in the following way: firstly, the main common components of this type of hardening rules are described; secondly, a set of definitions is given where the concept of stable and asymptotic limit state is introduced and finally examples of a sand and a clay model are given and compared with equivalent hypoplastic popular models. Throughout this chapter index notation will be used, therefore it should be recalled that: $\hat{A}_{ij} = A_{ij}/A_{kk}$, $A^*_{ij} = A_{ij} - 1/3A_{kk}\delta_{ij}$, $\|A_{ij}\|^2 = A_{ij}A_{ij}$ and $\vec{A}_{ij} = A_{ij}/\|A_{ij}\|$

2.1. GOVERNING EQUATIONS

Infinitesimal strains are assumed where strain can be additively decomposed into the elastic part and the plastic part, where the total strain is:

$$\varepsilon_{ij} = \varepsilon^e_{ij} + \varepsilon^p_{ij} \qquad i = 1,...,3 \qquad j = 1,...,3 \tag{2.1}$$

where ε^e_{ij} is the elastic strain tensor and ε^p_{ij} is the plastic strain tensor. The stress is related to the elastic strains though the linear elasticity tensor D^e_{ijkl}

$$\sigma_{ij} = D^e_{ijkl}\varepsilon^e_{kl} \tag{2.2}$$

where σ_{ij} is the stress tensor, the model is associated and the yield surface and potential surface are identical, being defined as a hypersphere or radious equal to m:

$$f = \left\|\sigma_{ij} - \alpha^T_{ij}\right\| - m = 0 \tag{2.3}$$

In this particular sense and for the sake of generalisation, α_{ij}^{T} is the sum of a set of internal variables $\alpha_{ij}^{(k)}$, named "backstress" being representative of the position of the centre of such hypersphere:

$$\alpha_{ij}^{T} = \sum_{k} \alpha_{ij}^{(k)} \tag{2.4}$$

The flow rule is obtained through:

$$\dot{\varepsilon}_{ij}^{p} = \dot{\lambda} \frac{\partial f}{\partial \sigma_{ij}} = \dot{\lambda} \vec{n}_{ij} \tag{2.5}$$

where $\dot{\lambda}$ is the plastic multiplier and is strictly positive. The final equations required to complete the model are the rate of the history variables. A general expression of the hardening rules is defined through a function h_{ij}, which is rate independent and is defined as:

$$\dot{\alpha}_{ij}^{(k)} = \dot{\lambda} h_{ij}(\vec{n}_{ij}, \alpha_{ij}^{(k)}) \tag{2.6}$$

2.2. GEOMETRIC IMPLICATIONS OF THE YIELD SURFACE SHAPE

This section demonstrates the implications of the yield surface shape when combined to non-linear kinematic hardening (NLKH) rules. Firstly, it must be noted that if the yield surface is chosen to be a hypersphere with no isotropic hardening the elastic region can only move. Therefore during yield the consistency condition $\dot{f} = 0$ imposes the following condition

$$\left(\sigma_{ij} - \alpha_{ij}\right)\left(\dot{\sigma}_{ij} - \dot{\alpha}_{ij}\right) = 0 \tag{2.7}$$

Given an arbitary perturbation of the backstress, only two solutions of (2.7) exist for the rate of stress: pure translation where $\dot{\sigma}_{ij} = \dot{\alpha}_{ij}$, or the rate of the normal orthogonal to the normal of the yield surface (pure rotation).

The first solution of (2.7)is obvious, while the second solution is not that trivial. To prove that all other solutions of the rate of stress which are not the trivial, let us generalise any possible solution of the rate of stress as:

$$\dot{\sigma}_{ij} = \dot{\alpha}_{ij} + \dot{\omega} S_{ijkl} (m \vec{n}_{kl}) \tag{2.8}$$

where $\dot{\omega}$ is an arbitrary scalar greater than zero, $\vec{n}_{kl}$ is the unitary normal of the yield surface, *m* is the radious of the hypersphere and S_{ijkl} is an arbitary skew-symmetric fourth order tensor. It should be noted that expression (2.8) fulfils the consistency condition (2.7) as:

$$\vec{n}_{kl} S_{ijkl} \vec{n}_{kl} = 0 \tag{2.9}$$

Taking the differential of the normal of the yield surface

$$d\vec{n}_{ij} = \frac{1}{\left\| \sigma_{kl} - \alpha_{kl} \right\|} \left(\delta_{ik} \delta_{jl} - \vec{n}_{ij} \vec{n}_{kl} \right) \left(\dot{\sigma}_{kl} - \dot{\alpha}_{kl} \right) \tag{2.10}$$

Substituting (2.8) into (2.10) and owing the fact that $\vec{n}_{ij} S_{ijkl} \vec{n}_{kl} = 0$, expression (2.10) gives:

$$d\vec{n}_{ij} = \dot{\omega} S_{ijkl} \vec{n}_{kl} \tag{2.11}$$

Equation (2.11) is a linear differential equation, whose solution is:

$$\vec{n}_{ij} (t_0 + \Delta t) = \exp\left(\omega \Delta t S_{ijkl} \right) \vec{n}^0_{kl} \tag{2.12}$$

where $\vec{n}^0_{kl}$ is the normal at the start of the plastic step and $\vec{n}_{ij}(t)$ is the solutions of the normal over time. Given the fact that the exponential of an antisymmetric tensor is a rotation tensor and that the set of possible solutions are defined by (2.8). Only when $\dot{\omega} = 0$ (trivial solutiuon) the rotation tensor becomes the identity and the normal of the yield surface does not change, otherwise if $\dot{\sigma}_{ij} \neq \dot{\alpha}_{ij}$ the only possible solution is elastic neutral loading. In conclusion, the stress rate is in reality imposed by the backstress rate, which, combined with the definition of adequate hardening non-linear kinematic model, is the backbone of the whole modelling strategy adopted in this thesis.

The previous conclusion implies that constitutive models expressed in rate form of the stress, such as generalized plasticity (Pastor et al., 1990, Lubliner et al., 1993) , endochronic models (Valanis, 1971, Bazant, 1978, Valanis and Peters, 1991) or hypoplastic models (Wu, 1992, von Wolffersdorff, 1996, Masin, 2005, Masin, 2013), can be “encapsulated” in a non-linear

kinematic hardening rule. The following sub-sections show some examples for endochronic and hypoplastic models.

2.2.1. DEFINITION OF "ENCAPSULATION"

Given the previous implications of the yield surface and NLKH rules the term "encapsulated model" is introduced. An encapsulated model is a NLKH model which adapts its hardening rule to mimic the rate of stress form of a model such as an endochronic model, generalised plasticity, etc. This is achieved by enforcing the plastic strain to resemble the total strain, and the rate of backstress to the stress rate. It must be said that the models are not identical as for an encapsulated model a blurred region of valid stresss rate solutions exists, while for the rate form model the solution is unique. However, as shown in the further chapters, for practical applications the differences are not significant and the NLKH acccomodates well models without yield surfaces such as endochronic models or hypoplasticity.

2.2.2. EXAMPLE: ENCAPSULATED ENDOCHRONIC MODEL

A simple case of endochronic model can be defined using constants instead of kernel functions to capture shear volumetric coupling. The example endochronic model can be formulated in its deviatoric and volumetric incremental parts following a similar methodology as described in Bazant (1978). In this sense any total strain increment can be defined by a plastic and elastic part as:

$$\begin{aligned} d\varepsilon_{ij}^{*} &= \frac{d\sigma_{ij}^{*}}{2G} + d\varepsilon_{ij}^{*p} \\ d\varepsilon_{kk} &= \frac{d\sigma_{kk}}{3K} + d\varepsilon_{kk}^{p} \\ dz &= dz_h = dz_d = \left\| d\varepsilon_{ij}^{*} \right\| \end{aligned} \tag{2.13}$$

where e_{ij} it the deviatoric part of the total strain and ε_{kk} is the volumetric strain and $\boldsymbol{K}$ and $\boldsymbol{G}$ represent the elastic stiffness in the volumetric and deviatoric direction, respectively. The variable "z" is the endrochronic time and it is a strictly increasing variable, with the endochronic loading functions defined as:

$$\sigma_{ij}^{*} = 3M_f \sigma_{kk} \frac{d\varepsilon_{ij}^{*p}}{dz}$$
$$\sigma_{kk} = \frac{1}{M_c}\sigma_{kk}\frac{d\varepsilon_{kk}^{p}}{dz} + \frac{1}{3M_c}\sigma_{ij}^{*}\frac{d\varepsilon_{ij}^{*p}}{dz} \tag{2.14}$$

where M_f and M_c are model parameters. Combining expressions (2.13) and (2.14)

$$d\sigma_{ij}^{*} = 2G\left(d\varepsilon_{ij}^{*} - \frac{1}{3M_f\sigma_{kk}}\sigma_{ij}^{*}dz\right)$$
$$d\sigma_{kk} = \frac{K}{3}\left(d\varepsilon_{kk} + M_c\left(\frac{1}{M_c M_f}\left(\frac{\left\|\sigma_{ij}^{*}\right\|}{3\sigma_{kk}}\right)^2 - 1\right)dz\right) \tag{2.15}$$

Expression (2.15) fully defines the endochronic model in rate form, and it can be observed that the model does not need history variables or a yield surface. For this particular expression it can be anticipated that the volumetric part of equation (2.15) is equivalent to the dissipation expression used in critical state soil mechanics (Schofield and Wroth, 1968).

$$\sigma_{ij}^{*} = M_f 3\sigma_{kk}\frac{d\varepsilon_{ij}^{*p}}{dz}$$
$$M_c\left\|d\varepsilon_{ij}^{*p}\right\|\sigma_{kk} = \sigma_{kk}d\varepsilon_{kk}^{p} + 1/3\sigma_{ij}^{*}d\varepsilon_{ij}^{*p} \tag{2.16}$$

Given this simple endochronic model in rate form and the conclusions derived from section 2.2, the rate of the stress from Equation (2.15) can be transformed into a non-linear kinematic hardening rule using the yield surface defined in Equation (2.3). Therefore the hardening rule becomes:

$$\dot{\alpha}_{ij}^{*} = 2G\left(\dot{\varepsilon}_{ij}^{*p} - \frac{3}{M_f}\hat{\alpha}_{ij}^{*}\left\|\dot{\varepsilon}_{ij}^{*p}\right\|\right)$$
$$\dot{\alpha}_{kk} = \frac{K}{3}\left(\dot{\varepsilon}_{kk}^{p} + M_c\left(\frac{9}{M_c M_f}\left\|\hat{\alpha}_{ij}^{*}\right\|^2 - 1\right)\left\|\dot{\varepsilon}_{ij}^{*p}\right\|\right) \tag{2.17}$$

The former expression can be implemented into a local constitutive driver and integrated over a constant purely deviatoric stress direction. The results of two numerical tests at different initial stress values are shown in Figure 13 over two cycles and at failure. As expected, the

response is akin to any endochornic model with shear-volumetric coupling. It can be also observed in the upper left figure how the stress is bounded into the typical Drucker-Prager limit surface imposed by the value of M_c in equation (2.17).

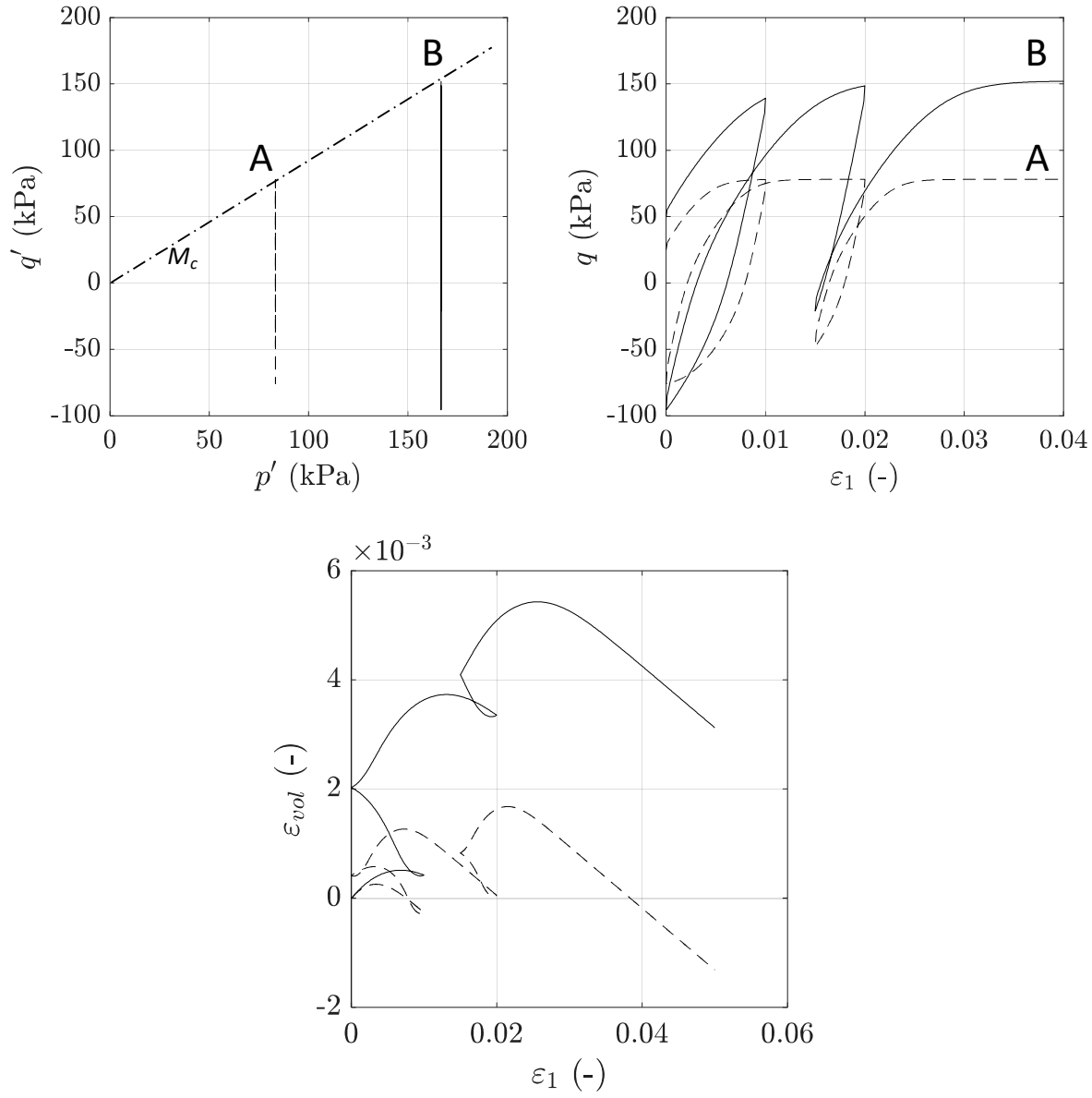
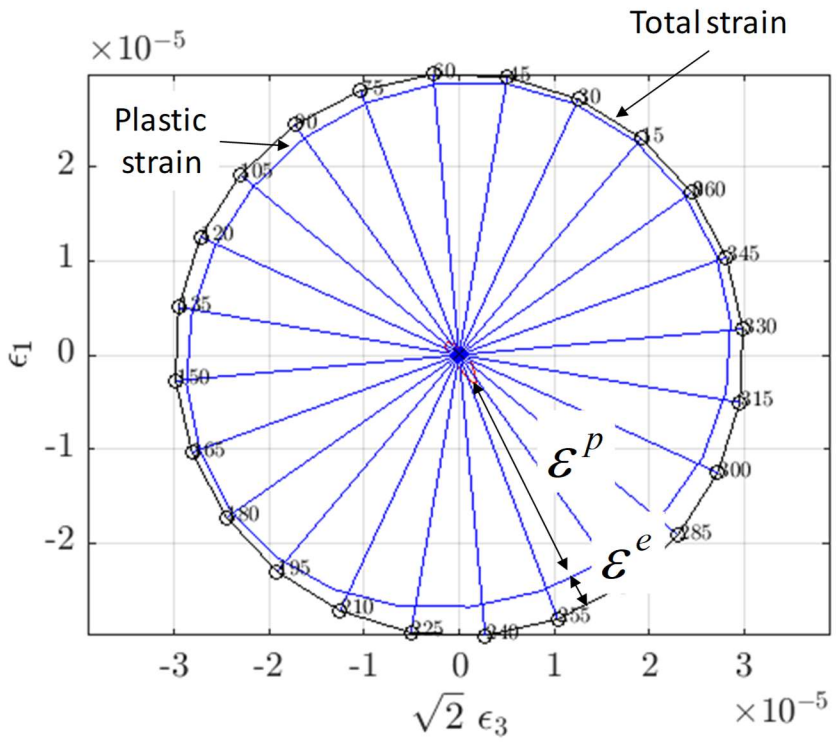


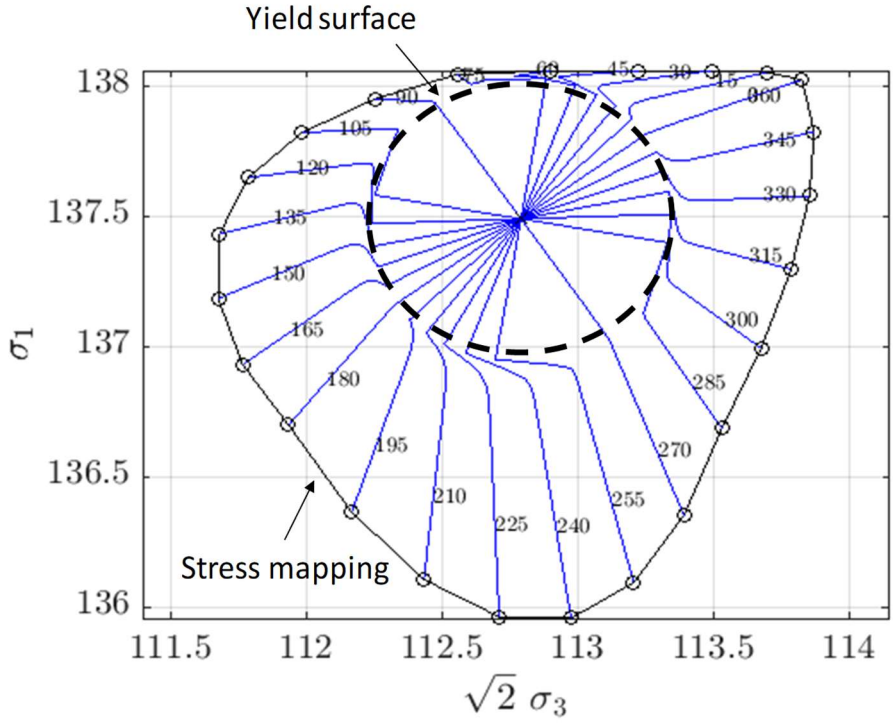
Figure 13: Simple encapsulated-endochronic model stress controlled tests for $M_c = 0.2/3\sqrt{1.5}; M_f = 1/3\sqrt{1.5}$

When using this type of "encapsulation" it is useful to define two scales at which to consider the stress-strain relationship: local and incremental. The local scale corresponds to the infinitesimal scale corresponding to the plastic rate equations, while the incremental scale corresponds to a small region where re-alignment of the normal to fulfil $\dot{\sigma}_{ij} = \dot{\alpha}_{ij}$ occurrs. Note that the incremental scale has nothing to do with the concept of small strains, it is only linked with the mathematical formulation, and this incremental region may be much smaller than 10^{-5}, depending on the yield surface and the elastic stiffness.

To illustrate the previous concept of scale, a set of numerical probes on the previous "encapsulated model" are carried out. The numerical probes consist of very small stress and strain perturbations carried out in all directions in the Rendulic plane, performed over many increments akin to "exact" numerical integration. The stress-strain results are shown in Figure 14, where it can be observed how the realignment between the rate of stress and backstress corresponds to neutral loading, until $\dot{\sigma}_{ij} = \dot{\alpha}_{ij}$ is reached. In Figure 14(a) and (b) the numbers corresponding to each of the stress-strain paths are shown. Figure 14(a) shows the fraction of elastic strain and plastic strain of the strain probe, where it can be observed how a large fraction of the total strain is plastic regardless of the total strain perturbation being small (~10^{-5}).



(a)



(b)

Figure 14: Small strain probes for the "encapsulated" endochronic model

2.2.3. EXAMPLE: ENCAPSULATED HYPOPLASTICITY

It is relativelly simple to encapsulate any model holding a rate stress formulation regardless of its complexity. Following the same methodology as in the previous example, two non-linear kinematic models based on the hypoplastic model of von Wolffersdorff (1996) and Masin (2005), have been reformulated as NLKH and numerically been implemented in a local constitutive driver. The same trends as the original models are observed as presented in in Figure 15 and Figure 16 for TXD and TXU tests. The relations shown correspond to a sand under loose and dense states in drained conditions and to a clay under undrained triaxial compression conditions for various initial OCRs (>20 to 1). All input parameters are summarized in Table 1 and Table 2 respectively.

Table 1: Input parameters for encapsulated hypoplastic sand model

Elastic param.			**Plastic param.**							
m	**K**	**G**	e_{i0}	e_{d0}	e_{c0}	h_s	**n**	α	β	φ_{cr}
3.16	$5\ 10^5$	$2\ 10^5$	1.25	0.55	0.85	10^5	0.25	0.25	1.0	33.0

Table 2: Input parameters for encapsulated hypoplastic clay model

Elastic params.			**Plastic params.**				
m	**K**	**G**	**N**	λ^*	κ^*	φ_{cr}	**r**
1.73	$5\ 10^5$	$2\ 10^5$	1.19	0.095	0.015	21.9	0.2

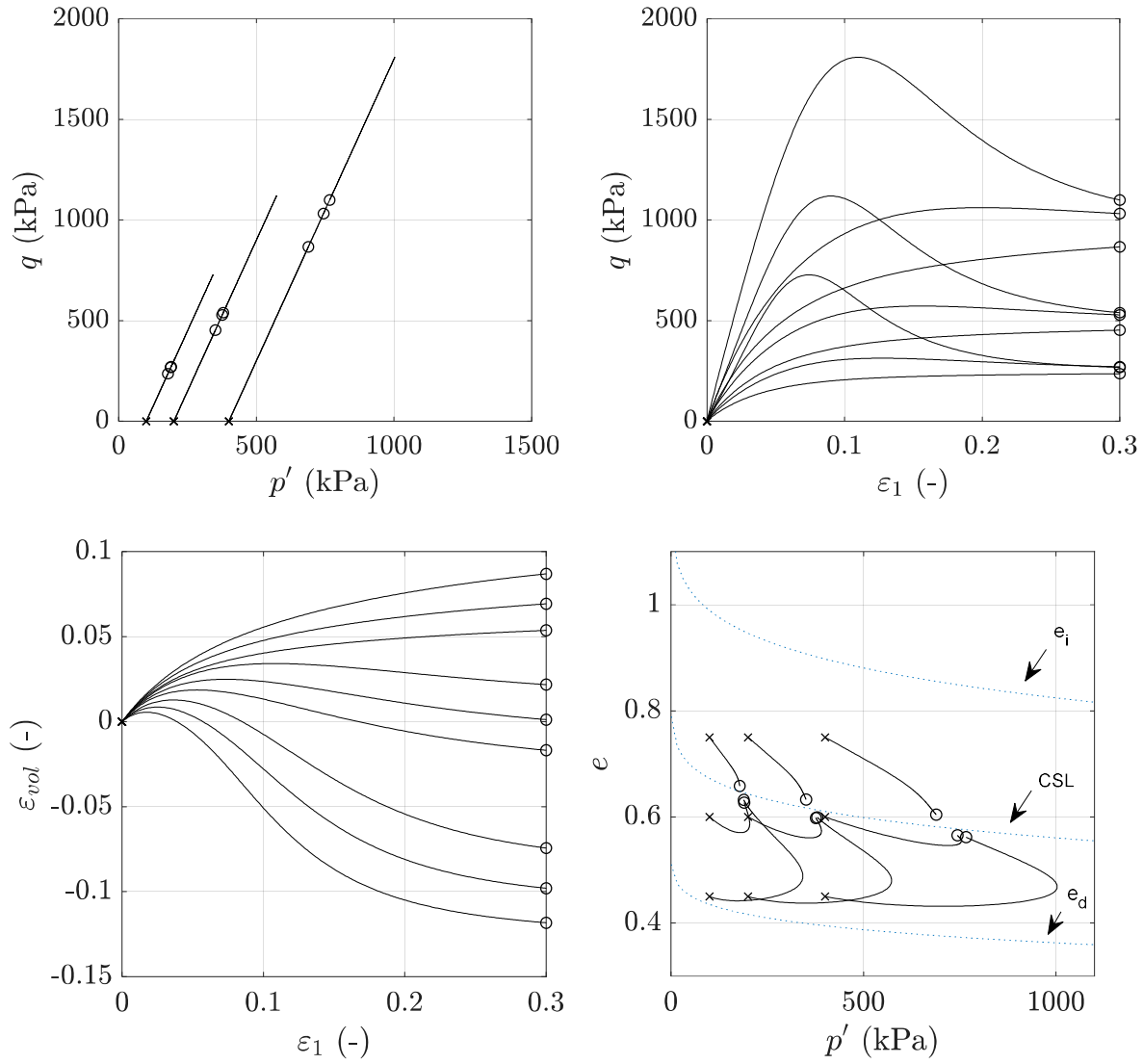


Figure 15:Drained triaxial test of "encapsulated" Von Wolfendorff model

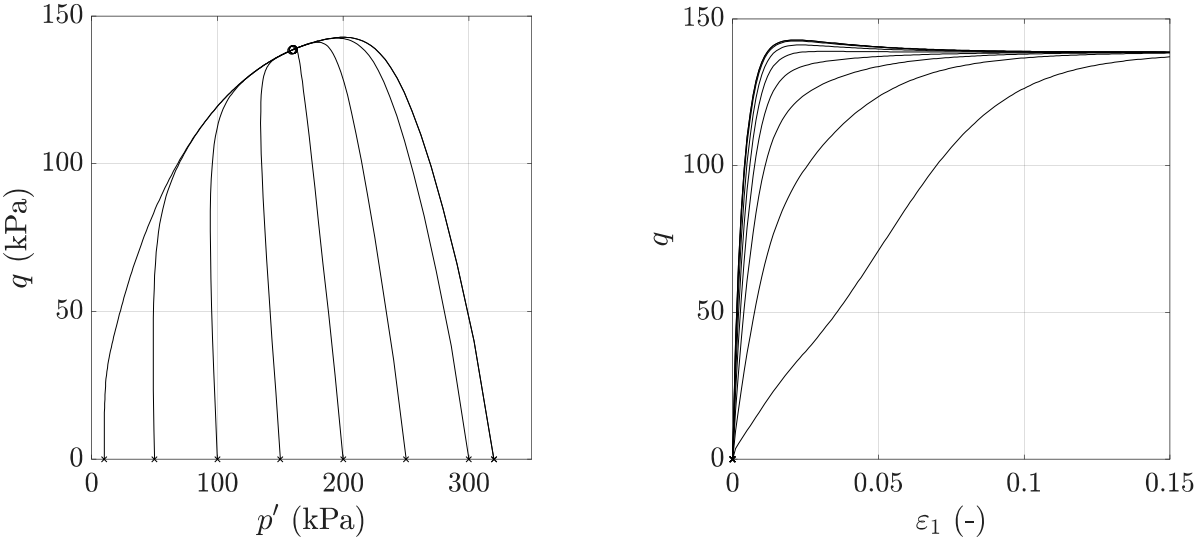


Figure 16:Undrained triaxial test of "encapsulated" Clay Hypoplastic model

2.2.4. ASYMPTOTIC PROPERTIES

Asymptotic behaviour is a typical property observed in soil behaviour. For example in clays, assymptotic behaviour was obserbed by Schofield and Wroth (1968) and Roscoe and Burland (1968) which combined the existence of critical states and compression asymptotic states into a unified framework of critical state soil mechanics.

More generally, the idea that asymptotic states are attractors in the stress-strain space was firstly postulated by Gudehus (1977) and then proved by Goldscheider (1982) for granular materials. They proposed that each direction of strain rate with a volume decrease is uniquely linked to a particular asymptotic stress ratio and a particular path in the mean stress versus void ratio plane (normal compression line).

The hypothesis of asymptotic behaviour has been the subject of further experimental investigation, compression asymptotic states are confirmed and well documented by true and axisymmetric triaxial tests on sands with strain path control (Chu and Lo, 1994). They observed a unique relationship between the strain path direction and asymptotic stress ratio. Asymptotic behaviour has also been studied by testing fine-grained soils by Topolnicki et al. (1990). Also it has been confirmed though DEM analysis (Masin, 2012a). The definition of a material with asymptotic properties is:

1. Along a compressive strain path (whose trace is negative, meaning compression), the resultant stress path will tend towards a straight line with constant stress ratio, $\dot{\hat{\sigma}}_{ij} = 0$, regardless of the initial state.
2. Each direction of strain rate is related to a given asymptotic state in the p-e plane.

The demonstration of a model to exhibit asymptotic conditions is shown very elegantly in Niemunis (2002). If a strain path is calculated as a sequence of mappings $\sigma_{ij}, H_{ij}(\sigma_{ij}), H_{ij}(H_{ij}(\sigma_{ij})), \ldots$ for any strain rate it must correspond an asymptotic stress value. Based on the previous hypothesis, given a perturbation defined as $\varsigma_{ij} = \sigma_{ij} - \sigma_{ij}^{assimp}$, it can be decomposed into its parallel part $\varsigma_{ij}^{//} = \vec{\sigma}_{ij}^{assimp} \vec{\sigma}_{kl}^{assimp} \varsigma_{kl}$ and its orthogonal part

$\varsigma_{ij}^{\perp} = \left(\delta_{ik}\delta_{jl} - \vec{\sigma}_{ij}^{assimp}\vec{\sigma}_{kl}^{assimp}\right)\varsigma_{kl}$. The condition for asymptotic behaviour implies that in every mapping the orthogonal distance of the perturbation must decrease, which can only mean that:

$$H_{ij}(\sigma_{ij}^{assimp} + \varsigma_{ij}^{\perp}) - H_{ij}(\sigma_{ij}^{assimp}) < 0 \tag{2.18}$$

When $\varsigma_{ij}^{\perp} \to 0_{ij}$, expression (2.18) becomes the directional derivative which is equivalent to

$$\frac{\partial H_{ij}}{\partial \sigma_{kl}}\varsigma_{kl}^{\perp} < 0 \tag{2.19}$$

then the model is assymptotic if:

$$\varsigma_{ij}^{\perp}\frac{\partial H_{ij}}{\partial \sigma_{kl}}\varsigma_{kl}^{\perp} < 0 \tag{2.20}$$

where for models using the rate the stress is, naturally:

$$\varsigma_{ij}^{\perp}\frac{\partial \dot{\sigma}_{ij}}{\partial \sigma_{kl}}\varsigma_{kl}^{\perp} < 0 \tag{2.21}$$

while for non-linear kinematic hardening models based on 2.1 is:

$$\varsigma_{ij}^{\perp}\frac{\partial \dot{\alpha}_{ij}}{\partial \alpha_{kl}}\varsigma_{kl}^{\perp} < 0 \tag{2.22}$$

All the models proposed in this thesis exhibit asymptotic behaviour.

2.3. FUNDAMENTAL COMPONENTS OF MODELS

In this section the general components common to all proposed models are described. The presented concepts are as general as possible and include ideas developed in generalised hypoplasticity (Niemunis, 2002), endochronic theory (Valanis, 1980) and cyclic plasticity (Chaboche, 1991, Ohno and Wang, 1993a, Ohno and Wang, 1993b). Each hardening rule has the following components:

- Limit surface Y
- Goal function $\vec{\Upsilon}_{ij}$
- Mapping tensor L_{ijkl}
- Metric tensor Σ_{ijkl}

and typically reads as

$$\dot{\alpha}_{ij} = f_e f_p L_{ijkl}\left(\dot{\varepsilon}^p_{kl} - Y\vec{\Upsilon}_{kl}\dot{z}\right) \tag{2.23}$$

where f_e and f_p are scalar functions and the variable "z" is a measure of the plastic strain akin to the endochronic time. In this case a simple model parameter "$\boldsymbol{k}$" affecting the measure of the volumetric plastic strain is proposed, which is defined as:

$$z^2 = \varepsilon^p_{ij}\Sigma_{ijkl}\Sigma_{klmn}\varepsilon^p_{mn} = \left\|\varepsilon^{*p}_{ij}\right\|^2 + \frac{k}{3}\left|\varepsilon^p_{kk}\right|^2 \tag{2.24}$$

The definition of the strain metric may admit more advanced definitions, (Erlicher and Point, 2006) and can be redefined to exhibit a behaviour similar to that corresponding to the Bouc-Wen family of models. The general form provides a gateway to include advanced relations between stiffness and strain directions, or dependencies with other strain history variables. In this thesis the definition of the endochronic time has only been studied for simple metric modifications, however a general form of the metric tensor has been included for future developments.

2.3.1. DEFINITION OF LIMIT SURFACE AND GOAL FUNCTION

Firstly, the limit surface and goal function are defined. These two functions are only dependent on the backstress internal variable. The limit surface, Y , and the goal function, $\vec{\Upsilon}_{ij}$ include a dependence on the intermediate eigenvalue of the backstress through the inclusion of the $g(\theta)$ function. In this case a Van Eekelen (Van Eekelen, 1980) general deviatoric shape has been chosen, defined as:

$$g(\theta) = \frac{XF}{(1 + YF \sin 3\theta)^{ZF}} \tag{2.25}$$

where **XF**, **YF** and **ZF** are inputs parameters and θ is the Lode's angle. The limit surface is defined as:

$$Y = f_d \left(\frac{3\sqrt{2}}{2g(\theta)} \left\| \hat{\alpha}_{ij}^* \right\| \right)^{\vartheta} = f_d \tilde{Y} \tag{2.26}$$

where ϑ is an input parameter that controls the curvature of the limit surface, and f_d is a scalar function. Goal functions define a tensor field of the backstress tensor, and are unitary in all the domain as well as coaxial with the backstress. Two possible expressions have been studied based on the dependence or not on the scalar function f_d:

<u>Case 1: Goal functions dependent on f_d</u>

$$\begin{aligned} \beta &= \left(\ln\left(\frac{\sqrt{3}}{ob_{\max}} + 1 \right) \right)^{1/\delta} \\ ob^{GF} &= ob_{\min} \exp\left(-\left(\beta \tilde{Y} / f_d \right)^{\delta} \right) + ob_{\max} \left(1 - \exp\left(-\left(\beta \tilde{Y} / f_d \right)^{\delta} \right) \right) \\ \vec{\Upsilon}_{ij}^{f_d} &= \left(\sqrt{1 - (ob^{GF})^2 / 3} \right) \vec{\alpha}_{ij}^* + \frac{ob^{GF}}{3} \delta_{ij} \end{aligned} \tag{2.27}$$

Case 2: Goal functions independent of f_d

$$\begin{aligned}
&\beta = \left(\ln\left(\frac{\sqrt{3}}{ob_{\max}} + 1 \right) \right)^{1/\delta} \\
&ob^{GF} = ob_{\min} \exp\left(-\left(\beta \tilde{Y} \right)^{\delta} \right) + ob_{\max} \left(1 - \exp\left(-\left(\beta \tilde{Y} \right)^{\delta} \right) \right) \\
&\vec{\Upsilon}_{ij} = \left(\sqrt{1 - (ob^{GF})^2 / 3} \right) \vec{\alpha}^*_{ij} + \frac{ob^{GF}}{3} \delta_{ij}
\end{aligned} \tag{2.28}$$

Where **ob$_{min}$** and **ob$_{max}$** are input parameters that control the minimum and maximum trace of the goal funtion, while **δ** controls its evolution. To aid visualization of the former definitions Figure 17 shows the value of the limit function (2.26) in an isomorphic space of the first and second invariants of the backstress tensor.

$$\begin{aligned}
&J_\alpha = \sqrt{1/2 \alpha^*_{ij} \alpha^*_{ij}} \\
&p_\alpha = \alpha_{kk} / 3
\end{aligned} \tag{2.29}$$

Figure 18 shows the tensor field $\vec{\Upsilon}_{ij}$ of (2.28) in the same isomorphic space. Also included in a greyscale is the value of the trace of the tensor field, $\vec{\Upsilon}_{kk}$. As will be described in next section, to capture the critical state conditions (CSL) the trace of the goal function must be zero, $\vec{\Upsilon}_{kk} = 0$, and the limit surface must be one, $Y = 1$.

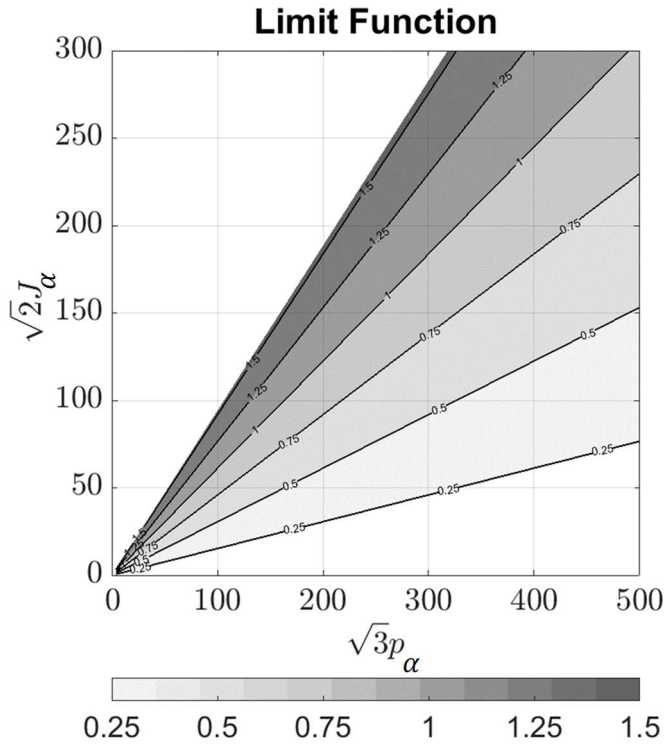


Figure 17: Graphical representation of the Limit surface for f_d = 1 and ϑ =1

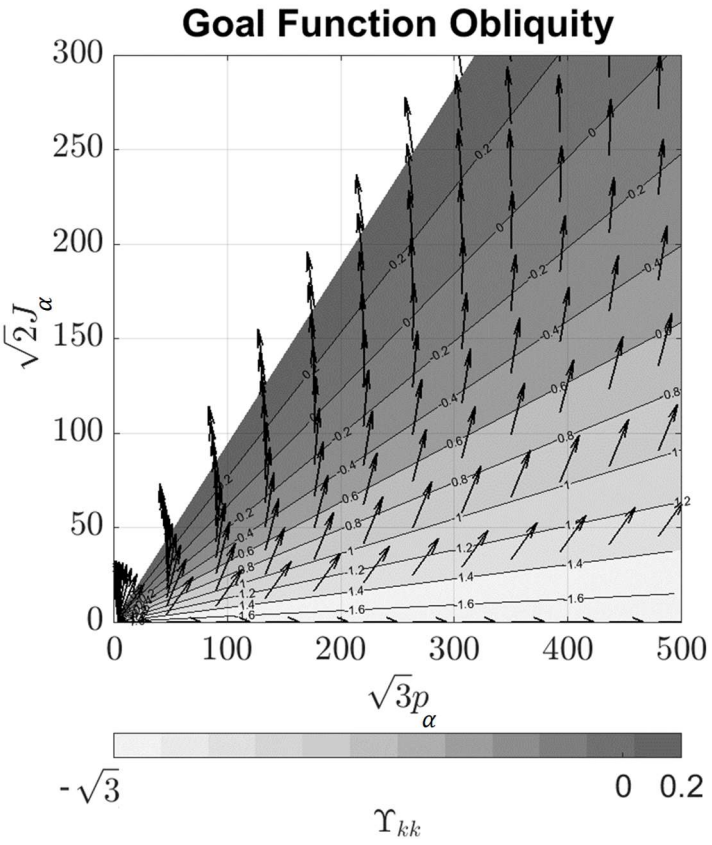
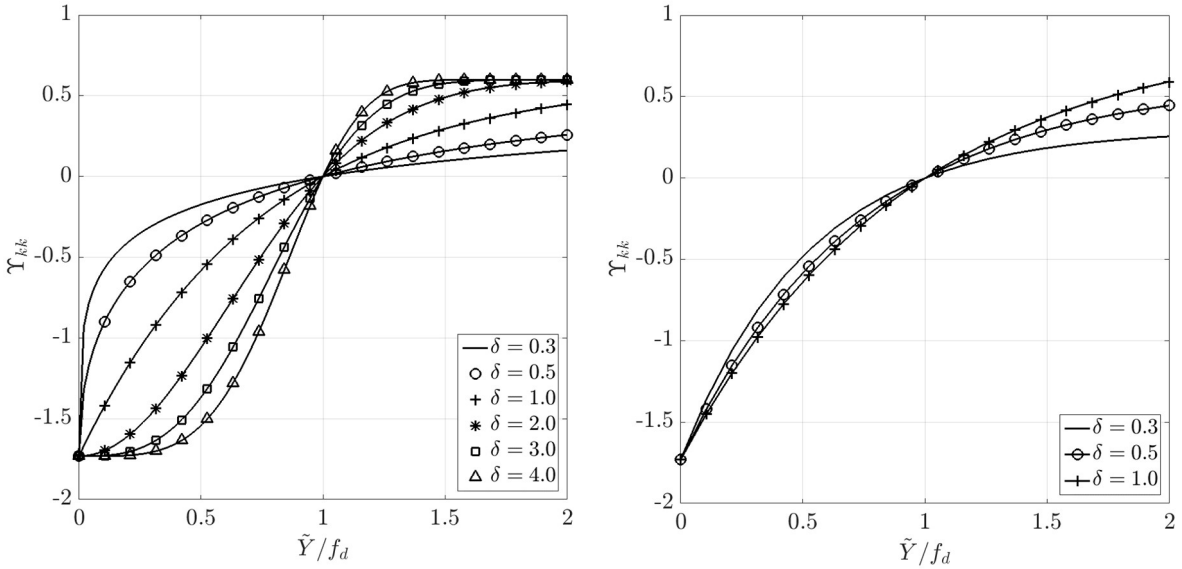


Figure 18: Graphical representation of the Goal Funtions f_d = 1 and ϑ =1

The expression of the goal function is as a combination of two kernels functions. Figure 19 illustrates an example of the possible shapes of the trace of the goal function in relation with the limit surface, where each curve represents one possible goal function field for different ob_{max}, ob_{min} and δ inputs. The axes of the figures correspond to the trace of the goal function and the limit surface **Y**, which are measures akin to the stress ratio J/p and dilatancy, respectively.



ob_{max} = 0.6; ob_{min} = -1.7321; f_d = 1 ob_{max} = 0.3; ob_{min} = -1.7321; δ=1.0; f_d = 1

Figure 19: Parametric study of the Goal Function

The combination of goal function, f_d function and limit surface define the non-linear "recall term", being a subtraction of the linear term of the kinematic hardening rule which does not share the direction of the plastic strain, namely:

$$\dot{\alpha}_{ij} = f_e f_p L_{ijkl} \left(\underbrace{\dot{\varepsilon}^p_{kl}}_{\substack{Linear \\ Term}} - \underbrace{Y\vec{\Upsilon}_{kl}\dot{z}}_{\substack{\text{Recall} \\ Term}} \right) \tag{2.30}$$

2.3.2. IMPLICATIONS OF THE RECALL TERM: STABLE ATTRACTORS

Once the limit surface and the goal function have been defined, the concept of stable attractor can be introduced. However, before entering into the description of soil behaviour, it can be noted that equation (2.30) has the form of a Bernoulli ordinary differential equation, therefore a stable attractor is the pair $(\dot{\varepsilon}_{ij}^{p}, \alpha_{ij})$ for which (2.30) becomes zero, which is no more than an equilibrium point, such as:

$$\dot{\varepsilon}_{ij}^{p} = f_d \tilde{Y} \vec{\Upsilon}_{ij} \dot{z} \tag{2.31}$$

The position of the stable attractor in the backstress and strain rate direction has been studied as a function of the previously defined goal functions, limit functions and f_d functions. In this case the function f_d has been considered constant and is arbitrarily defined between the value of 0.5 and 1.5. Equation (2.31) can be rewritten using the endochronic time measure "z" from Equation (2.24) and for convenience the variable obliquity *"ob"* is introduced, which corresponds to the trace of the unitary normal of the yield surface ($\vec{n}_{kk} = ob$). Therefore, Equation (2.31) can be rewritten as:

$$\vec{n}_{ij} - f_d \tilde{Y} \sqrt{1 + \frac{(k-1)}{3} \left| \vec{n}_{kk} \right|^2} \vec{\Upsilon}_{ij} = 0 \qquad ob = \vec{n}_{kk} \tag{2.32}$$

Expression (2.32) can be split into deviatoric and volumetric part and can be rewritten in the form of two residuals.

$$\begin{aligned} r_{Vol} \frac{1}{3} \delta_{ij} &= ob - f_d \tilde{Y} ob^{GF} \left(\sqrt{1 + \frac{(k-1)}{3} ob^2} \right) \frac{1}{3} \delta_{ij} \\ r_{Dev} \vec{n}_{ij}^{*} &= \left[\sqrt{1 - (ob)^2 / 3} - f_d \tilde{Y} \sqrt{\left(1 + \frac{(k-1)}{3} (ob)^2 \right) \left(1 - \left(ob^{GF} \right)^2 / 3 \right)} \right] \vec{n}_{ij}^{*} \end{aligned} \tag{2.33}$$

The points where both residuals are zero will be defined as “stable attractors”. Therefore, a stable attractor will correspond to points in the stress - plastic strain rate space where the backstress does not evolve in any direction. This concept is described in Jiang and Kurath (1996) for non-linear kinematic hardening models, while for hypoplasticity the appropriate reference is Wu and Niemunis (1996).

The location of couples $(\dot{\varepsilon}_{ij}^{p}, \alpha_{ij})$ fulfilling the (2.32) requirements is governed by the values of f_d and α_{kk}. Indeed with a few manipulations it can be observed that the couples $(\dot{\varepsilon}_{ij}^{p}, \hat{\alpha}_{ij})$ fulfilling (2.33) are unique, indicating that only a stable attractor can be found at a given J/p ratio for a given strain rate direction. The former discussion is illustrated graphically in Figure 20 and Figure 21, where it is shown that the expressions from (2.33), presented in the obliquity – limit function space (*ob - Y*), are akin to strain direction – J/p ratio. The intersection of both residuals lines (the stable attractor) is marked in the figures, one representing the goal functions dependent of f_d and the other independent of f_d.

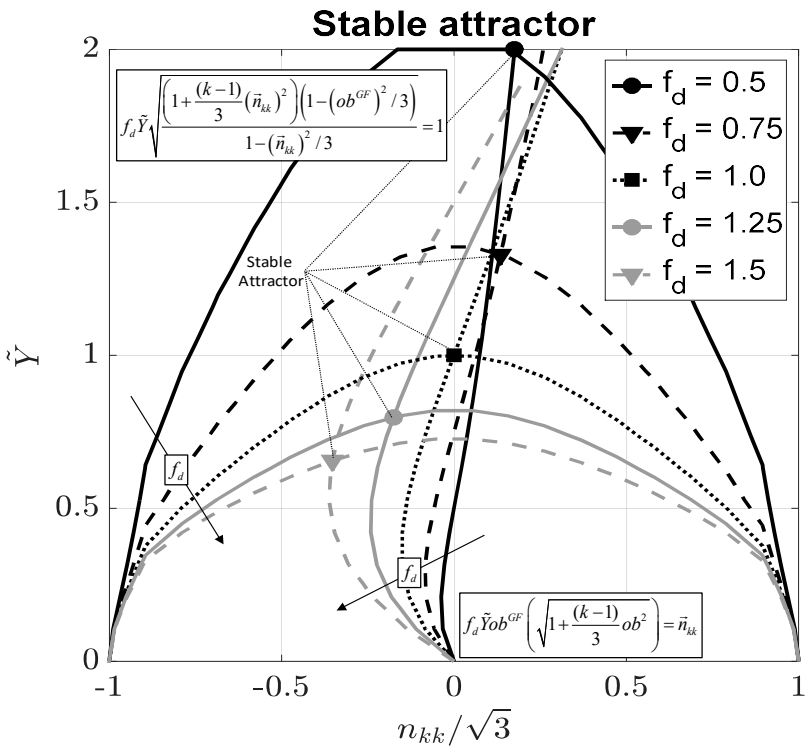


Figure 20: Stable attractors for goal function dependent of f_d $\vec{\Upsilon}_{ij}^{f_d}$

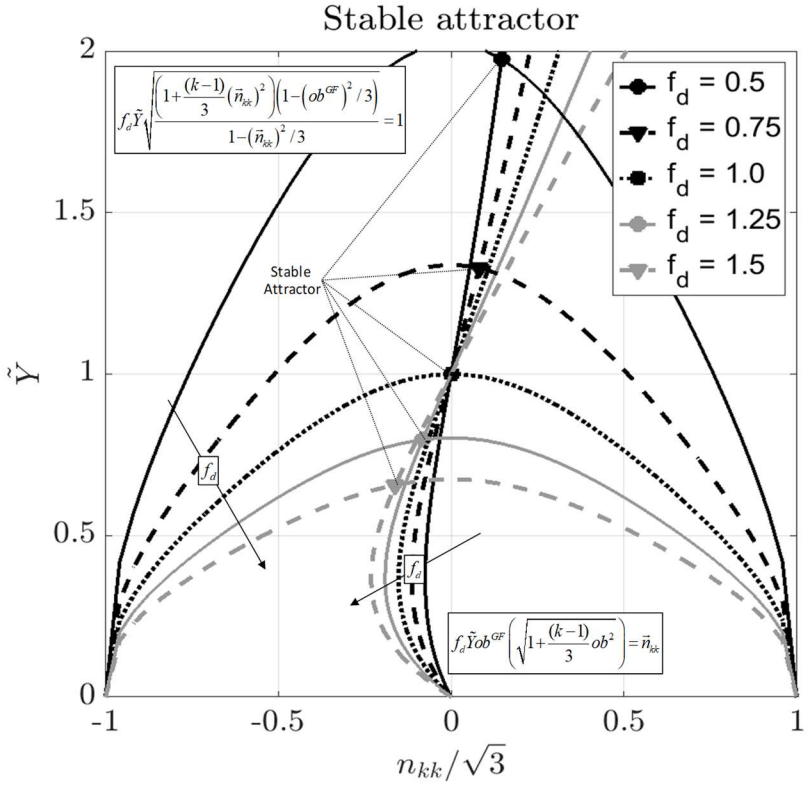


Figure 21: Stable attractors for goal function independent of f_d $\vec{\Upsilon}_{ij}$

The illustrations of expression (2.33) in Figure 20 and Figure 21 show that the value of f_d controls the position of the stable attractor couples $(\dot{\varepsilon}_{ij}^{p}, \hat{\alpha}_{ij})$. It must be noticed that if $f_d < 1$ the attractor falls in a region where the material is prone to swell (obliquity>0), and if $f_d > 1$ (ob<0) where the material is prone to contract. The situation of f_d=1 corresponds to the only case where the stable attractor lies in a region where the change in volume is zero, therefore strict critical state conditions can only occur when this condition is met.

In Figure 21 the volumetric residual marks a region that depends on the limit surface and the direction of the strain rate. That line determines the direction in which the trace of the backstress rate $\dot{\alpha}_{kk}$ will follow. For example, for cases when undrained conditions apply, if f_d > 1.0 then the stress path will tend to follow a contractive path until it reaches a zero value of the mean backstress. On the other hand, if f_d < 1.0 the stress path will show an initial contractant path until it crosses the residual line, where it will then show a dilatant behaviour indefinitely. The mathematical form of this type of rule includes implicitly the concept of phase transformation line.

In summary, the value of f_d is crucial when using this modelling framework in combination with the limit functions and goal functions defined previously, as it governs the location of the stable attractors. Typically, f_d is described as a function of the void ratio or other history variables. By doing so it is possible to model contractant or dilatant behaviour of soils and critical state conditions for sand and clay.

2.3.3. IMPLICATIONS OF THE RECALL TERM: ASYMPTOTIC STATES

Asymptotic states are defined as stress conditions where a constant stress ratio $\hat{\sigma}_{ij} = \sigma_{ij} / \sigma_{kk}$ is reached after a sufficiently long strain path under a constant strain direction, $\vec{\varepsilon}_{ij}$, regardless of its initial state. The models proposed here must comply with the previous condition to reproduce soil appropriately. Therefore, it is important to study the conditions under which $\dot{\hat{\alpha}}_{ij} = 0$ occurs. By definition, an asymptotic state must also correspond to a backstress rate $\dot{\alpha}_{ij}$, for which the following condition must hold:

$$\frac{\partial \hat{\alpha}^*_{ij}}{\partial \alpha_{kl}} \dot{\alpha}_{kl} = \frac{1}{\alpha_{kk}} \left(\delta_{ik}\delta_{jl} - \frac{1}{3}\delta_{ij}\delta_{kl} - \hat{\alpha}^*_{ij}\delta_{kl} \right) \dot{\alpha}_{kl} = 0_{ij} \tag{2.34}$$

As in this case $\hat{\alpha}_{ij}$ is coaxial with $\vec{\Upsilon}_{ij}$ and $\alpha_{kk} < 0$, expression (2.34) can be rewritten as:

$$\frac{\partial \hat{\alpha}^*_{ij}}{\partial \alpha_{kl}} h_{kl} = \frac{1}{\alpha_{kk}} \left(\delta_{ik}\delta_{jl} - \frac{1}{3}\delta_{ij}\delta_{kl} + \left\| \hat{\alpha}^*_{ij} \right\| \vec{n}^*_{ij}\delta_{kl} \right) h_{kl} = 0_{ij} \tag{2.35}$$

where h_{kl} is the general hardening rule of Equation (2.6) normalised by the strain metric. Using the residuals from (2.33), and considering the mapping tensor to be the fourth order identity ($L_{ijkl} \propto \delta_{ik}\delta_{jl}$), substituting (2.33) into (2.35) leads to the following equation dependent on the residuals described in (2.33):

$$r_{Dev}\vec{n}^*_{ij} + \left\| \hat{\alpha}^*_{ij} \right\| \vec{n}^*_{ij} r_{Vol} = 0 \tag{2.36}$$

Examining the previous expression, it must be noted that any absolute stress attractor is also an asymptotic attractor. Expression (2.36) can be plotted in the same axes as the stable attractors of Figure 20 and Figure 21. The surface obtained corresponds to the asymptotic $\hat{\sigma}_{ij} = \sigma_{ij} / \sigma_{kk}$ ratios reached after a constant strain direction. Figure 22 and Figure 23 show the surfaces defined by (2.36) for different input values of the goal function, endochronic time and f_d values:

- the goal function is **dependent** on f_d ($\vec{\Upsilon}_{ij}^{f_d}$), (equation (2.27))

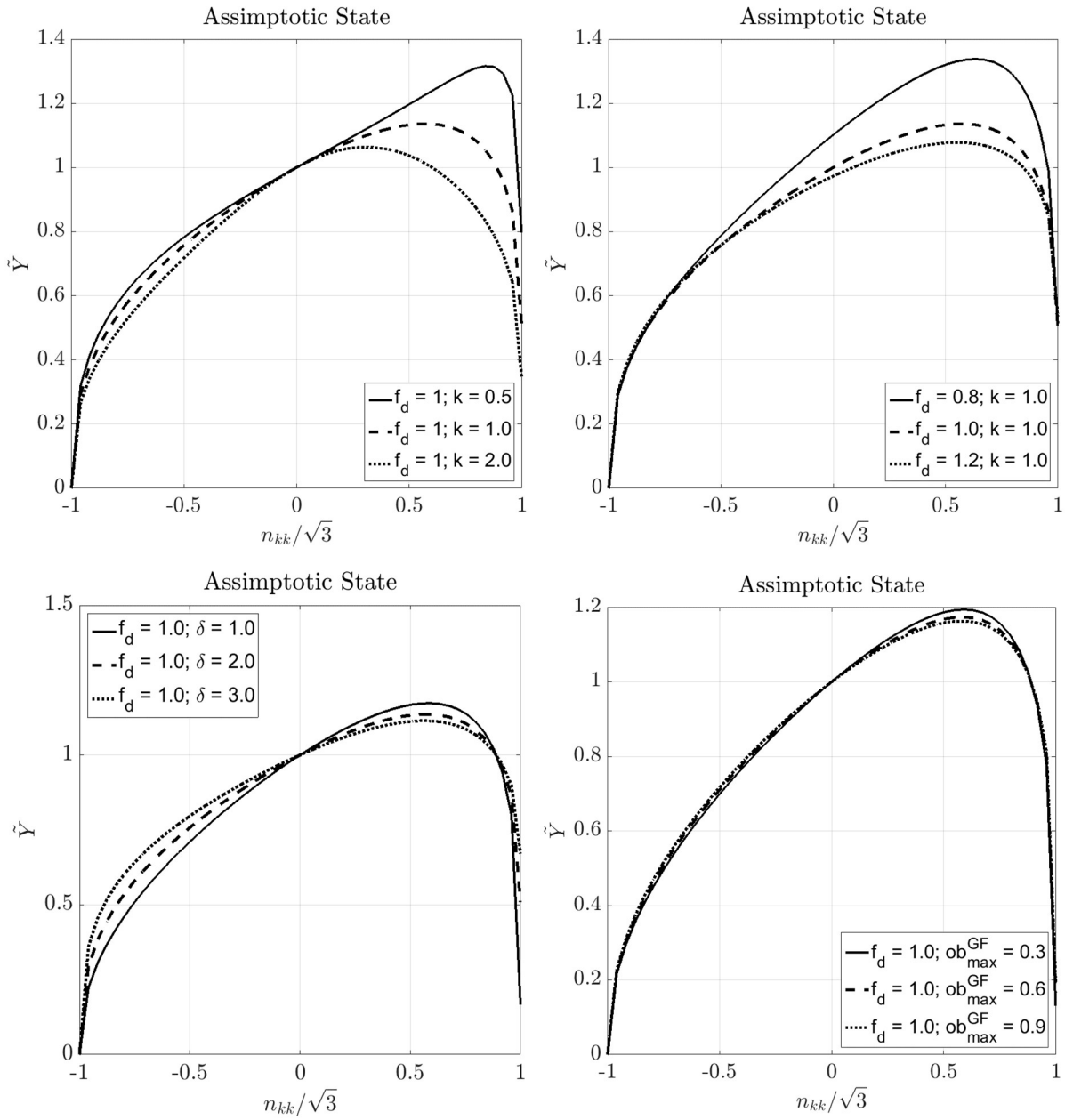


Figure 22: Parametric study of asymptotic attractors. Goal Function dependent on f_d

- the goal function is **independent** of $f_d(\vec{\Upsilon}_{ij})$ (equation (2.28))

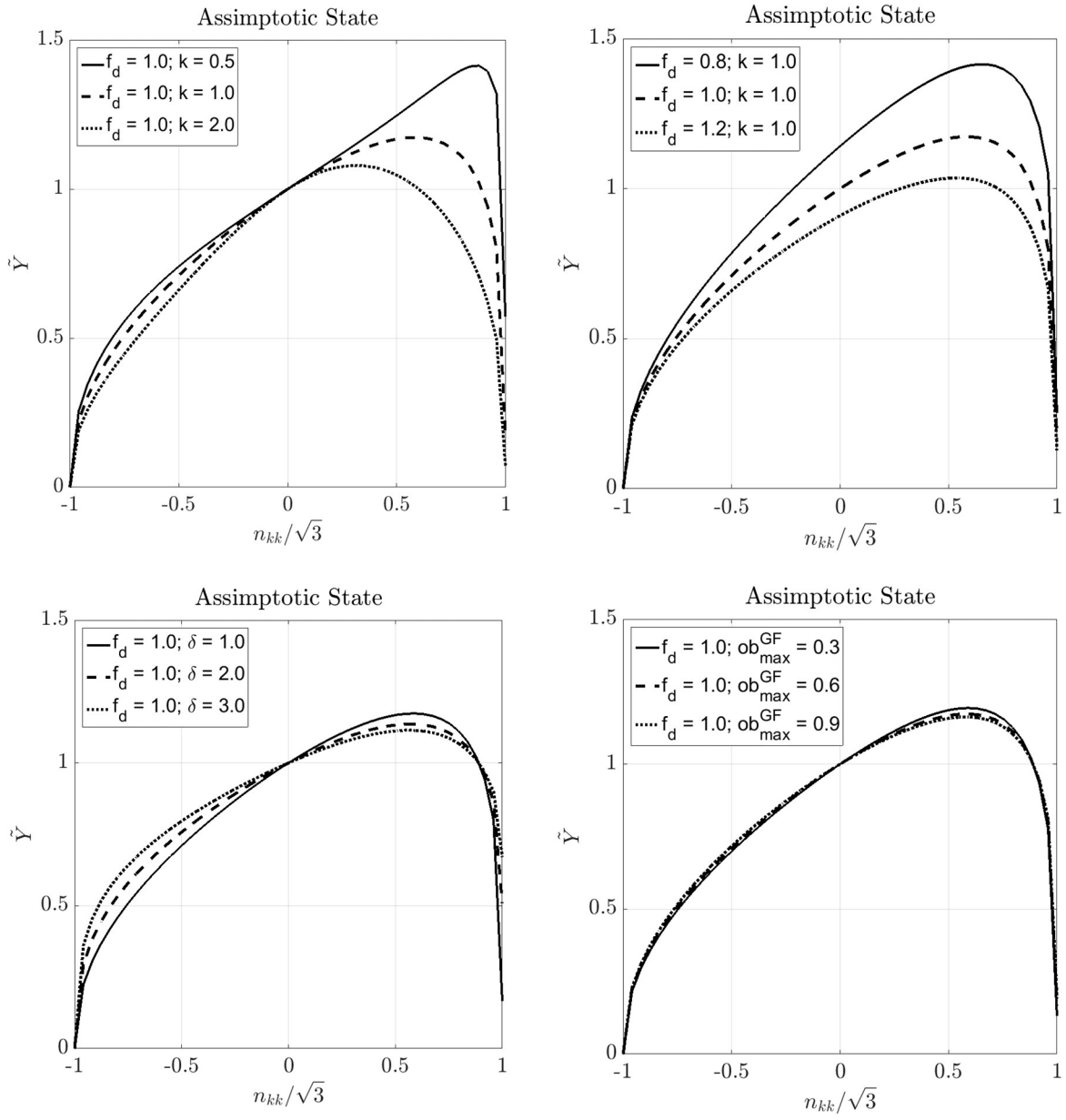


Figure 23: Parametric study of asymptotic attractors Goal Function independent of f_d

To re-illustrate the concept of asymptotic attractor through an example, a set of asymptotic probes, for two different initial states, has been carried out for the model defined by the general expression (2.23) and the inputs given in Table 3. This type of probes corresponds to numerical tests where the strain increments maintain a constant direction and the stress path is plotted. The stress paths are plotted in Figure 24, where it is included the predicted envelope of asymptotic attractors obtained though (2.35), showing that all stress paths end on the predicted

limit surface of equation (2.36) indicated by points A and B. Also, the asymptotic properties of the expression (2.36) can be verified, showing that regardless of the initial states (solid and dashed lines) the stress paths travel towards their associated asymptotic attractors. The lower right figure indicates all the strain directions studied for this example:

Table 3: Parametric inputs for asymptotic probes

f_d	$g(\theta)$	**ob**min	**ob**max	δ	ϑ	**k**
1.5	0.75	$-\sqrt{3}$	0.6	2.0	1.0	1.0

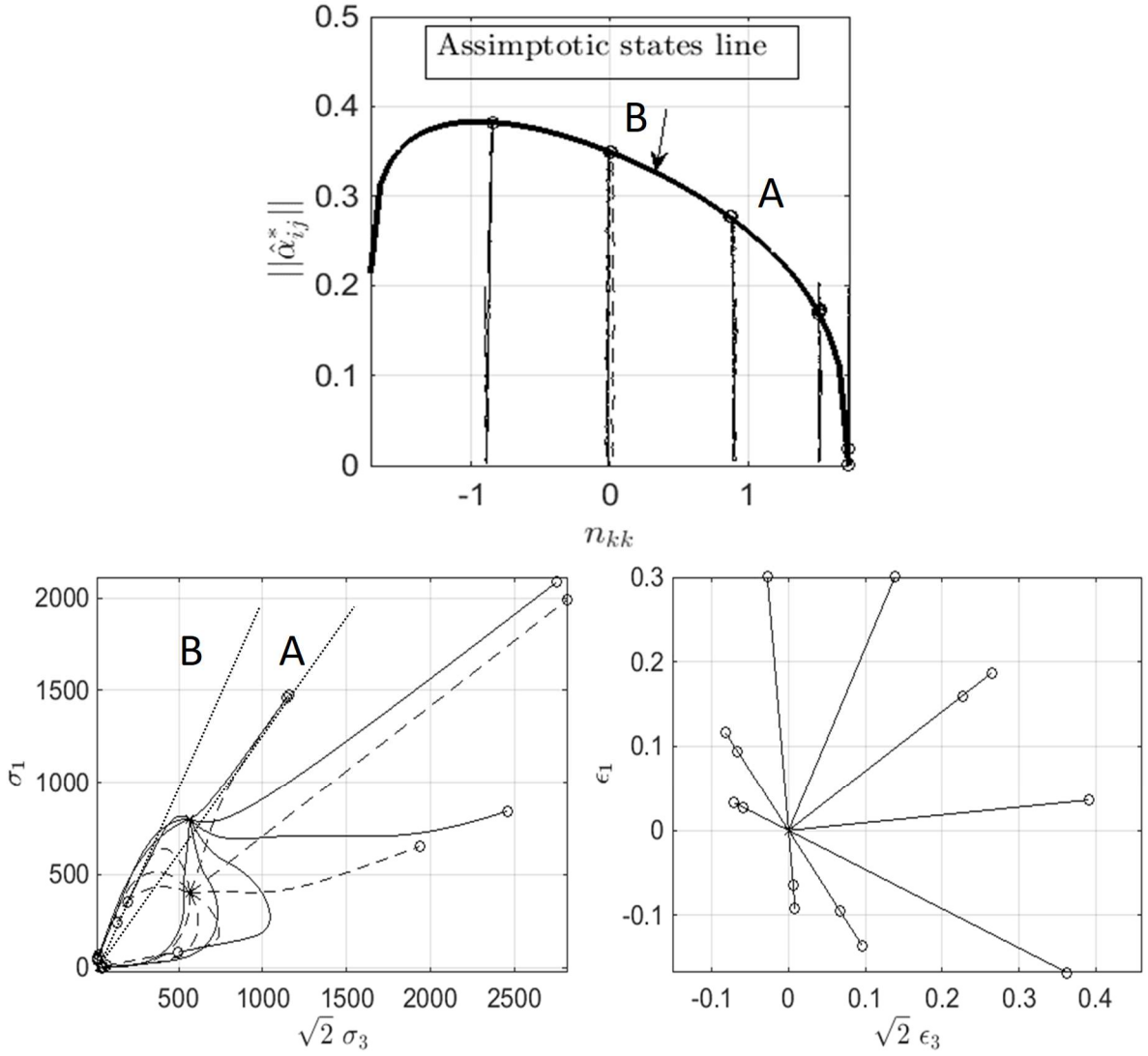


Figure 24: Asymptotic probes for f_d = 1.5

The rate at which the stress path reaches the asymptote will depend on the magnitude of plastic strain, mapping tensor and stiffness functions f_e and f_p. It is important to mention that for low values of f_d the asymptotic attractors may exhibit excessively large $\hat{\sigma}_{ij}$ ratios, which may produce unrealistic behaviour for soils. For example, for low values of f_d , the stress path of an oedometer test may travel towards a $\hat{\sigma}_{ij}$ asymptote higher than a purely deviatoric strain test with a higher f_d value. This is illustrated in Figure 25 where oedometric and TXU conditions are marked. To capture soil behaviour realistically it is necessary to tune expressions of f_d in a way that the value of the function f_d increases or decreases accordingly. As it is described in detail later, the rate of f_d shall travel towards 1 when subjected to shearing, or shall exhibit a rate of zero. For strain directions where $n_{kk}<0$, a $\dot{f}_d < 0$ situation is likely to result in unrealistic J/p asymptotes, and should therefore be avoided.

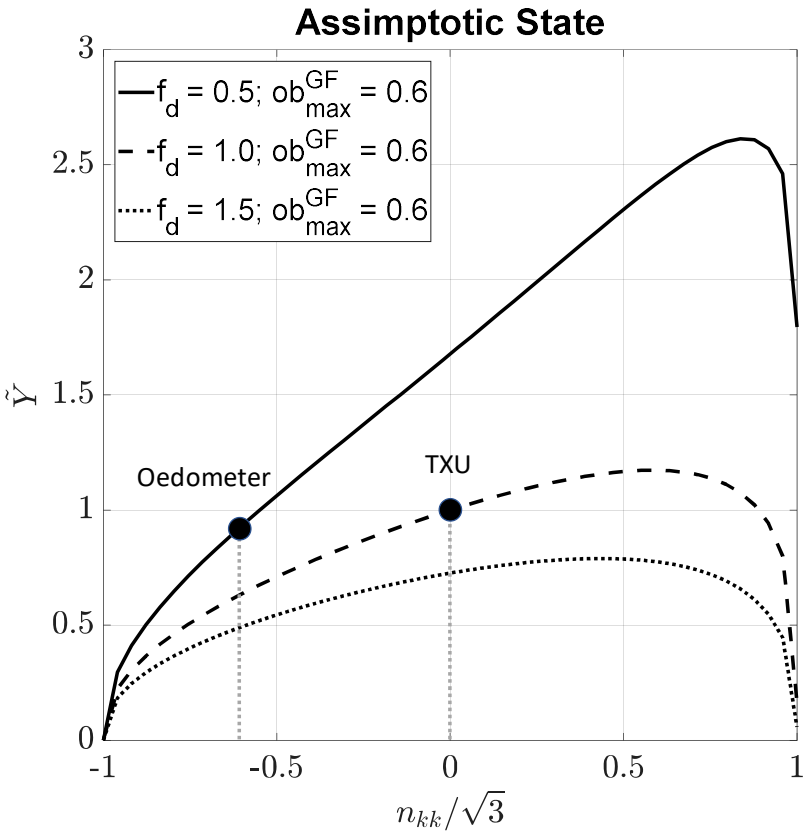


Figure 25: Envelope of asymptotic strain paths for both goal functions

2.3.4. MAPPING TENSOR

The mapping tensor controls the stiffness of the hardening rule at a local scale and does not have influence on the stable attractors, however it may affect the asymptotic attractors if not chosen appropriately. The mapping tensor is a positive defined fourth order tensor L_{ijkl} and is linear with respect to the linear term and the recall term as shown in eq (2.30). Following the same methodology as in section 2.3.3, when a mapping tensor is used, the asymptotic attractors are obtained though:

$$\left(\delta_{ip}\delta_{jq}-\frac{1}{3}\delta_{ij}\delta_{pq}-\hat{\alpha}^{*}_{ij}\delta_{pq}\right)L_{pqrs}\left(\dot{\varepsilon}^{p}_{kl}-Y\vec{\Upsilon}_{kl}\dot{z}\right)=0_{ij} \tag{2.37}$$

Although the mapping tensor does not affect the absolute attractors, it may (in some cases) change the asymptotic attractors. It is therefore a good practice to use mapping tensor that share the principal directions of the directional derivative of $\hat{\alpha}^{*}_{ij}$ and also are orthogonal to it, for example:

1. Projector sharing directional derivative $\frac{\partial\hat{\alpha}^{*}_{ij}}{\partial\alpha_{kl}}$ and its orthogonal counterpart

$$L_{ijkl}=\lambda^{dev}\left(\frac{\lambda^{vol}}{\lambda^{dev}}\left(\frac{1}{3}\delta_{ij}\delta_{kl}+\hat{\alpha}^{*}_{ij}\delta_{kl}\right)+\left(\delta_{ik}\delta_{jl}-\frac{1}{3}\delta_{ij}\delta_{kl}-\hat{\alpha}^{*}_{ij}\delta_{kl}\right)\right) \tag{2.38}$$

where the ratio $\lambda^{vol}/\lambda^{dev}$ controls the shape of the mapping tensor.

2. The hypoplastic mapping tensor, von Wolffersdorff (1996)

$$L_{ijkl}=\frac{1}{\hat{\alpha}_{ij}\hat{\alpha}_{ij}}\left(F^{2}\delta_{ik}\delta_{jl}+a^{2}\hat{\alpha}_{ij}\hat{\alpha}_{kl}\right) \tag{2.39}$$

where **a** and **F** are scalars. The following section proves that the hypoplastic tensor and the projector tensor are both idempotent with respect to the directional derivative of $\hat{\alpha}^{*}_{ij}$. As a result, the asymptotic attractors will be unaffected if any of the previous mapping tensors defined by (2.38) or (2.39) are used. The fact that the mapping tensors of case 1 are constructed with orthogonal projections makes them a friendlier choice for our mapping tensor than the standard

hypoplastic tensor, as this orthogonal property becomes very useful when superposing backstresses, as will be shown in Chapter 4.

- Mapping tensor 1: Othogonal projectors:

$$
\begin{aligned}
&P^1_{ijkl} = \delta_{ik}\delta_{jl} - \frac{1}{3}\delta_{ij}\delta_{kl} - \hat{\alpha}^*_{ij}\delta_{kl} \\
&P^2_{ijkl} = \frac{1}{3}\delta_{ij}\delta_{kl} + \hat{\alpha}^*_{ij}\delta_{kl} \\
&P^1_{ijmn}P^1_{mnkl} = P^1_{ijkl} \\
&P^2_{ijmn}P^2_{mnkl} = P^2_{ijkl} \\
&P^1_{ijmn}P^2_{mnkl} = 0_{ijkl}
\end{aligned}
\tag{2.40}
$$

Proof

$$
\begin{aligned}
&\left(\delta_{im}\delta_{jn} - \frac{1}{3}\delta_{ij}\delta_{mn} - \hat{\alpha}^*_{ij}\delta_{mn}\right)\left(\delta_{mk}\delta_{nl} - \frac{1}{3}\delta_{mn}\delta_{kl} - \hat{\alpha}^*_{mn}\delta_{kl}\right) = \\
&= \delta_{im}\delta_{jn} - \frac{1}{3}\delta_{ij}\delta_{mn} - \hat{\alpha}^*_{ij}\delta_{mn} - \frac{1}{3}\delta_{mn}\delta_{kl} + \frac{1}{3}\delta_{mn}\delta_{kl} + \hat{\alpha}^*_{ij}\delta_{mn} - \hat{\alpha}^*_{mn}\delta_{kl} = \\
&= \delta_{im}\delta_{jn} - \frac{1}{3}\delta_{ij}\delta_{mn} - \hat{\alpha}^*_{ij}\delta_{mn}
\end{aligned}
\tag{2.41}
$$

- Hypoplastic tensor

$$
\begin{aligned}
&L_{ijkl} = \frac{1}{\hat{\alpha}_{ij}\hat{\alpha}_{ij}}\left(F^2\delta_{ik}\delta_{jl} + a^2\hat{\alpha}_{ij}\hat{\alpha}_{kl}\right) \\
&P_{ijkl} = \delta_{ik}\delta_{jl} - \frac{1}{3}\delta_{ij}\delta_{kl} - \hat{\alpha}^*_{ij}\delta_{kl} \\
&P_{ijmn}L_{mnkl} = \lambda P_{ijmn} \\
&\lambda = \frac{F^2}{\hat{\alpha}_{ij}\hat{\alpha}_{ij}}
\end{aligned}
\tag{2.42}
$$

$$
\begin{aligned}
&\left(\delta_{ik}\delta_{jl} - \frac{1}{3}\delta_{ij}\delta_{kl} - \hat{\alpha}^*_{ij}\delta_{kl}\right)\frac{1}{\hat{\alpha}_{ij}\hat{\alpha}_{ij}}\left(F^2\delta_{ik}\delta_{jl} + a^2\hat{\alpha}_{ij}\hat{\alpha}_{kl}\right) = \\
&= F^2\delta_{ik}\delta_{jl} + a^2\hat{\alpha}_{ij}\hat{\alpha}_{kl} - \frac{1}{3}F^2\delta_{ij}\delta_{kl} - \frac{a^2}{3}\delta_{ij}\hat{\alpha}_{kl} - F^2\hat{\alpha}^*_{ij}\delta_{kl} - a^2\hat{\alpha}^*_{ij}\hat{\alpha}_{kl} = \\
&= F^2\left(\delta_{ik}\delta_{jl} - \frac{1}{3}\delta_{ij}\delta_{kl} - \hat{\alpha}^*_{ij}\delta_{kl}\right) = \frac{F^2}{\hat{\alpha}_{ij}\hat{\alpha}_{ij}}P_{ijmn}
\end{aligned}
\tag{2.43}
$$

2.3.4.1. Comparison of mapping tensors

The hypoplastic tensor is excellent to characterise the behaviour if one backstress is used, but becomes difficult to distinguish its orthogonal direction if it is separated into volumetric and deviatoric directions. It can be proved that the terms a and F are combinations of the eigenvalues of the following family of orthogonal projections, where λ_1, λ_2 are the eigenvalues.

$$\underbrace{\lambda_1\left(\delta_{ik}\delta_{jl}-\vec{\hat{\alpha}}_{ij}\vec{\hat{\alpha}}_{kl}\right)}_{P^1_{ijkl}}+\lambda_2\underbrace{\vec{\hat{\alpha}}_{ij}\vec{\hat{\alpha}}_{kl}}_{P^2_{ijkl}} \tag{2.44}$$

Recalling the hypoplasticity mapping tensor, it is clear that

$$\begin{aligned}
L_{ijkl}&=\frac{1}{\hat{\alpha}_{ij}\hat{\alpha}_{ij}}\left(F^2\delta_{ik}\delta_{jl}+a^2\hat{\alpha}_{ij}\hat{\alpha}_{kl}\right)=\left(\frac{F^2}{\left\|\hat{\alpha}_{ij}\right\|^2}\delta_{ik}\delta_{jl}+a^2\vec{\hat{\alpha}}_{ij}\vec{\hat{\alpha}}_{kl}\right)=\\
&=\left(\frac{F^2}{\left\|\hat{\alpha}_{ij}\right\|^2}\delta_{ik}\delta_{jl}-\frac{F^2}{\left\|\hat{\alpha}_{ij}\right\|^2}\vec{\hat{\alpha}}_{ij}\vec{\hat{\alpha}}_{kl}+\frac{F^2}{\left\|\hat{\alpha}_{ij}\right\|^2}\vec{\hat{\alpha}}_{ij}\vec{\hat{\alpha}}_{kl}+a^2\vec{\hat{\alpha}}_{ij}\vec{\hat{\alpha}}_{kl}\right)=\\
&=\underbrace{\frac{F^2}{\left\|\hat{\alpha}_{ij}\right\|^2}}_{\lambda_1}\left(\delta_{ik}\delta_{jl}-\vec{\hat{\alpha}}_{ij}\vec{\hat{\alpha}}_{kl}\right)+\underbrace{\left(\frac{F^2}{\left\|\hat{\alpha}_{ij}\right\|^2}+a^2\right)}_{\lambda_2}\vec{\hat{\alpha}}_{ij}\vec{\hat{\alpha}}_{kl}
\end{aligned} \tag{2.45}$$

However, the problem of the hypoplasticity tensor appears when the mapping tensor needs to be separated into a preferential direction, where its principal direction does not share a clear deviatoric or volumetric direction after mapping.

$$\begin{aligned}
&F^2\delta_{ik}\delta_{jl}+a^2\hat{\alpha}_{ij}\hat{\alpha}_{kl}=\underbrace{F^2\delta_{ik}\delta_{jl}-\frac{1}{3}F^2\delta_{ij}\delta_{kl}+a^2\hat{\alpha}^*_{ij}\hat{\alpha}_{kl}}_{A^1_{ijkl}}+\underbrace{\frac{1}{3}F^2\delta_{ij}\delta_{kl}+a^2\delta_{ij}\hat{\alpha}_{kl}}_{A^2_{ijkl}}\\
&A^1_{ijkl}A^2_{ijkl}=+a^2F^2\hat{\alpha}^*_{ij}\delta_{kl}+3a^4\hat{\alpha}^*_{ij}\hat{\alpha}_{kl}\neq 0
\end{aligned} \tag{2.46}$$

To illustrate the differences between both mapping tensors, Figure 26 shows graphically the small strain probes (Gudehus and Mašín, 2009) carried out at three different J/p ratios and at the same initial p'in the Rendulic plane.

The values chosen for the hypoplastic tensor are: a = 3 and F = 1**,** while for the orthogonal projection tensor the eigenvalues are $\lambda^{vol} / \lambda^{dev} = 3$. In general, no significant differences appear in terms of the trend as the stress ratio increases. The most significant difference is the rotation of the mappings corresponding to the strain directions that are preferentially deviatoric. This is natural since the orthogonal mapping tensor (Tensor 1) does not have a major symmetry with the term $\hat{\alpha}^{*}_{ij}\delta_{kl}$.

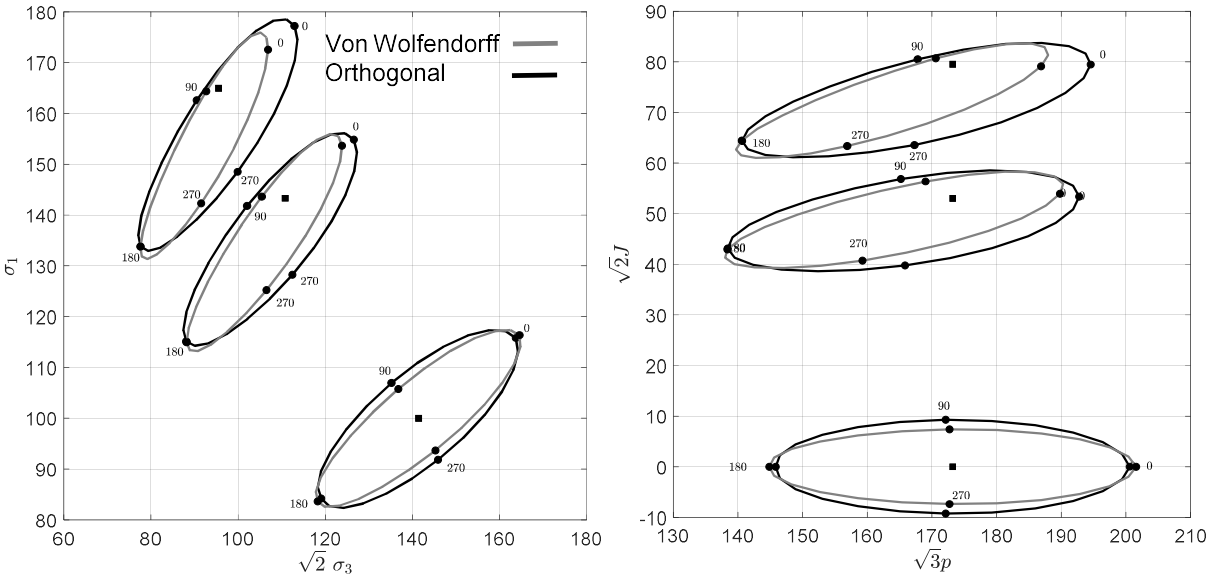


Figure 26: Comparison of mapping tensors

2.3.4.2. Positive definiteness of the proposed tensor

Althought the tensor proposed from orthogonal projectors in 2.3.4 is not super-symmetric it is positive definite as far as the eigenvalues are positive $\lambda^{dev} \geq 0 \qquad \lambda^{vol} \geq 1$. The othogonal tensor can be rewritten as

$$L_{ijkl} = \lambda^{dev}\delta_{ik}\delta_{jl} + (\lambda^{vol} - 1)\hat{\alpha}_{ij}\delta_{kl} \tag{2.47}$$

Obviously the only term without major symmetry can be expressed as

$$\hat{\alpha}_{ij}\delta_{kl} = \underbrace{\frac{1}{2}\left(\delta_{ij}\hat{\alpha}_{kl} + \hat{\alpha}_{ij}\delta_{kl}\right)}_{A_{ijkl}} + \underbrace{\frac{1}{2}\left(\delta_{ij}\hat{\alpha}_{kl} - \hat{\alpha}_{ij}\delta_{kl}\right)}_{S_{ijkl}} \tag{2.48}$$

Where $A_{ijkl}$is super-symmetric and positive defined and S_{ijkl} is skew-symmetric $a_{ij}S_{ijkl}a_{kl} = 0$.

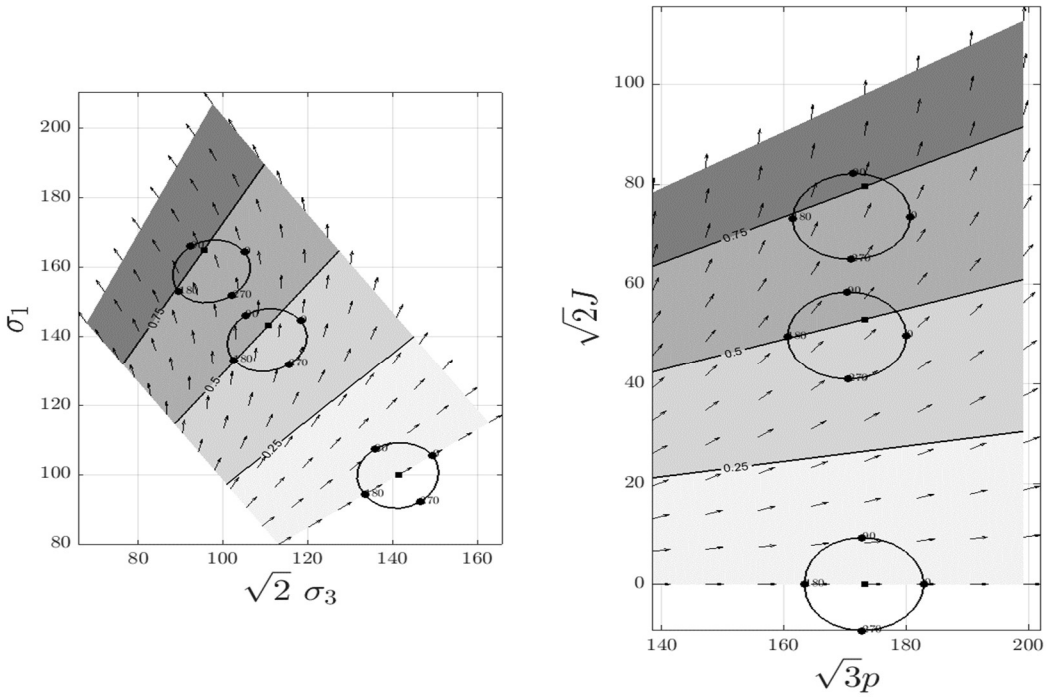
2.3.5. INFLUENCE OF MODEL PARAMETERS

In this section, a graphical representation of the models is shown using the methodology described in Gudehus and Mašín (2009). All the figures correspond to small finite strain perturbations, at initial stress ratios associated with a limit surface value of $\tilde{Y}$=[0.0,0.5,0.75] respectively. The mean effective stress considered for all cases is 100 kPa. Five combinations of parameters f_d, k, $\lambda^{vol}/\lambda^{dev}$ are plotted, to illustrate the implications of using different parameters. Three cases (1, 2 and 4) do not incorporate the effect of the mapping tensor, while cases 3 and 5 include the mapping tensor described by (2.38). Finally, Cases 3 and 5 show the effect of modifying the "metric" of the strain space through the endochronic time. The parameters for all cases are summarised in Table 4:

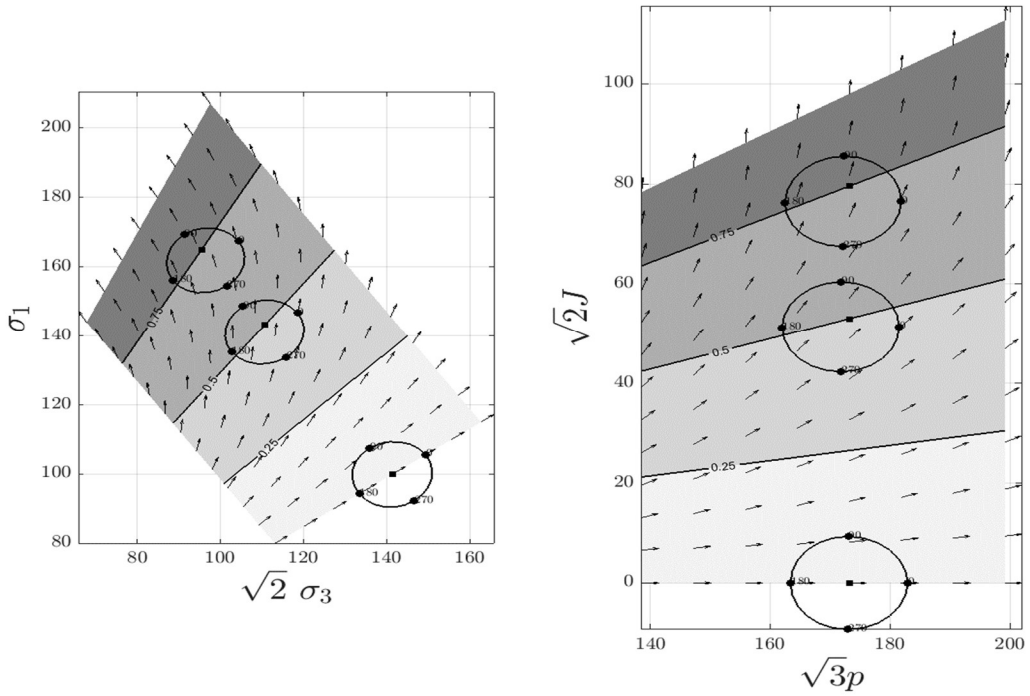
Table 4: Parametric inputs

	$\mathbf{f_d}$	**k**	$\boldsymbol{\lambda^{vol}/\lambda^{dev}}$
Case 1	1.0	1.0	1.0
Case 2	0.5	1.0	1.0
Case 3	1.0	1.0	2.0
Case 4	1.0	2.0	1.0
Case 5	1.0	2.0	2.0

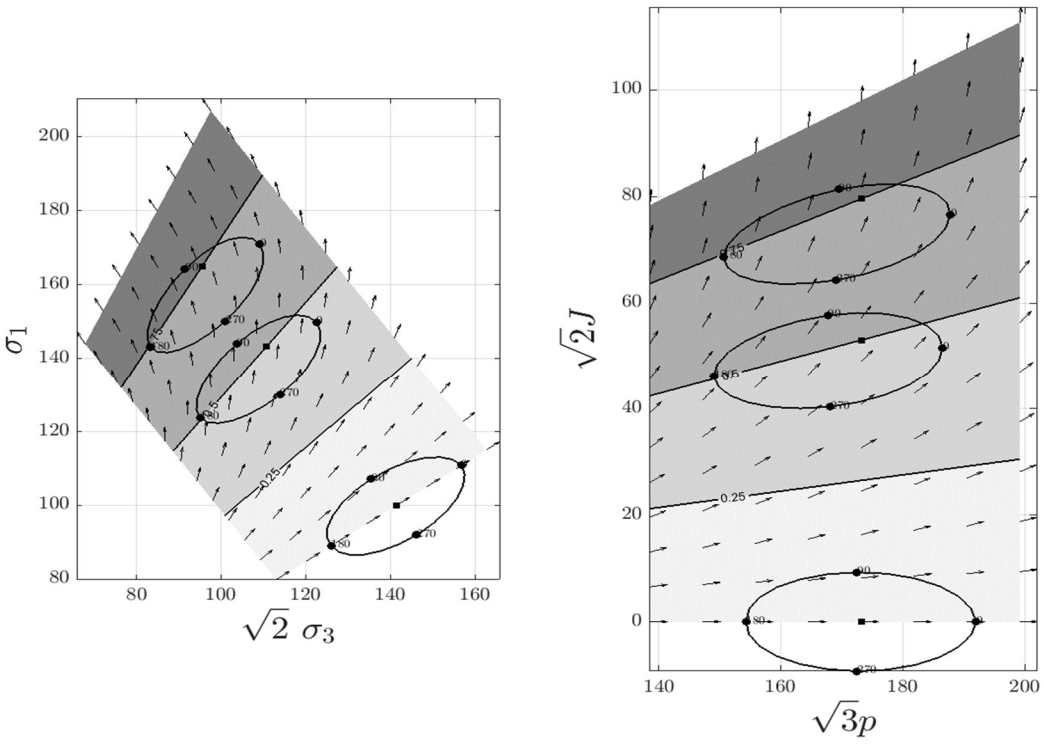
In Figure 16, the square dots inside the mapping correspond to the initial stress of the probe, the bullet dots on top of the mapping represent the purely volumetric or deviatoric strain directions in loading or unloading conditions. The value of the limit surface, is plotted in the background in a greyscale. The tensor field of the goal functions is also included, to aid visualisation. All figures are plotted in both the Rendulic plane and the invariant isomorphic space.



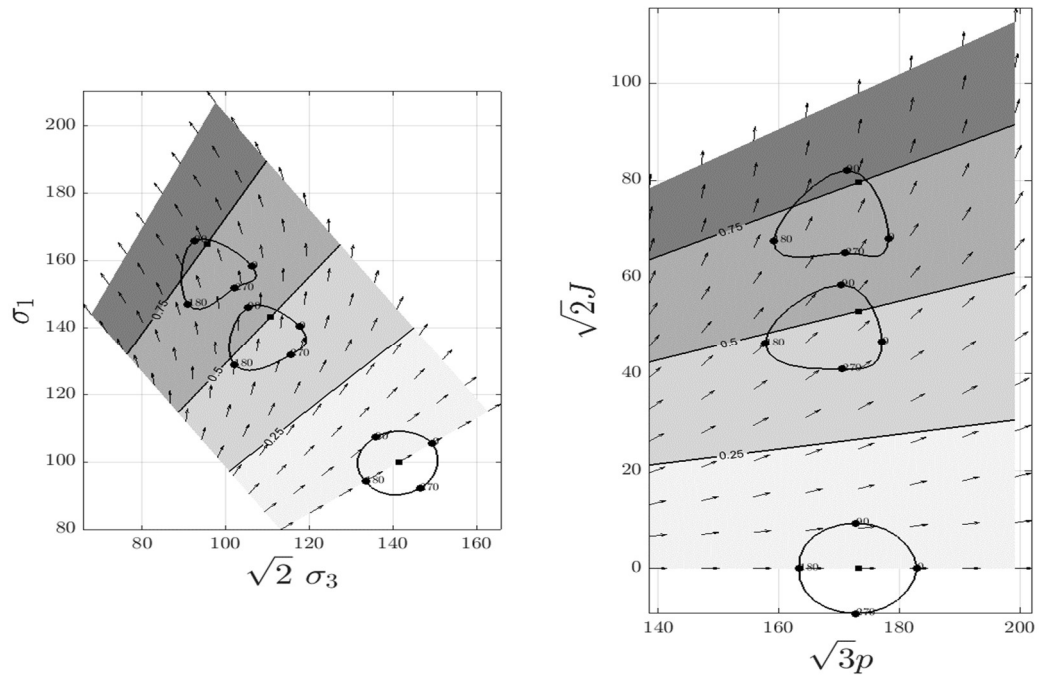
Case 1: $f_d = 1.0$, $k = 1.0$, $\lambda^{vol}/\lambda^{dev} = 1.0$



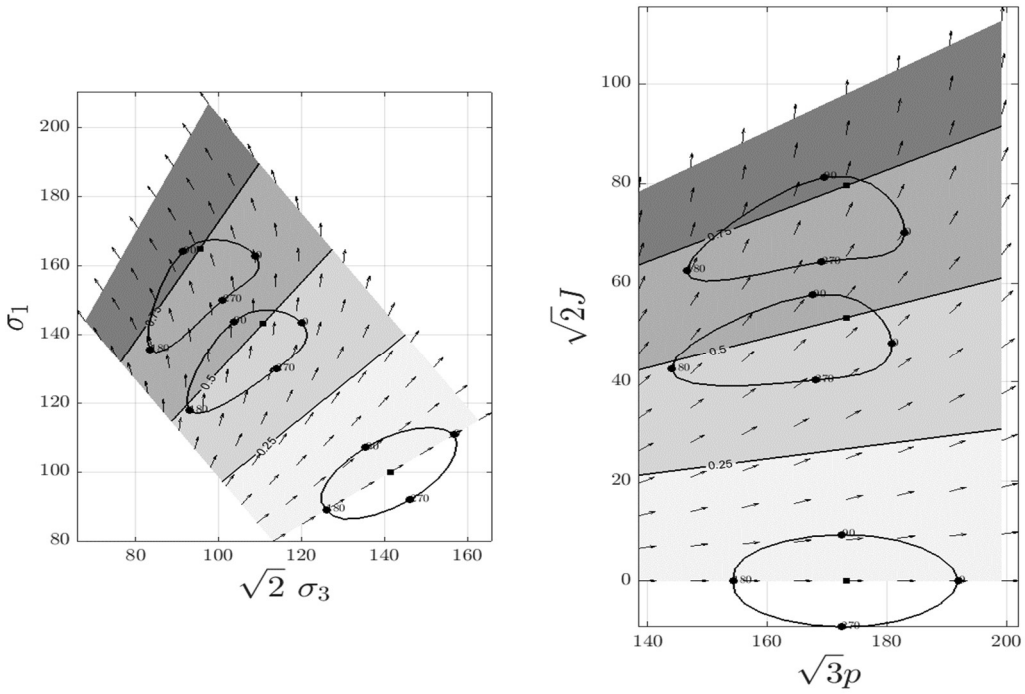
Case 2: $f_d = 0.5$, $k = 1.0$, $\lambda^{vol}/\lambda^{dev} = 1.0$



Case 3: $f_d = 1.0$, $k = 1.0$, $\lambda^{vol}/\lambda^{dev} = 2.0$



Case 4: $f_d = 1.0$, $k = 2.0$, $\lambda^{vol}/\lambda^{dev} = 1.0$



Case 5: $f_d = 1.0$, $k = 2.0$, $\lambda^{vol}/\lambda^{dev} = 2.0$

Figure 27: Strain perturbations mapping for $\tilde{Y} = [0.0, 0.5, 0.75]$*: (a) Case 1, (b) Case 2, (c) Case 3, (d) Case 4 and (e) Case 5.*

All mappings correspond to a sphere whose centre is shifted in the direction of $\vec{\Upsilon}_{ij}$ by a magnitude $Y = f_d \tilde{Y}$ and further distorted by the influence of the mapping tensor. Figure 28 shows a graphic interpretation of the effects of the mapping tensors and metric. It illustrates the effect of the mapping tensor L_{ijkl}, which causes an increase of the size of the mapping, distorting the sphere towards a more elliptic shape. On the other hand, when the metric of the strain is changed the space becomes curvilinear producing a more "egg-shaped" mapping. In other words, the mapping is linear in the space $\tilde{\varepsilon}^p_{ij}$ but when transformed to ε^p_{ij} the mapping becomes curved.

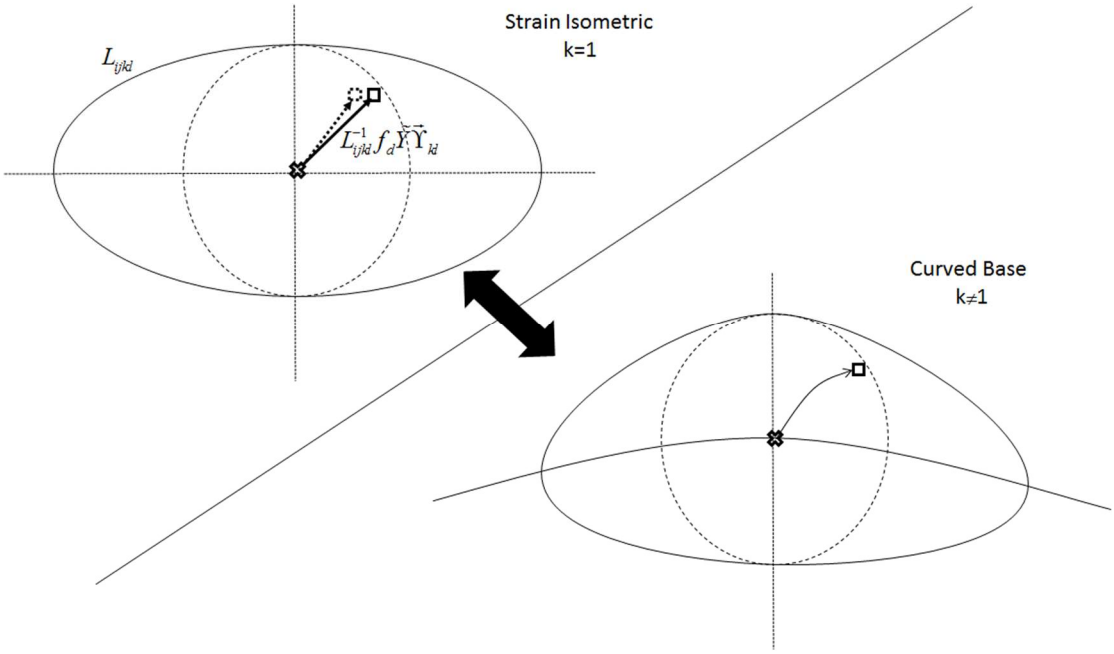


Figure 28: Graphical interpretation of the metric of plastic strain

2.3.6. INVERSION OF THE NLKH – PSEUDO FLOW RULE

So far it has been shown that non-linear kinematic rules are characterised by a linear term with respect to the plastic strain rate (linear term) and a non-linear term (recall term). It must be mentioned that this type of models do not comply with the normality condition (Lemaitre and Chaboche, 1994) and can be classified as standard implicit materials (de Saxce and Bousshine, 2002), however, their solution is unique and can allow inversion. Any non-linear kinematic hardening rule defined as (2.23) can be inverted following the methodology described in Wu and Niemunis (1996) and it can be rewritten in the form of strain rate as a function of the stress perturbation, e.g. $\dot{\varepsilon}^p_{ij}(\dot{\alpha}_{ij})$. In order to invert the hardening rule, it is needed firstly to transform the "metric" of the plastic strain.

$$\left\| A_{ij} \right\|_{\Sigma_{ijkl}} = \sqrt{A_{ij}\Sigma_{ijmn}\Sigma_{mnkl}A_{kl}} \tag{2.49}$$

The "endochronic" time defined by (2.49) is essentially a distance in the plastic strain space, and equation (2.23) can then be rewritten as

$$\dot{\alpha}_{ij} = L_{ijkl}\left(\dot{\varepsilon}^p_{kl} - f_d\tilde{Y}\vec{\Upsilon}_{kl}\sqrt{\dot{\varepsilon}^p_{mn}\left(\left(\delta_{mp}\delta_{nq} - \frac{1}{3}\delta_{mn}\delta_{pq}\right) + k\frac{1}{3}\delta_{mn}\delta_{pq}\right)\dot{\varepsilon}^p_{pq}}\right) \tag{2.50}$$

Now applying a linear transformation of the new metric to the plastic strain, a pseudo-plastic strain $\tilde{\varepsilon}^p_{ij}$ can be obtained where

$$\begin{aligned}\tilde{\varepsilon}^p_{ij} &= \Sigma_{ijkl}\varepsilon^p_{ij} \\ \Sigma_{ijkl} &= \left(\delta_{ik}\delta_{jl} - \frac{1}{3}\delta_{ij}\delta_{kl}\right) + \sqrt{k}\frac{1}{3}\delta_{ij}\delta_{kl}\end{aligned} \tag{2.51}$$

Expression (2.51) for Σ_{ijkl} must be invertible with k>0. Applying the variable change and substituting in (2.50):

$$\dot{\alpha}_{ij} = L_{ijmn}\left(\Sigma^{-1}_{mnkl}\dot{\tilde{\varepsilon}}^p_{kl} - f_d\tilde{Y}\vec{\Upsilon}_{mn}\left\|\dot{\tilde{\varepsilon}}^p_{ij}\right\|\right) \tag{2.52}$$

Contracting both sides by $\Sigma_{ijmn}L^{-1}_{mnkl}$:

$$\Sigma_{ijmn}L^{-1}_{mnkl}\dot{\alpha}_{kl} = \dot{\tilde{\varepsilon}}^p_{ij} - f_d\tilde{Y}\Sigma_{ijkl}\vec{\Upsilon}_{kl}\left\|\dot{\tilde{\varepsilon}}^p_{ij}\right\| \tag{2.53}$$

and grouping the terms gives:

$$\dot{\tilde{\varepsilon}}^p_{ij} = \underbrace{\Sigma_{ijmn}L^{-1}_{mnkl}\dot{\alpha}_{kl}}_{A_{ij}} + f_d\tilde{Y}\underbrace{\Sigma_{ijkl}\vec{\Upsilon}_{kl}}_{B_{ij}}\left\|\dot{\tilde{\varepsilon}}^p_{ij}\right\| \tag{2.54}$$

Taking the norm of (2.54):

$$\left\|\dot{\tilde{\varepsilon}}^p_{ij}\right\|^2 = A_{ij}A_{ij} + 2A_{ij}B_{ij}f_d\tilde{Y}\left\|\dot{\tilde{\varepsilon}}^p_{ij}\right\| + (f_d\tilde{Y})^2B_{ij}B_{ij}\left\|\dot{\tilde{\varepsilon}}^p_{ij}\right\|^2 \tag{2.55}$$

and rearranging (2.55), the second order polynomial is obtained:

$$\left((f_d\tilde{Y})^2B_{ij}B_{ij} - 1\right)\left\|\dot{\tilde{\varepsilon}}^p_{ij}\right\|^2 + 2A_{ij}B_{ij}f_d\tilde{Y}\left\|\dot{\tilde{\varepsilon}}^p_{ij}\right\| + A_{ij}A_{ij} = 0 \tag{2.56}$$

where the only admissible solution is

$$\left\|\dot{\tilde{\varepsilon}}_{ij}^{p}\right\| = \frac{A_{ij}B_{ij}f_d\tilde{Y} + \sqrt{\left(A_{ij}B_{ij}f_d\tilde{Y}\right)^2 + \left(1-(f_d\tilde{Y})^2 B_{ij}B_{ij}\right)A_{ij}A_{ij}}}{\left(1-(f_d\tilde{Y})^2 B_{ij}B_{ij}\right)} \tag{2.57}$$

Substituting (2.57) in (2.54) leads to:

$$\dot{\tilde{\varepsilon}}_{ij}^{p} = \underbrace{\Sigma_{ijmn}L^{-1}_{mnkl}\dot{\alpha}_{kl}}_{A_{ij}} + f_d\tilde{Y}\underbrace{\Sigma_{ijkl}\vec{\Upsilon}_{kl}}_{B_{ij}}\frac{A_{ij}B_{ij}f_d\tilde{Y} + \sqrt{\left(A_{ij}B_{ij}f_d\tilde{Y}\right)^2 + \left(1-(f_d\tilde{Y})^2 B_{ij}B_{ij}\right)A_{ij}A_{ij}}}{\left(1-(f_d\tilde{Y})^2 B_{ij}B_{ij}\right)} \tag{2.58}$$

Transforming (2.58) to the standard plastic strain metric using (2.51), finally gives:

$$\dot{\varepsilon}_{ij}^{p} = L^{-1}_{mnkl}\dot{\alpha}_{kl} + f_d\tilde{Y}\vec{\Upsilon}_{kl}\frac{A_{ij}B_{ij}f_d\tilde{Y} + \sqrt{\left(A_{ij}B_{ij}f_d\tilde{Y}\right)^2 + \left(1-(f_d\tilde{Y})^2 B_{ij}B_{ij}\right)A_{ij}A_{ij}}}{\left(1-(f_d\tilde{Y})^2 B_{ij}B_{ij}\right)} \tag{2.59}$$

where

$$\begin{aligned} A_{ij} &= \Sigma_{ijmn}L^{-1}_{mnkl}\dot{\alpha}_{kl} \\ B_{ij} &= \Sigma_{ijkl}\vec{\Upsilon}_{kl} \end{aligned} \tag{2.60}$$

The tensor L^{-1}_{mnkl} only affects the mapping of the rate of backstress, while the endochronic time measure affects the magnitude but not the direction of the non-linear contribution. Despite the unfriendly form of equation (2.59), it unveils one of the most interesting properties of this framework. The plastic strain can be decomposed in one term that is linear with respect to the backstress rate and a second term whose direction is controlled by the goal function only, and whose magnitude depends on the projection of the rate of backstress over the goal function, the limit surface and the plastic strain metric tensor, i.e:

$$\dot{\varepsilon}_{ij}^{p} = \underbrace{L^{-1}_{ijkl}\dot{\alpha}_{kl}}_{Linear} + \underbrace{f_d\tilde{Y}\frac{A_{ij}B_{ij}f_d\tilde{Y} + \sqrt{\left(A_{ij}B_{ij}f_d\tilde{Y}\right)^2 + \left(1-(f_d\tilde{Y})^2 B_{ij}B_{ij}\right)A_{ij}A_{ij}}}{\left(1-(f_d\tilde{Y})^2 B_{ij}B_{ij}\right)}}_{Magnitude}\underbrace{\vec{\Upsilon}_{ij}}_{Direction} \tag{2.61}$$

Examining more closely (2.61) the denominator $1-(f_d\tilde{Y})^2 B_{ij}B_{ij}$ becomes zero when the limit surface approaches one. In comparison with the plasticity framework, the goal function acts as

a “pseudo” flow rule and the limit surface as the “distance” to a hypothetical limit bounding surface. The elegance of this framework is that it keeps the associated behaviour of the plasticity equations, but manages to include a shear-volumetric coupling without sacrificing the associativity of the model.

The Figure 29, Figure 30, Figure 31 show graphically (Gudehus and Mašín, 2009) the relationship (2.61) in the Rendulic space. All the figures show two stress probes, marked in black and blue with a dashed line, where its strain response is drawn on the right hand side of the figure. The mappings, shown in the figures, correspond to the inverse problem, where the stress is perturbed by a constant finite magnitude of the stress and the strain is mapped. The initial conditions for all stress probes correspond to a limit surface of $\tilde{Y} = 0.75$ and $\tilde{Y} = 0.5$, the figure on the left shows the stress perturbation as a circle while that on the right is the mapped strain. The figure on the left includes the direction of goal functions and the magnitude of the limit surface in grayscale. By examining expression (2.61) it can be identified that the mapping of the strain with respect to the stress perturbation corresponds to an ellipse, which is a result of the inversion of the mapping tensor plus a component sharing the direction of the goal function by a certain magnitude. This component becomes more significant as the limit surface value increases and f_d increases. This is seen in Figure 29 where the probe at lower limit surface value does not exhibit a marked accumulated strain in the direction of the goal function, while the probe at higher limit surface (solid line) clearly has a significant contribution of the plastic strain in the goal function direction. Three different set of parameters have been chosen to illustrate the pseudo-flow rule.

Table 5: Parametric inputs

	f_d	k
Case 1	1.0	1.0
Case 2	0.5	1.0
Case 3	1.0	2.0

Case 1 illustrates the contribution of the non-linear term as the backstress state is closer to the limit surface. The solid line envelope is in that situation the limit surface ($f_d\tilde{Y}$) and $\tilde{Y}$ coincide while the dashed perturbation is in a region where the non-linear contribution is much less

significant than the situation closer to the limit surface, it is clear that as the recal term becomes stronger the response is more non-linear with respect to the backstress perturbations. Secondly, notice how the strain accumulation coincides with the direction of the goal function.

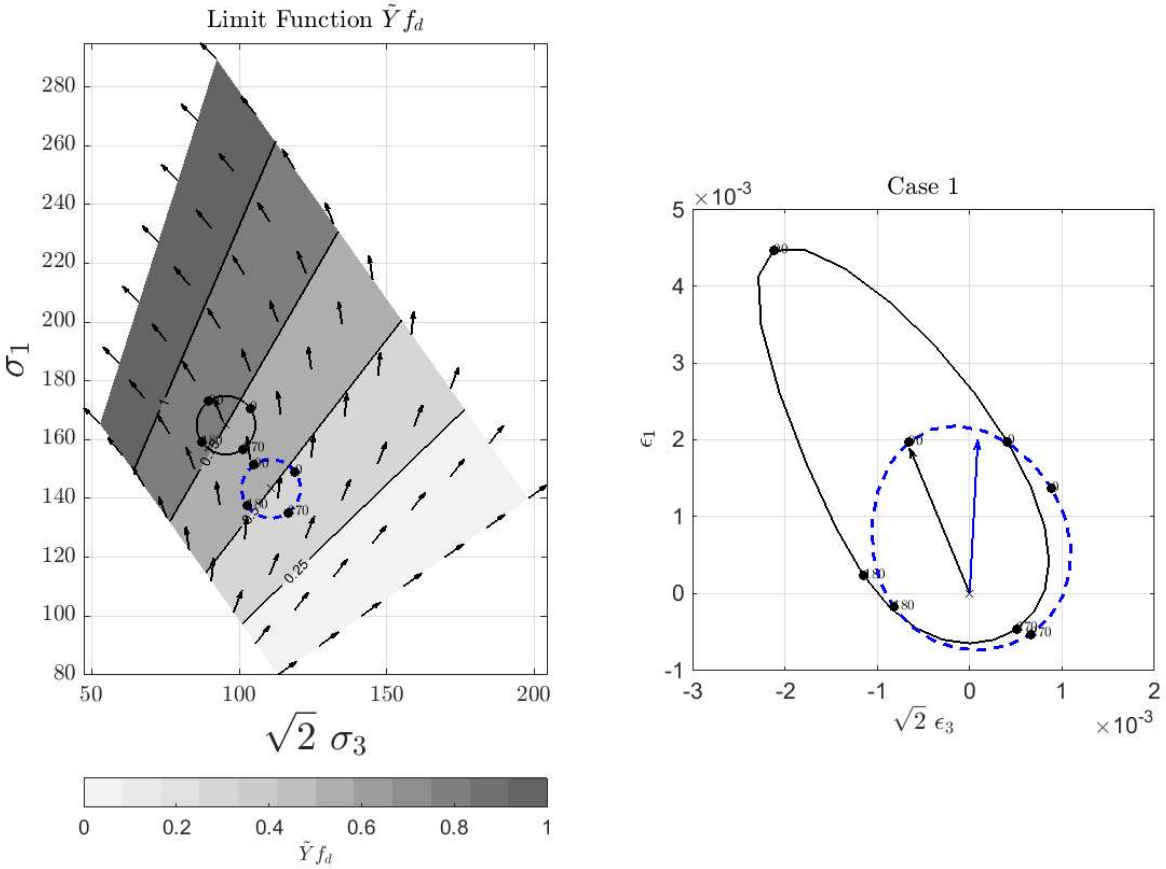


Figure 29: Stress probe for Case 1

Case 2 corresponds to a situation where f_d is small, therefore the limit surface will have a much lower value than case 1. In such condition the non-linear contribution is less significant and the linear part of the mapping governs the behaviour. Figure 30 outlines the importance of the f_d function as it is a substantial part of the recall term.

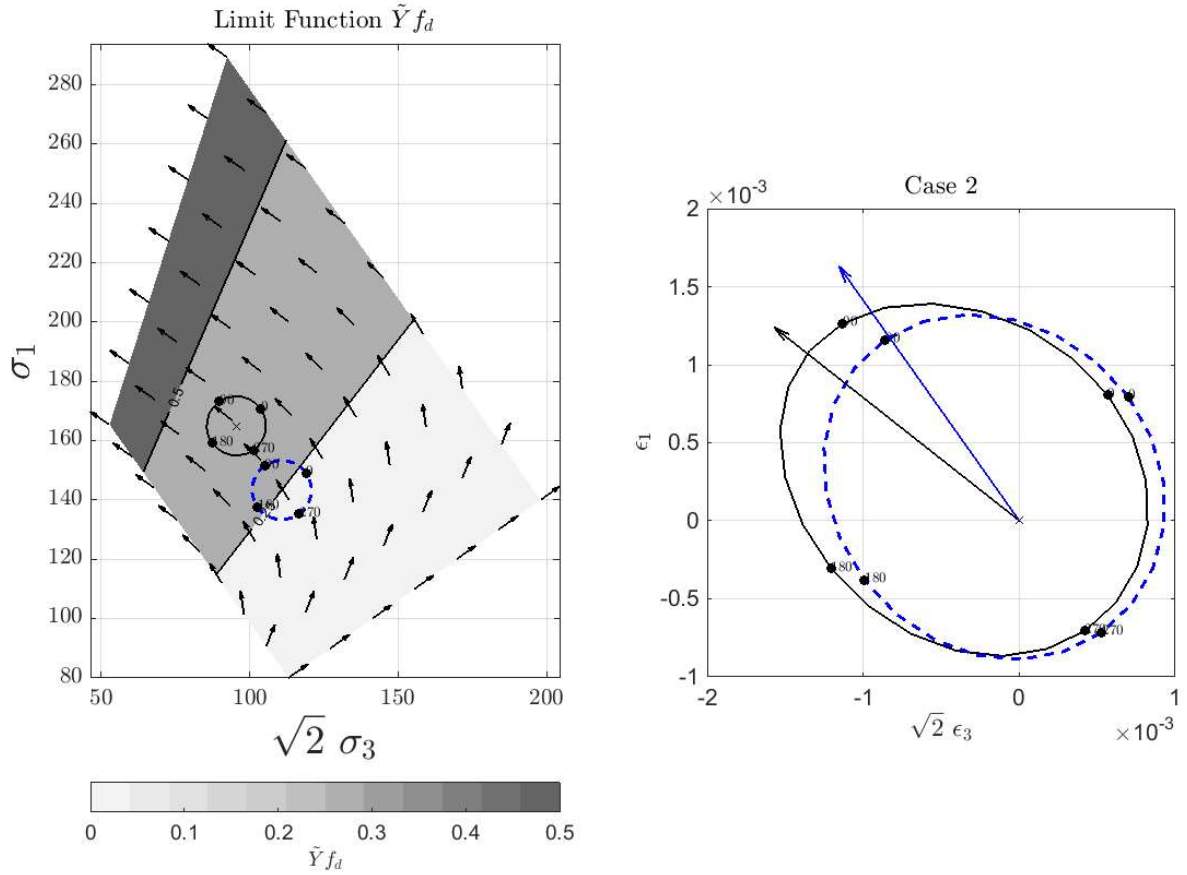


Figure 30: Stress probe for Case 2

Case 3 corresponds to similar conditions as case 1, but the metric of the strain has been perturbed. In this case the response follows the same trends as in case 1, but the mapping has a different shape as it is affected by the metric tensor Σ_{ijkl}.

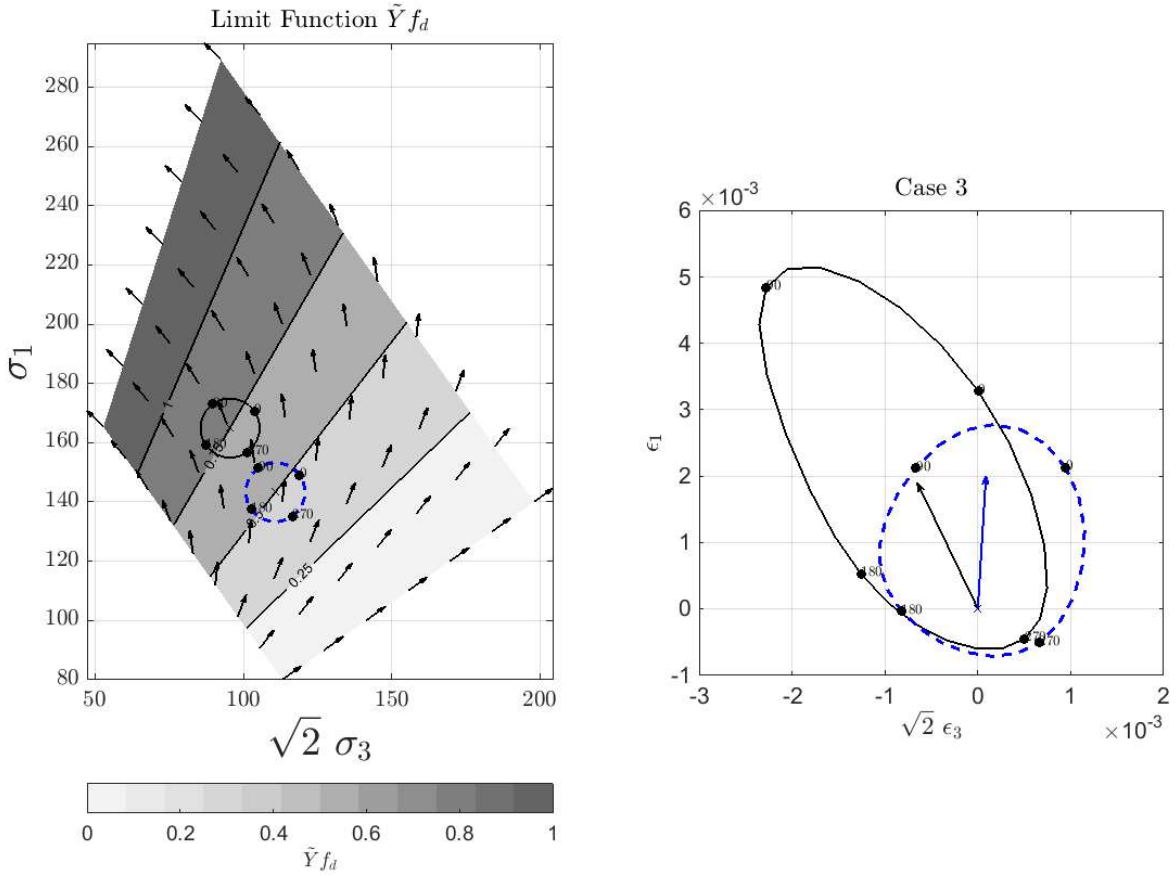


Figure 31: Stress probe for Case 3

The previous examples show the influence that the recall term has in the accumulation of plastic strain under a given backstress direction. It can be concluded that both the f_d function and the limit function have a significant effect on the magnitude of the plastic strain, while the goal function acts as a director of that "extra" plastic strain induced by the recall term. The mapping tensor can be interpreted as a stiffness tensor which is linear with respect to the rate of backstress producing plastic, but recoverable, strain, while the parameter "k" of the metric affects both the direction and magnitude of non-linear strain accumulation. As will be shown in the following section, this mathematical structure where the plastic strain can be decomposed into linear and non-linear parts with respect to the rate of backstress, is fundamental for ratchetting modelling.

2.3.7. REDUCTION OF NLKH RULE TO A DIFFERENTIAL EQUATION

It has been mentioned in the previous section that this type of hardening rules share the mathematical form of a Bernoulli ordinary differential equation. In this section, a less conventional treatment of the hardening rule is shown, akin to a classic ordinary differential equation (ODE) is carried out. The procedure reduces the system to two equations using the metric of the plastic strain:

$$\dot{\alpha}_{ij} = L_{ijkl}(\dot{\varepsilon}^{p}_{kl} - f_d \tilde{Y} \vec{\Upsilon}_{kl} \dot{z}) \tag{2.62}$$

The metric of the plastic strain can be transformed as:

$$\begin{aligned} \tilde{\varepsilon}^{p}_{ij} &= \Sigma_{ijkl} \dot{\varepsilon}^{p}_{ij} \\ \Sigma^{-1}_{ijkl} &= \left(\delta_{ik}\delta_{jl} - \frac{1}{3}\delta_{ij}\delta_{kl} \right) + \frac{1}{\sqrt{k}} \frac{1}{3} \delta_{ij}\delta_{kl} \end{aligned} \tag{2.63}$$

So:

$$\dot{\alpha}_{ij} = L_{ijkl} \left(\Sigma^{-1}_{klmn} \dot{\tilde{\varepsilon}}^{p}_{mn} - f_d \tilde{Y} \vec{\Upsilon}_{kl} \left\| \dot{\tilde{\varepsilon}}^{p}_{ij} \right\| \right) \tag{2.64}$$

The mapping tensor chosen is the orthogonal tensor, which constitutes the orthogonal projectors:

$$L_{ijkl} = \lambda^{vol} \left(\frac{1}{3}\delta_{ij}\delta_{kl} + \hat{\alpha}^{*}_{ij}\delta_{kl} \right) + \lambda^{dev} \left(\delta_{ik}\delta_{jl} - \frac{1}{3}\delta_{ij}\delta_{kl} - \hat{\alpha}^{*}_{ij}\delta_{kl} \right) \tag{2.65}$$

The limit surface is:

$$Y = f_d \left(\frac{3\sqrt{2}}{2g(\theta)} \left\| \hat{\alpha}^{*}_{ij} \right\| \right)^{\vartheta} = f_d \tilde{Y} \tag{2.66}$$

and the goal function is independent of f_d:

$$\begin{aligned}
&\vec{\Upsilon}_{ij} = \left(\sqrt{1-(ob^{GF})^2/3}\right)\vec{\alpha}^*_{ij} + \frac{ob^{GF}}{3}\delta_{ij} \\
&\beta = \left(\ln\left(\frac{\sqrt{3}}{ob_{\max}}+1\right)\right)^{1/\delta} \\
&ob^{GF} = ob_{\min}\exp\left(-\left(\beta\tilde{Y}\right)^{\delta}\right) + ob_{\max}\left(1-\exp\left(-\left(\beta\tilde{Y}\right)^{\delta}\right)\right)
\end{aligned} \tag{2.67}$$

With the previous ingredients the volumetric part of (2.64) is:

$$\dot{\alpha}_{kk} = \frac{\lambda^{vol}}{\sqrt{k}}\dot{\tilde{\varepsilon}}^p_{kk} - f_d\tilde{Y}(ob^{GF})\left\|\dot{\tilde{\varepsilon}}^p_{ij}\right\| \tag{2.68}$$

Also, as $\dot{\hat{\alpha}}^*_{ij} = \frac{\partial\hat{\alpha}^*_{ij}}{\partial\alpha^*_{kl}}\dot{\alpha}^*_{kl}$, expression (2.64) can be rewritten as:

$$\dot{\hat{\alpha}}^*_{ij} = \frac{\lambda^{dev}}{\alpha_{kk}}\left(\dot{\tilde{\varepsilon}}^{*p}_{ij} - \frac{1}{\sqrt{k}}\dot{\tilde{\varepsilon}}^p_{kk}\hat{\alpha}^*_{ij} - f_d\tilde{Y}\left(\left(\sqrt{1-(ob^{GF})/3}\right)\vec{\alpha}^*_{ij} + (ob^{GF})\hat{\alpha}^*_{ij}\right)\left\|\dot{\tilde{\varepsilon}}^p_{ij}\right\|\right) \tag{2.69}$$

Both expressions (2.68) and (2.69) are volumetric and deviatoric, and they conform to a first order differential equation:

$$\begin{aligned}
&\dot{\hat{\alpha}}^*_{ij} = \frac{\lambda^{dev}}{\alpha_{kk}}\left(\dot{\tilde{\varepsilon}}^{*p}_{ij} - \frac{1}{\sqrt{k}}\dot{\tilde{\varepsilon}}^p_{kk}\hat{\alpha}^*_{ij} - f_d\tilde{Y}\left(\left(\sqrt{1-(ob^{GF})^2/3}\right)\vec{\alpha}^*_{ij} + (ob^{GF})\hat{\alpha}^*_{ij}\right)\left\|\dot{\tilde{\varepsilon}}^p_{ij}\right\|\right) \\
&\dot{\alpha}_{kk} = \lambda^{vol}\left(\frac{1}{\sqrt{k}}\dot{\tilde{\varepsilon}}^p_{kk} - f_d\tilde{Y}(ob^{GF})\left\|\dot{\tilde{\varepsilon}}^p_{ij}\right\|\right)
\end{aligned} \tag{2.70}$$

Owing to the fact that there is coaxiality between the backstress and the plastic strain rate, expression (2.70) can be rewritten using the two invariants p_α and $\eta = J_\alpha/|p_\alpha|$ in a friendlier way:

$$\dot{\eta} = \frac{\sqrt{2}\lambda^{dev}}{2p}\left(\frac{\sqrt{2}}{2}\dot{\tilde{E}}_d^p - \left|\dot{\tilde{\varepsilon}}_{kk}^p\right|\frac{\sqrt{2}}{3\sqrt{k}}\eta - f_d\left(\frac{\eta}{g(\theta)}\right)^{\vartheta}\left(\left(\sqrt{1-(ob^{GF})^2/3}\right)+(ob^{GF})\frac{\sqrt{2}}{3}\eta\right)\left\|\dot{\tilde{\varepsilon}}_{ij}^p\right\|\right)$$
$$\dot{p}_\alpha = 3\lambda^{vol}\left(\frac{1}{\sqrt{k}}\dot{\tilde{\varepsilon}}_{kk}^p - f_d\left(\frac{\eta}{g(\theta)}\right)^{\vartheta}(ob^{GF})\left\|\dot{\tilde{\varepsilon}}_{ij}^p\right\|\right) \quad (2.71)$$

The system described in (2.71) is rate independent. The measure $\dot{z} = \left\|\dot{\tilde{\varepsilon}}_{ij}^p\right\|$ can be transformed into a time measure (akin to endochronic time) and the system can be further reduced, using the following quantities:

$$\dot{\tilde{E}}_d^p = \sqrt{2}\sqrt{\left\|\dot{\tilde{\varepsilon}}_{ij}^p\right\|^2 - 1/3\left|\dot{\tilde{\varepsilon}}_{kk}^p\right|^2}$$
$$ob^{\sim} = \frac{\dot{\tilde{\varepsilon}}_{kk}^p}{\left\|\dot{\tilde{\varepsilon}}_{ij}^p\right\|} \quad (2.72)$$

Substituting (2.72) into (2.71), equation (2.71) can be rewritten as rate form where the metric of plastic strains, "z", corresponds to the time (or endochronic time) and the obliquity, $ob^{\sim}$, represents the strain direction. Therefore, the derivative of η with respect to the endocronic time "z" can be defined as $\overset{z}{\eta}$, which is:

$$\overset{z}{\eta} = \frac{\sqrt{2}\lambda^{dev}}{2p}\left(\pm\sqrt{1-1/3\left|ob^{\sim}\right|^2} - \left|ob^{\sim}\right|\frac{\sqrt{2}}{3\sqrt{k}}\eta - f_d\left(\frac{\eta}{g(\theta)}\right)^{\vartheta}\left(\left(\sqrt{1-(ob^{GF})^2/3}\right)+(ob^{GF})\frac{\sqrt{2}}{3}\eta\right)\right) \quad (2.73)$$

$$\overset{z}{p}_\alpha = 3\lambda^{vol}\left(\frac{1}{\sqrt{k}}ob^{\sim} - f_d\left(\frac{\eta}{g(\theta)}\right)^{\vartheta}(ob^{GF})\right) \quad (2.74)$$

The expressions for λ^{dev} and λ^{vol} can be chosen arbitrarily without affecting the asymptotic values of η as discussed in 0. Given the form of equation (2.73) and (2.74), the phase portraits of the obtained ordinary differential equations for any given obliquity $ob^{\sim}$ can be drawn for any value of f_d. Figure 32 shows examples of phase portraits for equations (2.73) and (2.74) for obliquities of [-1,0,1] and f_d values of [0.5,1.0,1.5]

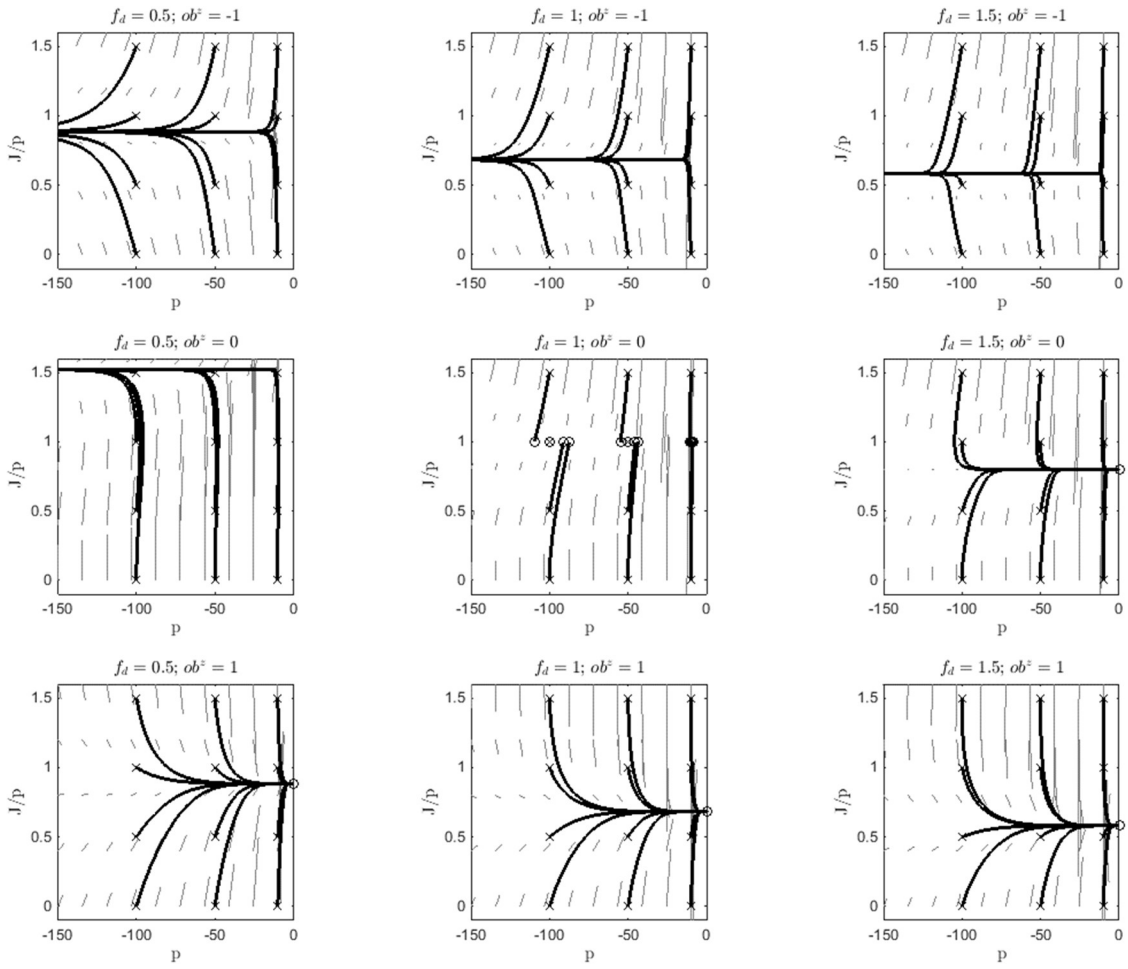


Figure 32: Phase portraits of J/p – p for equations (2.73) and (2.74) $\lambda^{dev} = 4000$ $\lambda^{vol} = 200$

In summary, it can be concluded that the rate equations (2.62) can be reduced to two equations using the obliquity and the endochronic time. Further discussion between endochronic time scales and non-linear kinematic hardening rules can be found in Watanabe and Atluri (1986a) and Erlicher and Point (2006).

2.3.8. RESPONSE UNDER STRESS CYCLES

In the previous section a description of the modelling framework has been given under static conditions. In this section it will be illustrated why this framework is useful to capture cyclic behaviour and the consequences of the pseudo flow rule described in the earlier section. As described in Wu and Niemunis (1996) and Jiang and Kurath (1996), a second property, being the key to model ratcheting, is that, given a closed backstress cycle, the direction of the strain accumulation can be predetermined. This is due to the fact that the linear terms of the hardening rule cancel out during the cycle leaving only the recall term to produce ratchetting. Therefore given a closed stress cycle the accumulated strain per cycle is:

$$\Delta\dot{\tilde{\varepsilon}}_{ij}^{p(Acc)} = \dot{\tilde{\varepsilon}}_{ij}^{p(+)} - \dot{\tilde{\varepsilon}}_{ij}^{p(-)} = 2 f_d \tilde{Y} \vec{\Upsilon}_{ij} \frac{A_{ij} B_{ij} f_d \tilde{Y} + \sqrt{\left(A_{ij} B_{ij} f_d \tilde{Y}\right)^2 + \left(1 - (f_d \tilde{Y})^2 B_{ij} B_{ij}\right) A_{ij} A_{ij}}}{\left(1 - (f_d \tilde{Y})^2 B_{ij} B_{ij}\right)} \quad (2.75)$$

Where

$$\begin{aligned} A_{ij} &= \Sigma_{ijmn} L^{-1}_{mnkl} \dot{\alpha}_{kl} \\ B_{ij} &= \Sigma_{ijkl} \vec{\Upsilon}_{kl} \end{aligned} \quad (2.76)$$

This is only exactly true for an infinitesimal closed cycle, however for a medium size stress cycle the backstress value in the centre of the circle still gives a good approximation as shown in chapter 4. To illustrate the consequences of (2.75), a set of closed cyclic stress perturbations with a magnitude of 10 kPa are run for the same cases described in section 2.3.6. Figure 33 and Figure 34 present the stress path of a cyclic probe, which consists of various two-way stress probes under constant stress direction. The cyclic probes in Figure 33 and Figure 34 correspond to two cycles and three stress directions (A-A', B-B', C-C') at different initial limit surface values. The figure on the right represents the strain path followed by the stress cycle and is represented by thin dotted lines. The strain envelope under static conditions for the first half cycle is also included, with an arrow indicating the direction of the goal function. The figure on the left depicts the goal function field and the limit surface is included to aid visualisation. It can be appreciated how the ratchetting, accumulation of strains after a stress cycle, always

follows the direction of the goal function regardless of the direction of the stress cycle, as obtained from expression (2.75).

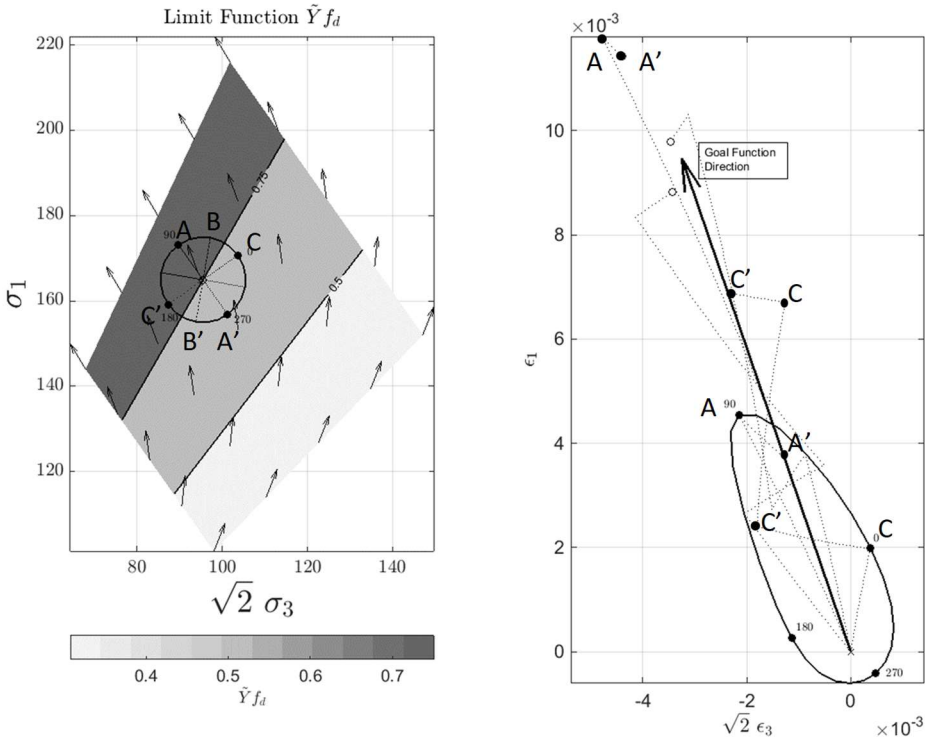


Figure 33: Ratcheting accumulation over 2 cycles for Case 1a

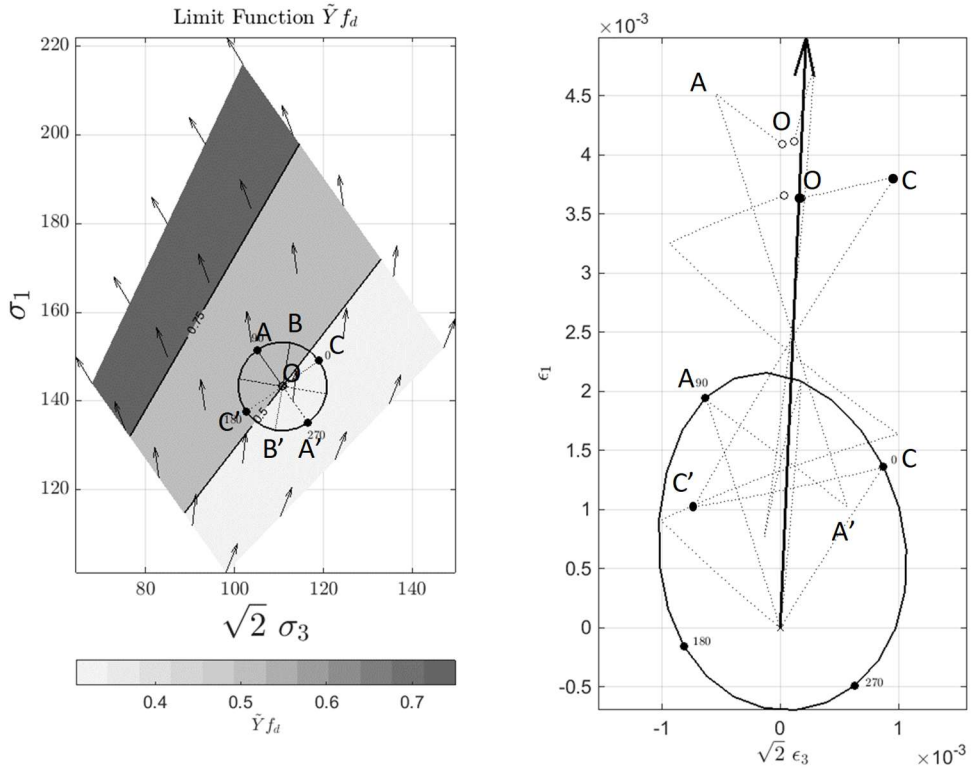


Figure 34: Ratcheting accumulation over 2 cycles for Case 1b

2.3.9. RESPONSE UNDER STRAIN CYCLES

Similar to derivations carried out in the previous section, it can be proved that non-linear kinematic hardening models always find a stable cycle under strain-controlled conditions (Lemaitre and Chaboche, 1994). This can be proven by integrating (2.62) over a closed cycle of strain, where z is the metric of the plastic strain and n_{ij} the normal of the yield surface:

$$\Delta\overset{N}{\alpha}_{ij} = \oint_{z} L_{ijkl}\vec{n}^{p}_{kl} - f_d\tilde{Y}L_{ijkl}\vec{\Upsilon}_{kl}dz = -2\int_{0}^{z} f_d\tilde{Y}L_{ijkl}\vec{\Upsilon}_{kl}dz \tag{2.77}$$

As the normal of the yield surface changes sign upon a reversal, the linear term of the integral cancels out and the only term affecting the backstress relaxation is the nonlinear term. A stable cycle will be defined by a situation where expression (2.77) is zero. In general, the backstress is going to relax in a direction opposite to the goal function until the backstress relaxation reaches $\Delta\alpha_{ij} = 0$. In the following section a quick method to obtain the stable cycles in the J/p - E_d plane using equation (2.73) is shown.

Proof:

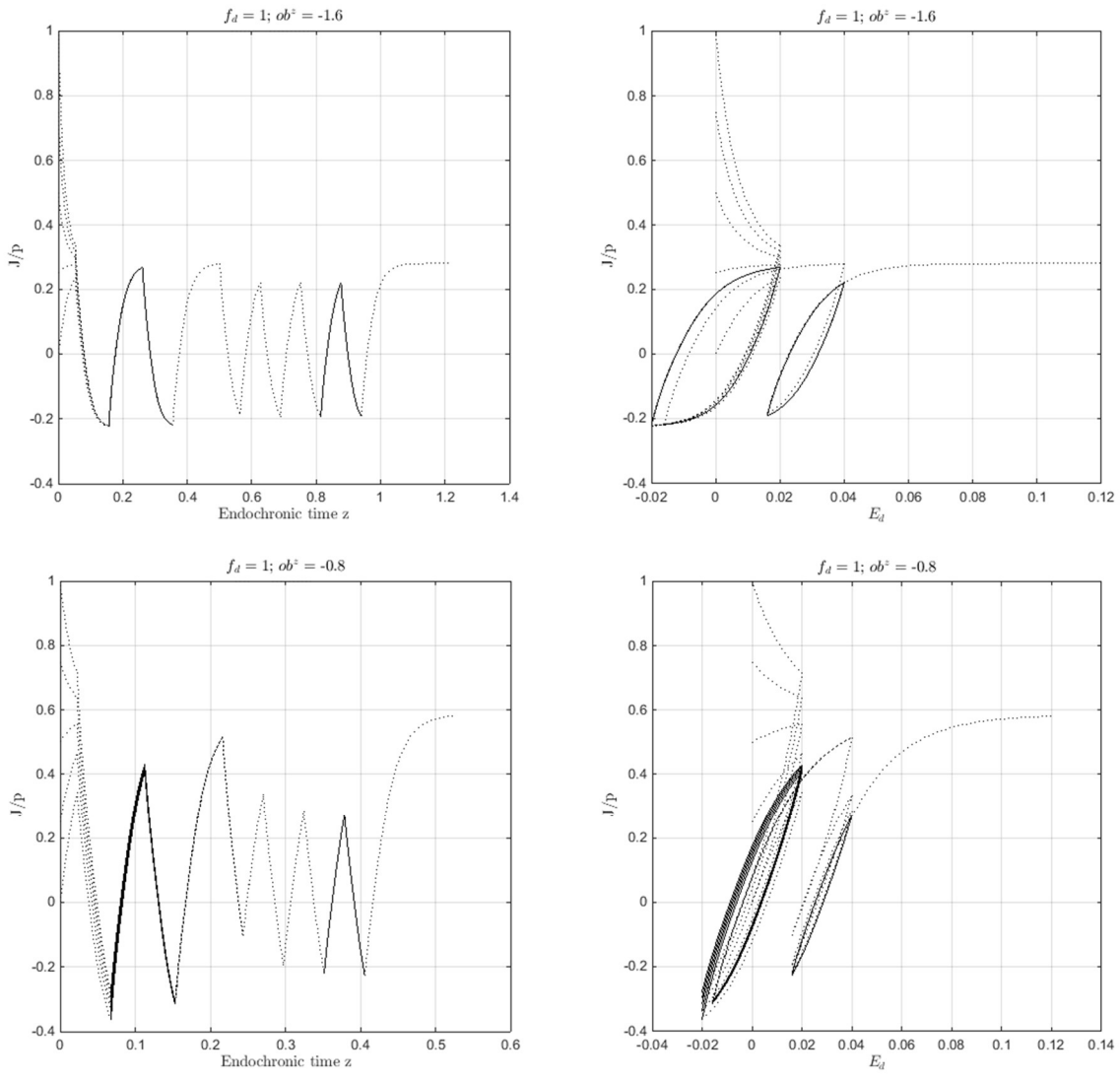
As, by definition, a stable cycle is a closed stress cycle where no ratcheting occurs, the method consists of finding the stress loop at which the stable condition is met. As the goal functions and limit surface are symmetric with respect to the p' axis, a condition (2.77) equal to zero is met in a cycle symmetric with respect to the axis p'. The previous property can be illustrated using expression (2.73) and the deviatoric strain instead of endochronic time. Owing to the fact that the rate of $\dot{\tilde{E}}^{p}_{d}$ can be negative but the rate of endochronic time is always positive, $\dot{z} > 0$, the pseudo-deviatoric strain can be defined depending on whether loading or unloading occurs:

$$\dot{\tilde{E}}^{p}_{d} = \pm\sqrt{2}\sqrt{\dot{z}^2 - 1/3\left|ob^{\sim}\right|^2} \tag{2.78}$$

For the condition where $\lambda^{dev} = 3p\tilde{\lambda}^{dev}$ equation (2.73) can be rewritten as:

$$\overset{z}{\eta}=\frac{3\sqrt{2}\tilde{\lambda}^{dev}}{2}\left(Sg(\dot{\tilde{E}}_d^p)\sqrt{1-1/3\left|ob^{\sim}\right|^2}-\left|ob^{\sim}\right|\frac{\sqrt{2}}{3\sqrt{k}}\eta-f_d\left(\frac{\eta}{g(\theta)}\right)^{\vartheta}\left(\left(\sqrt{1-(ob^{GF})^2/3}\right)+(ob^{GF})\frac{\sqrt{2}}{3}\eta\right)\right) \quad (2.79)$$

The former equation will always exhibit a stable symmetric cycle in the $\eta-E_d^p$ space. In addition, its area over a cycle in the $\eta-z$ space will be zero at the stable cycle. To illustrate the former property, Figure 35 shows various cycles obtained from expression (2.79), at various initial stress ratios, and under the obliquities $ob^{\sim}=\begin{bmatrix}-1.6 & -0.8 & 0.0\end{bmatrix}$. The figure shows the backstress in the J/p – z space on the left, while on the right the same path is shown in the J/p - E_d space. The stable cycle is marked with a solid line, while a dashed line indicates the stress path. It can be verified that, upon a closed strain cycle, the loop will always accommodates in a stable cycle regardless of the initial point.



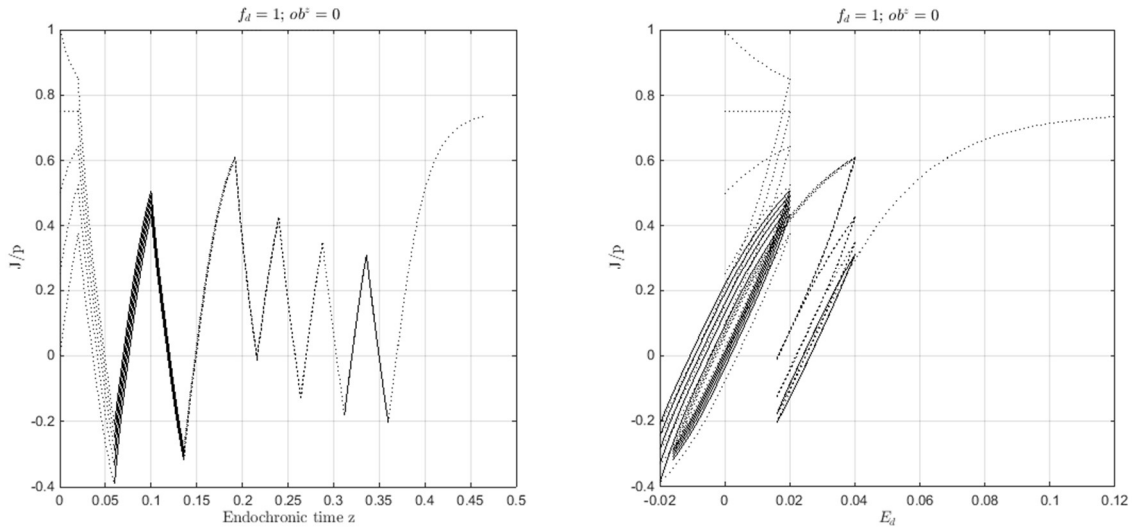


Figure 35: Stable cycles for equation (2.73) for different combinations of f_d and ob

2.3.10. SUPERPOSITION OF BACKSTRESSES

The concept of superposition of backstreses is used firstly in the field of metals (Chaboche, 1991) and differs from the concept of superposition in soil mechanics being not related with linear elastic response superposition.

From the previous sections it can be concluded that under asymmetric loading a unique hardening rule will produce a constant amount of accumulated strain per cycle. To improve the cyclic response of a single rule and to reduce the magnitude of the accumulated strain over a cycle, various strategies can be followed. The first one is the introduction of another history variable that reduces the influence of the limit surface over each cycle, which is normally achieved by reducing the effect of the recall term (Niemunis and Herle, 1997). A second strategy consists of the use of a combination of several backstress rules that cancel its ratchetting contribution (Chaboche, 1991). To illustrate the effect of combining backstresses, a simple example is shown corresponding to a basic rule plus a linear hardening rule. Under these conditions the amplitude of backstress is the sum of both hardening rules, therefore:

$$\begin{aligned} \alpha_{ij}^{T} &= \alpha_{ij}^{(1)} + \alpha_{ij}^{(2)} \\ \dot{\alpha}_{ij}^{(1)} &= f_e f_p L_{ijkl}\left(\dot{\varepsilon}_{kl}^{p} - Y\vec{\Upsilon}_{kl}\dot{z}\right) \\ \dot{\alpha}_{ij}^{(2)} &= C\dot{\varepsilon}_{ij}^{p} \end{aligned} \tag{2.80}$$

From expression (2.77) it can be observed that the linear rule cannot produce any ratchetting as the recall term is zero. Figure 36 and Figure 37 show in detail the stress path of the model described in (2.80) under triaxial conditions. It can be appreciated in Figure 37 how the system exhibits shakedown. More complex combinations of backstresses are presented in Chapter 4 with specialised hardening rules, but the fundamental idea remains the same.

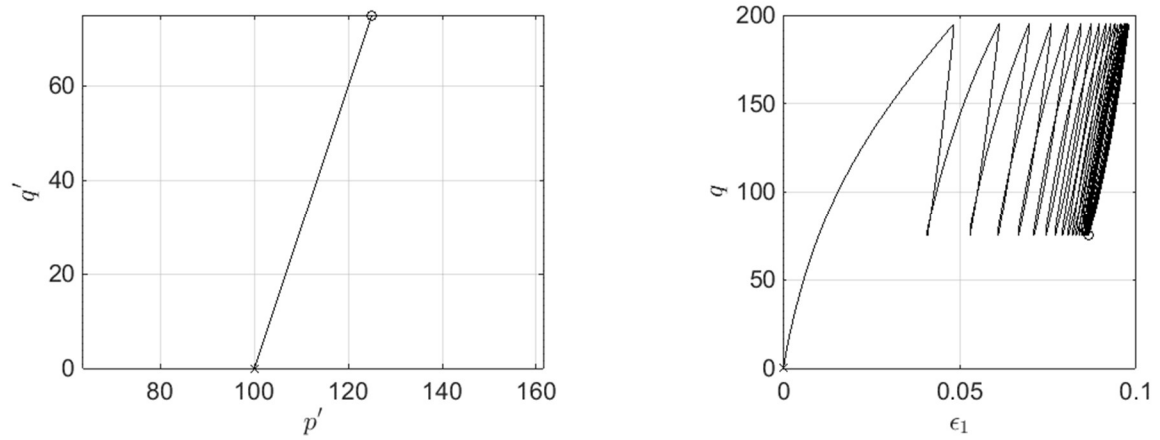


Figure 36: Response of a TXC with extra backstress

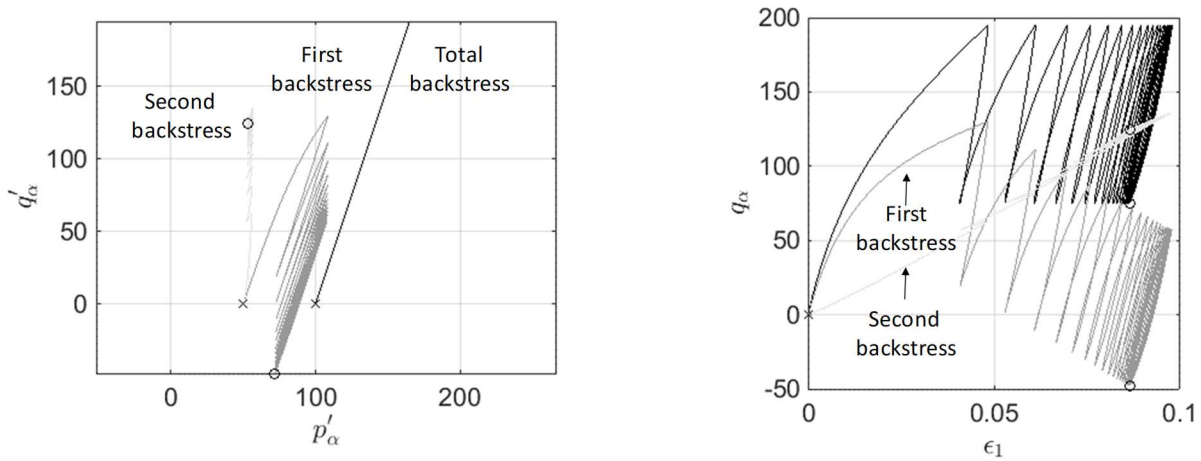


Figure 37: Detail of First and Second backstress (grey) and total stress black

2.4. THERMODYNAMIC ADMISIBILITY

This section provides some insight in the thermodynamic admissibility of the constitutive models proposed in this thesis. Several thermomechanical approaches exists to verify that a constitutive model complies with the Clausius-Duhem inequality. Good examples of the frameworks can be found in de Saxce (1992) or in Collins and Houlsby (1997) which later was further developed to the theory of hyperplasticity (Houlsby and Puzrin, 2007). In this thesis a similar methodology as described in de Saxce (1992) has been used as the concept of bipotentials and pseudo-potentials (Moreau, 1970) is more general and less strict than the Ziegler's orthogonality principle (Ziegler, 1977). In this section it is demonstrated that the general system of rate-independent equations described in section can be classified as an "*implicit standard material"* (de Saxce & Bousshine, 2002) and admits a bipotential form as described in Appendix I. The final part of the section studies under what conditions the thermodynamic admissibility is maintained for the general expression (2.23). A general set of definitions are included in Appendix I on the application of non-smooth mechanics to plasticity theory.

In order to keep a similar formalism than the mathematical formulation of de Saxce (1992), let us introduce the kinematical hardening variables $X_{ij} \in E$ (where *E* denotes strain space) and the endochronic time $z \in R$, with its corresponding associated variables being, respectively, the backstresses $\alpha_{ij} \in S$ (where S denotes stress) and the yield stress $m \in R$. These variables can be grouped in a velocity vector as $\dot{\kappa} = (\dot{\varepsilon}_{ij}^{p}, -\dot{X}_{ij}, -\left\|\dot{\varepsilon}_{ij}^{p}\right\|) \in E \times E \times R$ whose corresponding associated variables or thermodynamic forces are $\pi = (\sigma_{ij}, \alpha_{ij}, m) \in S \times S \times R$. Secondly, the "sets" corresponding to the elastic region are introduced as:

$$K_2 = \left\{ (\sigma_{ij}, m) \in S \times R \quad such \quad that \quad \left\|\sigma_{ij}\right\| - m \le 0 \right\} \tag{2.81}$$

and the elastic domain is defined by

$$K = \left\{ \pi = (\sigma_{ij}, \alpha_{ij}, m) \in F \quad such \quad that \quad (\sigma_{ij} - \alpha_{ij}, m) \in K_2 \right\} \tag{2.82}$$

The rate of endochronic time is defined as a measure of the strain rate, where:

$$f^*(\dot{\varepsilon}_{ij}^p, -z) = \sqrt{\dot{\varepsilon}_{ij}^p \Sigma_{ijkl} \Sigma_{klmn} \dot{\varepsilon}_{mn}^p} - \dot{z} \leq 0 \tag{2.83}$$

and the general non-linear kinematic hardening rule is given by:

$$\dot{X}_{ij} = \dot{\varepsilon}_{ij}^p - Y(\alpha_{ij}) \vec{\Upsilon}_{ij}(\alpha) \dot{z} \tag{2.84}$$

which is related linearly to the backstress by a positive definite fourth order tensor:

$$\alpha_{ij} = L_{ijkl} X_{kl} \tag{2.85}$$

It can be proved that the previous model admits a bipotential equal to

$$b(\dot{\kappa}, \pi) = \alpha_{ij} \vec{\Upsilon}_{ij}(\alpha_{ij}) Y(\alpha_{ij}) \dot{z} \tag{2.86}$$

where $\vec{\Upsilon}_{ij}(\alpha_{ij})$ is a unitary tensor field coaxial with α_{ij} and $Y(\alpha_{ij})$ is a tensor scalar function of α_{ij}. Equation (2.86) can be rewritten owing to the fact that the solution must belong to the set $(\sigma_{ij} - \alpha_{ij}, m) \in K_2$ and that (2.84) must be satisfied, therefore it can be rewritten as:

$$\begin{aligned} b(\dot{\kappa}, \pi) &= \alpha_{ij} \vec{\Upsilon}_{ij}(\alpha_{ij}) Y(\alpha_{ij}) \dot{z} + \coprod_{f^*}(\dot{\varepsilon}_{ij}^p, -z) + \\ &+ \coprod_{K_2}(\sigma_{ij} - \alpha_{ij}, m) + \coprod \left(\dot{X}_{ij} + Y(\alpha_{ij}) \vec{\Upsilon}_{ij}(\alpha) \dot{z} - \dot{\varepsilon}_{ij}^p \right) \end{aligned} \tag{2.87}$$

The next step is to prove that (2.87) is a bipotential, therefore it must be proved that

$$\forall (\dot{\kappa}', \pi') \in V \times F, \quad b(\dot{\kappa}', \pi') \geq \dot{\kappa}' : \pi' \tag{2.88}$$

And also that for each extremal couple the following condition holds:

$$b(\dot{\kappa}, \pi) = \varphi(\dot{\kappa}) + \chi(\pi) = \pi : \dot{\kappa} \Leftrightarrow \pi \in \partial_{\dot{\kappa}} b \Leftrightarrow \dot{\kappa} \in \partial_{\pi} b \tag{2.89}$$

To do so it must be shown that for any set of generalised velocities and stresses, such that $(\sigma_{ij} - \alpha_{ij}, m) \in K_2$, fulfilling the constrain (2.84) the definition of bipotential holds, therefore:

$$\forall \dot{\varepsilon}_{ij}^p, \dot{X}_{ij}, \left\| \dot{\varepsilon}_{ij}^p \right\| \quad \forall \sigma_{ij}, \alpha_{ij}, m \qquad \alpha_{ij} \vec{\Upsilon}_{ij}(\alpha_{ij}) Y(\alpha_{ij}) \dot{z} \geq \sigma_{ij} \dot{\varepsilon}_{ij}^p - \alpha_{ij} \dot{X}_{ij} - m \left\| \dot{\varepsilon}_{ij}^p \right\| \tag{2.90}$$

According to $(\sigma_{ij}-\alpha_{ij},m)\in K_2$, and remembering Cauchy-Schwarz inequality, the following inequality is always true

$$m\left\|\dot{\varepsilon}_{ij}^{p}\right\|\geq\left\|\sigma_{ij}-\alpha_{ij}\right\|\left\|\dot{\varepsilon}_{ij}^{p}\right\|\geq(\sigma_{ij}-\alpha_{ij})\dot{\varepsilon}_{ij}^{p} \tag{2.91}$$

But also using (2.84) in (2.91)

$$m\left\|\dot{\varepsilon}_{ij}^{p}\right\|\geq\left\|\sigma_{ij}-\alpha_{ij}\right\|\left\|\dot{\varepsilon}_{ij}^{p}\right\|\geq(\sigma_{ij}-\alpha_{ij})\dot{\varepsilon}_{ij}^{p}=\sigma_{ij}\dot{\varepsilon}_{ij}^{p}-\alpha_{ij}\left(\dot{X}_{ij}+Y(\alpha_{ij})\vec{\Upsilon}_{ij}(\alpha)\dot{z}\right) \tag{2.92}$$

which, rearranging, becomes

$$\alpha_{ij}Y(\alpha_{ij})\vec{\Upsilon}_{ij}(\alpha)\dot{z}=\sigma_{ij}\dot{\varepsilon}_{ij}^{p}-\alpha_{ij}\dot{X}_{ij}-(\sigma_{ij}-\alpha_{ij})\dot{\varepsilon}_{ij}^{p} \tag{2.93}$$

Substituting (2.91) in (2.93) shows that the following inequality is always true, which corresponds to the bipotential described in (2.86)

$$b(\dot{\kappa},\pi)=\alpha_{ij}Y(\alpha_{ij})\vec{\Upsilon}_{ij}(\alpha)\dot{z}\geq\sigma_{ij}\dot{\varepsilon}_{ij}^{p}-\alpha_{ij}\dot{X}_{ij}-m\left\|\dot{\varepsilon}_{ij}^{p}\right\| \tag{2.94}$$

Therefore it is proved that (2.86) is a bipotential. The next step is to show that any extremal couple for the bipotential fulfills (2.89) and that the subdifferential constituties the multivalued constitutive rule. Assuming any couple $(\dot{\kappa},\pi)$ such that $(\sigma_{ij}-\alpha_{ij},m)\in K_2$ fulfilling the constrains (2.84), then if the couple is extremal:

$$b(\dot{\kappa},\pi)=\dot{\kappa}:\pi \tag{2.95}$$

The condition of differential inclusion must hold, then for any extremal couple

$$\forall\pi' \qquad b(\dot{\kappa},\pi')-b(\dot{\kappa},\pi)\geq\dot{\kappa}:(\pi'-\pi) \tag{2.96}$$

$$\forall\dot{\kappa}' \qquad b(\dot{\kappa}',\pi)-b(\dot{\kappa},\pi)\geq(\dot{\kappa}'-\dot{\kappa}):\pi \tag{2.97}$$

To prove (2.96) π' is firstly substituted into the constraint (2.84), then it must be written:

$$\dot{X}_{ij}=\dot{\varepsilon}_{ij}^{p}-Y'\vec{\Upsilon}'_{ij}\,\dot{z} \tag{2.98}$$

Subtracting (2.98) and (2.84) the constrain holds:

$$(Y\vec{\Upsilon}_{ij} - Y'\vec{\Upsilon}'_{ij})\dot{z} = 0 \tag{2.99}$$

Secondly evaluating expression (2.87) on (2.96) is:

$$\begin{pmatrix} \coprod_{K_2}(\sigma'_{ij} - \alpha'_{ij}, m') - \coprod_{K_2}(\sigma_{ij} - \alpha_{ij}, m) \\ + \left(\alpha'_{ij} Y' \vec{\Upsilon}'_{ij} - \alpha_{ij} Y \vec{\Upsilon}_{ij}\right)\dot{z} \end{pmatrix} \geq (\sigma'_{ij} - \sigma_{ij})\dot{\varepsilon}^p_{ij} - (\alpha'_{ij} - \alpha_{ij})\dot{X}_{ij} \tag{2.100}$$

Taking (2.99) and the fact that $\dot{z} \geq 0$, equation (2.100) becomes:

$$\begin{pmatrix} \coprod_{K_2}(\sigma'_{ij} - \alpha'_{ij}, m') - \coprod_{K_2}(\sigma_{ij} - \alpha_{ij}, m) \\ + \left(\alpha'_{ij} - \alpha_{ij}\right) Y \vec{\Upsilon}_{ij}\dot{z} \end{pmatrix} \geq (\sigma'_{ij} - \sigma_{ij})\dot{\varepsilon}^p_{ij} - (\alpha'_{ij} - \alpha_{ij})\dot{X}_{ij} \tag{2.101}$$

Rearranging and substituting (2.84) the following condition is obtained:

$$\left(\alpha'_{ij} - \alpha_{ij}\right)\underbrace{\left(\dot{X}_{ij} + Y\vec{\Upsilon}_{ij}\dot{z}\right)}_{\dot{\varepsilon}^p_{ij}} \geq (\sigma'_{ij} - \sigma_{ij})\dot{\varepsilon}^p_{ij} \tag{2.102}$$

Substituting (2.102) into (2.101)

$$\coprod_{K_2}(\sigma'_{ij} - \alpha'_{ij}, m') - \coprod_{K_2}(\sigma_{ij} - \alpha_{ij}, m) \geq \left[(\sigma'_{ij} - \alpha'_{ij}) - (\sigma_{ij} - \alpha_{ij})\right]\dot{\varepsilon}^p_{ij} \tag{2.103}$$

Which is the flow rule, as a normality condition of the yield surface :

$$\dot{\varepsilon}^p_{ij} \in \partial \coprod_{K_2}(\sigma_{ij} - \alpha_{ij}, m) \tag{2.104}$$

As for extremal couples, the equality (2.94) must be reached, the dissipation “D” is equal to the bipotential for the extremal couples:

$$D = b(\dot{\kappa}, \pi) = \alpha_{ij}\vec{\Upsilon}_{ij}(\alpha_{ij})Y(\alpha_{ij})\dot{z} \tag{2.105}$$

Therefore, the general form is thermodynamically admissible as long as

$$b(\dot{\kappa}, \pi) = \alpha_{ij}Y(\alpha_{ij})\vec{\Upsilon}_{ij}(\alpha)\dot{z} \geq 0 \tag{2.106}$$

where “D” is the thermomechanical dissipation. According to (2.106), as far as the trace of the goal function is negative, expression (2.105) is always positive. The thermodynamic admissibility depends on the definition of the goal function, $\vec{\Upsilon}_{ij}$, and the input parameters. In

order to prove how the general equations that govern the material can be obtained (flow rule, hardening rule, Lagrange multipliers) the following example is provided using the bipotential in (2.86). In this respect, it is known that the bipotenial becomes the dissipative potential at extreme couples, then any set of extreme couples $(\dot{\kappa}, \pi)$ must be related by:

$$\inf_{\dot{\kappa}} (b(\dot{\kappa}, \pi) - \dot{\kappa} : \pi) = \inf_{\pi} (b(\dot{\kappa}, \pi) - \dot{\kappa} : \pi) = 0 \tag{2.107}$$

The constraints imposed in (2.87) need to be added to the optimization problem, and the former expression is then rewritten as:

$$b = \max \left(\sigma_{ij} \dot{\varepsilon}_{ij}^{p} - \alpha_{ij} \dot{X}_{ij} - m \left\| \dot{\varepsilon}_{ij}^{p} \right\| \right), \quad subjected \quad \begin{cases} f(\sigma_{ij} - \alpha_{ij}, m) \le 0 \\ \dot{X}_{ij} - \dot{\varepsilon}_{ij}^{p} + Y(\alpha_{ij}) \vec{\Upsilon}_{ij}(\alpha) \dot{z} = 0 \\ f^{*}(\dot{\varepsilon}_{ij}^{p}, -z) \le 0 \end{cases} \tag{2.108}$$

whose optimal objective value is

$$D = \alpha_{ij} \vec{\Upsilon}_{ij}(\alpha_{ij}) Y(\alpha_{ij}) \dot{z} \tag{2.109}$$

The former problem can be solved using Lagrangian multipliers where the Lagrangian is:

$$\begin{aligned} L = & -\sigma_{ij} \dot{\varepsilon}_{ij}^{p} + \alpha_{ij} \dot{X}_{ij} + m \left\| \dot{\varepsilon}_{ij}^{p} \right\| + \alpha_{ij} \vec{\Upsilon}_{ij}(\alpha_{ij}) Y(\alpha_{ij}) \dot{z} + \\ & + \lambda_{ij}^{(1)} \left(\dot{X}_{ij} - \dot{\varepsilon}_{ij}^{p} + Y(\alpha_{ij}) \vec{\Upsilon}_{ij}(\alpha) \dot{z} \right) + \lambda^{(2)} \left(\left\| \sigma_{ij} - \alpha_{ij} \right\| - m \right) + \lambda^{(3)} \left(\sqrt{\dot{\varepsilon}_{ij}^{p} \Sigma_{ijkl} \Sigma_{klmn} \dot{\varepsilon}_{mn}^{p}} - \dot{z} \right) \end{aligned} \tag{2.110}$$

with

$$\begin{aligned} & \frac{\partial L}{\partial \dot{\kappa}} = 0 \quad \frac{\partial L}{\partial \lambda_{ij}^{(1)}} \le 0 \qquad L = 0 \\ & \frac{\partial L}{\partial \pi} = 0 \quad \frac{\partial L}{\partial \lambda^{(2)}} \le 0 \quad \frac{\partial L}{\partial \lambda^{(3)}} \le 0 \end{aligned} \tag{2.111}$$

which leads to the flow rule and hardening rules, the yield surface is already defined in the set K_2:

$$\frac{\partial L}{\partial(-\dot{X}_{ij})} = -\alpha_{ij} - \lambda_{ij}^{(1)} = 0 \Leftrightarrow \lambda_{ij}^{(1)} = -\alpha_{ij}$$

$$\frac{\partial L}{\partial(\sigma_{ij})} = -\dot{\varepsilon}_{ij}^{p} + \lambda^{(2)} \frac{\sigma_{ij} - \alpha_{ij}}{\left\|\sigma_{ij} - \alpha_{ij}\right\|} = 0 \Leftrightarrow \dot{\varepsilon}_{ij}^{p} = \lambda^{(2)} \frac{\sigma_{ij} - \alpha_{ij}}{\left\|\sigma_{ij} - \alpha_{ij}\right\|} = \lambda^{(2)} \frac{\partial f}{\partial \sigma_{ij}}$$

$$\frac{\partial L}{\partial(m)} = \left\|\dot{\varepsilon}_{ij}^{p}\right\| - \lambda^{(2)} = 0 \Leftrightarrow \lambda_{ij}^{(2)} = \left\|\dot{\varepsilon}_{ij}^{p}\right\| \tag{2.112}$$

$$\frac{\partial L}{\partial \lambda_{ij}^{(1)}} = \left(\dot{X}_{ij} - \dot{\varepsilon}_{ij}^{p} + Y(\alpha_{ij})\vec{\Upsilon}_{ij}(\alpha)\dot{z}\right) \leq 0$$

$$\frac{\partial L}{\partial \lambda_{ij}^{(3)}} = \left(\dot{z} - \sqrt{\dot{\varepsilon}_{ij}^{p}\Sigma_{ijkl}\Sigma_{klmn}\dot{\varepsilon}_{mn}^{p}}\right) \leq 0$$

As $\dot{X}_{ij}$ and α_{ij} are related linearly by (2.85), from (2.112) the final expression is obtained:

$$\dot{\alpha}_{ij} = L_{ijkl}\left(\dot{\varepsilon}_{kl}^{p} - Y(\alpha_{ij})\vec{\Upsilon}_{kl}(\alpha)\dot{z}\right) \tag{2.113}$$

2.5. APPLICATION OF NON-LINEAR KINEMATIC HARDENING RULES TO SOILS

This section describes how to include dependencies on the void ratio and other history variables for non-linear kinematic hardening models following expression (2.23). The section initially provides some general definitions, going on to introduce two examples for sand and clay using the general expression. It can be concluded that, in general, the structure of the equations presented so far is similar to hypoplasticity *amorphous* models, which are characterized by a rate form only dependent on the backstress (Kolymbas, 1991b).

$$\dot{\alpha}_{ij}(\dot{\varepsilon}^p_{kl},\alpha_{ij}) = L_{ijkl}\left(\dot{\varepsilon}^p_{kl} - f_d\tilde{Y}\vec{\Upsilon}_{kl}\dot{z}\right) \tag{2.114}$$

The following properties apply for *amorphous* models as far as they use tensors $\hat{a}_{ij}$ or functions coaxial with α_{ij}:

$$\begin{aligned}\dot{\alpha}_{ij}(\lambda\dot{\varepsilon}^p_{kl},\alpha_{ij}) &= \lambda\dot{\alpha}_{ij}(\dot{\varepsilon}^p_{kl},\alpha_{ij})\\ \dot{\alpha}_{ij}(\dot{\varepsilon}^p_{kl},\lambda\alpha_{ij}) &= \lambda\dot{\alpha}_{ij}(\dot{\varepsilon}^p_{kl},\alpha_{ij})\end{aligned} \tag{2.115}$$

However, when a dependence of the void ratio is included in the recall term via f_d function, the models are named *endomorphous*. When a dependency of f_d as a function is included, the previous property becomes relaxed and is true if and only if:

$$\begin{aligned}&\dot{\alpha}_{ij}(\lambda\dot{\varepsilon}^p_{kl},\alpha_{ij}) = \lambda\dot{\alpha}_{ij}(\dot{\varepsilon}^p_{kl},\alpha_{ij})\\ &\dot{\alpha}_{ij}(\dot{\varepsilon}^p_{kl},\lambda\alpha_{ij}) = \lambda\dot{\alpha}_{ij}(\dot{\varepsilon}^p_{kl},\alpha_{ij}) \qquad \textit{if} \qquad \dot{f}_d = 0\end{aligned} \tag{2.116}$$

Both proposed clay and sand models are *endomorphous*.

2.5.1. NON-LINEAR KINEMATIC HARDENING RULE FOR SAND

This section describes how to build a model for sand using the general expression (2.23). To do so the same expression of Gudehus (1996) and Bauer (1996) for the function f_d is used

$$f_d = \left(\frac{e - e_d}{e_c - e_d} \right)^{\alpha} \tag{2.117}$$

where the inputs are dependent on the backstress internal variable, the other auxiliary functions being:

$$\begin{aligned} e_d &= e_{d0} \exp\left(-\left(\frac{-\alpha_{kk}^T}{h_s} \right)^n \right) \\ e_c &= e_{c0} \exp\left(-\left(\frac{-\alpha_{kk}^T}{h_s} \right)^n \right) \end{aligned} \tag{2.118}$$

with $e_{c0}, h_s, n\ e_{d0}$ being input parameters representing the critical state line (CSL) position in the e-p plane and the maximum density line. Condition $\dot{f}_d = 0$ occurs if the total backstress path travels along any line defined by:

$$e \sim \exp\left(-\left(\frac{-\alpha_{kk}^T}{h_s} \right)^n \right) \tag{2.119}$$

The condition at which $\dot{f}_d = 0$ needs to be explored, differentiating expression (2.117):

$$\dot{f}_d = \frac{\alpha}{e - e_d} f_d \dot{e} + \left(\alpha e_c \left(\frac{|\alpha_{kk}|}{h_s} \right)^n |\alpha_{kk}|^{-1} - \frac{\alpha (e - e_c) e_d}{(e - e_d)} \left(\frac{|\alpha_{kk}|}{h_s} \right)^n |\alpha_{kk}|^{-1} \right) \frac{f_d n}{e_c - e_d} \dot{\alpha}_{kk} \tag{2.120}$$

The previous equation can be combined with (2.73), considering that, in practical terms, all the volumetric strain is plastic and therefore:

$$\dot{\varepsilon}_{kk}^p \approx \frac{\dot{e}}{1 + e} \tag{2.121}$$

The void ratio can be transformed in the metric of $\dot{\tilde{\varepsilon}}_{ij}^{p}$ similarly as carried out in the previous section:

$$\tilde{\varepsilon}_{ij}^{*p}+\frac{\sqrt{k}}{3}\tilde{\varepsilon}_{kk}^{p}\delta_{ij}=\varepsilon_{ij}^{p} \tag{2.122}$$

Then

$$\dot{e}=(1+e)\sqrt{k}\dot{\tilde{\varepsilon}}_{kk}^{p} \tag{2.123}$$

Substituting (2.123) in (2.120)

$$\dot{f}_d=\frac{\alpha}{e-e_d}f_d(1+e)\sqrt{k}\dot{\tilde{\varepsilon}}_{kk}^{p}+\left(\alpha e_c\left(\frac{|\alpha_{kk}|}{h_s}\right)^{n}|\alpha_{kk}|^{-1}-\frac{\alpha(e-e_c)e_d}{(e-e_d)}\left(\frac{|\alpha_{kk}|}{h_s}\right)^{n}|\alpha_{kk}|^{-1}\right)\frac{f_d n}{e_c-e_d}\dot{\alpha}_{kk} \tag{2.124}$$

which, in invariant form, is:

$$\dot{f}_d=\frac{\alpha}{e-e_d}f_d(1+e)\sqrt{k}\dot{\tilde{\varepsilon}}_{kk}^{p}+\left(\alpha e_c\left(\frac{|3p|}{h_s}\right)^{n}|3p|^{-1}-\frac{\alpha(e-e_c)e_d}{(e-e_d)}\left(\frac{|3p|}{h_s}\right)^{n}|3p|^{-1}\right)\frac{3f_d n}{e_c-e_d}\dot{p} \tag{2.125}$$

Using the endochronic time z the above expression becomes:

$$\overset{z}{f}_d=\frac{\alpha}{e-e_d}f_d(1+e)\sqrt{k}ob^{\sim}+\left(\alpha e_c\left(\frac{|3p|}{h_s}\right)^{n}|3p|^{-1}-\frac{\alpha(e-e_c)e_d}{(e-e_d)}\left(\frac{|3p|}{h_s}\right)^{n}|3p|^{-1}\right)\frac{3f_d n}{e_c-e_d}\overset{z}{p} \tag{2.126}$$

This equation is auxiliary and helps to evaluate the evolution of f_d as a function of void ratio, backstress and obliquity. The system of ordinary differential equations to solve follows a similar structure as (2.73), but is enriched by another equation including the dependency on the void ratio. The system of differential equations becomes:

$$\overset{z}{\eta}=\frac{\sqrt{2}\lambda^{dev}}{2p}\left(\pm\sqrt{1-1/3|ob^{\sim}|^{2}}-|ob^{\sim}|\frac{\sqrt{2}}{3\sqrt{k}}\eta-f_d\left(\frac{\eta}{g(\theta)}\right)^{\vartheta}\left(\left(\sqrt{1-(ob^{GF})^{2}/3}\right)+(ob^{GF})\frac{\sqrt{2}}{3}\eta\right)\right) \tag{2.127}$$

$$\overset{z}{p}=3\lambda^{vol}\left(\frac{1}{\sqrt{k}}ob^{\sim}-f_d\left(\frac{\eta}{g(\theta)}\right)^{\vartheta}(ob^{GF})\right) \tag{2.128}$$

$$\overset{z}{e}=(1+e)\sqrt{k}ob^{\sim} \tag{2.129}$$

The rate of f_d can be used as a constraint, as $\overset{z}{f}_d<0$ is an undesirable condition for some strain paths where $ob^{\sim}<0$. Then the constraint to impose uses the following complementary function:

$$\overset{z}{f}_d=\frac{\alpha}{e-e_d}f_d(1+e)\sqrt{k}ob^{\sim}+\left(\left(\alpha e_c-\frac{\alpha(e-e_c)e_d}{(e-e_d)}\right)\left(\frac{|3p|}{h_s}\right)^n|3p|^{-1}\right)\frac{3f_dn}{e_c-e_d}\overset{z}{p} \tag{2.130}$$

As mentioned in the previous section, a situation where $\dot{f}_d<0$ and the stress path does not travel to an absolute attractor is undesirable as it may lead to and exessively high asymptotic attractor. For good practice the following constraints are enforced:

$$f_d<1 \qquad \overset{z}{f}_d\geq 0 \qquad for \qquad ob^{\sim}\in[-\sqrt{3},0] \tag{2.131}$$

$$f_d>1 \qquad \overset{z}{f}_d\leq 0 \qquad for \qquad ob^{\sim}\in[-\sqrt{3},0] \tag{2.132}$$

As a consequence, λ^{vol} and λ^{dev} in equations (2.127) and (2.128) must be chosen so that the previous conditions are fulfilled. A good rule of thumb that later renders the model easier to calibrate is to use the slope of the critical state line (CSL) as a reference stiffness. In this case the CSL follows a slope defined by:

$$e\sim\exp\left(-\left(\frac{-\alpha_{kk}}{h_s}\right)^n\right) \tag{2.133}$$

whose stiffness is:

$$\dot{\alpha}_{kk}=3(1+e)\frac{h_s}{en}\left(\frac{|\alpha_{kk}|}{h_s}\right)^{1-n}\dot{\varepsilon}^p_{kk} \tag{2.134}$$

Under isotropic conditions the backstress follows a slope parallel to the CSL, however for different obliquities the backstress path travels to a constant η asymptote. To do so the extra contribution of the mapping tensor to the volumetric stiffness is normalised as:

$$\begin{aligned}
\vec{L}_{ijkl} &= \frac{1}{1+\left|S_f-1\right|\left(1+1/3\left\|\hat{\alpha}_{ij}^{*}\right\|\right)} L_{ijkl} \\
L_{ijkl} &= \left(\delta_{ik}\delta_{jl}-\frac{1}{3}\delta_{ij}\delta_{kl}-\hat{\alpha}_{ij}^{*}\delta_{kl}\right)+S_f\left(\frac{1}{3}\delta_{ij}\delta_{kl}+\hat{\alpha}_{ij}^{*}\delta_{kl}\right) \\
S_f &= \frac{\lambda^{vol}}{\lambda^{dev}}
\end{aligned} \tag{2.135}$$

Also, it is known that the system will travel towards an asymptote that is unknown exactly "a priori", however it is well known that this condition $\eta^{Assimp} \leq \frac{\eta}{g(\theta) f_d}$ is always true. Substituting into (2.128) it can be seen that, whatever the value of η^{Assimp}, it supposes a subtraction of the volumetric stiffness as:

$$\dot{\alpha}_{kk} = \frac{\lambda^{vol}}{\sqrt{k}}\dot{\tilde{\varepsilon}}_{kk}^{p} - f_d\tilde{Y}(\eta^{Assimp})(ob^{GF}(\eta^{Assimp}))\left\|\dot{\tilde{\varepsilon}}_{ij}^{p}\right\| \tag{2.136}$$

Therefore, to compensate, an extra contribution to the stiffness as a function of η needs to be included. After all the corrections, the stiffness function f_p is:

$$\begin{aligned}
f_p = \lambda_{dev} &= \frac{(1+e)\frac{h_s}{en}\left(\frac{|\alpha_{kk}|}{h_s}\right)^{1-n}\left(1+3/2\tilde{Y}\left\|n_{ij}^{*}+k/3n_{kk}\delta_{ij}\right\|\right)}{1+\left|S_f-1\right|\left(1+1/3\left\|\hat{\alpha}_{ij}^{*}\right\|\right)} \\
L_{ijkl} &= \left(\delta_{ik}\delta_{jl}-\frac{1}{3}\delta_{ij}\delta_{kl}-\hat{\alpha}_{ij}^{*}\delta_{kl}\right)+S_f\left(\frac{1}{3}\delta_{ij}\delta_{kl}+\hat{\alpha}_{ij}^{*}\delta_{kl}\right) \\
S_f &= \frac{\lambda^{vol}}{\lambda^{dev}}
\end{aligned} \tag{2.137}$$

where the shape factor S_f is an input to the model. Function f_p only takes into account the dependence on the mean total backstress but does not include a dependence with the void ratio. To include a dependence on the void ratio another function borrowed from hypoplasticity is used, which is defined as:

$$f_e = \left(\frac{e_c}{e} \right)^{\beta} \tag{2.138}$$

This function introduces the dependence of the stiffness on the void ratio and reinforces the asymptotic character of f_d for $_{ob}\tilde{} = \left[-\sqrt{3}, 0 \right]$. When the state is below the critical state line in the e-p plane, f_e becomes greater than one $f_e > 1$. On the other hand, if state is above the CSL, $f_e < 1$ and the stiffness is reduced, bringing the backstress closer to the CSL as the slope is lower than the reference CSL slope.

2.5.1.1. Stress paths for sand model

Following the same methodology described in 2.3.7 the implications of the chosen functions are illustrated using the methodology described in 2.3.7. The void ratio has been added to the diagrams as a new unknown, the range of obliquities studied goes from $_{ob}\tilde{} = \left[-\sqrt{3}, 0.5 \right]$ and the inputs are shown in Table 6. Two different cases, with and without considering the f_e function are shown.

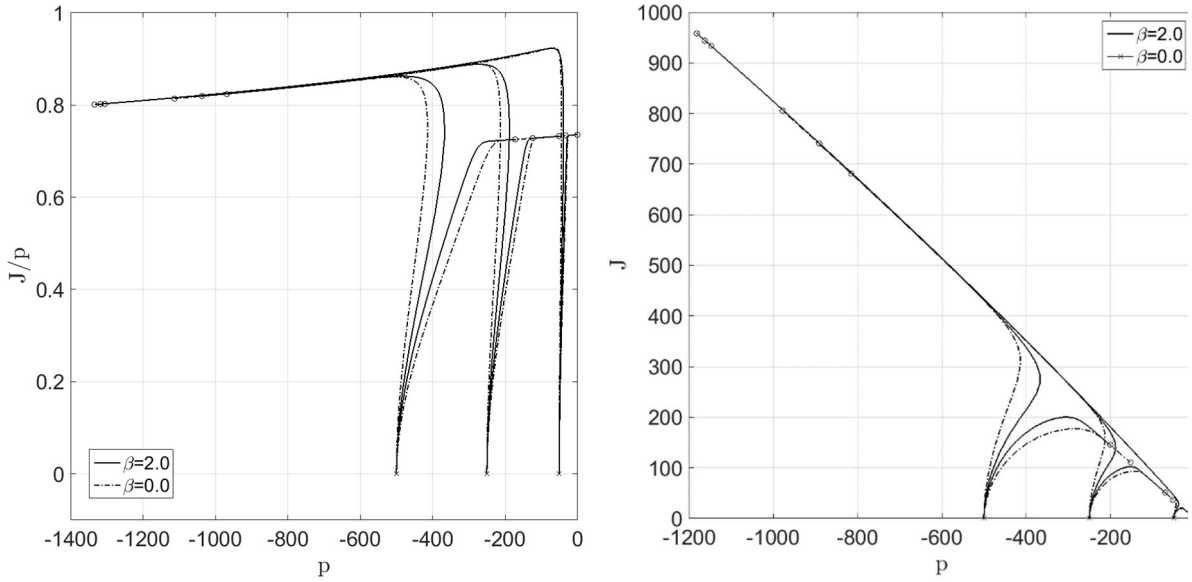
Table 6: Input values for sand model

	e_{c0}	e_{d0}	h_s	n	α	β	g(θ)	$\mathcal{G}$	S_f	ob_{min}	ob_{max}	δ	k
Reference	1.05	0.65	25E3	0.85	0.24	2.0	0.75	0.9	2.0	-1.73	0.8	1.8	1.0
No fe func.	1.05	0.65	25E3	0.85	0.24	0.0	0.75	0.9	2.0	-1.73	0.8	1.8	1.0

Figure 38, Figure 39, Figure 40 and Figure 41 present the backstress paths under a constant strain direction for various initial conditions. Three initial stresses are investigated at two different void ratios for dense and loose conditions (0.75 and 1.1). A total of 12 stress paths is shown in each figure where the dashed line represents the cases where the function f_e is taken to be the unity. Each figure represents the independent variables of the ODE: J/p – p spaces, and e – p spaces, the stress paths in the f_d – e and J-p spaces have been included to assess the validity of the proposed model.

Pure deviatoric strain (ob=0)

Figure 38 shows the stress path under purely deviatoric conditions, which is representative of undrained shear tests. It can be observed how the stress path travels towards critical state conditions (f_d=1) for both the loose and dense states (Figure 38c). The model behaves as a typical sand where the cases above the CSL it behaves as a loose sand and below the CSL as a dense sand (Figure 38b). Secondly it can be appreciated how the function f_e alters the stiffness of the model modifying its overall response (Figure 38a, Figure 38b).



(a) (b)

Figure 38: Strain-Backstress paths for pure deviatoric strain conditions (ob=0)

Purely Isotropic compression

Figure 39 shows the stress paths corresponding to the minimum possible obliquity of $-\sqrt{3}$, which corresponds to purely isotropic compression conditions. As the reference stiffness is taken from the CSL any isotropic compression test will be parallel to it and f_d does not evolve reaching $\dot{f}_d = 0$, this only occurs when the function f_e is not used, on the other hand, when f_e comes into action the stress path will converge to the CSL and once there they will follow the CSL.

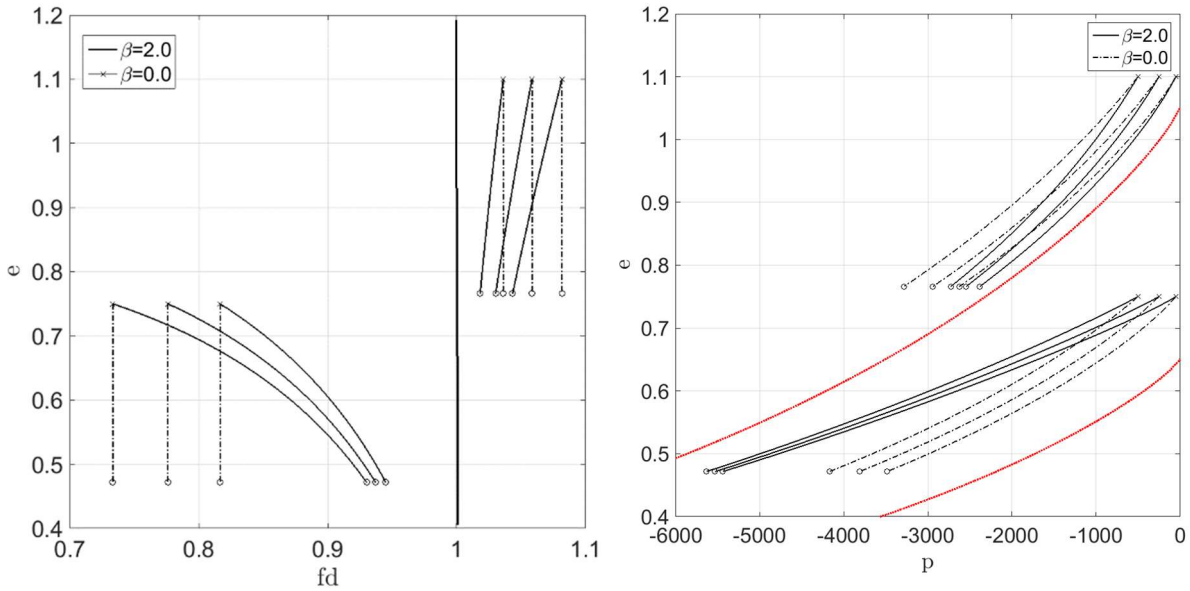


Figure 39: Strain-Backstress paths for isotropic conditions (ob=−√3)

Oedometric conditions

Figure 40 shows the model response under oedometric conditions, which corresponds to an obliquity of -1. The stress path will reach an asymptote which depends on its initial void ratio (Figure 40a) and the stress-strain paths will exhibit a larger stiffness in the volumetric direction than predicted in isotropic conditions. In general the stress path will travel towards a value of f_d that does not need to be 1 and will depend on the inputs of the goal function and the limit surface.

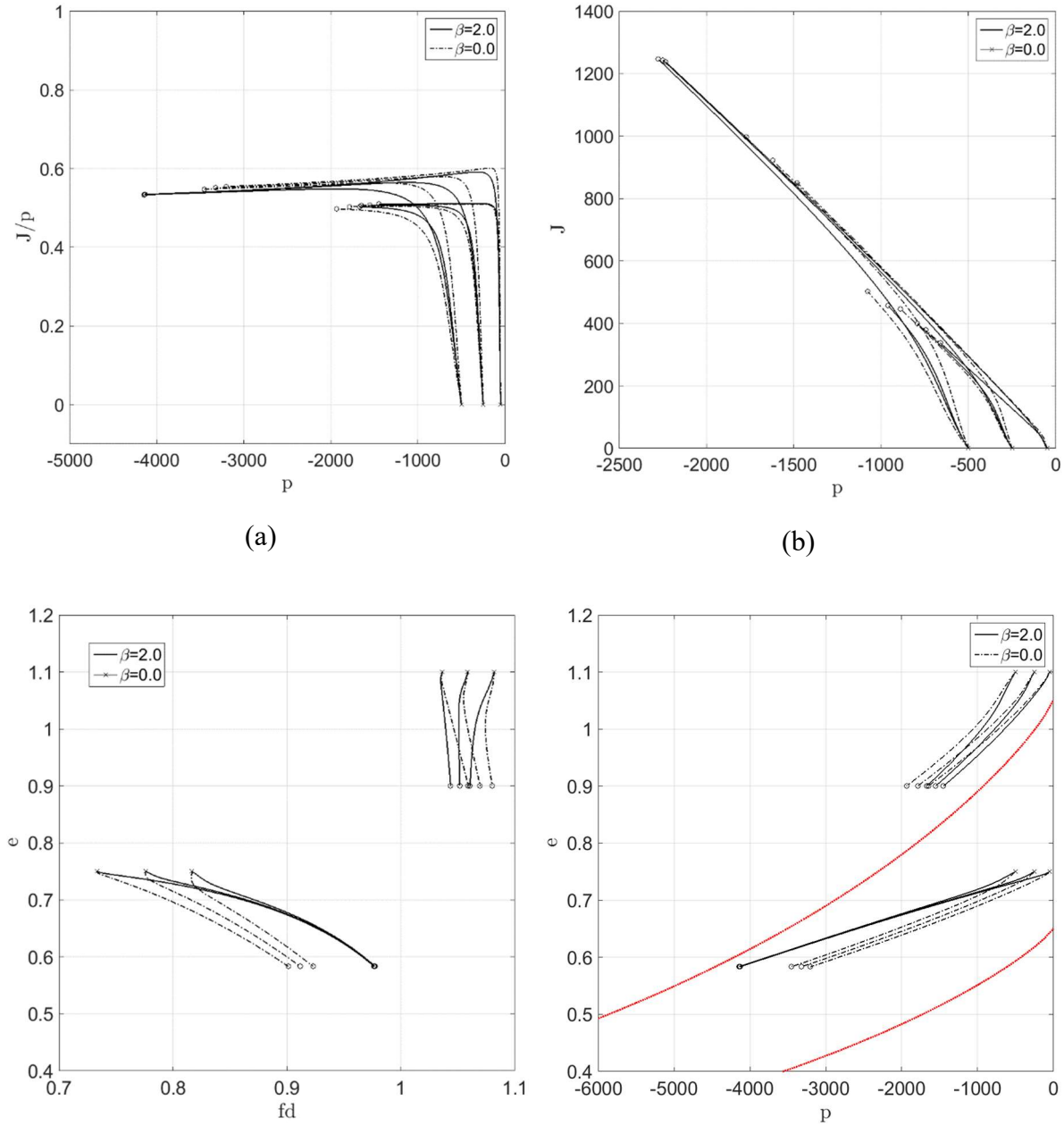
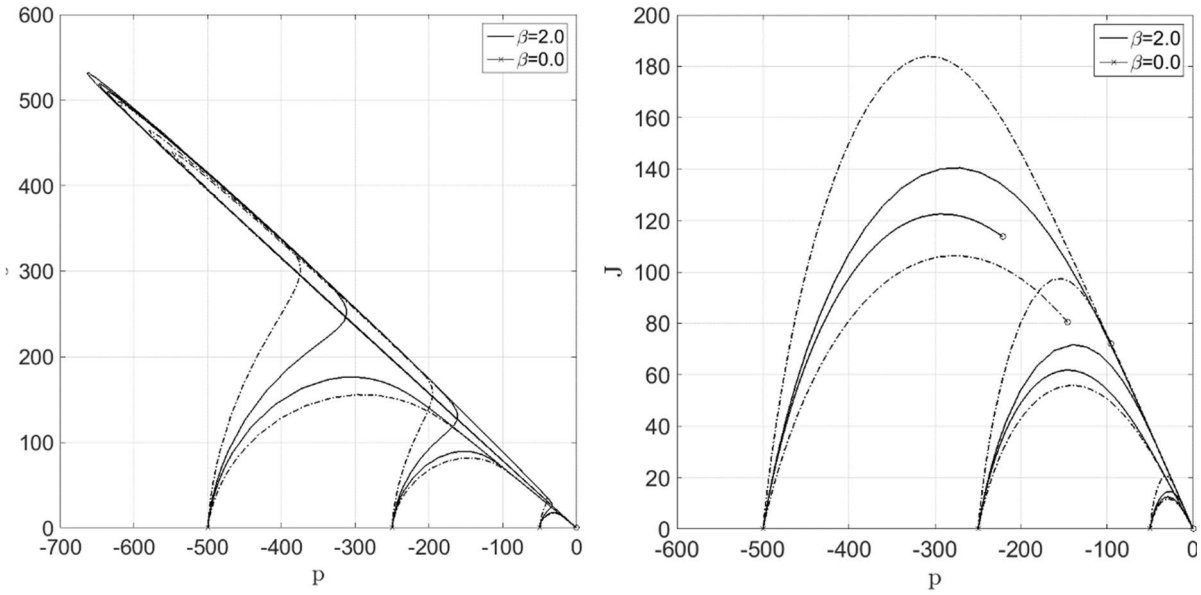


Figure 40: Strain-Backstress path for oedometric conditions (ob=-1)

Zero mean effective strees attractor: Liquefaction ob > 0

Any strain path with a positive obliquity will sooner or later travel to p' = 0 as it is swelling, which corresponds to an stable attractor as described in 0. This condition occurs even for the cases with low positive obliquities as can be observed in Figure 41 where the responses for ob = 0.1 and ob = 0.5 are shown. Obviously, the larger the obliquity of the strain path the larger will be the effect that will enforce the stress path to travel towards zero. It is curious to mention that even for the case of a low positive obliquity the stress path exhibits phase transformation similarly an in undrained test conditions (ob=0), but eventually ends in the zero mean stress attractor following its associated asymptote (see Figure 41a).



(a) (b)

Figure 41; Liquefaction backstreess paths for positive obquiquity: (a) ob = 0.1, (b) ob = 0.5

2.5.2. COMPARISON OF BASIC SAND MODEL WITH VON WOLFFERSDORFF (1996) MODEL

In this section the performance of the proposed model is compared to the reference hypoplastic model for sands (von Wolffersdorff, 1996), denoted here as VW model, under monotonic conditions. The basic sand model can be adapted to yield the VW model thanks to the general form adopted for the goal function and limit surface. Table 7 shows the two sets of inputs, as an example to illustrate the similarities between the two models.

Table 7: Input parameters of Sand model and VW model used for comparison

	e_{c0}	e_{d0}	e_{i0}	h_s	n	α	β	φ'	XV	YF	ZF	ϑ	S_f	ob_{min}	ob_{max}	δ
VW	0.83	0.55	0.95	1000	2.5	0.24	1.5	32								
Basic Sand	0.83	0.55		1000	2.5	0.1	1.5		0.75	0.0	0.1	0.3	3.0	-1.73	0.6	1.8

To show the similarities between the two models the expression employed by the VW model is recalled here:

$$\dot{\alpha}_{ij} = f_p^{VF} f_e \left(L_{ijkl}^{VF} \dot{\varepsilon}_{kl}^{p} + f_d N_{ij}^{VF} \left\| \dot{\varepsilon}_{kl}^{p} \right\| \right) \tag{2.139}$$

The former expression can be rearranged into an equivalent limit function and goal functions as:

$$Y^{VF} = \left\| (L_{ijkl}^{VF})^{-1} N_{kl}^{VF} \right\| \qquad \vec{\Upsilon}_{ij}^{VF} = \frac{-(L_{ijkl}^{VF})^{-1} N_{kl}^{VF}}{\left\| (L_{ijkl}^{VF})^{-1} N_{kl}^{VF} \right\|} \tag{2.140}$$

The limit and goal functions are then plotted in Figure 42 in an isomorphic space for general comparison. The results show significant similarities between the models for both the limit function and the goal function.

Basic sand	Von Wolffersdorff

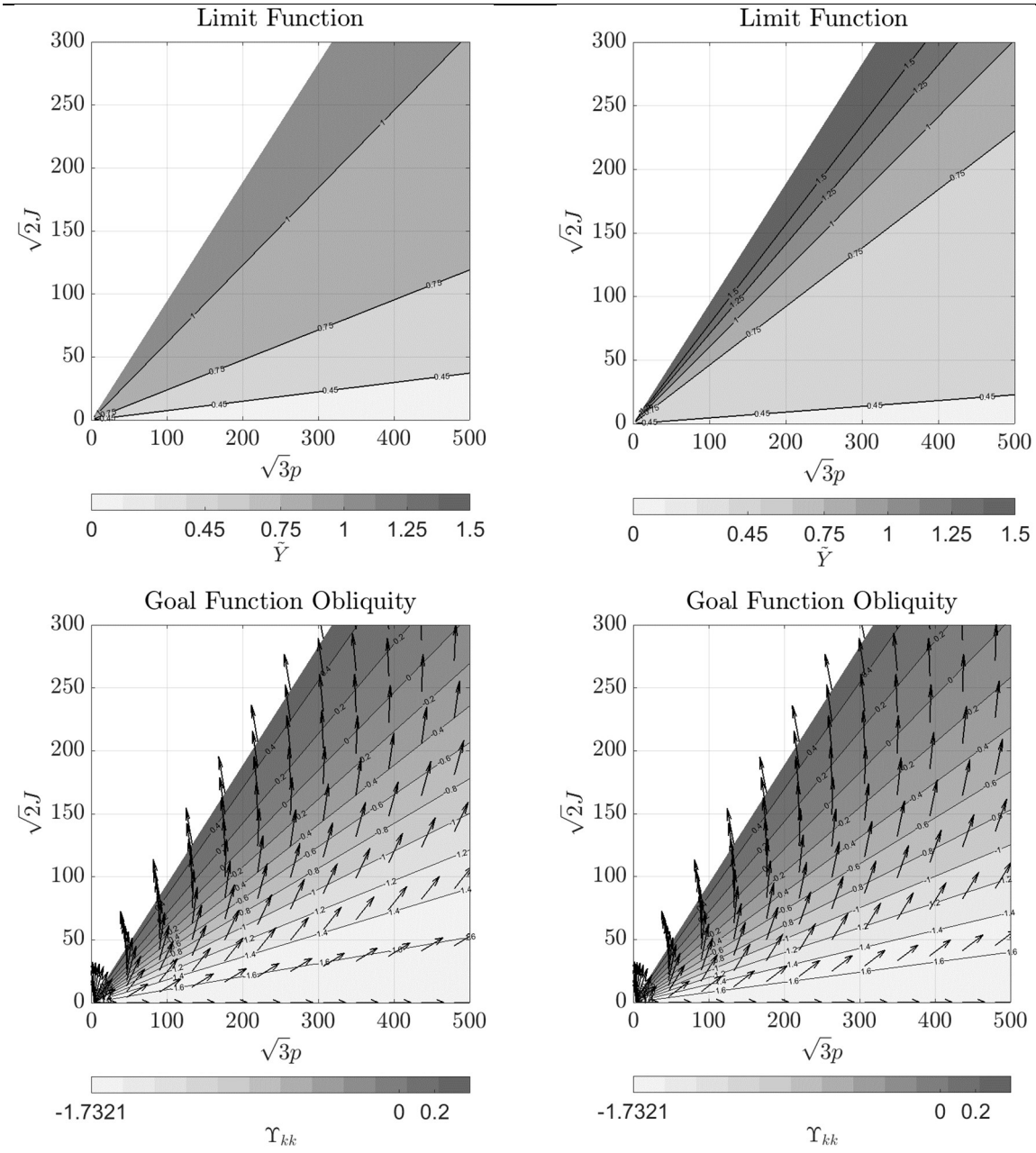


Figure 42: Comparison of equivalent goal function for basic sand and Von Wolffersdorff

In the following subsections a set of strain probes using both models and typical soil tests (TXD, TXU, OED, ISO) are shown and compared.

2.5.2.1. Strain probes

A set of numerical finite strain perturbations following the methodology of Gudehus and Mašín (2009) have been carried out under the same initial conditions. The results in Figure 43 show the stress envelopes mapped in an isomorphic space. These results show that the overall stiffness of the basic sand model is higher (i.e. the same strain perturbations lead to larger stress mappings) than the VW model, which is expected since the two models use a different definition of f_p. The basic sand model tends to give higher stiffness as it enforces $\dot{f}_d > 0$ more drastically under compressive conditions generaly exhibiting higher stiffness.

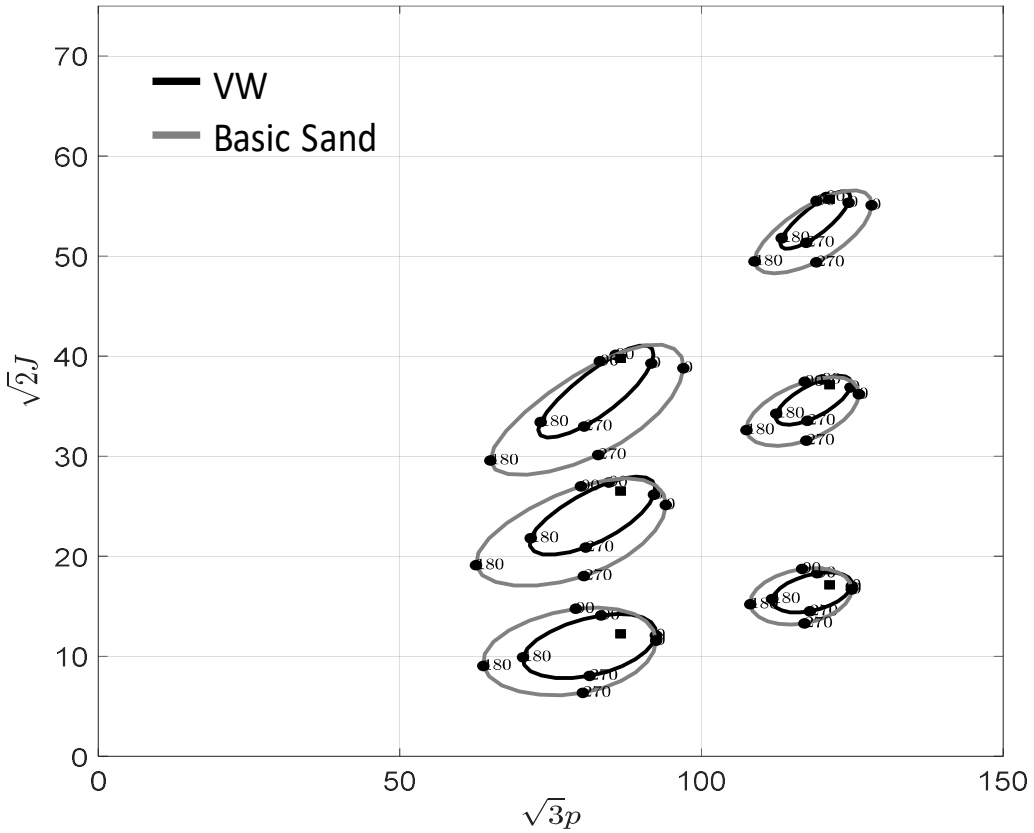


Figure 43: Finite perturbation for VW (black) and Basic Sand (grey), initial void ratio e = 0.8

Despite the differences in magnitude the overall stiffness mapped in Figure 43 is very similar in terms of the shape. The most significant differences appear for higher stress ratios and for mainly deviatoric strain directions (90, 270), while for purely volumetric (0, 180) states the

principal directions of the responses are more similar. As discussed in the previous section this differences come from the different mapping tensors of both models.

2.5.2.2. Drained Triaxial test

Figure 44 shows a set of stress-strain curves under triaxial conditions for the basic sand model and the VW model, for different initial void ratios, with all tests starting from isotropic conditions and $p' = 50$ kPa. The equivalence between models is quite clear in this conditions, however it must be said that the inputs listed in Table 7 for the basic sand model were obtained by enforcing a similar response to that yielded by the VW model under triaxial compression conditions. In this sense the similarities are clearly enforced, further conventional tests are investigated in the followoign sections.

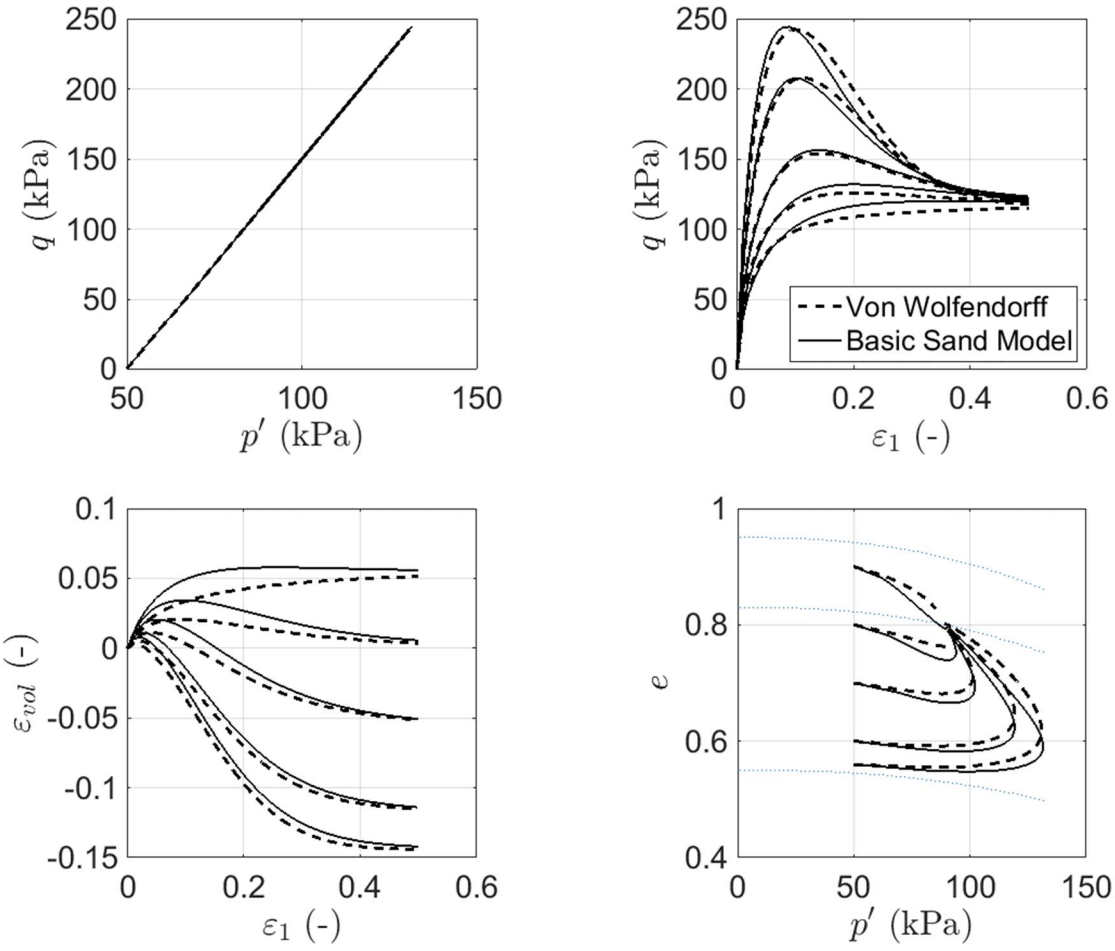


Figure 44: Comparison triaxial compression response of Basic Sand model and Von Wolffersforff for various initial void ratios

2.5.2.3. Undrained triaxial tests

With the inputs parameters listed in Table 7 a set of undrained triaxial tests has been carried out with both models. More significant differences are manifested than when considering the response obtained for the drained triaxial tests, in particular with the sharpness of the pore pressure generation. Stress paths are shown in Figure 45 where it can be observed how the basic model enforces a sharper phase transformation than the VW model, the reason for this being principally the differences in stiffness in the volumetric direction and in the limit surface value. Both models exhibit the same type of asymptotic behaviour as it is mostly controlled by the goal functions which are very similar between the two models.

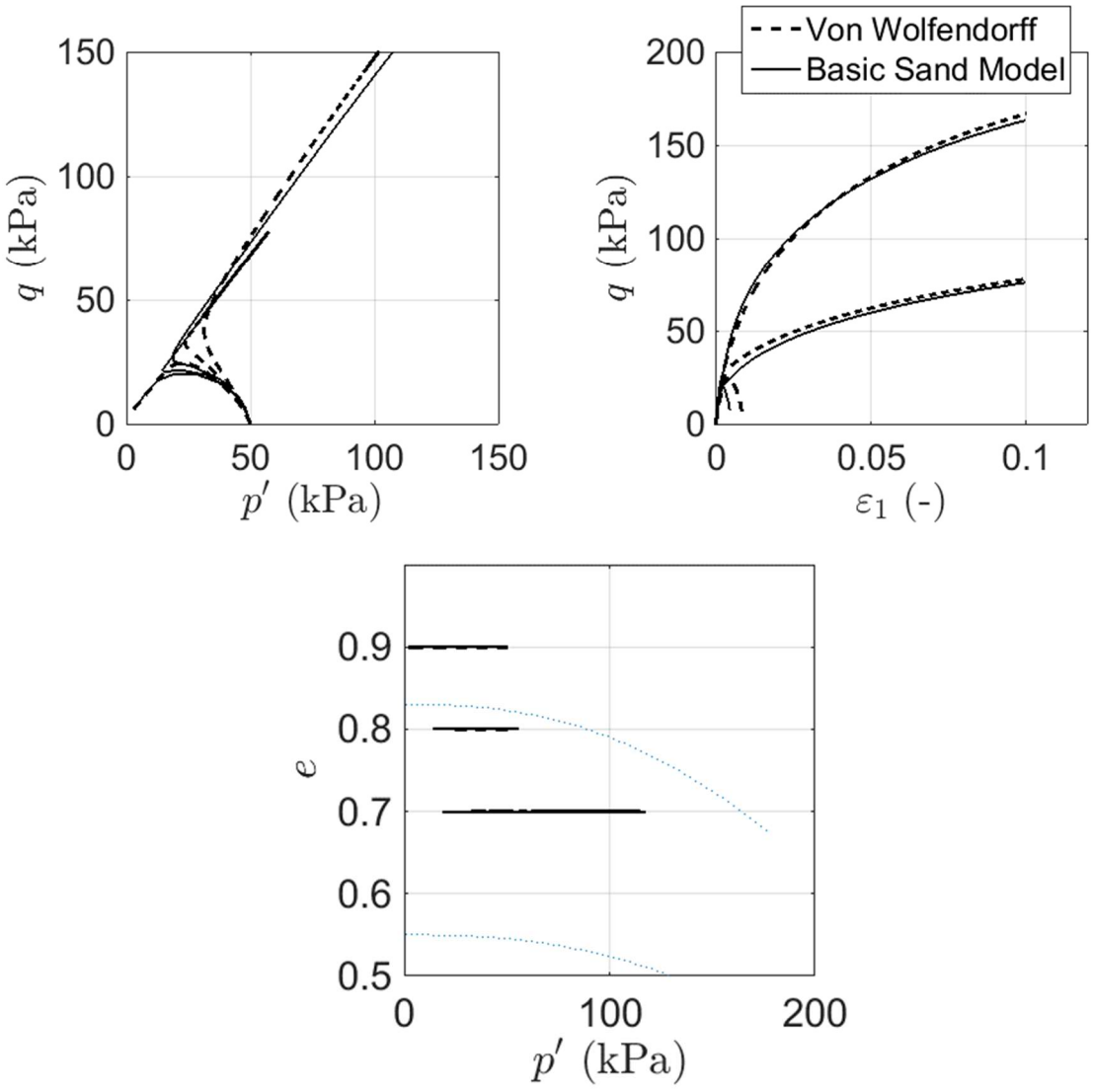


Figure 45: Comparison of undrained triaxial response of Basic Sand model and Von Wolffersforff for various initial void ratios

2.5.2.4. Oedometric conditions

On the other hand, for compressive tests, such as oedometeric compression in dense and loose states (Figure 46, Figure 47), small differences are manifested in terms of stiffness and asymptotic behaviour. The similarities in the asymptotic behaviour come from the fact that the goal functions and limit functions of both models are very similar. Also, the stiffness is tuned for both models to be consistent with the CSL slope, which obviously is also the same as discussed in the previous section.

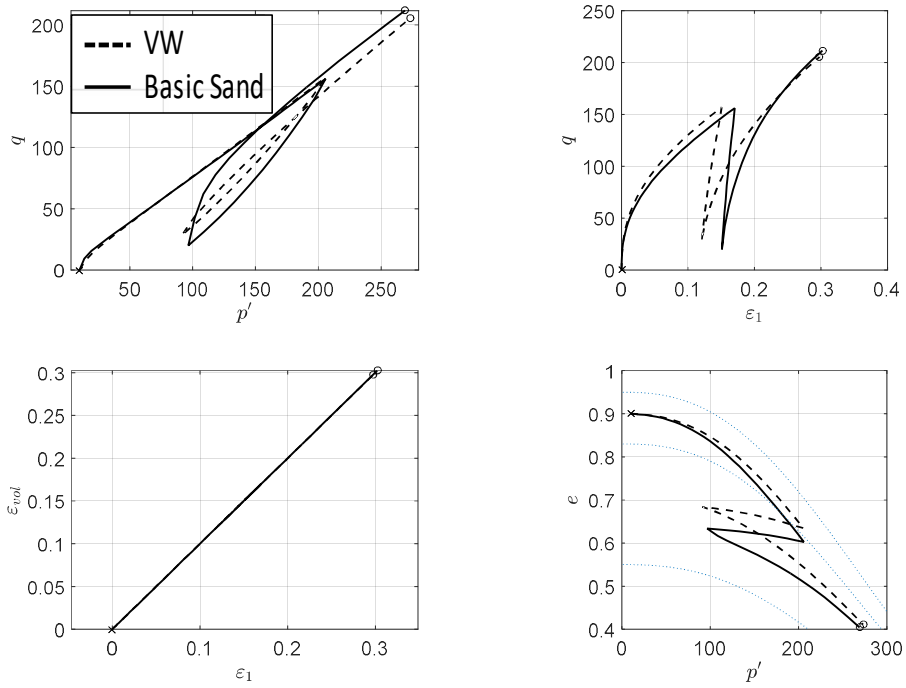


Figure 46: Comparison oedometric response of Basic Sand model and Von Wolffersforff exporession for loose state

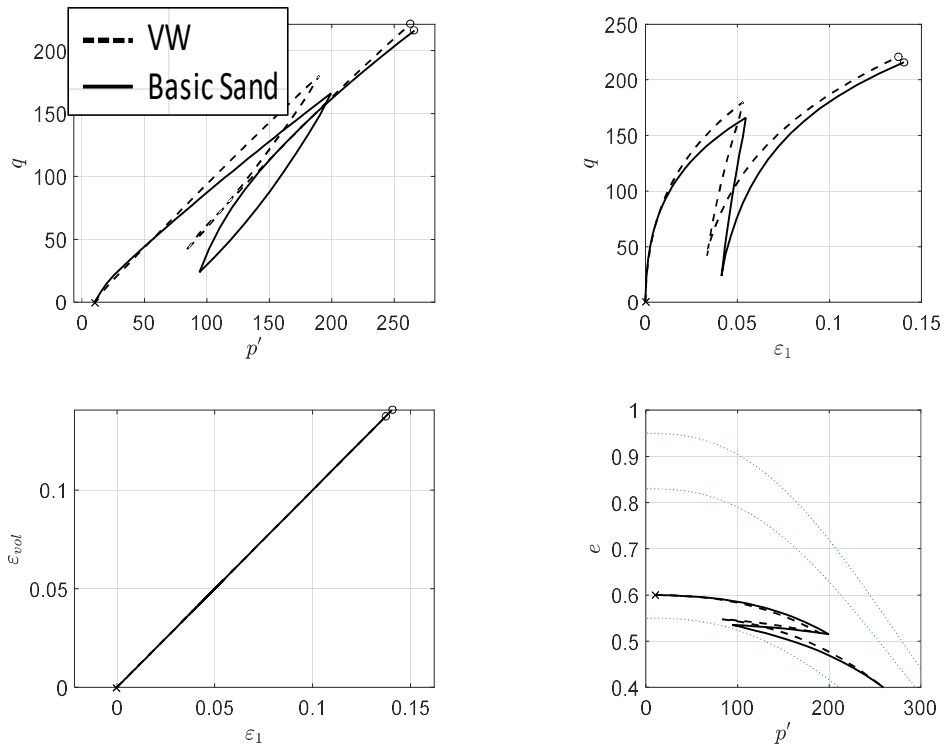


Figure 47: Comparison oedometric response of Basic Sand model and Von Wolffersorff exporession for dense state

2.5.2.5. Summary

In summary, the proposed structure of the sand model is flexible enough to exhibit the same response as the VW hypoplastic model. Despite the difference in the tensorial expression, the inputs can be accomodated to exhibit similar responses as the VW hypoplastic model. It can be observed how the basic model has a well balanced formulation capturing the main aspects of soil behaviour while keeping a simple but general mathematical form. This simpler mathematical form can be decomposed in orthogonal directions, which helps in the development of future extensions, and for backstress superposition as subsequently described in Chapter 4.

2.5.3. NON-LINEAR KINEMATIC HARDENING RULES FOR CLAYS

The first model that adapted hypoplasticity for clays was proposed by Herle and Kolymbas (2004), as modification of the von Wolffersdorff (1996) hypoplastic model. Subsequently, Masin (2005) proposed a hypoplastic model for clays within the critical state framework (Figure 48), that was later refined (Masin, 2012b). The method that we will use here to adapt the general form of hardening rule to model clays following the method described in Masin (2013) which allows to define explicitly the asymptotic states.

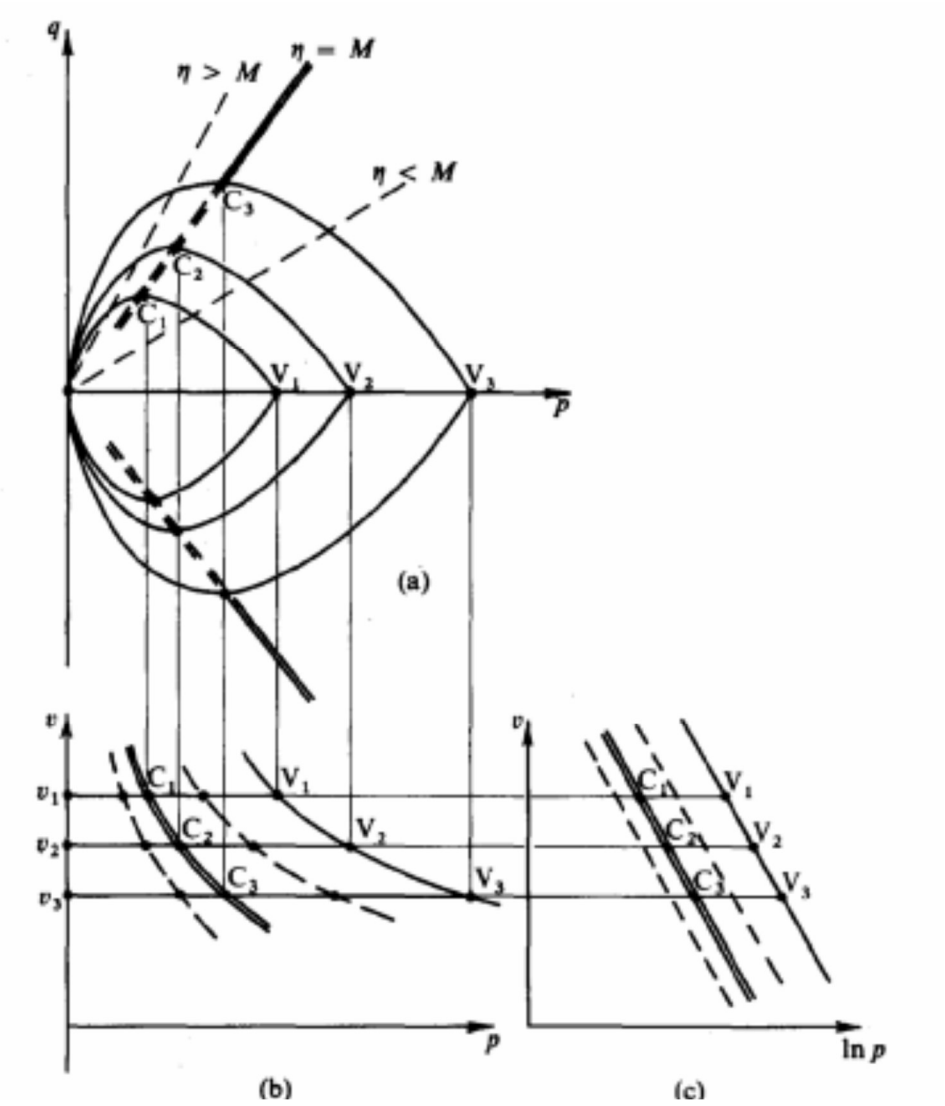


Figure 48: Critical state framework (Schofield and Wroth, 1968)

The method is based on the fact that the asymptotic state surface does not change in shape with respect to the Hvorslev equivalent pressure p_e^*.

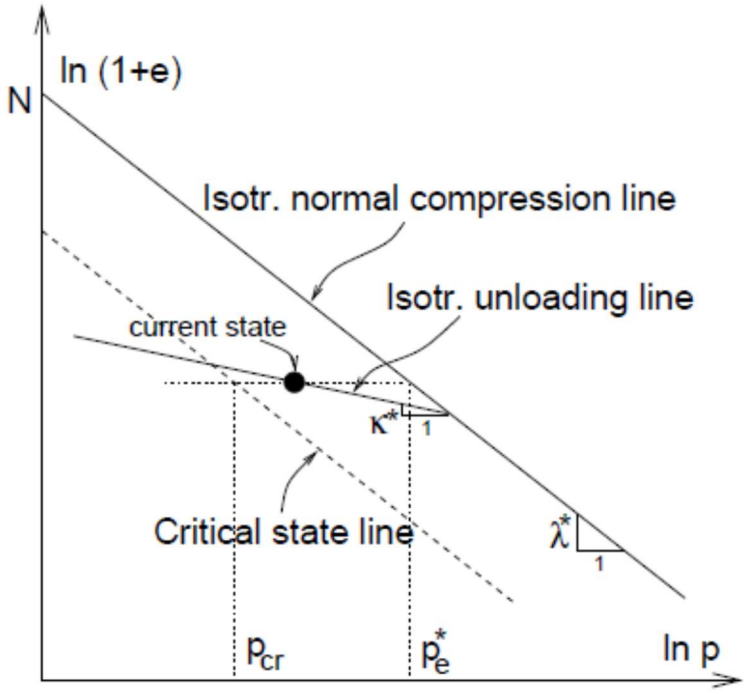


Figure 49: Definition of N, λ^*, κ^* and p_e, from Masin (2005)

As the CSL line lies at half of the Hvorlev pressure, f_d must be defined as

$$f_d = \left(\frac{2p_\alpha}{p_e^*} \right)^\alpha \tag{2.141}$$

Where p_e^* is the equivalent Hvorslev pressure, α is a model parameter and $3p_\alpha$ is the trace of the backstress. The CSL line definition is taken from Butterfield (1979)

$$p_e^* = \exp\left(\frac{N - \ln(1+e)}{\lambda^*} \right) \tag{2.142}$$

As the shape of asymptotic boundary surface does not change in shape, the tensor $\hat{\alpha}_{ij}^e = \alpha_{ij} / p_e^*$ needs to be constant, therefore

$$\dot{\hat{\alpha}}_{ij}^{e}=\frac{1}{p_e^*}\left(\dot{\alpha}_{ij}-\frac{\alpha_{ij}}{p_e^*}\dot{p}_e^*\right)=0 \tag{2.143}$$

Where

$$\dot{p}_e^*=-p_e^*\frac{\dot{\varepsilon}_{kk}^{p}}{\lambda^*} \tag{2.144}$$

Expression (2.143) is the condition for maintaining the shape of the critical state framework constant. Expression (2.143) can be combined with the general rule (2.23), therefore expression (2.143) becomes:

$$\begin{aligned}\dot{\hat{\alpha}}_{ij}^{e}&=\frac{f_s}{p_e^*}L_{ijkl}(\vec{n}_{kl}^{p}-f_dY\vec{\Upsilon}_{kl})+\frac{\alpha_{ij}}{p_e^*}\frac{1}{\lambda^*}\vec{n}_{kk}\\ \hat{\alpha}_{ij}^{e}&=\frac{\alpha_{ij}}{p_e^*}\end{aligned} \tag{2.145}$$

Where the mapping tensor is the orthogonal tensor defined in the previous section

$$L_{ijkl}=S_f\left(\frac{1}{3}\delta_{ij}\delta_{kl}+\hat{\alpha}_{ij}^{*}\delta_{kl}\right)+S_d\left(\delta_{ik}\delta_{jl}-\frac{1}{3}\delta_{ij}\delta_{kl}-\hat{\alpha}_{ij}^{*}\delta_{kl}\right) \tag{2.146}$$

As the model needs to be asymptotic it implies that upon a constant plastic strain direction $\vec{n}_{ij}$ the rate of $\hat{\alpha}_{ij}^{e}$ must be zero, then

$$f_sL_{ijkl}(\vec{n}_{kl}^{p}-f_dY\vec{\Upsilon}_{kl})+\alpha_{ij}\frac{1}{\lambda^*}\vec{n}_{kk}=0 \tag{2.147}$$

Rearranging the terms in (2.147) becomes

$$\left(f_sL_{ijkl}+\frac{1}{\lambda^*}\alpha_{ij}\delta_{kl}\right)\vec{n}_{kl}=f_sf_dYL_{ijkl}\vec{\Upsilon}_{kl} \tag{2.148}$$

The following constrains need to be imposed

1. The CS asymptote is imposed when $f_dY=1$ and $\vec{n}_{kk}=0$

2. Isotropic compression: $Y = 0$ and $\vec{n}_{kk} = -\sqrt{3}$
3. Oedometric conditions impose $K_0 \approx 1 - \sin\varphi_{cs}$

The previous conditions can be achieved enforcing a Modified Cam Clay yield surface shape as asymptotic limit surface (2.148). Therefore, when the backstress lies on the MCC surface asymptotic behaviour is enforced. Therefore implying:

$$\vec{n}_{kl} = \vec{\Upsilon}_{kl} \qquad f_d = f_d^A \tag{2.149}$$

Where f_d^A is the value of f_d evaluated at the asymptote $\eta^A = J_\alpha^A / p_\alpha^A$. Recalling (2.141) one obtains

$$f_d^A = \left(\frac{2 p_\alpha^A}{p_e^*} \right)^\alpha \tag{2.150}$$

The yield surface of the modified Cam-Clay can be written as:

$$p_\alpha^A = \frac{p_e^*}{1 + \tilde{Y}^2} \tag{2.151}$$

where

$$\tilde{Y} = \left(\frac{\eta}{g(\theta)} \right)^\vartheta \tag{2.152}$$

Substituting and rearranging, the following equality must be always true, then:

$$Y \vec{\Upsilon}_{ij} = \frac{1}{f_d^A} \left(\delta_{ik}\delta_{jl} + \frac{1}{f_s \lambda} L^{-1}_{ijmn} \alpha_{mn} \delta_{kl} \right) \vec{\Upsilon}_{kl} \tag{2.153}$$

Recalling the general form of non-linear kinematic as:

$$\dot{\alpha}_{ij} = \dot{\lambda} h_{ij} = \dot{\lambda} f_s L_{ijkl} (\vec{n}^p_{kl} - f_d Y \vec{\Upsilon}_{kl}) \tag{2.154}$$

Substituting (2.153) in (2.154) the final form of the clay model is

$$\dot{\alpha}_{ij} = f_s L_{ijkl} \dot{\varepsilon}^p_{kl} - \frac{f_d}{f_d^A} \left(f_s L_{ijkl} + \frac{1}{\lambda} \alpha_{mn} \delta_{kl} \right) \vec{\Upsilon}_{kl} \left\| \dot{\varepsilon}^p_{kl} \right\| \tag{2.155}$$

Where the function f_s is borrowed from Masin (2005):

$$f_s = 3\, p_\alpha \left(\frac{1}{\kappa} + \frac{1}{\lambda} \right) \tag{2.156}$$

To illustrate the model performance, in the following section we run a set of typical soil tests with the following parameters,

Table 8: Input parameters for Clay study

	N	**λ**	**κ**	**Sf**	**X**	**Y**	**Z**	**α**	**obmin**	**obmax**	δ^{GF}	ϑ
Reference	1.0	0.1	0.01	0.6	0.72	0.0	0.0	2.0	-1.73	0.6	1.8	1.2

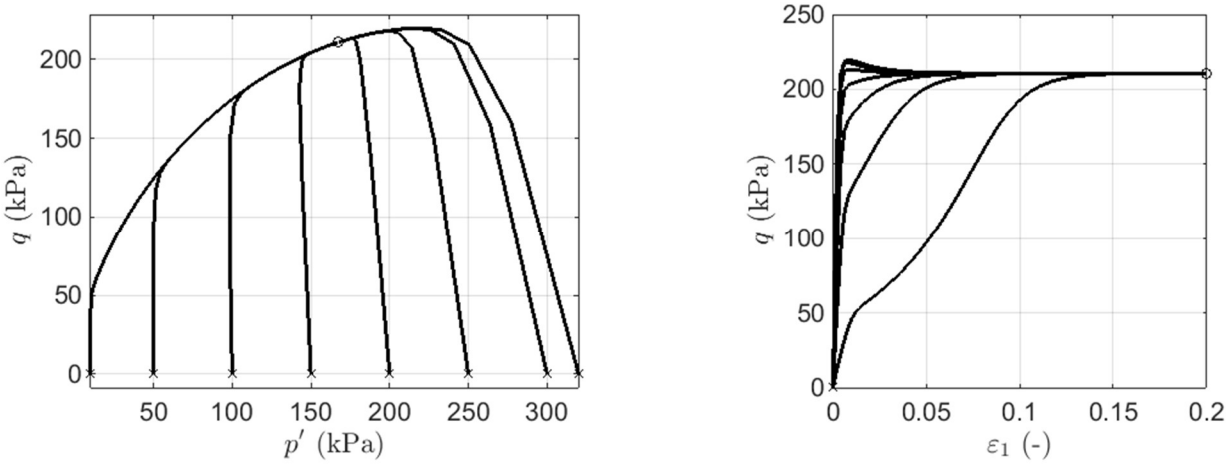


Figure 50: Undrained triaxial tests for various OCRs

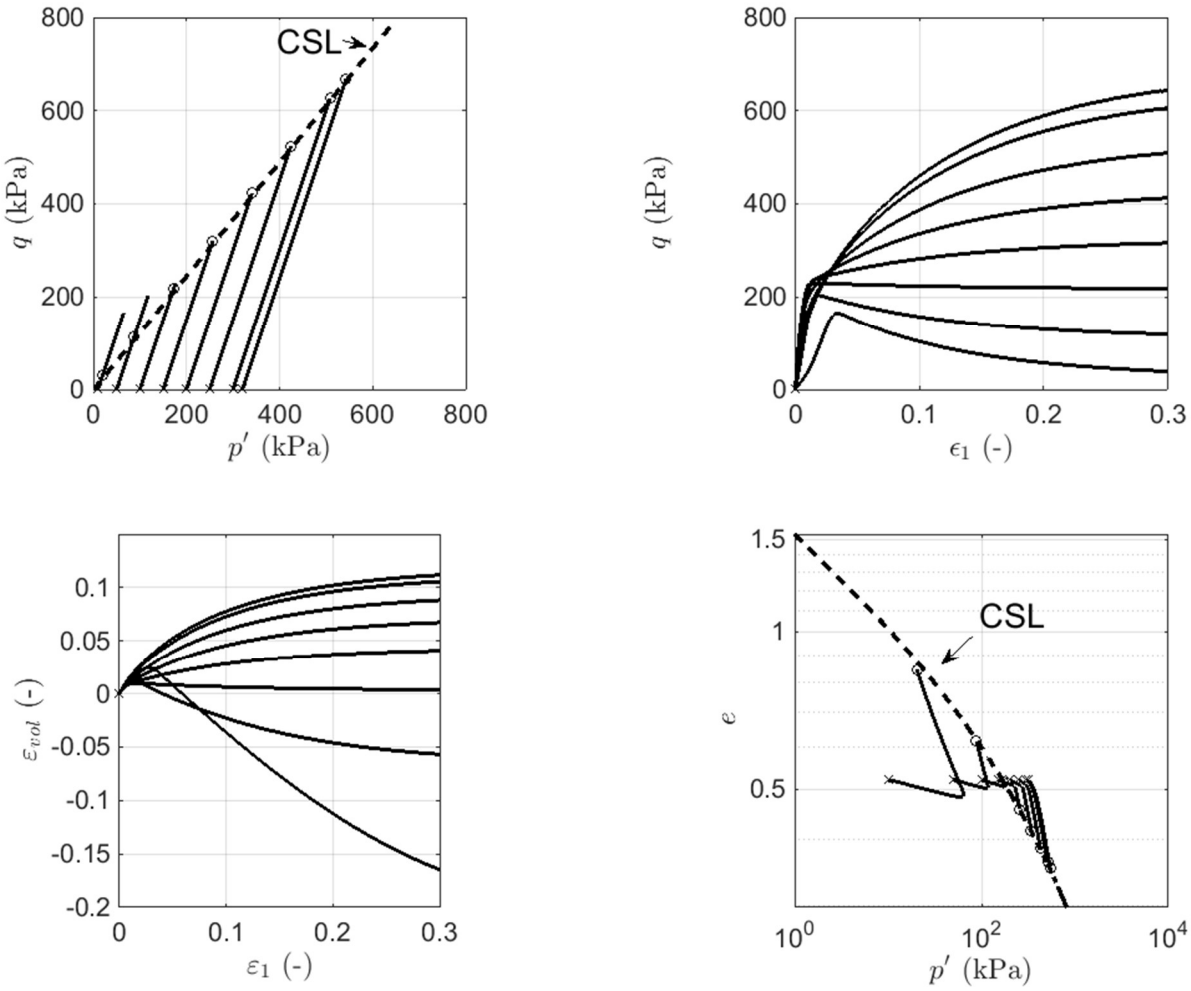
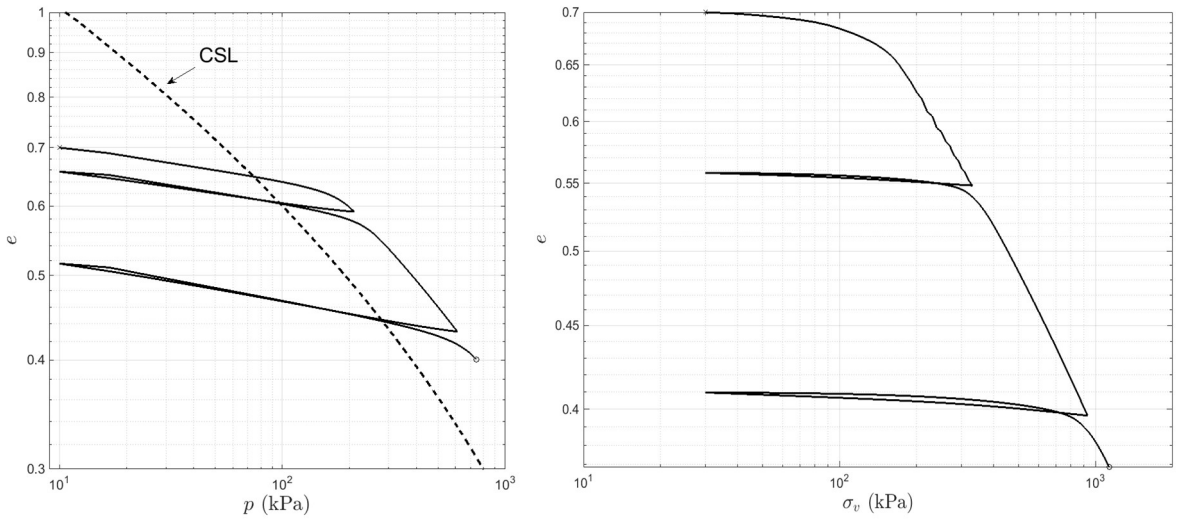


Figure 51: Drained triaxial tests for various OCRs



(a) (b)

Figure 52: Compression tests. (a) isotropic, (b) oedometric

2.5.4. COMPARISON OF BASIC CLAY MODEL WITH MASIN (2013) MODEL

Similar to the sand model, the basic clay model can be compared to the Masin (2013) model. The equivalent limit surface and equivalent goal function $\vec{\Upsilon}_{ij}^{eq}$ between both models can be obtained as:

$$Y = \left\| \frac{1}{f_d^A} \left(\vec{\Upsilon}_{kl} + \frac{\vec{\Upsilon}_{kk}}{f_s \lambda^*} L_{ijmn}^{-1} \alpha_{mn} \right) \right\| \qquad \vec{\Upsilon}_{ij}^{eq} = \frac{1}{Y} \left(\vec{\Upsilon}_{kl} + \frac{\vec{\Upsilon}_{kk}}{f_s \lambda^*} L_{ijmn}^{-1} \alpha_{mn} \right) \tag{2.157}$$

Substituting (2.157) the general form described can be recovered as:

$$\dot{\alpha}_{ij} = f_s L_{ijkl} \left[\dot{\varepsilon}_{kl}^{p} - f_d Y \vec{\Upsilon}_{kl}^{eq} \left\| \dot{\varepsilon}_{kl}^{p} \right\| \right] \tag{2.158}$$

where the function f_s is the same as that defined in Masin (2013):

$$f_s = 3 p_\alpha \left(\frac{1}{\kappa} + \frac{1}{\lambda} \right) \tag{2.159}$$

The equations of the model to compare against are described in Masin (2013). The following equations transcribe the expressions published in a backstress form, transforming the equations into non-linear kinematic models under for infinitesimal strain conditions. The hypoplastic model is:

$$\dot{\sigma}_{ij} = f_s L_{ijkl} \dot{\varepsilon}_{kl} - \frac{f_d}{f_d^A} A_{ijkl} \vec{d}_{kl}^{A} \left\| \dot{\varepsilon}_{kl} \right\| \tag{2.160}$$

where:

$$L_{ijkl} = \delta_{ik} \delta_{jl} + \frac{\nu}{1 - 2\nu} \delta_{ij} \delta_{kl} \tag{2.161}$$

$$A_{ijkl} = f_s L_{ijkl} + \frac{1}{\lambda^*} \sigma_{ij} \delta_{kl} \tag{2.162}$$

and:

$$f_s = \frac{\sigma_{kk}}{2}\left(\frac{1}{\lambda^*}+\frac{1}{\kappa^*}\right)\frac{1-2\nu}{1+\nu} \tag{2.163}$$

The function f_d is the same as the original hypoplastic model, on the other hand f_d^A in Masin (2013) has a more complex form of "asymptotic surface" than the one used in the basic clay model, where:

$$f_d^A = 2^{\alpha}(1-F_m)^{\alpha/\omega} \tag{2.164}$$

Where F_m is the Matsuoka-Nakai parameter:

$$F_m = \frac{9I_3 + I_2 I_1}{I_3 + I_2 I_1} \tag{2.165}$$

and the exponent ω is:

$$\omega = -\frac{\ln(\cos^2\varphi_c)}{\ln 2} + 0.3(F_m - \sin^2\varphi_c) \tag{2.166}$$

The asymptotic strain directions (goal functions) are:

$$\begin{aligned} \vec{d}_{kl}^{\,A} &= \frac{d_{kl}^A}{\left\| d_{kl}^A \right\|} \\ d_{kl}^A &= -\hat{\sigma}_{kl}^* + \delta_{kl}\left(\frac{2}{3} - \frac{1+\cos 3\theta}{4}F_m^{1/4}\right)\frac{F_m^{\xi/2} - \sin^{\xi}\varphi_c}{1-\sin^{\xi}\varphi_c} \end{aligned} \tag{2.167}$$

where θ is the Lode's angle and ξ:

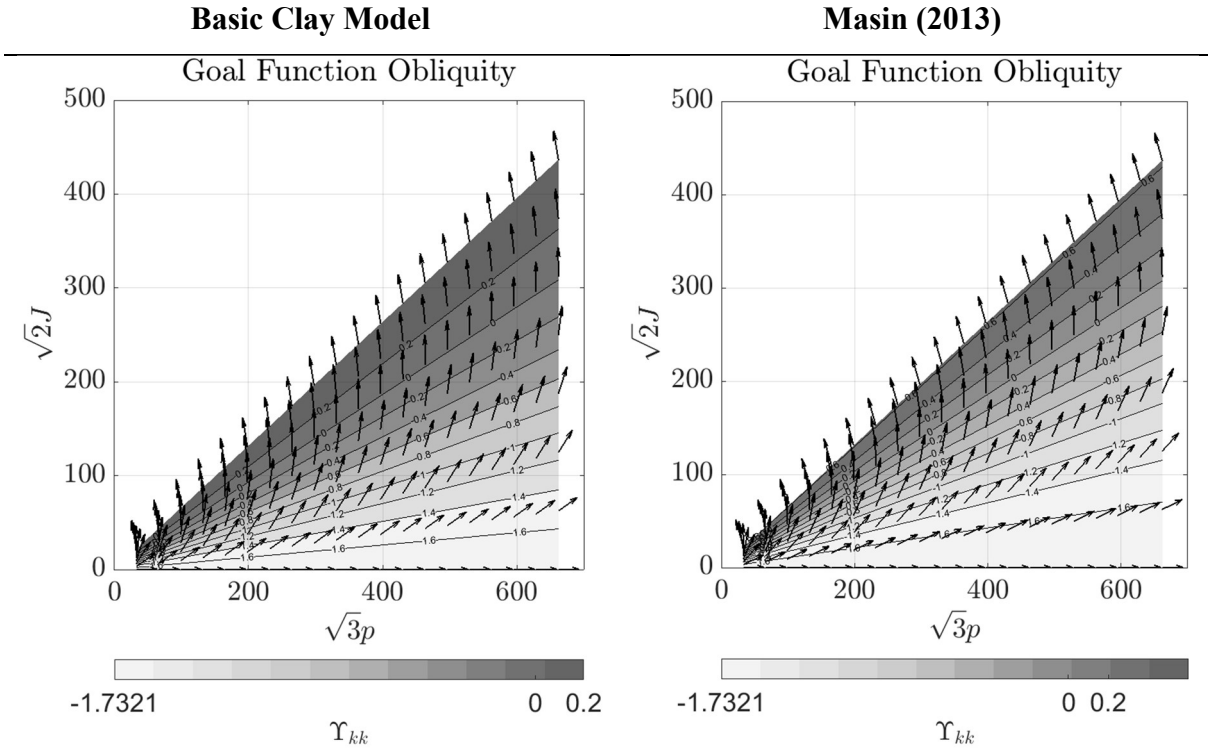
$$\xi = 1.7 + 3.9\sin^2\varphi_c \tag{2.168}$$

The comparison of both models is illustrated following the same approach as with the VW model. The set of parameters given in Table 9 is chosen to provide an equivalent response in drained and undrained triaxial conditions and the rest of the tests are compared using the same chosen inputs.

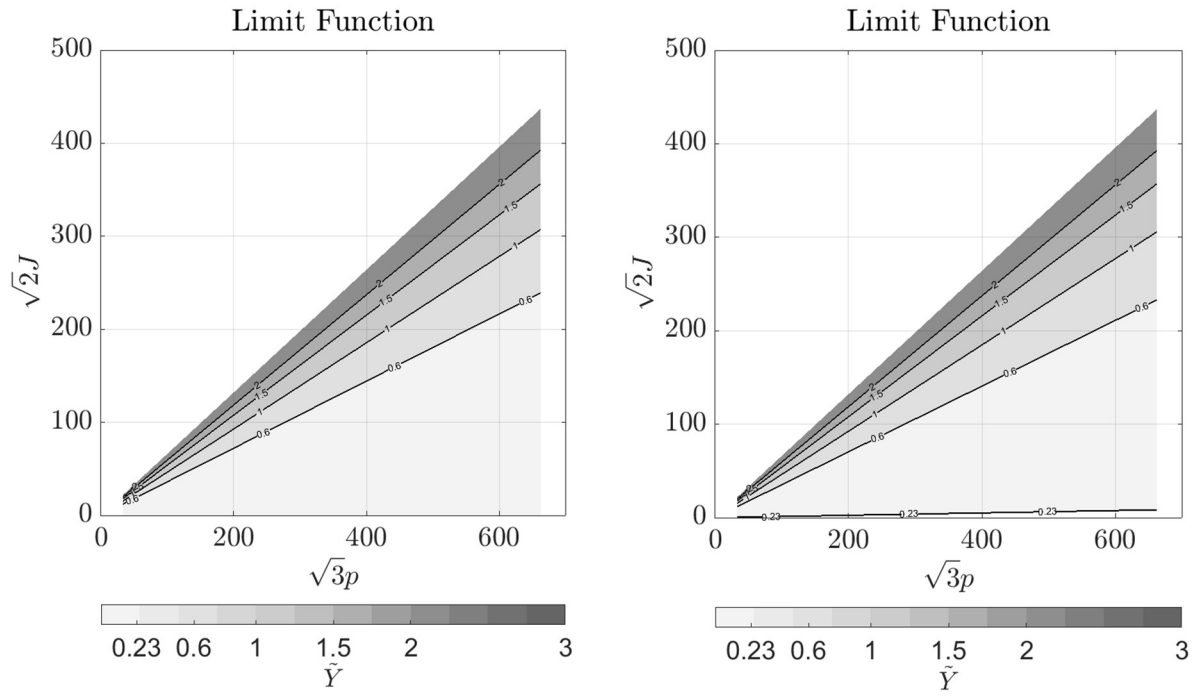
Table 9: Input parameters for Basic Clay model comparison

	N	**λ**	**κ**	**Sf**	**X**	**Y**	**Z**	**α**	**obmin**	**obmax**	δ^{GF}	ϑ
Basic Clay	1.0	0.1	0.01	1.3	0.57	0.0	0.1	2.0	-1.73	0.6	1.8	1.2
	N	λ	κ	ν	φ_c							
(Masin, 2013)	1.0	0.1	0.01	0.2	25							

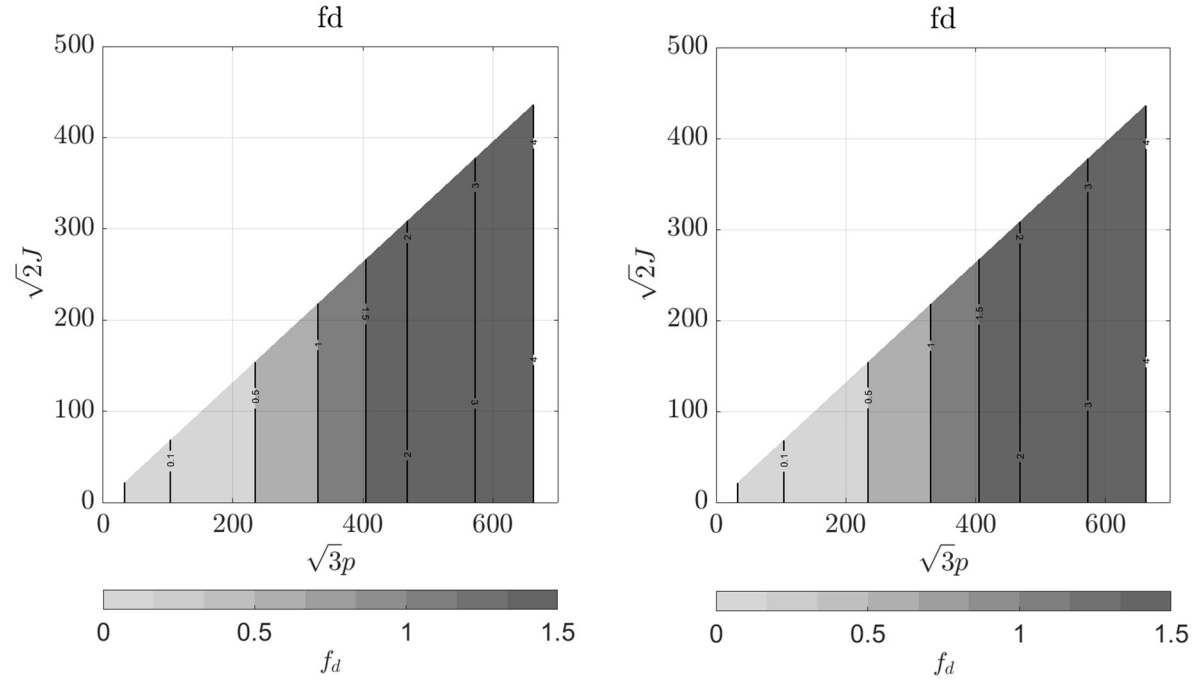
The equivalent goal functions, limit surfaces and f_d functions of both models are plotted in Figure 53 in the isomorphic space, where it can be appreciated that they compare similarly well as in the case of the sand model.



(a)



(b)



(c)

Figure 53: Comparison of equivalent goal function (a), limit surfaces (b) and f_d functions (c) for Basic Clay and Masin (2013) models

Following the same methodology as in the sand model, strain probes and conventional tests are carried out for comparing both models.

2.5.4.1. Strain probes

Numerical finite perturbations of the strain for various overconsolidation ratios (OCRs) and initial J/p' ratios are carried out to compare the local stiffness of the model. Figure 54 shows the stress mapping upon a numerical perturbation of the strain for both models, in which the square dot corresponds to the initial stress of the perturbation and the circles correspond to the mapping for purely isotropic (0,180 degrees) or purely deviatoric conditions (90, 270 degrees). The Basic Clay model exhibits a higher stiffness than that of the Masin (2013) model, which particularly occurs in the deviatoric plane where the mapping tensor of the basic clay includes a term dependent on J/p', while the hypoplastic clay model does not (as it uses the isotropic stiffness tensor).

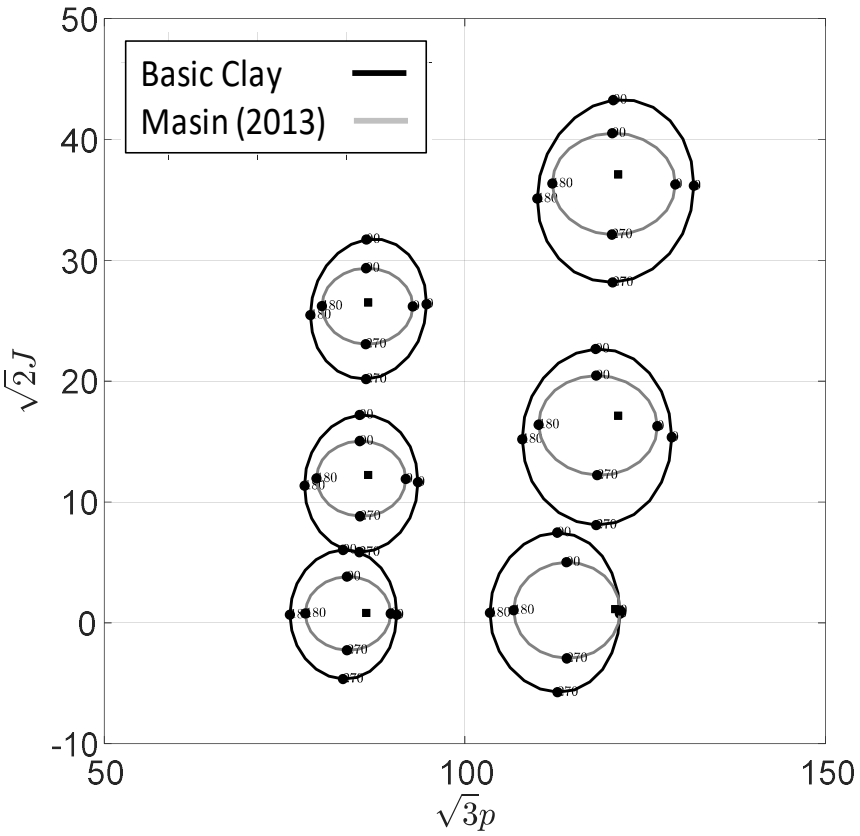


Figure 54:Mapping of a finite perturbation of the Basic clay model and hypoplasticity clay with explicitly defined asymptotic states

2.5.4.2. Drained triaxial tests

A set of drained triaxial tests has been carried out for various initial ORCs and the obtained results are shown in Figure 55, where it can be observed that the response is similar for both models, exhibiting the same type of peak strength for the overconsolidated states and same critical state failure envelope. The two models appear to lead to slightly different evolutions of dilatancy and hardening rate, however the response is comparable.

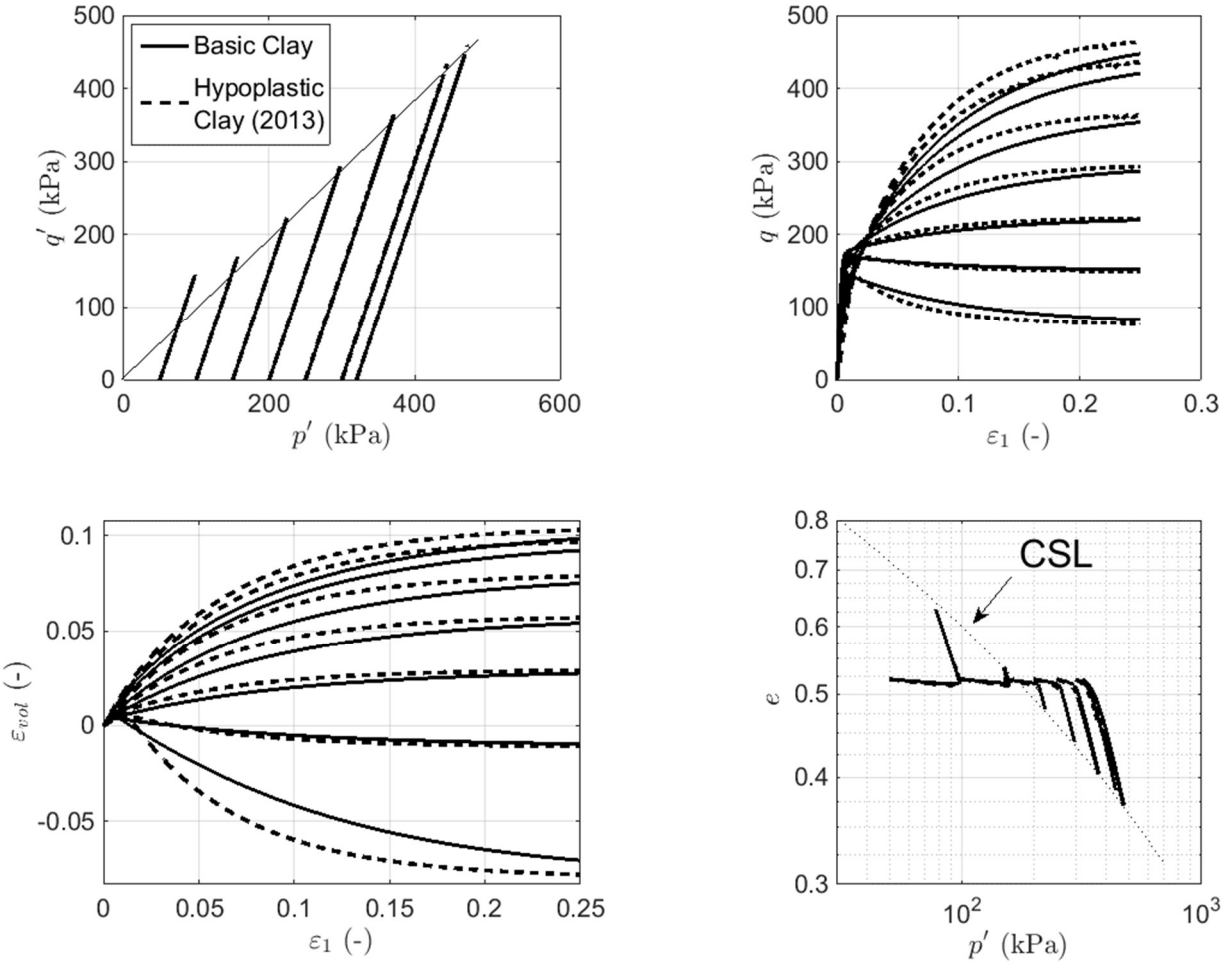


Figure 55: Drained triaxial tests for various initial OCRs

2.5.4.3. *Undrained triaxial tests*

Similar to the drained triaxial tets a set of ondrained tests has been carried out at different initial OCRs and the stress paths have been plotted in the p-q space. Clearly, the q-p' failure enevelope is similar between both models, although perhaps Masin (2013) model has a sharper transition for normally consolidatd stes when compared to the basic clay model as it has a stronger contractant contribution of the goal functions and limit surfaces.

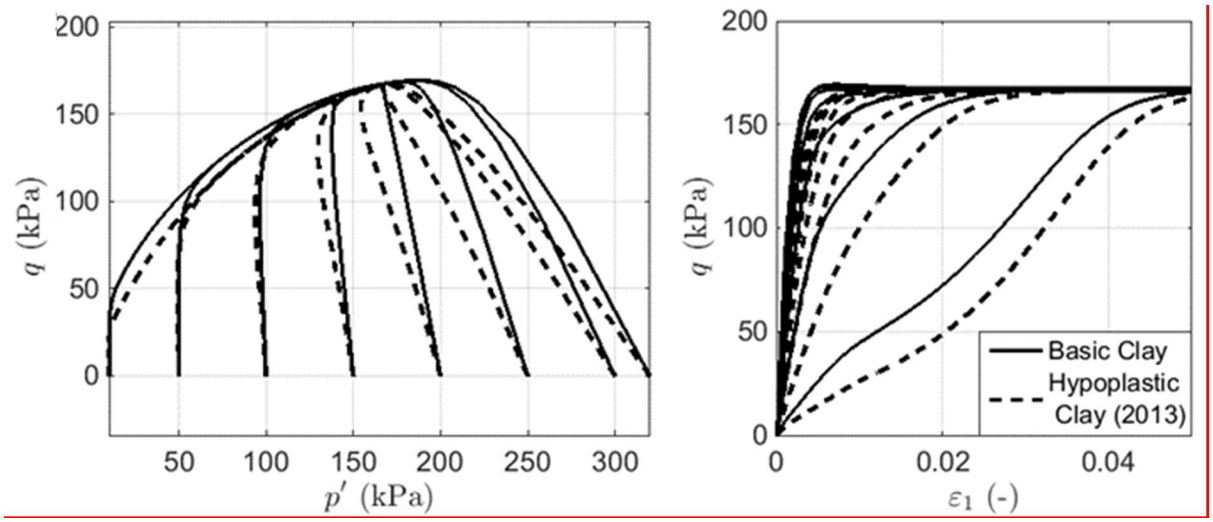


Figure 56: Undrained triaxial tests for various initial OCRs

2.5.4.4. *Isotropic and oedometric compression tests*

Lastly, a set of isotropic and oedometric tests including loading and reloading stages are carried out. Figure 57 and Figure 58 show the isotropic responses and oedometric responses predicted by both models. Slight differences appear in the oedometric tests with respect to the asymptotic states as the assimptic limit surfaces of both models are different. Nevertheless, since the backbone of the formulation of hypoplasticity is the consistency with the ICL both models enforce this condition and the yield surface to become an assimptote, it is obvious that the response of both models in this conditions will be practically the same.

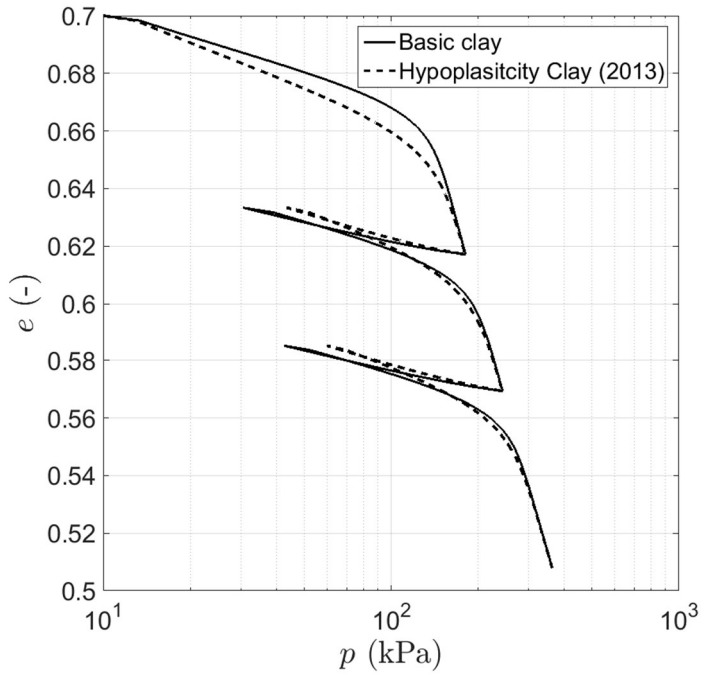


Figure 57: Comparison of models under isotropic conditions

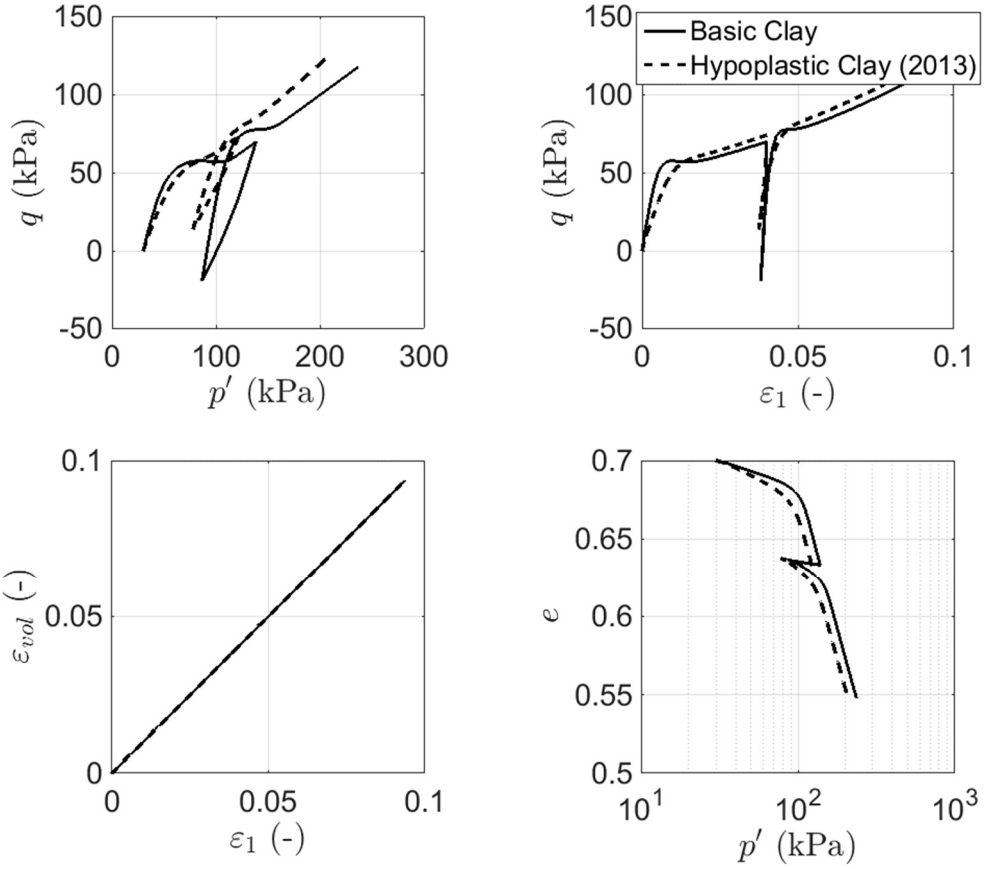


Figure 58: Comparison of models under oedometric conditions

2.5.4.5. Summary

Regardless of the differences in terms of local stiffness (Figure 54), the basic clay model can produce a similar response as clay hypoplastic models (Masin, 2013). The basic model replicates the general features of clay behaviour for typical laboratory tests. In this sense, it is proven that the expresions developed in this chapter are general enough to also replicate clay behaviour without having to sacrifice its generality.

2.6. SUMMARY OF CHAPTER

In this chapter it has been illustrated:

- That models in rate form (endochronic, hypoplastic,…) can be "encapsulated" with a non-linear kinematic hardening rule;
- A general form of functions and mapping tensors to be used in the formulation of NLKH have been proposed and accomodated to reproduce sands and clays.
- Each component of the general form has been studied and its implications have been discussed;
- A methodology to reduce the model to a simple autonomous ODE has been shown though a redefiniton of the strain metric;
- The cyclic properties of the modelling framework have been introduced and illustrated, including the superposition principle.
- Cualitative demonstration of numerical laboratory monotonic tests for sand and clay are provided.
- It has been shown that the models admit a bipotential and their themodynamical admissibility has been assesed.
- Both basic sand and basic clay models are compared with advanced hypoplastic models where their similarities and differences are illustrated at a local level and under common laboratory test conditions.

CHAPTER 3: NUMERICAL INTEGRATION

This chapter covers the local integration of the constitutive relations described in the previous chapter. The chapter is structured in three main parts: The first part briefly describes the programming logic of the constitutive driver developed during this Phd. The second part covers the integration challenges of this type of constitutive equations, giving a description of the explicit and implicit algorithms used for the local integration. Finally the third part benchmarks the performance of the local solver algorithms for two constitutive models: a simple encapsulation of the Wu (1992) model and the basic sand model proposed in the previous chapter.

3.1. OBJECT ORIENTED LOCAL INTEGRATION DRIVER

Before introducing the numerical aspects of the problem, the programming logic followed to explore the possible constitutive relations and their local integration is described. The programming logic of the local solver has followed an Object-Oriented logic paradigm similar to Patzak and Bittnar (2001). The advantage of this logic structure is that the code becomes modular so that the classes created for the local solver do not experience scalability issues and can be re-used for commercial Finite Element (FE) programs. The defined classes are:

- Material
- State or Integration Point
- Numerical Control
- Numerical Test
- Numerical Benchmark

The “Material” class contains the attributes of the constitutive model while the “state” or “integration point” class corresponds to the current state of the material (stress, strain, time, internal variables…). The methods associated with the “state” are typically: evaluation of yield

surface, calculation of normal of the yield surface, plastic modulus, second derivatives, stiffness matrix, etc.

The class “Numerical control” contains the tolerances and parameters affecting the type of integration and the type of local solver. The “Load Control” class is a class defined exclusively for the constitutive driver and is not used when the driver is integrated in a FE program. “Load control” class contains the constrains for each type of test or load condition following Bardet and Choucair (1991).

Finally, the “Numerical Test” and “Numerical Benchmark” are classes that involve one or more Numerical tests. The object “Numerical Test" contains an array of State Objects representing the history of the material and at least a method to solve itself. The method computes new states for each increment by pointing to Load control object for the type of increment and to Numerical Control for the type of solver. The class “Numerical Benchmark” follows the same concept but one step further, in that the object “Numerical Benchmark” contains an array of “Numerical Tests” that solve themselves. Numerical benchmark is very useful in the calibration of large sets of data, carrying out thousands of tests, probes or validation benchmarks which, when combined with genetic algorithms, become a powerful tool to calibrate large sets of laboratory data. Figure 59 shows the logic structure of the driver developed in this research, while Figure 60 shows how to integrate the constitutive driver logic in a Finite Element program.

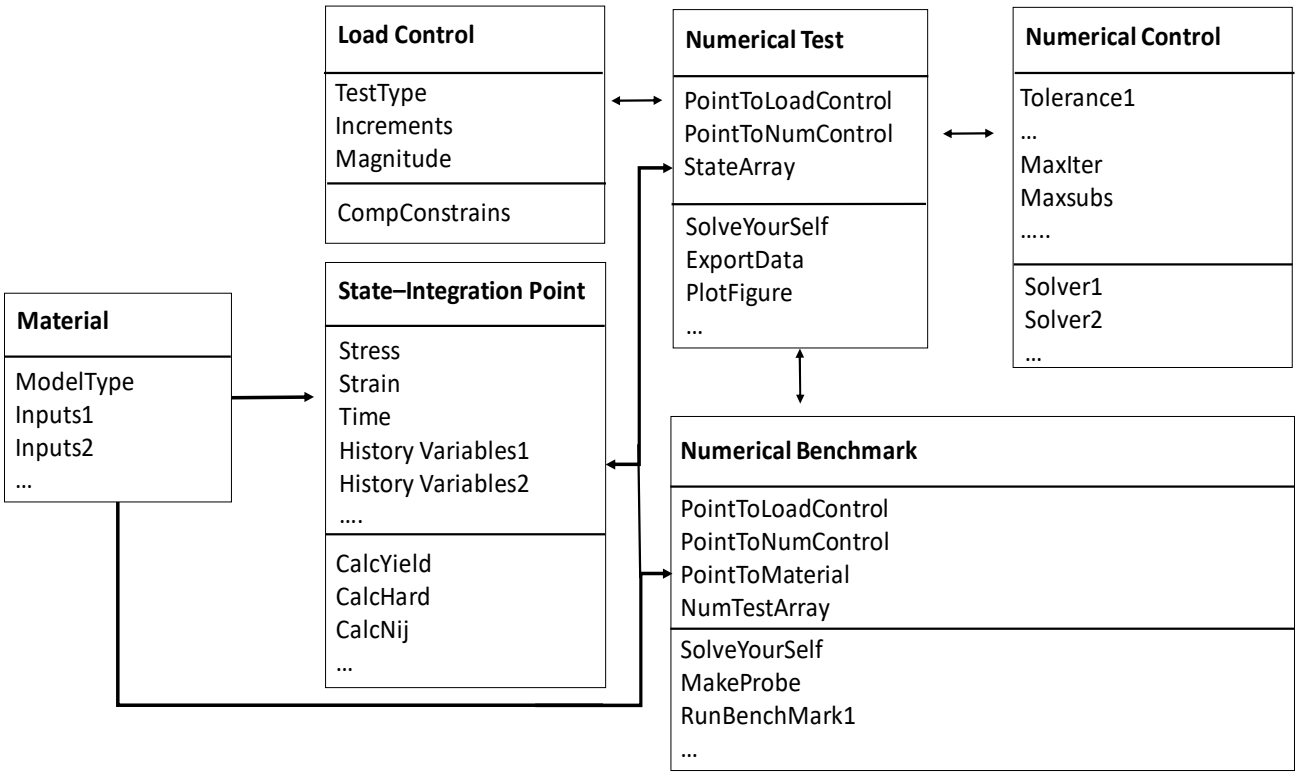


Figure 59: General structure of the object-oriented solver

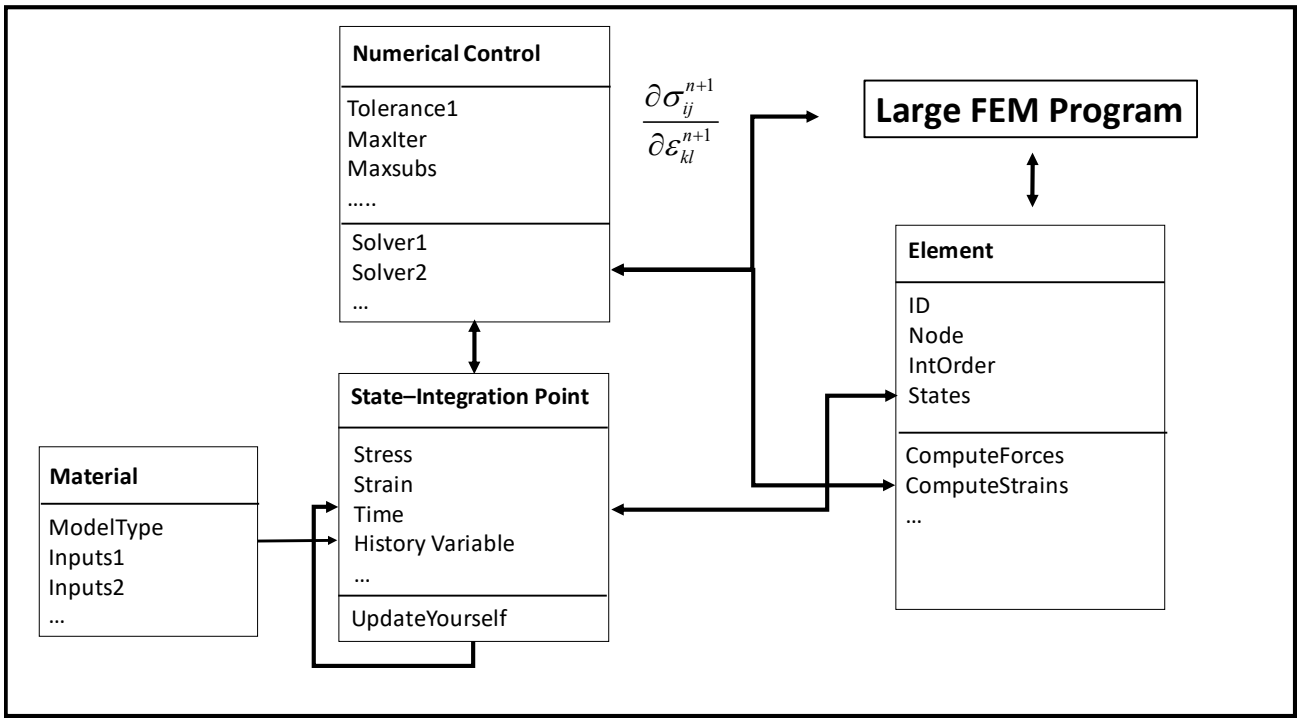


Figure 60: Integration in a Finite Element Program

3.2. LOCAL INTEGRATION

This section contextualises the challenges of the local integration of this type of equations and describes the solvers used in this thesis for the local integration of the constitutive equations. The structure of the section covers firstly a contextualisation of previous studies for similar families of this type of equations, followed by a description of the explicit and the implicit integration strategies. The final part of the section describes the modifications carried out to add constrains on the explicit solvers and implicit solver in order to perform mixed controlled numerical element tests.

3.2.1. CONTEXT

The equations used in this thesis share concepts of plasticity theory and hypoplasticity. In this sense all the models presented and described in this thesis require the existence of a yield surface with associated behaviour and all the ingredients of any elastoplastic model. On the other hand the form of the non-liner hardening rule and the orthogonality of the normal of the yield surface with the rate of stress minus backstress enforces the response to be practically identical to any hypoplastic model.

From the perspective of plasticity, many are the authors (Chaboche and Cailletaud, 1996), (Lubarda and Benson, 2002), (Kobayashi and Ohno, 2002), that have proposed various types of discretisation for the implicit integration of J-plasticity non-linear kinematic hardening models. On the other hand from the perspective of hypoplasticity examples of integration methods for the rate equations both implicitly and explicitly can be found in Tamagnini et al. (2000), Batista et al. (2003) and Fellin et al. (2009). However, perhaps for the type of problem considered here the most relevant conclusions can be derived from Chaboche and Cailletaud (1996) and Tamagnini et al. (2000), where similarities exists in the performance of various solution strategies. For example, both consider that the better performance for an implicit discretisation occurs when a semi-mid-point rule is used and that explicit second order Runge-Kutta (substep) with optimised step size performs equivalently to semi-implicit methods with uniform step size.

Here is an extract from Chaboche and Cailletaud (1996) conclusions:

- *The convergence study has shown for all the constitutive equations that the implicit integration ($\theta = 1$) leads to a linear convergence and is more stable in the case of large steps. Conversely, the semi-implicit integration for $\theta = l/2$ leads to a much better quadratic convergence in the low error range (small steps).*
- *The semi-implicit method applied with a uniform step size gives similar results compared to an explicit second order Runge-Kutta method with an optimised step size. Much better properties of the semi-implicit algorithm are then expected for such conditions where an optimised step would be used.*

while below is one from Tamagnini et al. (2000) conclusions:

- *The performance of the "First-order GMM-10 method is generally unsatisfactory both in terms of accuracy and efficiency, while the sixth-order adaptive RKF-56 method performs definitely better than all other methods examined when high accuracy of the global solution is needed.*
- *The performance of the two second-order methods (GMM-05, implicit; and RKF-12, explicit) has been found to be generally comparable for the initial conditions and loading paths considered. However, the adaptive nature of the sub stepping scheme adopted by the RKF-12 method may represent a major advantage in practical applications, in that it allows to avoid the a priori definition of an appropriate sub step size for which no rules of general applicability are available.*

While the study carried out by Tamagnini et al. (2000) concluded that the most efficient algorithm is the Runge-Kutta-56, later Batista et al. (2003), using the first hypoplastic model formulated (Wu, 1992), found the RK-56 to be unstable for large steps suggesting a semi-implicit Rosenbrock scheme to integrate the equations. In the light of the previous work carried by such authors it is interesting to explore the implicit and explicit local integration to benchmark the performance of the algorithms under the proposed eqautions. Two models are chosen: a simple encapsulated model akin to Wu (1992), and the previously proposed basic sand Model which shares similarities with the Cloe model (Chambon et al., 1994) which was benchmarked by Tamagnini et al. (2000).

Secondly, it is important to note that the size of the yield surface in these models is small and that the elastic stiffness is high. In this sense it is expected that when integrating this type of equations implicitly the predictors will lie in a region very far away from the solution. Therefore it has been considered of interest to explore the global convergence of the algorithms when integrating large steps implicitly. To do so the strategies covered in Scalet and Auricchio (2017) are used, in particular the constrained and augmented Lagrangian formulations of the closest projection method (CPPM) (Perez-Foguet and Armero, 2002), and commercial trust region solvers (Conn et al., 2000) for the implicit integration of the equations.

3.2.2. EXPLICIT METHODS: SUBSTEPPING SOLVER

The explicit solver chosen is the a substepping algorithm (Sloan, 1987), in particular the implementation has followed the one described in Potts and Zdravkovic (1999), which includes a drift correction (Potts and Gens, 1985). For the strain controlled problem the algorithm implemented in this thesis is the same, however for the constrained problem an adaptation of it had to be made to be consistent with the linearization process, as detailed in the following section. The unconstrained algorithm uses the first step to determine the increment of elastic stress as:

$$\Delta\sigma_{ij} = D^{e}_{ijkl}\Delta\varepsilon_{ij} \tag{3.1}$$

At the end of the iterative procedure, if the yield surface is not crossed, dε and dσ are updated. On the other hand, in case that at the end of the step the stress state is outside the yield surface, i.e. $F(\sigma + d\sigma, k) > 0$, the α must be determined in order that $F(\sigma + \alpha d\sigma, k) = 0$. This is done through an iterative procedure until a tolerance is reached (1.0E-5 was adopted here):

$$\alpha_{i+1} = \alpha_i - \frac{f(\sigma + \alpha_i \Delta\sigma, k)}{f(\sigma + \alpha_i \Delta\sigma, k) - f(\sigma + \alpha_{i-1} \Delta\sigma, k)}(\alpha_i - \alpha_{i-1}) \tag{3.2}$$

Therefore the elastic stress and strain can be evaluated as

$$\Delta\varepsilon^{e}_{ijkl} = \alpha\Delta\varepsilon_{ij} \tag{3.3}$$

The objective of this algorithm is to integrate the elasto-plastic constitutive matrix D_{ijkl}^{ep} over the elastoplastic strain step, splitting the step into a series of smaller substeps using a second order Euler approximation. The steps of the algorithm are:

i) Initialise at a given stress in the yield surface

$$\begin{aligned} T &= 0 \\ \Delta T &= 1 \end{aligned} \tag{3.4}$$

ii) Set the substep equal to

$$\Delta\varepsilon_{ij}^{ss} = \Delta T \Delta\varepsilon_{ij}^{s} \tag{3.5}$$

iii) Get the first estimate of the stress, plastic strain and hardening parameters.

$$\begin{aligned} \Delta\sigma_{ij}^{1} &= D^{ep}(\sigma_{ij}, k)\Delta\varepsilon_{ij}^{ss} \\ \Delta\varepsilon_{ij}^{p(1)} &= \lambda(\sigma_{ij}, k, \Delta\varepsilon_{ij}^{ss})\frac{\partial f(\sigma_{ij}, m)}{\partial\sigma_{ij}} \\ \Delta k^{(1)} &= k(\Delta\varepsilon_{ij}^{p(1)}) \end{aligned} \tag{3.6}$$

iv) Using the above quantities, the stresses and hardening/softening parameters of the first estimate, a second estimate can be obtained with the updated parameters using the previous methodology.

$$\begin{aligned} \Delta\sigma_{ij}^{2} &= D^{ep}(\sigma_{ij} + \Delta\sigma_{ij}^{1}, k + \Delta k^{1})\Delta\varepsilon_{ij}^{ss} \\ \Delta\varepsilon_{ij}^{p(2)} &= \lambda(\sigma_{ij} + \Delta\sigma_{ij}^{1}, k + \Delta k^{1}, \Delta\varepsilon_{ij}^{ss})\frac{\partial f(\sigma_{ij}, m)}{\partial\sigma_{ij}} \\ \Delta k^{(2)} &= k(\Delta\varepsilon_{ij}^{p(2)}) \end{aligned} \tag{3.7}$$

v) It is now possible to know a more accurate Euler estimate of stress, plastic strains and hardening/softening parameters for the strain increment

$$\begin{aligned} \Delta\sigma_{ij} &= 0.5(\Delta\sigma_{ij}^{1} + \Delta\sigma_{ij}^{2}) \\ \Delta\varepsilon_{ij}^{p} &= 0.5(\Delta\varepsilon_{ij}^{p(1)} + \Delta\varepsilon_{ij}^{p(2)}) \\ \Delta k &= 0.5(\Delta k^{1} + \Delta k^{2}) \end{aligned} \tag{3.8}$$

vi) Convergence criteria is only based on stress

$$SR = \frac{\left\| (\Delta\sigma_{ij}^{1} - \Delta\sigma_{ij}^{2}) \right\|}{\left\| 0.5(\Delta\sigma_{ij}^{1} + \Delta\sigma_{ij}^{2}) \right\|} < STOL \tag{3.9}$$

vii) If the error is acceptable the step is accepted and move to viii), else the substep is reduced by β depending which convergence condition has been violated and back to ii)

$$\beta = 0.8\left[\frac{STOL}{SR}\right]^{0.5} \tag{3.10}$$

viii) Stress, strain and history parameters are updated as

$$\begin{aligned} \sigma_{ij} &= \sigma_{ij} + \Delta\sigma_{ij} \\ \varepsilon_{ij}^{p} &= \varepsilon_{ij}^{p} + \Delta\varepsilon_{ij}^{p} \\ k &= k + \Delta k \end{aligned} \tag{3.11}$$

ix) Normally after the integration process the final step does not yield exactly in the yield surface and a new condition $F(\sigma, k) \le YTOL$ must be fulfilled. If satisfied, the stress is updated and the process continues until T = 1. If not a drift correction is applied as follows,

$$\Delta\sigma_{ij}^{drift} = -\Lambda^{drift} D_{ijkl}^{e} \frac{\partial P}{\partial \sigma_{kl}} \tag{3.12}$$

$$\Lambda^{drift} = \frac{F(\sigma, k)}{\frac{\partial F}{\partial \sigma_{ij}} D_{ijkl}^{e} \frac{\partial P}{\partial \sigma_{kl}} - \frac{\partial F}{\partial k_{i}} \Delta k_{i}} \tag{3.13}$$

and therefore corrections also include strain drift

$$\begin{aligned} \Delta\varepsilon_{ij}^{p} &= \Lambda^{drift} \frac{\partial P}{\partial \sigma_{ij}} \\ \Delta k &= \Lambda^{drift} \Delta k \left(\frac{\partial P}{\partial \sigma_{ij}} \right) \end{aligned} \tag{3.14}$$

x) Update stress and history parameters, store variables and update T. Go back to 1 while T < 1

Only the second order modified Euler scheme has been studied, however higher order Runge-Kutta schemes are perfectly possible to use without having to modify the drift correction. Future implementations will include the RK-15 where only the correction factor needs to be corrected to:

$$\beta = 0.8\left[\frac{STOL}{SR}\right]^{1/5} \tag{3.15}$$

3.2.3. IMPLICIT INTEGRATION

The implicit integration is perhaps the section where more possible combinations on the treatment of the equations can be done. In this sense the section is subdivided into a number of parts covering the discretisation of the non-linear equations and the solvers of the non-linear system of equations.

3.2.3.1. Time discretisation

As mentioned earlier, the formulations of most constitutive models lie between the cyclic plasticity framework and hypoplasticity. As the hardening rule is a rate independent function it can be treated as a function:

$$\dot{\alpha}_{ij}^{(k)} = \dot{\lambda} h_{ij}(\vec{n}_{ij}, \alpha_{ij}^{(k)}) \tag{3.16}$$

where $\vec{n}_{ij}$ is the normal of the yield surface, $\alpha_{ij}^{(k)}$ the backstress and $\dot{\lambda}$ the plastic multiplier, coincident with $\left\|\dot{\varepsilon}_{ij}^{p}\right\|$. Therefore the intermediate evaluations for the normal and the backstress can be controlled by θ_n, θ_α controlling the evaluation of the backstress and the normal of the yield surface, where

$$\alpha_{ij}^{n+\theta_\alpha} = \theta_\alpha \alpha_{ij}^{n+1} + (1-\theta_\alpha)\alpha_{ij}^{n} \tag{3.17}$$

and

$$\vec{n}_{ij}^{n+\theta_n} = \frac{\theta_n\left(\sigma_{ij}^{n+1} - \alpha_{ij}^{n+1}\right) + (1-\theta_n)\left(\sigma_{ij}^{n} - \alpha_{ij}^{n}\right)}{\left\|\theta_n\left(\sigma_{ij}^{n+1} - \alpha_{ij}^{n+1}\right) + (1-\theta_n)\left(\sigma_{ij}^{n} - \alpha_{ij}^{n}\right)\right\|} \tag{3.18}$$

The first challenge for integration of this equations is where to evaluate the normal. This issue has already been treated by Chaboche and Cailletaud (1996). The root of the problem is that, due to the shape of the yield surface, it is impossible to guarantee the consistency condition at the end of the step if everything is evaluated at the mid of the step (stress, backstress or normal), producing a "saw-tooth" solution type for large integration steps. This is addressed by solving the hardening rule at the mid-point, while solving the consistency at the end of the step (Ortiz and Popov, 1985).

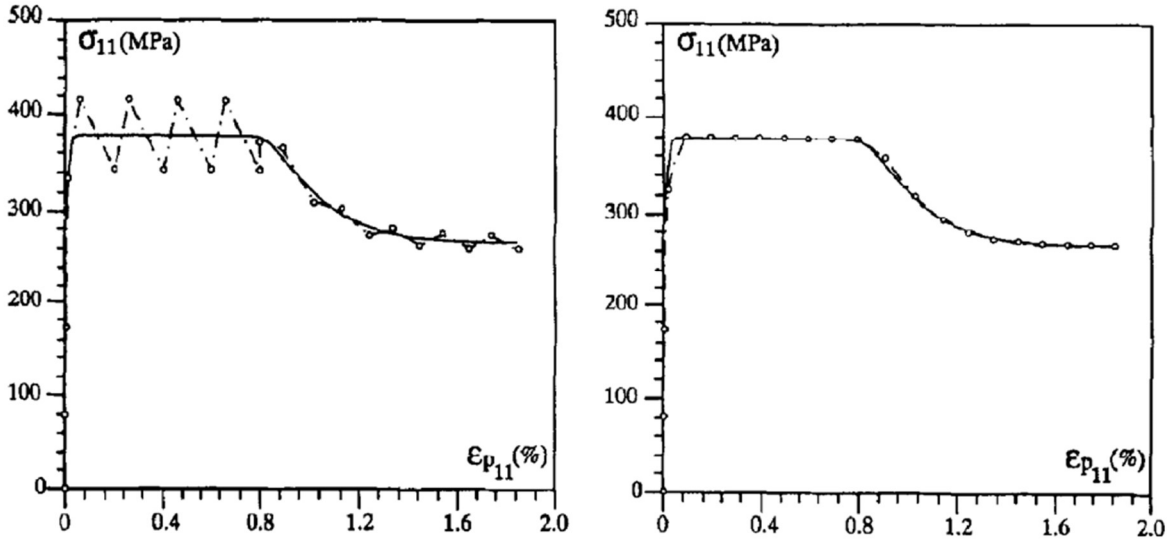


Figure 61: Biaxial loading for Non-linear kinematic hardening model. All equations solved at the mid of the step (left). Mixed discretisation, hardening rule solved in the mid step and consistency condition at the end of the step (right). (Chaboche and Cailletaud, 1996)

Therefore the direction of the plastic strain can be evaluated at the middle of the step but the consistency must be enforced ate the end of the step. Two semi-implicit discretisations are studied here:

Trapezoidal discretisation (TZ)

$$\sigma_{ij}^{n+1} = \left(\sigma_{ij}^{PR} + \sigma_{ij}^{n}\right) - \lambda^{n+1} D_{ijkl}^{e} \vec{n}_{kl}^{n+\theta_n} \tag{3.19}$$

$$\alpha_{ij}^{n+1} = \alpha_{ij}^{n} + \lambda^{n+1}\left((1-\theta_\alpha) h_{ij}(\alpha_{ij}^{n}, \vec{n}_{kl}^{n+\theta_n}) - \theta_\alpha h_{ij}(\alpha_{ij}^{n+1}, \vec{n}_{kl}^{n+\theta_n})\right) \tag{3.20}$$

$$f^{n+1} = 0 \tag{3.21}$$

Midpoint discretisation (MID)

$$\sigma_{ij}^{n+1} = \left(\sigma_{ij}^{PR} + \sigma_{ij}^{n}\right) - \lambda^{n+1} D_{ijkl}^{e} \vec{n}_{kl}^{n+\theta_n} \tag{3.22}$$

$$\alpha_{ij}^{n+1} = \alpha_{ij}^{n} + \lambda^{n+1} h_{ij}(\alpha_{ij}^{n+\theta_\alpha}, \vec{n}_{ij}^{n+\theta_n}) \tag{3.23}$$

$$f^{n+1} = 0 \tag{3.24}$$

It is noted that both time discretisation become the classic backward Euler when both values of θ are 1. The time discretisations studied in this thesis are shown in the following table.

Table 10: Cases of time step discretisations for implicit integration

		θ_n	θ_α
BE	***Backward Euler***	1.0	1.0
MID05	***Mid-Point***	0.5	0.5
MID1	***Half Mid-Point***	1.0	0.5
TZ1	***Half Trapezoidal***	1.0	0.5

3.2.3.2. Reduced system for $\theta_n = 1$

If the normal is evaluated at the end of the step ($\theta_n = 1$) regarding the type of discretisation or where the backstress is evaluated, the general systems of equations (3.19)-(3.21) and (3.22)-(3.24) can be reduced, eliminating the 6 stress unknowns, as:

$$\sigma_{ij}^{n+1} = \left(\sigma_{ij}^{PR} + \sigma_{ij}^{n}\right) - \lambda^{n+1} D_{ijkl}^{e} \vec{n}_{kl}^{n+1} \tag{3.25}$$

For the trapezoidal discretisation:

$$\alpha_{ij}^{n+1} = \alpha_{ij}^{n} + \lambda^{n+1}\left((1-\theta_\alpha) h_{ij}(\alpha_{ij}^{n}, \vec{n}_{ij}^{n}) - \theta_\alpha h_{ij}(\alpha_{ij}^{n+1}, \vec{n}_{ij}^{n+1})\right) \tag{3.26}$$

while for the mid-point:

$$\alpha_{ij}^{n+1} = \alpha_{ij}^{n} + \lambda^{n+1} h_{ij}\left(\alpha_{kl}^{n+\theta}, \vec{n}_{kl}^{n+1}\right) \tag{3.27}$$

Rearranging (3.25) results in:

$$m\vec{n}_{ij}^{n+1} = \left(\sigma_{ij}^{PR} + \sigma_{ij}^{n}\right) - \lambda^{n+1} D_{ijkl}^{e} \vec{n}_{kl}^{n+1} - \alpha_{ij}^{n+1} \tag{3.28}$$

A fourth order tensor A_{ijkl} dependant on λ^{n+1} is obtained isolating $\vec{n}_{ij}^{n+1}$:

$$\begin{aligned}
&A_{ijkl}(\lambda^{n+1}) = (m + 2G\lambda^{n+1})\delta_{ik}\delta_{jl} + \left(K - 2/3G\right)\lambda^{n+1}\delta_{ij}\delta_{kl} \\
&A_{ijkl}^{-1}(\lambda^{n+1}) = \frac{1}{m + 2G\lambda^{n+1}}\left(\delta_{ik}\delta_{jl} - \frac{\left(\frac{K - 2/3G}{m + 2G\Delta\lambda}\right)\lambda^{n+1}}{1 + 3\left(\frac{K - 2/3G}{m + 2G\Delta\lambda}\right)\lambda^{n+1}}\delta_{ij}\delta_{kl}\right) \\
&A_{ijkl}\vec{n}_{kl}^{n+1} = \sigma_{ij}^{PR} + \sigma_{ij}^{n} - \alpha_{ij}^{n+1}
\end{aligned} \tag{3.29}$$

Finally, a relation between the unknowns $\vec{n}_{ij}^{n+1}$ and α_{ij}^{n+1} can be obtained:

$$\vec{n}_{ij}^{n+1} = L_{ijkl}^{-1}\left(\sigma_{kl}^{PR} + \sigma_{kl}^{n} - \alpha_{kl}^{n+1}\right) \tag{3.30}$$

Therefore it only needs to solve α_{ij}^{n+1} and λ^{n+1}, substituting (3.30) into (3.26) and imposing the consistency condition. For the trapezoidal integration the following system of equations to be solved is

$$\begin{aligned} r_\alpha &= \alpha_{ij}^{n+1} - \alpha_{ij}^{n} - \lambda^{n+1}\left((1-\theta_\alpha)h_{ij}(\alpha_{ij}^{n},\vec{n}_{ij}^{n+1}) - \theta_\alpha h_{ij}(\alpha_{ij}^{n+1},\vec{n}_{ij}^{n+1})\right) \\ r_\lambda &= \left\| L_{ijkl}^{-1}\left(\sigma_{kl}^{PR} + \sigma_{kl}^{n} - \alpha_{kl}^{n+1}\right)\right\| - 1 \end{aligned} \tag{3.31}$$

while if for the midpoint rule the system to solve is

$$\begin{aligned} r_\alpha &= \alpha_{ij}^{n+1} - \alpha_{ij}^{n} - \lambda^{n+1} h_{ij}\left((\theta_\alpha\alpha_{ij}^{n+1} + (1-\theta_\alpha)\alpha_{ij}^{n}),\vec{n}_{ij}^{n+1}\right) \\ r_\lambda &= \left\| L_{ijkl}^{-1}\left(\sigma_{kl}^{PR} + \sigma_{kl}^{n} - \alpha_{kl}^{n+1}\right)\right\|^2 - 1 \end{aligned} \tag{3.32}$$

This discretisation has less unknowns at the cost of adding complexity on the residual functions. The final system is:

$$\begin{aligned} r_\alpha &= \alpha_{ij}^{n+1} - \alpha_{ij}^{n} - \Delta\lambda h_{ij}\left((\theta_\alpha\alpha_{ij}^{n+1} + (1-\theta_\alpha)\alpha_{ij}^{n}),\vec{n}_{ij}^{n+1}\right) \\ r_\lambda &= \left\| L_{ijkl}^{-1}\left(\sigma_{kl}^{PR} + \sigma_{kl}^{n} - \alpha_{kl}^{n+1}\right)\right\|^2 - 1 \end{aligned} \tag{3.33}$$

and the Jacobian can be obtained through:

$$\frac{\partial r}{\partial x} = \begin{bmatrix} \delta_{ik}\delta_{jl} - \lambda^{n+1}\theta_\alpha \dfrac{\partial h_{ij}^{n+\theta_n}}{\partial \alpha_{kl}^{n+1}} & -h_{ij}(\alpha_{ij}^{n+\theta_\alpha}, L_{ijkl}^{-1}\left(\sigma_{kl}^{PR} + \sigma_{kl}^{n} - \alpha_{kl}^{n+1}\right) - \lambda^{n+1}\theta_\alpha \dfrac{\partial h_{ij}^{n+\theta_n}}{\partial \lambda^{n+1}}) \\ -2L_{ijmn}^{-1}L_{mnpq}^{-1}\left(\sigma_{pq}^{PR} + \sigma_{pq}^{n} - \alpha_{pq}^{n+1}\right) & 2\left(\sigma_{pq}^{PR} + \sigma_{pq}^{n} - \alpha_{pq}^{n+1}\right)\dfrac{\partial L_{ijkl}^{-1}}{\partial \lambda} L_{ijkl}^{-1} \end{bmatrix} \tag{3.34}$$

$$x = \begin{bmatrix} \alpha_{ij}^{n+1} \\ \lambda^{n+1} \end{bmatrix}$$

where

$$\begin{aligned} L_{ijkl}(\Delta\lambda) &= (m + 2G\Delta\lambda)\delta_{ik}\delta_{jl} + \left(K - 2/3G\right)\Delta\lambda\delta_{ij}\delta_{kl} \\ L_{ijkl}^{-1}(\Delta\lambda) &= \frac{1}{m + 2G\Delta\lambda}\left(\delta_{ik}\delta_{jl} - \frac{\left(\dfrac{K - 2/3G}{m + 2G\Delta\lambda}\right)\Delta\lambda}{1 + 3\left(\dfrac{K - 2/3G}{m + 2G\Delta\lambda}\right)\Delta\lambda}\delta_{ij}\delta_{kl}\right) \\ \frac{\partial L_{ijkl}^{-1}}{\partial \lambda} &= -L_{ijpq}^{-1}D_{pqrt}^{e}L_{rtkl}^{-1} \end{aligned} \tag{3.35}$$

3.2.3.3. Non-linear solvers

It is well known that Newton-Raphson methods (as a Closest Projection Point Method, CPPM) have quadratic convergence in the neighbourhood of the solution, but they are not globally convergent. Due to the fact that the elastic predictor is very large it is very likely that classic CPPMs may not converge, or they explore regions of the space of solutions that do not fulfil the Kuhn-Tucker conditions. Also, apart from being far from the solution a classic Newton-Raphson procedure may experience a deficient rate of convergence. In this sense the classic CPPM against globally convergent schemes (Armero and Perez-Foguet, 2002, Perez-Foguet and Armero, 2002) has been explored for medium-large excursions of the strain increment. Finally a radical approach to solve plasticity equations has been explored using a general-purpose solver for non-linear optimization (Conn et al., 2000). In summary the non-linear solvers used are:

- Closest Projection Point method (CPPM)
- Primal Closest Projection method – Line search (primal-CPPM)
- Augmented Primal Closest projection method (augmented-primal-CPPM)
- Dogleg-Trust-Region method (DTM)

3.2.3.4. *Closest Projection Point method (CPPM)*

The system to resolve consists of the following residuals:

$$r_\sigma = \sigma_{ij}^{n+1} - \left(\sigma_{ij}^{PR} + \sigma_{ij}^{n}\right) + \lambda D_{ijkl}^{e} \vec{n}_{kl}^{n+\theta_n} \tag{3.36}$$

$$r_\alpha = \alpha_{ij}^{n+1} - \alpha_{ij}^{n} - \lambda h_{ij}(\alpha_{ij}^{n+\theta_\alpha}, \vec{n}_{ij}^{n+\theta_n}) \tag{3.37}$$

$$r_f = f^{n+1} = \left\| \sigma_{ij}^{n+1} - \alpha_{ij}^{n+1} \right\| - m \tag{3.38}$$

where the Jacobian is

$$\frac{\partial r}{\partial x} = \begin{bmatrix} \delta_{ik}\delta_{jl} + \lambda^{n+1}\theta_n D_{ijmn}^{e} \dfrac{\partial \vec{n}_{mn}^{n+\theta_n}}{\partial \sigma_{kl}^{n+1}} & -\lambda^{n+1}\theta_n D_{ijkl}^{e} \dfrac{\partial \vec{n}_{kl}^{n+\theta_n}}{\partial \sigma_{ij}^{n+1}} & D_{ijkl}^{e}\vec{n}_{kl}^{n+\theta_n} \\ -\lambda^{n+1}\theta_n \dfrac{\partial h_{ij}^{n+\theta_n}}{\partial \sigma_{kl}^{n+1}} & \delta_{ik}\delta_{jl} - \lambda^{n+1}\left(\theta_\alpha \dfrac{\partial h_{ij}^{n+\theta_n}}{\partial \alpha_{kl}^{n+1}} + (\theta_n - \theta_\alpha)\dfrac{\partial h_{ij}^{n+\theta_n}}{\partial \vec{n}_{ij}^{n+\theta_n}} \dfrac{\partial \vec{n}_{ij}^{n+\theta_n}}{\partial \alpha_{kl}^{n+1}}\right) & -h_{ij}(\alpha_{ij}^{n+\theta_\alpha}, \vec{n}_{ij}^{n+\theta_n}) \\ \vec{n}_{ij}^{n+1} & -\vec{n}_{ij}^{n+1} & 0 \end{bmatrix}$$

$$x = \begin{bmatrix} \sigma_{ij}^{n+1} \\ \alpha_{ij}^{n+1} \\ \lambda^{n+1} \end{bmatrix}$$

(3.39)

The iterative procedure until a solution is reached within the predefined tolerance is:

$$x^{(k+1)} = x^{(k)} + dx^{(k)} = x^{(k)} - \left[\frac{\partial r(x^{(k)})}{\partial x}\right]^{-1} r(x^{(k)}) \tag{3.40}$$

3.2.3.5. *Line search (CPPM-LS)*

A line search technique can be included in the CPPM to improve convergence. The line search technique requires two extra numerical inputs appearing in equations (3.43), in this case the recommendations of Perez-Foguet and Armero (2002) have been followed and the values of

$\eta^{LS}=0.1$ and $\beta^{LS}=10^{-4}$ has been used for all the analyses. The line search technique affects the magnitude of the iterative corrector $dx^{(k)}$ but not its direction. Following the CPPM notation described in 0, given $dx^{(k)}, x^{(k)}, r^k$ where $r^k = r(x^{(k)})$, the linear search (LS) works as:

1. Initialise j = 0,

$$\begin{aligned} \gamma_{(0)}^{(k)} &= 1 \\ \hat{M}^{(k)} &= \frac{1}{2} r^{(k)} r^{(k)} \\ \hat{M}'^{(k)} &= -2\hat{M}^{(k)} \end{aligned} \tag{3.41}$$

2. Compute new merit function

$$\begin{aligned} x_{(j)}^{(k+1)} &= x^{(k)} + \gamma_{(j)}^{(k)} dx^{(k)} \\ r_{(j)}^{(k+1)} &= r(x_{(j)}^{(k+1)}) \\ \hat{M}_{(j)}^{(k+1)} &= \frac{1}{2} r_{(j)}^{(k+1)} r_{(j)}^{(k+1)} \end{aligned} \tag{3.42}$$

3. Check Goldstein condition $\hat{M}_{(j)}^{(k+1)} \le (1-2\beta^{LS}\gamma_{(j)}^{(k)})\hat{M}_{(j)}^{(k)}$
   - True ➔ EXIT and set $x_{(j)}^{(k+1)} = x^{(k)} + \gamma_{(j)}^{(k)} dx^{(k)}$
   - False➔ Compute $\gamma_{(j+1)}^{(k)}$

$$\gamma_{(j+1)}^{(k)} = \max\left(\eta^{LS}\gamma_{(j)}^{(k)}, \frac{(\gamma_{(j)}^{(k)})^2 \hat{M}^{(k)}}{\hat{M}_{(j)}^{(k+1)} - \left(1-2\gamma_{(j)}^{(k)}\right)\hat{M}^{(k)}} \right) \tag{3.43}$$

4. Set j = j +1 and go to 2

3.2.3.6. Constrained closest projection point (Primal-CPPM)

If the predictor is too far away the first iterations of $dx^{(k)}$ may go to a region where $\lambda^{n+1} < 0$, violating Kuhn-Tucker conditions. The described algorithm includes a constrain to avoid the situation (primal-CPPM) when the Kuhn-Tucker conditions are not fulfilled. The algorithm and the constrained Jacobian reads:

1. IF $\lambda^{(k)n+1} = 0$ THEN $g = n_{ij}\left(\sigma_{ij}^{(k)} - \sigma_{ij}^{PR} + \sigma_{ij}^{n} + \alpha_{ij}^{(k)} - \alpha_{ij}^{n}\right)$

   1.1. IF $g \le 0$

$$dx^{(k)} = -\left[\frac{\partial r(x^{(k)})}{\partial x}\right]^{-1} r(x^{(k)}) \tag{3.44}$$

   1.2. ELSE

$$\begin{aligned}
\left[D^{(k)}\right]_{ij} &= \begin{cases} \left[\left(J^{(k)}\right)^{-1}\left(J^{(k)}\right)^{-T}\right]_{ij} & i,j \neq n_x \quad i=j=n_x \\ 0 & i,j=n_x \quad i \neq j \end{cases} \\
dx^{(k)} &= -D^{(k)}\left(J^{(k)}\right)^{T} r(x^{(k)}) \\
J^{(k)} &= \left[\frac{\partial r(x^{(k)})}{\partial x}\right]
\end{aligned} \tag{3.45}$$

while the constrained line search has a standard form when $\lambda^{(k)n+1} > 0$, but if $\lambda^{(k)n+1} = 0$ then:

1. Initialise j = 0,

$$\begin{aligned}
\gamma_{(0)}^{(k)} &= 1 \\
\hat{M}'^{(k)} &= r^{(k)} J^{(k)} d^{(k)}
\end{aligned} \tag{3.46}$$

2. Compute new merit function

$$\begin{aligned}
x_{(j)}^{(k+1)} &= \left\langle x^{(k)} + \gamma_{(j)}^{(k)} dx^{(k)} \right\rangle_n \\
r_{(j)}^{(k+1)} &= r(x_{(j)}^{(k+1)}) \\
\hat{M}_{(j)}^{(k+1)} &= \frac{1}{2} r_{(j)}^{(k+1)} r_{(j)}^{(k+1)}
\end{aligned} \tag{3.47}$$

3. Check Goldstein condition $\hat{M}_{(j)}^{(k+1)} \le \hat{M}_{(j)}^{(k)} + \beta^{LS} r^{(k)} J^{(k)} (x_{(j)}^{(k+1)} - x^{(k)})$

   - True ➔ EXIT and set $x_{(j)}^{(k+1)}$
   - False➔ Compute $\gamma_{(j+1)}^{(k)}$

$$\gamma_{(j+1)}^{(k)} = \max\left(\eta^{LS}\gamma_{(j)}^{(k)}, \frac{-(\gamma_{(j)}^{(k)})^2 \hat{M}'^{(k)}}{2\left(\hat{M}_{(j)}^{(k+1)} - \hat{M}^{(k)} - \gamma_{(j)}^{(k)}\hat{M}'^{(k)}\right)}\right) \tag{3.48}$$

4. Set j = j +1 and go to 2

3.2.3.7. Augmented closest projection point (Aug-CPPM)

The algorithm uses an augmented form of the variational formulation of the system of equations (3.36) (3.37) and (3.38). A more detailed description of the algorithm can be found in Armero and Perez-Foguet (2002). The solver requires a numerical input "***c***" as penalty term on the plastic multiplier. Through numerical investigation a value of "***c****"* in the range of [1E-2,1E-4] has been found to provide a good performance for the system of equations proposed. The augmented system of equations is:

$$r_\sigma = \sigma_{ij}^{n+1} - \left(\sigma_{ij}^{PR} + \sigma_{ij}^{n}\right) + c\left\langle \frac{\lambda}{c} + f^{n+1} \right\rangle D_{ijkl}^{e} \vec{n}_{kl}^{n+\theta_n} \tag{3.49}$$

$$r_\alpha = \alpha_{ij}^{n+1} - \alpha_{ij}^{n} - c\left\langle \frac{\lambda}{c} + f^{n+1} \right\rangle h_{ij}(\alpha_{ij}^{n+\theta_\alpha}, \vec{n}_{ij}^{n+\theta_n}) \tag{3.50}$$

$$r_f = \left\langle \frac{\lambda}{c} + f^{n+1} \right\rangle - \frac{\lambda}{c} \tag{3.51}$$

The Jacobian here is:

$$\frac{\partial r}{\partial x}=\begin{bmatrix} \delta_{ik}\delta_{jl}+\theta_n c\left\langle \frac{\lambda^{n+1}}{c}+f^{n+1}\right\rangle D^e_{ijmn}\frac{\partial \vec{n}^{n+\theta_n}_{mn}}{\partial \sigma^{n+1}_{kl}}+s^{(n+1)}\theta_n c\vec{n}^{n+1}_{ij}D^e_{klmn}\vec{n}^{n+\theta_n}_{mn} & -c\left\langle \frac{\lambda^{n+1}}{c}+f^{n+1}\right\rangle \theta_n D^e_{ijkl}\frac{\partial \vec{n}^{n+\theta_n}_{kl}}{\partial \sigma^{n+1}_{ij}}-s^{(n+1)}\theta_n c\vec{n}^{n+1}_{ij}D^e_{klmn}\vec{n}^{n+\theta_n}_{mn} & s^{(n+1)}D^e_{ijkl}\vec{n}^{n+\theta_n}_{kl} \\ -c\left\langle \frac{\lambda^{n+1}}{c}+f^{n+1}\right\rangle \theta_n \frac{\partial h^{n+\theta_n}_{ij}}{\partial \sigma^{n+1}_{kl}}-s^{(n+1)}c\vec{n}^{n+1}_{ij}h^{n+\theta_n}_{kl} & \delta_{ik}\delta_{jl}-c\left\langle \frac{\lambda^{n+1}}{c}+f^{n+1}\right\rangle \theta_\alpha \frac{\partial h^{n+\theta_n}_{ij}}{\partial \alpha^{n+1}_{kl}}-s^{(n+1)}c\vec{n}^{n+1}{}_n h_{kl}(\alpha^{n+\theta_\alpha}_{ij},\vec{n}^{n+\theta_n}_{ij}) & -s^{(n+1)}h_{ij}(\alpha^{n+\theta_\alpha}_{ij},\vec{n}^{n+\theta_n}_{ij}) \\ s^{(n+1)}\vec{n}^{n+1}_{ij} & -s^{(n+1)}\vec{n}^{n+1}_{ij} & (s^{(n+1)}-1)\frac{1}{c} \end{bmatrix}$$

$$x=\begin{bmatrix}\sigma^{n+1}_{ij}\\ \alpha^{n+1}_{ij}\\ \lambda^{n+1}\end{bmatrix}$$

(3.52)

where

$$\frac{\partial h^{n+\theta_n}_{ij}}{\partial \alpha^{n+1}_{kl}}=\frac{\partial h^{n+\theta_n}_{ij}}{\partial \alpha^{n+\theta_n}_{kl}}\frac{\partial \alpha^{n+\theta_n}_{kl}}{\partial \alpha^{n+1}_{kl}}=\theta_n\frac{\partial h^{n+\theta_n}_{ij}}{\partial \alpha^{n+\theta_n}_{kl}}$$

Given $dx^{(k)}, x^{(k)}, r^k$, it is combined with the unconstrained Line search algorithm described in 3.2.3.5.

3.2.3.8. Dogleg-Trust-Region method (DTM)

The Dogleg-Trust-Region-Method (Conn et al., 2000) is an optimization method that searches for the minimum of an objective function $F(x): \mathbb{R}^n \to \mathbb{R}$. It solves a series of sub-problems by using a Taylor approximation of second order to estimate the function in the neighbourhood of the evaluation point as:

$$F(x_{ij}^k + h\vec{\varepsilon}_{ij}) \approx Q(h\vec{\varepsilon}_{ij}) = F(x_{ij}^k) + \left.\frac{\partial F}{\partial x_{mn}^k}\right|_k h\vec{\varepsilon}_{mn} + \frac{1}{2}h^2\vec{\varepsilon}_{ij}B_{ijkl}(x_{ij}^k)\vec{\varepsilon}_{kl} \tag{3.53}$$

where $\left.\frac{\partial F}{\partial x_{mn}^k}\right|$ is the gradient of the residual discretisation and B_{ijkl} is an estimate of the Hessian of ***F***. If a minimum has been found it implies that the gradient of the quadratic approximation $Q_{ij}(h\vec{\varepsilon}_{ij})$ is zero and then:

$$\left.\frac{\partial F}{\partial x_{mn}^k}\right|_k + B_{ijkl}(x_{ij}^k)h\vec{\varepsilon}_{kl} = 0 \tag{3.54}$$

The iterative procedure consists of solving (3.54) sub-problems given the radius *h*:

1. Set k = 0 and initial x_{ij}^k
2. Solve δ_{ij} from (3.54)
3. Update $x_{ij}^{k+1} = x_{ij}^k + \delta_{ij}$

In other words, the algorithm finds the minimum of an approximation of radius ***"h"*** in the space of solutions and updates the variables to find a new minimum. Once that new minimum is obtained, it may increase or decrease the radius ***"h"*** of the new approximation of $F(x)$. The algorithm has initially slow convergence until it finds the appropriate trust region, where it exhibits superlinear convergence.

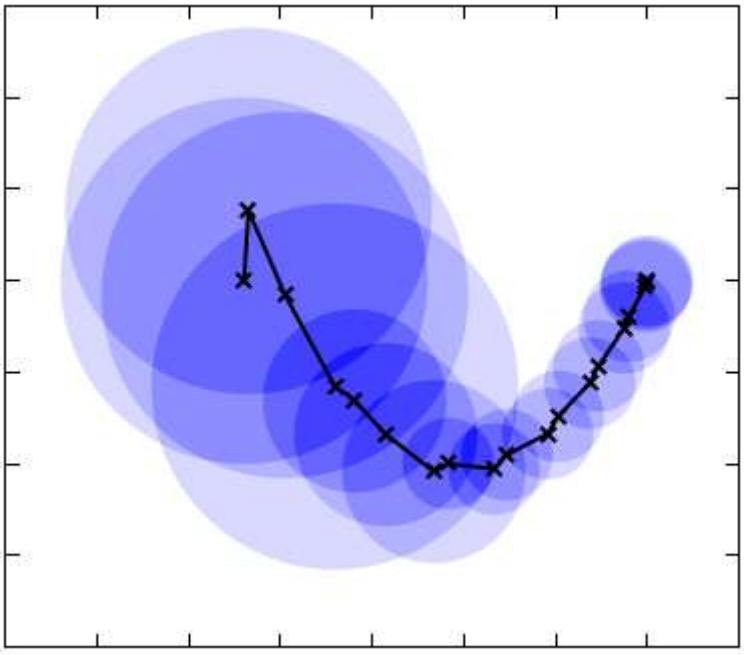


Figure 62: Illustration of trust-region method

In order to ensure that this method converges, it needs $B_{ijmnkl}(x_{ij}^{k})$ to be positive defined. This method is globally convergent, and Jacobian and Hessians are evaluated numerically.

3.2.3.9. Algorithmic consistent tangent modulus

For the system of equations of (3.36) (3.37) and (3.38) the algorithmic consistent tangent matrix can be obtained with the method described in de Souza Neto et al. (2008), for which the algorithmic consistent tangent matrix is:

$$D_{ijkl}^{n+1} = \frac{\partial \sigma_{ij}^{n+1}}{\partial \varepsilon_{ij}^{n+1}} \tag{3.55}$$

Recalling the system of equations of the midpoint discretisation:

$$\begin{Bmatrix} \sigma_{ij}^{n+1} - \left(\sigma_{ij}^{PR} + \sigma_{ij}^{n}\right) + \lambda D_{ijkl}^{e} \vec{n}_{kl}^{n+\theta_n} \\ \alpha_{ij}^{n+1} - \alpha_{ij}^{n} - \lambda h_{ij}(\alpha_{ij}^{n+\theta_\alpha}, \vec{n}_{ij}^{n+\theta_n}) \\ \left\| \sigma_{ij}^{n+1} - \alpha_{ij}^{n+1} \right\| - m \end{Bmatrix} = \begin{Bmatrix} 0 \\ 0 \\ 0 \end{Bmatrix} \tag{3.56}$$

After differentiation:

$$\begin{Bmatrix} d\sigma_{ij}^{n+1} + \lambda D_{ijpq}^{e} \dfrac{\partial \vec{n}_{pq}^{n+\theta_n}}{\partial \sigma_{kl}^{n+1}} d\sigma_{kl}^{n+1} + \lambda D_{ijpq}^{e} \dfrac{\partial \vec{n}_{pq}^{n+\theta_n}}{\partial \alpha_{kl}^{n+1}} d\alpha_{kl}^{n+1} + D_{ijmn}^{e} \vec{n}_{mn}^{n+\theta_n} d\lambda^{n+1} \\ d\alpha_{ij}^{n+1} - \lambda \dfrac{\partial h_{ij}^{n+\theta_n}}{\partial \sigma_{kl}^{n+1}} d\sigma_{kl}^{n+1} - \lambda \dfrac{\partial h_{ij}^{n+\theta_n}}{\partial \alpha_{kl}^{n+1}} d\alpha_{kl}^{n+1} - d\lambda h_{ij}^{n+\theta_n} \\ \vec{n}_{ij}^{n+\theta_n} (d\sigma_{kl}^{n+1} - d\alpha_{kl}^{n+1}) \end{Bmatrix} = \begin{Bmatrix} D_{ijpq}^{e} d\varepsilon_{ij} \\ 0 \\ 0 \end{Bmatrix} \tag{3.57}$$

Rearranging:

$$\begin{bmatrix} \left(D_{ijpq}^{e}\right)^{-1} + \lambda\theta_n \dfrac{\partial \vec{n}_{pq}^{n+\theta_n}}{\partial \sigma_{kl}^{n+1}} & -\lambda\theta_n \dfrac{\partial \vec{n}_{ij}^{n+\theta_n}}{\partial \sigma_{kl}^{n+1}} & \vec{n}_{ij}^{n+\theta_n} \\ -\lambda\theta_n \dfrac{\partial h_{ij}^{n+\theta_n}}{\partial \sigma_{kl}^{n+1}} & \delta_{ik}\delta_{jl} - \theta_\alpha \lambda \dfrac{\partial h_{ij}^{n+\theta_n}}{\partial \alpha_{kl}^{n+1}} & -h_{ij}^{n+\theta_n} \\ \vec{n}_{ij}^{n+1} & -\vec{n}_{ij}^{n+1} & 0 \end{bmatrix} \begin{Bmatrix} d\sigma_{ij}^{n+1} \\ d\alpha_{ij}^{n+1} \\ d\lambda \end{Bmatrix} = \begin{Bmatrix} d\varepsilon_{ij} \\ 0 \\ 0 \end{Bmatrix} \tag{3.58}$$

and inverting (3.58):

$$\begin{Bmatrix} d\sigma_{ij}^{n+1} \\ d\alpha_{ij}^{n+1} \\ d\lambda \end{Bmatrix} = \begin{bmatrix} D_{11} & D_{12} & D_{13} \\ D_{21} & D_{22} & D_{23} \\ D_{31} & D_{32} & D_{33} \end{bmatrix} \begin{Bmatrix} d\varepsilon_{ij} \\ 0 \\ 0 \end{Bmatrix} \tag{3.59}$$

The first column (D_{11} D_{21} D_{31}) is:

$$\begin{aligned} \frac{\partial \sigma_{ij}^{n+1}}{\partial \varepsilon_{kl}^{n+1}} &= D_{11} \\ \frac{\partial \alpha_{ij}^{n+1}}{\partial \varepsilon_{kl}^{n+1}} &= D_{21} \\ \frac{\partial \lambda}{\partial \varepsilon_{kl}^{n+1}} &= D_{31} \end{aligned} \tag{3.60}$$

Also differentiating (3.56) gives:

$$\begin{aligned}\frac{\partial \sigma_{ij}^{n+1}}{\partial \varepsilon_{kl}^{n+1}} &= -\lambda D_{ijkl}^{e} \frac{\partial \vec{n}_{kl}^{n+\theta_n}}{\partial \varepsilon_{kl}^{n+1}} - D_{ijmn}^{e} \vec{n}_{mn}^{n+1} \frac{\partial \lambda}{\partial \varepsilon_{kl}^{n+1}} \\ \frac{\partial \vec{n}_{kl}^{n+\theta_n}}{\partial \varepsilon_{kl}^{n+1}} &= \frac{\partial \vec{n}_{kl}^{n+\theta_n}}{\partial \alpha_{mn}^{n+1}} \frac{\partial \alpha_{mn}^{n+1}}{\partial \varepsilon_{kl}^{n+1}} + \frac{\partial \vec{n}_{kl}^{n+\theta_n}}{\partial \sigma_{mn}^{n+1}} \frac{\partial \sigma_{mn}^{n+1}}{\partial \varepsilon_{kl}^{n+1}}\end{aligned} \tag{3.61}$$

Using the terms obtained in (3.60) and (3.61), the algorithmic consistent tangent matrix is obtained.

3.2.4. CONSTRAINED SUBSTEPPING SOLVER

To carry out mixed controlled tests as a constrained problem, the explicit sub-stepping solver (Sloan, 1987) has been modified to include constraints during sub-stepping and also during the drift correction (Potts and Gens, 1985). In this sense the constrained problem needs to be linearised. The algorithm first determines the increment of elastic stress as:

$$\begin{cases} (S_{ijkl} \cdot D_{klmn}^{e} + E_{ijmn}) \Delta \varepsilon_{mn} = \Delta Y_{ij} \\ \Delta \sigma_{ij} = D_{ijkl}^{e} \Delta \varepsilon_{kl} \end{cases} \tag{3.62}$$

At the end of the step if the yield surface is not crossed $\Delta\varepsilon$ and $\Delta\sigma$ are updated. On the other hand, in case that at the end of the step the stress state is outside the yield surface, $F(\sigma + d\sigma, k) > 0$, α must be determined in order that $F(\sigma + \alpha\, d\sigma, k) = 0$. This is done through an iterative procedure until a tolerance of 1.0E-5 is reached:

$$\alpha_{i+1} = \alpha_i - \frac{F(\sigma + \alpha_i \Delta\sigma, k)}{F(\sigma + \alpha_i \Delta\sigma, k) - F(\sigma + \alpha_{i-1} \Delta\sigma, k)} (\alpha_i - \alpha_{i-1}) \tag{3.63}$$

Therefore the elastic stress and strain can be evaluated as

$$\Delta \varepsilon_{ijkl}^{e} = \alpha \Delta \varepsilon_{ij} \tag{3.64}$$

The objective of this algorithm is to integrate the elasto-plastic constitutive matrix over the elastoplastic strain step, splitting the step into a series of smaller sub-steps using a second order Euler approximation. The steps of the algorithm are:

i) Initialise at a given stress in the yield surface:

$$\begin{aligned} T &= 0 \\ \Delta T &= 1 \end{aligned} \tag{3.65}$$

ii) Set the sub-step equal to

$$\Delta Y_{ij}^{ss} = \Delta T \Delta Y_{ij}^{s} \tag{3.66}$$

iii) Solve the linear system of equations to obtain $\Delta\varepsilon_{ij}^{1}$ and get the first estimate of the stress, plastic strain and hardening parameters.

$$\begin{cases} (S_{ijkl} \cdot D_{klmn}^{ep(1)}(\sigma, k) + E_{ijmn})\Delta\varepsilon_{mn}^{1} = \Delta Y_{ij}^{ss} \\ \Delta\sigma_{ij}^{1} = D_{ijkl}^{ep}\Delta\varepsilon_{kl}^{1} \\ \Delta\varepsilon_{ij}^{p(1)} = \Lambda^{1}(\sigma, k, \Delta\varepsilon_{mn}^{1})\dfrac{\partial P(\sigma, m)}{\partial\sigma} \\ \Delta k^{1} = k(\Delta\varepsilon_{ij}^{p(1)}) \end{cases} \tag{3.67}$$

iv) Using the above quantities, the stresses and hardening/softening parameters of the first estimate, a second estimate can be built with the updated parameters using the previous methodology:

$$\begin{cases} (S_{ijkl} \cdot D_{klmn}^{ep(2)}(\sigma + \Delta\sigma_{ij}^{1}, k + \Delta k^{1}) + E_{ijmn})\Delta\varepsilon_{mn}^{2} = \Delta Y_{ij}^{ss} \\ \Delta\sigma_{ij}^{2} = D_{ijkl}^{ep}\Delta\varepsilon_{kl}^{2} \\ \Delta\varepsilon_{ij}^{p(2)} = \Lambda^{2}(\sigma + \Delta\sigma_{ij}^{1}, k + \Delta k^{1}, \Delta\varepsilon_{mn}^{2})\dfrac{\partial P(\sigma + \Delta\sigma_{ij}^{1}, m)}{\partial\sigma} \\ \Delta k^{(2)} = k(\Delta\varepsilon_{ij}^{p(2)}) \end{cases} \tag{3.68}$$

v) It is now possible to know a more accurate Euler estimate of stress and strains, plastic strains and hardening/softening parameters for an increment ΔY:

$$\begin{aligned} \Delta\sigma_{ij} &= 0.5(\Delta\sigma_{ij}^{1} + \Delta\sigma_{ij}^{2}) \\ \Delta\varepsilon_{ij} &= 0.5(\Delta\varepsilon_{ij}^{(1)} + \Delta\varepsilon_{ij}^{(2)}) \\ \Delta\varepsilon_{ij}^{p} &= 0.5(\Delta\varepsilon_{ij}^{p(1)} + \Delta\varepsilon_{ij}^{p(2)}) \\ \Delta k &= 0.5(\Delta k^{1} + \Delta k^{2}) \end{aligned} \tag{3.69}$$

vi) Convergence criteria is only based on stress, strain or energy respectively as:

$$S^*R = \frac{\left\|(\Delta\sigma_1 - \Delta\sigma_2)\right\|}{\left\|0.5(\Delta\sigma_1 + \Delta\sigma_2)\right\|} < S^*TOL \tag{3.70}$$

$$EPS^*R = \frac{\left\|(\Delta\varepsilon_1 - \Delta\varepsilon_2)\right\|}{\left\|0.5(\Delta\varepsilon_1 + \Delta\varepsilon_2)\right\|} < EPS^*TOL \tag{3.71}$$

$$E^*R = \frac{(\Delta\sigma_1 - \Delta\sigma_2)^T(\Delta\varepsilon_1 - \Delta\varepsilon_2)}{0.25(\Delta\sigma_1 + \Delta\sigma_2)^T(\Delta\varepsilon_1 + \Delta\varepsilon_2)} < E^*TOL \tag{3.72}$$

vii) If the error is acceptable, the step is accepted and moves to viii), else the substep is reduced by β depending on which convergence condition has been violated and directed back to ii)

$$\beta = 0.8\left[\frac{*TOL}{*R}\right]^{0.5} \tag{3.73}$$

viii) Stress, strain and history parameters are updated as

$$\begin{aligned} \sigma &= \sigma + \Delta\sigma \\ \varepsilon &= \varepsilon + \Delta\varepsilon \\ \varepsilon_p &= \varepsilon_p + \Delta\varepsilon_p \\ k &= k + \Delta k \end{aligned} \tag{3.74}$$

ix) Normally after the integration process the final step does not yield exactly in the yield surface, a new condition must be fulfilled. So if $F(\sigma,k) \le YTOL$ is fulfilled, the stress is updated and the process continues until T = 1. If not, a drift correction is applied as follows, however as the system is constrained:

$$S_{ijkl} \cdot \Delta\sigma_{kl} = -E_{ijmn}\Delta\varepsilon_{mn} \tag{3.75}$$

where:

$$\Lambda^{drift} = \frac{F(\sigma,k)}{\frac{\partial F}{\partial\sigma_{ij}}\left(S_{ijkl} + E_{ijmn}\left(D^e_{mnkl}\right)^{-1}\right)^{-1}E_{klpq}\frac{\partial P}{\partial\sigma_{pq}} - \frac{\partial F}{\partial k_m}k_m\left(\frac{\partial P(\sigma,k)}{d\sigma}\right)} \tag{3.76}$$

Therefore the stress drift is:

$$\Delta\sigma_{ij}^{drift} = -\Lambda^{drift}\left(S_{ijkl} + E_{ijmn}\left(D_{mnkl}^{e}\right)^{-1}\right)^{-1} E_{klpq}\frac{\partial P}{\partial \sigma_{pq}} \tag{3.77}$$

But also the corrections also include strain drift:

$$\begin{aligned}
\Delta\varepsilon_{ij}^{drift} &= \left(D_{ijkl}^{e}\right)^{-1}\Delta\sigma_{kl}^{drift} + \Delta\varepsilon_{ij}^{p(drift)} \\
\Delta\varepsilon_{ij}^{p(drift)} &= \Lambda^{drift}\frac{dP}{\partial\sigma} \\
\Delta k^{drift} &= \Lambda^{drift} k\left(\frac{dP}{\partial\sigma}\right)
\end{aligned} \tag{3.78}$$

x) Update stress and history parameters, store variables and update T. Go back to 1 while T < 1.

3.2.5. CONSTRAINED IMPLICIT SOLVER

When the normal of the yield surface is evaluated at the end of the step with a midpoint integration strategy the constrains on stress and strain can be rewritten in a simple way as:

$$S\Delta\sigma_{ij}^{n+1} + E\Delta\varepsilon_{ij}^{n+1} = dY \tag{3.79}$$

$$\Delta\alpha_{ij}^{n+1} = \lambda^{n+1} h_{ij}(\alpha_{ij}^{n+\theta_\alpha}, \vec{n}_{ij}^{n+1}) \tag{3.80}$$

$$f^{n+1}(\Delta\sigma_{ij}^{n+1}, \Delta\alpha_{ij}^{n+1}) = 0 \tag{3.81}$$

Owing the fact that,

$$\Delta\varepsilon_{ij}^{n+1} = C_{ijkl}^{e}\Delta\sigma_{ij}^{n+1} + \lambda^{n+1}\vec{n}_{kl}^{n+1} \tag{3.82}$$

$$\vec{n}_{kl}^{n+1} = \frac{\sigma_{ij}^{n} + \Delta\sigma_{ij}^{n+1} - \alpha_{ij}^{n} - \Delta\alpha_{ij}^{n+1}}{\left\|\sigma_{ij}^{n} + \Delta\sigma_{ij}^{n+1} - \alpha_{ij}^{n} - \Delta\alpha_{ij}^{n+1}\right\|} \tag{3.83}$$

The unknows of the system are $\Delta\sigma_{ij}^{n+1}, \Delta\alpha_{ij}^{n+1}, \lambda^{n+1}$ which can be expressed as

$$r_{ij}^{1} = S\Delta\sigma_{ij}^{n+1} + E\left(C_{ijkl}^{e}\Delta\sigma_{ij}^{n+1} + \lambda^{n+1}\vec{n}_{kl}^{n+1}\right) - dY \tag{3.84}$$

$$r_{ij}^{2} = \Delta\alpha_{ij}^{n+1} - \lambda^{n+1} h_{ij}(\alpha_{ij}^{n+\theta_\alpha}, \vec{n}_{ij}^{n+1}) \tag{3.85}$$

$$r^{3} = f^{n+1}(\Delta\sigma_{ij}^{n+1}, \Delta\alpha_{ij}^{n+1}) \tag{3.86}$$

The solution of this equations can be carried out with any of the non-linear solvers described in the previous sections.

3.3. NUMERICAL STUDY: WU ENCAPSULATED MODEL (WU, 1992)

As discussed in 2.2, hypoplastic models can be encapsulated with a a non-linear kinematic hardening rule. This section presents a numerical study on the encapsulated Wu (1992) amorphous model, which corresponds to one of the first proposed hypoplastic models. The model does not depend on void ratio and uses four constants as inputs without physical relevance. The same input values as described in Batista et al. (2003) have been used and a high elastic stiffness has been included in combination with a small yield surface. The hardening rule is expressed as:

$$h_{ij}(\vec{n}_{ij}, \alpha_{ij}) = C_1 \alpha_{kk} \vec{n}_{ij} + C_2 \alpha_{kl} \vec{n}_{kl} \frac{\alpha_{ij}}{\alpha_{nn}} + C_3 \frac{\alpha_{ik}\alpha_{kj}}{\alpha_{nn}} + C_4 \frac{\alpha_{ik}^{*}\alpha_{kj}^{*}}{\alpha_{nn}} \tag{3.87}$$

Where the input parameters are:

$$C_1 = -106.5 \qquad C_2 = -801.5 \qquad C_3 = -797.1 \qquad C_4 = 1077.7 \tag{3.88}$$

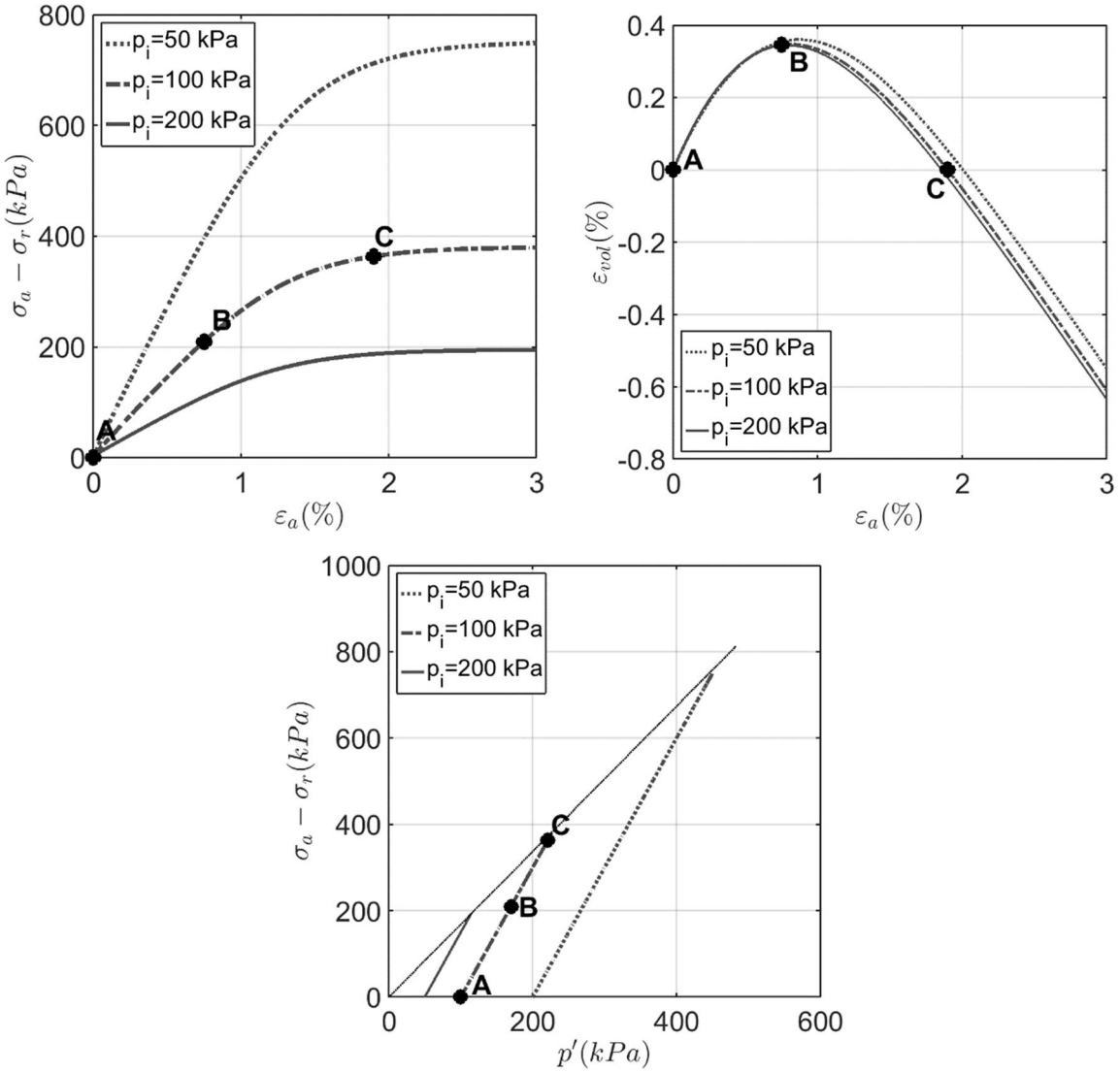
and the elastic parameters are:

$$K = 500.000 \qquad G = 200.000 \qquad m = \sqrt{10} \tag{3.89}$$

where K is the bulk modulus, G the shear modulus and m the size of the yield surface

3.3.1. MODEL PERFORMANCE IN TRIAXIAL CONDITIONS

A set of triaxial tests at various initial stresses has been simulated in order to assess the ability of the encapsulated model to reproduce the features of soil behaviour with the chosen set of parameters. Such features are shear-volumetric coupling and a *J*/*p* envelope of the backstress similar to a Drucker-Prager yield surface. Figure 63 shows the results of local integration under drained and undrained triaxial conditions illustrating how the model reponse exhibits initial contractant behaviour until a J/p ratio where it phase-transforms exhibiting dilatant behaviour, finally the stress path reaches its limit corresponding to a J/p' asymptote with a constant strain rate direction.



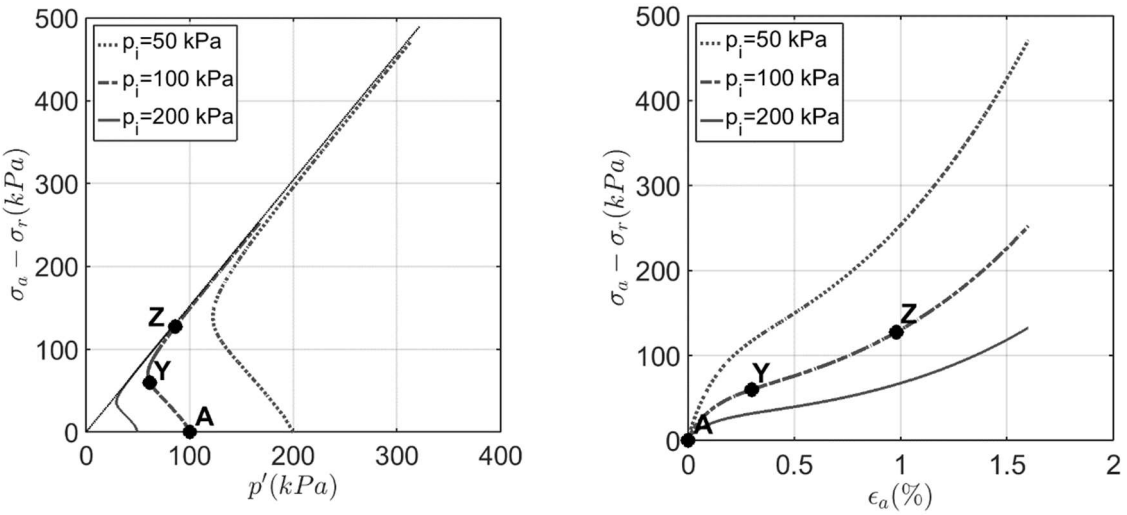


Figure 63: Evaluation of Wu (1992) "encapsulated" model in Triaxial conditions (TXC)

For qualitative comparsion, despite the inputs used between Batista and the next figures are different, they prove useful to illustrate the validity of the chosen parameters used by Batista. The following figure shows some predictions included in Wu (1992) which exhibit the same trends than those shown in Figure 63. As expected, in practical terms using a NLKH rule or a hypoplastic model has no substancial differences when applied to real laboratory data as discussed in Chapter 2.

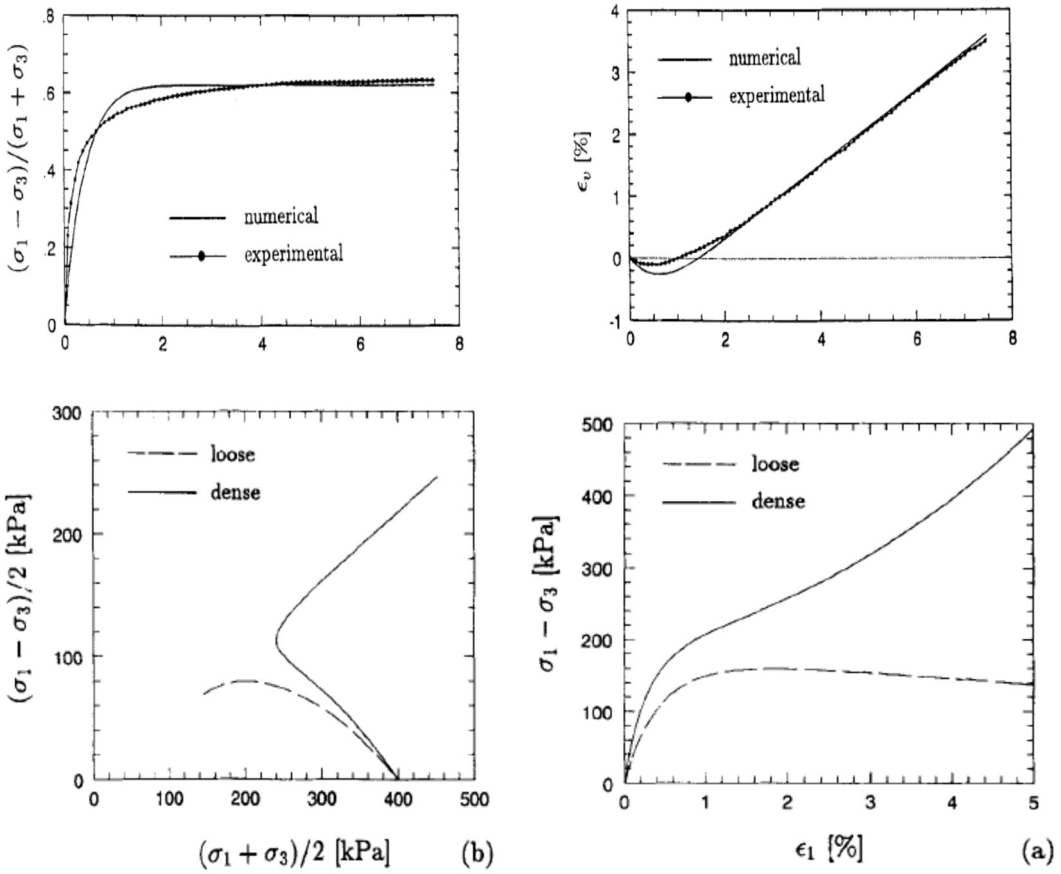


Figure 64: Numerical triaxial tests detailed from Wu (1992)

3.3.2. ANALYTICAL DERIVATIVES

In order to build the Jacobians used by the implicit integration methods the second derivatives of the yield surface and the hardening rules, need to be provided. This section describes the derivatives of the Wu encapsulated model which are:

$$\frac{\partial^2 f(\sigma_{ij},\alpha_{ij})}{\partial\sigma_{ij}\partial\sigma_{kl}} = -\frac{\partial^2 f(\sigma_{ij},\alpha_{ij})}{\partial\alpha_{ij}\partial\alpha_{kl}} = \frac{1}{\left\|\sigma_{ij}-\alpha_{ij}\right\|}\left(\delta_{ik}\delta_{jl} - \vec{n}_{ij}\vec{n}_{kl}\right) \tag{3.90}$$

Derivatives for the hardening rule (3.87) can be obtained through the chain rule, firstly:

$$\frac{\partial h_{ij}(\alpha_{ij},\vec{n}_{ij})}{\partial\vec{n}_{kl}} = C_1\alpha_{kk}\delta_{ik}\delta_{jl} + C_2\frac{\alpha_{ij}\alpha_{kl}}{\alpha_{nn}} \tag{3.91}$$

Also

$$\frac{\partial h_{ij}(\alpha_{ij},\vec{n}_{ij})}{\partial \alpha_{ij}} = C_1 \vec{n}_{ij}\alpha_{kl} + C_2\left(\frac{\vec{n}_{mn}\alpha_{mn}}{\alpha_{kk}}\delta_{ik}\delta_{jl} + \frac{\alpha_{ij}\delta_{kl}}{\alpha_{kk}} - \frac{\alpha_{mn}\delta_{mn}}{\alpha_{kk}\alpha_{kk}}\alpha_{ij}\delta_{kl}\right) + C_3\left(\frac{1}{\alpha_{kk}}\frac{\partial(\alpha_{im}\alpha_{ml})}{\partial \alpha_{kl}} - \frac{1}{\alpha_{kk}\alpha_{kk}}\alpha_{im}\alpha_{mj}\delta_{kl}\right) + C_4\left(\frac{1}{\alpha_{kk}}\frac{\partial(\alpha^*_{im}\alpha^*_{mj})}{\partial \alpha_{kl}} - \frac{1}{\alpha_{kk}\alpha_{kk}}\alpha^*_{im}\alpha^*_{mj}\delta_{kl}\right) \tag{3.92}$$

where

$$\begin{aligned}\frac{\partial(\alpha_{im}\alpha_{ml})}{\partial \alpha_{kl}} &= \alpha_{lj}\delta_{ik} + \alpha_{ik}\delta_{lj} \\ \frac{\partial(\alpha^*_{im}\alpha^*_{mj})}{\partial \alpha_{kl}} &= \frac{\partial(\alpha_{im}\alpha_{ml})}{\partial \alpha_{kl}} - \frac{2\alpha_{kk}}{3}\delta_{ik}\delta_{jl} - \frac{2}{3}\alpha_{ij}\delta_{kl} + \frac{2\alpha_{kk}}{9}\delta_{ij}\delta_{kl}\end{aligned} \tag{3.93}$$

Finally, assembling and using the chain rule

$$\begin{aligned}\frac{dh_{ij}(\alpha_{ij},\vec{n}_{ij})}{d\alpha_{kl}} &= \frac{\partial h_{ij}(\alpha_{ij},\vec{n}_{ij})}{\partial \alpha_{kl}} - \left(C_1\alpha_{kk}\delta_{ip}\delta_{jq} + C_2\frac{\alpha_{ij}\alpha_{pq}}{\alpha_{nn}}\right)\frac{\partial \vec{n}_{pq}}{\partial \alpha_{kl}} \\ \frac{dh_{ij}(\alpha_{ij},\vec{n}_{ij})}{d\sigma_{kl}} &= \left(C_1\alpha_{kk}\delta_{ip}\delta_{jq} + C_2\frac{\alpha_{ij}\alpha_{pq}}{\alpha_{nn}}\right)\frac{\partial \vec{n}_{pq}}{\partial \sigma_{kl}}\end{aligned} \tag{3.94}$$

The obtained second derivatives are used in the computation of the Jacobian for the implicit schemes discussed in this chapter.

3.3.3. ISOERROR MAPS

Once all the ingredients are described (discretisation, derivatives, inputs…) the performance of the different algorithm can be explored. To do so, firstly, a set of isoerror maps have been computed in order to study the effect of the discretisation as discussed in Section 3.3.2. Due to the fact that non-linear kinematic hardening models cannot be reduced in form of invariants, two types of strain probes have been explored: the Rendulic plane, in order to explore the numerical performance for the cases where the diagonal of the tensors is dominant, and plane strain conditions where the non-diagonal terms are more common. The chosen starting point is point A shown in Figure 63, with stress components summarised in Table 2

Table 11: initial conditions for Iso-Error maps Wu encapsulated model

	σ_{xx}	σ_{yy}	σ_{zz}	σ_{xy}	σ_{xz}	σ_{yz}
Point A	-100.0	-100.0	-100.0	0.0	0.0	0.0

The error is defined as,

$$error = 100 \frac{\left\| \sigma_{ij}^{EXACT} - \sigma_{ij}^{NUM} \right\|}{\left\| \sigma_{ij}^{EXACT} \right\|} \tag{3.95}$$

where the "exact" solution corresponds to the same strain increment but carried out in 100 sub-increments with strict convergence criteria. The convergence criteria for the explicit solvers corresponds to a minimum of 100 sub-steps per increment and a relative error tolerance of 10E-6, while for the implicit solvers 100 sub-steps using the second order discretization has been used with a residual tolerance of 10E-12. In this sense both "exact" solutions from both integration strategies have been compared on one another with a maximum relative error of ~10E-6 (as expected), which corresponds to the upper bound of precision of this numerical exercise.

The implicit time step discretisations are summarized in Table 12 depending on whether the normal of the yield surface or the backstress are evaluated in the middle of the step or at the end of the step. Four cases are investigated: backward Euler (all at the end), midpoint (all in the middle), half midpoint (normal at the end, backstress in the middle) and half trapezoidal (normal at the end and backstress in the middle).

Table 12: Cases of time step discretisation for implicit integration

		θ_n	θ_α
BE	***Backward Euler***	1.0	1.0
MID05	***Mid-Point***	0.5	0.5
MID1	***Half Mid-Point***	1.0	0.5
TZ1	***Half Trapezoidal***	1.0	0.5

All the investigated time discretisation can be generalized by the following set of equations:

$$\sigma_{ij}^{n+1} = D_{ijkl}^{e}\Delta\varepsilon_{kl} + \sigma_{ij}^{n} - \lambda^{n+1}D_{ijkl}^{e}\vec{n}_{kl}^{n+\theta_n} \tag{3.96}$$

$$f^{n+1} = \sqrt{(\sigma_{ij}^{n+1} - \alpha_{ij}^{n+1})(\sigma_{ij}^{n+1} - \alpha_{ij}^{n+1})} - m \tag{3.97}$$

If midpoint

$$\alpha_{ij}^{n+1} = \alpha_{ij}^{n} + \lambda^{n+1}L_{ijkl}(\alpha_{ij}^{n+\theta_\alpha})\vec{n}_{kl}^{n+\theta_n} + \lambda^{n+1}N_{ij}(\alpha_{ij}^{n+\theta_\alpha}) \tag{3.98}$$

If trapezoidal

$$\begin{aligned}\alpha_{ij}^{n+1} &= \alpha_{ij}^{n} + \lambda^{n+1}(1-\theta_\alpha)\left(L_{ijkl}(\alpha_{ij}^{n})\vec{n}_{kl}^{n+\theta_n} + N_{ij}(\alpha_{ij}^{n})\right) + \\ &+\theta_\alpha\lambda^{n+1}\left(L_{ijkl}(\alpha_{ij}^{n+1})\vec{n}_{kl}^{n+\theta_n} + N_{ij}(\alpha_{ij}^{n+1})\right)\end{aligned} \tag{3.99}$$

where tensor functions are:

$$\begin{aligned}L_{ijkl}(\alpha_{ij}) &= C_1\alpha_{mm}\delta_{ik}\delta_{jl} + C_2\frac{\alpha_{ij}\alpha_{kl}}{\alpha_{mm}} \\ N_{ij}(\alpha_{ij}) &= C_3\frac{\alpha_{ik}\alpha_{kj}}{\alpha_{nn}} + C_4\frac{\alpha_{ik}^{*}\alpha_{kj}^{*}}{\alpha_{nn}}\end{aligned} \tag{3.100}$$

3.3.3.1. Isoerror maps in the Rendulic plane

A total of 2500 "excursions" (strain tests) for each discretisation shown in Table 12 have been carried out and plotted in Figure 65 to Figure 68. All the data is presented in an isomorphic plane where the calculated error is plotted in the Rendulic stress space and the strain space. A maximum value of 30% of error has been taken as threshold for the figures. From the isoerror results shown in Figure 65 to Figure 68 it is clear that the first order discretisation backward Euler (BE), although stable, does not approximate as well as the other second order discretisations the solution for medium size strain increments, exhibiting more than 1% of error for strain excursion of the order of 10^{-3}

In this sense to obtain good precision a significantly larger number of substeps will be required than when using any of the other discretisations (second order). Amongst the second order discretisations (MID05, MID1, TZ1) the one exhibiting better precision corresponds to the half mid-point discretisation MID1, corresponding to $\theta_n = 1$ and $\theta_\alpha = 0.5$. This is in line with the

observed behaviour in J-plasticity Amstrong-Frederick family models (Lubarda and Benson, 2002) (Chaboche and Cailletaud, 1996), but also amongst the implicit integration strategies for the hypoplasticity with the Cloe model (Tamagnini et al., 2000). The reason for this good performance of the MID1 discretisation comes from the implication of the yield surface shape. As discussed in 2.2, as the elasticity tensor is large compared to the plastic modulus, then when $\dot{\sigma}_{ij} \neq \dot{\alpha}_{ij}$ the yield sphere only rotates enforcing neutral loading. The direction of the normal $\vec{n}_{ij}$ is quasi-parallel to the imposed strain increment $\Delta\varepsilon_{ij}$, so evaluating the normal at the end is actually closer to the exact solution at the end of the step than in the middle, this is particularly significant during loading reverals. This is clear comparing Figure 66 with Figure 67, where evaluating the middle precision does not improve and the isoerror maps are practically a copy of each other. Owing to the fact that the half-mid-point rule (MID1) can be rearranged to reduce the number of unknowns by 6, as pointed out in the previous section the MID1 discretisation is superior.

Regarding the differences between the half trapezoidal (TZ1) and the half mid-point (MID1) discretisation, both exhibit second order accuracy and can experience a reduction of its number of unknowns. However, the mid-point discretisation performs better under strain directions where the volumetric strain is near to zero, on the other hand under isotropic conditions no significant differences are encountered.

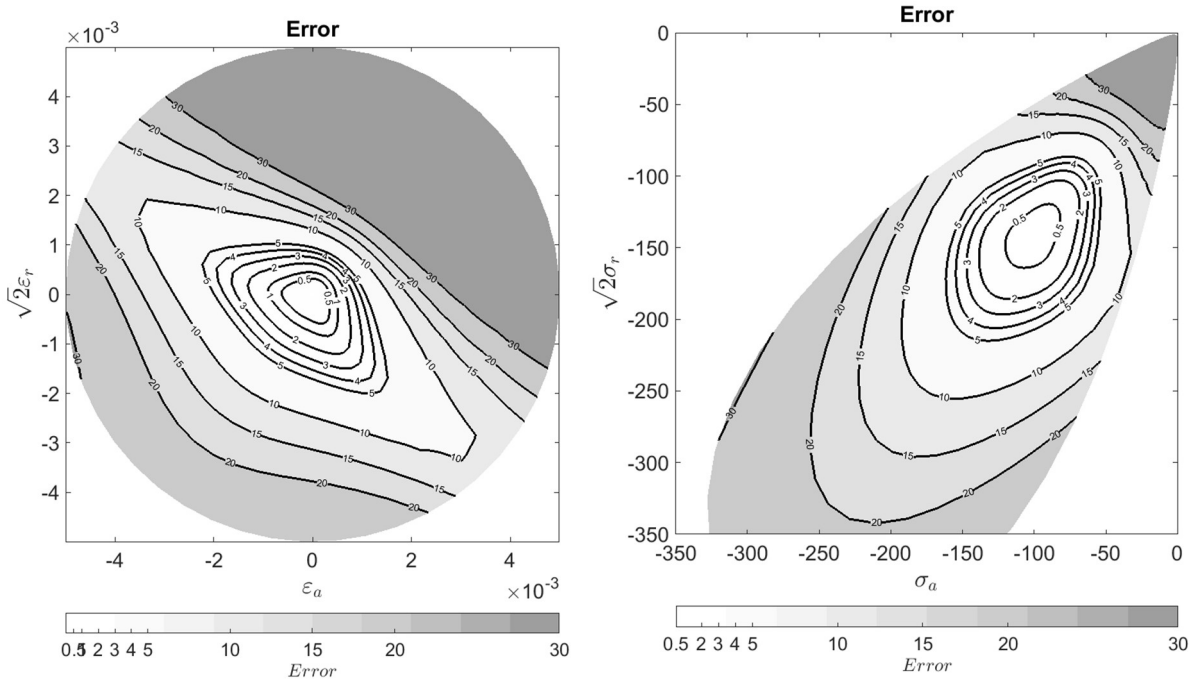


Figure 65: Backward Euler (BE)

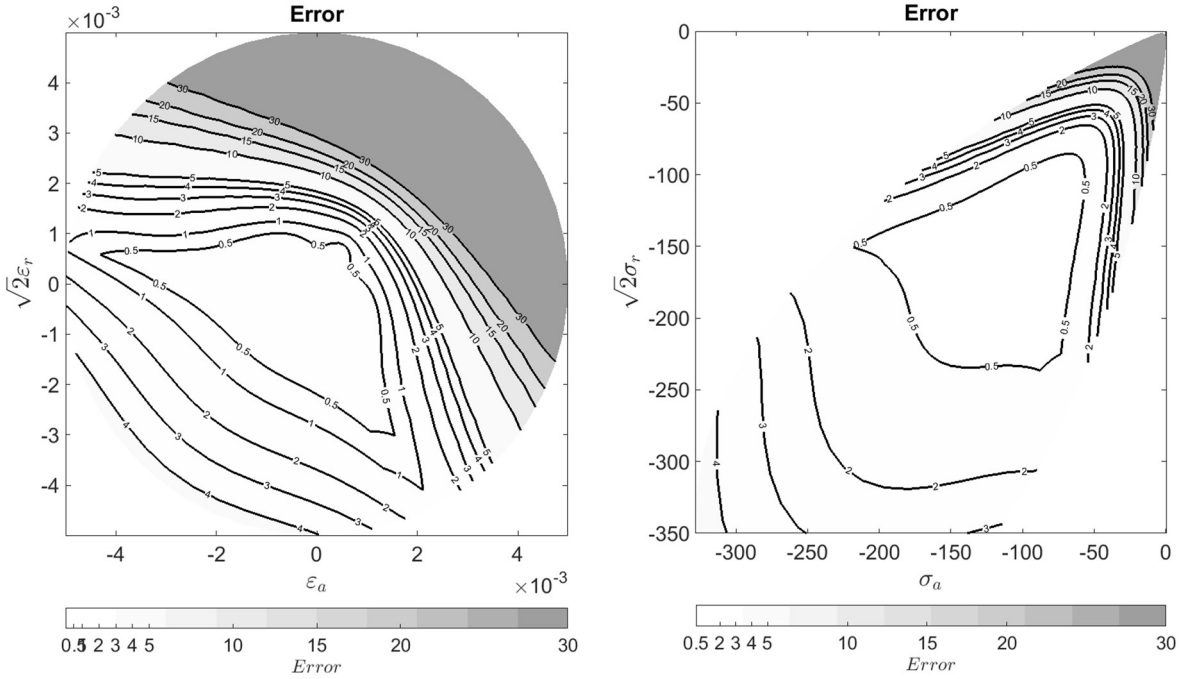


Figure 66: Mid-Point (MID05)

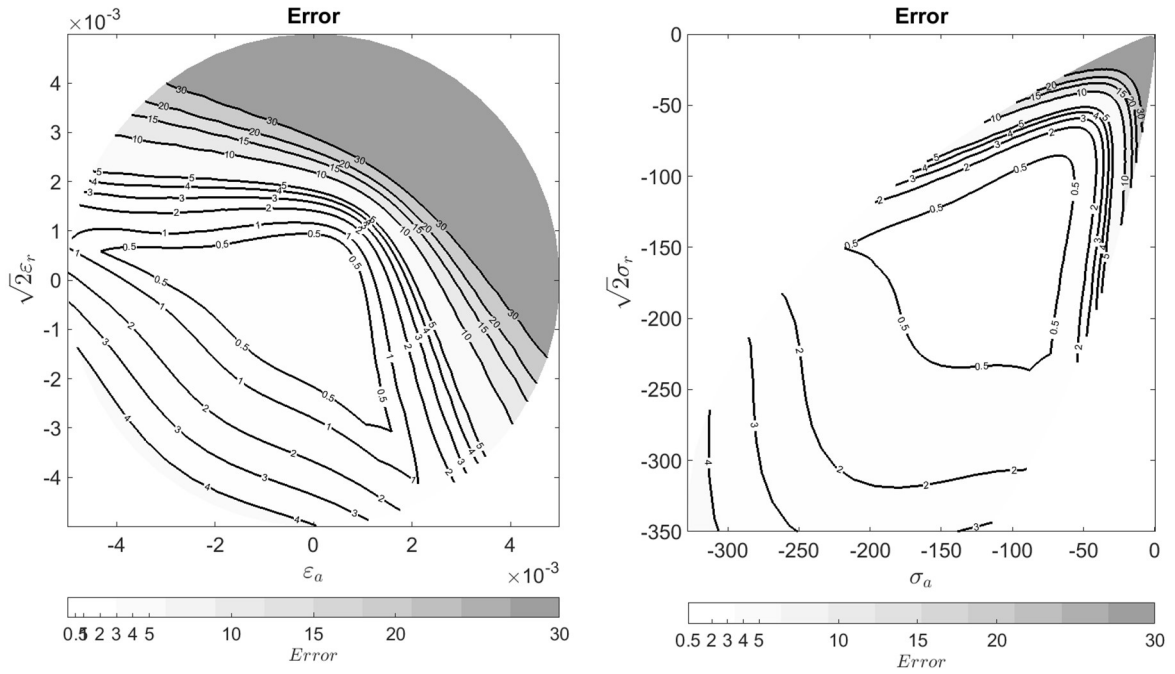


Figure 67: Half Mid-Point (MID1)

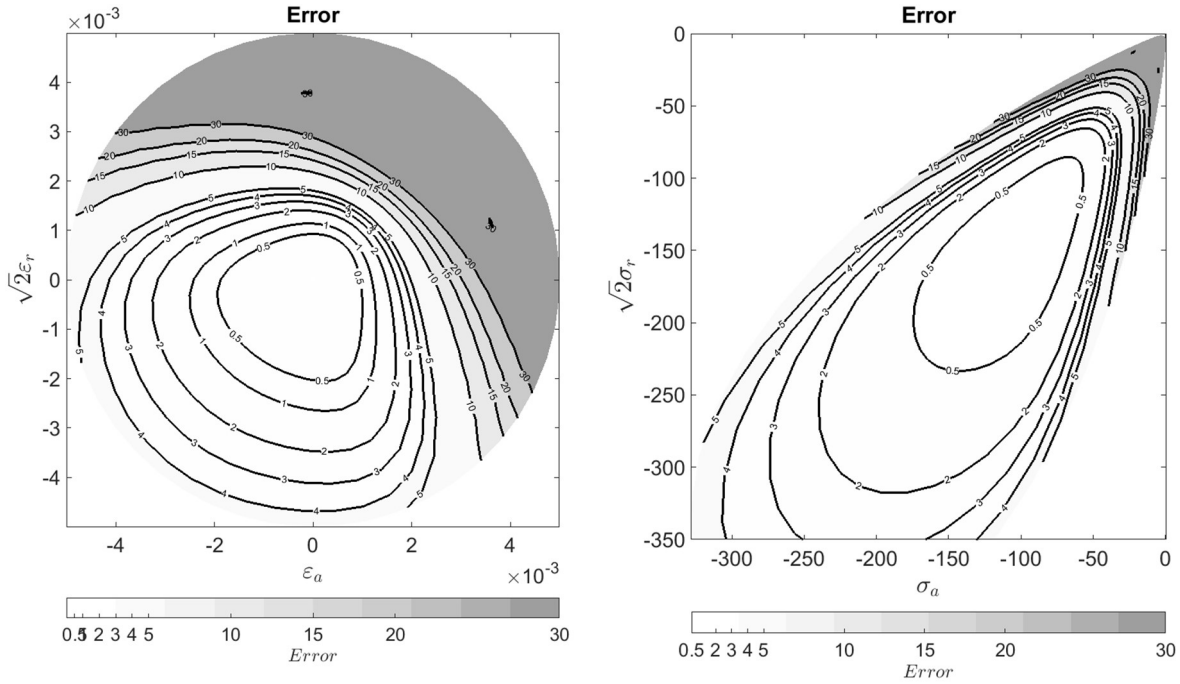


Figure 68: Half Trapezoidal (TZ1)

3.3.3.2. Isoerror maps under plane strain conditions

Similar to the previous section, two sets of 2500 tests per discretisation have been carried out. A total of 20,000 strain excursions have been explored for the four discretisations in Table 12. The directions explored are in plane $\varepsilon_{xx} - \varepsilon_{xy}$, $\varepsilon_{yy} = 0$, $\varepsilon_{zz} = 0$, (non-diagonal excursions) and under $\varepsilon_{xx} - \varepsilon_{yy}, \varepsilon_{xy} = 0, \varepsilon_{zz} = 0$ conditions (diagonal). Figure 69 to Figure 76 presents the error for all the previous cases as described in (3.95), where the stress and strain at the end of the "excursion" is shown, but no longer in an isomorphic space.

Similar conclusions as in the previous section can be extracted when comparing the backward Euler (BE). In general, the first order discretisation exhibits more than 1% of error for strain excursions of the order of 10^{-3}. Regarding the midpoint (MID05) and the half-midpoint (MID1), few differences appear in terms of the accuracy provided by both discretisations. Secondly, in general, the half midpoint discretisation (MID1) shows a much better performance in terms of precision than the half trapezoidal (TZ1) for medium to large size steps, which is clearly seen comparing Figure 73 and Figure 74 with Figure 75 and Figure 76. The MID1 discretisation shows a superior performance, in particular in strain directions where the volumetric strain is small compared to the deviatoric strain. Finally, it is a general trend that for all discretisations that the integration is more precise under compressive strain paths. This is due to the dependence of the hardening rule with the mean backstress and the asymptotic nature of the model. Under a strain path where the change in volume is positive (swelling) the stress path will be forced to reach earlier its associated asymptote, providing a much more non-linear stress path to integrate. In this sense it is recommended to divide the step into a series of substeps in low mean effective stress regions and particularly under positive volumetric strain directions when using an implicit integration strategy.

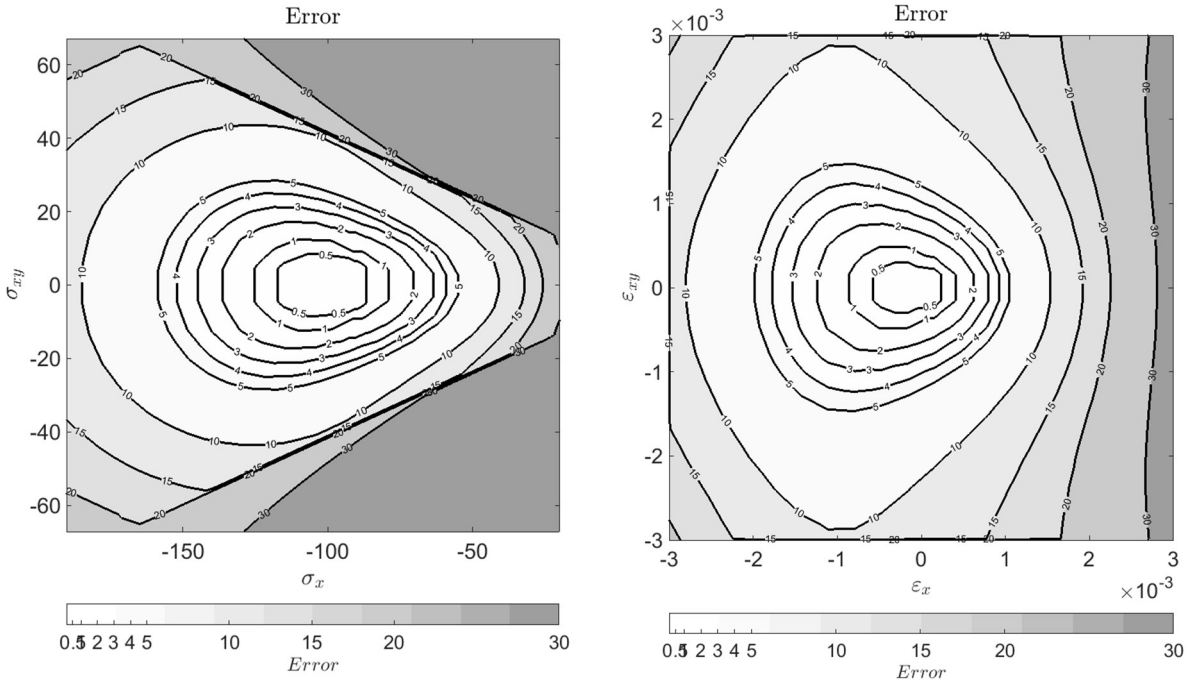


Figure 69: Backward-Euler (BE) in Plane Strain Conditions for non-diagonal excursions

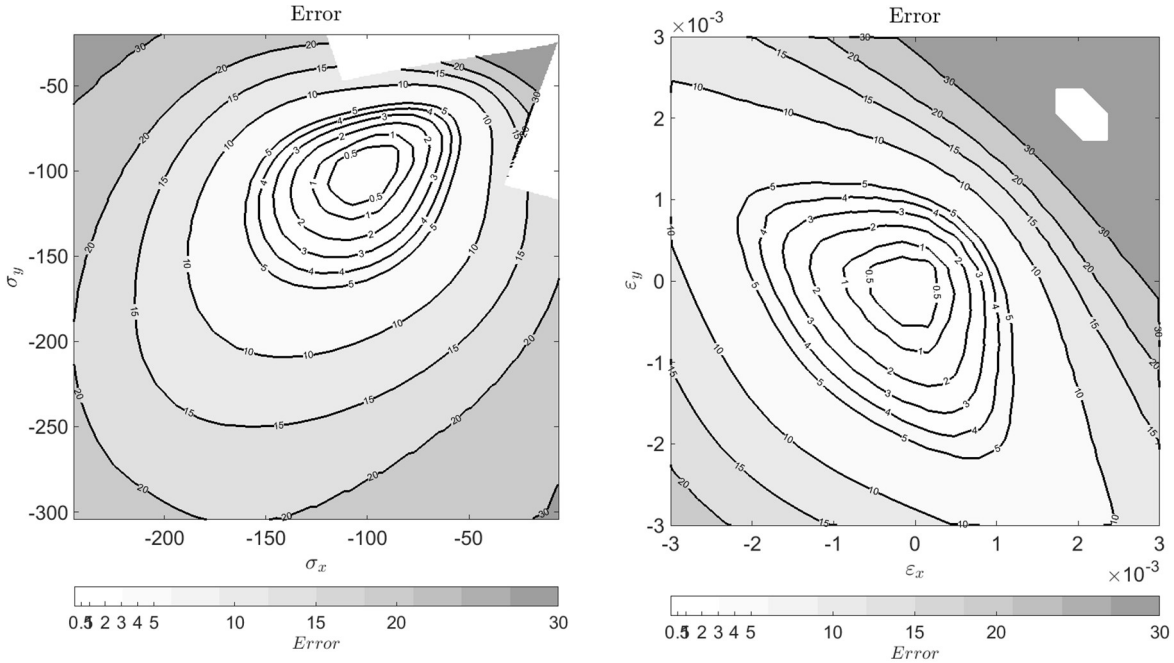


Figure 70: Backward Euler (BE) in Plane Strain Conditions for diagonal excursions

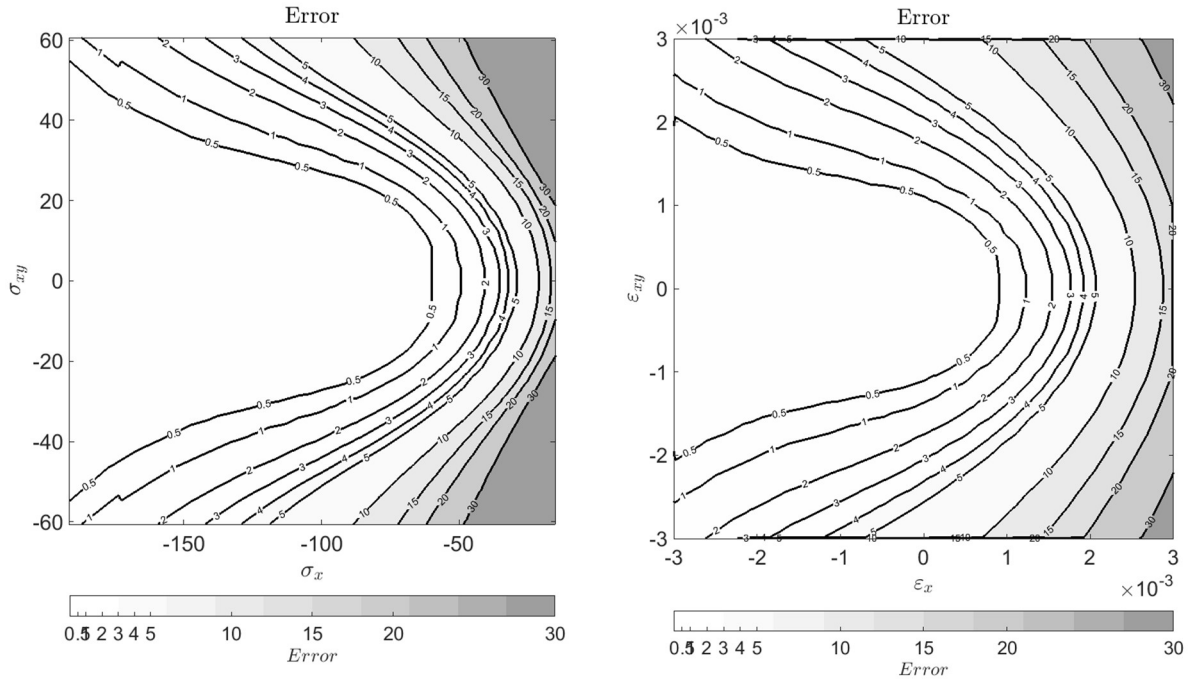


Figure 71: Mid-Point (MID05) in Plane Strain Conditions for non-diagonal excursions

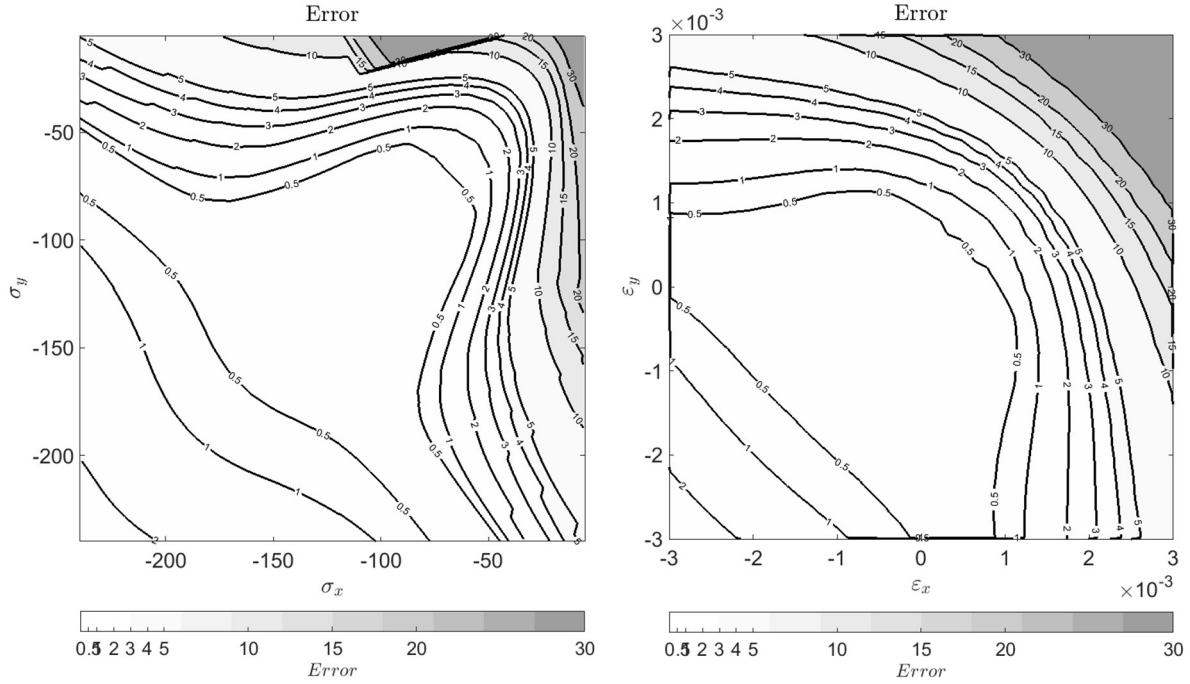


Figure 72: Mid-Point (MID05) in Plane Strain Conditions for diagonal excursions

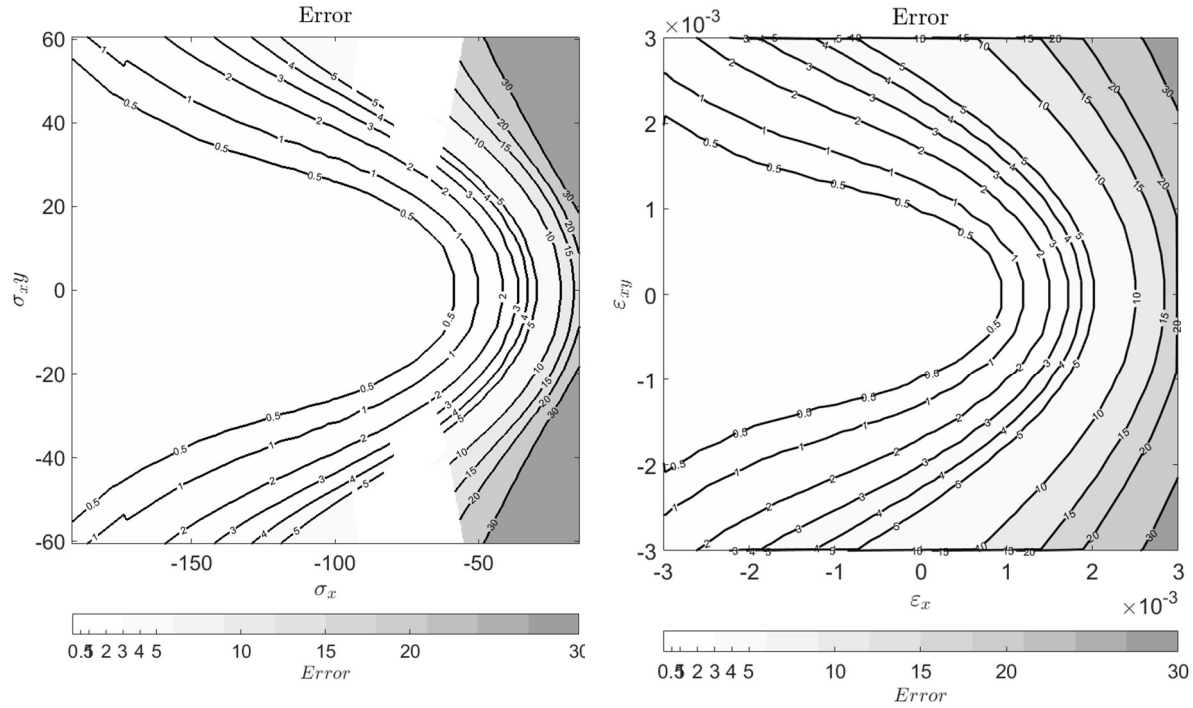


Figure 73: Half-Mid-Point (MID1) in Plane Strain Conditions for non-diagonal excursions

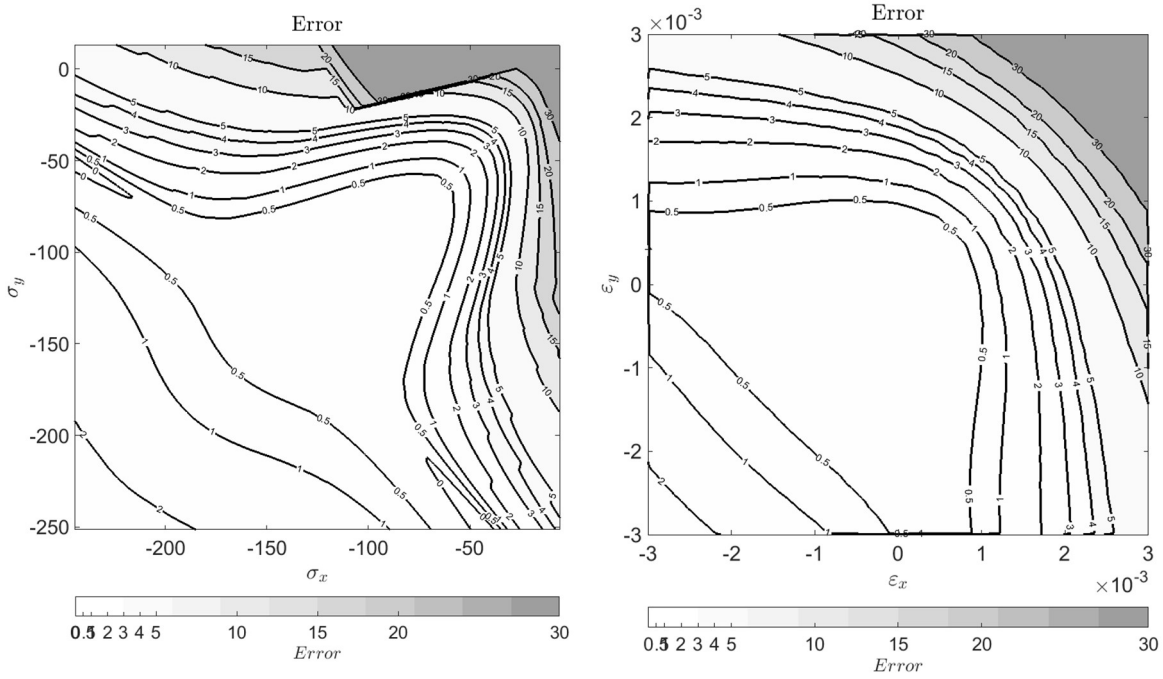


Figure 74: Half Mid-Point (MID1) in Plane Strain Conditions

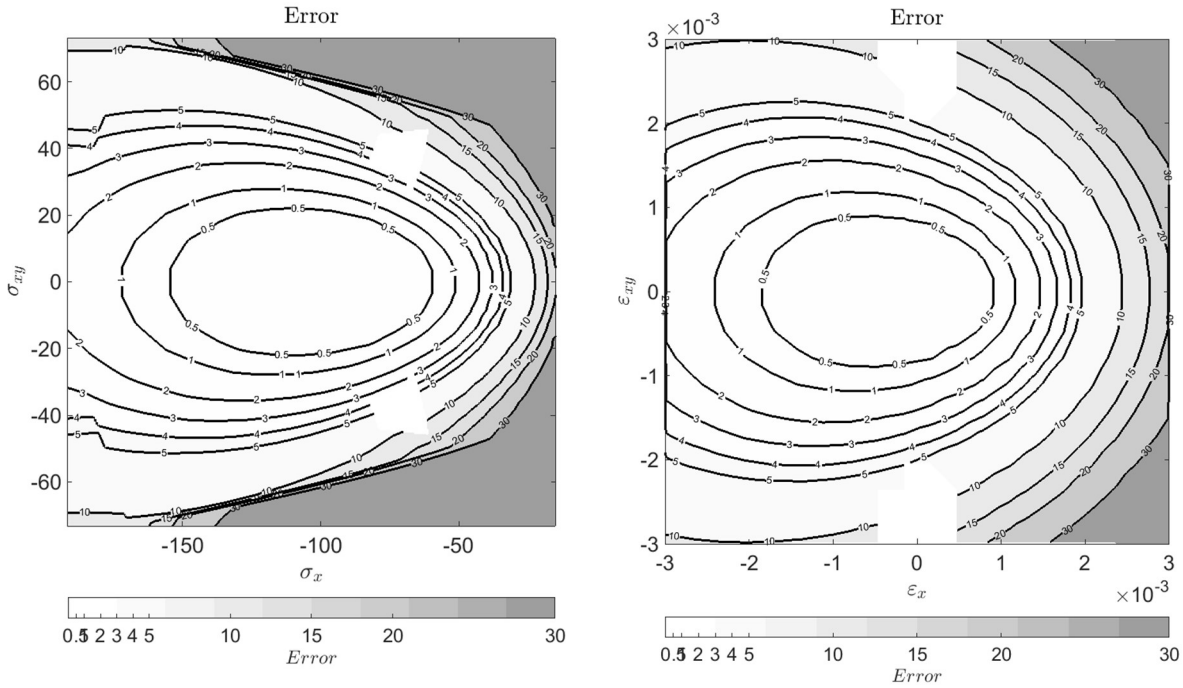


Figure 75: Half trapezoidal (TZ1) in Plane Strain Conditions for non-diagonal excursions

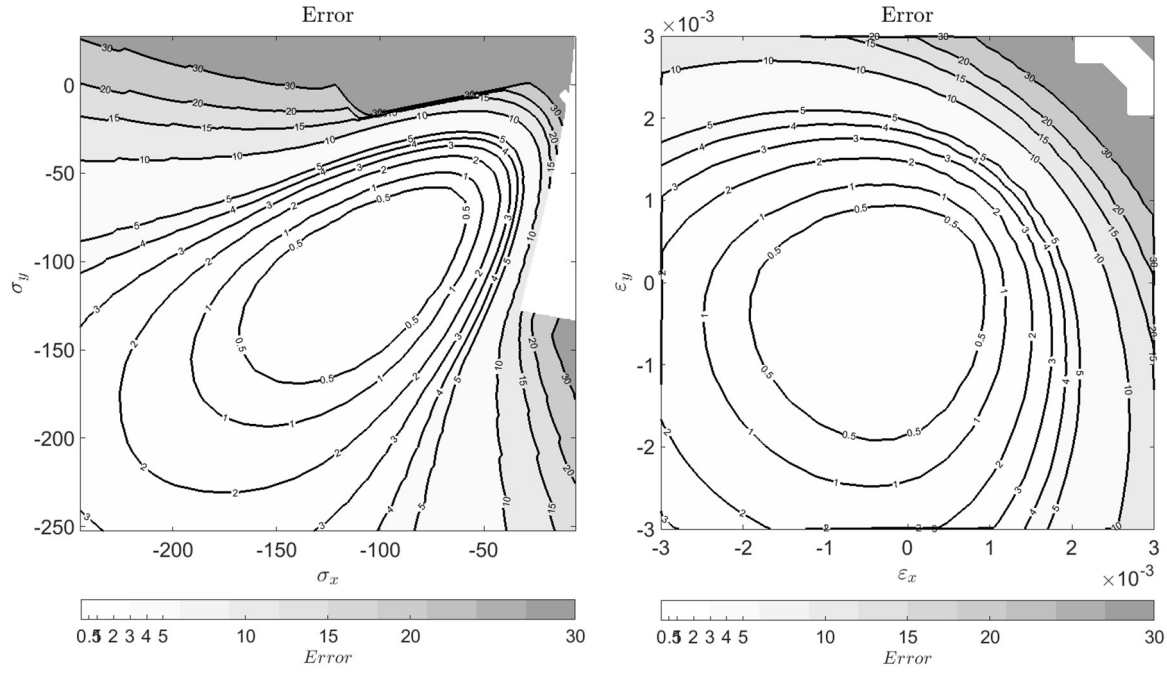


Figure 76: Half trapezoidal (TZ1) in Plane Strain Conditions for diagonal excursions

3.3.4. PRECISISON FOR ZIG-ZAG STRAIN PATH

Following the conclusions obtained from the isoerror maps, to examine the findings a zig-zag strain path has been tested for all discretisations under one step, and compared with the exact solution. The strain path used has a number of reversals in all strain directions and the magnitude of the strain step is of the order of 10^{-3}. The strain path is defined in the Table 4:

Table 13: Zig-Zag strain test

INCREMENT	ε_{xx}	ε_{yy}	ε_{zz}	ε_{xy}	ε_{xz}	ε_{yz}
1	-1E-3	0.0	0.0	0.0	0.0	0.0
2	-2E-3	0.0	0.0	0.0	0.0	0.0
3	-2E-3	-1E-3	0.0	0.0	0.0	0.0
4	-2E-3	-1E-3	0.0	0.0	0.0	0.0
5	-2E-3	-2E-3	0.0	0.0	0.0	0.0
6	-1E-3	-2E-3	0.0	0.0	0.0	0.0
7	-1E-3	-2E-3	-1E-3	0.0	0.0	0.0
8	-1E-3	0.0	-2E-3	0.0	0.0	0.0
9	-1E-3	-1E-3	-1E-3	0.0	0.0	0.0
10	-2E-3	-2E-3	-2E-3	0.0	0.0	0.0

Figure 77 shows the comparison between the exact solution and the Backward – Euler discretisation. While Figure 78 shows the comparison between the exact solution and both midpoint discretisations. As expected, the second order approximations show a much better accuracy when compared with the exact solution when integrating over a step. Also, it can be concluded that, regardless of the number of reversals, evaluating the normal at the end or at the middle of the step has practically no influence on the solution as both stress paths are practically identical in Figure 78.

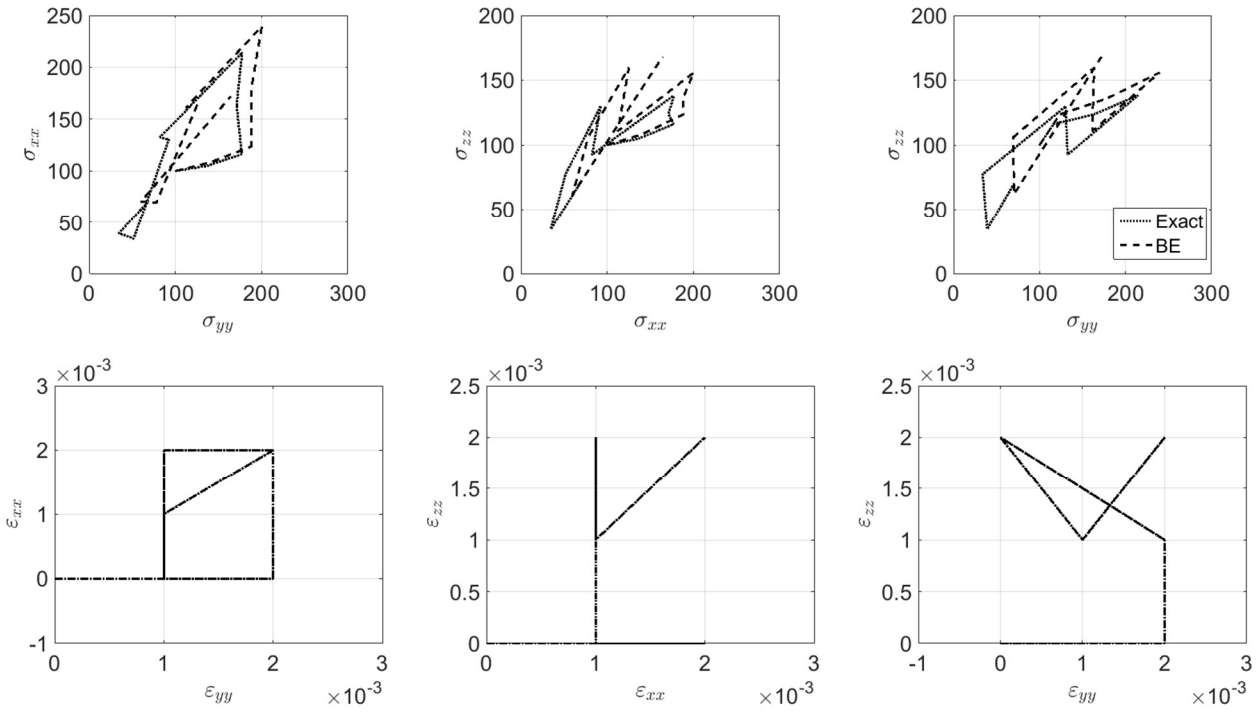


Figure 77: Zig-Zag strain test exact solution versus Backward-Euler discretisation.

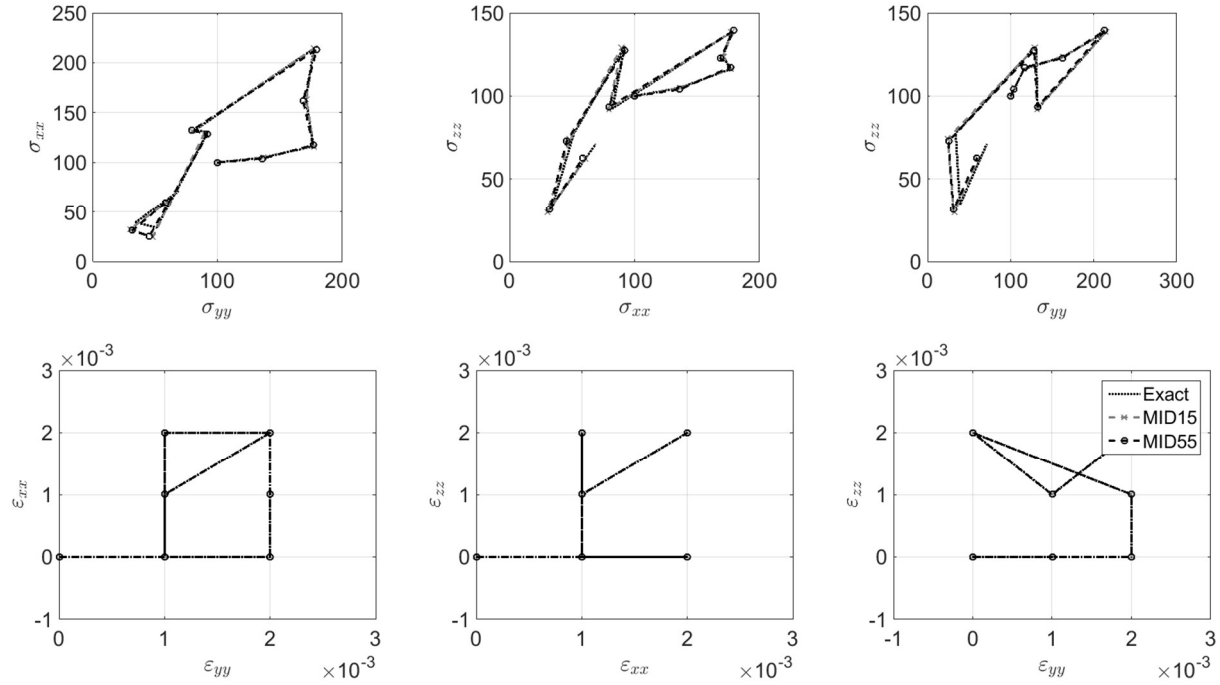


Figure 78: Zig-Zag strain test exact solution versus Mid-Point and Half-Mid-Point discretisations

3.3.5. CONVERGENCE RATE

To study the behaviour of each of the non-linear solvers described in chapter-section 3.2.3.3, the rate of convergence for four mid-size steps under different strain directions has been studied. The initial conditions correspond to those described in 0and the strain directions are representative of the isoerror maps. Figure 79 presents the norm of the residuals versus the number of iterations for four particular cases $\Delta\varepsilon_{xy} = 0.002$, $\Delta\varepsilon_{xx} = 0.002$ $\Delta\varepsilon_{xx} = -0.002$ and $\Delta\varepsilon_{vol} = 0.009$.

Figure 79 summarizes the rate of convergence for all four strain increments, where the augmented-CPPM shows better overall performance than the rest of the solvers. All the algorithms show quadratic convergence rate in the neighbourhood of the solution, however before achieving quadratic convergence a significant number of iterations is required. This is particularly high for the classic CPPM where the number of iterations often goes beyond 30, where in many cases the residuals increase over some iterations, exhibiting poor convergence properties. On the other hand, the primal-CPPM and Trust region algorithms show a reduction of the residual over each iteration until the residuals reach quadratic convergence. A feature that has not been explored is the initial guess used for the globally convergent algorithms.

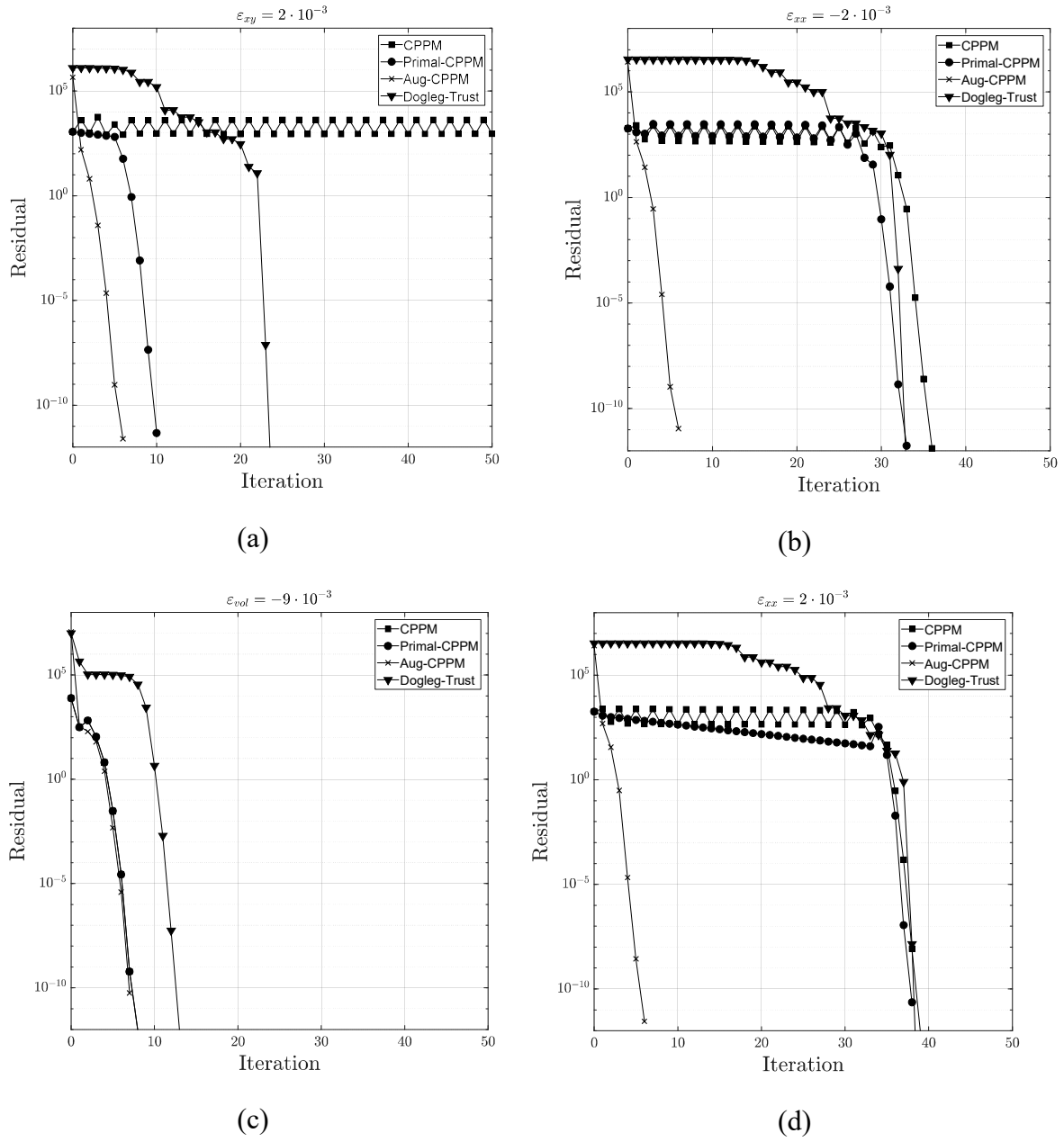


Figure 79: Rate of converge of each of the algorithms for pure deviatoric strain(a), oedometric compresion strain path(b), isotropic compresion strain path(c) and oedometric swelling strain path (d)

As can be concluded from Figure 79, the aug-CPPM seems to perform better than the other solvers for this four cases, reaching all solutions in less than 7 iterations, while the other solvers require on average 10-30 iterations in some cases. In comparison with the other solvers, the aug-CPPM requires an extra numerical input, Figure 80 shows the effect that this term has on the rate of convergence of the aug-CPPM for the worst case (Figure 79d). A value of c = 0.001 has been found to provide the best performance.

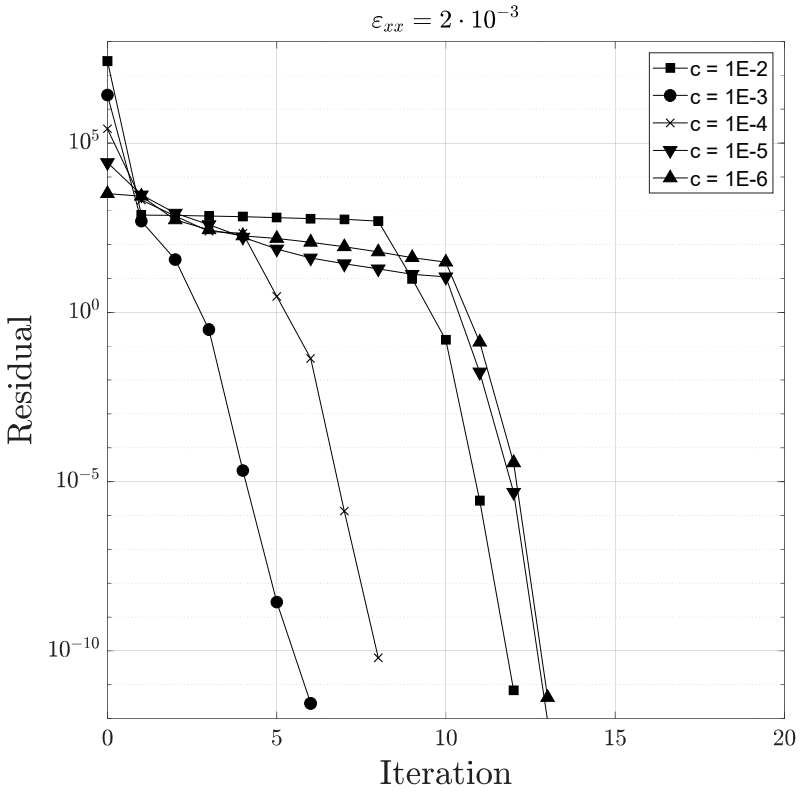
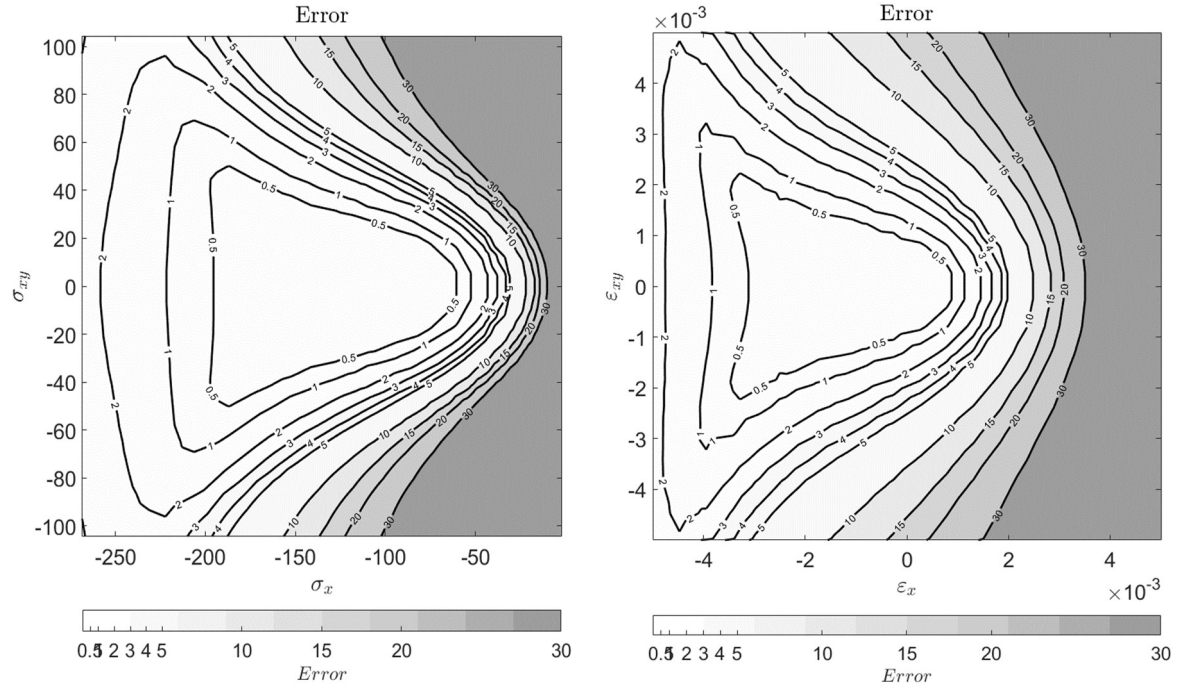


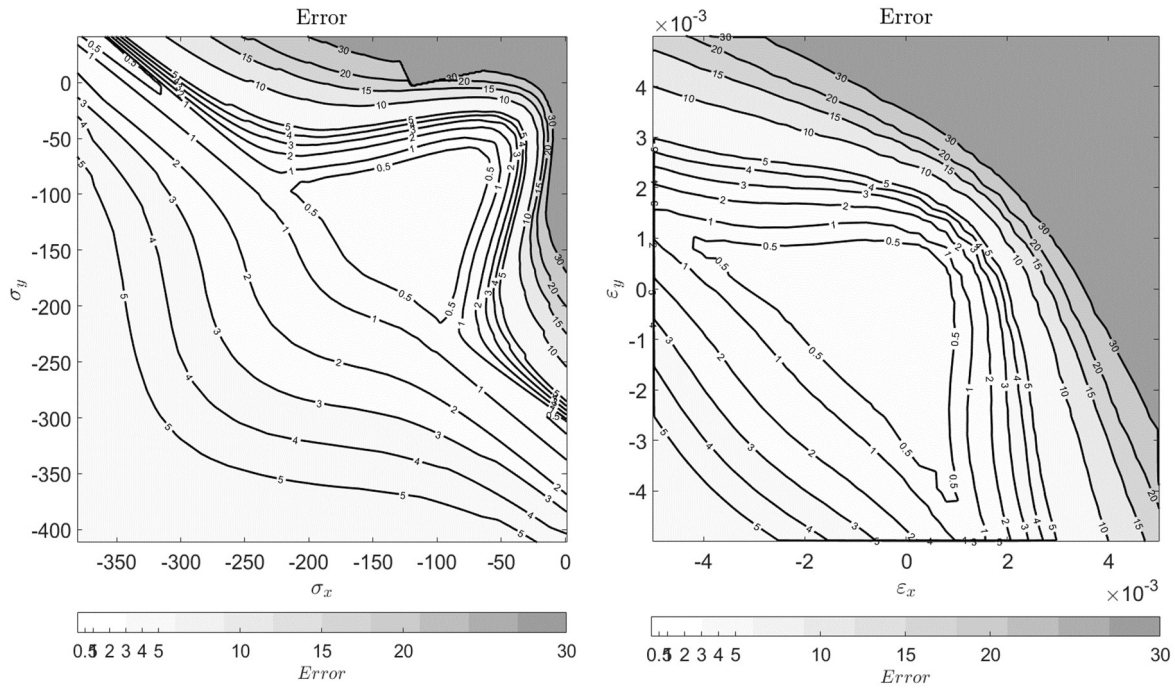
Figure 80: Rate of converge for aug-CPPM for various penalty terms 1E-2 to 1E-6 for oedometric swelling strain path

3.3.6. GLOBAL CONVERGENCE

As concluded with the isoerror maps, the most convenient discretisation is the half-mid-point (MID1) when integrating the equations in one step in terms of error accuracy. Also, from the previous results on the rate of convergence of the non-linear solvers, it has been found that a classic CPPM exhibits poor global convergence properties in the examined cases and that augmented formulation of the CPPM algorithm excels in terms of convergence, regardless of the distance of the stress predictor. In this section the global convergence properties of the algorithms described in chapter subsection 3.2.3.3 are studied for the half-mid-point time discretisation (MID1). To do so the number of iterations required to reach the solution is plotted for a given number of strain excursions. Figure 82 to Figure 85 show the number of iterations required to reach solution of equations (3.96) to (3.98), all mappings have been obtained using a tolerance of 10^{-8}. The solution obtained with all non-linear solvers is the same, exhibiting the same precision regardless of the non-linear solver. Detail of the size of the stress and strain excursions carried out in these analyses is plotted in Figure 81, where the isoerror maps are shown.



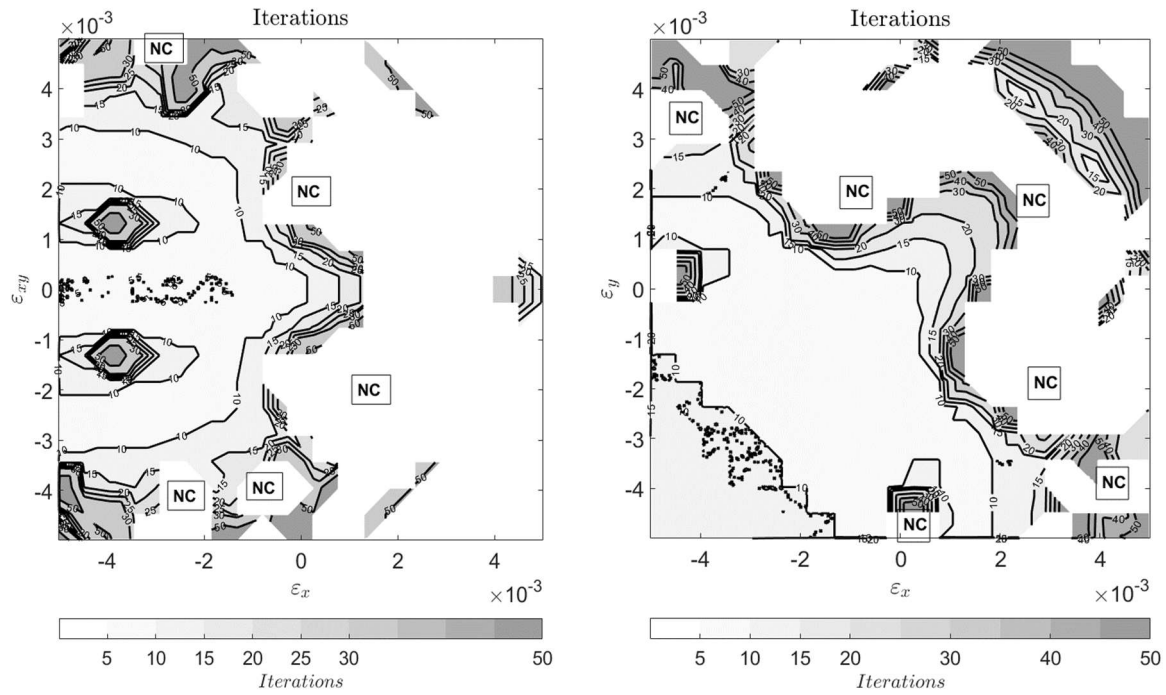
(a)



(b)

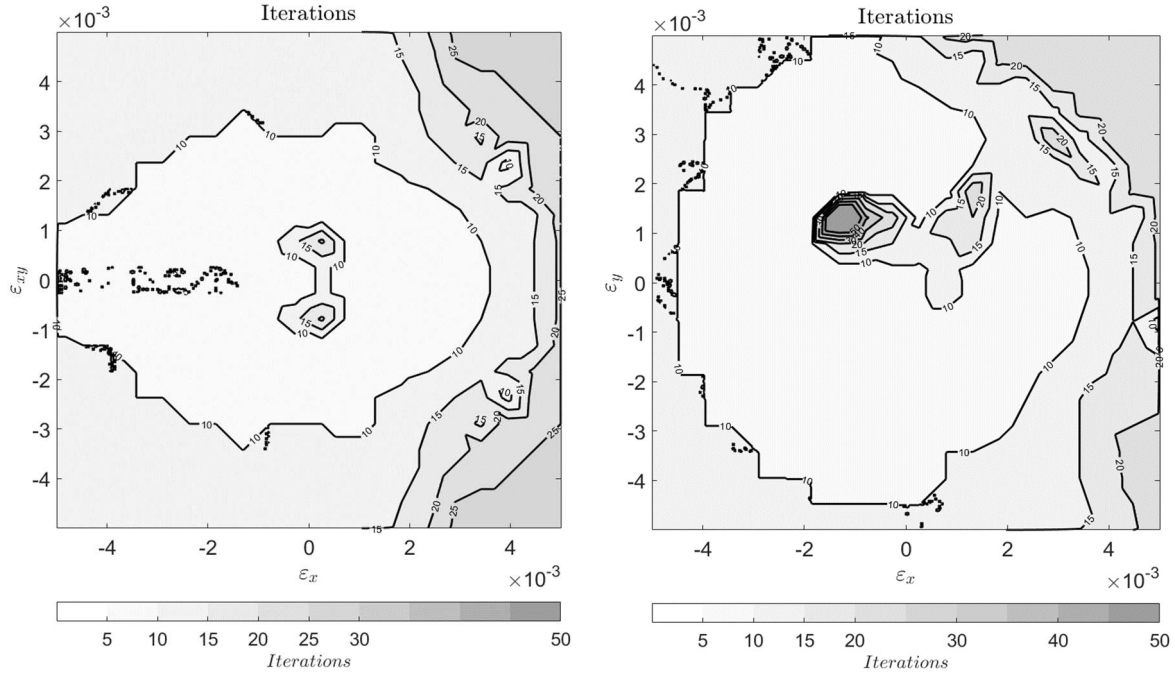
Figure 81: Isoerrors for global convergence test. (a) non-diagonal excursions, (b) diagonal excursions

As expected the classic Newton-Raphson (CPPM) exhibits poor global convergence for large strain excursions, which occurs in particular for situations where the elastic predictor falls in the tensile region, typically when $\Delta\varepsilon_{xx} > 0$ (see Figure 82). Under this strain direction it is likely to violate the Khun-Tucker conditions. Figure 82 includes the sign "NC", meaning "not converged". It can be seen that under one step integration the classic CPPM does not provide enough stability, especially when the prediction lies in a tensile stress region. On the other hand, the constrained CPPM (primal-CPPM) and trust region algorithm converged for all the strain excursions, requiring less iterations for the primal-CPPM with respect to the trust region algorithm (DTM). However, there is no doubt that the augmented Lagrangian closest projection method (aug-CPPM) is superior in all aspects to the other solvers for the examined cases. Firstly it is globally convergent, and secondly only requires at maximum of 7 iterations to reach the solution regardless of the strain direction and magnitude.



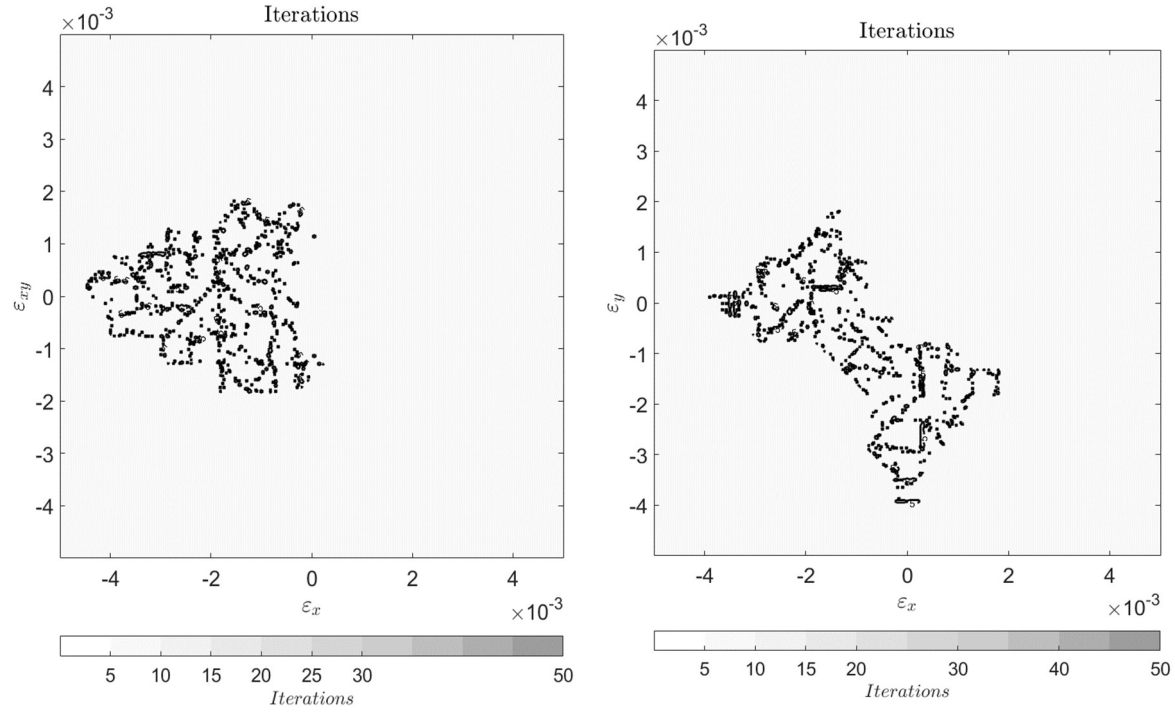
(a) (b)

Figure 82: Iterations map for closest-Projection-Point Method (CPPM), non-diagonal excursions (a), diagonal excursions (b)



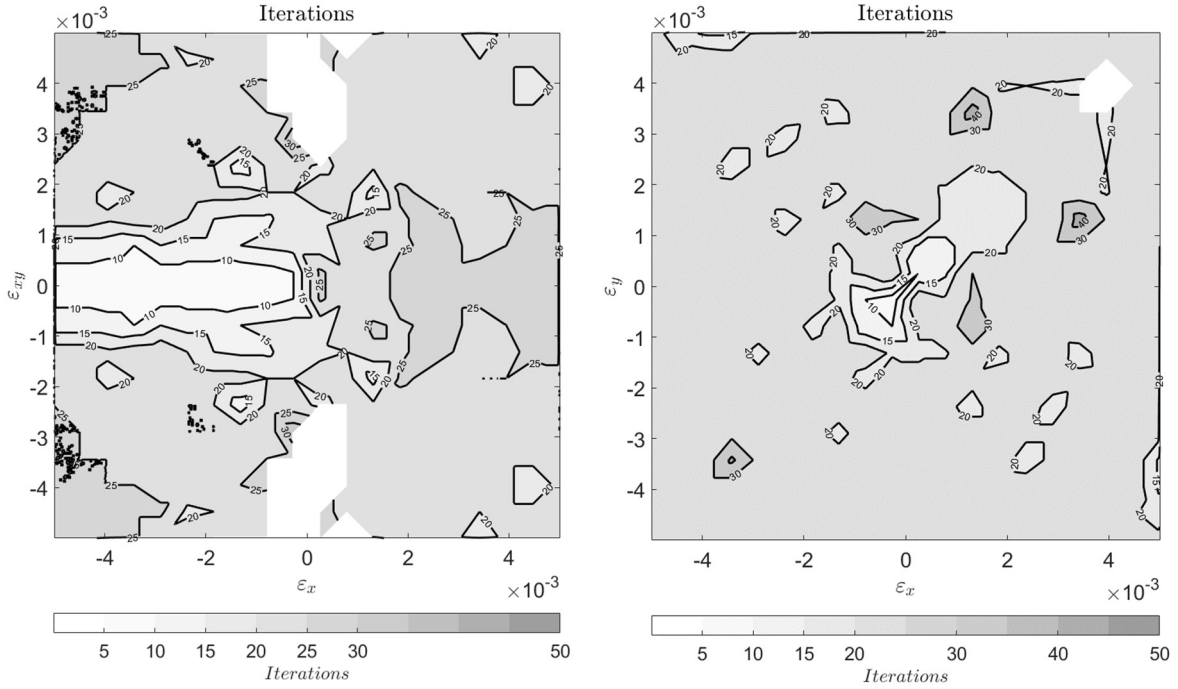
(a) (b)

Figure 83: Iterations map for constrained-Closest-Projection-Point Method (primal-CPPM), non-diagonal excursions (a), diagonal excursions (b)



(a) (b)

Figure 84: Iterations map for augmented-Closest-Projection-Point Method (augmented-CPPM), non-diagonal excursions (a), diagonal excursions (b)



(a) (b)

Figure 85: Dogleg-Trust-Region method (DTM), non-diagonal excursions (a), diagonal excursions (b)

3.4. NUMERICAL STUDY: BASIC SAND MODEL

The previous section presented the numerical study of an *amorphous version* of encapsulated hypoplasticity with no dependence on the void ratio. Having validated the methodology with the "simple" encapsulated Wu model (Wu, 1992), it is the turn now to explore the response and performance with a much more advanced model, such as the basic sand model proposed in 2.5.1, the inputs chosen are:

Table 14: Inputs of Basic Sand Model used in this numerical study

e_{c0}	e_{d0}	h_s	n	α	β	XF	YF	ZF	ς	S_f	ob_{min}	ob_{max}	δ
1.05	0.55	400E3	0.45	0.15	1.7	0.52	0.77	0.24	0.4	4.0	-1.73	1.0	2.0

Similarly, as done in the previous section, the model performance, precision of the discretisation, global convergence and quality of the integration of standard tests are presented, and the overall performance of the algorithms is compared.

3.4.1. MODEL RESPONSE IN TRIAXIAL CONDITIONS

A set of numerical triaxial tests is carried out until 30 % of axial strain to assess the response of the model. The initial mean stresses in Figure 86 are 100 and 200 kPa and the initial void ratios vary from 0.7 to 1.1, covering loose sand, medium-dense sands and dense sand, the critical state line (CSL) has been included in the figure for reference.

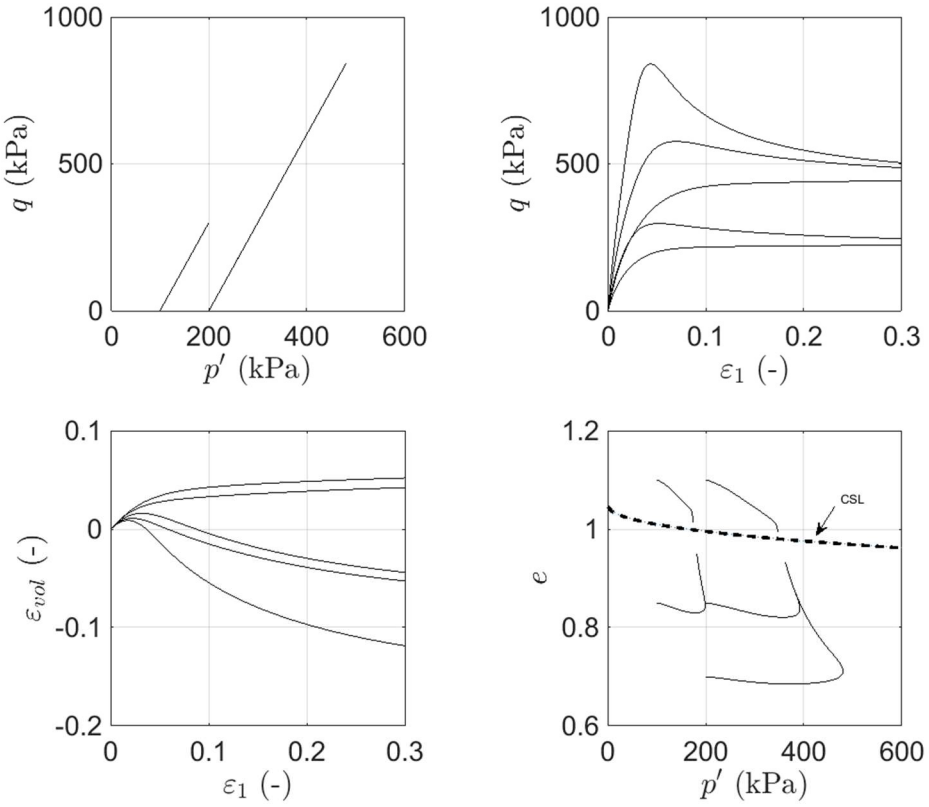


Figure 86: Model response in triaxial conditions

3.4.2. ANALYTICAL DERIVATIVES

To evaluate the Jacobians of the residuals, the derivatives of the hardening rules with respect to stress and backstress are needed. For simplicity a type of hardening rule where the metric is not modified, ($\dot{z} = \left\| \dot{\varepsilon}_{ij}^{p} \right\| = \lambda$), has been chosen. Under those conditions the hardening rule is:

$$\dot{\alpha}_{ij} = \lambda h_{ij} = f_e f_b L_{ijkl} \left(\vec{n}_{kl} - f_d \tilde{\vec{Y}} \vec{\Upsilon}_{kl} \right) \tag{3.101}$$

$$L_{ijkl} = S_f \left(\frac{1}{3} \delta_{ij} \delta_{kl} + \hat{\alpha}_{ij}^{*} \delta_{kl} \right) + \left(\delta_{ik} \delta_{jl} - \frac{1}{3} \delta_{ij} \delta_{kl} - \hat{\alpha}_{ij}^{*} \delta_{kl} \right) \tag{3.102}$$

The derivative of the normal of the yield surface is:

$$\frac{\partial \vec{n}_{ij}}{\partial \alpha_{kl}} = -\frac{1}{\left\| \sigma_{ij} - \alpha_{ij} \right\|} \left(\delta_{ik}\delta_{jl} - \vec{n}_{ij}\vec{n}_{kl} \right) \tag{3.103}$$

The derivative of the hardening rule with respect to the stress is:

$$\frac{dh_{ij}(\alpha_{ij}, \vec{n}_{ij})}{d\sigma_{kl}} = \left(f_e f_b L_{ijpq} \right) \frac{\partial \vec{n}_{pq}}{\partial \sigma_{kl}} \tag{3.104}$$

The goal function $\vec{\Upsilon}_{kl}$ is an isotropic function of one tensor and in this case its derivative can be obtained using the general method described in de Souza Neto (2004). To do so, the backstress needs to be decomposed into eigenvalues and eigenprojectors as:

$$\alpha_{ij} = \sum_{p=1}^{3} \alpha_p E_{ij}^p \tag{3.105}$$

The derivative of the goal function with respect to the eigenvalues is:

$$\begin{aligned} &\frac{d\left(\vec{\Upsilon}_p(\alpha_1, \alpha_2, \alpha_3, \tilde{Y}) \right)}{d\alpha_m} = \vec{\alpha}_p^* \frac{\partial\left(\sqrt{1-(ob^{GF})^2/3} \right)}{\partial \alpha_m} + \\ &+ \left(\sqrt{1-(ob^{GF})^2/3} \right) \frac{\partial \vec{\alpha}_p^*}{\partial \alpha_m} + \frac{1}{3}\delta_p \frac{\partial (ob^{GF})}{\partial \alpha_m} \qquad m = 1,..,3 \quad p = 1,..,3 \end{aligned} \tag{3.106}$$

where

$$\begin{aligned} &\frac{\partial \vec{\alpha}_{ij}^*}{\partial \alpha_{kl}} = \frac{1}{\left\| \alpha_{ij}^* \right\|} \left(\delta_{ik}\delta_{jl} - \frac{1}{3}\delta_{ij}\delta_{kl} - \vec{\alpha}_{ij}^* \vec{\alpha}_{kl}^* \right) \\ &\frac{\partial (ob^{GF})}{\partial Y} = \frac{\delta \exp\left(-\left(Y^{1/\vartheta} \sqrt[\delta]{\ln\left(\frac{ob_{\max} + \sqrt{3}}{ob_{\max}} \right)} \right)^{\delta} \left(ob_{\max} - ob_{\min} \right) \left(Y^{1/\vartheta} \sqrt[\delta]{\ln\left(\frac{ob_{\max} + \sqrt{3}}{ob_{\max}} \right)} \right)^{\delta} \right)}{\vartheta Y} \end{aligned} \tag{3.107}$$

For this case the goal function and the backstress are coaxial and, inserting (3.106) and (3.105) in the method proposed by de Souza Neto (2004), the derivative of the goal function can be obtained as:

$$\frac{d\vec{\Upsilon}_{ij}}{d\alpha_{kl}} = \sum_{a=1}^{3} \frac{\Upsilon_a}{(\alpha_a - \alpha_b)(\alpha_a - \alpha_c)} \begin{pmatrix} \frac{\partial \alpha_{ij}^2}{\partial \alpha_{kl}} - (\alpha_b - \alpha_c)\prod_4 \\ -\left[(\alpha_a - \alpha_b) + (\alpha_a - \alpha_c)\right] E_{ij}^a E_{kl}^a \\ -(\alpha_b - \alpha_c)\left[E_{ij}^b E_{kl}^b - E_{ij}^c E_{kl}^c \right] \\ -\sum_{i=1}^{3}\sum_{j=1}^{3} \frac{\partial \Upsilon_i}{\partial \alpha_j} E_{ij}^i E_{kl}^j \end{pmatrix} \tag{3.108}$$

where $\prod_4$ is the super-symmetric fourth order identity. In a similar way, the derivative of the limit function from its eigenvalues can be obtained using any standard symbolic math package such as Mathematica, SimPy or Matlab:

$$\frac{\partial \tilde{Y}(\alpha_1, \alpha_2, \alpha_3)}{\partial \alpha_p} \qquad p = 1,..,3 \tag{3.109}$$

The derivative of the limit surface is simpler, as expression $\frac{\partial Y}{\partial \alpha_k}$ has been already computed and can be reused in the general space as:

$$\frac{\partial Y}{\partial \alpha_{ij}} = \sum_{p=1}^{3} \frac{\partial Y}{\partial \alpha_p} E_{ij}^p \tag{3.110}$$

As the mapping tensor can be split into a constant term and backstress dependent term then

$$\begin{aligned} L_{ijkl} &= L_{ijkl}^{CTE} + \left(S_f - 1\right)\hat{\alpha}_{ij}^{*}\delta_{kl} \\ L_{ijkl}^{CTE} &= \left(\delta_{ik}\delta_{jl} - \frac{1}{3}\delta_{ij}\delta_{kl}\right) + S_f\left(\frac{1}{3}\delta_{ij}\delta_{kl}\right) \end{aligned} \tag{3.111}$$

After applying the chain rule the derivative is

$$\frac{dh_{ij}}{d\alpha_{kl}} = f_e f_b \left[\begin{array}{l} L^{CTE}_{ijpq} \left(\dfrac{\partial \vec{n}_{pq}}{\partial \alpha_{kl}} - f_d \left(\vec{\Upsilon}_{pq} \dfrac{\partial \tilde{Y}}{\partial \alpha_{kl}} + \tilde{Y} \dfrac{\partial \vec{\Upsilon}_{pq}}{\partial \alpha_{kl}} \right) - \tilde{Y} \vec{\Upsilon}_{ij} \dfrac{\partial f_d}{\partial \alpha_{kl}} \right) + \\ \left(S_f - 1 \right) \left(\dfrac{\partial \left(\vec{n}_{kk} \hat{\alpha}^*_{ij} \right)}{\partial \alpha_{kl}} - f_d \dfrac{\partial \left(Y \vec{\Upsilon}_{kk} \hat{\alpha}^*_{ij} \right)}{\partial \alpha_{kl}} - Y \vec{\Upsilon}_{kk} \hat{\alpha}^*_{ij} \dfrac{\partial f_d}{\partial \alpha_{kl}} \right) \end{array} \right] + h_{ij} \frac{\partial (f_e f_b)}{\partial \alpha_{kl}} \tag{3.112}$$

where for the tensors

$$\frac{\partial \left(Yob^{GF} \hat{\alpha}^*_{ij} \right)}{\partial \alpha_{kl}} = \hat{\alpha}^*_{ij} \frac{\partial (Yob^{GF})}{\partial \alpha_{kl}} + \tilde{Y} ob^{GF} \frac{\partial \hat{\alpha}^*_{ij}}{\partial \alpha_{kl}} \tag{3.113}$$

$$\frac{\partial (Yob^{GF})}{\partial \alpha_{kl}} = ob^{GF} \frac{\partial (Y)}{\partial \alpha_{kl}} + Y \frac{\partial (ob^{GF})}{\partial \alpha_{kl}} = \left(ob^{GF} + Y \frac{\partial (ob^{GF})}{\partial Y} \right) \frac{\partial (Y)}{\partial \alpha_{kl}} \tag{3.114}$$

$$\frac{\partial \left(\vec{n}_{pp} \hat{\alpha}^*_{ij} \right)}{\partial \alpha_{kl}} = \left(\hat{\alpha}^*_{ij} \frac{\partial \vec{n}_{pp}}{\partial \alpha_{kl}} + \vec{n}_{kk} \frac{\partial \hat{\alpha}^*_{ij}}{\partial \alpha_{kl}} \right) \tag{3.115}$$

$$\frac{\partial \vec{n}_{pp}}{\partial \alpha_{kl}} = - \frac{1}{\left\| \sigma_{ij} - \alpha_{ij} \right\|^2} \left(\left\| \sigma_{ij} - \alpha_{ij} \right\| \delta_{kl} - (\sigma_{kk} - \alpha_{kk}) \vec{n}_{kl} \right) \tag{3.116}$$

Once the tensorial derivatives are carried out, the scalar functions f_e, f_b and f_d need to be differentiated:

$$\frac{e_d}{e_{d0}} = \frac{e_c}{e_{c0}} = \exp \left[- \left(\frac{-\alpha_{kk}}{h_s} \right)^n \right] \tag{3.117}$$

$$f_d = \left(\frac{e - e_d}{e_c - e_d} \right)^{\alpha} \tag{3.118}$$

$$f_e = \left(\frac{e_c}{e} \right)^{\beta} \tag{3.119}$$

$$f_b = \frac{(1+e)\dfrac{h_s}{en}\left(\dfrac{|\alpha_{kk}|}{h_s}\right)^{1-n}\left(1+2\tilde{Y}\right)}{1+\left|S_f-1\right|\left(1+1/3\left\|\hat{\alpha}_{ij}^{*}\right\|\right)} \tag{3.120}$$

where

$$\frac{\partial e_c}{\partial \alpha_{ij}} = e_{c0}\frac{n\left(\dfrac{|\alpha_{kk}|}{h_s}\right)^{n}\exp\left(-\left(\dfrac{|\alpha_{kk}|}{h_s}\right)^{n}\right)}{|\alpha_{kk}|}\delta_{ij} \tag{3.121}$$

$$\frac{\partial e_d}{\partial \alpha_{ij}} = e_{d0}\frac{n\left(\dfrac{|\alpha_{kk}|}{h_s}\right)^{n}\exp\left(-\left(\dfrac{|\alpha_{kk}|}{h_s}\right)^{n}\right)}{|\alpha_{kk}|}\delta_{ij} \tag{3.122}$$

$$\frac{\partial f_e}{\partial \alpha_{ij}} = \left(\frac{e_{c0}}{e}\right)^{\beta}\frac{\beta n\left(\dfrac{|\alpha_{kk}|}{h_s}\right)^{n}\left(\exp\left(-\left(\dfrac{|\alpha_{kk}|}{h_s}\right)^{n}\right)\right)^{\beta}}{|\alpha_{kk}|}\delta_{ij} \tag{3.123}$$

$$\frac{\partial f_d}{\partial \alpha_{ij}} = -\alpha f_d\left(\frac{e_{d0}}{e-e_d}\frac{n\left(\dfrac{|\alpha_{kk}|}{h_s}\right)^{n}\exp\left(-\left(\dfrac{|\alpha_{kk}|}{h_s}\right)^{n}\right)}{|\alpha_{kk}|}\delta_{ij}+\frac{n\left(\dfrac{|\alpha_{kk}|}{h_s}\right)^{n}}{|\alpha_{kk}|}\delta_{ij}\right) \tag{3.124}$$

$$\frac{\partial f_b}{\partial \alpha_{ij}} = \frac{\partial f_b}{\partial Y}\frac{\partial Y}{\partial \alpha_{ij}}+\frac{\partial f_b}{\partial \eta_\alpha}\frac{\partial \eta_\alpha}{\partial \alpha_{ij}}+\frac{\partial f_b}{\partial p_\alpha}\frac{\partial p_\alpha}{\partial \alpha_{ij}} \tag{3.125}$$

And finally the last auxiliary terms of (3.125) are:

$$\frac{\partial f_b}{\partial p_\alpha} = \frac{(1+e)\dfrac{h_s}{en}\left(1+2\tilde{Y}\right)}{1+\left|S_f-1\right|\left(1+\dfrac{\sqrt{2}}{9}|\eta_\alpha|\right)}\left(\frac{|3|}{h_s}\right)^{1-n}(1-n)\,p\,|p|^{-(1+n)} \tag{3.126}$$

$$\frac{\partial f_b}{\partial Y} = 2\tilde{Y}\frac{(1+e)\dfrac{h_s}{en}\left(\dfrac{|\alpha_{kk}|}{h_s}\right)^{1-n}}{1+\left|S_f-1\right|\left(1+1/3\left\|\hat{\alpha}_{ij}^{*}\right\|\right)} \tag{3.127}$$

$$\frac{\partial f_b}{\partial \eta_\alpha} = -\frac{9\sqrt{2}(1+e)\frac{h_s}{en}\left(\frac{|3p|}{h_s}\right)^{1-n}\left(1+2\tilde{Y}\right)\left|S_f-1\right|\eta_\alpha}{\left(\sqrt{2}\left|S_f-1\right|\left|\eta_\alpha\right|+9\left|S_f-1\right|+9\right)^2\left|\eta_\alpha\right|} \qquad (3.128)$$

$$\frac{\partial \eta_\alpha}{\partial \alpha_{ij}} = \frac{1}{p_\alpha}\left(\frac{\sqrt{2}}{2}\vec{\alpha}^*_{ij} - \frac{1}{3}\eta_\alpha \delta_{ij}\right)$$

The final derivative can be obtained assembling (3.112). This section presented the terms in the form of a large chain rule derivative.

3.4.3. ISOERROR MAPS

As carried out in the encapsulated Wu model, the isoerror maps in plane strain conditions and in the Rendulic plane have been explored, however in this exercise the number of excursions in the strain space is 20.000 numerical tests per case studied, where the a maximum magnitude of the strain step is 10^{-2}. In this sense there will be strain excursions that in one step will suppose an increment over 1,000 kPa and others whose solution should be in a liquefied state, with a mean backstress of 0.0. The reference case studied is a medium-dense sand, with an initial p' of 300kPa and a initial void ratio of 0.85.

3.4.3.1. Isoerror maps in the rendulic plane

Similar conclusions as with the encapsulated Wu model can be obtained regarding the discretisation, despite that the sand model exhibits a higher degree of non-linearity the trends are similar. In this sense the half mid point (MID1) continues being the most convenient discretisation as it can admit a reduced system of residulas. Figure 87 to Figure 90 show the isoerror maps in the Rendulic plane in an isomorphic space. No valid solutions where found in the tensile region confirming the robustness of the constitutive model. In general terms the error for the second order discretisations lies below 1% for excursions of a magnitude below 1E-3 strain.

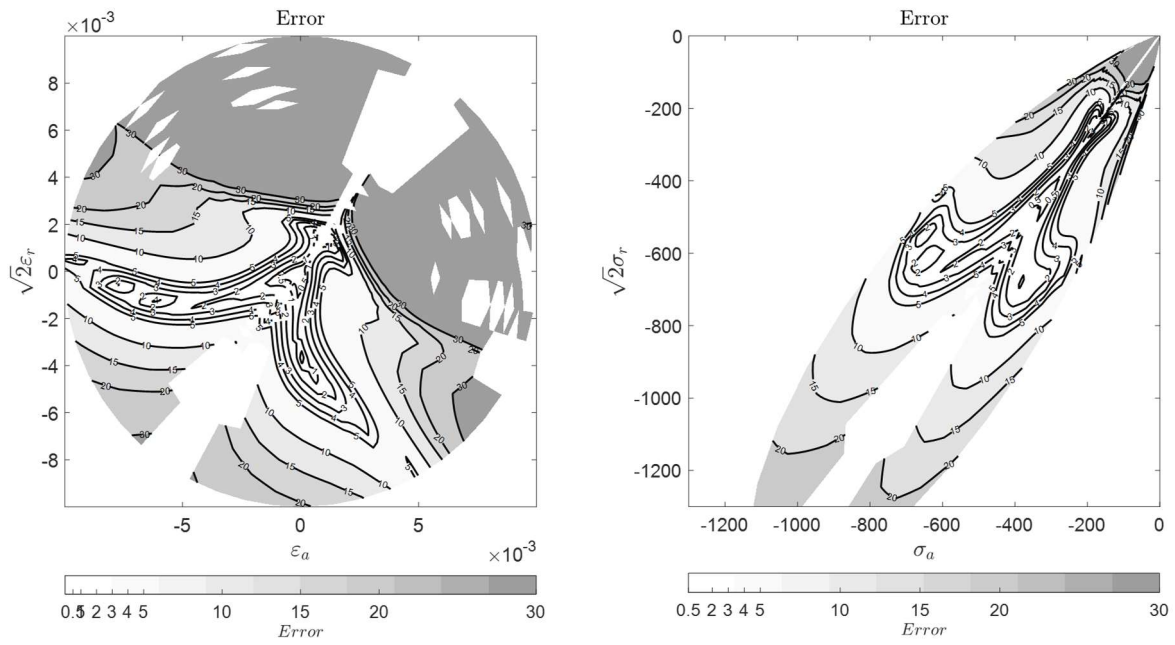


Figure 87: Backward Euler (BE)

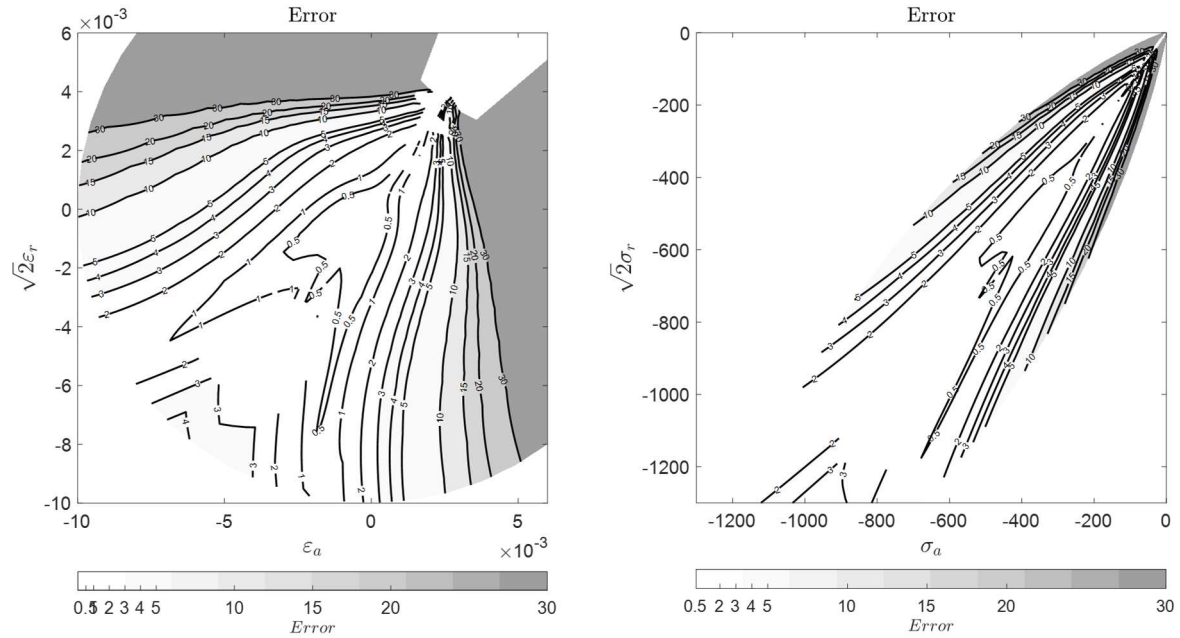


Figure 88: Half-Mid-Point (MID1)

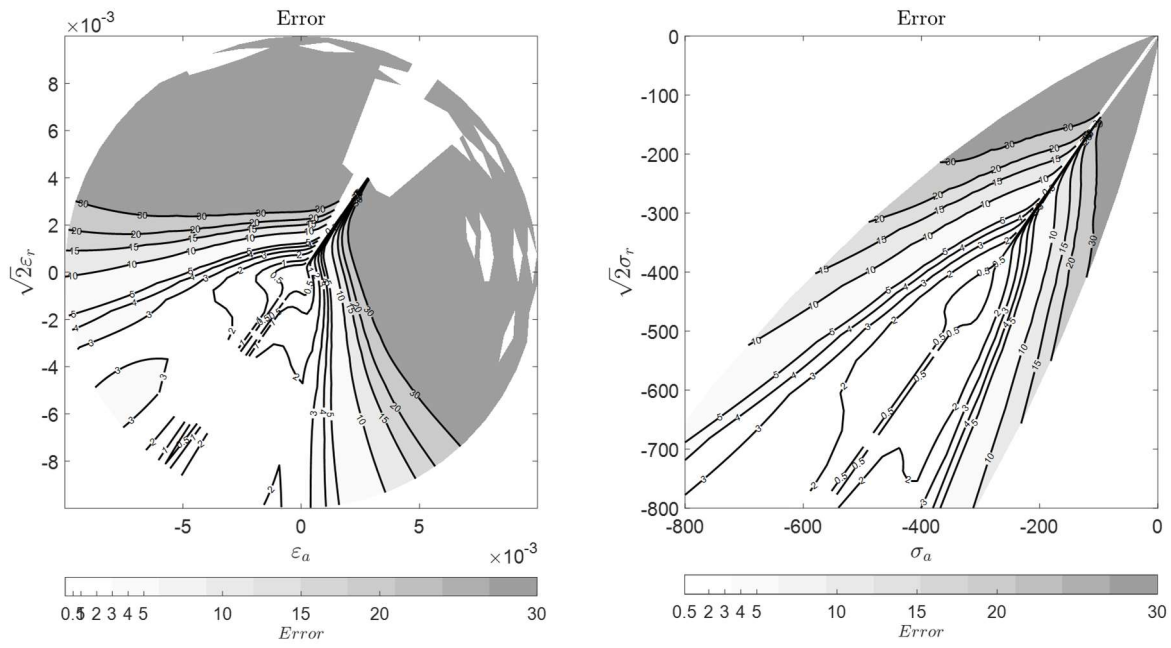


Figure 89: Mid-Point (MID05)

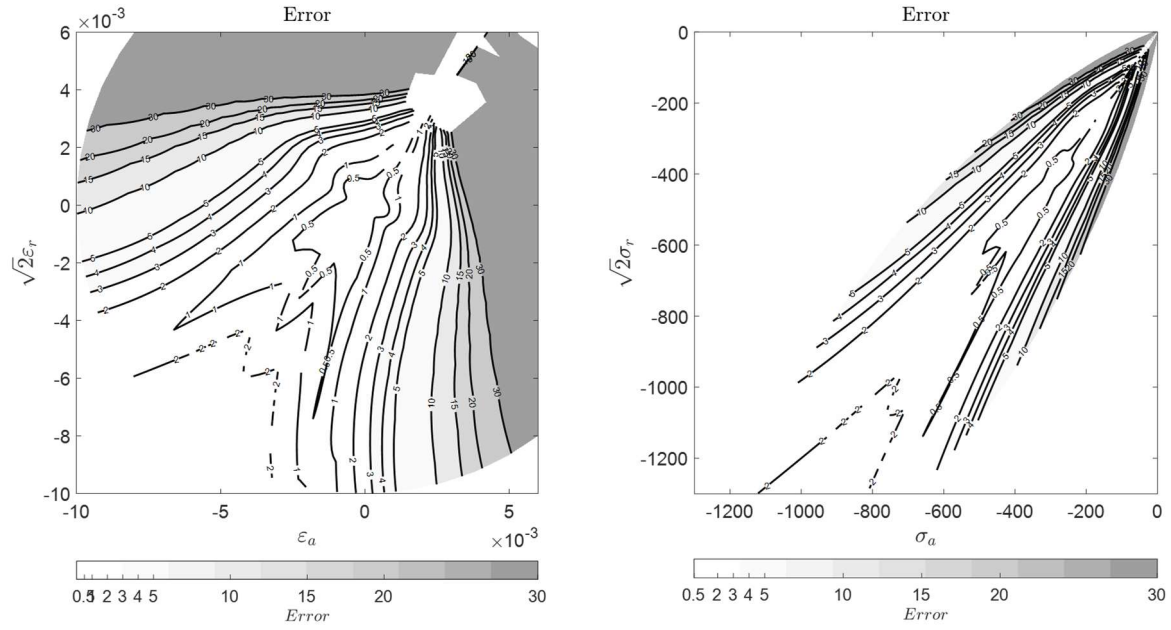


Figure 90: Trapezoidal discretisation (TZ1)

3.4.3.2. Plane Strain

A similar study has been carried out as in the Wu encapsulated model, in this case for strain excursion in the mid-range 1E-3 under plane strain conditions, a slightly smaller order of magnitude than the study for the rendulic plane with values between -3E-3 and +3E-3. The initial conditions correspond to the same ones described in the previous section with an initial p' of 300kPa and a void ratio of 0.85. Same conclusions as in the Wu encapsulated model can be extracted.

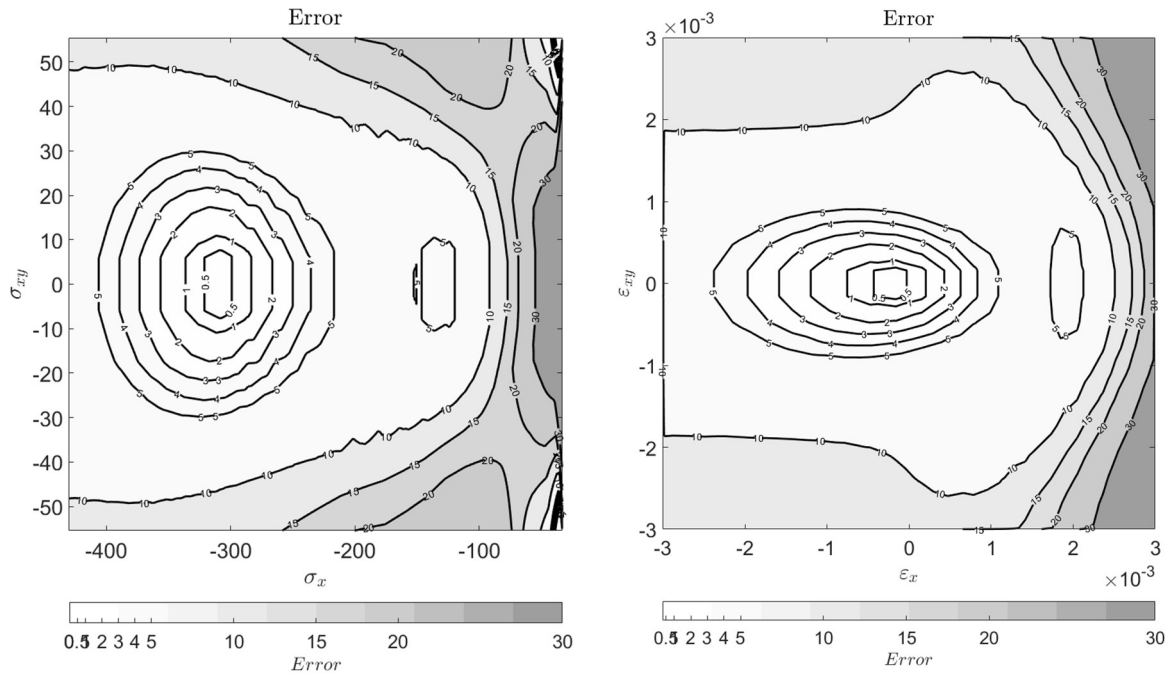


Figure 91: BackWard-Euler (BE) in Plane Strain Conditions for non-diagonal excursions

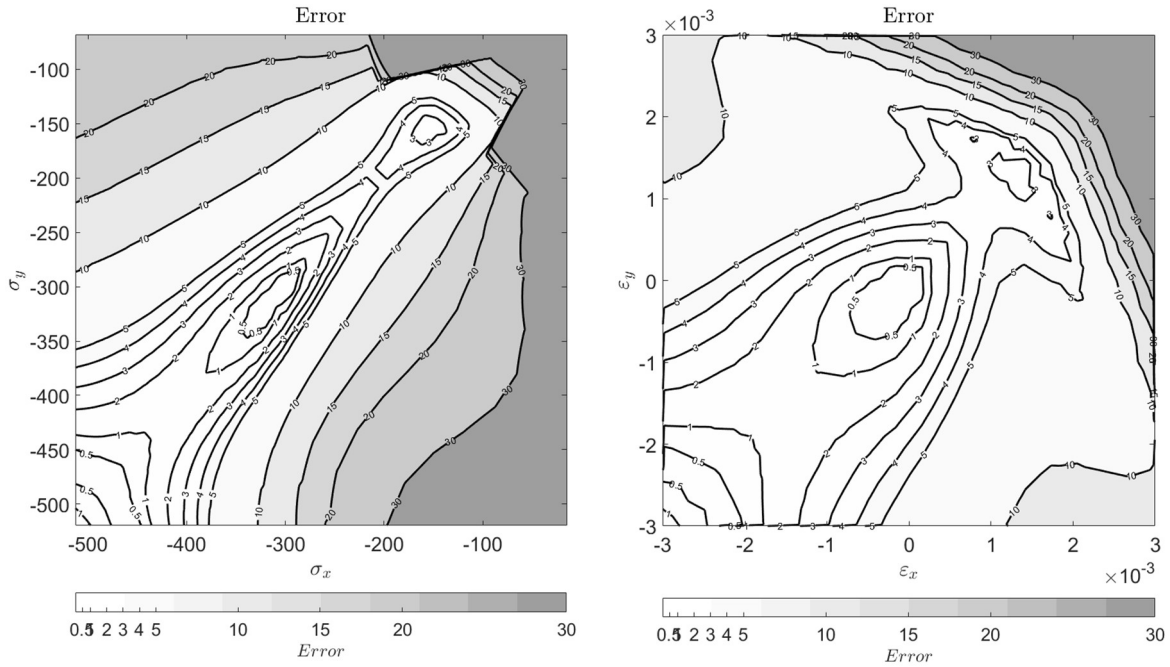


Figure 92: BackWard-Euler (BE) in Plane Strain Conditions for diagonal excursions

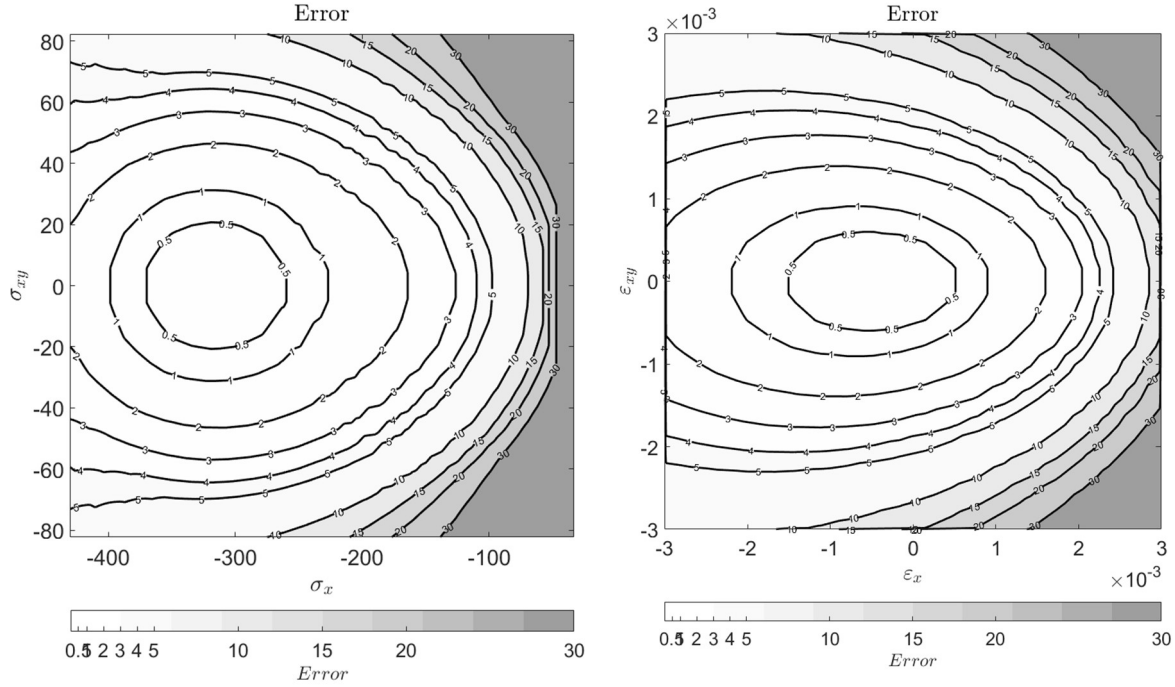


Figure 93: Half Mid-Point (MID1) in Plane Strain Conditions for non-diagonal excursions

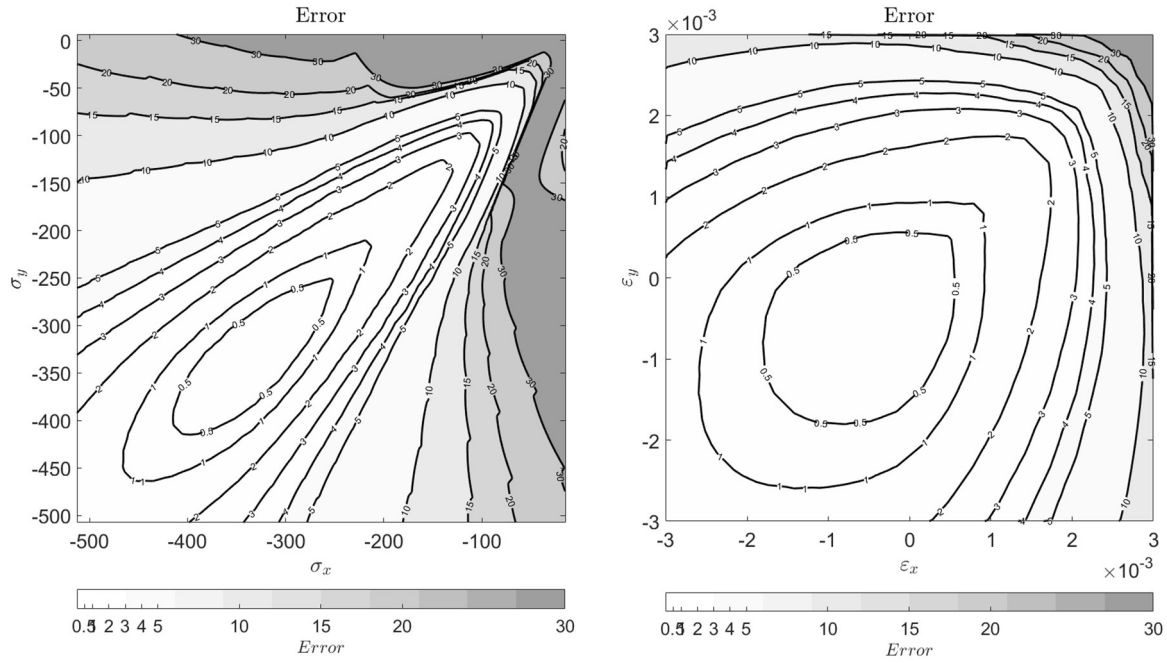


Figure 94: Half Mid-Point (MID1) in Plane Strain Conditions for diagonal excursions

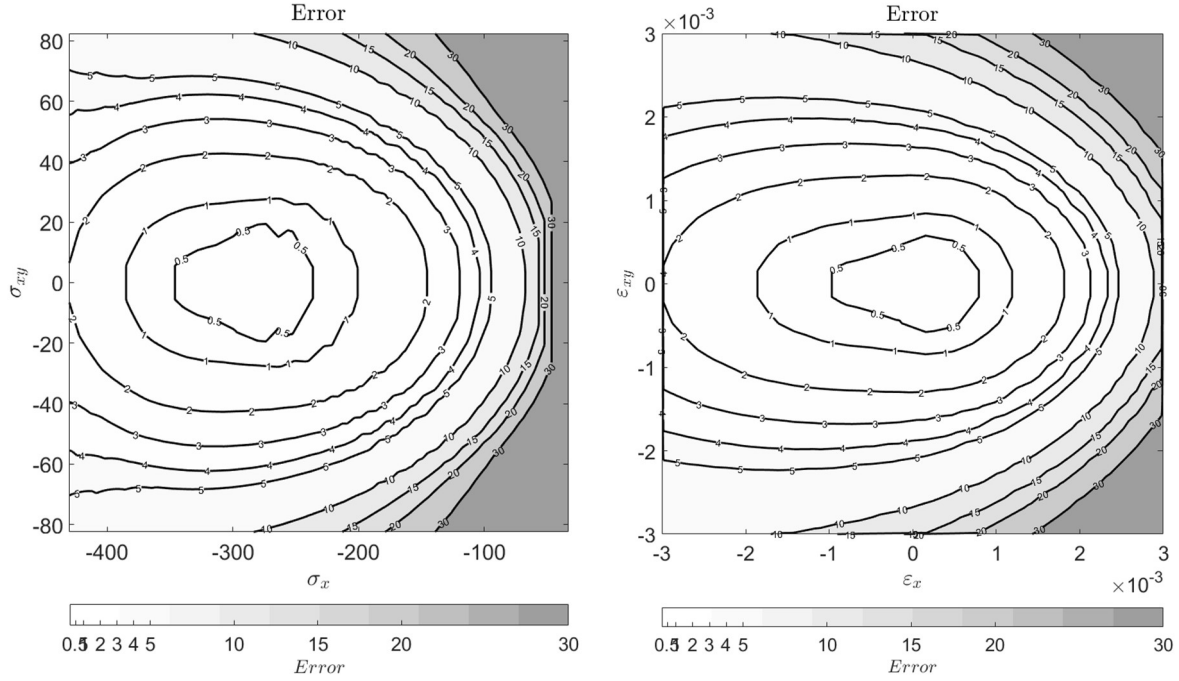


Figure 95: Mid-Point (MID05) in Plane Strain Conditions for non-diagonal excursions

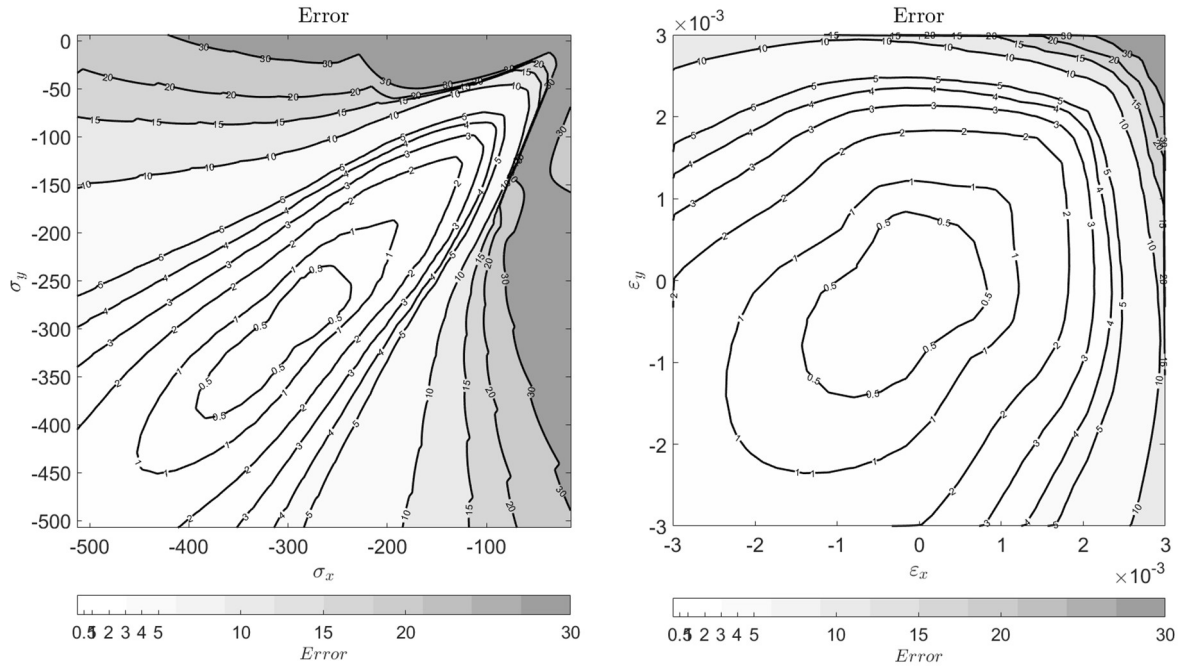


Figure 96: Mid-Point (MID05) in Plane Strain Conditions for diagonal excursions

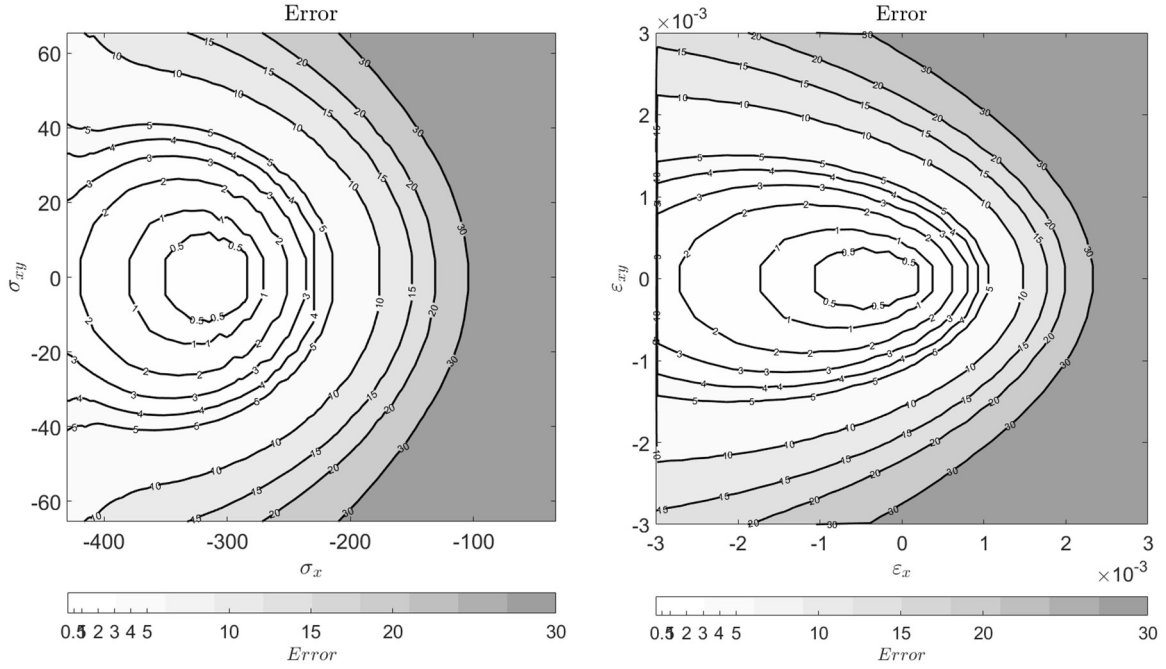


Figure 97: Trapezoidal (TZ) in Plane Strain Conditions for non-diagonal excursions

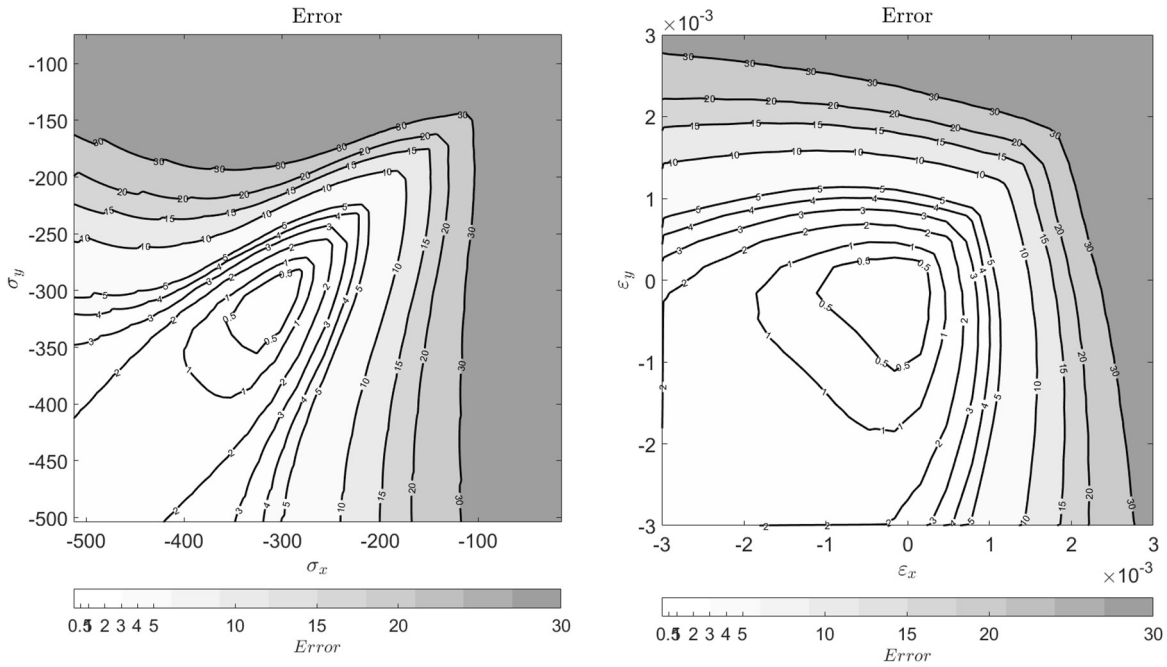


Figure 98: Trapezoidal (TZ) in Plane Strain Conditions for diagonal excursions

3.4.4. CONVERGENCE RATE

The rate of convergence of the non-linear solvers has been studied using the same methodology of 3.3.5. Initial conditions are akin to those used for the isoerror maps with a mean effective stress of 300 kPa and initial void ratio of 0.85. Residual tolerance has been set to 10^{-10} and the inputs chosen are the ones corresponding in Table 12. Figure 99 shows the obtained norm of residual versus the number of iterations where curiously for this cases the CPPM can converge below 30 iterations, however it can be appreciated how for some cases (Figure 99b and Figure 99d) the norm of the residual increases until quadratic convergence rate is achieved. In general terms it can be observed how the augmented closest projection method (aug-CPPM) is superior to the other solvers, as observed for the Wu encapsulated model, followed by the primal-CPPM, the DTM and the classic CPPM.

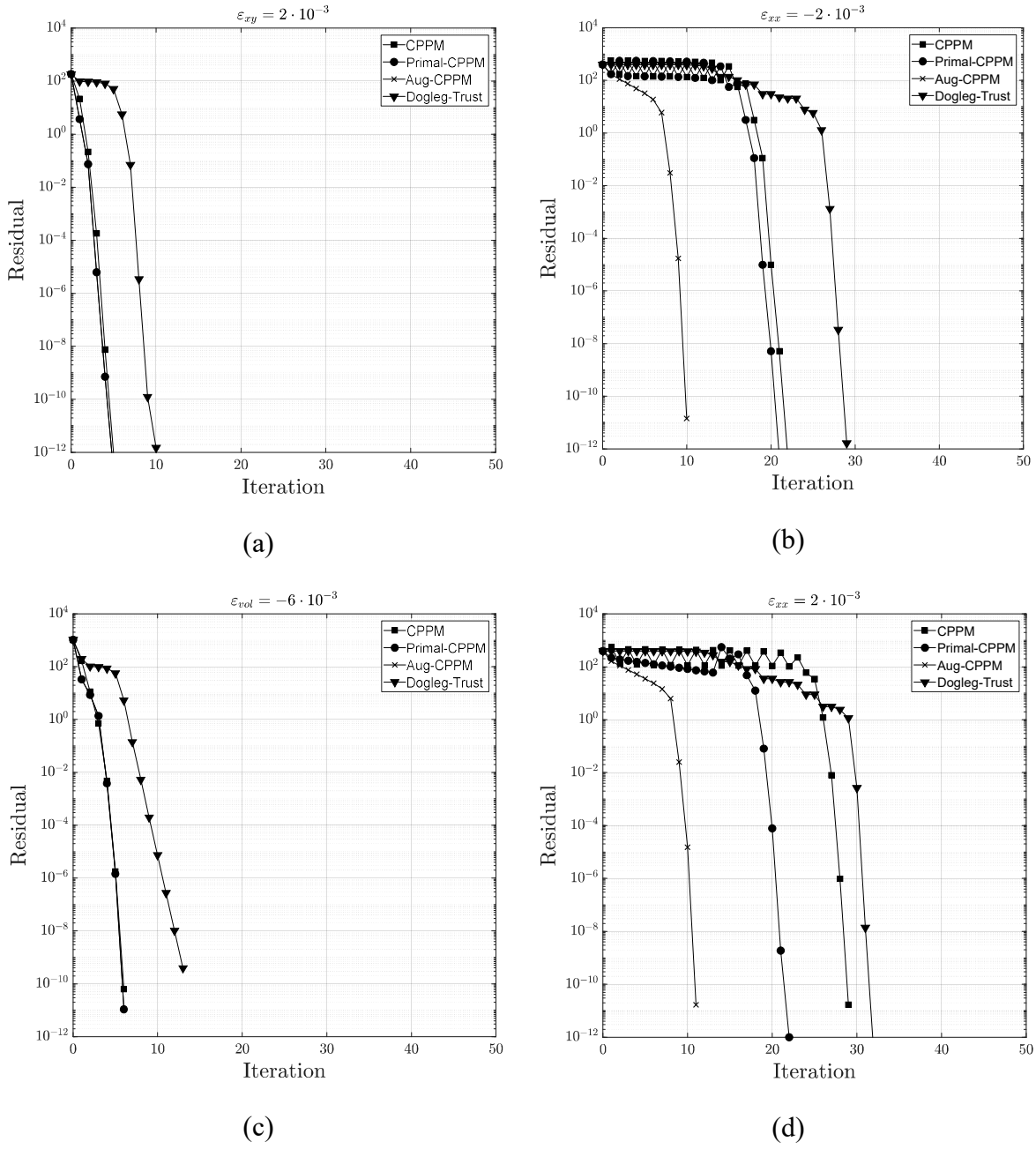


Figure 99: Rate of converge of each of the algorithms for pure deviatoric strain(a), oedometric compresion strain path(b), isotropic compresion strain path(c) and oedometric swelling strain path (d)

3.4.5. GLOBAL CONVERGENCE

Similarly, as in the previous numerical study the performance of the non-linear solvers CPPM, primal-CPPM, aug-CPPM and DTM has been investigated in plane strain conditions for the half mid-point discretisation. Again, the performance of the aug-CPPM seems to be superior to all the other non-linear solvers for this type of model, exhibiting the same trends as seen in the previous study. In this sense the performance of the non-linear solvers from more to less performance in one step is the aug-CPPM, followed by the primal-CPPM, the classic CPPM and the DTM solver. From results of all figures it seems that the strain direction that supposes more difficulties for all the solver corresponds to cases where the volumetric strain rate is small when compared to the deviatoric strain corresponding to small obliquities of the strain rate direction. For all the cases studied the aug-CPPM did not require re-calibration of the penalty term *"c"* where a value of 1E-3 still exhibited good performance.

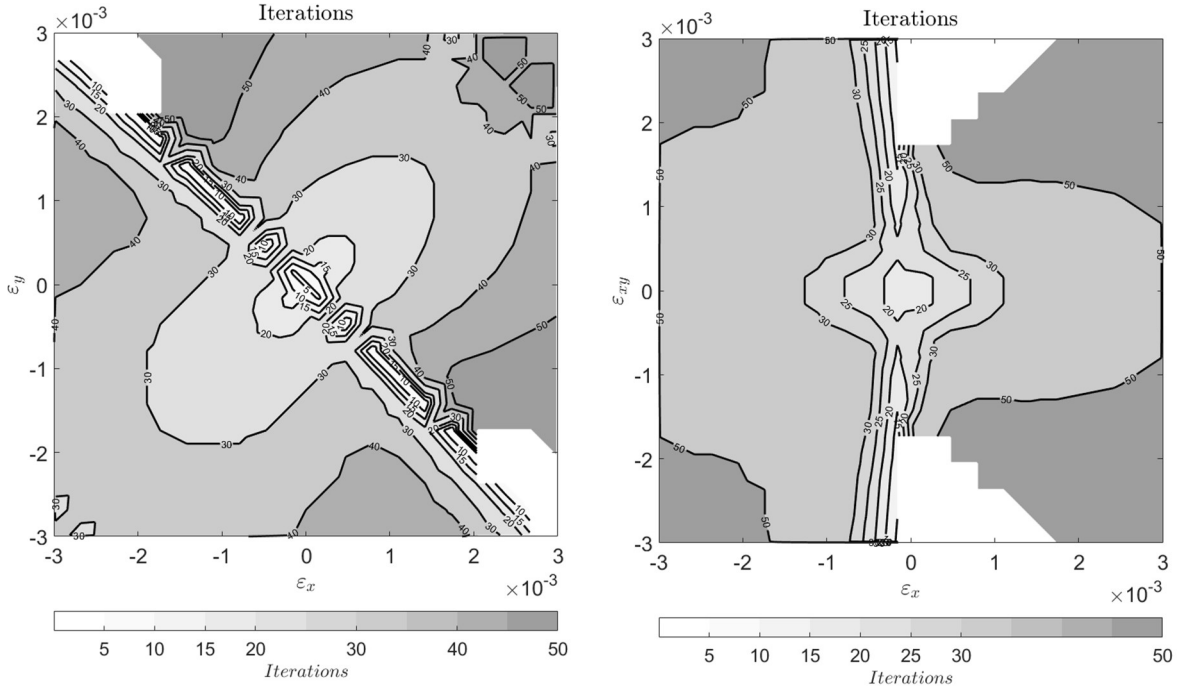


Figure 100: Convergence mapping of CPPM for half-Mid-Point discretisation

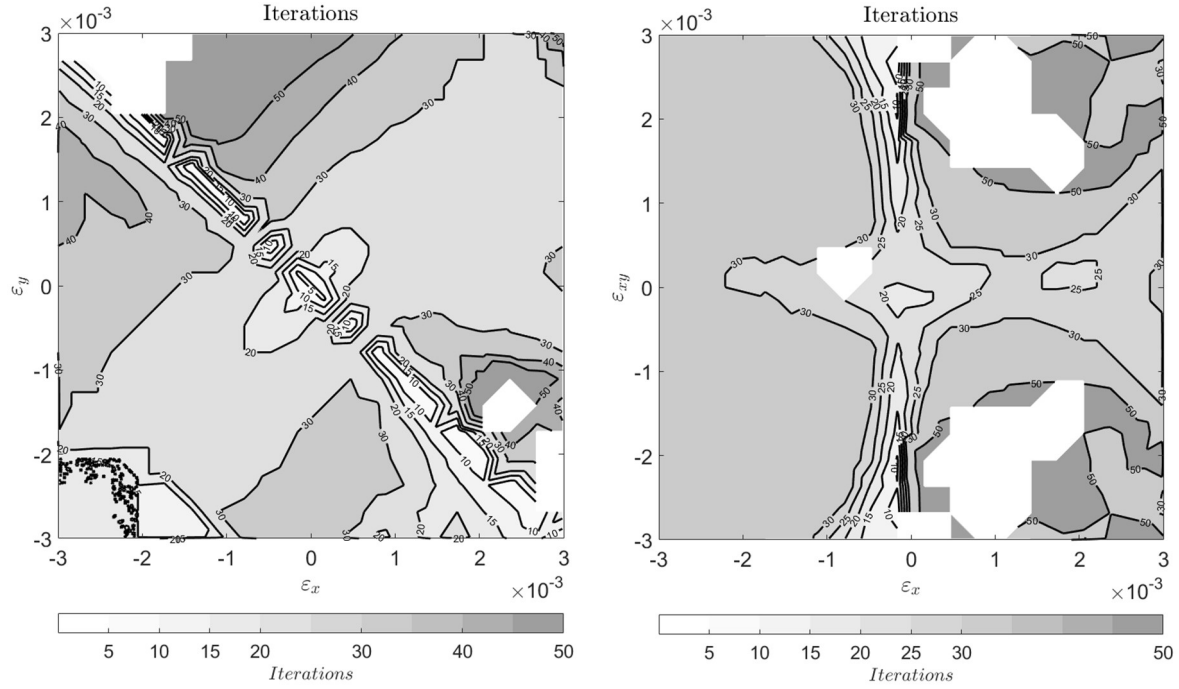


Figure 101: Convergence mapping of primal-CPPM for half-Mid-Point discretisation

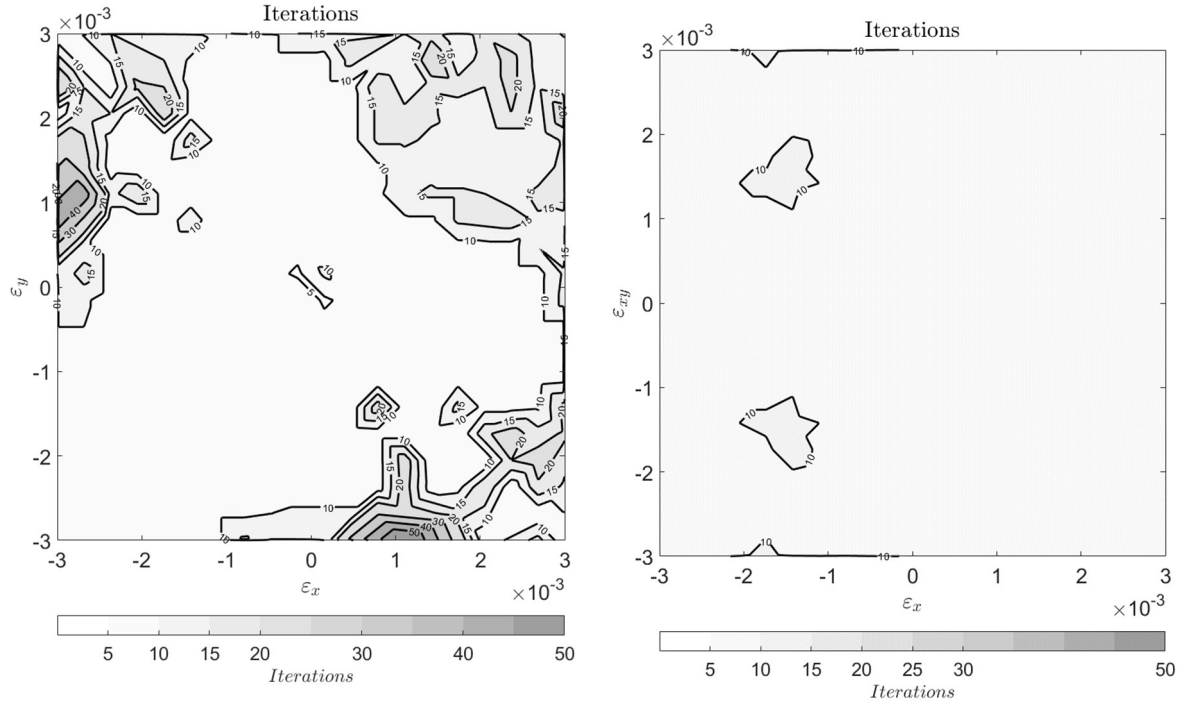


Figure 102: Convergence mapping of augmented-CPPM for half-Mid-Point discretisation

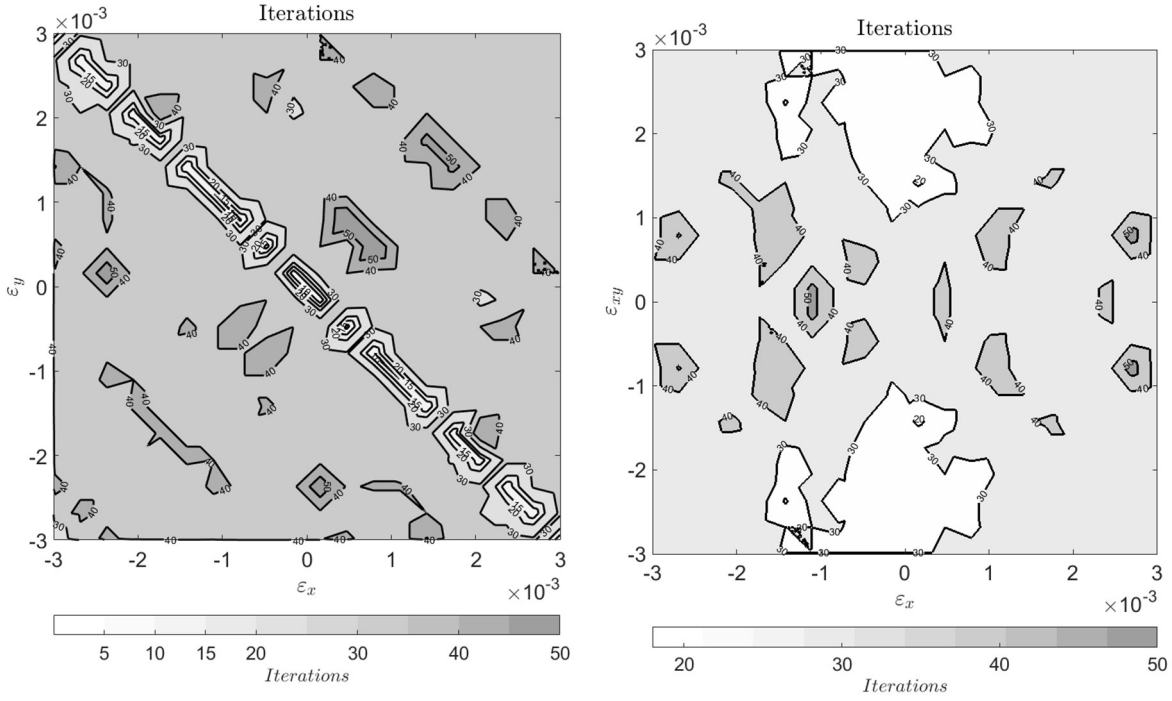


Figure 103: Convergence mapping of Trust-Dogleg-Method (DTM) for half-Mid-Point discretisation

3.4.6. COMPUTATIONAL COST OF THE SUBSTEPPING ALGORITHM

Following a similar methodology as in the previous sections the computing cost of the sub-stepping algorithm can be illustrated. In this sense the algorithm used is described in 3.2.2 where the tolerance has been chosen following the recommendations of Potts and Zdravkovic (1999) with a value for the stress tolerance upon integration of 10^{-4}. Under the previous conditions a set of tests in the rendulic plane and in plane strain conditions has been run and the number of sub-steps required to reach the solution plotted in Figure 105 and Figure 104. The errors have been not included as the sub-stepping algorithm gives practically the exact solution as it uses a small step size.

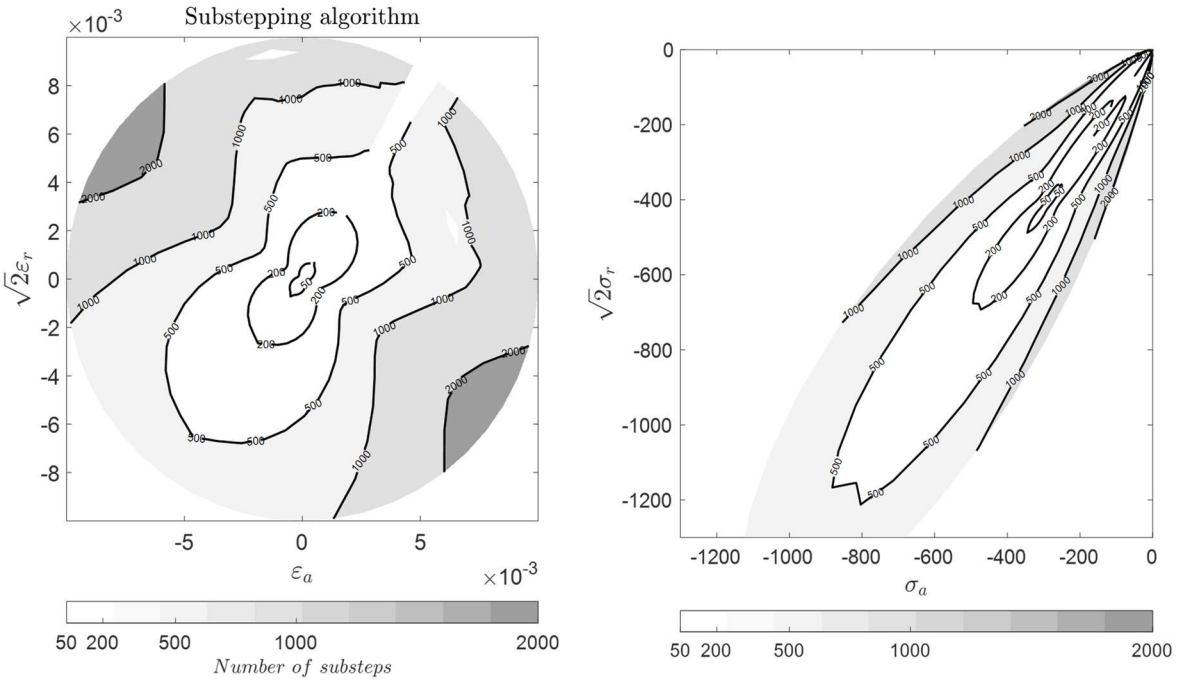


Figure 104: Substepping mapping in the rendulic plane

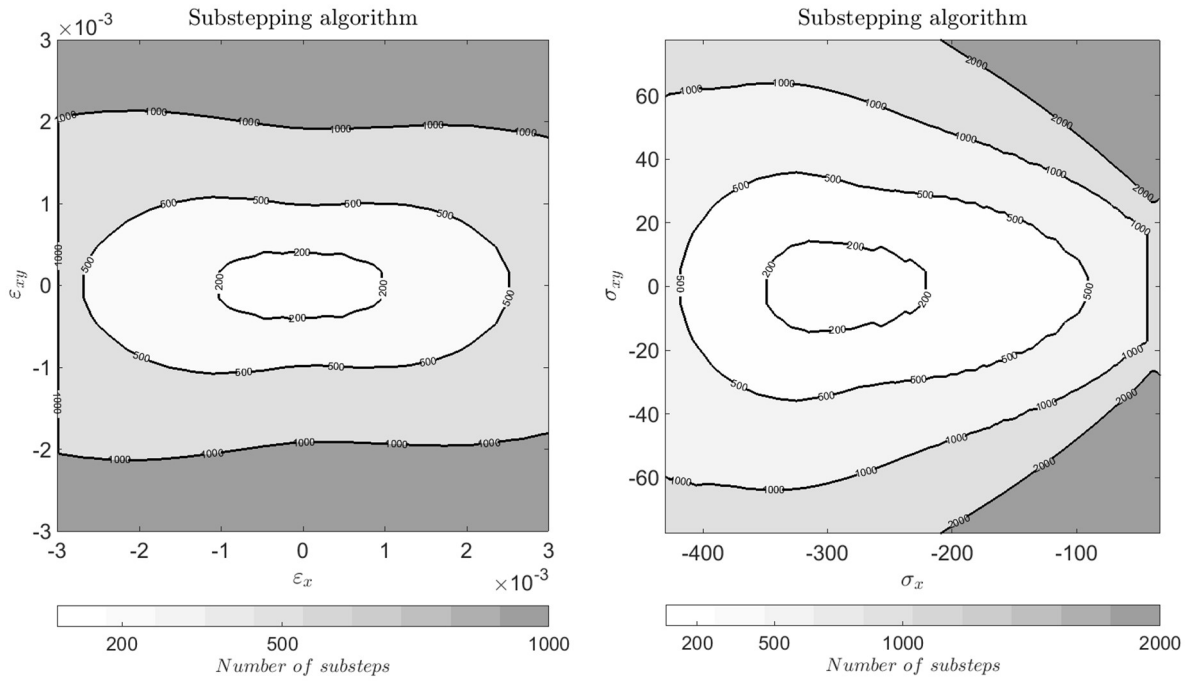


Figure 105: Substepping mapping in plane strain conditions

In terms of computation cost each substep involves the evaluation of the hardening rule twice plus one more if it a drift correction is required, which usually does due to the small size of the yield surface. In general, a strain increment of the order of 10E-3 requires around 200 substeps, which involves more than 400-600 evaluations of the hardening rule. Conversely, a half-midpoint rule can integrate the equations exhibiting an error around 0.5% in one step and less than 10 hardenign function evaluations. The following section studies in detail the performance of all the algorithms.

3.5. ALGORITHM PERFORMANCE

In this section a set of drained and undrained triaxial test for the sand model are studied in order to benchmark the efficiency of all the algorithms. In this section the explicit or implicit integration strategy is compared carrying out an exercise similar to Chaboche and Cailletaud (1996). In this sense three cyclic triaxial tests (two undrained and one drained) of 10, 48 and 105 increments are proposed using the constrained solver described in chapter subsection 3.2.4 under very strict convergence criteria. Once the tests are run, the strain history is extracted and

used to benchmark the unconstrained algorithms, in this sense the influence of the constrains is avoided and the problem is strictly strain controlled, with no controlability problems.

3.5.1. TRIAXIAL TESTS CASES AND METHODOLOGY

Three numerical tests are investigated, one drained and two undrained tests under cyclic conditions for small and large strain increments. The exact solution of each of this tests has been obtained using a total of 10.000 substeps for both the implicit integration and 50.000 substeps and SSTOL of 10E-6 for the substepping algorithm. Both exact solutions have been compared yielding a difference in terms of stress of 10E-5 in absolute value, in this the upper bound of precision rounds a relative error of ~10E-6 for all the increments.

Table 15: Characteristics of the tests for numerical benchmarking

	Increments	Axial strain
TXU1	48 INC	1.9E-4
TXU2	[3, 3, 4] 10 INC	[5E-4, 1E-3, 5E-3]
TXD1	50 INC	Variable

To compare the precision of all solvers a constant sub-incrementation technique has been added to the implicit solvers, while the automatic sub-incrementation of the sub-stepping solver has been kept according to Sloan (1987). In this sense the increments defined in Table 15 can be integrated by the implicit solvers in smaller steps of constant size. A measure of the relative error of each test can be obtained as:

$$error_k = 100 \frac{\left\| \sigma_{ij}^{EXACT} - \sigma_{ij}^{NUM} \right\|}{\left\| \sigma_{ij}^{EXACT} \right\|} \qquad k = 1, ..., N \tag{3.129}$$

Where $error_k$ is an array and N the number of each increment, as for every increment it is possible to know the number of substeps required by the solver a measure of the precision can be stablished comparing the average number of substeps N_{av} per increment with the average relative error E_{av}. Using this methodology, it is possible to obtain a "number" that represents

the overall performance the local integration algorithms by increasing of reducing SSTOL in the substepping algorithm or by modifying the number of substeps in the implicit solvers.

Figure 106, Figure 107 and Figure 108 show a detail of the stress path of the tests used for numerical benchmark, where a detail of the increments is included. Case TXU1 and TXU2 corresponds to undrained conditions, where TXU1 has small increments and TXU2 has larger increments, the case TXD1 corresponds to a case with variable strain increments as it has been extracted from a stress controlled test.

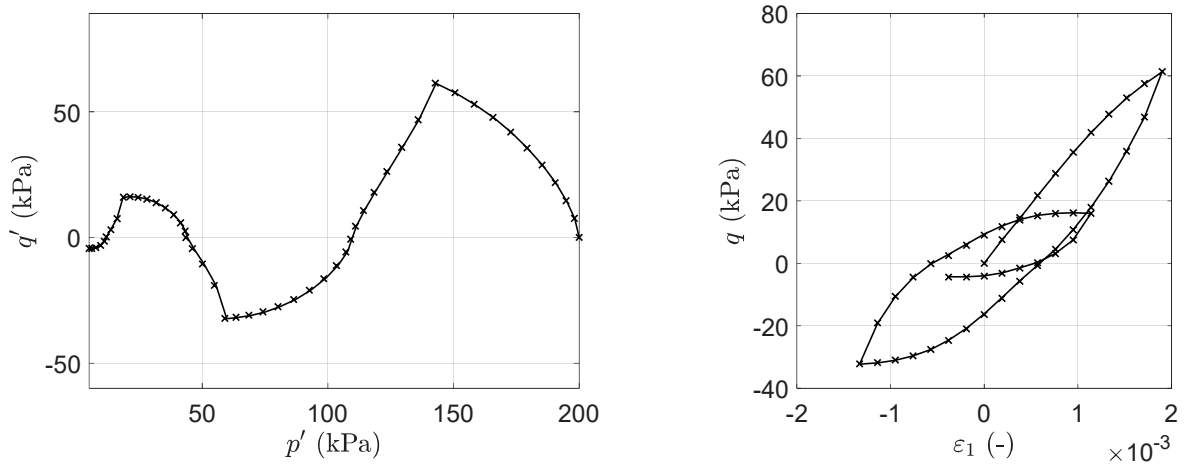


Figure 106: Undrained triaxial case for performance benchmark TXU1: small increments

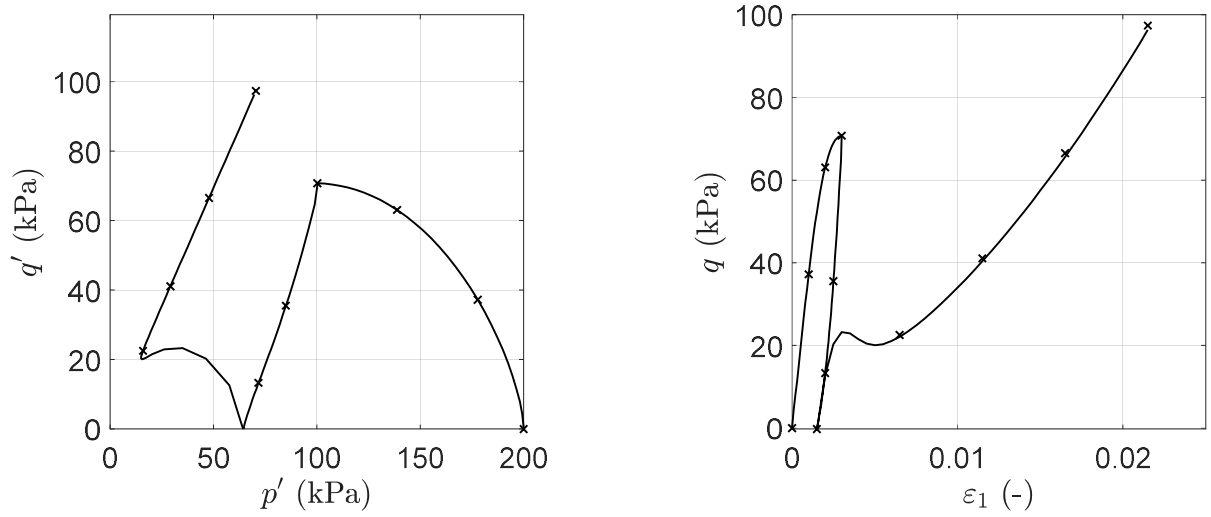


Figure 107: Undrained triaxial case for performance benchmark TXU2: Large increments

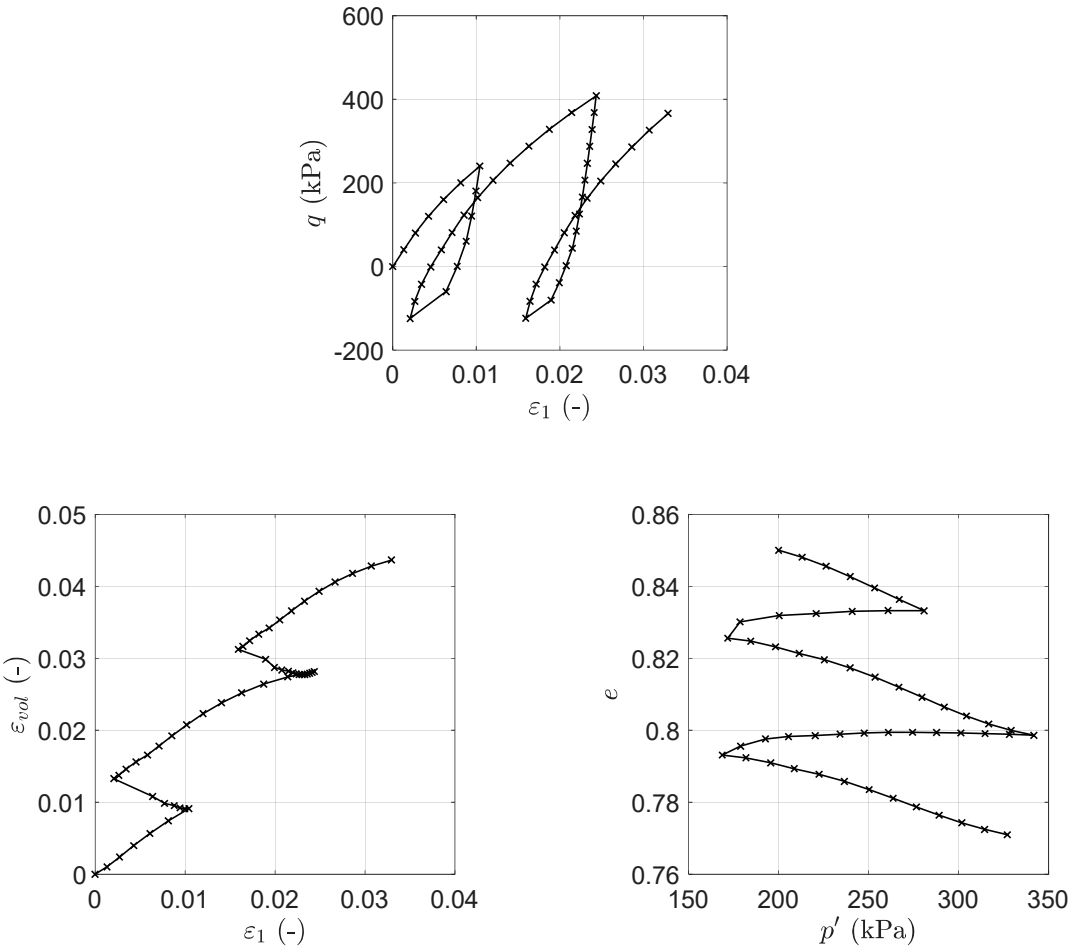


Figure 108: Drained triaxial case for performance benchmark TXD1

Figure 109, Figure 110 and Figure 111 show the results of convergence for the previous benchmark tests where the backward-Euler, half-midpoint, half trapezoidal and substepping algorithms are compared. It can be observed that for small increments (Figure 109) in the mid-low relative error range [10E-4-10E-2] the implicit integration with less than 100 substeps provides better accuracy than the substepping algorithm, however beyond that threshold the substepping algorithm improves significantly its precision with the number of average substeps. Only in the small step high error range [<1E-5] (Figure 109) the substepping provides a better performance, for the same number of average substeps.

Regarding the implicit methods it is clear that the trapezoidal (TZ1) and the half-mid-point (MID1) perform significantly better that the backward Euler due to their second order approximation. However it is interesting to note that for small increment range the order of the implitic discretisation is not very significant. A different story occurs with the numerical tets

consisting in larger increments where the second order methods exhibit a significantly better performance than the backward Euler (Figure 110), consistant with what has been observed in the iso-error maps shown in the previous sections.

For the large increment undrained triaxial (TXU2) consisting into larger increments, the performance of the second order approximations (TZ1, MID1) excels over the substepping algorithm in both the small and high error range. It can be appretiated in Figure 110 that for an strict average relative error of 1E-5 the MID1 requires of the order of 300 substeps while the SS requires beyond 2000 substeps.

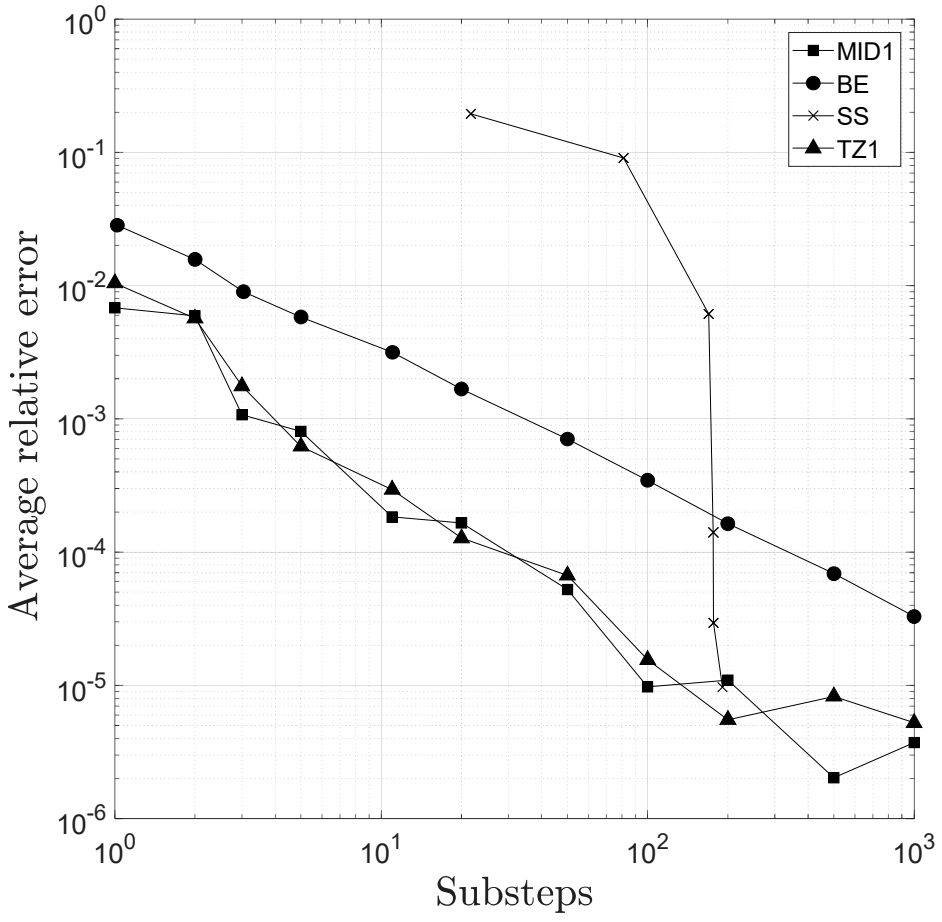


Figure 109: Convergence study for TXU1 (small increments) for basic sand

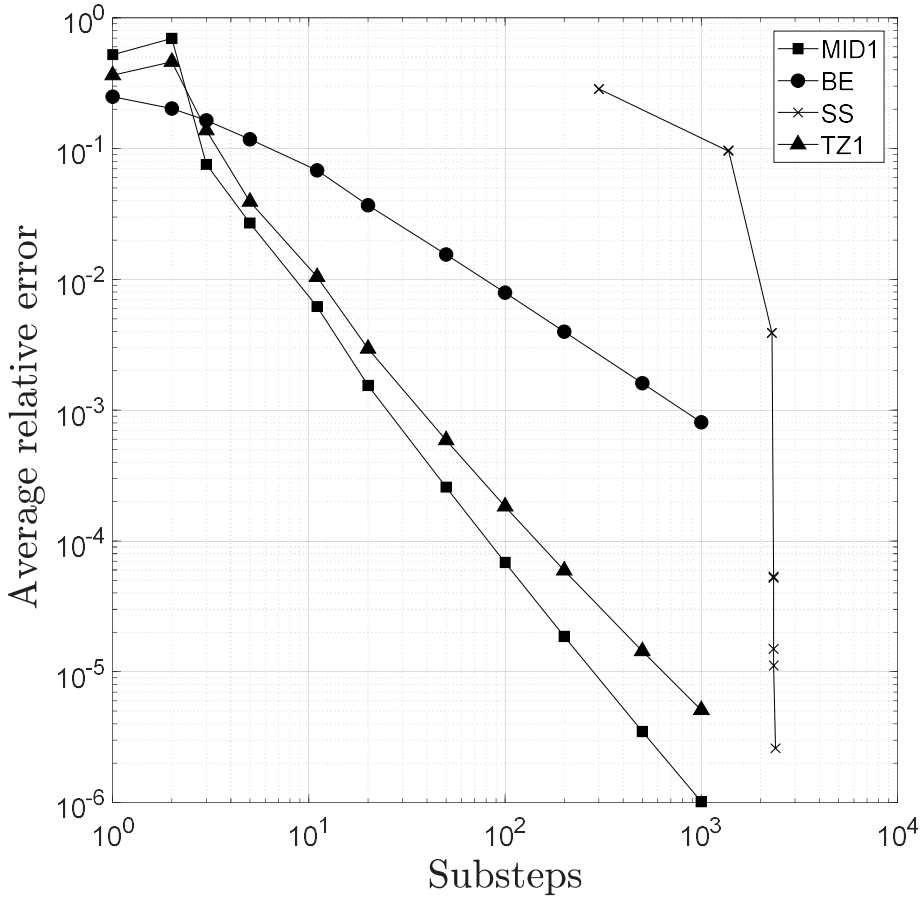


Figure 110: Convergence study for TXU2 (large increments) for basic sand

Finally, the last case (drained triaxial TXD1) covers small and large strain increments and also is helpful to see the effect of the change in the void ratio. Figure 111 shows the convergence-performance lines where again in the low error range the implicit integration (MID1) performs better than the substepping algorithm while in the high precision range the performance of the substepping and the second order discretizations is similar. It is interesting to see how the performance of the TZ1 and the MID1 discretisations converge as the substeppinng become smaller, indicating that there is a threshold (probably governed by the precision of the float type) at which their solutions do not differ, this can be observed in Figure 111 corresponding to the drained triaxial with mid size increments, where beyond 100 substeps the performance of TZ1 and MID1 become similar.

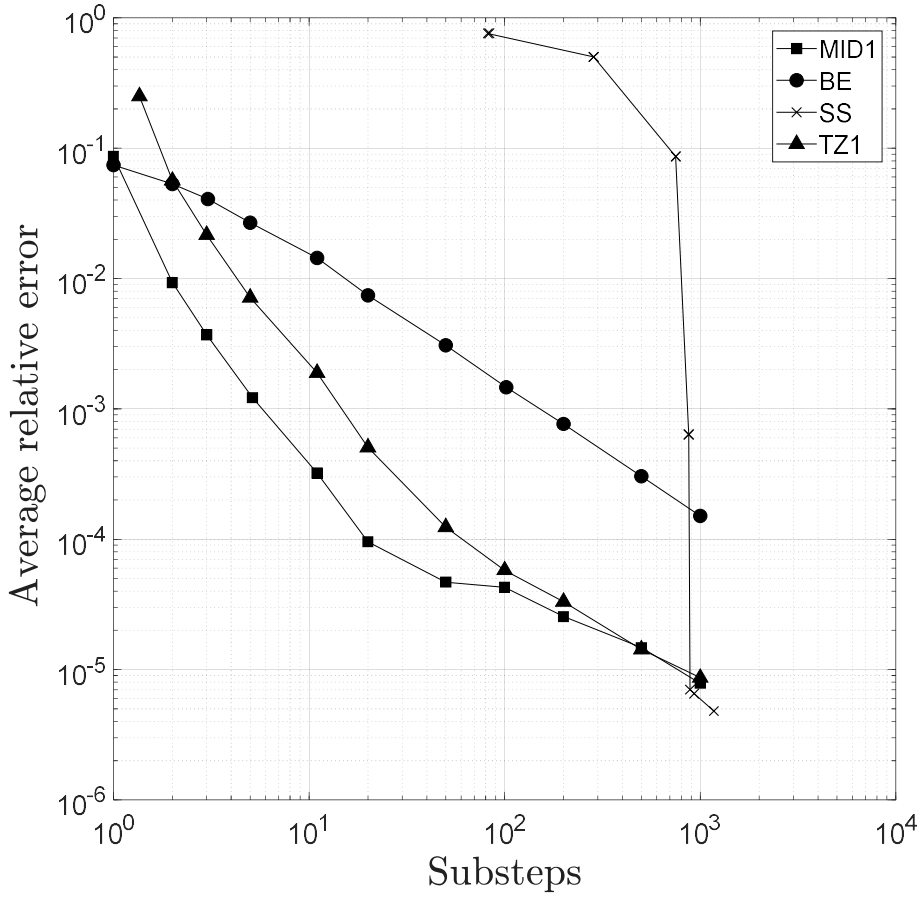


Figure 111: Convergence study for TXD1 for basic sand

In general terms, the half-midpoint is superior than the backward Euler discretisation at the same computational cost. Figure 112 and Figure 113 shows a comparison of the obtained response of the backward euler versus the midpoint under one step integration of case TXU1 where the MID1 provides practically an approximation to the exact solution below 1E-2.

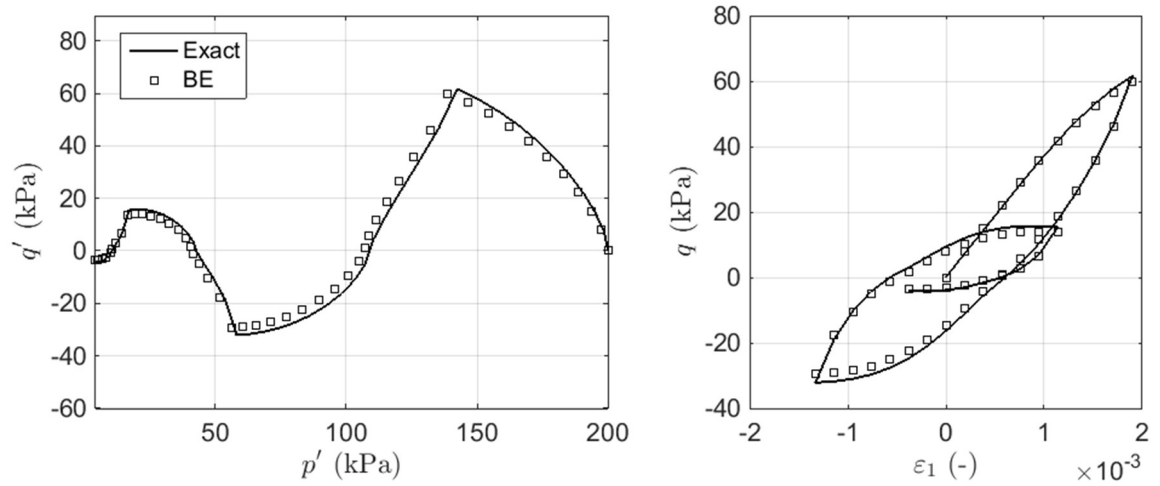


Figure 112: Comparison of "exact" solution with Backward-Euler discretisation for TXU cyclic conditions

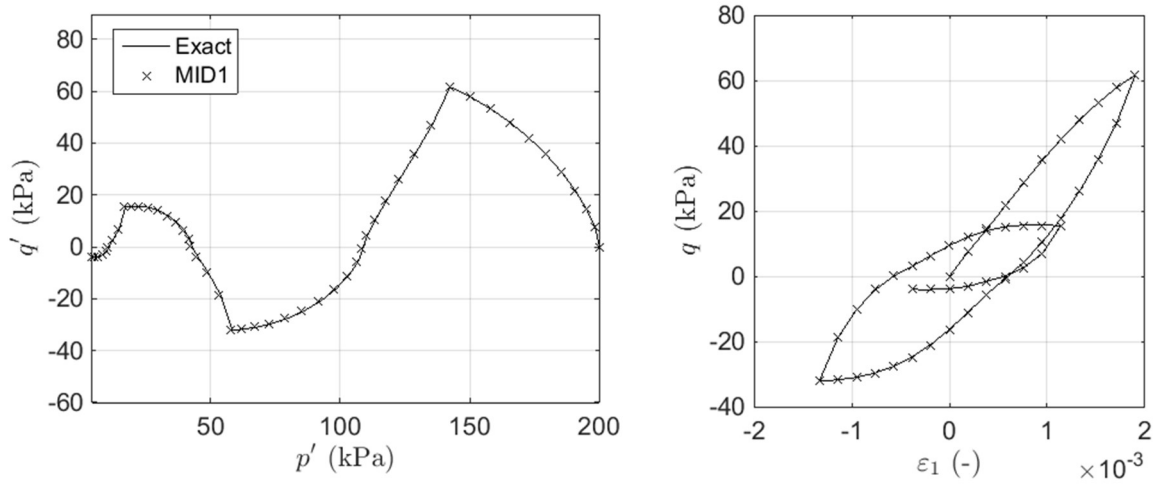


Figure 113: Comparison of "exact" solution with Half-Mid-Point discretisation for TXU cyclic conditions

In summary, it can be concluded that the substepping algorithm becomes only superior to the implicit integration when subjected to small increments as in the other cases it requires of the order of 1000 to 2000 substeps to integrate appropriately the equations. The half mid-point on the other hand provides an appropriate balance between performance and accuracy but lacks the adaptability of the optimized step subincrementation technique, requiring a fixed substep size as it cannot have an estimate during integration.

In terms of implementation, the substepping algorithm is much simpler to implement than an aug-CPPM as there are no second derivatives required, however it lacks the possibility of an algorithmic consistent tangent matrix affecting the performance of the global problem. However, in can be concluded that in the range of FEA analysis where it is acceptable a tolerance of the error around [10E-3,1E-4] the aug-CPPM exhibits a much better performance over the substepping algorithm.

3.5.2. NUMERICAL DERIVATIVES OR ANALYTICAL?

A severe overhead and a drawback of the hardening rules proposed in the previous chapter is the computation of the second derivatives of the hardening rule. This section explores if it is possible to outmanuver the tedious process of differenciation at the cost of numerical overhead. Owing the fact that the exact derivatives for the Wu and basic sand model have been obtained in subsections 3.3.2and 3.4.2 a benchmark of the numerical overhead between the exact and numerical derivatives has beed carried out. Numerical derivatives have been computed following Perez-Foguet et al. (2000a) and Perez-Foguet et al. (2000b) using a second order central difference scheme and taking the length of the perturbation to be $\sqrt[3]{eps}$ where *eps* is the machine precision, in this particular case double precision has been used.

$$\frac{\partial F_{ij}(A_{ij})}{\partial A_{kl}} = \frac{F_{ij}(A_{ij} + h\vec{X}_{kl}) - F_{ij}(A_{ij} - h\vec{X}_{kl})}{2h} + E_{ijkl}(h^2) \tag{3.130}$$

Where

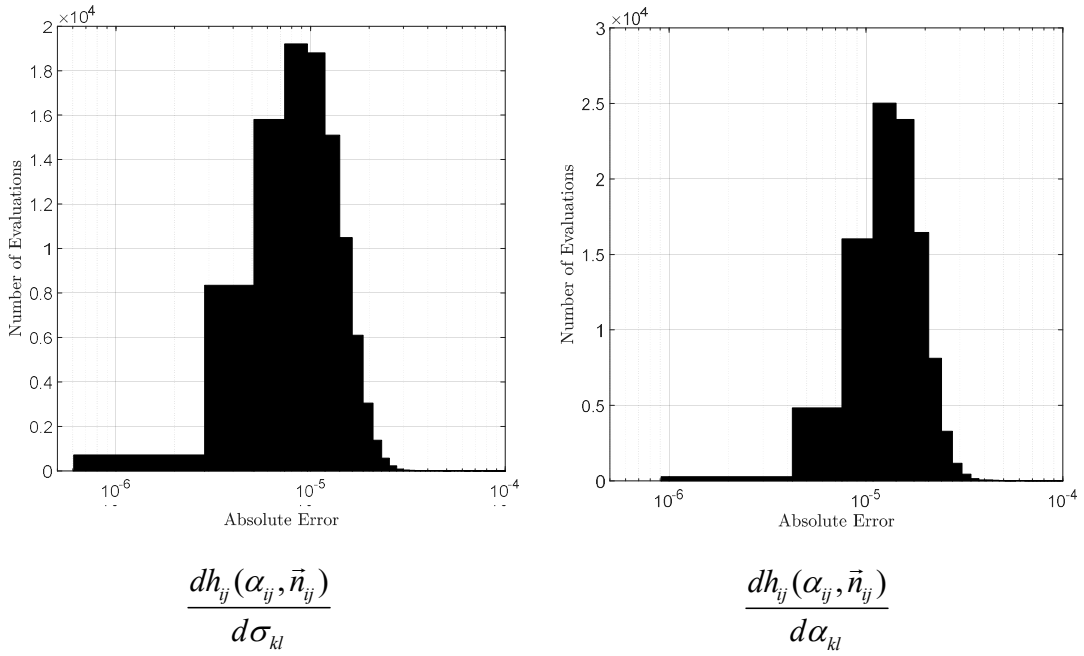
$$h = \sqrt[3]{eps} \tag{3.131}$$

Thanks to the symmetry of the stress, strain and backstress to compute the numerical derivative the hardening function has to be evaluated 12 times.

Wu Model

To evaluate the accuracy of the numerical derivative a numerical benchmark has been performed involving 10^6 random evaluations. The values of σ_{ij} and α_{ij} are based on a uniform distribution from [-500 -1] for the diagonal terms $(\sigma_{xx}, \sigma_{yy}, \sigma_{zz})$ and from [-250 +250] for the non-diagonal terms $(\sigma_{xy}, \sigma_{xz}, \sigma_{yz})$. Figure 114 shows the obtained distribution of absolute error for the 10^6 cases.

$$AbsError = \sqrt{\left(\frac{dh_{ij}^{NUM}(\alpha_{ij},\vec{n}_{ij})}{d\sigma_{kl}} - \frac{dh_{ij}(\alpha_{ij},\vec{n}_{ij})}{d\sigma_{kl}}\right)\left(\frac{dh_{ij}^{NUM}(\alpha_{ij},\vec{n}_{ij})}{d\sigma_{kl}} - \frac{dh_{ij}(\alpha_{ij},\vec{n}_{ij})}{d\sigma_{kl}}\right)} \quad (3.132)$$



$$\frac{dh_{ij}(\alpha_{ij},\vec{n}_{ij})}{d\sigma_{kl}} \qquad \frac{dh_{ij}(\alpha_{ij},\vec{n}_{ij})}{d\alpha_{kl}}$$

Figure 114: Benchmark of analytical and numerical derivatives for encapsulated Wu model

Results show that with a central difference scheme the absolute error is mainly grouped around 10^{-5} with and upper limit of 0.5 10^{-5}.

Basic sand model

To evaluate the accuracy of the numerical derivative a numerical benchmark has been performed involving 10^6 random evaluations. The values of σ_{ij} and α_{ij} are based on a uniform distribution from [-500 -1] for the diagonal terms ($\sigma_{xx}, \sigma_{yy}\sigma_{zz}$) and from [-250 +250] for the nondiagonal terms ($\sigma_{xy}, \sigma_{xz}\sigma_{yz}$), the void ratio ranges from 0.6 to 1.2. Figure 114 shows the obtained distribution of absolute error and relative errors for the 10^6 cases for $\frac{dh_{ij}(\alpha_{ij},\vec{n}_{ij})}{d\alpha_{kl}}$ of the sand model.

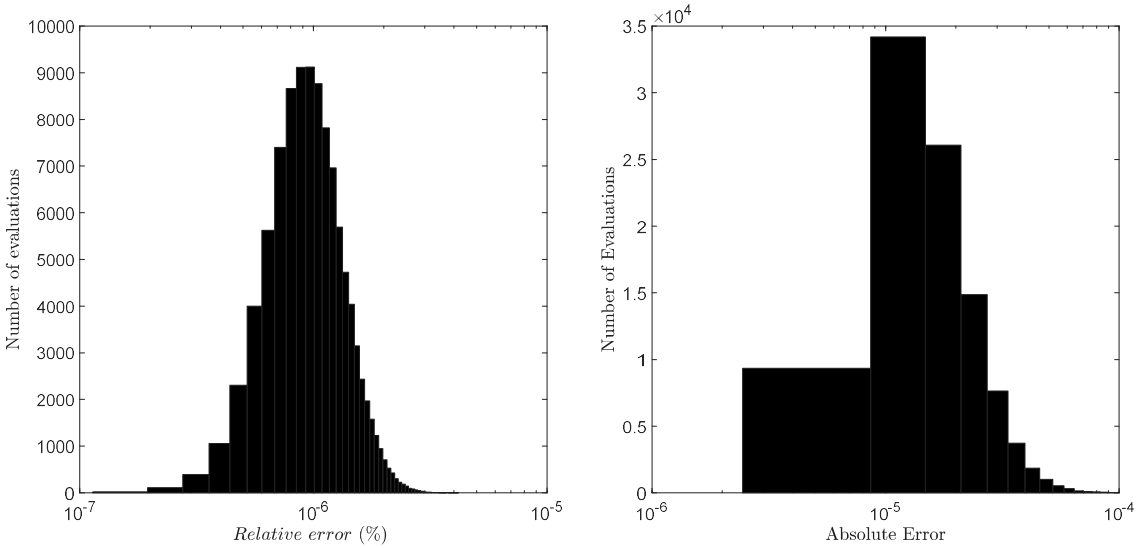


Figure 115: Benchmark of analytical and numerical derivatives for basic sand rule

Again for the domain of study, the error between the analytical and numerical derivative when using a central difference scheme is very small, no significant difference in the number of iterations or the precision has been found when running cases using the analytical or the numerical derivative. In terms of precision the numerical derivative yields practically the exact value, the only disadvantage of the numerical derivative is that they imply a heavy overhead of hardening function evaluations, 12 per derivative, 24 per iteration. Conversely, the analytical derivatives will require only one fucntion call, however, as models increase in complexity some

derivatives require the use of eigendecomposition and a large number of auxiliary routines to call, therefore the method to compute the derivatives will depend on the programming style and the libraries used for their computation.

3.5.3. COMPUTATIONAL EFFICIENCY

It can observed from Figure 109 that the quality of integration of the MID1 with one step is equivalent to the quality of integration of the SS for SSTOL = 1E-3 for that test. Wing that both algorithms provide the same response in terms of precision performance, it provides an opprotunity to asses computations performance. This section compares the computational cost of implicit versus the explicit strategy, in particular looking at the number of times that the hardening function needs to be evaluated. Three cases are evaluated, substepping, aug-CPPM-MID1 using exact second derivatives and aug-CPPM-MID1 with numerical derivatives. Figure 116 shows the ouput of explicit and implicit stress path, where it can be appreciated that the quality of the integration is very similar.

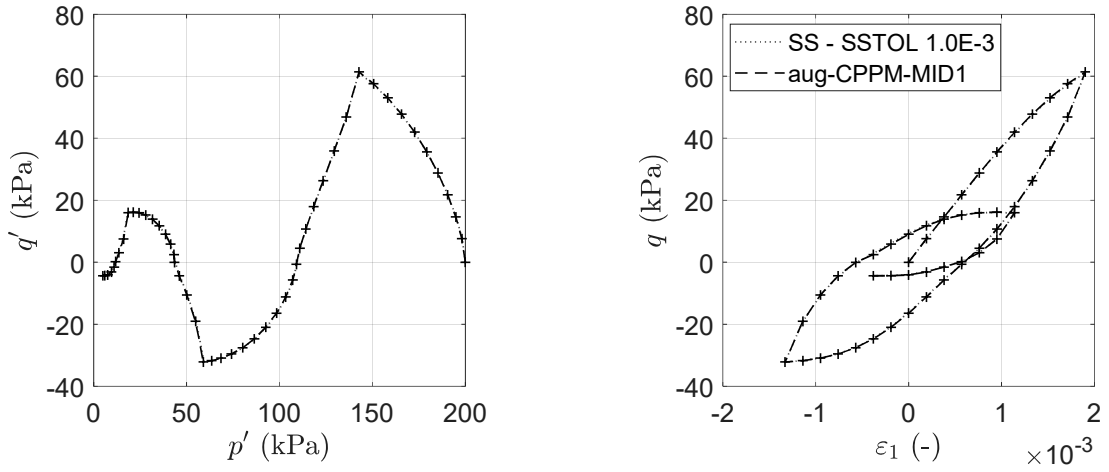


Figure 116: Same quality of integration for MID1 in one step and SS under SSTOL = 10-3. Relative average error of exact solution SS = 6.1E-3 MID1 = 6.8E-3

The results of the benchmark are presented in Table 16 showing that even using numerical derivatives, which reduces significantly the implementation difficulty, the half midpoint

MID1-aug-CPPM implicit strategy is superior to the substepping algorithm of Sloan (1987). This is due to the second order precision of the MID1 discretisation which combined with a reduction of the number of unknows combined with the efficiency of the aug-CPPM provides an excellent combination of features. In overall the algorithm is efficient, precise and globally convergent, and can accept implementations without the need of computing second derivatives.

Table 16: Numerical output of cyclic TXU

	INC	**Substeps**	**Iterations/Drift**	**Jacobian evals**	**Hardening func. evals**	**CPU Ratio with SS**
SS	48	8135	12737		29007	-
MID1-aug-CPPM	48	48	151	151	199	51.8
MID1-aug-CPPM (num. derivatives)	48	48	151	0		16.8

3.6. SUMARY OF CHAPTER

In this chapter it has been shown and extensive study of various integration strategies of the local problem at gauss point level for the type of rate equations described in chapter 2.

- Two NLKH models have been studied: an encapsulated version of the Wu model and the basic sand model proposed in chapter 2
- Implicit and explicit strategies have been benchmarked regarding precision, stability and computationl performance.
- The precision of three implicit discretization have been benchmarked under one step conditions in a wide range of strain directions
- Four algorithms to solve the implit set of equations have been studied, a standard CPPM, two globally convergent CPPM and a commercial trust region solver, on the other hand for the explicit integration strategy only the subbstepping algorithm is studied;
- The rate of convergence of the distinc algorithms is shown for large strain excursions

- The accuracy-computational performance of the algorithms has been studied for three cyclic tests where the MID1 aug-CPPM has shown the best performance for this type of equations.
- The effect in terms of precision and computational overhead of the exact derivatives and the numerical derivatives has also been described.

CHAPTER 4: MODEL EXTENSIONS, EVALUATION, AND IMPLEMENTATION

This chapter focuses on the evaluation of the proposed modelling framework and on its possible extensions, whether using superposition of specialised hardening rules or numerical artifices. The structure of the chapter covers firstly, extensions regarding specialised hardening rules that can be superposed with the basic hardenign rules described in chapter 2. Secondly, it provides a description of the calibration methodology for the sand model and the response is benchmarked for a extended soil test database (Wichtmann and Triantafyllidis, 2016a, Wichtmann and Triantafyllidis, 2016b). Finally, the last section covers numerical artifices on the proposed models to include practical FE modelling aspects such as safety factor analysis and Jump-in-Cycles methods.

4.1. SPECIALISED HARDENING RULES

The use of one backstress may be limiting if advanced aspects of soil behaviour, such as ratcheting or shakedown, need to be captured. As discussed in chapter 2, a single hardening rule is prone to produce excessive ratcheting when subjected under non-symmetric stress cycles. When using only one hardening rule, without extra hardening variables, a choice needs to be made: or either asymptotic behaviour or full-shakedown since both mechanisms require opposite strategies in the formulation of the recall terms. To improve the ratcheting response of the model under cyclic conditions and maintain its asymptotic properties, the typical strategy is to create hardening laws specialised that vanish at large straining conditions where the basic hardenign law is recovered.

This idea is not anew, for example, hypoplasticity uses the intergranular strain concept, which aside from the physical interpretation and from a purely material modelling perspective, uses a strain history variable that creates a limit strain region where the hardenign rule is linear. This is achieved by enforcing a penalty term in the recall term when the strain history variable lies within the defined surface. As a result, the model acts differently for small amplitudes and large amplitudes, improving ratchetting without sacrificing asymptotic properties. A second strategy, more common when modelling rubbers and metals, is the use of the principle of backstress

superposition (Chaboche, 1991) to improve the prediction of ratchetting. However, their calibration becomes more complex, normally requiring simple computer programs and solution of non-linear equations to predetermine the inputs.

The following section makes a compromise between both strategies, proposing a set of extra hardening rules and history variables that complement the basic hardening rules. In this sense, the superposition of backstress is used but with simpler hardening rules that vanish after sufficient straining. To help guiding the reader through this section, all the hardening rules detailed follow the same structure. Firstly, the drawbacks of the main hardening rule are presented, then the proposed extra rules are formulated and finally examples of its effects are illustrated.

4.1.1. DENSIFICATION HARDENING RULE

The current basic sand model accounts for the soil compressibility as a function of its stress state and void ratio. Under cyclic load conditions the term governing the ratcheting or stress relaxation corresponds only to the non-linear recall term. Therefore, the basic models will produce ratcheting dependent only on the direction of the goal function and the magnitude of the limit function, both dependent on the current backstress and void ratio. As a result, a single rule is prone to produce excessive ratchetting under stress cycles in the volumetric direction, as the trace of the goal function is only zero at critical state conditions. Also, the model will not take into account memory effects or any dependency with the strain rate direction. The inclusion of the specialised rule aims to correct this deficiency of the main hardening rule in oedometric and isotropic conditions.

One of the advantages of this framework is that it has associated behaviour. As a result, the normal of the yield surface will always share the principal directions of the total strain rate. Therefore, it is possible to include auxiliary hardening rules that are activated when certain conditions of the normal of the yield surface are verified. The hardening rules borrows the idea from Delobelle et al. (1995), and therefore can include a dependency of the soil response on the strain rate direction.

As it has been discussed, a unique hardening rule will produce excess ratchetting, additionally, as the asymptotic states are not bounded in the p' space, the correct concavity of the stress-strain loop cannot be appropriately captured with only one rule (Lemaitre and Chaboche, 1994). To improve this response, a second backstress has been included whose initial state is at zero mean stress and is bounded by the first backstress. The extra hardening rule is named "densification rule" and uses a non-invertible mapping tensor defined by the volumetric projector of the principal backstress mapping tensor, which is

$$P^{V}_{ijkl} = \frac{1}{3}\delta_{ij}\delta_{kl} + \hat{\alpha}^{*(1)}_{ij}\delta_{kl} \tag{4.1}$$

The fundamental hardening rule plus the specialised one can be described with the following set of equations:

$$\begin{aligned}
&L^{(1)}_{ijkl} = f_e f_p (1 + aSg(\vec{n}_{kk}) + a) S_f \left(\frac{1}{3}\delta_{ij}\delta_{kl} + \hat{\alpha}^{*(1)}_{ij}\delta_{kl} \right) + f_e f_p S_d \left(\delta_{ik}\delta_{jl} - \frac{1}{3}\delta_{ij}\delta_{kl} - \hat{\alpha}^{*(1)}_{ij}\delta_{kl} \right) \\
&\dot{\alpha}^{(1)}_{kk} = \lambda h_{ij} = C^{(1)} f_e f_b L^{(1)}_{ijkl} \left(\vec{n}_{kl} - \rho^{H} f_d \tilde{\vec{Y}} \vec{\Upsilon}_{kl} \right) \\
&\dot{\alpha}^{(2)}_{ij} = C^{(2)} \left(\frac{1}{3}\delta_{ij} + \hat{\alpha}^{*(1)}_{ij} \right) A(\vec{n}_{ij}, \alpha^{(1)}_{ij}) f_e f_p \left(\dot{\varepsilon}_{kk} - Sg(2r_\alpha - 1)\left|2r_\alpha - 1\right|^{g^{(2)}} \left|\dot{\varepsilon}_{kk}\right| \right) \\
&r_\alpha = \beta^{(2)} \frac{\left|\alpha^{(2)}_{kk}\right|}{\left|\alpha^{(1)}_{kk}\right|} \\
&\rho = (1 - r_\alpha) \\
&A(\vec{n}_{ij}, \alpha^{(1)}_{ij}) = R^{UR} H(\vec{n}_{kk} - ob^{\min(2)}) H(Y^{(1)} - Y^{\min(2)}) \\
&R^{UR} = \begin{cases} R^{UR} & \vec{n}_{kk} \le 0 \\ 1 & \vec{n}_{kk} > 0 \end{cases}
\end{aligned} \tag{4.2}$$

It must be noted that the first backstress acts as a history variable mirroring the second backstress, corresponding to the maximum mean stress to which the sand has been subjected. Under monotonic conditions when the material experiences negative volumetric strain the second backstress eventually will tend to a mean stress of 0.0, becoming inactive and the model will recover the basic hardening rule. The first and second backstress share the same principal direction, therefore the second backstress will always mirror the rate of the first backstress and vanish when $r_\alpha = 0$ or $r_\alpha = 1$ depending on whether the path is loading or unloading.

The function $A(\vec{n}_{ij}, \alpha_{ij}^{(1)})$ acts as a switch that can either disable or activate the second hardening rule depending, on the stress ratio and the obliquity of the plastic strain rate. A penalty term ρ^H is applied to the recall term of the basic rule in order to avoid excessive stress relaxation in the deviatoric plane. To illustrate the effect of this specialised hardening rule, a set of cyclic isotropic compression and oedometric tests has been simulated, where the effect of the different input parameters is shown and discussed.

Table 17: Parametric study of specialized densification rule

Main rule	e_{c0}	e_{d0}	h_s	**n**	α	β	**XV**	**YF**	**ZF**	θ	S_f	ob_{max}	δ	Y_{min}
(a)	1.05	0.65	4E5	0.45	0.24	2.0	0.74	0.0	0.1	0.7	5.0	1.0	1.35	0.1
Second rule	$C^{(2)}$	a	$\beta^{(2)}$	$\vartheta^{(2)}$	R_{ur}	H								
(b)	5.0	0.3	1.0	1.0	1.0	4.0								
(c)	5.0	0.3	1.0	3.0	1.0	4.0								
(d)	5.0	0.3	1.0	1.0	0.5	4.0								
(e)	5.0	0.11	0.8	1.0	1.0	4.0								

Figure 16 shows a set of cyclic isotropic tests for the model inputs described in Table 17.

Case (a), Figure 117 and Figure 118:

No specialised rule applied

Case (b), Figure 117 and Figure 119: Constant ratcheting:

Upon unloading (when active) the principal direction of the volumetric projector takes all its stiffness from the densification rule, which in this case has a higher stiffness. As a result, during a stress cycle the backstress of the first rule does not move, and the stress cycle is absorbed by the second backstress. As the second backstress has the form of the Amstrong-Frederick rule, the result is the simulation of constant ratcheting.

Case (c), Figure 117 and Figure 120: Constant ratcheting, smaller concavity of the loop:

Same as case (b), but the limit function has a different curvature, analogous to Ohno-Wang family of models (Ohno, 1990). The exponent forces the stress path to be more linear away

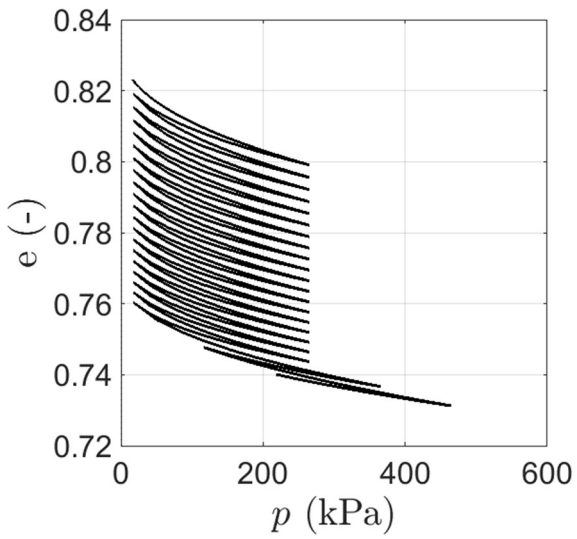
from the limit value and therefore the loops are less open, with lesser energy dissipation over each cycle.

Case (d), Figure 117 and Figure 121: Ratcheting decrease until residual ratcheting:

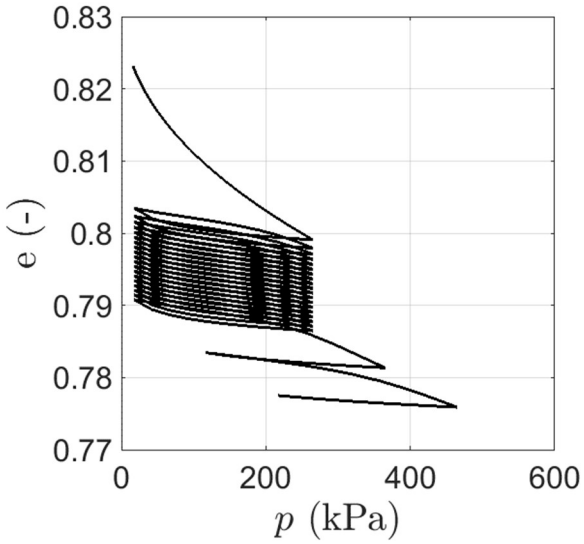
The input R_{ur} produces an imbalance in the stiffness of the second rule as a function of the sign of the obliquity of the plastic strain rate. As a result the second backstress loses its symmetry during a full cycle, enforcing the main hardening rule to accommodate a region in the backstress space where the produced ratcheting is minimum. Consequently, ratcheting is reduced progressively until both backstresses find stable regions, where the ratcheting per cycle is constant.

Case (e), Figure 117 and Figure 122 : Full shakedown:

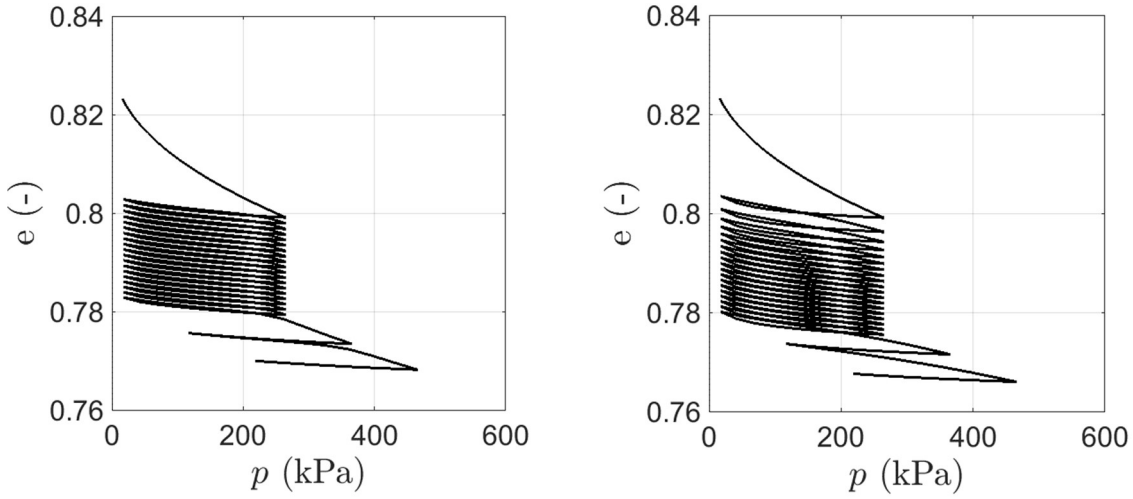
When parameter β is not 1.0, the second backstress has a smaller region where to accommodate the loop. As a result there will always exist a region where both rules will produce a symmetric stress loop, reducing ratcheting to zero and therefore exhibitng shakedown. That situation occurs naturally as the system will travel to minimum ratcheting, which in this case is zero.



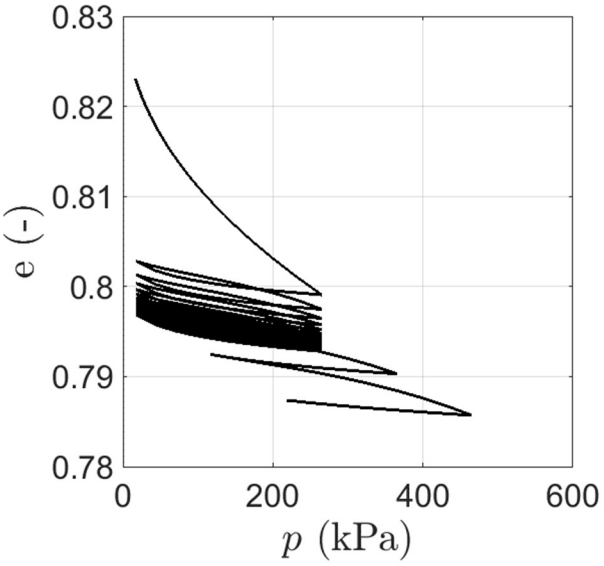
(a)



(b)



(c) (d)



(e)

Figure 117: Effect of the specialised densification rule under isotropic conditions: (a) no specialised rule, (b) constant ratcheting, (c) constant ratcheting with smaller concavity, (d) residual ratcheting and (e) full shakedown.

The following figures also show the effect of the densification rule in oedometric conditions.

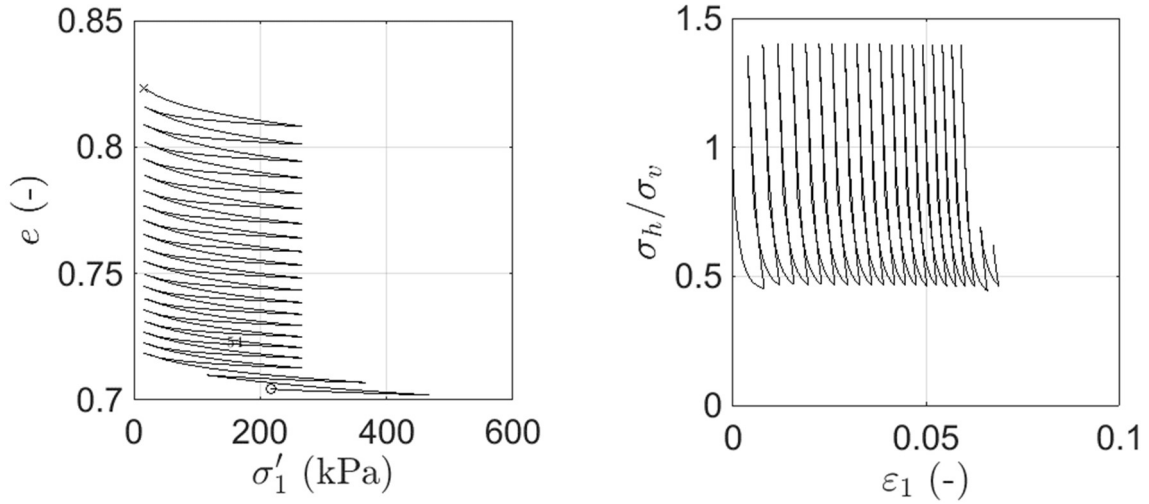


Figure 118: Effect of the specialized densification rule under oedometric conditions: (a) no specialized rule.

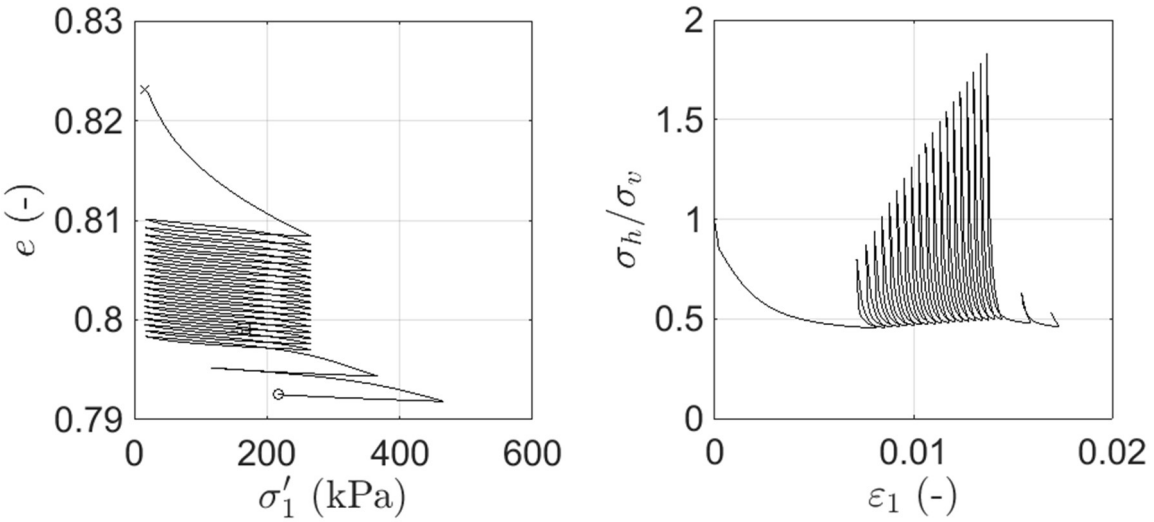


Figure 119: Effect of the specialized densification rule under oedometric conditions: (b) constant ratcheting

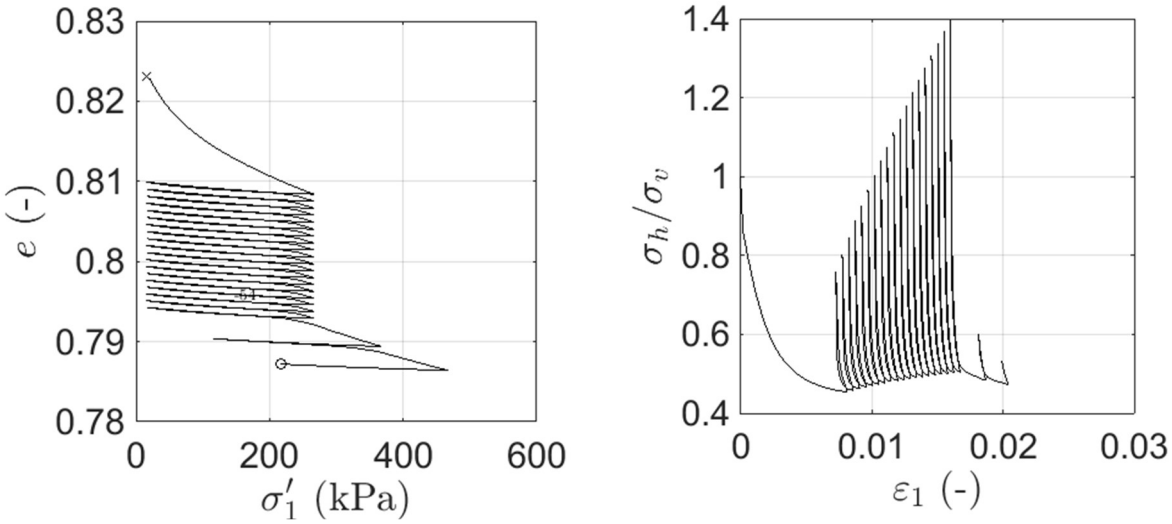


Figure 120: Effect of the specialized densification rule under oedometric conditions (c) constant ratcheting less concavity

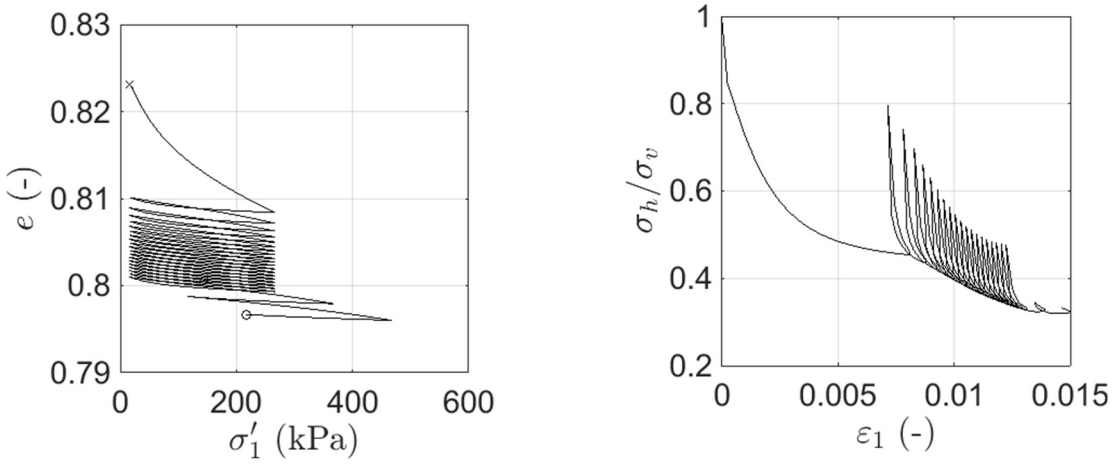


Figure 121: Effect of the specialized densification rule under oedometric conditions (d) residual ratcheting

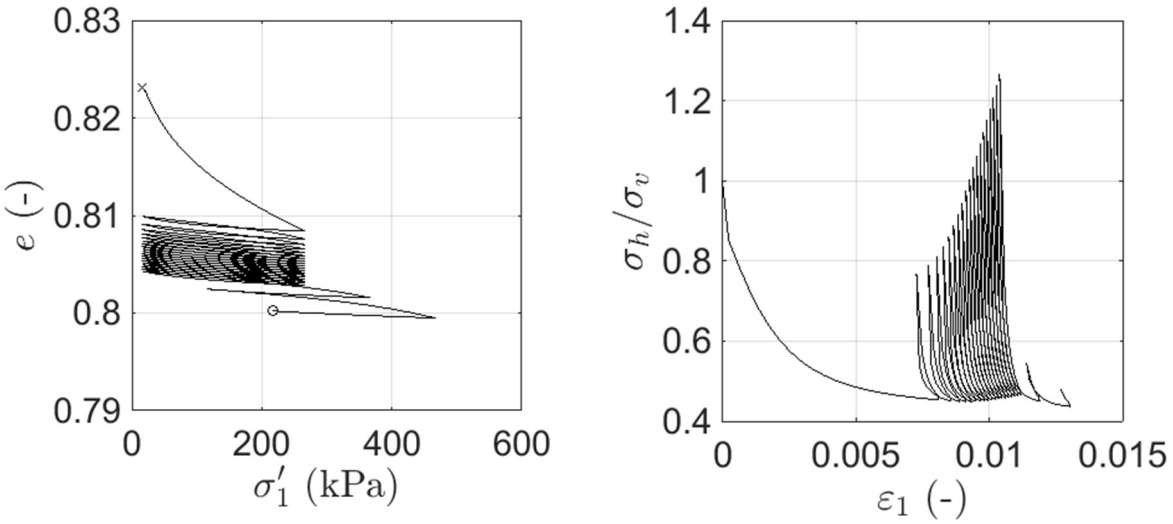


Figure 122: Effect of the specialized densification rule under oedometric conditions (e) full shakedown

4.1.1.1. Pitfalls

Care must be taken when calibrating this type of rules as while the first backstress always tends to produce densification, the second backstress produces swelling if left alone. With the combination of both rules, densification, shakedown, or residual ratcheting can be captured depending on the combination of parameters used. However, combinations of stable strain cycles must be studied, restricting combinations where the trace of the sum of both backstresses failling into swelling.

4.1.2. ENFORCED RATCHETING

As discussed in chapter 2 under a backstress perturbation, the hardening rule enforces a fraction of the plastic strain to share the direction of the goal function by a magnitude that depends on the limit surface and the direction of the backstress perturbation. Therefore, upon closed stress cycles, the goal function will control the direction at which ratcheting is accumulated. Conversely, upon a closed cycle of strain the backstress will tend to relax in the same direction (but with opposite sign) as the goal function. The limitation of the basic rule lies in the fact that the original goal and limit functions are calibrated to capture the asymptotic states under monotonic loading and not of cyclic loading. Unfortunately, that may not coincide with the direction of ratcheting seen in experiments of medium to small amplitudes (Wichtmann et al., 2014). The rule proposed below corrects this deficiency by acting on the goal function of the main hardening rule.

The new rule uses a new backstress variable that moves only in the deviatoric plane, bounded by a fraction of the limit surface of the main hardening rule. In effect, this specialised rule will borrow a fraction of the stress amplitude from the main rule thus reducing the ratcheting. Moreover, it will be used to define a stress threshold at which the goal function can be redefined locally. As a result, the ratcheting direction and magnitude can be adjusted and made dependent on the amplitude of the stress cycle. The hardening rule must be combined with the main hardening rule and can also be combined with any other specialised rule. The rule is defined as:

$$
\begin{aligned}
&\dot{\alpha}_{ij}^{(1)} = \lambda h_{ij} = C^{(1)} f_e f_b L_{ijkl}^{(1)} \left(\vec{n}_{kl} - \rho^{H(3)} f_d \tilde{Y} \vec{\Upsilon}_{kl}^{(3)} \right) \\
&\dot{\alpha}_{ij}^{*(3)} = C^{(3)} f_e f_b \left(\dot{\varepsilon}_{ij}^{p*} - \left(Y^{(3)} \right)^{g^{(3)}} \vec{\alpha}_{ij}^{(3)} \left\| \dot{\varepsilon}_{ij}^{p*} \right\| \right) \\
&Y^{(3)} = \frac{3 \left\| 0.5 \alpha_{ij}^{(3)} \right\|}{\beta_{(3)} g_{(1)}(\theta_{(1)}) \left| \alpha_{kk}^{(3)} \right|} \\
&ob_Y = (1 - Y_3^{X_3}) ob_{enf} + Y_3^{X_3} \vec{\Upsilon}_{kk}^{(1)} \\
&\vec{\Upsilon}_{kl}^{(3)} = \sqrt{1 - \frac{ob_Y^2}{3}} \frac{\alpha_{ij}^{*(1)}}{\left\| \alpha_{ij}^{*(1)} \right\|} + \frac{ob_Y}{3} \delta_{ij} \\
&\rho^{H(3)} = \left(Y^{(3)} \right)^H
\end{aligned}
\tag{4.3}
$$

where the required inputs are $C^{(3)}$, ob_{enf}, $\beta_{(3)}$, $\vartheta^{(3)}$, X_3 and H_3 controlling stiffness, enforced obliquity, limit surface, magnitude of the recall term and penalty on the first hardening rule. The next section presents a parametric study designed to illustrate the impact of various parameters (Table 18) on the behaviour obtained when simulating cyclic drained triaxial tests with large and mid-size loading amplitudes.

Table 18: Inputs for parametric study of enforced ratchetting hardening rule

Main rule	**e_{c0}**	**e_{d0}**	**h_s**	**n**	**α**	**β**	**XV**	**YF**	**ZF**	**θ**	**S_f**	**ob_{max}**	**δ**
(a)	1.05	0.65	4E5	0.45	0.24	2.0	0.74	0.0	0.1	0.7	5.0	1.0	1.35
Second rule	**$C^{(3)}$**	**$ob_{enf}^{(3)}$**	**$\beta^{(3)}$**	$\vartheta^{(3)}$	**$X^{(3)}$**	**H**							
(b)	1.0	1.0	0.2	1.0	1.0	0.0							
(c)	1.0	1.0	0.2	1.0	2.0	0.0							
(d)	2.0	1.7	0.1	0.3	3.0	0.0							
(e)	5.0	0.0	0.5	1.0	4.0	4.0							

Case (a), Figure 123:

No specialised rule, only basic sand rule.

Case (b), Figure 124:

Case (b) corresponds to a simple case where a fraction of the limit surface of the main hardening rule is borrowed from the simple rule. The weights acting on the goal function change are small and therefore only a reduction of ratcheting is seen, with little influence on the ratcheting direction.

Case (c), Figure 125:

Case (c) increases the weight acting on the redefinition of the goal function. As a consequence, a higher fraction of the stress cycle has positive obliquity, reducing drastically ratcheting in the volumetric direction as the principal rule and secondary rule cancel out.

Case (d), Figure 126:

In case (d) the stress region of the second backstress is reduced in size, but the weight acting on the redefinition of the goal function and the enforced obliquity impose a significantly higher obliquity. In that region, although smaller, the volumetric ratcheting becomes positive while the ratcheting in the deviatoric direction increases.

Case (e), Figure 127:

In case (e), a severe penalty is applied to the main hardening rule, transforming it into a practically linear rule, as long as the second backstress is not on the limit surface. Severe ratcheting reduction occurs as a consequence of the secondary rule absorbing a larger fraction of the cycle. Under these conditions the model will always produce shake-down for stress amplitudes below the limit surface defined by the secondary hardening rule.

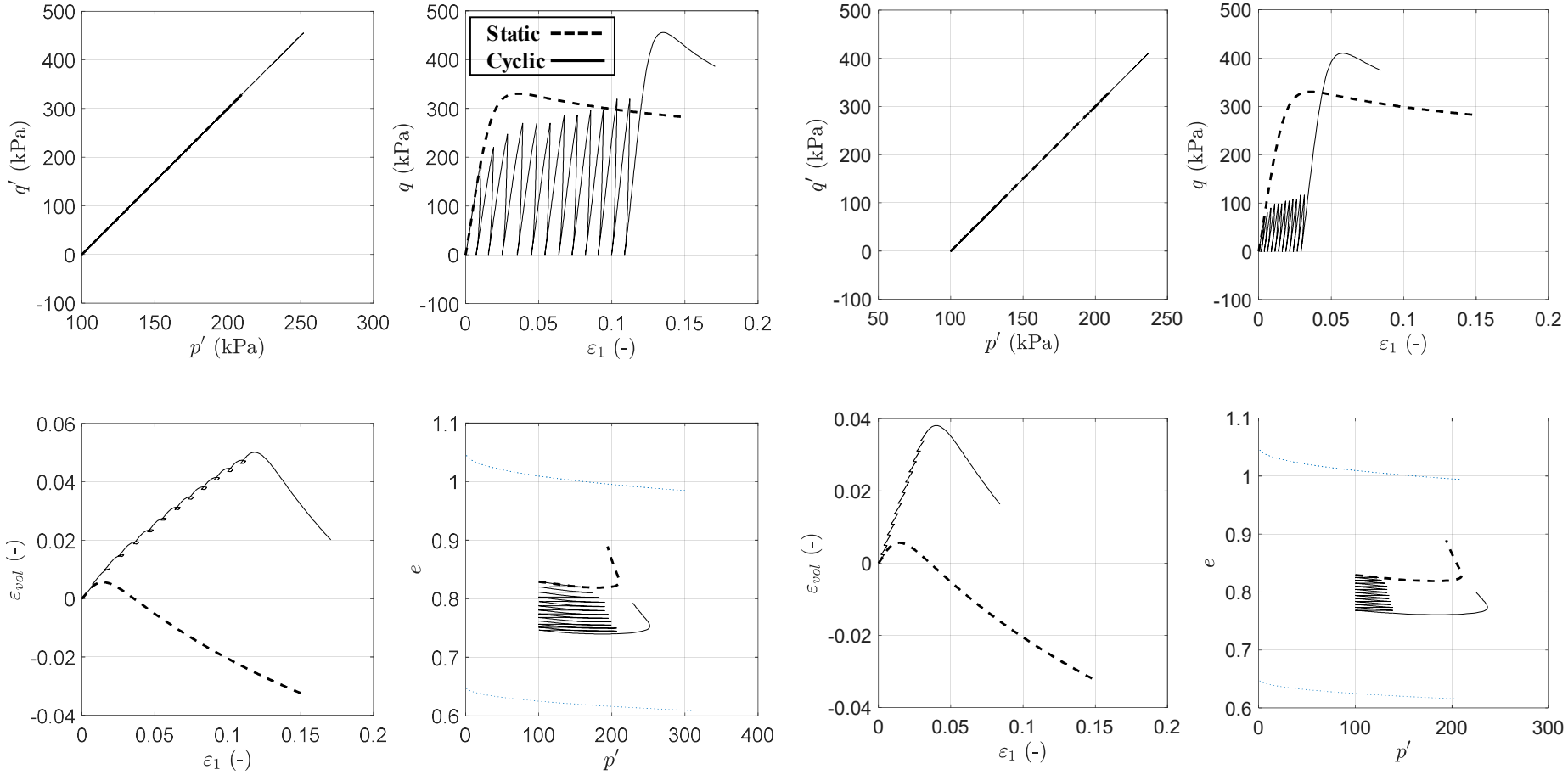


Figure 123: Case (a), basic sand model with no specialized rules, excessive ratchetting

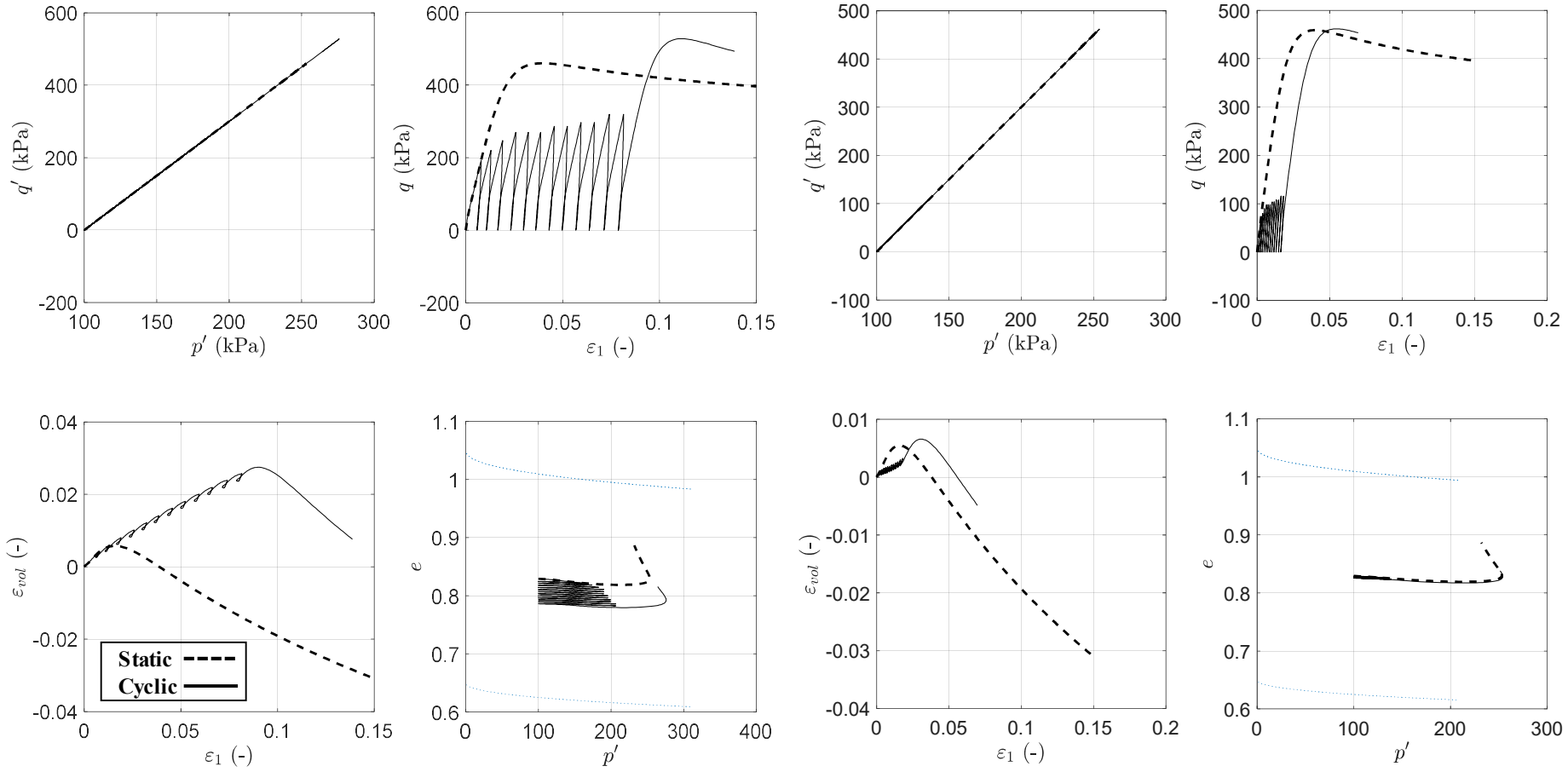


Figure 124: Case (b), simple contribution of the specialised rule, reduction of ratcheting for low amplitudes and no significant change in ratcheting direction

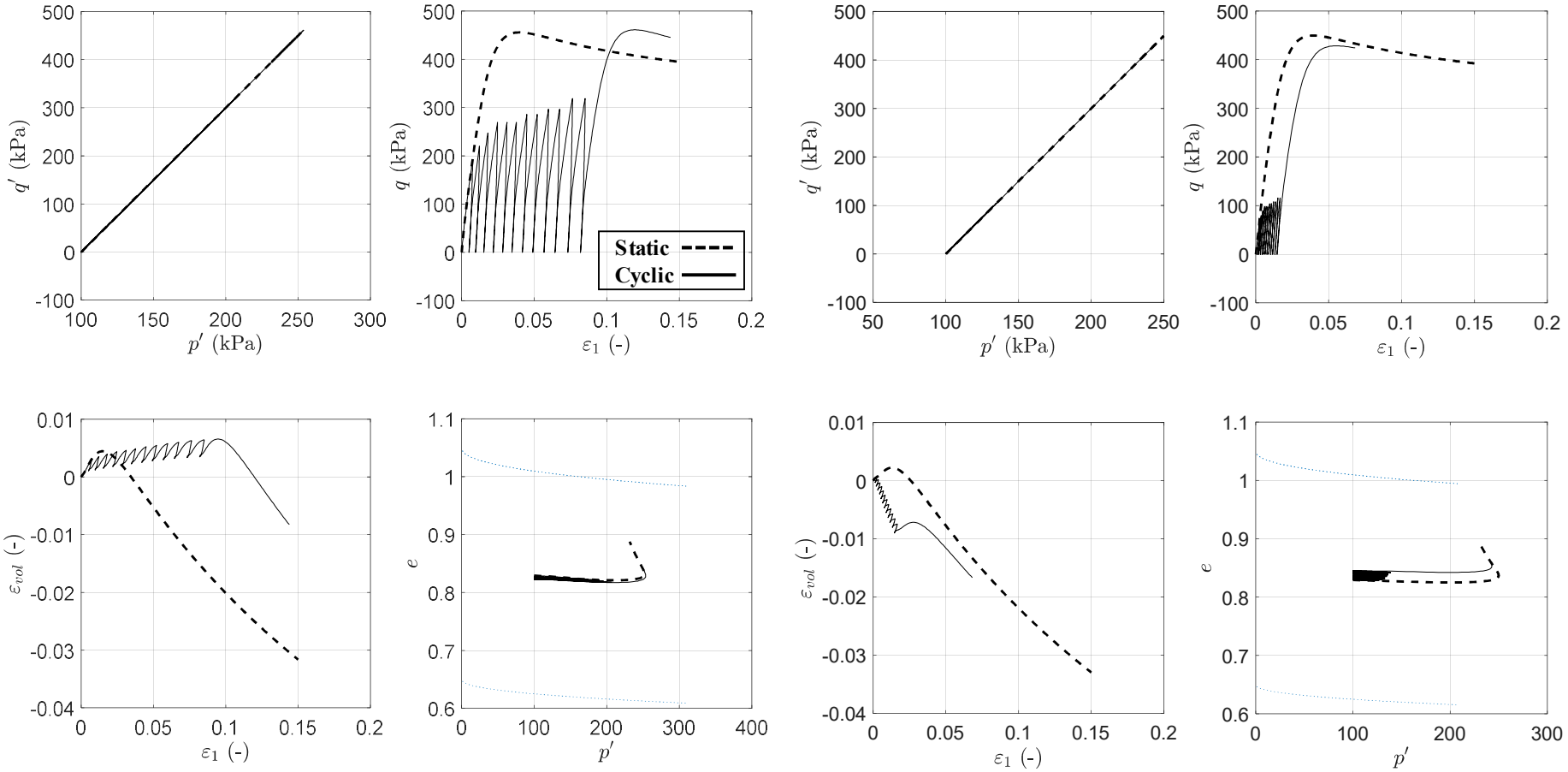


Figure 125: Case (c), reduction of ratcheting and change in ratcheting direction depending on the amplitude of the cycle

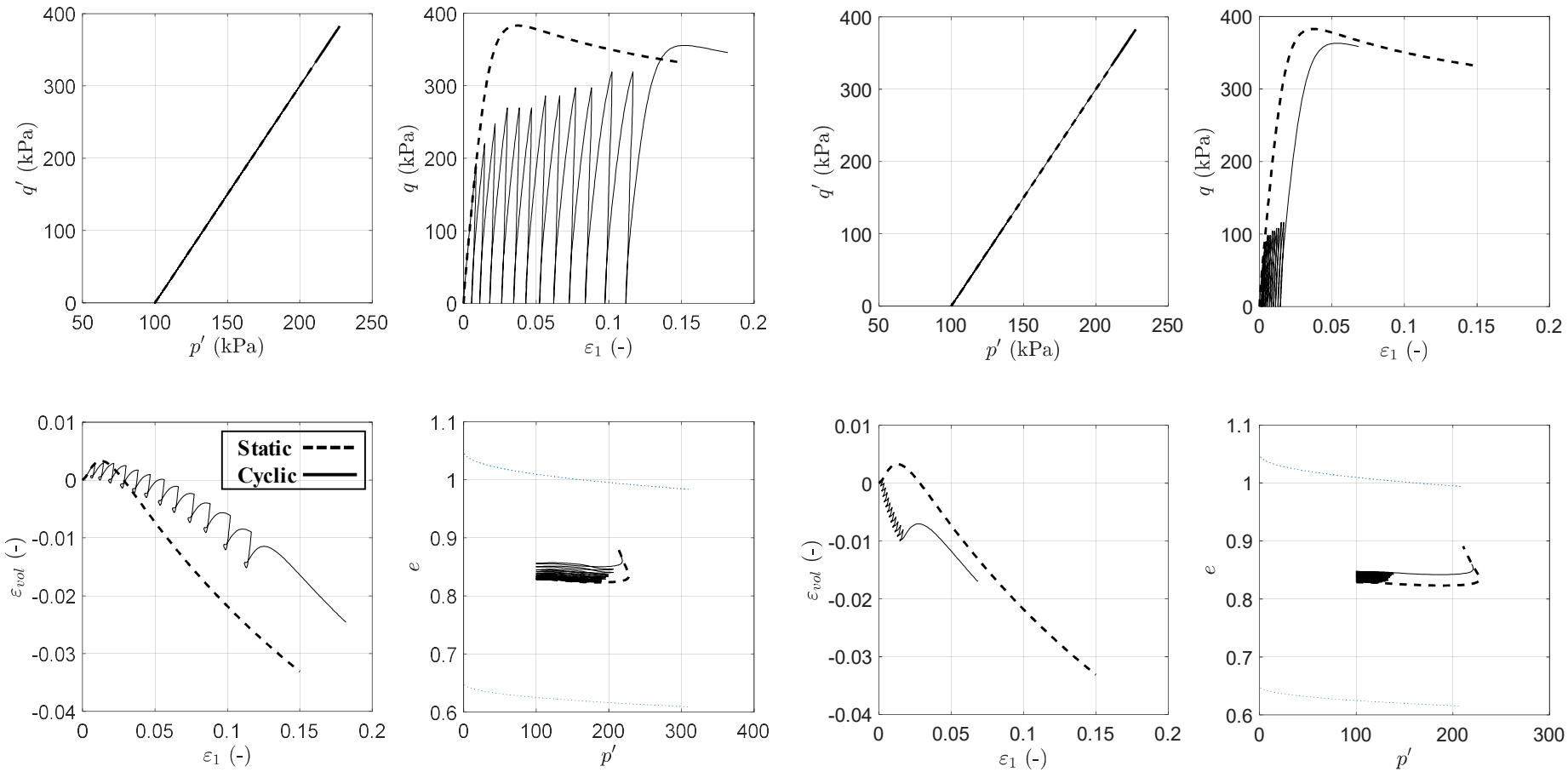


Figure 126: Case (d), smaller reduction of ratcheting but higher influence on the ratcheting direction

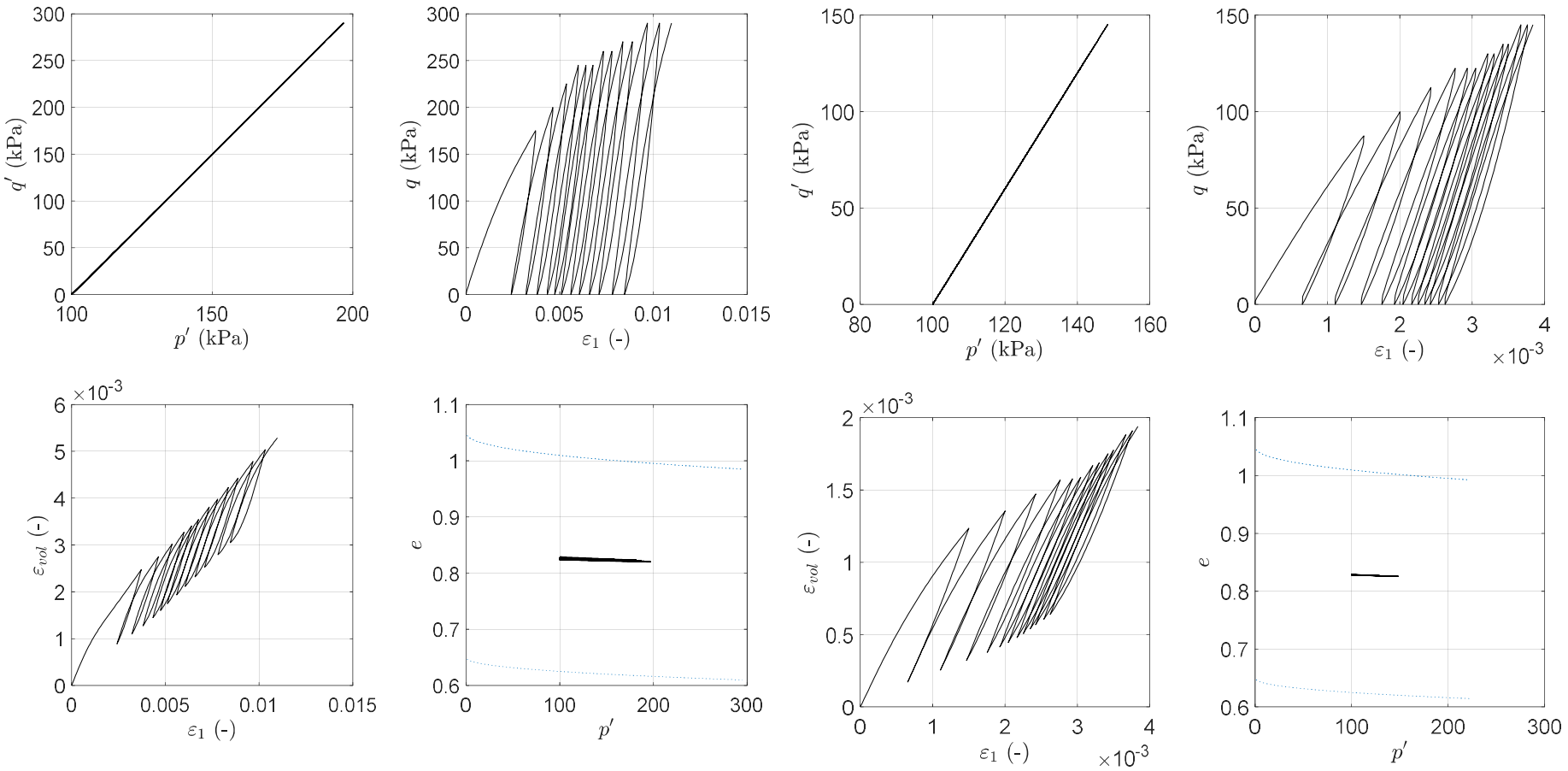


Figure 127: Case (e), residual ratcheting

The previous cases illustrate the outcomes of possible strategies in terms of modelling with the previous rule, where the system can be adjusted to such a large extent that even the creation of volumetric expansion upon cyclic loading, as in case (d), is possible. In the 11and as a result it would be practically impossible to reproduce swelling upon cyclic loading. This limitation can be overcome using this specialised hardening rule that creates a region in the stress space where the goal function is explicitly defined, while beyond that stress region the standard goal function is recovered.

4.1.3. STRAIN HISTORY SURFACE – INTERGRANULAR STRAIN

This section describes a way to include a concept similar to the intergranular strain used in hypoplasticity (Niemunis and Herle, 1997). To do so, a tensor-like variable in the strain space is defined, namely *"backstrain tensor"* or *"intergranular strain",* Σ_{ij}. The use of strain-like history variables to improve ratcheting was firstly used in the field of metals, in particular to improve the ratcheting response of the 316 stainless steel (Chaboche et al., 1979). Subsequently, Ohno (1982) generalised its formulation to create non-cyclic hardening regions.

In general, the use of a backstrain has the purpose of defining a region in the strain space where the recall term of the main hardening rule is affected. Affecting the stiffness and the response under cyclic loading. Therefore, the intergranular strain concept can be used to improve the cyclic response under small strain amplitudes.

To introduce this concept, since the *backstrain* is an internal variable, a rate evolution rule is required. The expression of Niemunis and Herle (1997) has been adopted in this work as it has been developed in the context of geo-materials and proven to reproduce appropriately soil behaviour in boundary problems (Hong et al., 2017, Heins and Grabe, 2017). The inputs required are: R, which affects the size of the strain region; M_d, M_v, affecting the stiffness of the principal directions of the mapping tensor; β_r affecting the rate of the backstrain; and X, affecting the recall term of the basic law. The rate of backstrain is defined as:

$$\dot{\Sigma}_{ij} = \begin{cases} \left(\delta_{ik}\delta_{jl} - \rho^{\beta r}\vec{\Sigma}_{ij}\vec{\Sigma}_{kl}\right)\dot{\varepsilon}^{p}_{kl} & \dot{\varepsilon}^{p}_{kl}\vec{\Sigma}_{ij} > 0 \\ \dot{\varepsilon}^{p}_{kl} & \dot{\varepsilon}^{p}_{kl}\vec{\Sigma}_{ij} < 0 \end{cases} \tag{4.4}$$

Where

$$\rho = \frac{\left\| \Sigma_{ij} \right\|}{R} \tag{4.5}$$

Expression (4.5) acts similar to a limit surface, but in the strain space. Expression (4.4) enforces the intergranular strain to be bounded by $\left\| \Sigma_{ij} \right\| = R$, while its direction will be defined by that of $\dot{\varepsilon}_{kl}^{p}$, as expression (4.4) contains a projector orthogonal to $\vec{\Sigma}_{ij}$.

Once the domain and evolution of Σ_{ij} are defined, their effect on the main hardening rule must be introduced. The two effects of the intergranular strain hardenign rule are: 1) to improve small strain behaviour under directional loading, and 2) to reduce excessive ratcheting for small amplitudes. These effects are achieved firstly by acting on the magnitude of principal directions of the mapping tensor and secondly on the magnitude of the recall term. The intergranular strain hardening rule has been adapted for the general expression and differs from that proposed in hypoplasticity (Niemunis and Herle, 1997) as it acts in the principal directions of the mapping tensor, in the present case the rule is defined as:

$$\begin{aligned} L_{ijkl}^{(1)} = {} & f_e f_p \left(S_f + M_d (1-\rho^{\chi}) \right) \left(\frac{1}{3} \delta_{ij} \delta_{kl} + \hat{\alpha}_{ij}^{*(1)} \delta_{kl} \right) + \\ & + f_e f_p \left(S_d + M_V (1-\rho^{\chi}) \right) \left(\delta_{ik} \delta_{jl} - \frac{1}{3} \delta_{ij} \delta_{kl} - \hat{\alpha}_{ij}^{*(1)} \delta_{kl} \right) \end{aligned} \tag{4.6}$$

and

$$\dot{\alpha}_{kk}^{(1)} = \lambda h_{ij} = \begin{cases} C^{(1)} f_e f_b L_{ijkl}^{(1)} \left(\vec{n}_{kl} - \rho^{\chi} f_d \tilde{Y} \vec{\Upsilon}_{kl} \right) & \Sigma_{ij} \vec{n}_{ij} > 0 \\ C^{(1)} f_e f_b L_{ijkl}^{(1)} \vec{n}_{kl} & \Sigma_{ij} \vec{n}_{ij} < 0 \end{cases} \tag{4.7}$$

The former equations illustrate how the response of the hardening rule becomes linear when a reversal occurs. Moreover, according to equation (4.7), when the backstrain history variable lies in the limit imposed by R ($\rho = 1$), the basic equations are recovered. The effect of the backstrain is illustrated in Figure 128 by comparing its prediction with a real strain-controlled undrained triaxial test (blue) described in Wichtmann and Triantafyllidis (2016b).

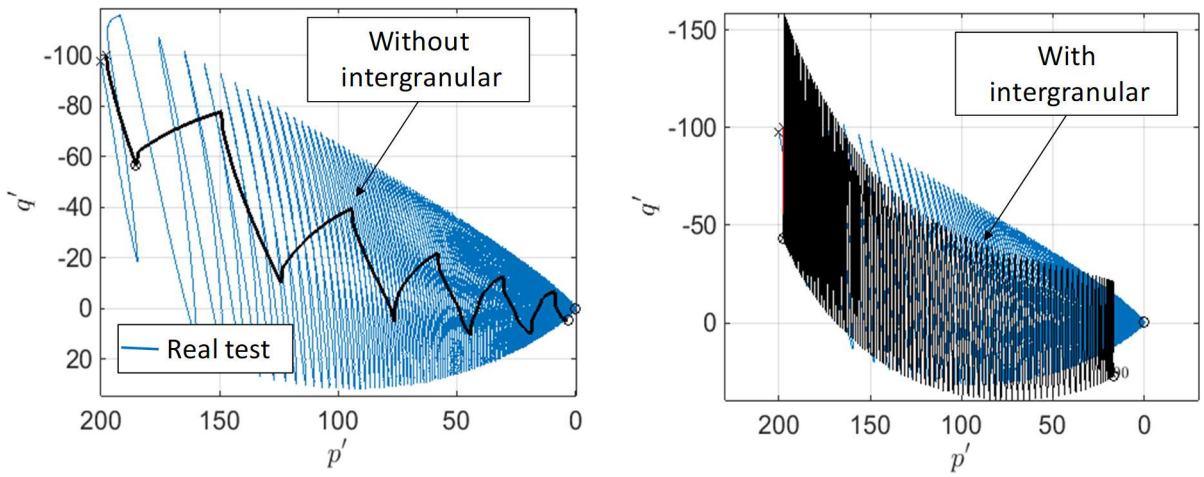


Figure 128: Numerical prediction of cyclic undrained test with and without intergranular "backstrain"

Similar to the previous section, a parametric study of a cyclic undrained triaxial tests under strain control conditions with N=50 cycles is carried out to illustrate and discuss the influence of each of the parameters, the set of parameters is shown in the following table.

Table 19: Parameters used parametric study for intergranular backstrain rule

Main	e_{c0}	e_{d0}	h_s	**n**	α	β	**XV**	**YF**	**ZF**	θ	S_f	ob_{max}	δ
(a)	1.02	0.55	4E5	0.45	0.15	1.7	0.53	0.77	0.24	0.4	3.5	1.0	2.5
Inter.	**R**	β^r	M_v	M_d	**X**								
(b)	6.0E-4	1.0	2.0	2.0	4.0								
(c)	1.2E-3	1.0	2.0	2.0	4.0								
(d)	6.0E-4	2.0	2.0	2.0	4.0								
(e)	6.0E-4	1.0	1.0	2.0	4.0								
(f)	6.0E-4	1.0	2.0	2.0	2.0								

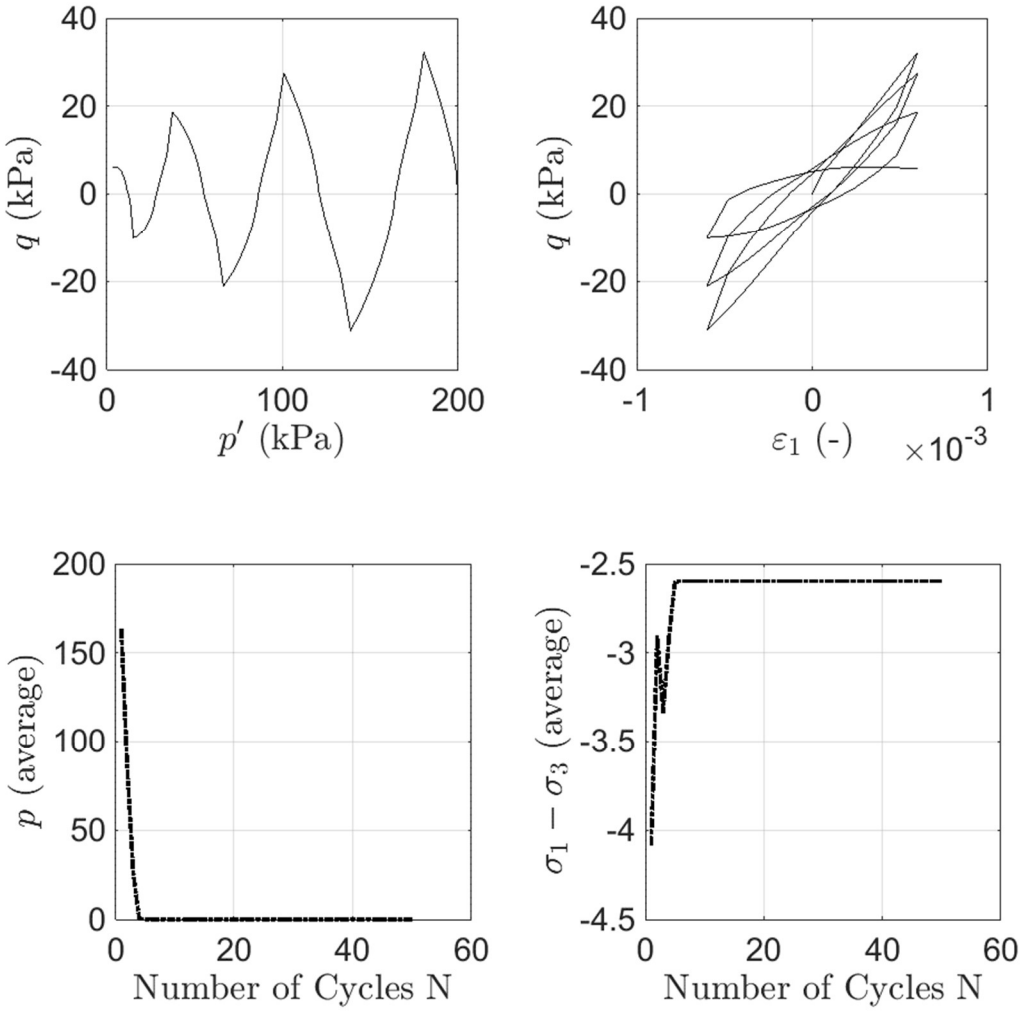
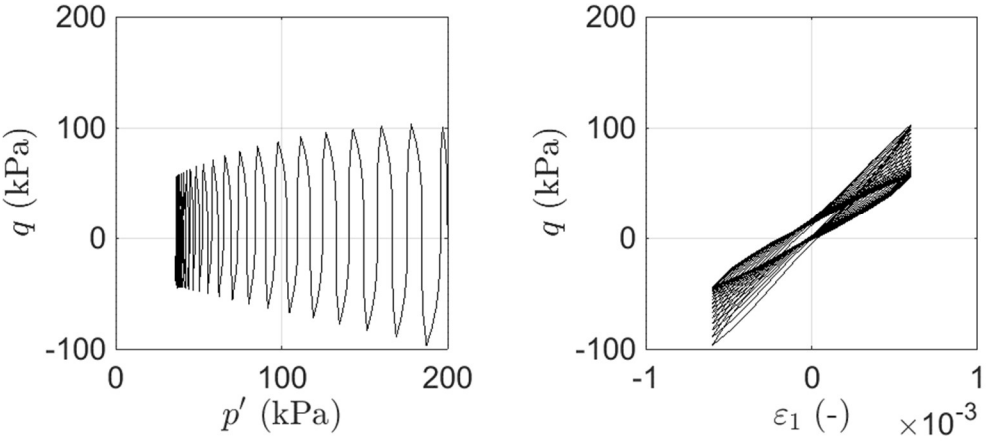


Figure 129:Case (a) No Intergranular strain



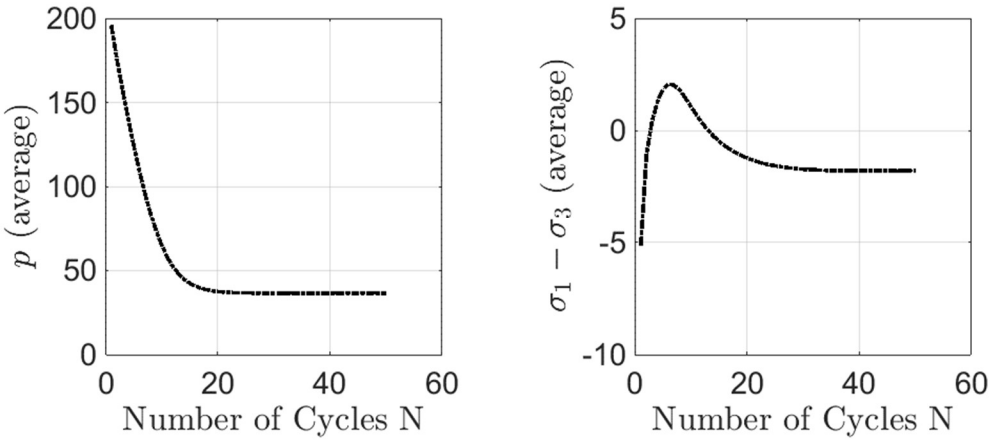


Figure 130:Case (b)

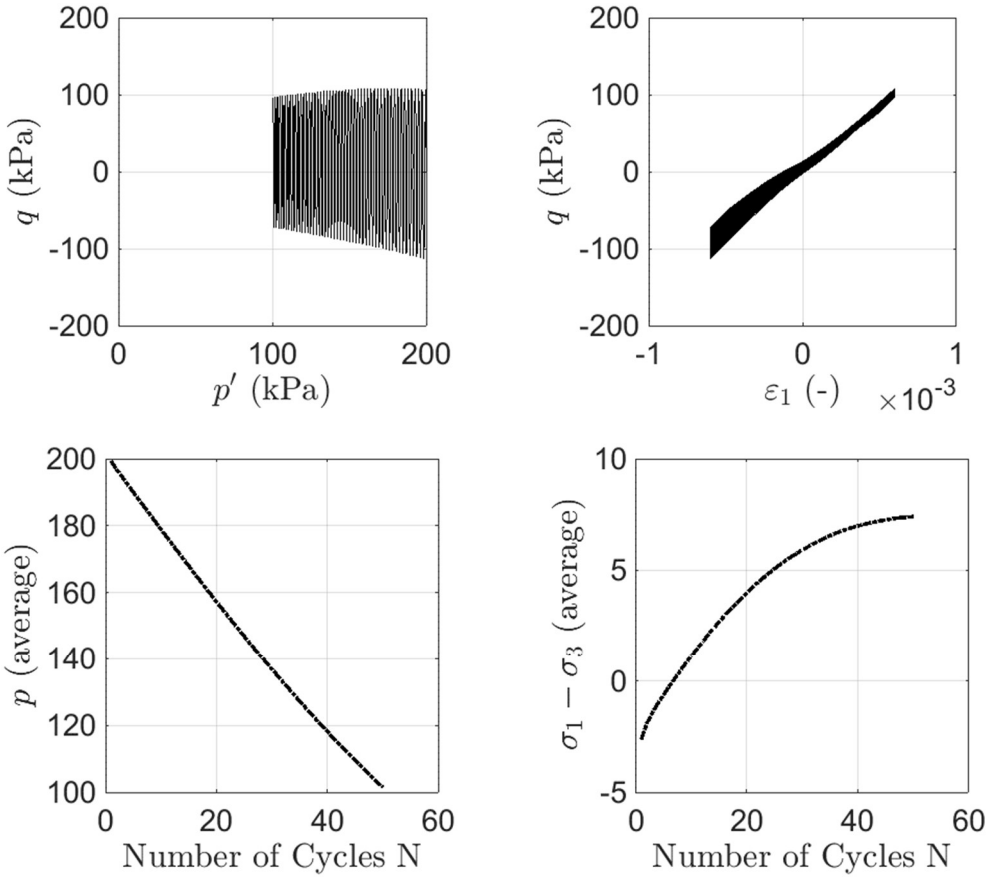


Figure 131:Case (c)

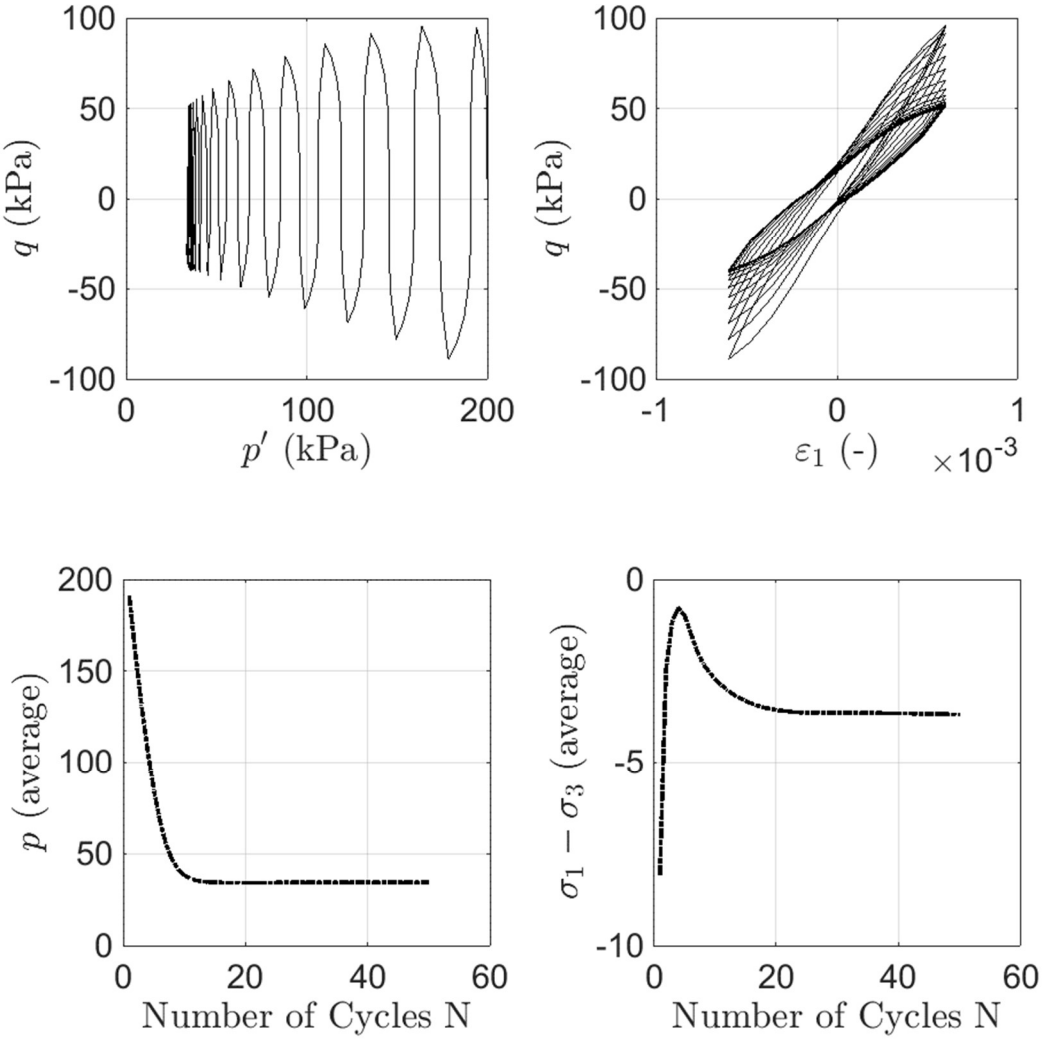
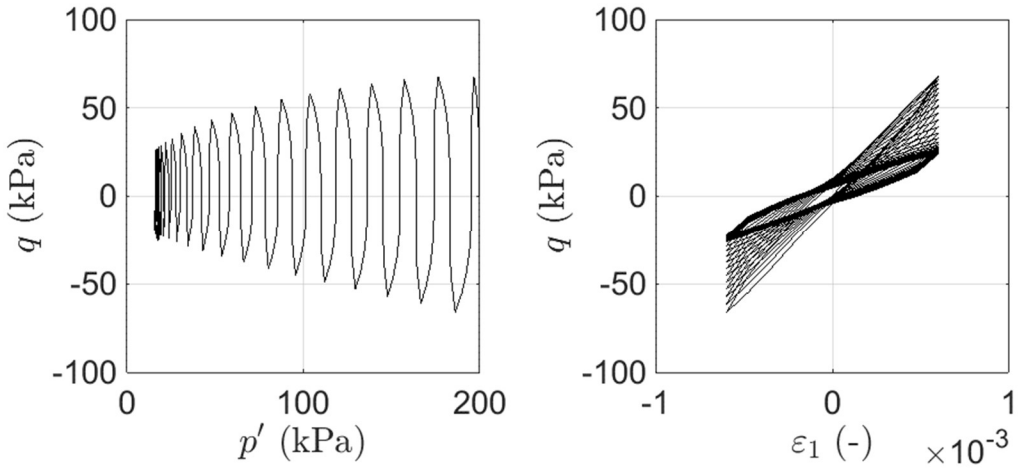


Figure 132:Case (d)



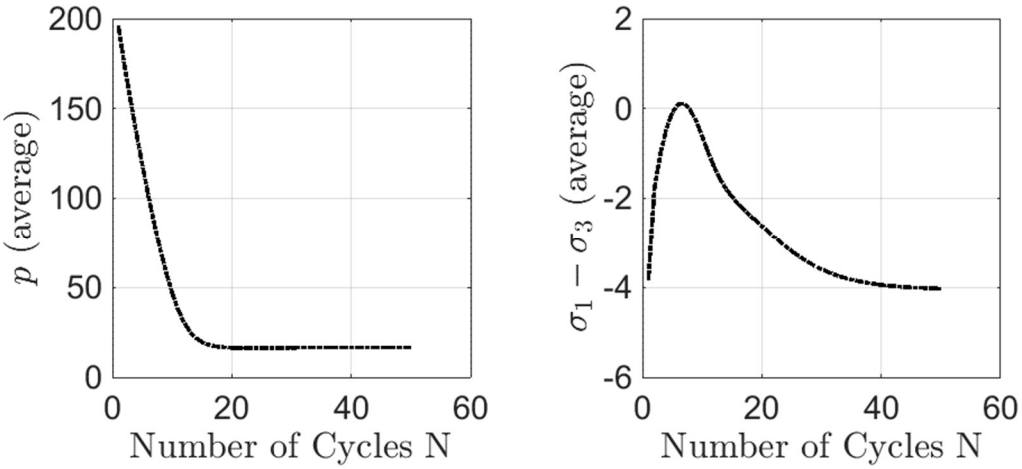


Figure 133:Case (e)

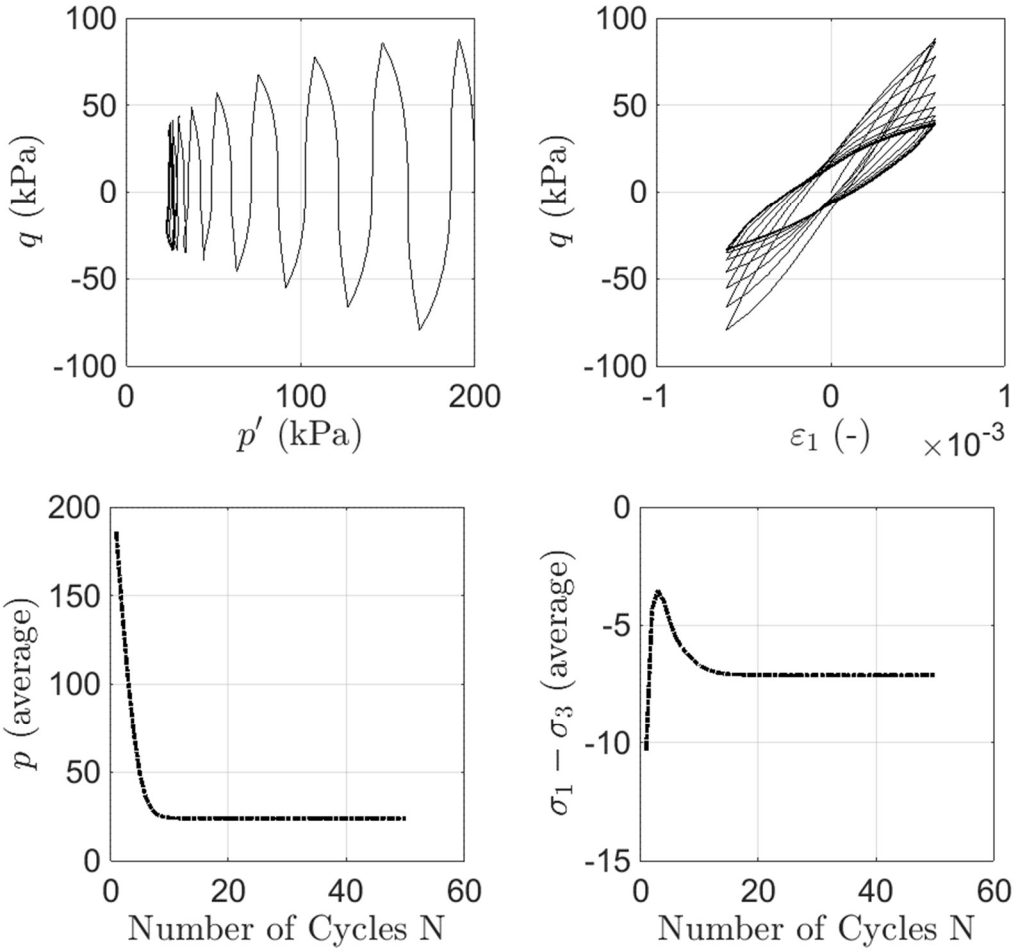


Figure 134:Case (f)

Case (a), Figure 129

No intergranular strain, excessive stress relaxation per cycle.

Case (b),Figure 130:

A region of 6E-4 strain magnitude is imposed by “R” where the weight acting on the rate of intergranular strain is small. As a result the intergranular strain evolves at a slower rate than the plastic strain, the numerical prediction reduces the ratchetting until a stable cycle is found at a mean effective stress of ~40 kPa.

Case (c), Figure 131:

A large region of 1.2E-3 strain magnitude is imposed by “R”. In this case the ratchetting per cycle is further reduced when compared to case (b) as the effect of the intergranular strain history variable is stronger.

Case (d), Figure 132:

An region as in case (b) is used, however the rate at which the intergranular strain evolves is different. Therefore, the stable stress cycle is located in the same region but the number of cycles to reach it is smaller since the intergranular starin evolves more rapidly with the plastic strain.

Case (e), Figure 133:

In this case the contribution of the intergranular strain in the volumetric projector principal direction is reduced, altering the stiffness of the model and shape of the mapping tensor, thus the stable cycle appears at a different average stress.

Case (f), Figure 134:

A significantly smaller penalty is applied to the recall term as a function of the intergranular strain, meaning the ratcheting increases as a result of a less linear main hardening rule.

4.2. KARLSRUHE SAND CALIBRATION BENCHMARK

In this section the laboratory tests described in the database of static and cyclic Karlsruhe sand tests (Wichtmann and Triantafyllidis, 2016a, Wichtmann and Triantafyllidis, 2016b) is used in combination with the basic sand model and the specialised hardening rules to evaluate its application to real sois. The type of tests and the calibrated parameters are described, with the aim to evaluate the capability of the model to capture soil behavior and at the same time illustrate the calibration process. All the tests benchmarked are described in the following table:

Table 20: Summary table of all tests used for benchmarking

Test ID	Initial p' (kPa)	Initial q (kPa)	Initial e (-)	Test Type
ISO1	48.8	0	0.97	Isotropic cyclic
ISO2	49.5	0	0.82	Isotropic cyclic
ISO3	49.1	0	0.69	Isotropic cyclic
ISO4	49.1	0	0.96	Isotropic cyclic
ISO5	49.0	0	0.82	Isotropic cyclic
ISO6	49.9	0	0.68	Isotropic cyclic
OEC1	-	-	1.0	Oed. cyclic
OEC2	-	-	0.89	Oed. cyclic
OEC3	-	-	0.79	Oed. cyclic
OEC4	-	-	0.76	Oed. cyclic
OE1	-	-	1.03	Oedometer
OE2	-	-	1.02	Oedometer
OE3	-	-	1.0	Oedometer
OE4	-	-	0.97	Oedometer
OE5	-	-	0.95	Oedometer
OE6	-	-	0.9	Oedometer
OE7	-	-	0.85	Oedometer
OE8	-	-	0.83	Oedometer
OE9	-	-	0.81	Oedometer
OE10	-	-	0.78	Oedometer
OE11	-	-	0.74	Oedometer
OE12	-	-	0.72	Oedometer
TMD1	~50	0.0	1.0	Monotonic drained triaxial
TMD2	~100	0.0	0.97	Monotonic drained triaxial
TMD3	~200	0.0	0.974	Monotonic drained triaxial
TMD4	~300	0.0	0.97	Monotonic drained triaxial
TMD5	~400	0.0	0.96	Monotonic drained triaxial
TMD6	~50	0.0	0.88	Monotonic drained triaxial
TMD7	~100	0.0	0.86	Monotonic drained triaxial
TMD8	~200	0.0	0.86	Monotonic drained triaxial
TMD9	~300	0.0	0.85	Monotonic drained triaxial
TMD10	~400	0.0	0.85	Monotonic drained triaxial

TMD11	~50	0.0	0.839	Monotonic drained triaxial
TMD12	~100	0.0	0.816	Monotonic drained triaxial
TMD13	~200	0.0	0.817	Monotonic drained triaxial
TMD14	~300	0.0	0.814	Monotonic drained triaxial
TMD15	~400	0.0	0.8	Monotonic drained triaxial
TMD16	~50	0.0	0.74	Monotonic drained triaxial
TMD17	~100	0.0	0.76	Monotonic drained triaxial
TMD18	~200	0.0	0.75	Monotonic drained triaxial
TMD19	~300	0.0	0.734	Monotonic drained triaxial
TMD20	~400	0.0	0.75	Monotonic drained triaxial
TMD21	~50	0.0	0.73	Monotonic drained triaxial
TMD22	~100	0.0	0.735	Monotonic drained triaxial
TMD23	~200	0.0	0.71	Monotonic drained triaxial
TMD24	~300	0.0	0.7	Monotonic drained triaxial
TMD25	~400	0.0	0.72	Monotonic drained triaxial
TMU1	~100	0.0	0.83	Undrained monotonic triaxial
TMU2	~200	0.0	0.81	Undrained monotonic triaxial
TMU3	~300	0.0	0.82	Undrained monotonic triaxial
TMU4	~400	0.0	0.82	Undrained monotonic triaxial
TMU5	~200	0.0	0.95	Undrained monotonic triaxial
TMU6	~200	0.0	0.72	Undrained monotonic triaxial
TMU7	~100	0.0	0.83	Undrained monotonic triaxial
TMU8	~200	0.0	0.85	Undrained monotonic triaxial
TMU9	~300	0.0	0.83	Undrained monotonic triaxial
TMU10	~400	0.0	0.83	Undrained monotonic triaxial
TMU11	~200	0.0	0.96	Undrained monotonic triaxial
TMU12	~200	0.0	0.7	Undrained monotonic triaxial
TCUE1	~200	~150	0.812	Undrained strain controlled small amplitudes
TCUE2	~200	~150	0.79	Undrained strain controlled small amplitudes
TCUE3	~200	~(-100)	0.85	Undrained strain controlled small amplitudes
TCUE4	~200	~150	0.83	Undrained strain controlled small amplitudes
TCUE5	~200	~100	0.79	Undrained strain controlled small amplitudes
TCUE6	~200	~150	0.91	Undrained strain controlled small amplitudes
TCUE7	~200	~150	0.75	Undrained strain controlled small amplitudes
TCUE8	~200	~230	0.8	Undrained strain controlled small amplitudes
TCUE9	~200	0	0.8	Undrained strain controlled small amplitudes
TCUE10	~200	~(-100)	0.84	Undrained strain controlled small amplitudes

TCUE11	~200	~(-150)	0.835	Undrained strain controlled small amplitudes
TCUE12	~50	~50	0.83	Undrained strain controlled small amplitudes
TCUE13	~100	~75	0.79	Undrained strain controlled small amplitudes
TCUE14	~300	~220	0.81	Undrained strain controlled small amplitudes
TCUE15	~200	~0.0	0.94	Undrained strain controlled large amplitudes
TCUE16	~200	~0.0	0.8	Undrained strain controlled large amplitudes
TCUE17	~200	~0.0	0.7	Undrained strain controlled large amplitudes
TCUE18	~100	~0.0	0.81	Undrained strain controlled large amplitudes
TCUE19	~700	~0.0	0.81	Undrained strain controlled large amplitudes
TCUE20	~200	~0.0	0.81	Undrained strain controlled large amplitudes
TCUE21	~200	~150	0.83	Undrained strain controlled large amplitudes
TCUE22	~100	~0.0	0.67	Undrained strain controlled large amplitudes
TCUE23	~700	~0.0	0.67	Undrained strain controlled large amplitudes

4.2.1. CALIBRATRION PROCEDURE

This section describes the suggested steps to calibrate the basic sand model. As discussed in previous chapters the basic sand model is based in critial state theory, which assumes critial state conditions as a particular assimptotic state. In this sense it is important to allocate the CSL initially. The inputs of the sand model are divided in blocks, where $\mathbf{e_{c0}}$, $\mathbf{h_s}$ and **n** control the position and slope of the CSL, $\mathbf{e_{d0}}$, β control the stiffness as function of the void ratio, **XV**, **YF** and **ZF** define the shape of the deviatoric failure envelope, $\mathbf{ob_{min}}$, $\mathbf{ob_{max}}$ and δ control the shear volumetric coupling and finally α and ϑ control the peak stength and post-peak behaviour. Finally $\mathbf{S_f}$ affects the mapping tensor controlling the stiffness in the direction of the J/p assymptote. The steps to calibrate the model are:

1) Determine the CSL line slope and dependence of stiffness with void ratio
2) Position the CSL to determine loose and dense responses under shear
3) Determine the deviatoric failure envelope (use other test than TXC)
4) Adjust dilatance and limit surface curvature (based on shear tests)
5) Once the monotonic response is captured, use specialised rules (densification, enforced ratcheting, intergranular strain) to improve limitations of a single basic law in cyclic conditions

The following figures detail the calibration process where each figure is representative of a calibration stage. A set of 5 TXD tests are extracted from the karlruhe database in combination with the isotropic compression tests for guiding the process. Figure 135 shows an example of calibration of the slope of the CSL where $\mathbf{e_{d0}}$, $\mathbf{e_{c0}}$, $\mathbf{h_s}$ and $\mathbf{n}$.

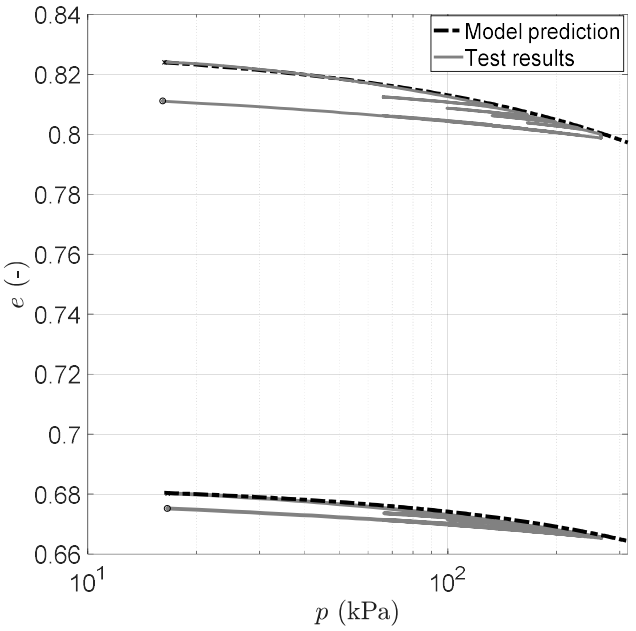


Figure 135: Step 1, adjust of the CSL slope with isotropic compression tests or oedometers. $\boldsymbol{e_{d0}}$, $\boldsymbol{e_{c0}}$, $\boldsymbol{h_s}$ and $\boldsymbol{n}$

Secondly, the CSL needs to be located in a region dividing dense to loose states as a funtion of p' and the void ratio. The following figure shows the chosen 5 TXD to be calibrated and a possible position of the CSL, after this process a final value of $\mathbf{e_{c0}}$ should be is obtained.

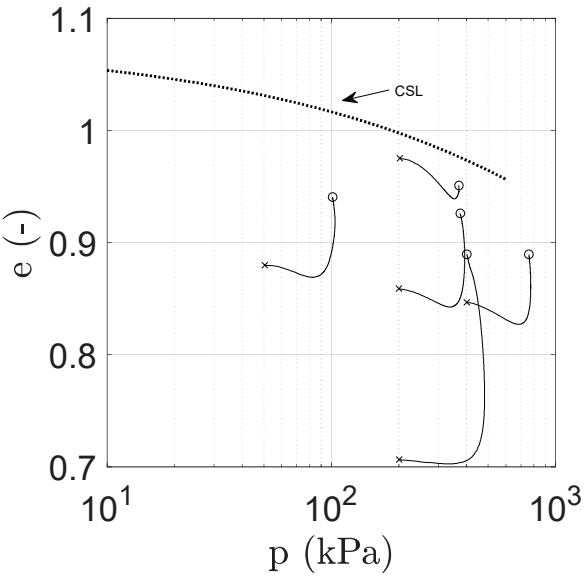


Figure 136: Step 2. Position the CSL slope for loose and dense states. Parameters adjusted e_{c0}

The deviatoric shape can be adjusted if TXE or using other tests such as shear tests. The following figure shows the calibration of XF, YF, ZF based on the undrained triaxial tests in compression and extension taken from the Karlruhe.

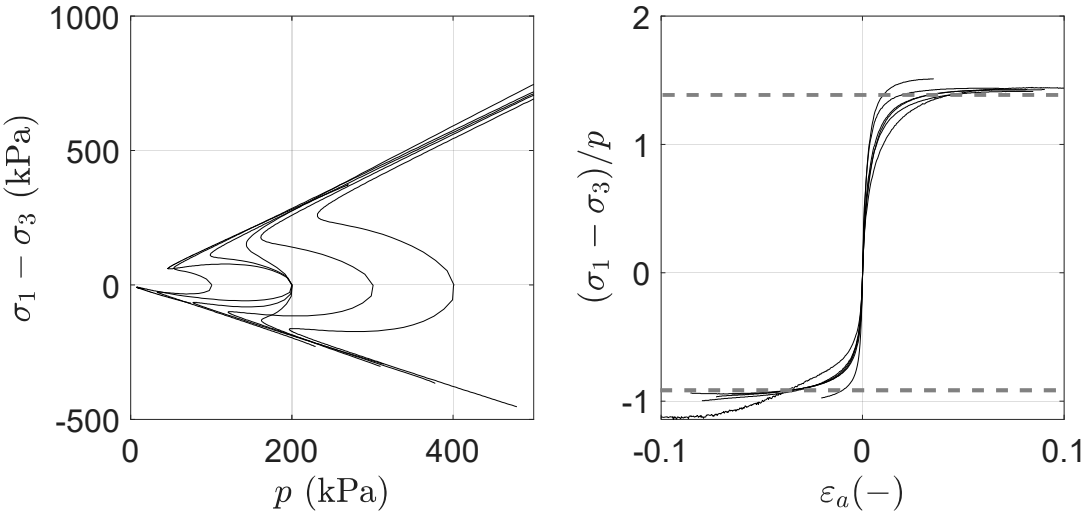


Figure 137: Step 3. Use shear tests (TXD, TXU, SS) to characterize the deviatoric shape. Parameters adjusted XF, YF, ZF

Once the strengh at critical state conditions is determined, the goal functions and limit surface curvature can be determined. The TXD stress paths of Figure 136 can be normalised with respect to the obliquity and the plastic metric versus the J/p ratio as shown in Figure 138. Once the stress path are plotted the goal function parameters (**ob**$_{min}$, **ob**$_{max}$ and δ) and the curvature of the limit surface (ϑ) can be adjusted.

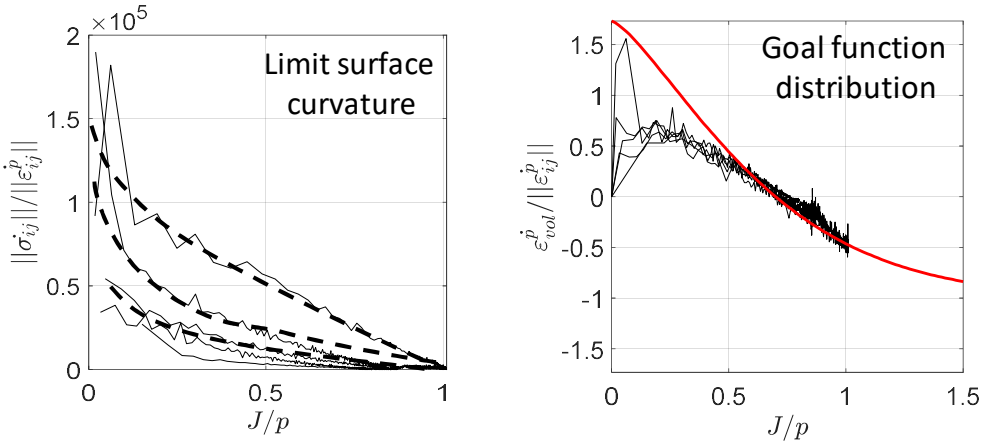


Figure 138: Step 4. Normalise drained shear tests (SS, TXD) to characterize the goal function distribution and the curvature of the limit surface with J/p. Parameters adjusted ***ob***$_{min}$, ***ob***$_{max}$, δ and ϑ

Finally, the rests of the parameters (S_f and α) can be adjusted by trial and error using a constitutive driver to better capture the peak strength value and its post-peak degradation, the result of the final calibration versus the laboratory tests for the five tests is shown in Figure 139.

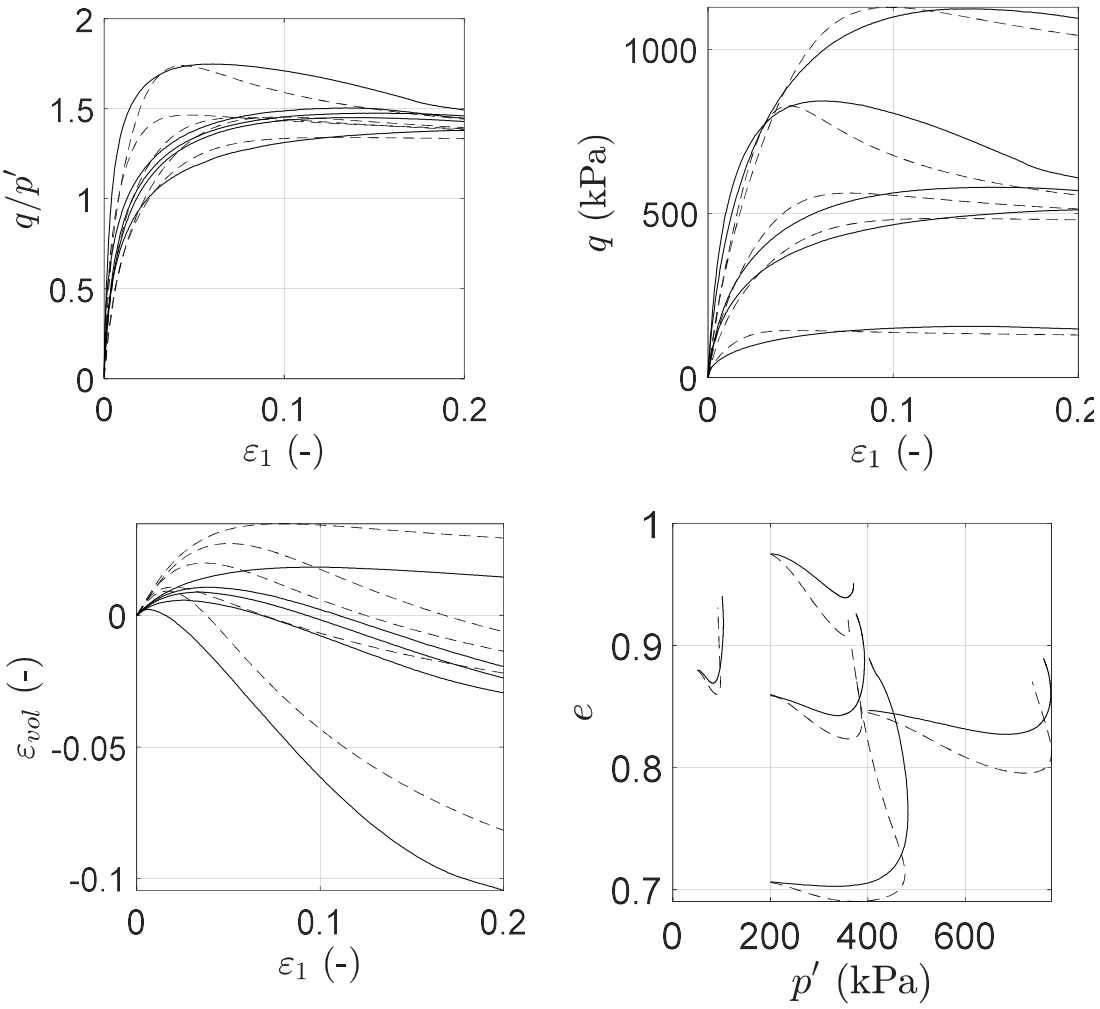


Figure 139: Example of calibration, final result

Once the basic law reproducing appropiatelly the static behaviour, the same parameters as the static model can be employed to asses the prediction under cyclic conditions. Is in this stage where the specialised laws described insection 4.1 can be used to enhance the model predictions, an example of this process is show in Figure 140.

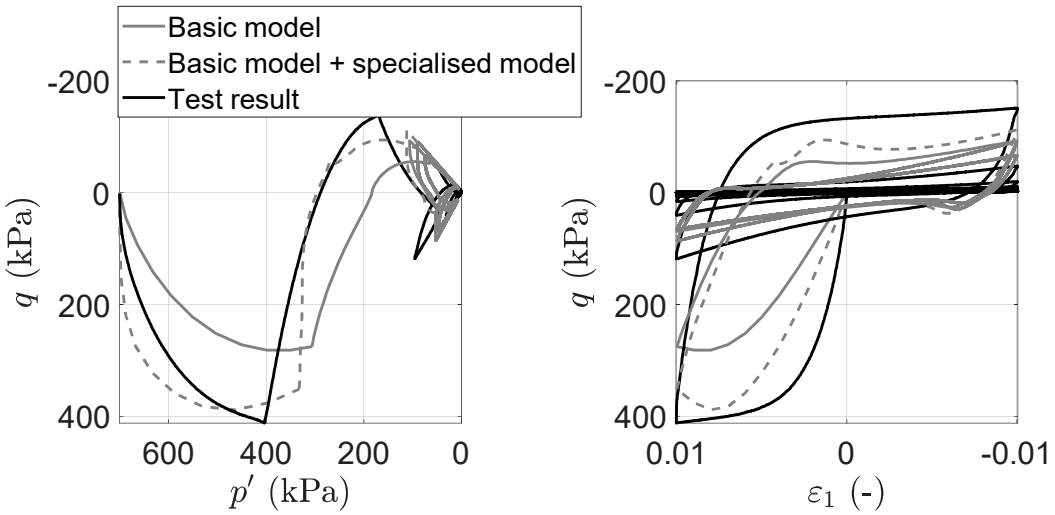


Figure 140: Example of use of specialised hardenign rules to improve cyclic predictions

In summary, the calibration methodology focuses on the calibration of the material for static conditions and uses the concept of backstress superposition to improve the limitations of a simple hardenign rule acting locally on the non-liner recal term of the main law. Next section covers in detail the calibration of the 82 tests detailed in 4.2.

4.2.2. BENCHMARK OF MODEL PREDICTIONS FOR ALL TESTS

The following section benchmarks the model using the previous methodology for all the tests listed in 4.2. The type of tests follow the steps detailed in the previous section.

4.2.2.1. Cyclic isotropic tests

A set of six isotropic cyclic tests of Karlsruhe sand is included in the database. The tests are performed with constant and variable amplitude of cycling for three different densities, from loose to very dense, and with the maximum mean effective stress below 300 kPa. Figure 35 shows the six laboratory tests in the e-p' plane.

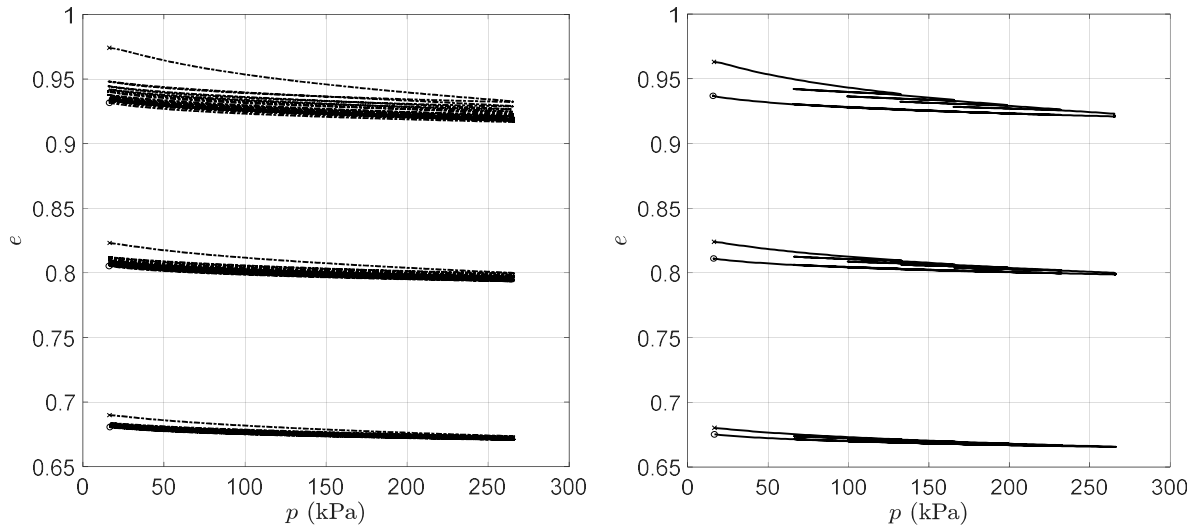


Figure:Cyclic isotropic test for Karlsruhe sand. (a) 20 cycles of equal amplitude, (b) different amplitudes

With these tests the inputs regarding f_b and f_e functions and the slope of the critical state line can be determined. Once the slope of the CLS is adjusted, the densification specialised hardening rule can be adjusted to match the loading-unloading paths and the densification of the soil upon isotropic stress cycles. The parameters obtained for calibration are shown in Table 21.

Table 21: Parameters determined with cyclic isotropic tests

Main rule	e_{c0}	e_{d0}	h_s	**n**	**α**	**β**	**XV**	**YF**	**ZF**	**θ**	S_f	ob_{min}	ob_{max}	**δ**
	-	0.55	4E5	0.45	-	2.5	-	-	-	-	-	-	-	-
Densification rule	$C^{(2)}$	**a**	$\beta^{(2)}$	$\theta^{(2)}$	R_{ur}	**H**								
	1.2	0.015	0.8	3.0	1.2	4.0								

In general, as shown in Figure 141, the numerical predictions agree well with the laboaratory data. In particular, it can be observed how the dependence of the stiffness with with the void ratio is accounted for due to the f_e function. Secondly, the addition of a specialised densification rule improves significantly the response under cyclic isotropic conditions, accurately capturing the reduction in voids per cycle for all the different initial void ratios (Figure 142, Figure 143 and Figure 144).

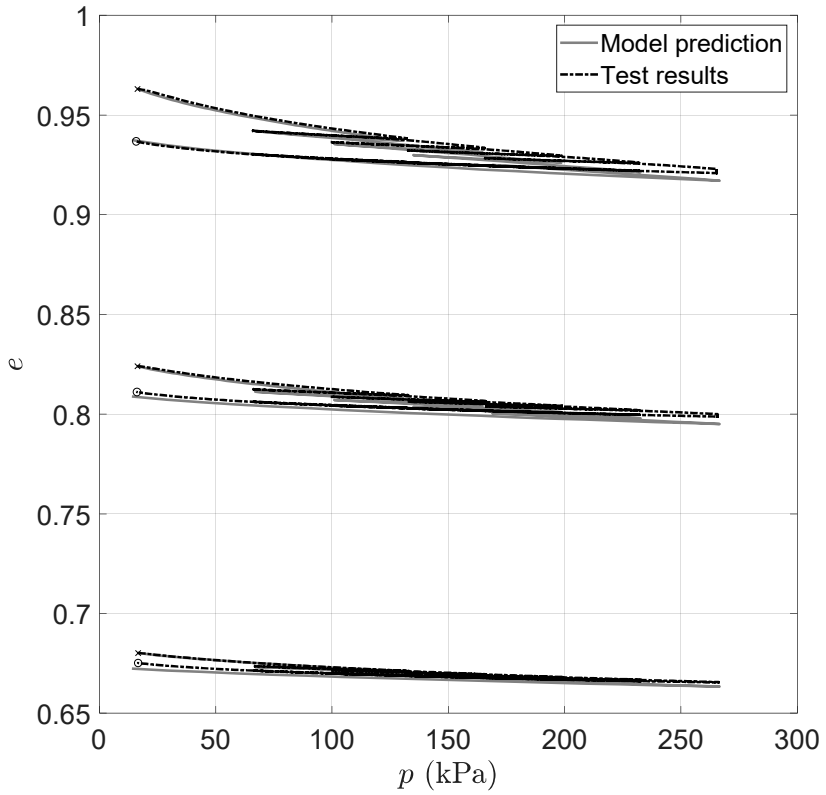


Figure 141: Calibration versus Test for non-constant amplitude

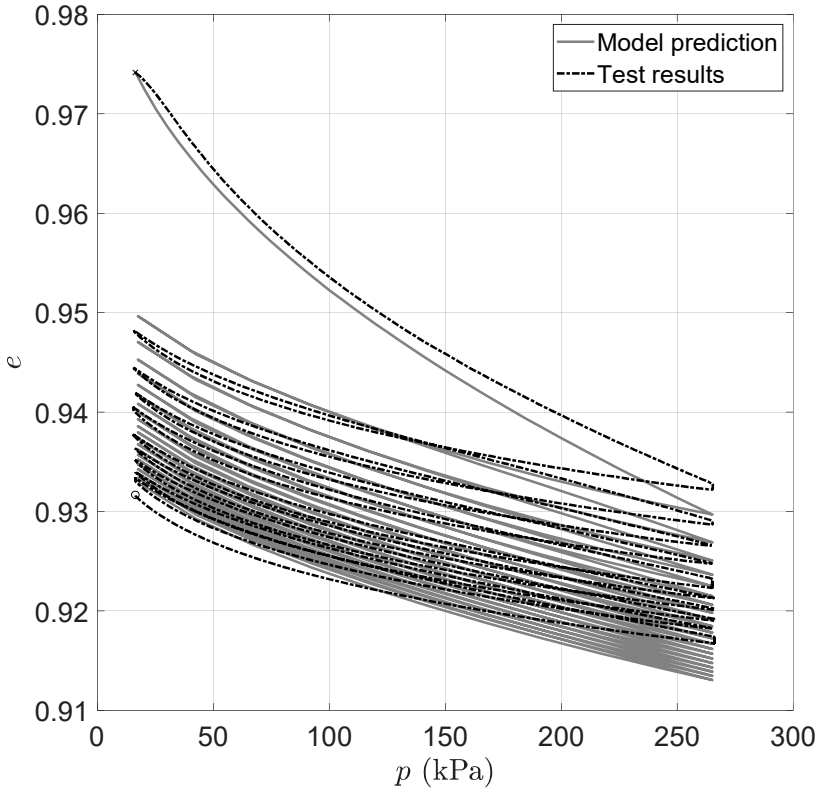


Figure 142: Calibration versus loose sand - isotropic cyclic test

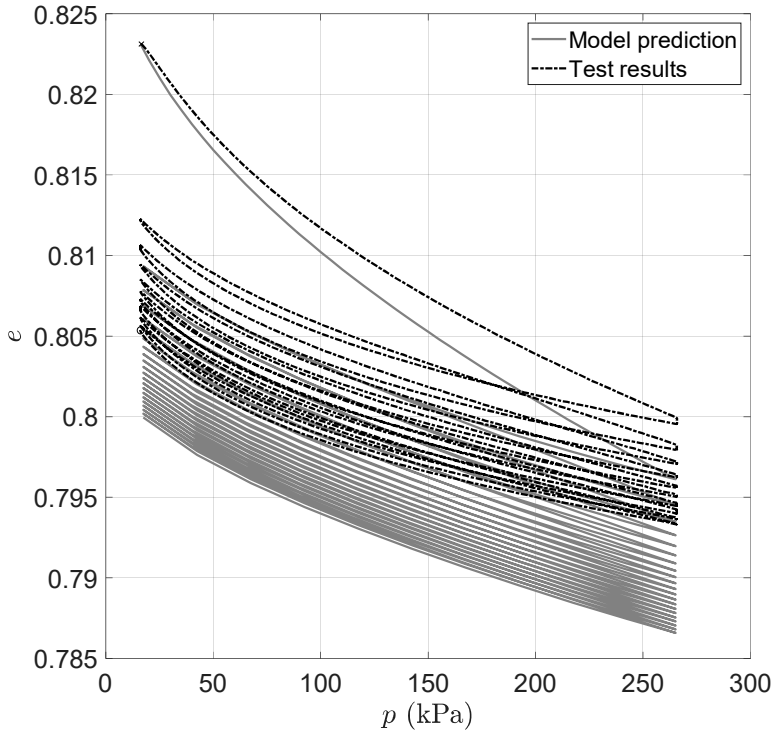


Figure 143: Calibration versus dense sand - isotropic cyclic test

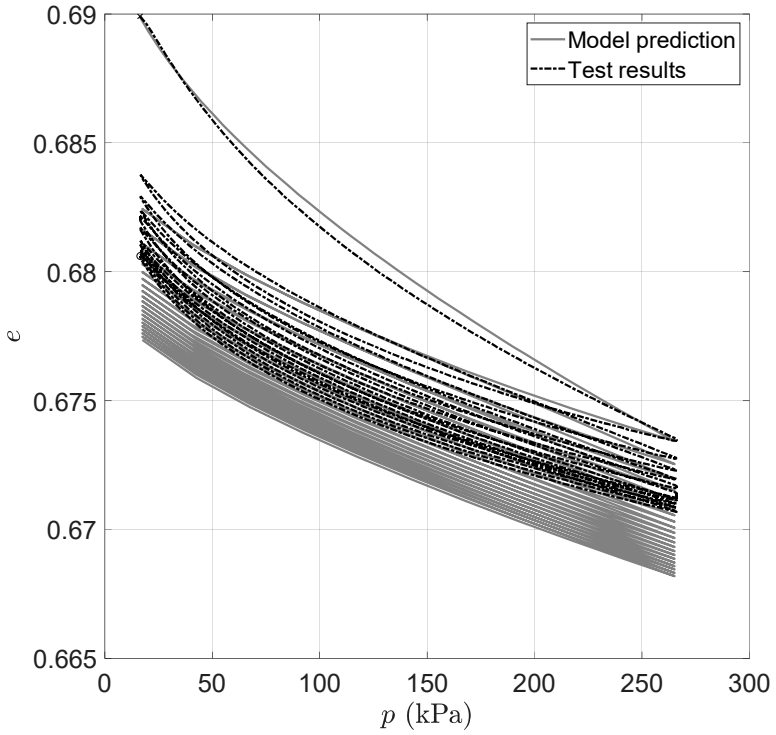


Figure 144: Calibration versus very dense sand - isotropic cyclic test

4.2.2.2. Monotonic drained triaxial tests

The next step after calibrating the stiffness in the volumetric principal direction is the determination of the strength parameters and shear stiffness. To do so, a set of 25 drained monotonic tests on Karlsruhe sand is used to calibrate the first hardening rule. Figure 145 shows all the tests used for calibration. In this particular case the position of the CSL is determined in combination with the strength and shear volumetric coupling.

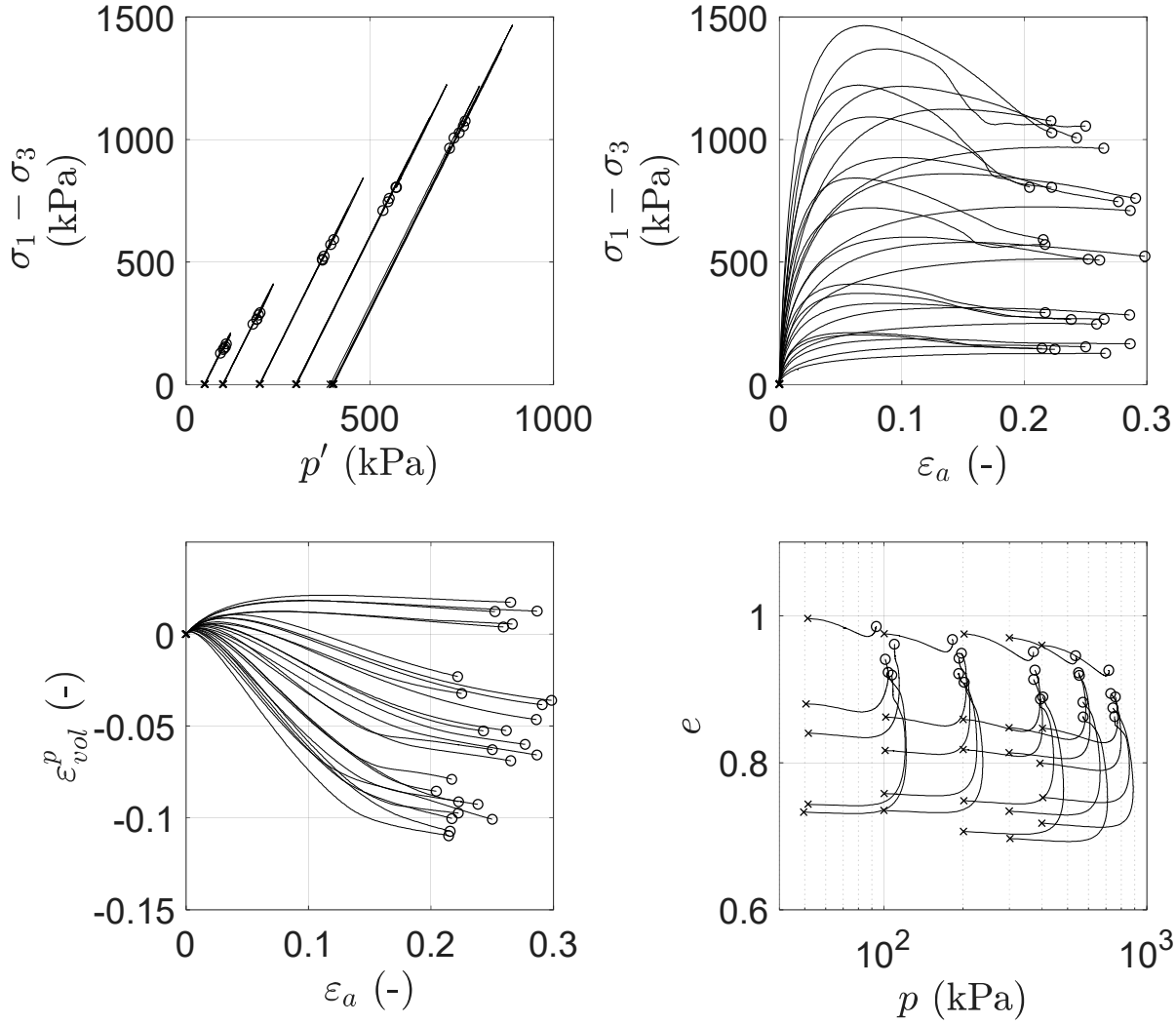


Figure 145: Karlsruhe sand drained triaxial compression tests

It should be noted that, despite the strain levels in shearing reaching more than 20%, as shown in Figure 145, critical state conditions are not completely achieved for all tests. However, there is a clear difference between the response of the looser states and the denser cases, and the position of the critical state line can be inferred as a boundary between the two regions.

Secondly once the CSL is determined, the test data shown in Figure 145 can be normalised to determine the goal function orientation and the shape and curvature of the limit surface. This normalization is shown in Figure 146, where the obliquity of goal function – limit surface value can be determined. Once the goal function and the limit surface curvature ϑ are determined, the next step is to capture the peak strength, and post peak degradation. This is mechanism is

controlled by the α and e_{d0} parameters which can be determined through trial-and-error process.

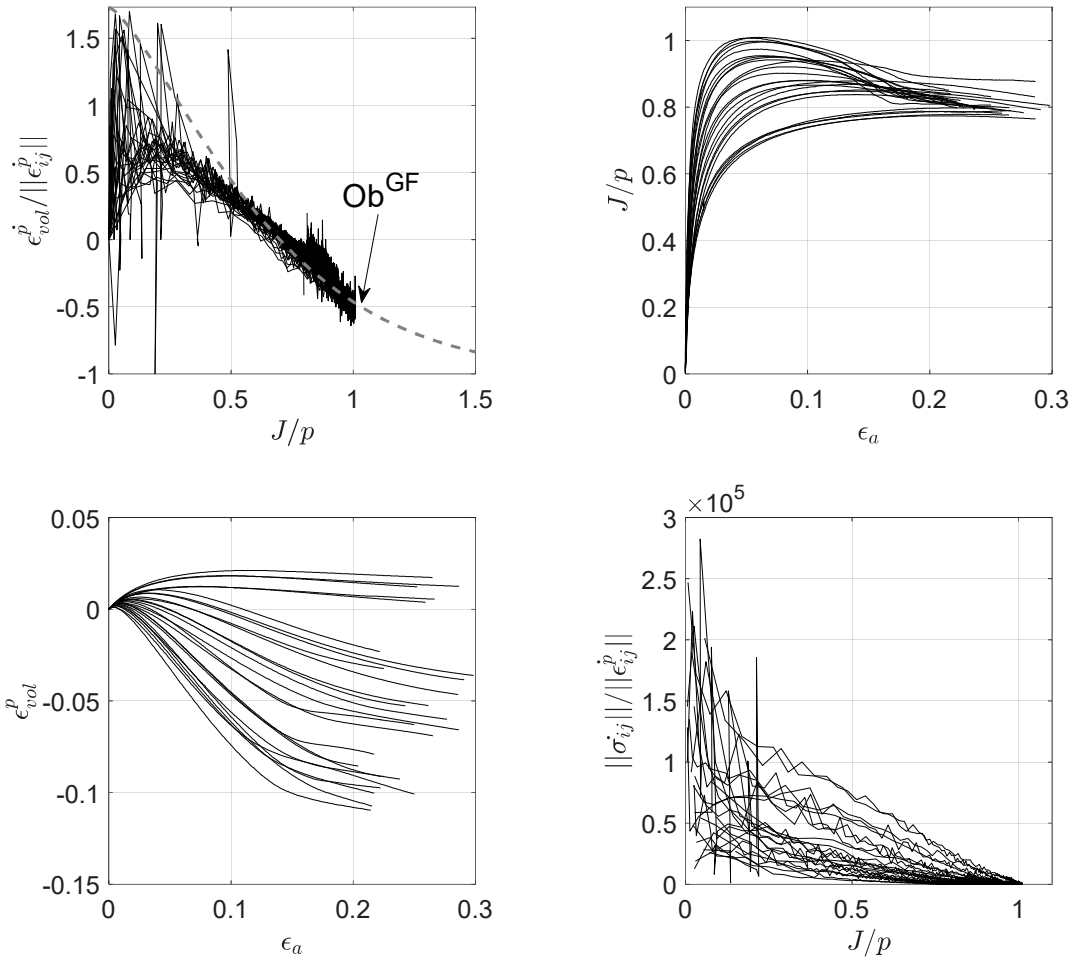


Figure 146: Normalized paths for Karlsruhe Drained triaxial test

Based on the results of the isotropic compression test (ISO) together with those of drained triaxial compression tests (TXD), the rest of the inputs missing in Table 21 can be determined. The completed set of parameters (ISO+TXD) are shown in Table 22, and the numerical prediction of the calibrated parameter are compared with the real test data in Figure 147 to Figure 151, where there is good agreement between model predictions and laboratory tests for a wide range of initial mean stress and void ratios.

Table 22: Parameters determined with ISO, TXD and TXU tests

Main rule	e_{c0}	e_{d0}	h_s	**n**	α	β	**XV**	**YF**	**ZF**	ϑ	S_f	ob_{max}	δ
	1.0	0.55	4E5	0.45	0.15	2.5	0.53	0.77	0.24	0.4	3.5	1.0	2.5

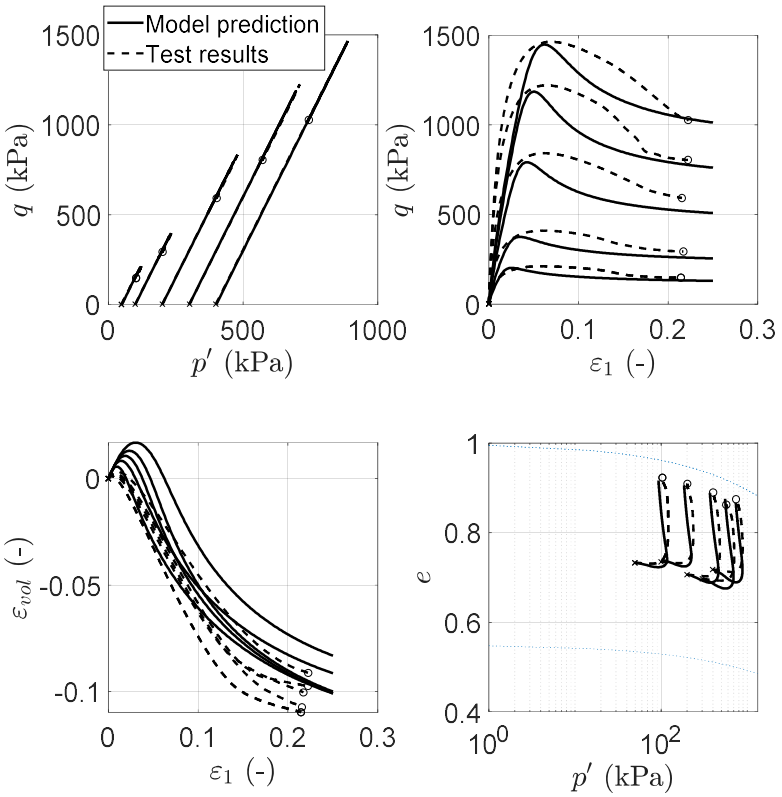


Figure 147: Triaxial test for very dense sand

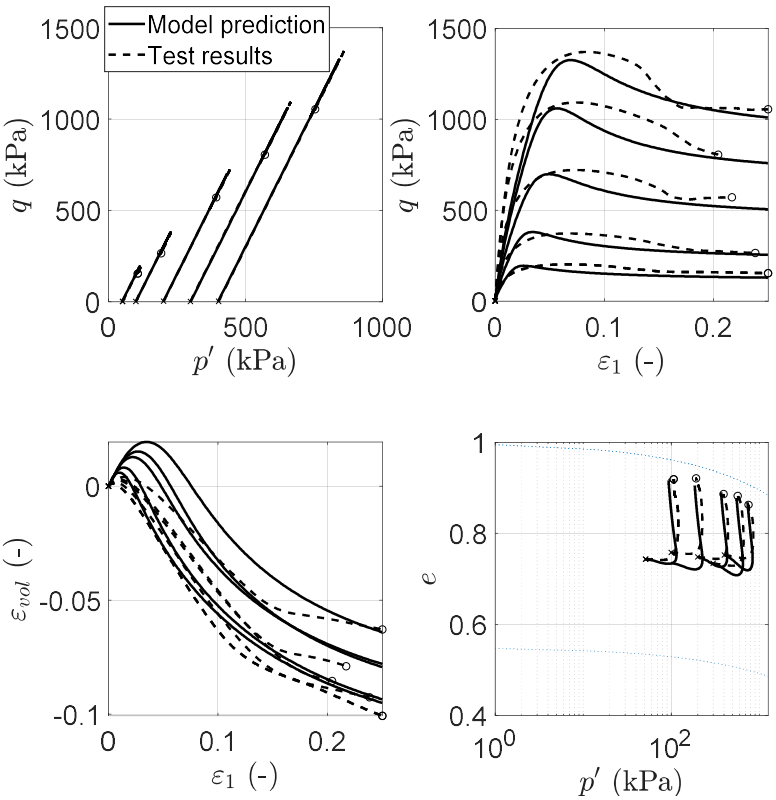


Figure 148: Triaxial test for dense sand

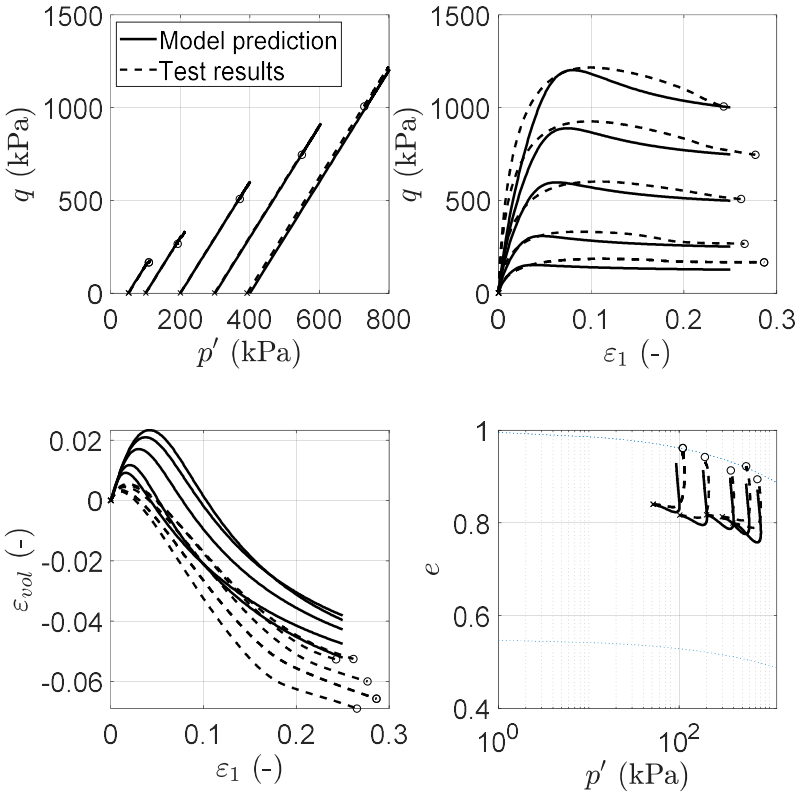


Figure 149: Traiaxila test for medium sand

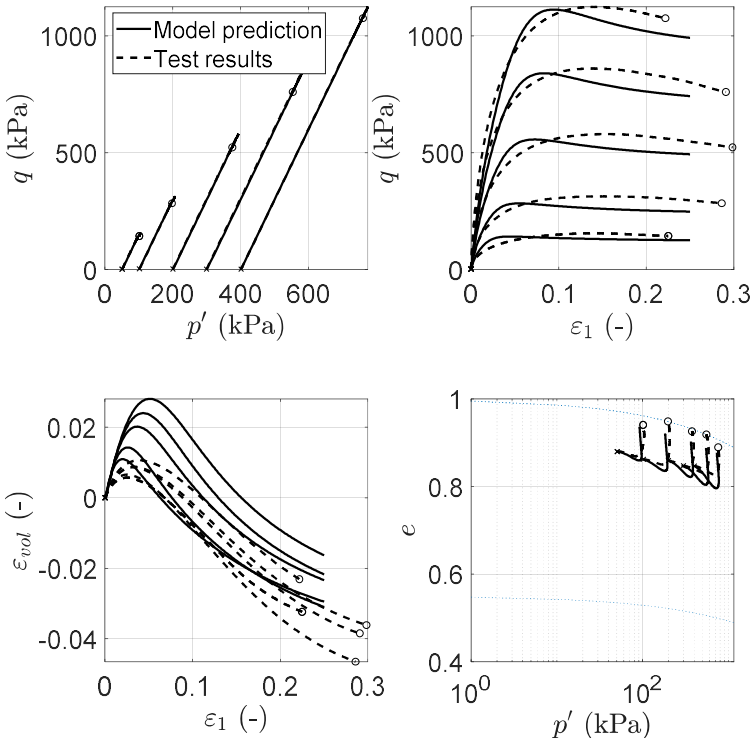


Figure 150: Triaxial test for medium dense sand

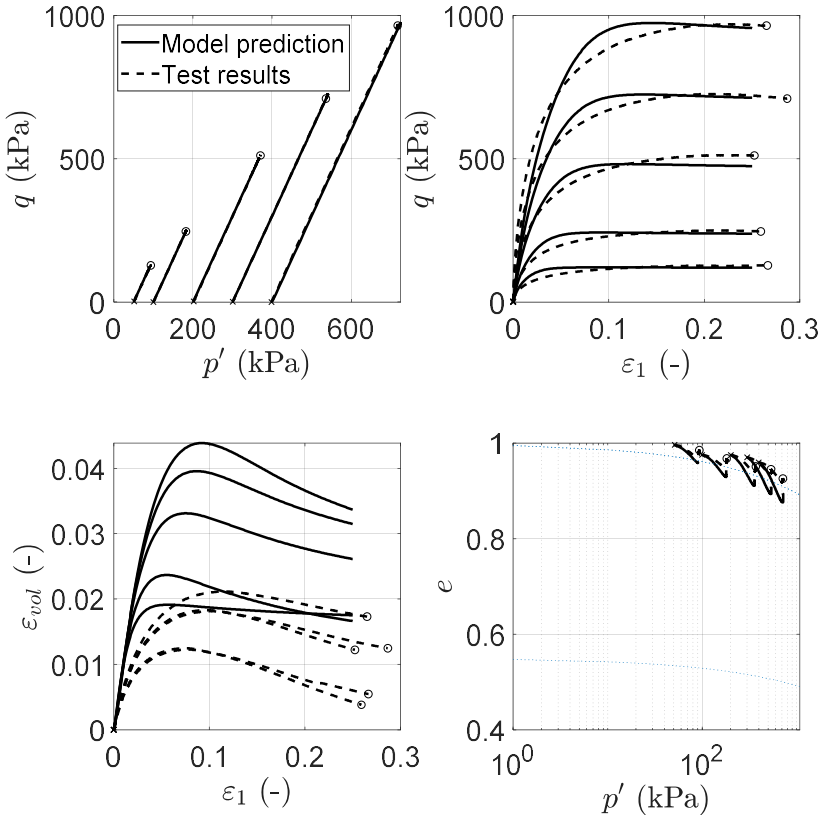


Figure 151: Triaxial test for loose sand

4.2.2.3. Monotonic undrained triaxial tests

At the time this calibration was carried out the Karlsruhe database did not include monotonic drained triaxial extension tests. However it included twelve monotonic triaxial compression and triaxial extension tests in undrained conditions. The initial void ratios and relative positions to the CSL line in e - p' space for these 12 tests are shown in Figure 152. Six tests correspond to undrained triaxial extension tests and six to undrained triaxial compression tests. The Van Eekelen (1980) deviatoric shape (parameters XF, YF, ZF) has been calibrated using these undrained triaxial tests.

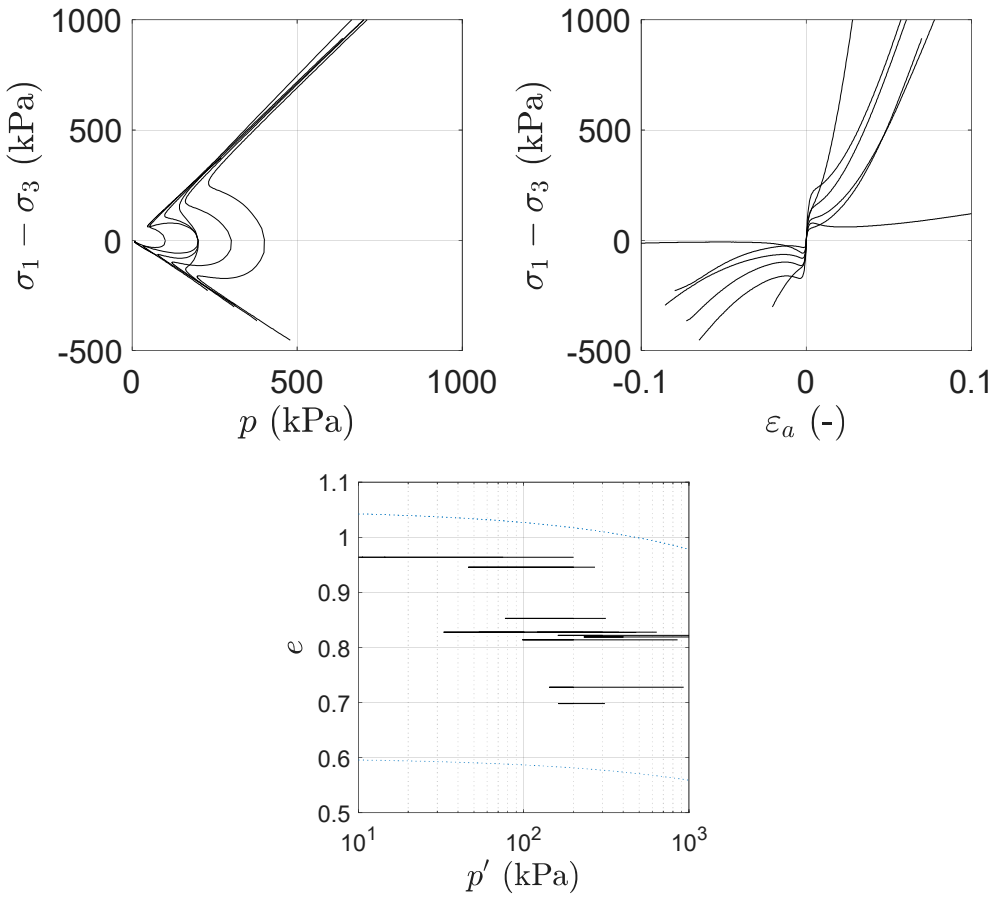


Figure 152: Karlsruhe sand undrained triaxial tests

The inputs used for the model are those described in Table 22 and the numerical predictions of the model with respect to the 12 undrained monotonic triaxial tests are shown in Figure 153 to Figure 158, where a good agreement between the experimental and numerical datasets can be observed. It is important to mention that in terms of stiffness a difference exists between the compression and extension tests, where the shear stiffness is well captured under triaxial compression conditions (see Figure 153, Figure 154 and Figure 155), but less well predicted for the triaxial extension cases (see Figure 156, Figure 157 and Figure 158). A possible improvement of the model could be the introduction of a dependence of the shape factor with the Lode's angle, an aspect of work which is left for future study.

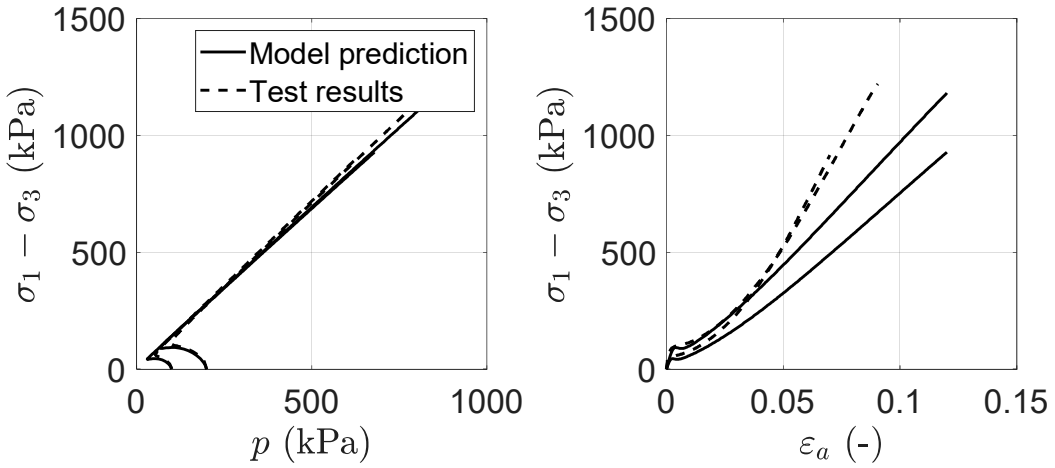


Figure 153: Undrained triaxial compression tests in dense sand versus numerical prediction (1)

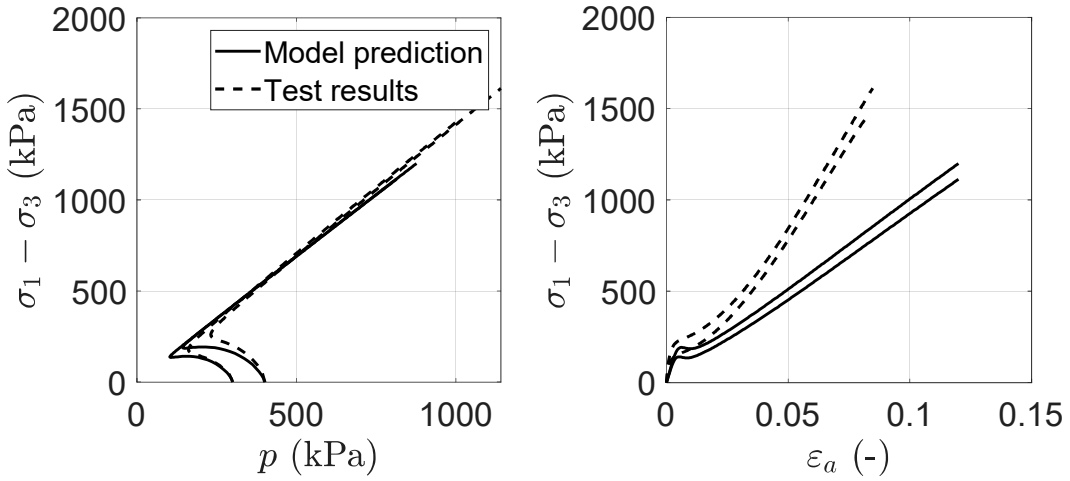


Figure 154: Undrained triaxial compression tests in dense sand versus numerical prediction (2)

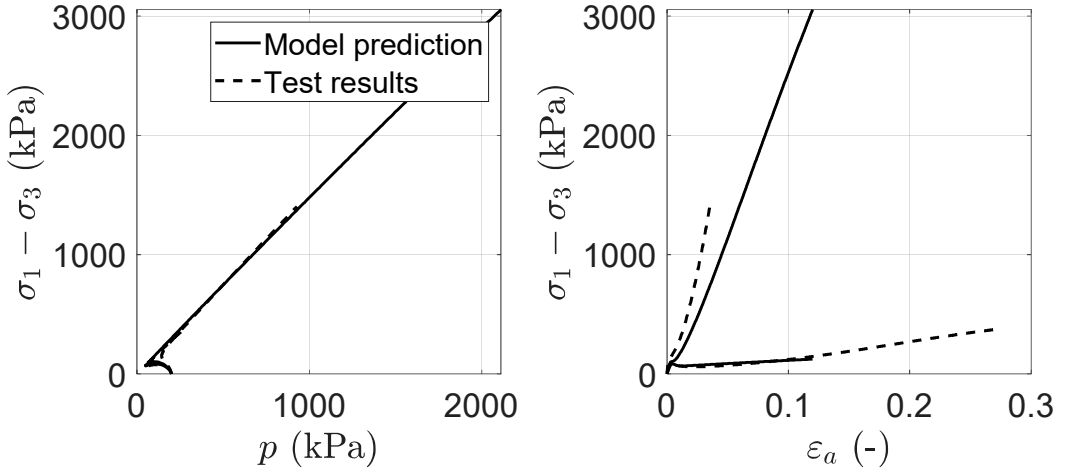


Figure 155: Undrained triaxial compression tests in loose and very dense sand versus numerical prediction (3)

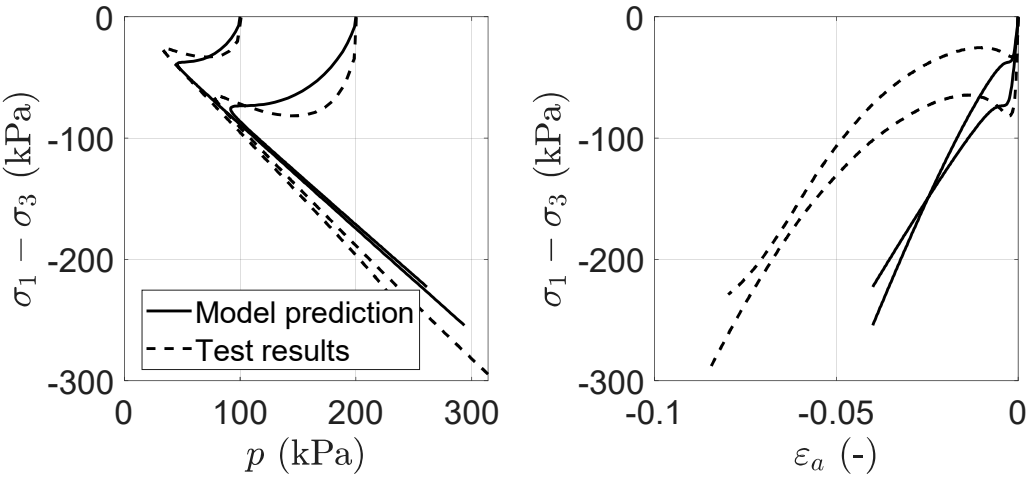


Figure 156: Undrained triaxial extension tests in dense sand versus numerical prediction (1)

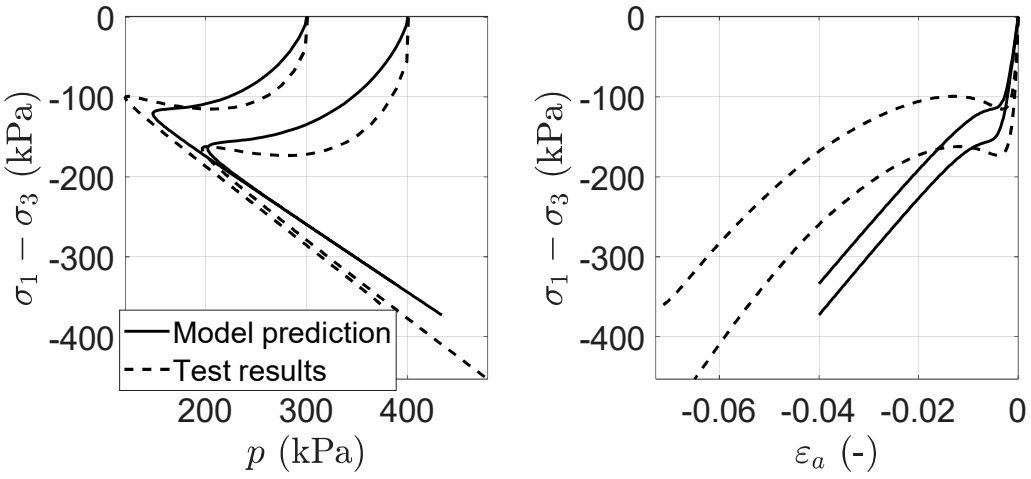


Figure 157: Undrained triaxial extension tests in dense sand versus numerical prediction (2)

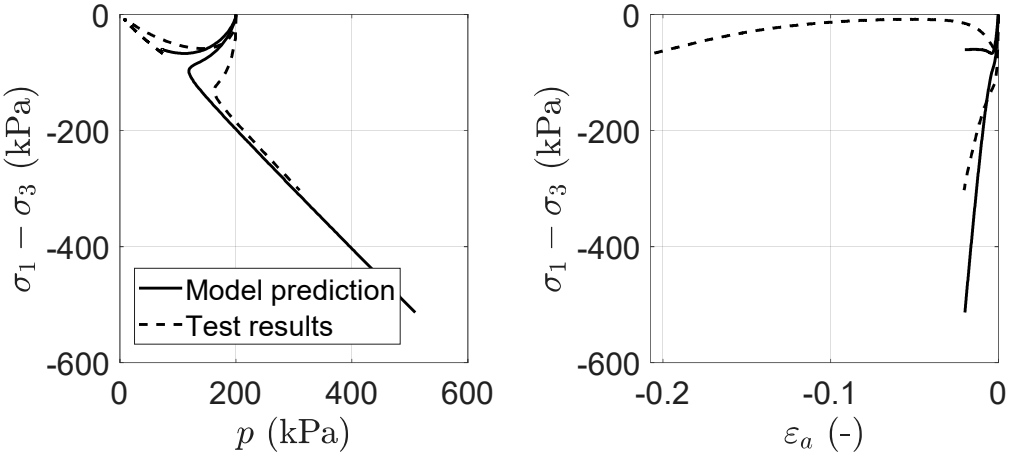


Figure 158: Undrained triaxial extension tests in dense sand versus numerical prediction (3)

4.2.2.4. Oedometer tests

The database of experimental data also includes a set of oedometer tests, 12 with one loading-reloading cycle and 4 involving a larger amount of loading reloading cycles. Figure 159 to Figure 161 show the comparison between the experimental data and model predictions for the parameters described in Table 22. The predicted response of the model is slightly softer that the observed in the laboratory data. The reason behind this difference in stiffness the fact that the model adjust its stiffness to enforce asymtotic conditions, which affects the stiffness in oedometric conditions as the f_b function acts on the stiffness to ensure $\dot{f}_d > 0$. The prediction of the model could be improved by adjusting the definition of f_b. Nevertheless, the response of the model is reasonably good for most of the tests, in particular the loading-unloading behaviour.

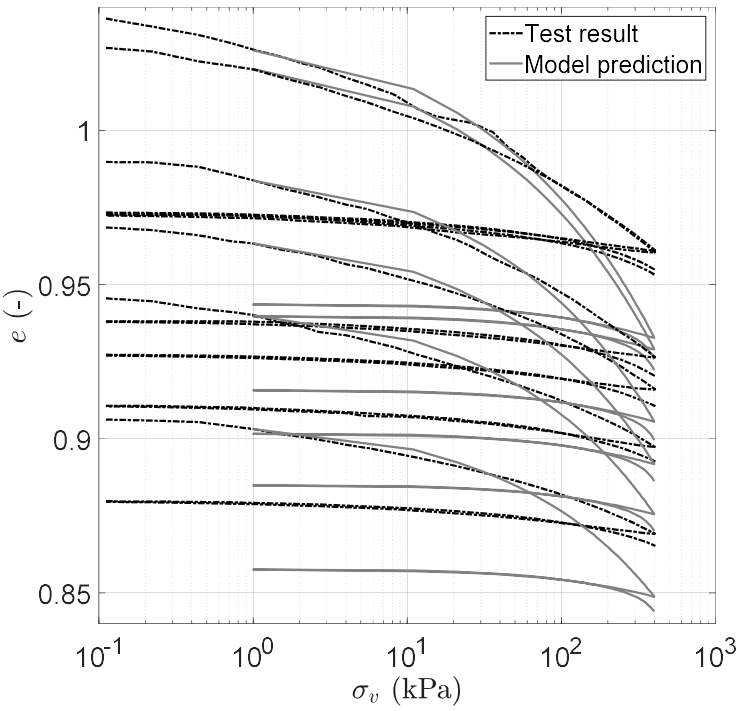


Figure 159: Load-unload oedometer tests for loose-dense versus numerical prediction

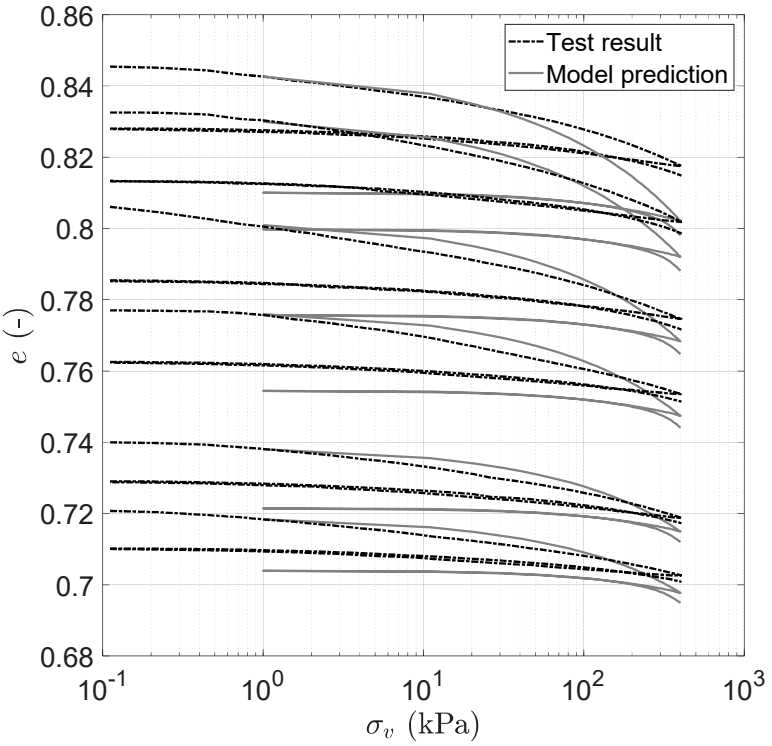


Figure 160: Load-unload oedometer tests for dense-very dense sand versus numerical prediction

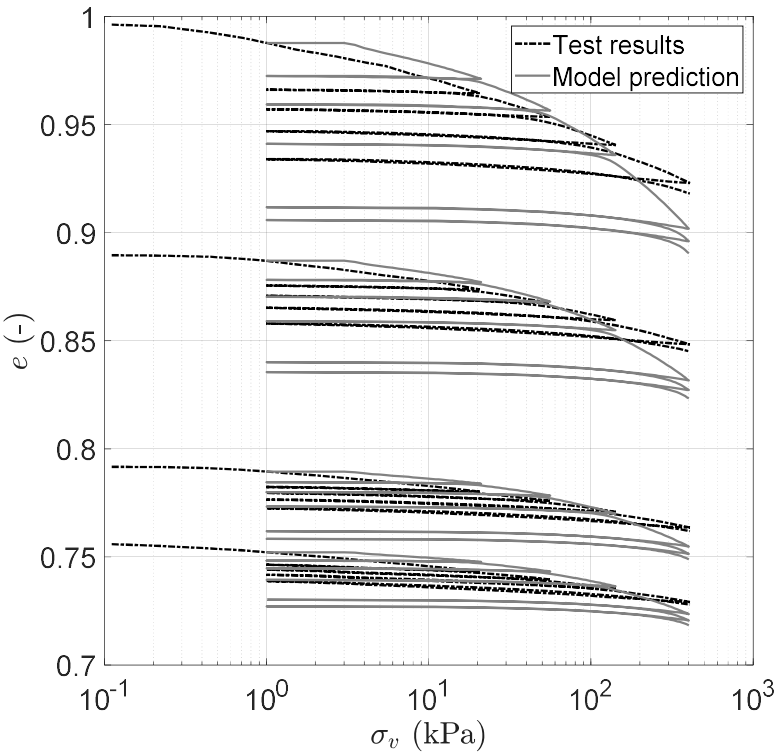


Figure 161: Cyclic oedometer tests versus numerical prediction

4.2.2.5. Strain-controlled undrained cyclic triaxial tests

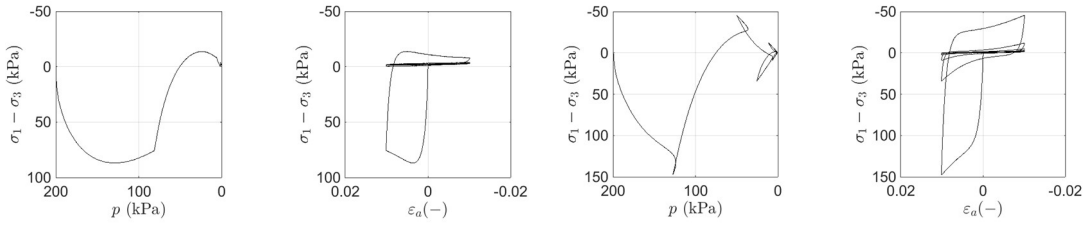
This section presents the model predictions for 23 axially strain-controlled undrained cyclic triaxial tests. The results are divided into two groups according to the amplitude of loading (small and large amplitudes). All tests are performed under symmetric strain-controlled conditions, where the large amplitude tests correspond to amplitudes ranging from 5E-2 to 1E-2, while small amplitudes tests are characterized by amplitudes between 5E-4 to 1E-3. In order to capture the response more accurately, the goal functions and limit surface curvature have been adapted to improve the prediction for the large amplitude tests. Moreover, in order to capture the behaviour for small strain amplitudes the intergranular strain rule defined in 4.1.3 has been included. The parameters used for the following tests are show in Table 23.

Table 23: Parameters determined with cyclic undrained triaxial test

Main rule	e_{c0}	e_{d0}	h_s	n	α	β	XV	YF	ZF	ϑ	S_f	ob_{min}	ob_{max}	δ
	1.0	0.55	4E5	0.45	0.15	2.5	0.53	0.77	0.24	0.7	4	-1.7	0.1	1.6
Inter	R	βr	Mv)	Md	X									
	3E-4	0.5	2.0	2.0	4.0									

(a) Large amplitudes

Of the 23 axial strain controlled undrained tests in the database, 9 correspond to tests with large amplitudes. The set explores different initial densities, from dense to loose states, and various initial stresses, particularly at different initial J/p' ratios. Figure 162 presents a summary of these tests, indicating their respective number (from 15 to 23).



(15) (16)

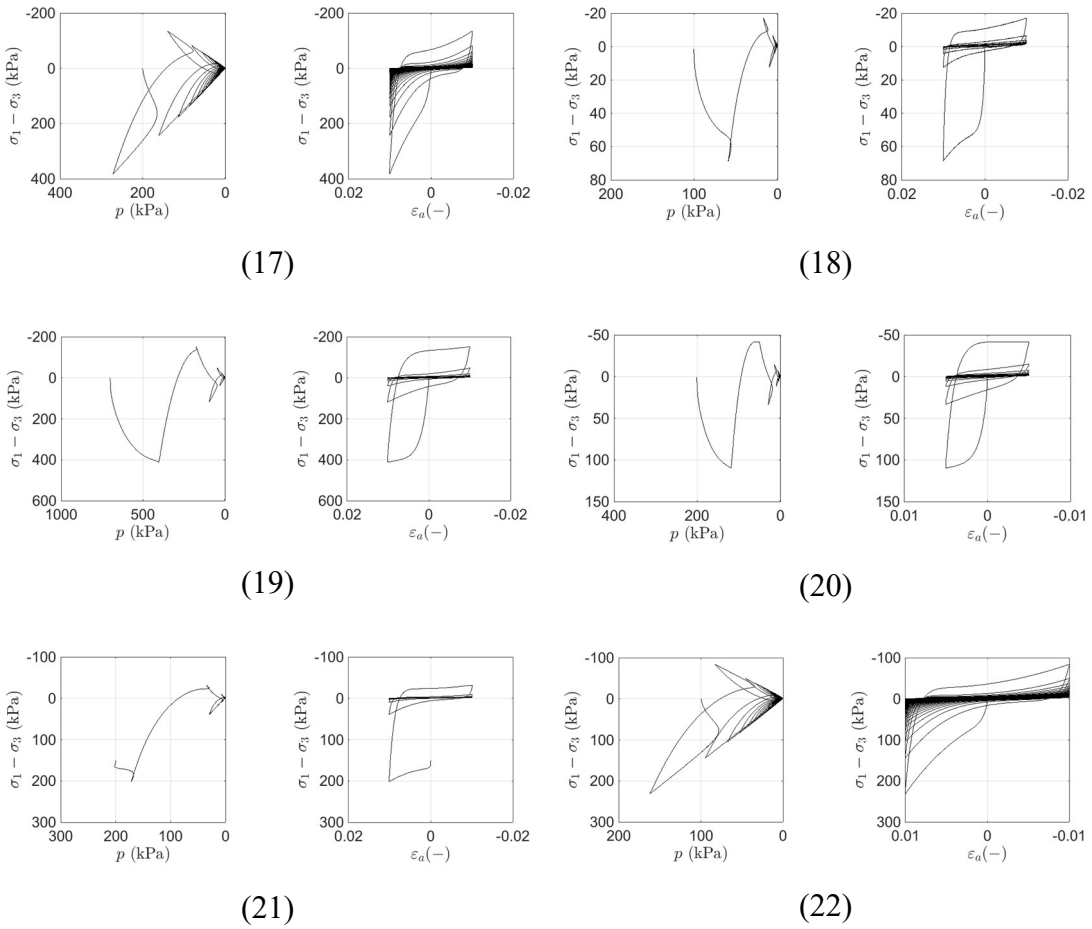


Figure 162: Large amplitude undrained strain controlled triaxial tests

The stress path on each cycle is characterised by an initial contractant stage followed by a dilatant stage, leading to the butterfly shape typically observed in this type of tests. Adjustments to the limit and goal functions can be performed to simulate accurately this aspect of the soil response. However, they must be carefully chosen as the nature of the model is to search for a stable cycle under strain controlled conditions (e.g. Figure 164, Figure 165, Figure 170). In effect, from a perspective of the formulation of the model, this type of tests are challenging as they go against the nature of this type of models, as NLKH under strain controlled conditions tends to search for a stable stress path. Therefore, the butterfly shape can only be achieved if the input parameters do not allow a stable cycle to exist, or if such stable cycle can only be found at very small mean effective stress levels (e. g. Figure 163, Figure 167, Figure 168).

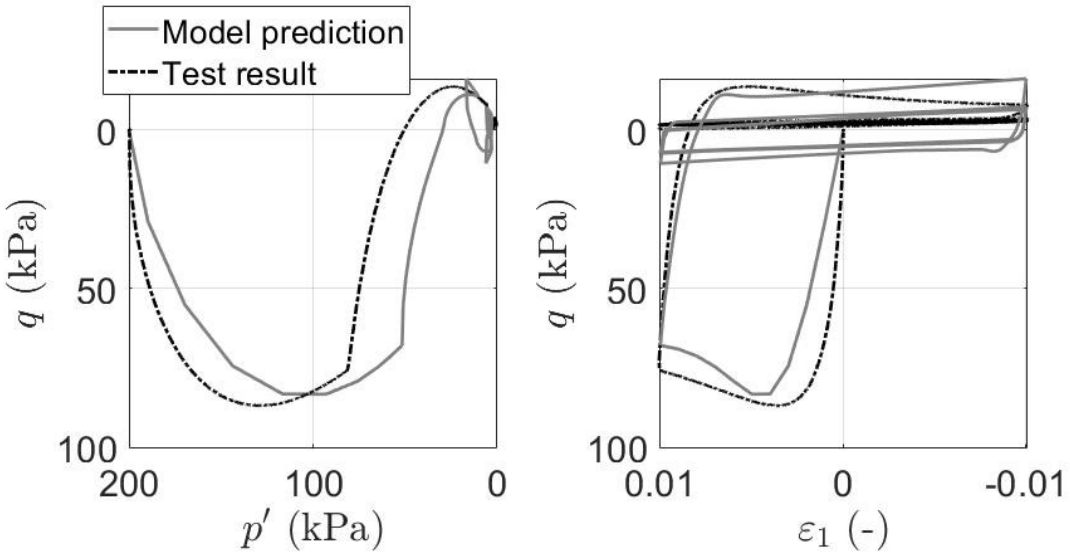


Figure 163: Large amplitude undrained strain controlled triaxial test 15 against numerical prediction

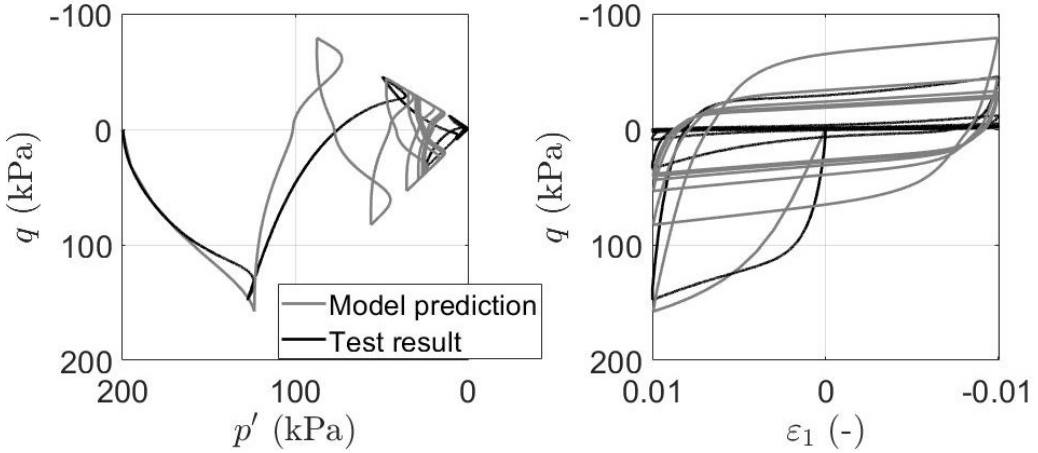


Figure 164: Large amplitude undrained strain controlled triaxial test 16 against numerical prediction

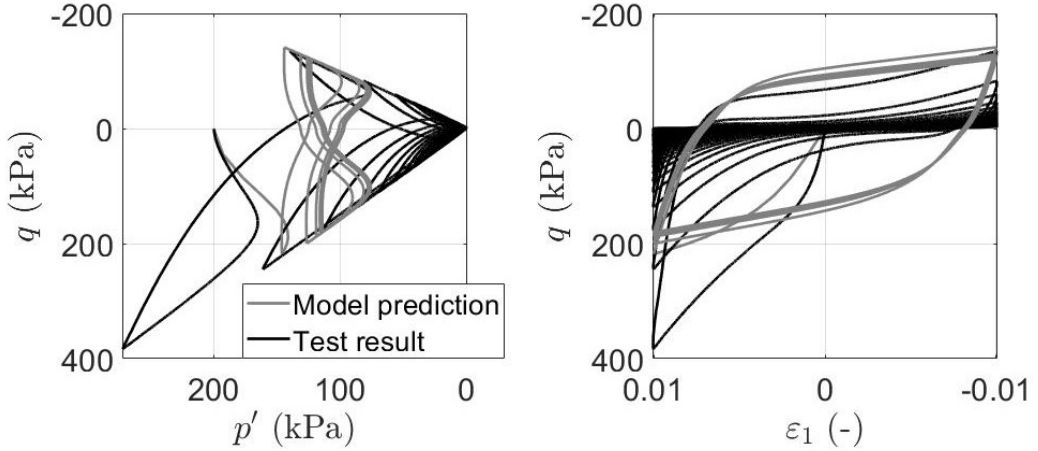


Figure 165: Large amplitude undrained strain controlled triaxial test 17 against numerical prediction

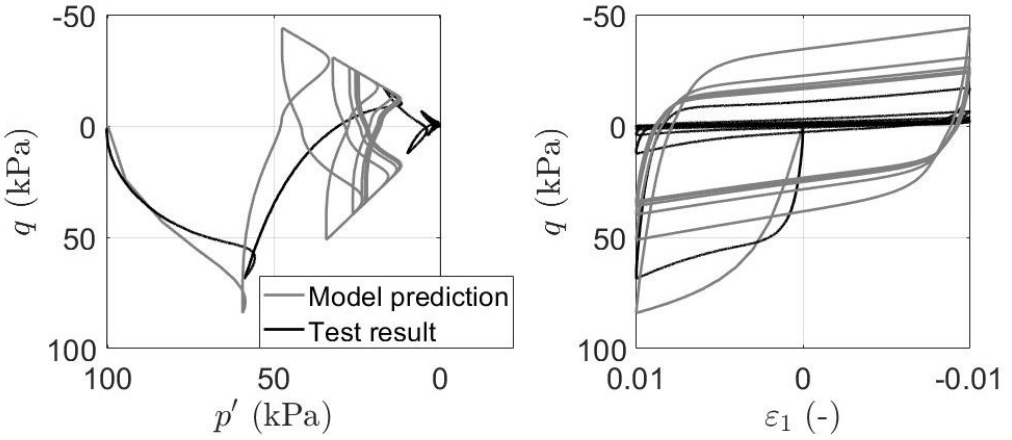


Figure 166: Large amplitude undrained strain controlled triaxial test 18 against numerical prediction

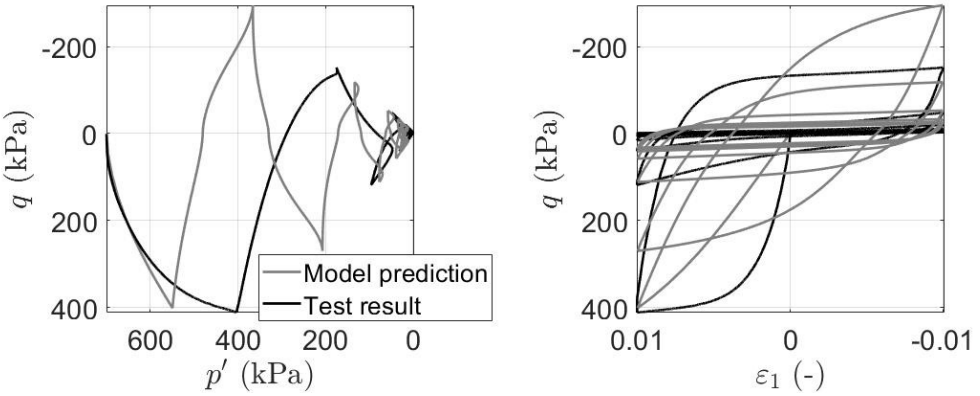


Figure 167: Large amplitude undrained strain controlled triaxial test 19 against numerical prediction

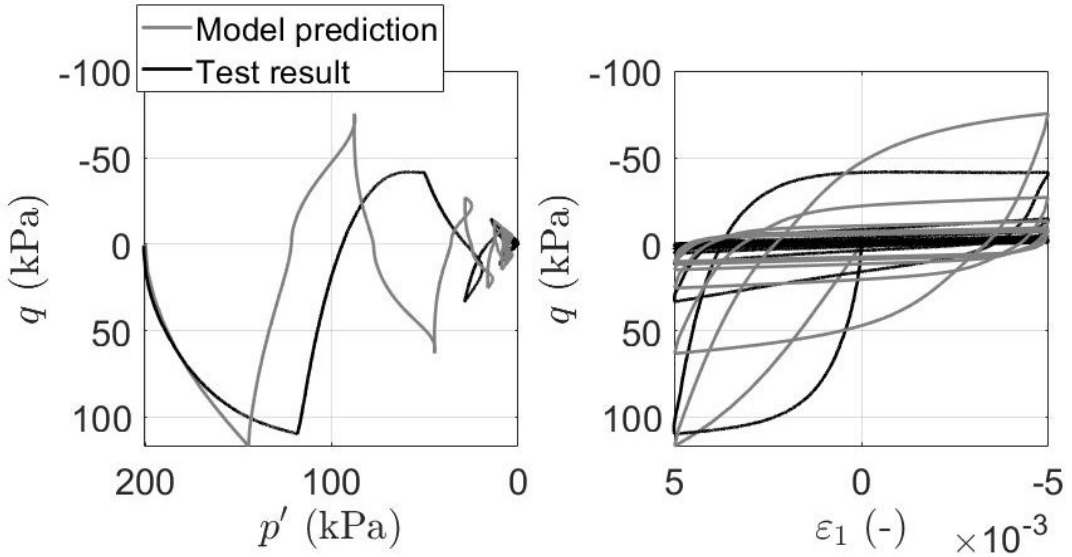


Figure 168: Large amplitude undrained strain controlled triaxial test 20 against numerical prediction

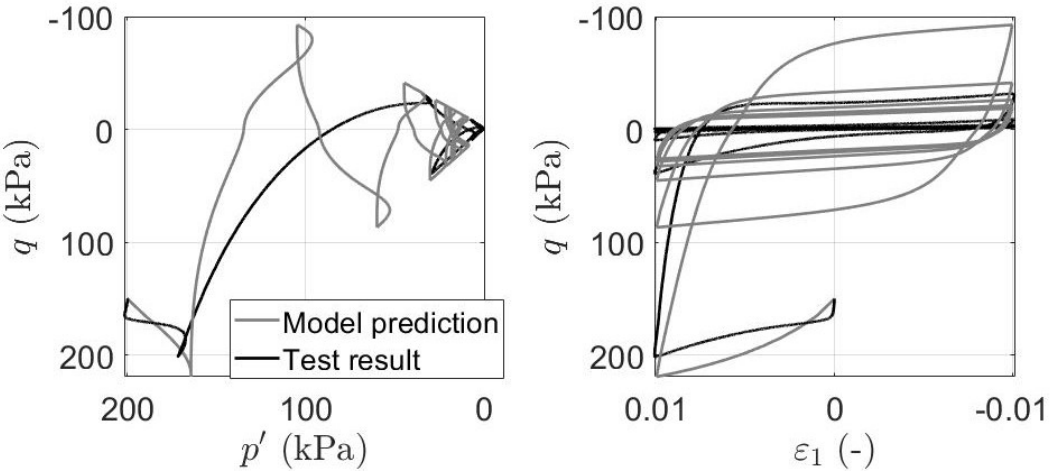


Figure 169: Large amplitude undrained strain controlled triaxial test 21 against numerical prediction

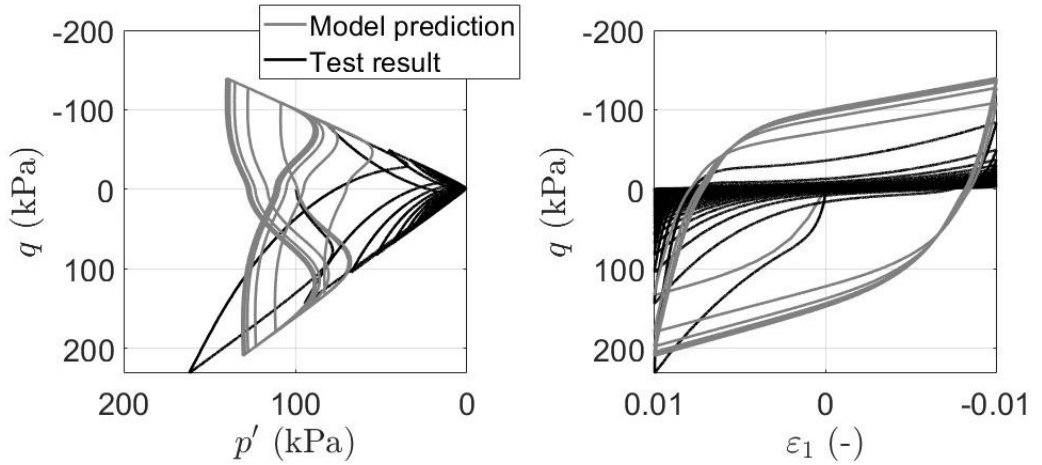


Figure 170: Large amplitude undrained strain controlled triaxial test 22 against numerical prediction

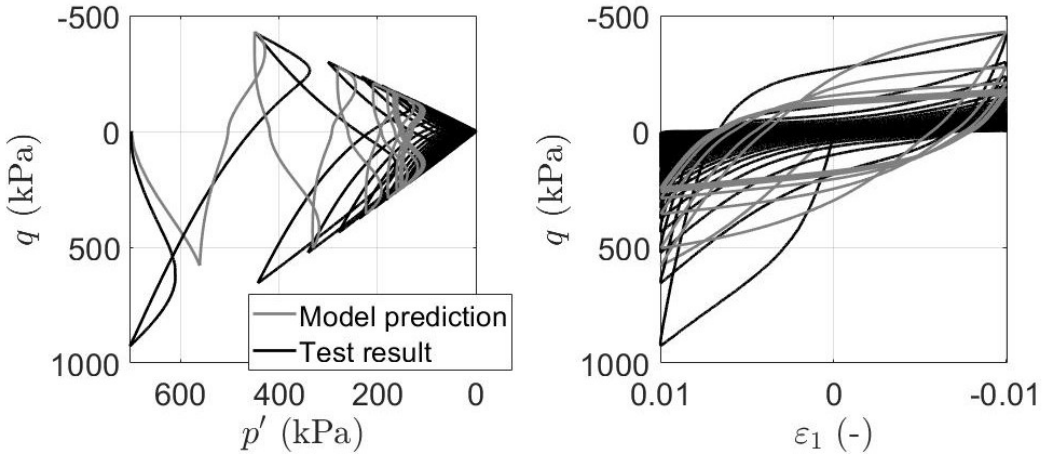
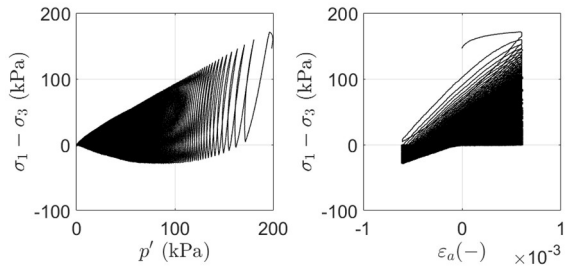


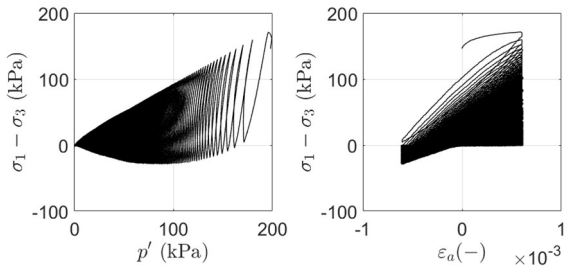
Figure 171: Large amplitude undrained strain controlled triaxial test 23 against numerical prediction

(b) Small amplitudes

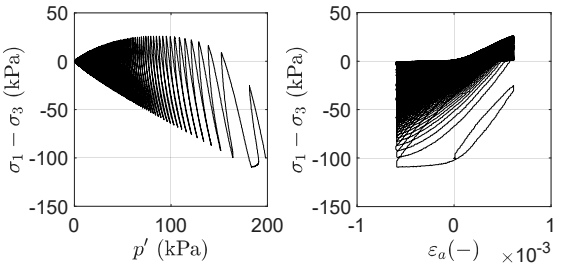
The database also includes 14 strain-controlled undrained triaxial tests with small amplitudes, under a significant number of cycles (>100). The set explores the effects of different initial densities, from dense to loose states, and various initial stresses, particularly at different initial J/p' ratios. All tests are performed under symmetric axial strain control conditions, with amplitudes varying between 5E-4 to 1E-3. Figure 172 summarises the whole set of tests, indicating their respective number.



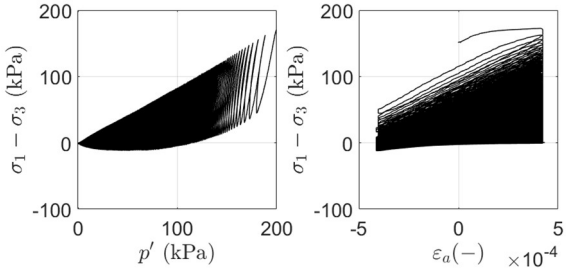
(1)



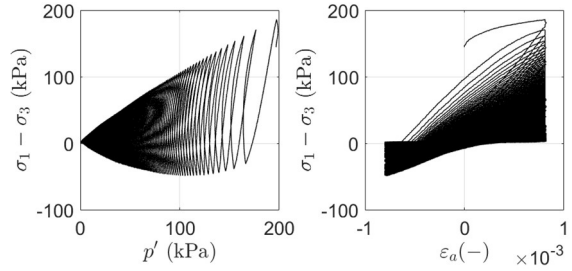
(2)



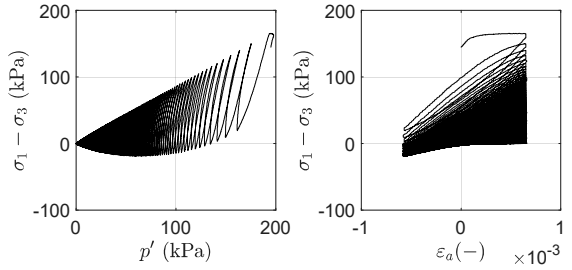
(3)



(4)



(5)



(6)

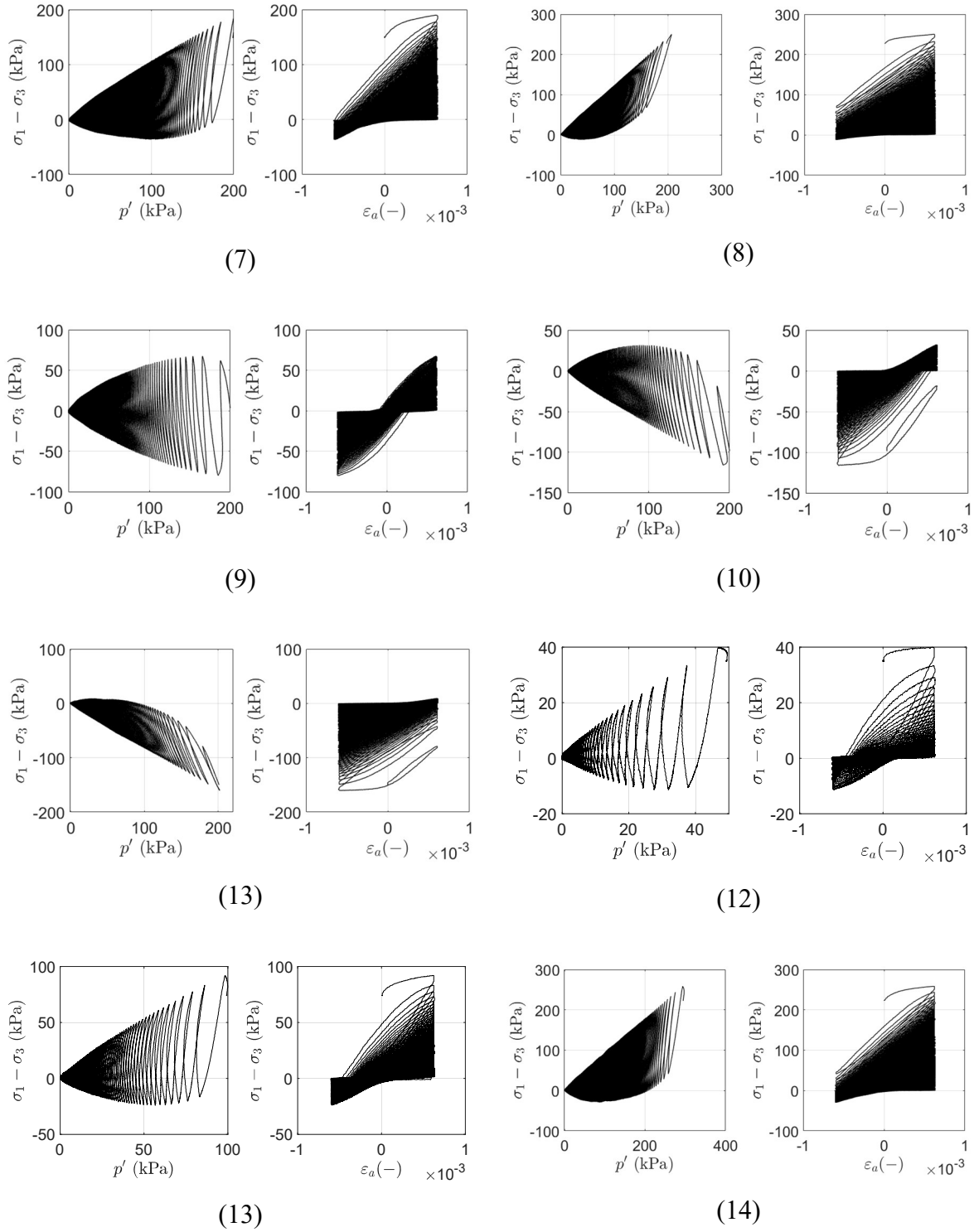


Figure 172: Small amplitude undrained strain controlled triaxial tests

It can be clearly seen in Figure 172 that for low amplitudes an increase in pore pressure over each cycle is produced. All stress path travel towards a mean effective stress of 0 kPa. The data can be processed to obtain the average stress of each cycle and therefore account for the stress

change over each cycle. Figure 173 shows the stress relaxation in p'- q space over the number of cycles. In terms of calibration, the main rule already accounts for stress relaxation in stress points below the critical state line, as the trace of the goal function of the main rule is negative when $f_d Y < 1$. In this sense, the limitation of the model lies in the fact that under a unique hardening rule the ratcheting (and therefore the reduction of mean stress with the numebr of cycles) becomes excessive. Therefore to improve the model predictions the intergranular strain rule has been used to adjust the magnitude of ratcheting. Figure 173 shows a the average mean stress and deviatoric stress of each cycle for the 14 tests shown in Figure 172, as an indicator on how much the stress cycle travels to a mean average value of zero.

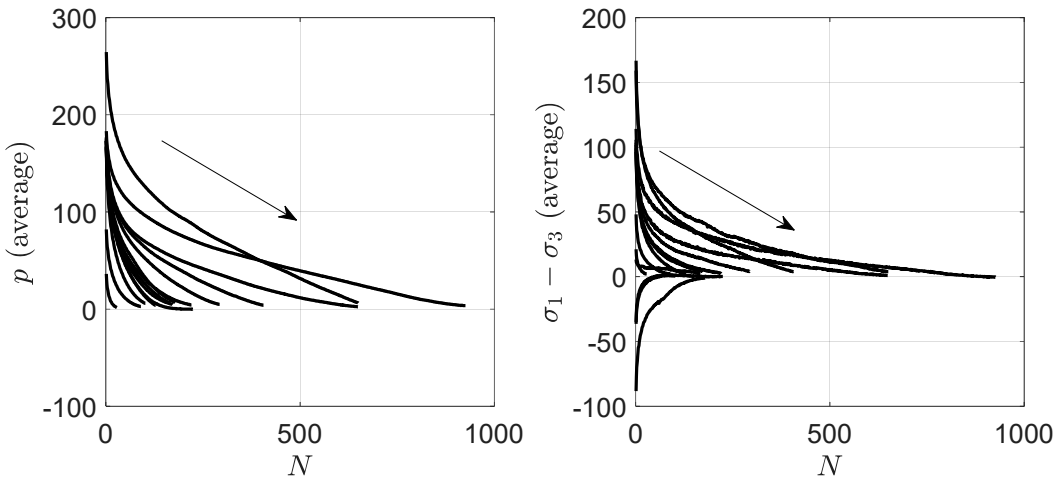


Figure 173: Stress relaxation over number of cycles for cyclic undrained strain controlled test

Figure 174 to Figure 187 show the model predictions when the intergranular strain rule is activated. The response is shown in terms of the variations of average mean stress and deviatoric stress with the number of cycles, as an illustration of the direction along which the average stress relaxes. In general, it can be observed how the intergranular rule reduces ratchetting as it acts by scaling the recall term. Nevertheless, the direction at which the stress relaxes per cycle is still governed by the goal function and the mapping tensor. Further improvements in this response can be achieved with extra hardening rules that act locally on the direction of the recall term, an issue which has been left for future study.

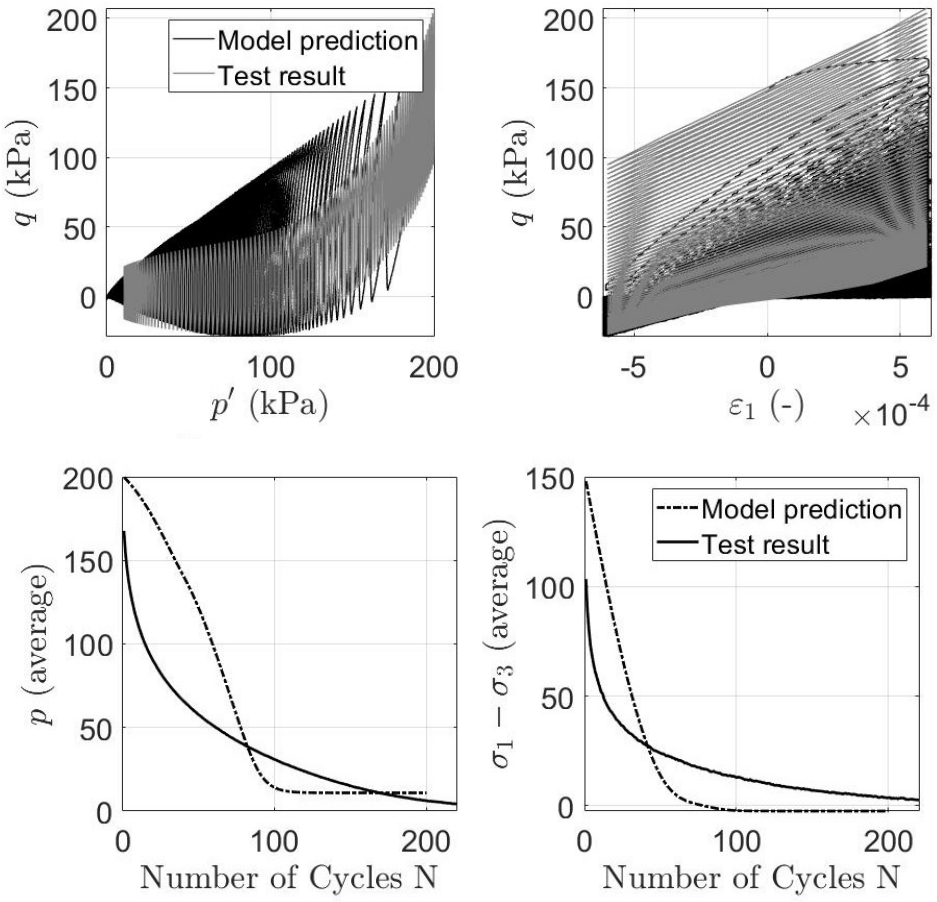
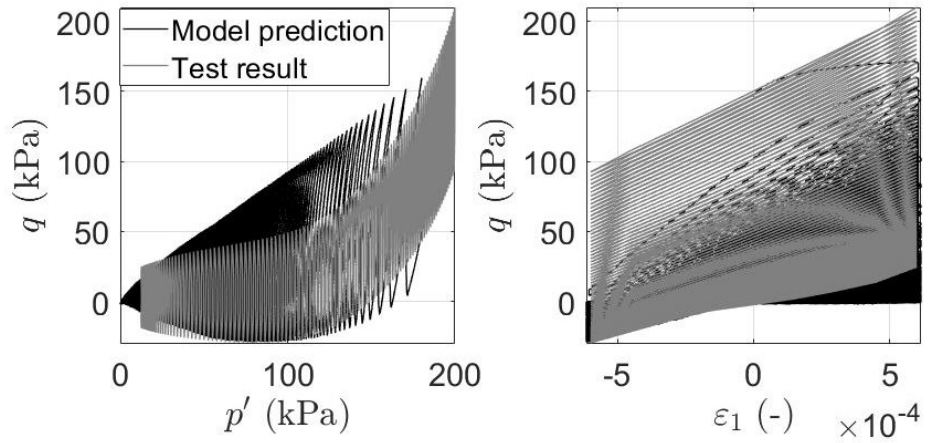


Figure 174: Small amplitude undrained strain controlled triaxial test 1 against numerical prediction



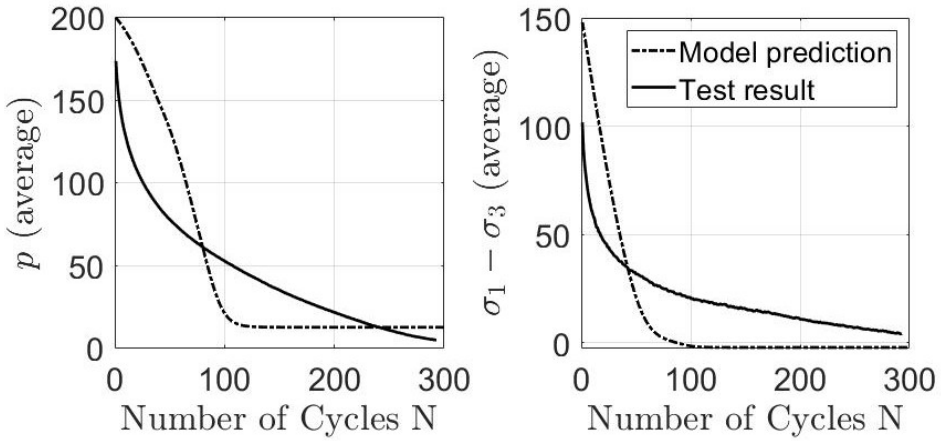


Figure 175: Small amplitude undrained strain controlled triaxial test 2 against numerical prediction

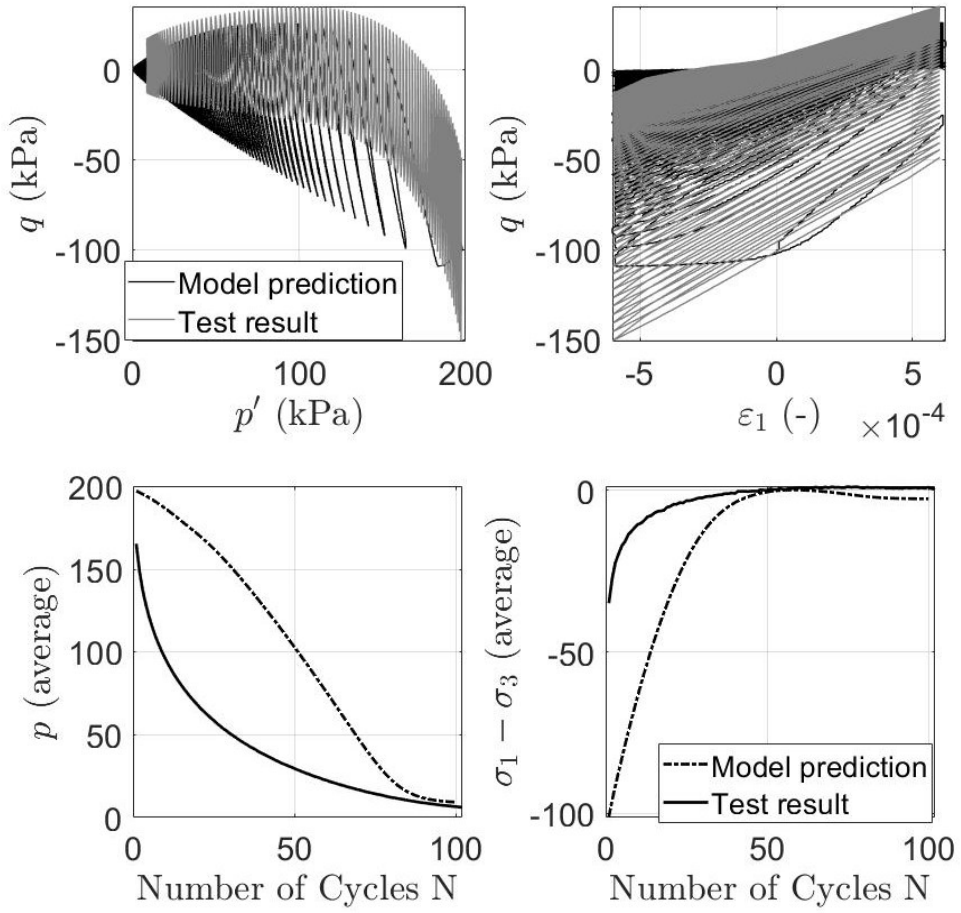


Figure 176: Small amplitude undrained strain controlled triaxial test 3 against numerical prediction

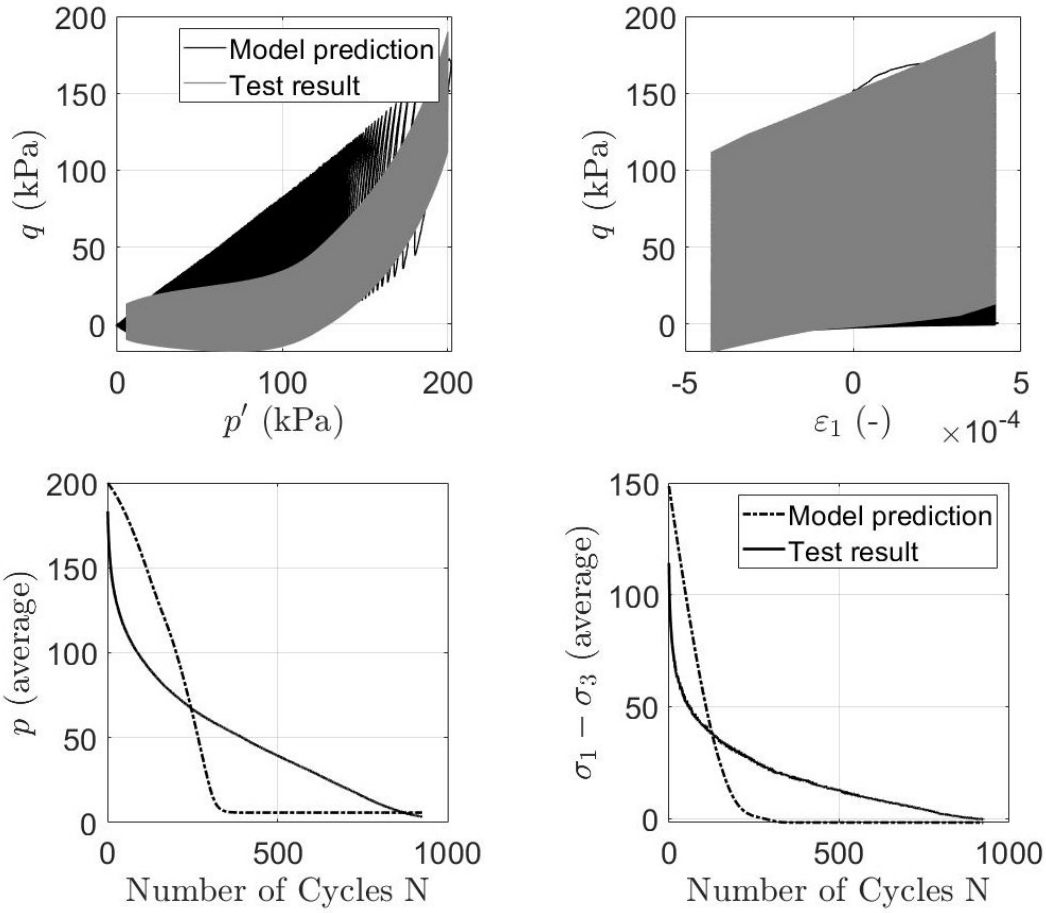
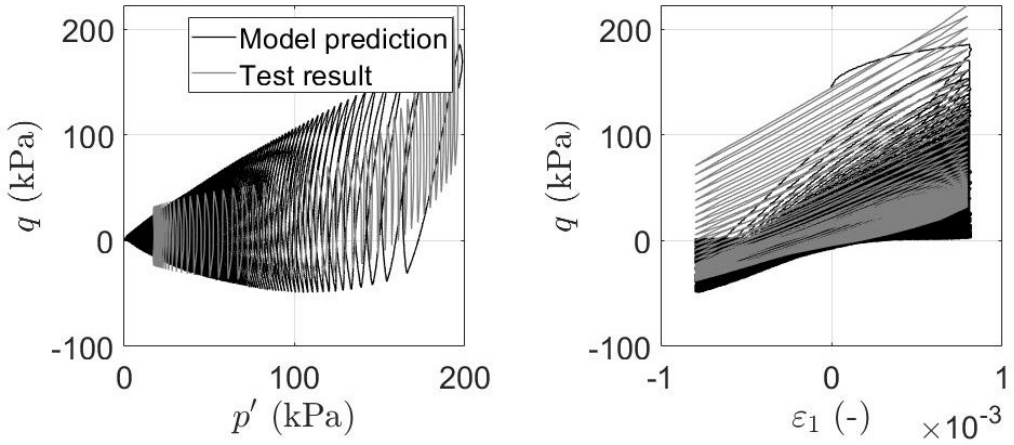


Figure 177: Small amplitude undrained strain controlled triaxial test 4 against numerical prediction



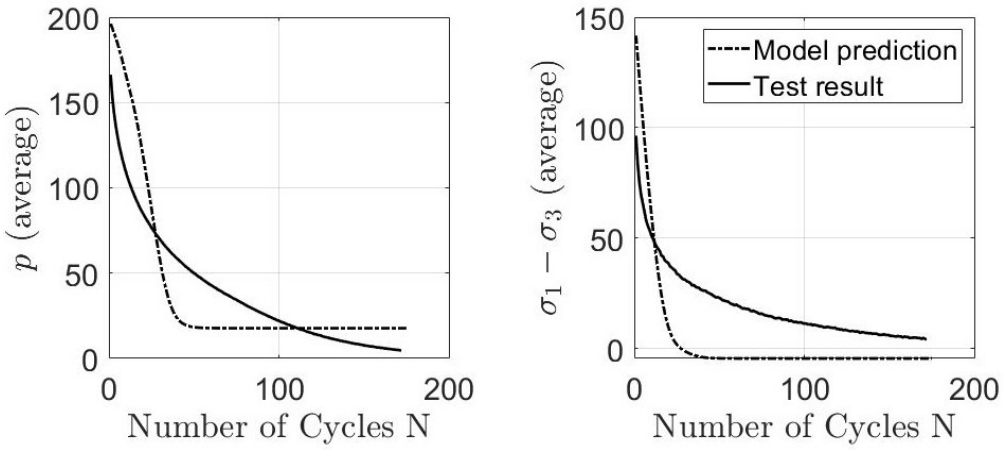


Figure 178: Small amplitude undrained strain controlled triaxial test 5 against numerical prediction

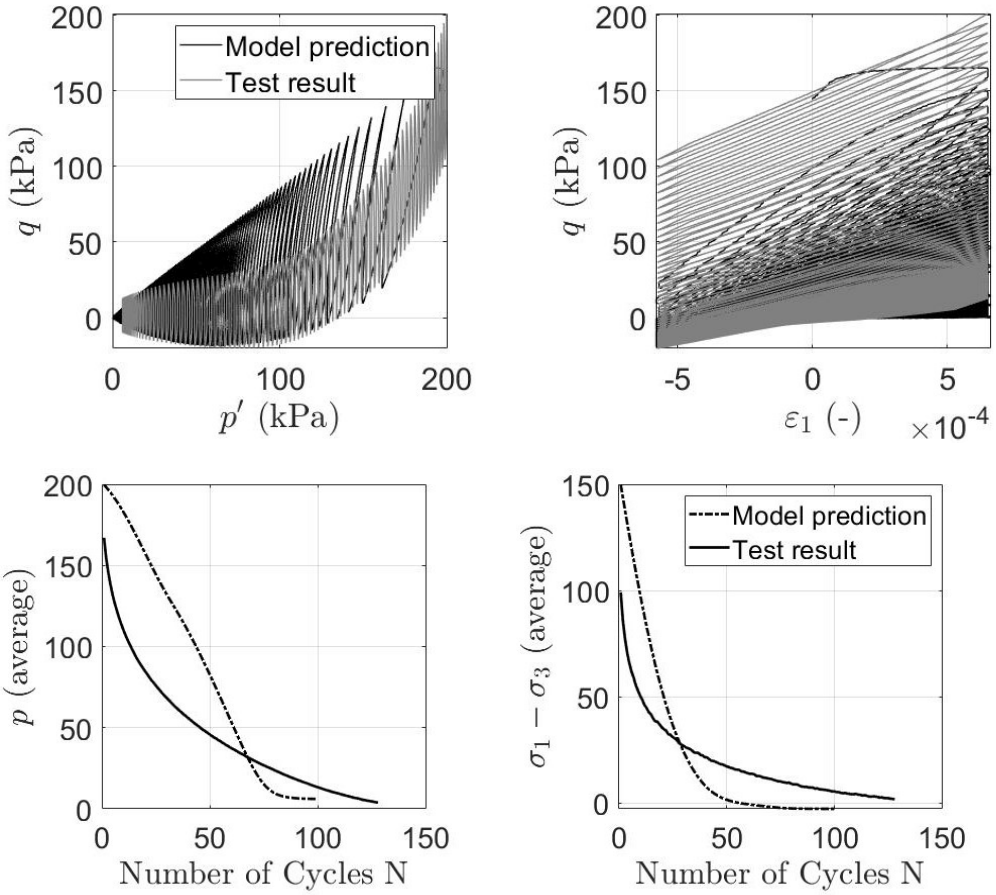


Figure 179: Small amplitude undrained strain controlled triaxial test 6 against numerical prediction

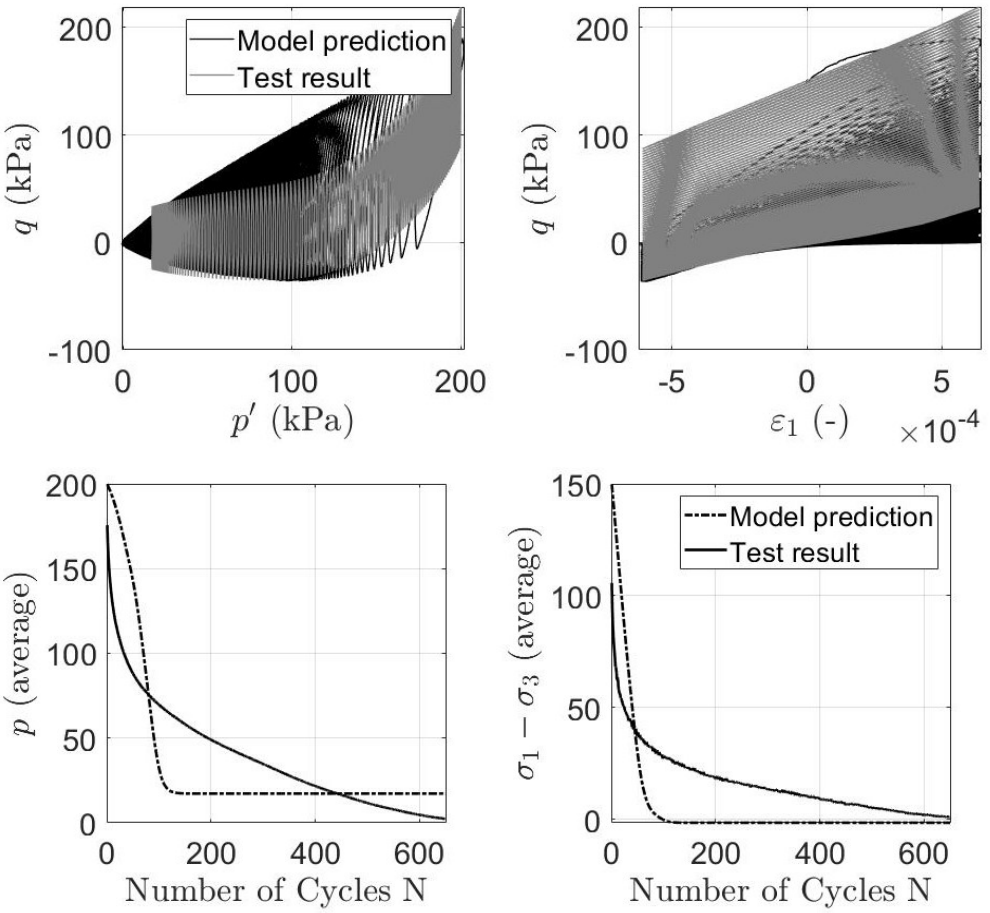
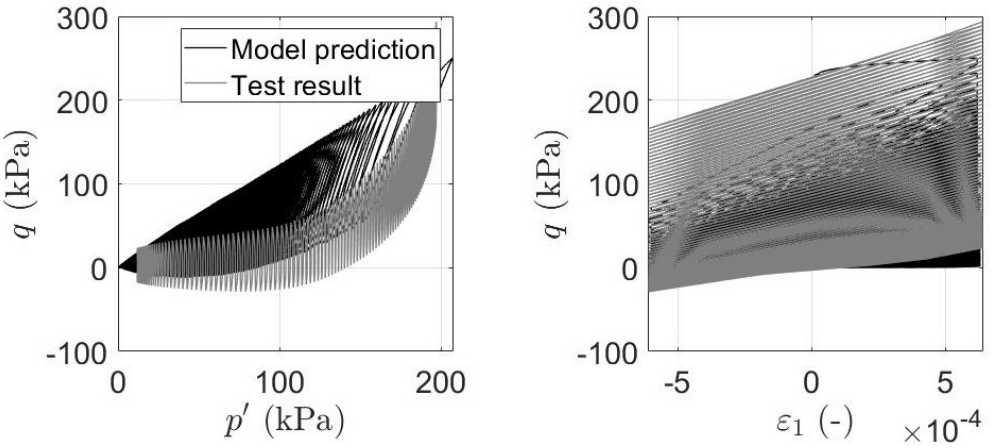


Figure 180: Small amplitude undrained strain controlled triaxial test 7 against numerical prediction



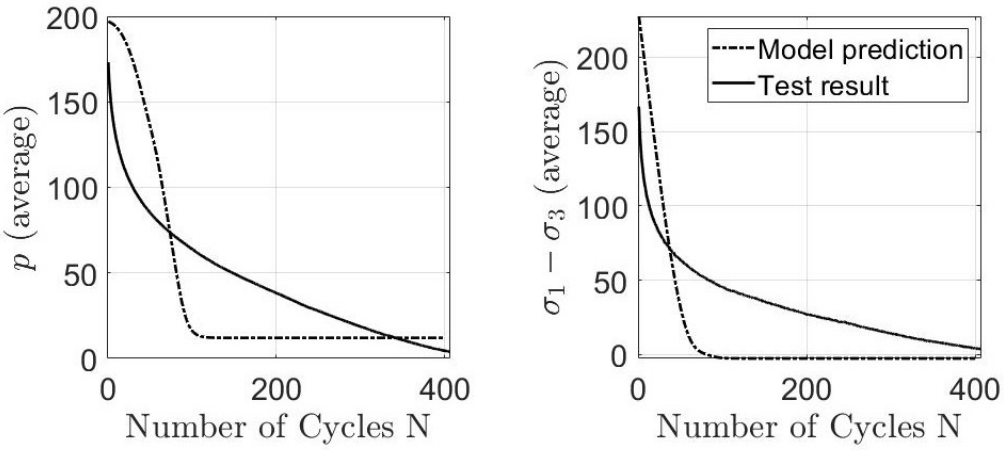


Figure 181: Small amplitude undrained strain controlled triaxial test 8 against numerical prediction

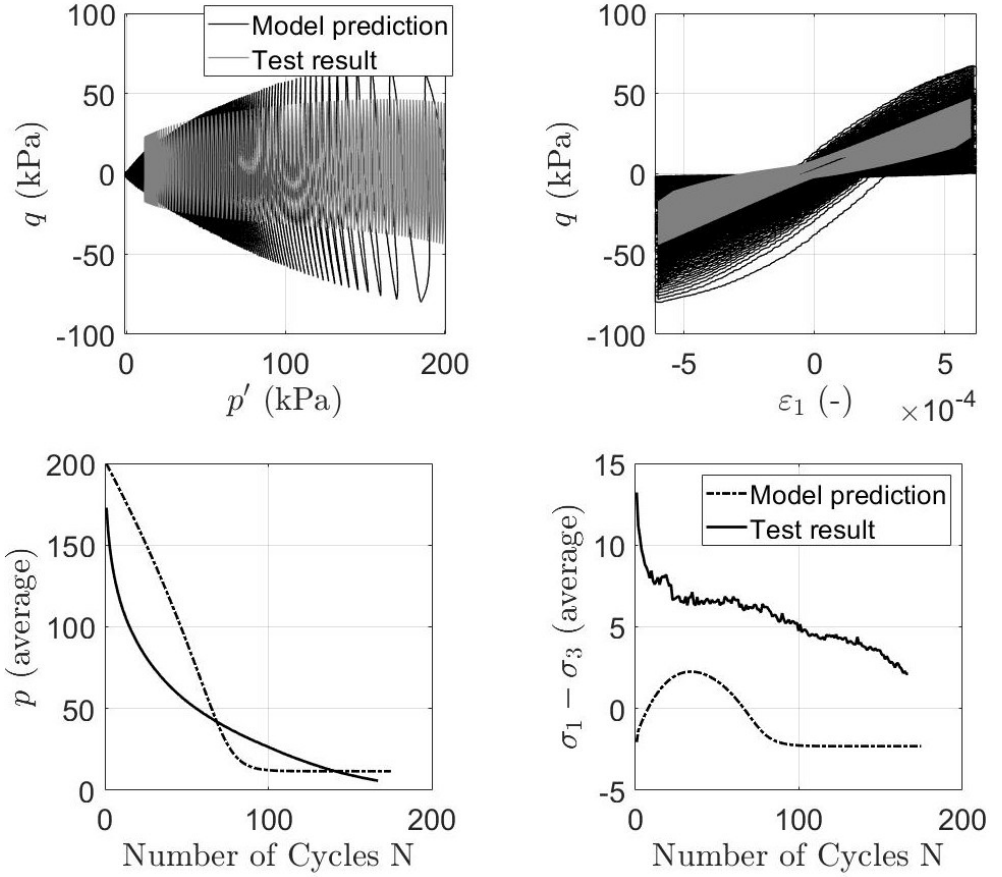


Figure 182: Small amplitude undrained strain controlled triaxial test 9 against numerical prediction

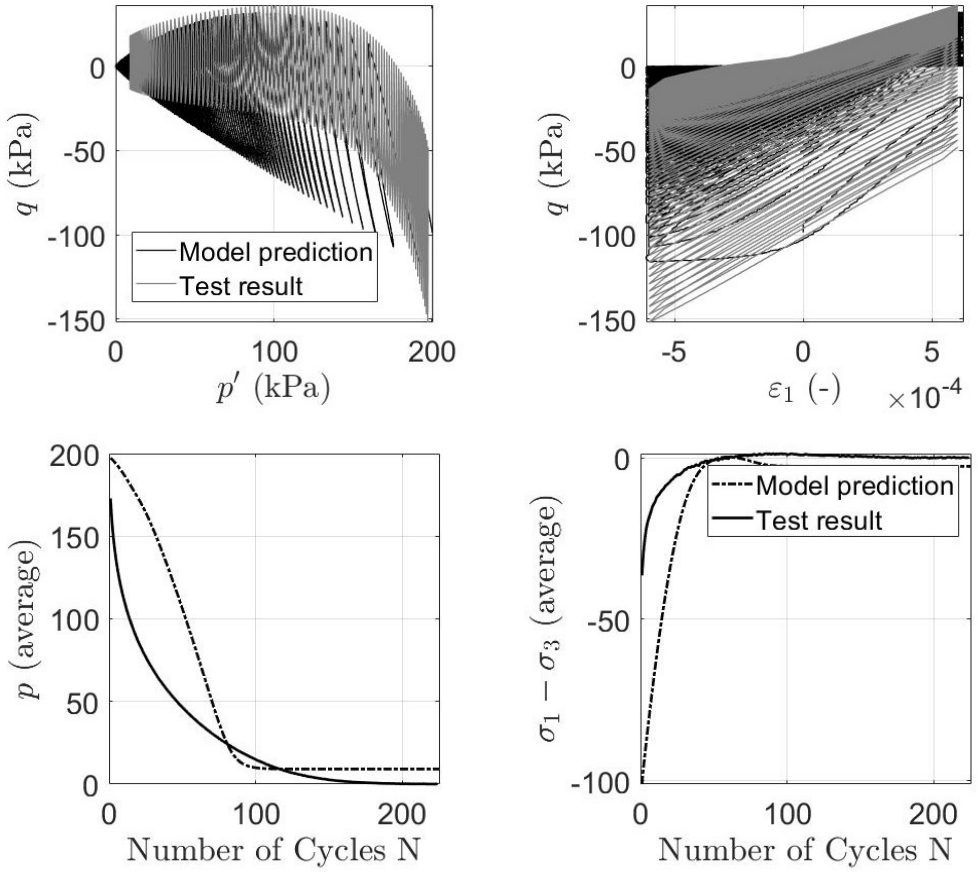
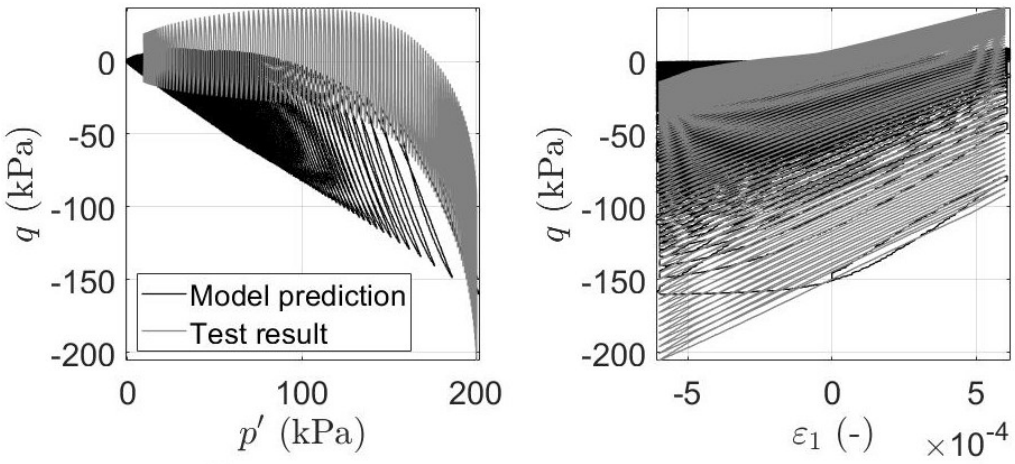


Figure 183: Small amplitude undrained strain controlled triaxial test 10 against numerical prediction



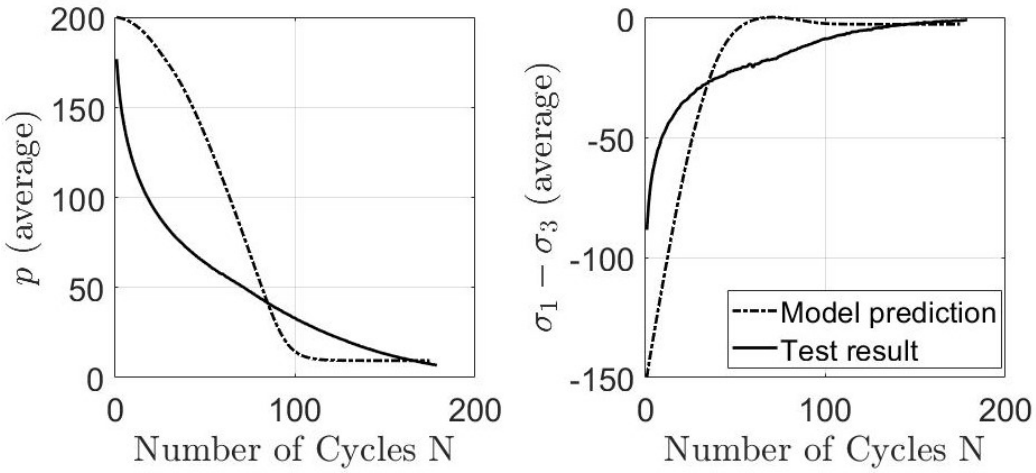


Figure 184: Small amplitude undrained strain controlled triaxial test 11 against numerical prediction

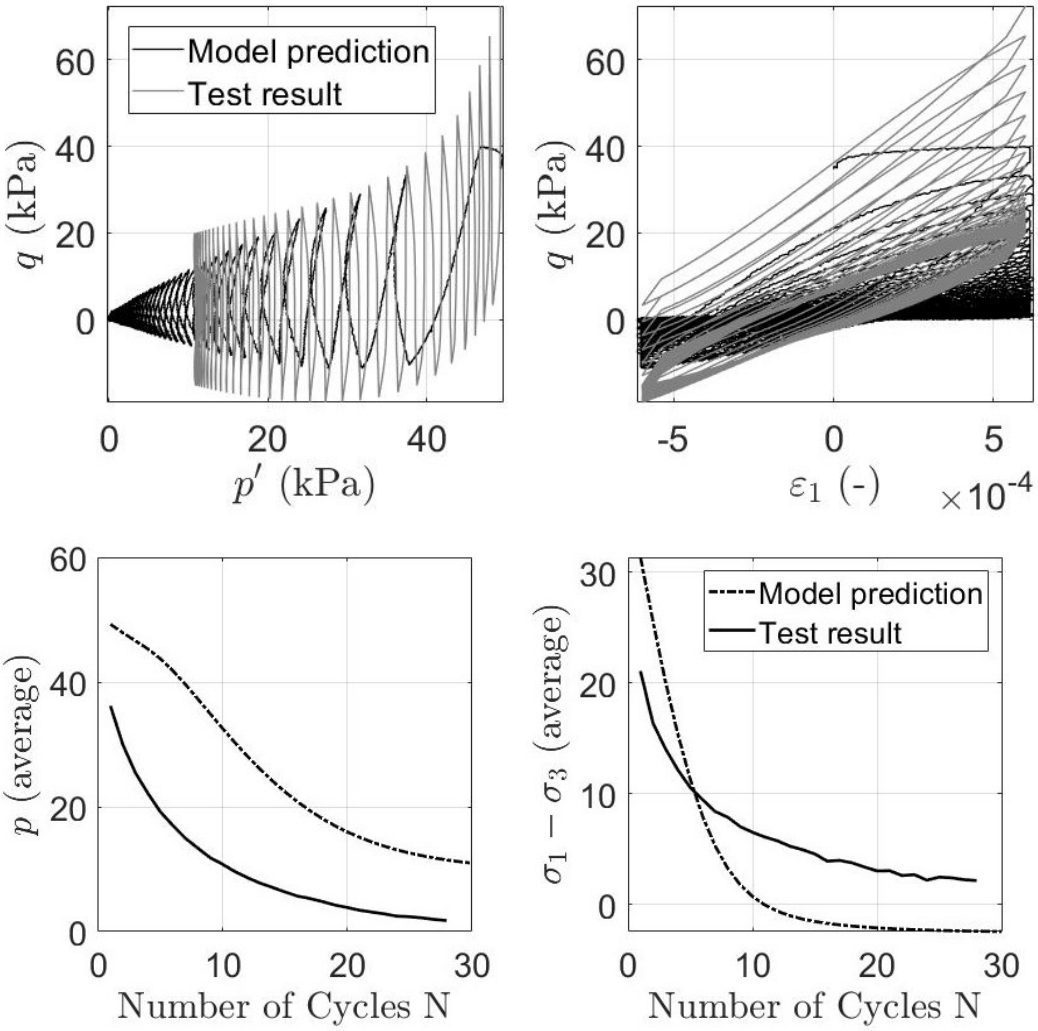


Figure 185: Small amplitude undrained strain controlled triaxial test 12 against numerical prediction

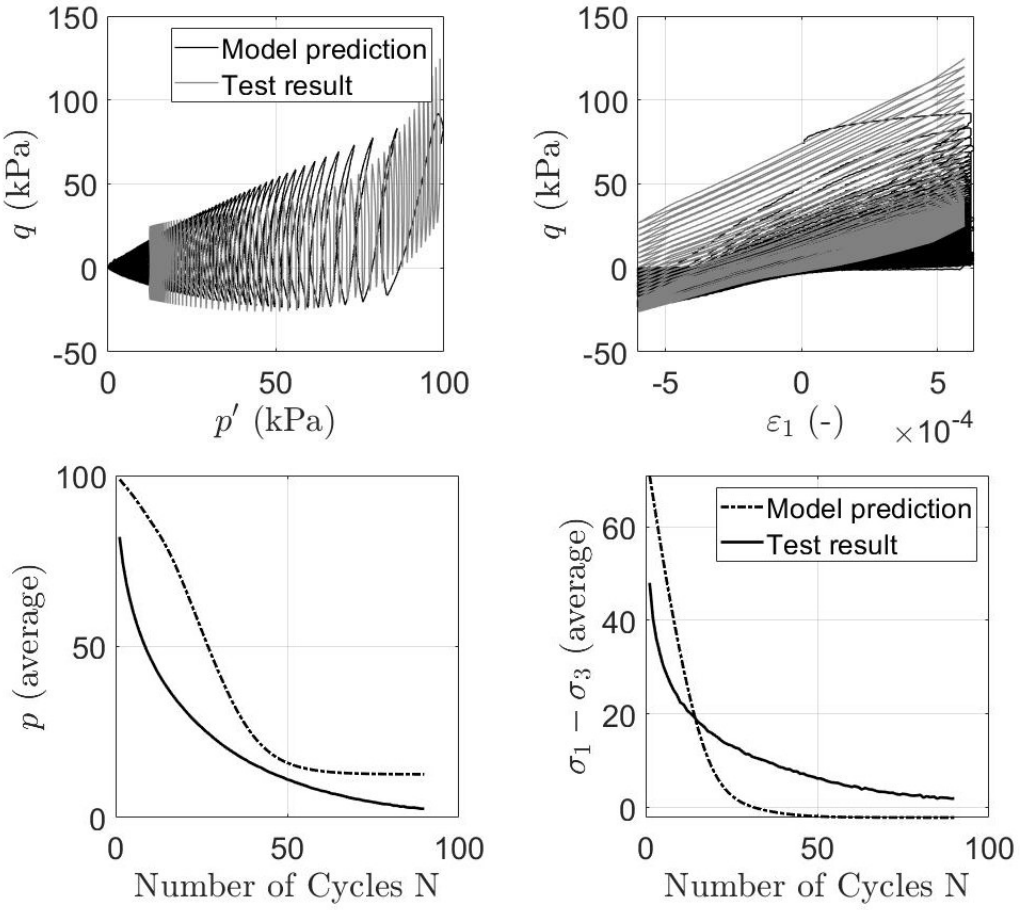
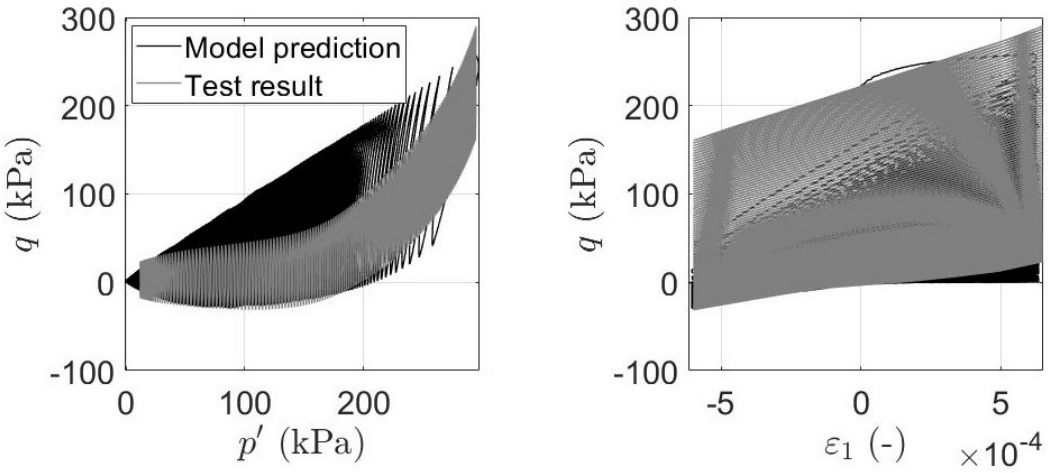


Figure 186: Small amplitude undrained strain controlled triaxial test 13 against numerical prediction



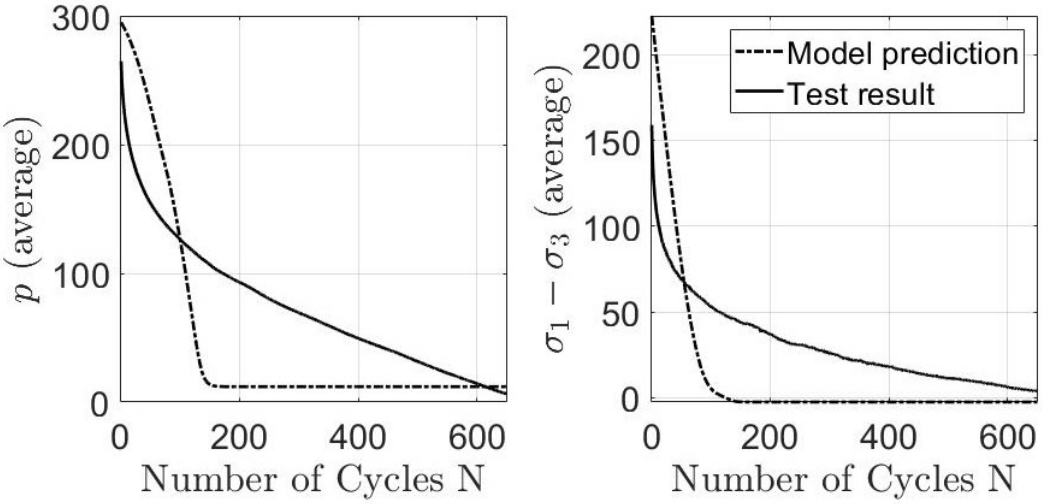


Figure 187: Small amplitude undrained strain controlled triaxial test 14 against numerical prediction

4.3. ADVANCED FE IMPLEMENTATION FEATURES

The material model described above and used at a single integration point has been implemented into the finite element software ICFEP (Potts and Zdravkovic, 1999) for the study of boundary value problems presented in Chapter 5. The coding structure of ICFEP requires the local integration at the Gauss point level to be explicit, therefore the algorithm employed to integrate the local equations is a sub-stepping algorithm (Sloan, 1987) and is combined with the drift correction of (Potts and Gens, 1985), as detailed in 3.2.4.

4.3.1. MODIFICATIONS FOR THE TENSILE REGION

The nature of the modelling framework enforces the backstress to travel towards a zero mean effective stress when the obliquity of the strain path is positive. Although this is consistent with asymptotic theory and with soil behaviour (e.g. liquefaction) numerical problems arise when the hardening rule is evaluated at a value of mean backstress equal to, or greater than, zero. This results from the sub-stepping algorithm requiring a second evaluation of the hardening rule at an Euler forward estimate, which may not fulfil the consistency condition. Therefore, even if the step is rejected it may evaluate the hardening rule in an undesirable region of the stress space, triggering numerical errors (or NaN evaluations). To overcome this issue, a threshold value is defined where the hardening rule switches to a purely deviatoric part, which creates a limit region equivalent to a Van Eekelen – Von Mises cone. The modification can be implemented as a condition within the sub-stepping algorithm, where if the mean backstress value is below a tolerance limit and $n_{kk} - f_d \tilde{Y} \vec{\Upsilon}_{kk} > 0.0$, the hardening rule becomes

$$\dot{\alpha}_{kk} = f_p f_e \left(\alpha_{kk} n_{ij}^* - \frac{\alpha_{ij}^*}{\sqrt{2} g(\theta)^{(k)}} \left\| n_{ij}^* \right\| \right) \tag{4.8}$$

Otherwise, the standard hardening rule is used. The model has been integrated in boundary value problems with a tolerance value in the range of 0.1 to 3, and is recommended to be linked to the size of the yield surface, m.

4.3.2. BACKSTRESS PERTURBATIONS: SAFETY FACTOR

The consistency condition enforces the stress to follow the same direction as the sum of backstresses. This proves advantageous because the backstress is an internal variable whose rate form can be defined more freely as long as it complies with the second principle of thermodynamics. The concept of safety factor can be included following a methodology similar to the one described in Potts and Zdravkovic (2012), where the safety factor is introduced as an extra history variable in the formulation of the yield surface. The family of models presented here does not use the yield surface to account for the limit states, instead the mathematical form of the hardening rule defines a set of asymptotic attractors to account for it. Therefore, the safety factor (SF) has to be included in the formulation of the hardening rule, resulting in the following differential form:

$$\Delta\alpha_{ij} = \Delta\lambda h_{ij}(\vec{n}_{ij}, \alpha_{ij}, SF) + \frac{\partial h_{ij}(\vec{n}_{ij}, \alpha_{ij}, SF)}{\partial SF}\Delta SF \tag{4.9}$$

where

$$h_{ij}(\vec{n}_{ij}, \alpha_{ij}, SF) = f_e f_b L_{ijkl}\left(\vec{n}_{kl} - f_d \tilde{Y}(SF)\vec{\Upsilon}_{kl}(SF)\right) \tag{4.10}$$

Using expression (4.9) the consistency condition can be rewritten as:

$$n_{ij}\left(\Delta\sigma_{ij} - \Delta\alpha_{ij}\right) = 0 \tag{4.11}$$

Rearranging, the plastic multiplier becomes

$$\Delta\lambda = \frac{n_{ij}D^e_{ijkl}\Delta\varepsilon_{kl} - n_{ij}\dfrac{\partial h_{ij}(\vec{n}_{ij}, \alpha_{ij}, SF)}{\partial SF}\Delta SF}{n_{ij}D^e_{ijkl}\vec{n}_{kl} + n_{ij}h_{ij}(\vec{n}_{ij}, \alpha_{ij}, SF)} \tag{4.12}$$

Due to the fact that:

$$\Delta\sigma_{ij} = D^e_{ijkl}\Delta\varepsilon_{kl} - \Delta\lambda D^e_{ijkl}\vec{n}_{kl} \tag{4.13}$$

then

$$\Delta\sigma_{ij} = \underbrace{\left(D^{e}_{ijkl} - \frac{n_{pq} D^{e}_{pqij} D^{e}_{kltz} \vec{n}_{tz}}{n_{ij} D^{e}_{ijkl} n_{kl} + n_{ij} h_{ij}(\vec{n}_{ij}, \alpha_{ij}, SF)} \right)}_{D^{ep}_{ijkl}} \Delta\varepsilon_{kl} + \underbrace{\frac{n_{ij} \dfrac{\partial h_{ij}(\vec{n}_{ij}, \alpha_{ij}, SF)}{\partial SF} D^{e}_{ijkl} \vec{n}_{kl}}{n_{ij} D^{e}_{ijkl} n_{kl} + n_{ij} h_{ij}(\vec{n}_{ij}, \alpha_{ij}, SF)} \Delta SF}_{\Delta\sigma^{SF}_{ij}} \tag{4.14}$$

Expression (4.14) shows that the stress increment will have the classical contribution, $D^{ep}_{ijkl} \cdot \Delta\varepsilon_{kl}$, plus the effect of the "numerical history" variable perturbation, in this case the safety factor, $\Delta\sigma^{SF}_{ij}$. For notation purposes the stress is redefined as in (4.15) in two components:

$$\begin{aligned}
\Delta\sigma_{ij} &= \Delta\sigma^{ep}_{ij} + \Delta\sigma^{SF}_{ij} \\
\Delta\sigma^{ep}_{ij} &= \left(D^{e}_{ijkl} - \frac{n_{pq} D^{e}_{pqij} D^{e}_{kltz} \vec{n}_{tz}}{n_{ij} D^{e}_{ijkl} n_{kl} + n_{ij} h_{ij}(\vec{n}_{ij}, \alpha_{ij}, SF)} \right) \Delta\varepsilon_{kl} \\
\Delta\sigma^{SF}_{ij} &= \frac{n_{ij} \dfrac{\partial h_{ij}(\vec{n}_{ij}, \alpha_{ij}, SF)}{\partial SF} D^{e}_{ijkl} \vec{n}_{kl}}{n_{ij} D^{e}_{ijkl} n_{kl} + n_{ij} h_{ij}(\vec{n}_{ij}, \alpha_{ij}, SF)} \Delta SF
\end{aligned} \tag{4.15}$$

Following the former structure, the safety factor or any other perturbation can be included as a right-hand-side external force vector without having to rearrange the formulation of the FE code. The right-hand side additional contribution that the perturbation of the hardening variable induces is computed easily as:

$$\Delta R^{SF} = \frac{1}{2} \int_{Vol} \left[B^{T} \right] \left\{ \Delta\sigma^{SF} \right\} dV \tag{4.16}$$

For simplicity, in the computation of the derivatives of the hardening rule, the change in the goal function with respect to the safety factor has been ignored. This is done as the goal function is a unitary tensor field and therefore any perturbation is orthogonal to itself, therefore resulting in a negligible value. As a result, the main component driving the reduction of capacity is the limit surface magnitude, where the safety factor comes in through $g(\theta)$. For the sand model, the perturbation of the backstress with respect to the SF is obtained through a simple chain rule. However, it should be noted that the derivative does not need to be exact for the safety factor and it could be defined arbitrarily as consistency is always enforced by (4.11):

$$\frac{\Delta h_{ij}(\vec{n}_{ij},\alpha_{ij},SF)}{\Delta SF}=\frac{\Delta h_{ij}}{\Delta \tilde{Y}}\frac{\Delta \tilde{Y}}{\Delta(g(\theta))}\frac{\Delta(g(\theta))}{\Delta SF} \tag{4.17}$$

where

$$Y=f_d\left(\frac{3\sqrt{2}}{2g(\theta)}\left\|\hat{\alpha}_{ij}^{*}\right\|\right)^{\vartheta}=f_d\tilde{Y} \tag{4.18}$$

For the Van-Eekelen deviatoric shape

$$g(\theta)=\frac{X}{(1+YF\,\sin 3\theta)^{Z}} \tag{4.19}$$

$$X=\frac{2\sqrt{3}(1-YF)^{Z}\sin\left(\tan^{-1}\left(\frac{\tan\varphi_{cs}}{FS}\right)\right)}{3-\sin\left(\tan^{-1}\left(\frac{\tan\varphi_{cs}}{FS}\right)\right)} \tag{4.20}$$

where

$$f_p=\frac{(1+e)\frac{h_s}{en}\left(\frac{\left|\sum_i \alpha_{kk}\right|}{h_s}\right)^{1-n}\left(1+1.75\tilde{Y}\left\|n_{ij}^{*}+k/3n_{kk}\delta_{ij}\right\|\right)}{1+\left|S_f-1\right|\left(1+1/3\left\|\hat{\alpha}_{ij}^{*}\right\|\right)} \tag{4.21}$$

Finally

$$\frac{\Delta h_{ij}}{\Delta \tilde{Y}}=-f_p f_e f_d\left(S_d\Upsilon_{ij}+\frac{(S_f-S_d)}{3}\Upsilon_{kk}\delta_{ij}+(S_f-S_d)\Upsilon_{kk}\hat{\alpha}_{ij}^{*}\right)$$

$$\frac{\Delta \tilde{Y}}{\Delta(g(\theta))}=-\vartheta\tilde{Y}\frac{1}{g(\theta)}$$

$$\frac{\Delta(g(\theta))}{\Delta SF}=-\frac{1}{(1+Y\sin 3\theta)^{Z}}\frac{\partial X}{\partial SF}$$

$$X = \frac{2\sqrt{3}x}{3-x}$$

$$x = \sin\left(\tan^{-1}\left(\frac{\tan\varphi_{cs}}{FS}\right)\right)$$

$$\frac{\partial X}{\partial x} = \frac{3(1-YF)^{Z}}{(3-x)^{2}}$$

$$\frac{\partial x}{\partial SF} = \frac{\sec^{2}(\varphi_{cs})}{FS\sqrt{\frac{\tan^{2}\varphi_{cs}}{FS^{2}}+1}} - \frac{\tan^{2}(\varphi_{cs})\sec^{2}(\varphi_{cs})}{FS^{3}\left(\frac{\tan^{2}\varphi_{cs}}{FS^{2}}+1\right)^{3/2}}$$

Implementing this perturbation in a FE code requires first a calculation of the friction force with a safety factor of 1:

$$f^{\varphi} = \tan\left(\sin^{-1}\frac{3XF}{2\sqrt{3}(1-YF)^{Z}+XF}\right) \tag{4.22}$$

which is then used to recalculate X^{SF} including the safety factor:

$$X^{SF} = \frac{2\sqrt{3}(1-YF)^{ZF}\sin\left(\tan^{-1}\left(\frac{f^{\varphi}}{FS}\right)\right)}{3-\sin\left(\tan^{-1}\left(\frac{f^{\varphi}}{FS}\right)\right)} \tag{4.23}$$

From there, the algorithm proceeds in the usual manner, though it now needs to include the contribution of the perturbation of the numerical history variable in the calculation of the plastic multiplier (4.12).

4.3.3. BACKSTRESS PERTURBATION: JUMP-IN-CYCLES METHOD

As shown in the previous section, the backstress can be perturbed arbitrarily by using an arbitrary history variable ς and then enforcing consistency of the yield surface. In a general way it can be rewritten as

$$n_{ij}\left(\Delta\sigma_{ij}-\Delta\lambda h_{ij}(\vec{n}_{ij},\alpha_{ij},\varsigma)-\frac{\Delta\alpha_{ij}}{\Delta\varsigma}\Delta\varsigma\right)=0 \tag{4.24}$$

where $\Delta\varsigma$ is a generic perturbation. Therefore, a perturbation based on the number of cycles can be built as $\Delta\alpha_{ij}/\Delta\mathrm{N}$, using a strain cycle based on the methodology described in 2.3.9. The previous concept, if combined with a good choice of the implicit discretisation described in 3.2.3.1, can be used to "jump-in" small to medium cycles maintaining good accuracy. The idea is illustrated here using the half-midpoint and half-trapezoidal discretisations as both have second order accuracy and the normal of the yield function is evaluated at the end of the step. First, an average backstress is defined as:

$$\alpha_{kl}^{n+1/2}=1/2\left(\alpha_{kl}^{n+1}+\alpha_{kl}^{n}\right) \tag{4.25}$$

Since the backstress is evaluated in the middle of the step, recalling the discretization in 3.2.3.1, it will result in:

For the Midpoint discretisation:

$$\alpha_{ij}^{n+1}=\alpha_{ij}^{n}+\lambda^{n+1}h_{ij}(\vec{n}_{kl}^{n+1},\alpha_{kl}^{n+1/2},e^{n+1/2}) \tag{4.26}$$

For the Trapezoidal discretisation:

$$\alpha_{ij}^{n+1}=\alpha_{ij}^{n}+\frac{1}{2}\lambda^{n+1}\left(h_{ij}(\vec{n}_{kl}^{n+1},\alpha_{kl}^{n+1},e^{n+1})+h_{ij}(\vec{n}_{kl}^{n+1},\alpha_{kl}^{n},e^{n})\right) \tag{4.27}$$

Upon a closed strain cycle a variable accounting for the backstress perturbation can be defined as

$$\frac{\Delta\alpha_{ij}}{\Delta N} = \alpha_{ij}^{n+2} - \alpha_{ij}^{n} \tag{4.28}$$

where α_{ij}^{n+2} would be the backstress at the end of the following half-cycle. The variables α_{ij}^{n+1}, α_{ij}^{n}, $\left\|\Delta\varepsilon^{p}\right\|$ and $\vec{n}_{kl}^{n+1}$ are already known. Figure 82 illustrates a sketch of the idea in 1D conditions.

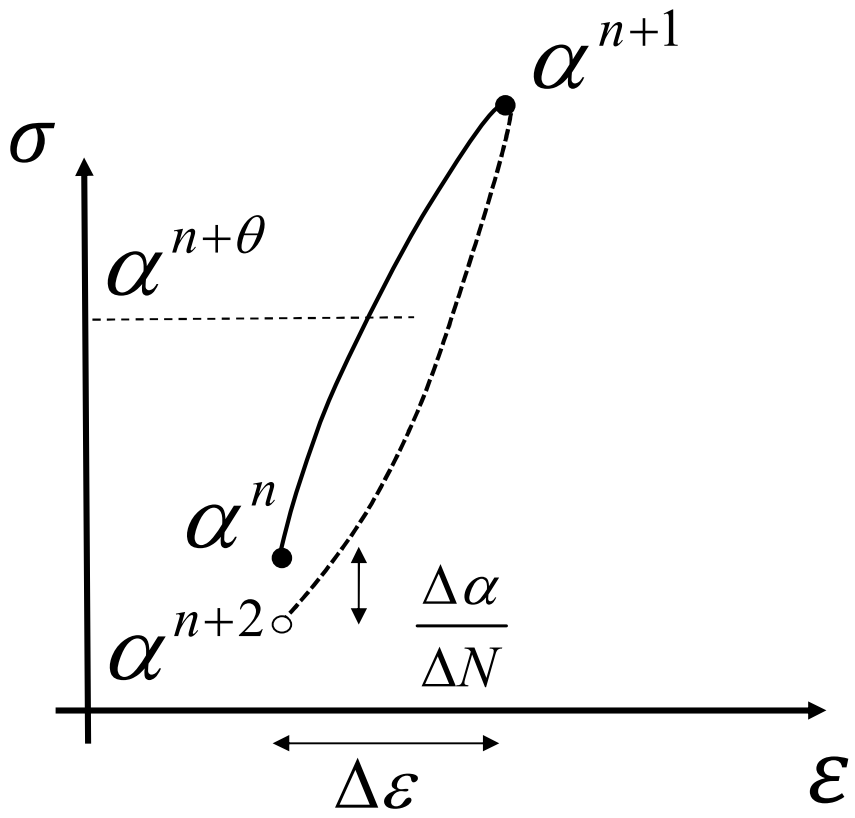


Figure 188: Graphical description of Jump-in-cycles method for one cycle.

The key of the problem for one cycle revolves around determining an accurate estimation of $\frac{\Delta\alpha_{ij}}{\Delta N}$, owing to the fact that only $\alpha_{ij}^{n+1}, \alpha_{ij}^{n}, \left\|\Delta\varepsilon^{p}\right\|$ and $\vec{n}_{kl}^{n+1}$ are known. In the following section four approaches to estimate $\frac{\Delta\alpha_{ij}}{\Delta N}$ are tested: two approximated methods, denoted as "explicit jump-in-cycle" methods, and two direct methods, denoted "implicit jump-in-cycle" methods.

4.3.3.1. Explicit approximations

The simplest of the methods is a combination of the half-mid point discretisation or trapezoidal discretisation, with assumptions on where the backstress on the next half-cycle is evaluated. The perturbation of the backstress $\left.\frac{\Delta\alpha_{ij}}{\Delta N}\right|^{E}$ can be computed under the following assumption:

$$\begin{aligned}\alpha_{kl}^{n+1/2} &= 0.5\left(\alpha_{ij}^{n+1}+\alpha_{ij}^{n}\right)\approx 0.5\left(\alpha_{ij}^{n+1}+\alpha_{ij}^{n+2}\right)\\ \lambda^{n+2} &= \lambda^{n+1}\end{aligned} \tag{4.29}$$

Therefore

$$\alpha_{ij}^{n+2}=\alpha_{ij}^{n+1}+\lambda^{n+2}h_{ij}(-\vec{n}_{kl}^{n+1},\alpha_{ij}^{n+1/2},e^{n+1/2}) \tag{4.30}$$

Depending on the discretisation used, combining (4.26) or (3.61) with (3.64), yields the following predictions of α_{ij}^{n+2}:

<u>For the Midpoint Explicit Jump-in-Cycle:</u>

$$\alpha_{ij}^{n+2}=\alpha_{ij}^{n}+\lambda^{n+1}h_{ij}(\vec{n}_{kl}^{n+1},\alpha_{ij}^{n+1/2},e^{n+1/2})+\lambda^{n+2}h_{ij}(-\vec{n}_{kl}^{n+1},\alpha_{ij}^{n+1/2},e^{n+1/2}) \tag{4.31}$$

<u>For the Trapezoidal Explicit Jump-in-Cycle:</u>

$$\alpha_{ij}^{n+2}=\alpha_{ij}^{n}+0.5\lambda^{n+1}\begin{pmatrix}h_{ij}(\vec{n}_{kl}^{n+1},\alpha_{ij}^{n},e^{n})+h_{ij}(\vec{n}_{kl}^{n+1},\alpha_{ij}^{n+1},e^{n+1})+\\ +h_{ij}(-\vec{n}_{kl}^{n+1},\alpha_{ij}^{n},e^{n})+h_{ij}(-\vec{n}_{kl}^{n+1},\alpha_{ij}^{n+1},e^{n+1})\end{pmatrix} \tag{4.32}$$

Substituting (4.28) for a cycle of half magnitude, where $\lambda^{n+1}=\lambda^{n+2}=\left\|\Delta\varepsilon_{ij}^{p}\right\|$ and where the direction $\vec{n}_{ij}$ is also known, the following solutions are obtained:

For the Midpoint Explicit Jump-in-Cycle:

$$\left.\frac{\Delta\alpha_{ij}}{\Delta N}\right|^{MID-E} = -2\left\|\Delta\varepsilon_{ij}^{p}\right\| f_e(\alpha_{kl}^{n+1/2}) f_p(\alpha_{kl}^{n+1/2}) L_{ijkl}(\alpha_{kl}^{n+1/2})\left(f_d(\alpha_{kl}^{n+1/2})\tilde{Y}(\alpha_{kl}^{n+1/2})\vec{\Upsilon}_{kl}(\alpha_{kl}^{n+1/2})\right)$$

(4.33)

For the Trapezoidal Explicit Jump-in-Cycle:

$$\left.\frac{\Delta\alpha_{ij}}{\Delta N}\right|^{TZ-E} = -\left\|\Delta\varepsilon_{ij}^{p}\right\|\left(\begin{array}{l} f_e(\alpha_{kl}^{n}) f_p(\alpha_{kl}^{n}) L_{ijkl}(\alpha_{kl}^{n})\left(f_d(\alpha_{kl}^{n})\tilde{Y}(\alpha_{kl}^{n})\vec{\Upsilon}_{kl}(\alpha_{kl}^{n})\right)+ \\ f_e(\alpha_{kl}^{n+1}) f_p(\alpha_{kl}^{n+1}) L_{ijkl}(\alpha_{kl}^{n+1})\left(f_d(\alpha_{kl}^{n+1})\tilde{Y}(\alpha_{kl}^{n+1})\vec{\Upsilon}_{kl}(\alpha_{kl}^{n+1})\right) \end{array}\right) \quad (4.34)$$

Which can be observed that are in line with the infinitesimal perturbation described in 2.3.9.

4.3.3.2. Implicit approximations

The estimate of $\left.\frac{\Delta\alpha_{ij}}{\Delta N}\right|^{I}$ can be computed implicitly preserving the second order accuracy of the integration method for both the midpoint and trapezoidal discretisations. This, however, is at the cost of higher complexity and number of computations. To estimate $\left.\frac{\Delta\alpha_{ij}}{\Delta N}\right|^{I}$ a system of six unknowns must be solved, where the equation to solve can be built without having to use approximations as the following equation is always true:

$$\begin{aligned} &\alpha_{kl}^{n+\theta 2} = 0.5\left(\alpha_{ij}^{n+1} + \alpha_{ij}^{n+2}\right) = 0.5\left(\alpha_{ij}^{n+1} + \alpha_{ij}^{n} + \left.\frac{\Delta\alpha_{ij}}{\Delta N}\right|^{I}\right) \\ &\lambda^{n+2} = \lambda^{n+1} \end{aligned} \quad (4.35)$$

where

$$\alpha_{ij}^{n+2} = \alpha_{ij}^{n} + \left.\frac{\Delta\alpha_{ij}}{\Delta N}\right|^{I} \quad (4.36)$$

Naturally, the system of equations to solve is obtained using the same methodology as in the previous section. The following equations are obtained depending on the implicit discretisation chosen:

For the Midpoint Implicit Jump-in-Cycle:

$$\alpha_{ij}^{n+2} = \alpha_{ij}^{n} + \lambda^{n+1} h_{ij}(\vec{n}_{kl}^{n+1}, \alpha_{kl}^{n+1/2}, e^{n+1/2}) + \lambda^{n+2} h_{ij}(-\vec{n}_{kl}^{n+1}, \alpha_{kl}^{n+\theta 2}, e^{n+1/2}) \tag{4.37}$$

For the Trapezoidal Implicit Jump-in-Cycle:

$$\begin{aligned} \alpha_{ij}^{n+2} &= \alpha_{ij}^{n} + \lambda^{n+1} 0.5\left(h_{ij}(\vec{n}_{kl}^{n+1}, \alpha_{kl}^{n+1}, e^{n+1}) + h_{ij}(\vec{n}_{kl}^{n+1}, \alpha_{kl}^{n}, e^{n})\right) \\ &+ \lambda^{n+2} 0.5\left(h_{ij}(-\vec{n}_{kl}^{n+1}, \alpha_{kl}^{n+2}, e^{n}) + h_{ij}(-\vec{n}_{kl}^{n+1}, \alpha_{kl}^{n+1}, e^{n+1})\right) \end{aligned} \tag{4.38}$$

It should be noted that now α_{kl}^{n+2} and $\alpha_{kl}^{n+2\theta}$ contain the solution $\frac{\Delta \alpha_{ij}}{\Delta N}$, where $\lambda^{n+1}, \vec{n}_{ij}$ α_{ij}^{n} α_{ij}^{n+1} are known. Equations (4.37) and (4.38) are non-linear and must be solved implicitly. This leads to a system of only six unknowns, where:

For the Midpoint Implicit Jump-in-Cycle:

$$R\left(\frac{\Delta \alpha_{ij}}{\Delta N}\right) = \frac{\Delta \alpha_{ij}}{\Delta N} - \lambda^{n+1}\left(h_{ij}(\vec{n}_{kl}^{n+1}, \alpha_{kl}^{n+1/2}, e^{n+1/2}) + h_{ij}(-\vec{n}_{kl}^{n+1}, \alpha_{kl}^{n+1/2} + 0.5\frac{\Delta \alpha_{ij}}{\Delta N}, e^{n+1/2})\right) \tag{4.39}$$

For the Trapezoidal Implicit Jump-in-Cycle:

$$R\left(\frac{\Delta \alpha_{ij}}{\Delta N}\right) = \frac{\Delta \alpha_{ij}}{\Delta N} - \frac{1}{2}\lambda^{n+1}\begin{pmatrix} h_{ij}(\vec{n}_{kl}^{n+1}, \alpha_{kl}^{n+1}, e^{n+1}) + h_{ij}(\vec{n}_{kl}^{n+1}, \alpha_{kl}^{n}, e^{n}) + \\ + h_{ij}(-\vec{n}_{kl}^{n+1}, \alpha_{ij}^{n} + \frac{\Delta \alpha_{ij}}{\Delta N}, e^{n}) + h_{ij}(-\vec{n}_{kl}^{n+1}, \alpha_{kl}^{n+1}, e^{n+1}) \end{pmatrix} \tag{4.40}$$

The system of equations can be solved using any non-linear solver where the initial starting point is estimated using one of the previously described jump-in-cycle explicit methods for better stability.

4.3.3.3. Comparison of jump-in-cycles approximations

To study the performance of the previous jump-in-cycle methods (explicit MID, explicit TZ, implicit MID, implicit TZ) a strain-controlled undrained triaxial test for large-mid strain excursions under unsymmetrical strain conditions has been carried out using the same inputs and initial conditions (p' = 300 kPa, e = 0.85) as in 3.4. The following table summarises the inputs that will be used in all forthcoming benchmarks.

Table 24: Input parameters for benchmark tests, same inputs as Chapter: Numerical Integration

	e_{c0}	e_{d0}	h_s	n	α	β	XV	YF	ZF	ϑ	S_f	ob_{min}	ob_{max}	δ
Basic Sand	1.05	0.55	4E5	0.45	0.15	1.7	0.52	0.77	0.24	0.4	4.0	-1.73	1.0	2.0

Figure 189 compares the stress path computed exactly, where the strain path is integrated conventionally, to the predictions obtained using each of the jump-in-cycles methods. The strain path corresponds to three closed strain controlled cycles where the material does not exhibit change in volume and is axially controlled, emulating conditions akin to undrained strain controlled conditions. The errors are computed using (4.41) and the error values are shown in Table 25. It can be observed how the most accurate methods corresponds to the Mid-implicit jump-in-cycles method.

$$ABS = \left\| \left| \frac{\Delta \alpha_{ij}}{\Delta N} \right|^{Exact} - \left| \frac{\Delta \alpha_{ij}}{\Delta N} \right|^{Num} \right\|$$
$$REL = 100 \frac{ABS}{\left\| \left| \frac{\Delta \alpha_{ij}}{\Delta N} \right|^{Exact} \right\|} \tag{4.41}$$

Table 25: Absolute and relative error for three large cycles

	Error Mid Explicit		**Error Mid Implicit**		**Error TZ Explicit**		**Error TZ Implicit**	
	REL (%)	ABS	REL (%)	ABS	REL (%)	ABS	REL (%)	ABS
Cycle 1	16.0	25.3	7.4	11.7	13.6	21.5	1.8	2.8
Cycle 2	7.1	8.0	1.5	1.7	84	94.4	14.6	16.4
Cycle 3	10.1	7.7	2.3	1.7	246.2	186.9	11.8	8.9

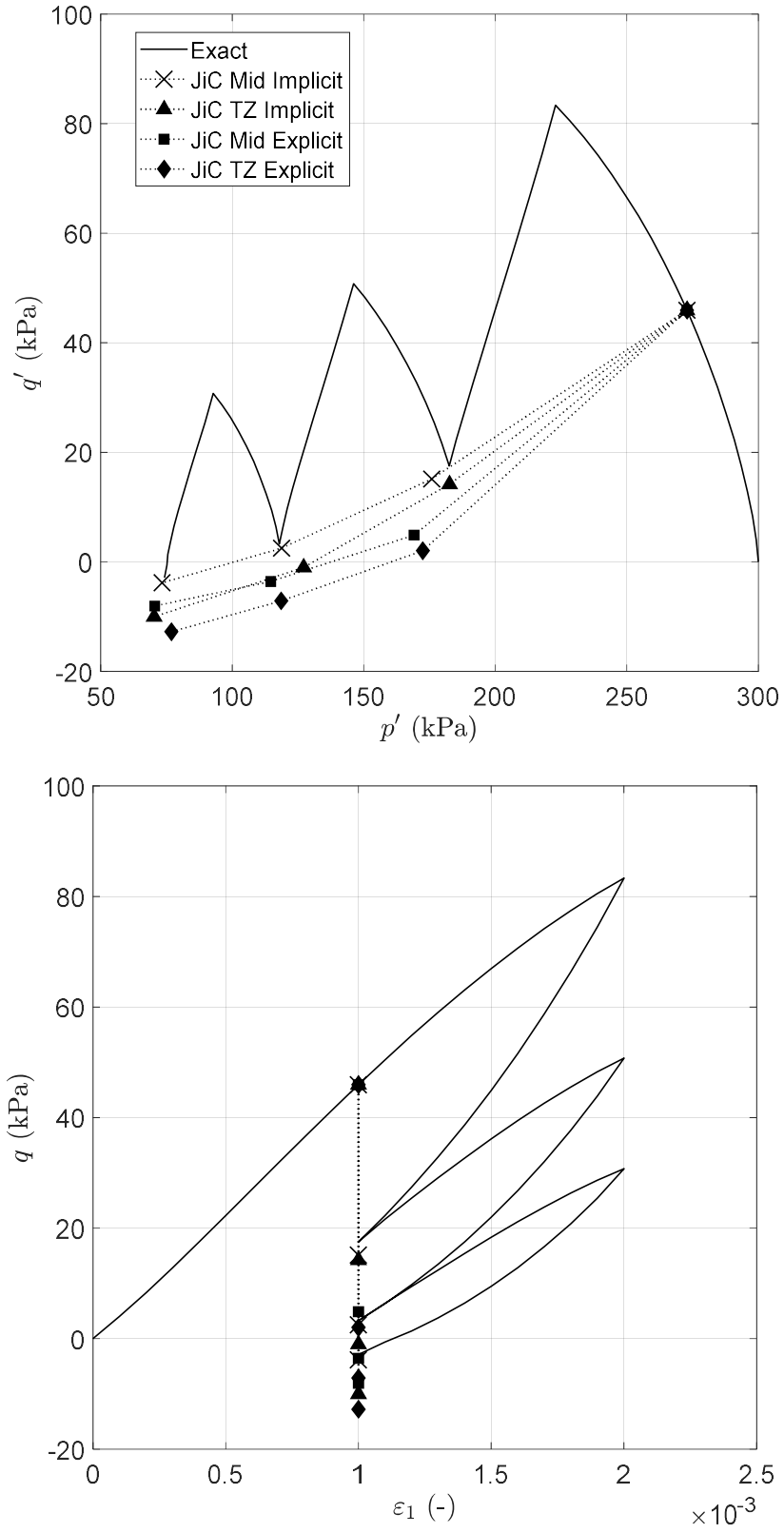


Figure 189: Benchmark of four proposed Jump-in-Cycles methods for mid size strain excursions, undrained strain controlled triaxial test

4.3.3.4. Recursive "Jump-in-Cycles" method

This section illustrates that the former idea of jumping one cycle can be extended to consider larger number of cycles using a recursion technique. The method will estimate $\frac{\Delta\alpha_{ij}}{\Delta N^{(m)}}$ where now $\Delta N^{(m)}$ is a batch of cycles with the same strain characteristics. The term $\frac{\Delta\alpha_{ij}}{\Delta N^{(n)}}$ can be computed following the methods described in the previous section where α_{ij}^{n+2m} is estimated. Therefore:

$$\frac{\Delta\alpha_{ij}}{\Delta N^{(m)}} = \alpha_{ij}^{n+2m} - \alpha_{ij}^{0} \tag{4.42}$$

Instead of estimating $\left.\frac{\Delta\alpha_{ij}}{\Delta N}\right|^{MID-I}$ for one cycle, the obtained value of α_{ij}^{n+2} can be re-used for future predictions. This process can be repeated recursively and therefore an estimate of the whole batch can be obtained by recursion. This is illustrated on the following example, where Equation (4.39) can be rearranged so that:

$$\begin{aligned} &r(\alpha_{ij}^{n+2}) = \alpha_{ij}^{n+2} - \alpha_{ij}^{n} - \lambda^{n+1} h_{ij}(\vec{n}_{kl}^{n+1}, \alpha_{kl}^{n+1/2}, e^{n+1/2}) \\ &-\lambda^{n+2} h_{ij}(-\vec{n}_{kl}^{n+1}, 0.5(\alpha_{kl}^{n+2} + \alpha_{kl}^{n+1}) +, e^{n+1/2}) \end{aligned} \tag{4.43}$$

α_{ij}^{n+2} is solved and used as an estimate for another half-cycle jump, which leads to α_{ij}^{n+3} as:

$$\begin{aligned} &r(\alpha_{ij}^{n+3}) = \alpha_{ij}^{n+3} - \alpha_{ij}^{n+1} - \lambda^{n+1} h_{ij}(-\vec{n}_{kl}^{n+1}, 0.5(\alpha_{kl}^{n+2} + \alpha_{kl}^{n+1}), e^{n+1/2}) \\ &-\lambda^{n+2} h_{ij}(\vec{n}_{kl}^{n+1}, 0.5(\alpha_{kl}^{n+3} + \alpha_{kl}^{n+2}), e^{n+1/2}) \end{aligned} \tag{4.44}$$

Which leads to α_{ij}^{n+4}, and so on…

$$
\begin{aligned}
&r(\alpha_{ij}^{n+4}) = \alpha_{ij}^{n+4} - \alpha_{ij}^{n+2} - \lambda^{n+1} h_{ij}(\vec{n}_{kl}^{n+1}, 0.5(\alpha_{kl}^{n+3} + \alpha_{kl}^{n+2}), e^{n+1/2}) \\
&-\lambda^{n+2} h_{ij}(-\vec{n}_{kl}^{n+1}, 0.5(\alpha_{kl}^{n+4} + \alpha_{kl}^{n+3}), e^{n+1/2}) \\
&\qquad\qquad\qquad\qquad \vdots \\
&r(\alpha_{ij}^{n+i}) = \alpha_{ij}^{n+i} - \alpha_{ij}^{n+i-1} - \lambda h_{ij}(\vec{n}_{kl}^{n+1}, 0.5(\alpha_{kl}^{n+i-1} + \alpha_{kl}^{n+i-2}), e^{n+1/2}) \\
&-\lambda h_{ij}(-\vec{n}_{kl}^{n+1}, 0.5(\alpha_{kl}^{n+i} + \alpha_{kl}^{n+i-1}), e^{n+1/2}) \\
&\qquad\qquad\qquad\qquad \vdots \\
&r(\alpha_{ij}^{n+2m}) = \alpha_{ij}^{n+2m} - \alpha_{ij}^{n+2(m-1)} - \lambda h_{ij}(\vec{n}_{kl}^{n+1}, 0.5(\alpha_{kl}^{n+2m-1} + \alpha_{kl}^{n+2m-2}), e^{n+1/2}) \\
&-\lambda h_{ij}(-\vec{n}_{kl}^{n+1}, 0.5(\alpha_{kl}^{n+2m} + \alpha_{kl}^{n+2m-1}), e^{n+1/2})
\end{aligned}
\tag{4.45}
$$

A final backstress value α_{ij}^{n+2m} can be estimated corresponding to all the "half-jumps" prescribed of one batch. Once this estimate is obtained, the perturbation of the backstress for that batch of cycles under the prescribed strain conditions is easily computed as:

$$
\frac{\Delta \alpha_{ij}}{\Delta N^{(m)}} = \alpha_{ij}^{n+2m} - \alpha_{ij}^{0} \tag{4.46}
$$

where α_{ij}^{0} is the initial backstress at the start of the jump-in-cycle. To further show the performance of this procedure over various cycles and strain magnitudes, an exercise involving three sets of cyclic probes has been undertaken. Its results are shown in Figure 190, Figure 187 and Figure 192.

Each cyclic probe consists of six unsymmetrical cyclic strain paths in the Rendulic plane under various directions. Magnitudes of 5E-4 and 1E-4 are explored for 1, 5, 10 and 20 cycles and 10, 20, 50, 100 and 200 cycles respectively. The figures show the stress path of the tests carried out classically in 101 increments for each strain direction, while the grey star points represent the stress value predicted at the end of a batch of cycles.

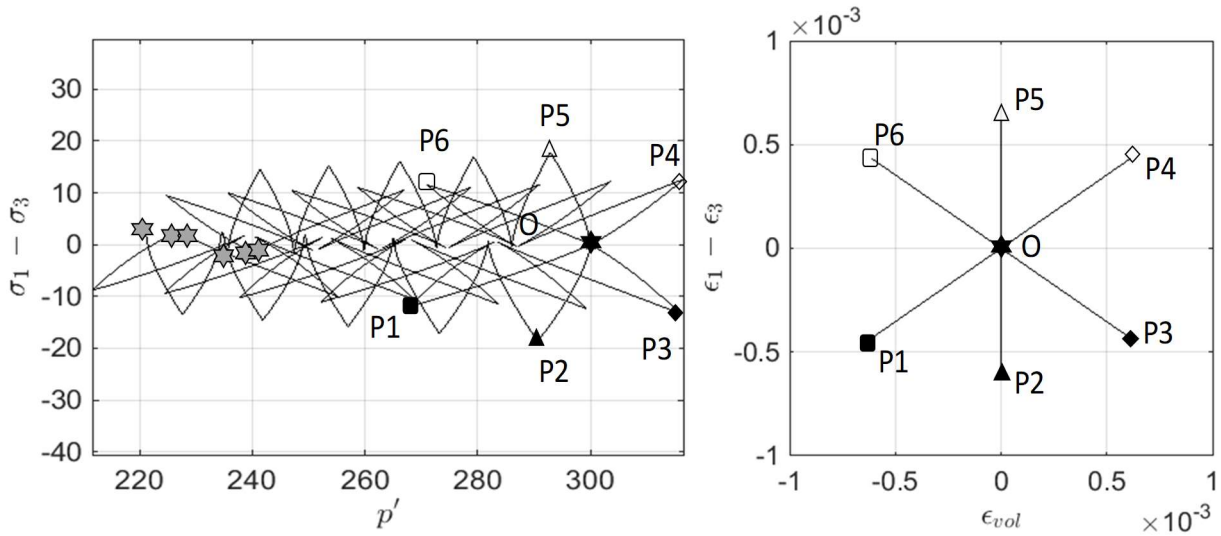


Figure 190: Illustration of benchmark analysis: cyclic strain controlled probes for N = 5

The errors calculated using (4.41) for all the cyclic probes and number of cycles are shown in Table 26 and Table 27, as a function of the strain amplitude and the number of cycles.

Table 26: Absolute and relative errors of cyclic strain probe 1 (5E-4)

Amplitude = 5E-4												
	P1		**P2**		**P3**		**P4**		**P5**		**P6**	
	Rel (%)	ABS	Rel (%)	ABS	Rel (%)	ABS	Rel (%)	ABS	Rel (%)	ABS	Rel (%)	ABS
N = 1	0.3	1.6	0.6	3.1	0.01	0.1	0.1	0.5	0.4	2.0	0.3	1.4
N = 5	0.9	3.7	3.3	12.6	0.1	0.5	0.5	2.1	2.1	8.7	1.2	5.0
N = 10	2.7	3.7	3.7	10.2	1.3	3.9	1.9	6.1	3.0	9.5	3.0	9.7
N = 20	23.8	35.7	16.0	29.0	24.4	36.7	15.5	28.2	15.5	28.1	15.6	28.5

It is interesting to see in Figure 191 a detail of the "exact" solution probes for 20 cycles (N = 20) with an amplitude of 5E-4, where the excursion of $\left\| \frac{\Delta \alpha_{ij}}{\Delta N^{(m)}} \right\|$ is more than 300 kPa. In these conditions the method fails to give good prediction (rel error ~20%). It is clear that the accuracy of the method is linked to the accuracy of discretization, and therefore it is dependent of the strain magnitude and the order of the discretisation used. It can be observed that for small number of cycles, results are in line with the isoerror maps shown in 3.4.3.

For smaller amplitudes, results in Figure 192 show a good performance of the half-mid discretisation, estimating with good accuracy up to 100 cycles for amplitudes of 1E-4 and excursions beyond 100 kPa in magnitude. This method is very efficient for small to medium perturbations suggesting that a significant reduction in computational cost can be achieved with little sacrifice in terms of the precision of the solution. In effect, the tests shown in Figure 191 would correspond to 4001 increments if each cycle were simulated "exactly", while the "jump-in–cycles" would correspond to a single increment.

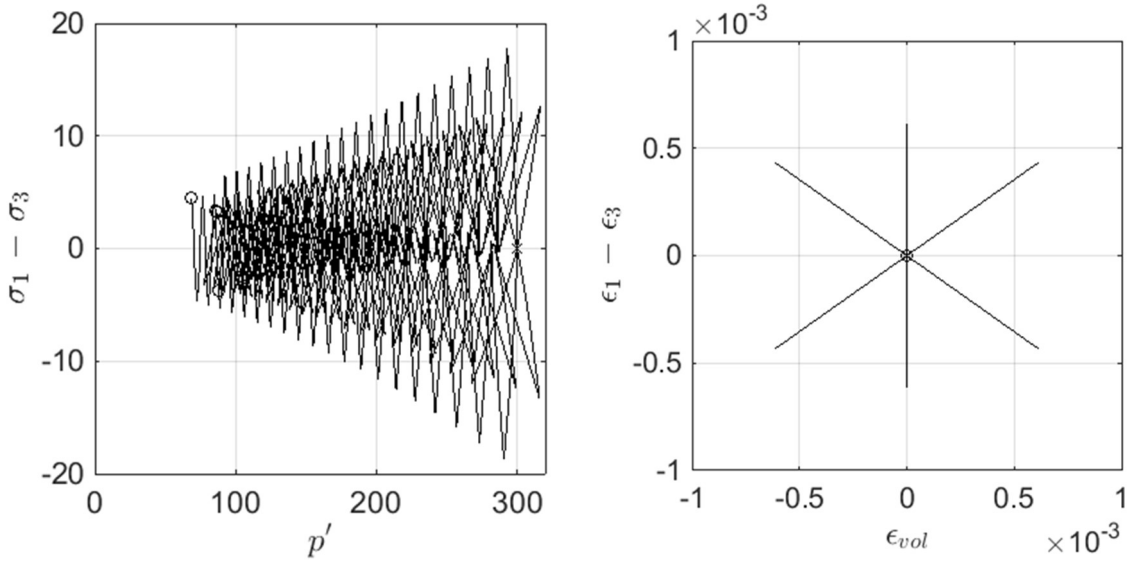
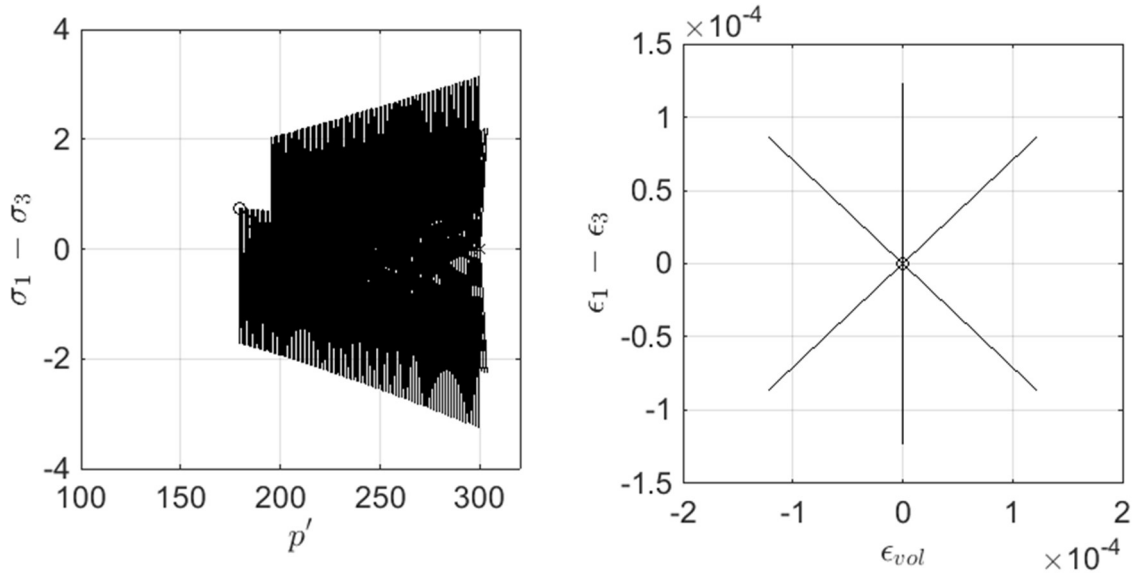


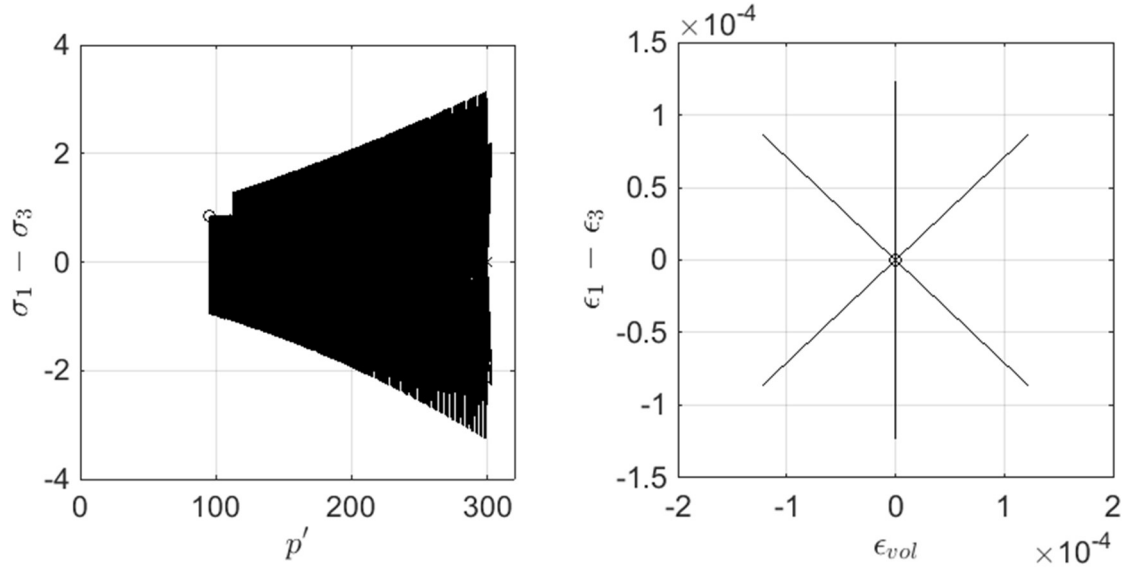
Figure 191: Cyclic strain probes for strain amplitude 1E-4

Table 27: Absolute and relative errors of cyclic strain probe (2) (1E-4)

Amplitude = 1E-4												
	P1		**P2**		**P3**		**P4**		**P5**		**P6**	
	Rel (%)	ABS	Rel (%)	ABS	Rel (%)	ABS	Rel (%)	ABS	Rel (%)	ABS	Rel (%)	ABS
N = 10	0.3	1.3	0.4	1.8	0.2	1.2	0.2	1.1	0.2	1.2	0.3	1.2
N = 20	0.4	2.2	0.8	3.7	0.4	1.9	0.4	2.1	0.5	2.5	0.5	2.3
N = 50	0.9	3.5	2.2	8.7	0.8	3.1	1.0	4.4	1.4	5.8	1.1	4.7
N = 100	1.9	6.1	3.4	1.7	1.7	5.6	2.3	8.2	2.3	7.8	2.5	8.7
N = 200	12.6	23.7	8.2	13.5	21.0	9.5	20.1	9.3	6.1	3.1	20.3	9.4



N = 100



N = 200

Figure 192: Cyclic strain probes for strain amplitude 1E-4

4.4. SUMARY OF CHAPTER

With respect to specialised hardenign rules

- Three examples of specialised hardening rules are presented enhancing the limitations of the basic rules, a parametric strudy detailing the effect of each of their inputs is shown;
- The limitations of the basic rule for sand have been underlined and its effect when combined with specialised hardening rules has been discussed.

With respect to Karlsruhe calibration:

- Over 82 tests have been compared versus the numerical predictions over a single set of parameters;
- Guidance on the calibration methodology of the basic model is given;
- The tests have been presented in subsections as described in the calibration methodology;
- The modelling framework has proven flexible enough to capture the complexity of cyclic tests under specific conditions;
- Due to time limitation the whole database has not been benchmarked, but it is left for future study.

With respect to implementation and “numerical artifices”:

- A description of the corrections needed to implement the model in ICFEP are described;
- Two artifices involving perturbations of the backstresses (safety factor, Jump-In-cycles method) have been described;
- Various methods to estimate the backstress perturbation over a number of cycles have been evaluated, where the most favorable discretization regarding the estimate of the batch corresponds to a implicit half-midpoint rule.

CHAPTER 5: MODEL APPLICATION

This chapter demonstrates the application of the sand version of the constitutive framework described in previous chapters. A set of boundary value problems is described, providing insight into the response of the model at Gauss point level and global level. This chapter covers, firstly, 2D cases for verification of the implementation of the model in a FEA code. The second part of the chapter applies the constitutive model to real 3D boundary value problems, focussing on reproducing the results of the tests on laterally loaded piles at Dunkirk, carried out as part of the PISA project. This last part includes the calibration of the constitutive model parameters based on monotonic triaxial tests performed on Dunkirk sand, the study of pile response to monotonic loading, the equivalent structural response and the determination of p-y reactions from the numerical analyses. The response of one of the large Dunkirk piles under cyclic loading conditions is also shown for different levels of complexity of the developed constitutive model.

5.1. VERIFICATION OF IMPLEMENTATION: RIGID FOOTING

To validate the implementation of the constitutive model in ICFEP and to identify possible numerical problems before simulating large scale boundary value problems, a rigid footing on sand was analysed. This type of boundary value problem has been chosen because the Gauss points in the mesh elements experience a wide range of strain directions, and because the expected failure mechanism mobilised in the sand can be preliminary assessed depending on the model response. Apart from the wide range of strain directions, the boundary value problem presents several challenging regions, e.g. around the edge of the footing the stress field experiences a discontinuity which could result in numerical problems at global level. The input parameters for the constitutive model used in this analysis for the main hardening rule are the same ones as the used in the isoerror maps in Chapter 3, reproduced in Table 28 below, to be consistent with previous benchmarks.

5.1.1. MESH, BOUNDARY AND INITIAL CONDITIONS

The mesh shown in Figure 193 consists of 235 8-noded quadrilateral displacement-based elements, adopting a reduced, 2x2, integration order. The boundary conditions restrict the horizontal displacement along the axis of symmetry (i.e. the left-hand-side vertical boundary of the mesh) and along the far vertical boundary on the right-hand-side. The base of the mesh is restricted from moving in both horizontal and vertical directions. The footing is simulated as rigid and fully rough, for which the boundary condition is that of applying uniform vertical displacements at nodes and zero horizontal displacements along the interface between the footing and the soil. Both a strip (plane strain analysis) and a circular footing (axi-symmetric analysis) are considered, with a width/diameter of 2m.

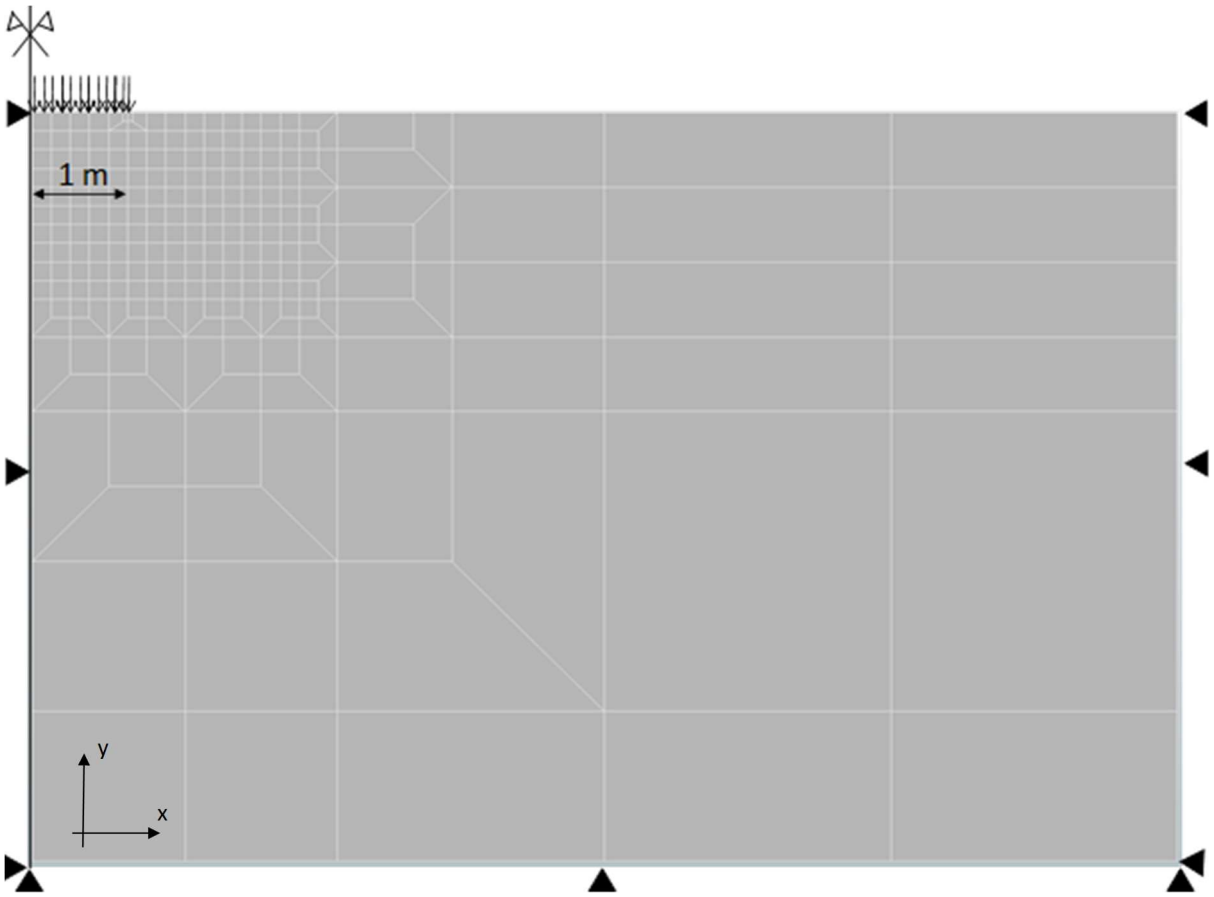


Figure 193: Detail of mesh used in footing analyses

The initial stresses are established assuming a bulk density γ=20.0 kN/m^3 and the water level is at the ground surface, with a hydrostatic pore water pressure in the ground. Three different initial void ratios, e_{in}, of 0.75, 1.0 and 1.2 are studied, with K_0 = 1 used for all cases. Under these conditions, the case of the dense material (i.e. $e_{in} = 0.75$) exhibits post-peak softening upon shearing, which could be affected by the element size in the mesh. However, this particular effect has not be examined at this stage. The model input parameters correspond to the same set used for all the numerical benchmarks and are shown in Table 28. The footing is loaded under drained conditions.

Table 28: Input parameters for benchmark tests, same inputs as Chapter: Numerical Integration

	e_{c0}	e_{d0}	h_s	n	α	β	XV	YF	ZF	ϑ	S_f	ob_{min}	ob_{max}	δ
Basic Sand	1.05	0.55	4E5	0.45	0.15	1.7	0.52	0.77	0.24	0.4	4.0	-1.73	1.0	2.0

Figure 194 shows a summary of the simulated response of the sand under drained triaxial compression conditions, at different initial mean effective stress, $p'(= 50, 10, 200$ kPa), which would correspond to different depths below the footing and assuming the three different initial void ratios, e_{in}. Overall, the model is capable of realistically capturing the diverse behaviour of sand at element (or integration point) level. The dense material shows softening in the $\varepsilon_1 - q$ plot at all stress levels, while the medium dense and loose samples shows a more ductile behaviour. In the $\varepsilon_1 - \varepsilon_{vol}$ plot all samples initially contract, with the medium dense and dense sand experiencing dilation. All stress path regarding of its initial void ration travel towards the CSL.

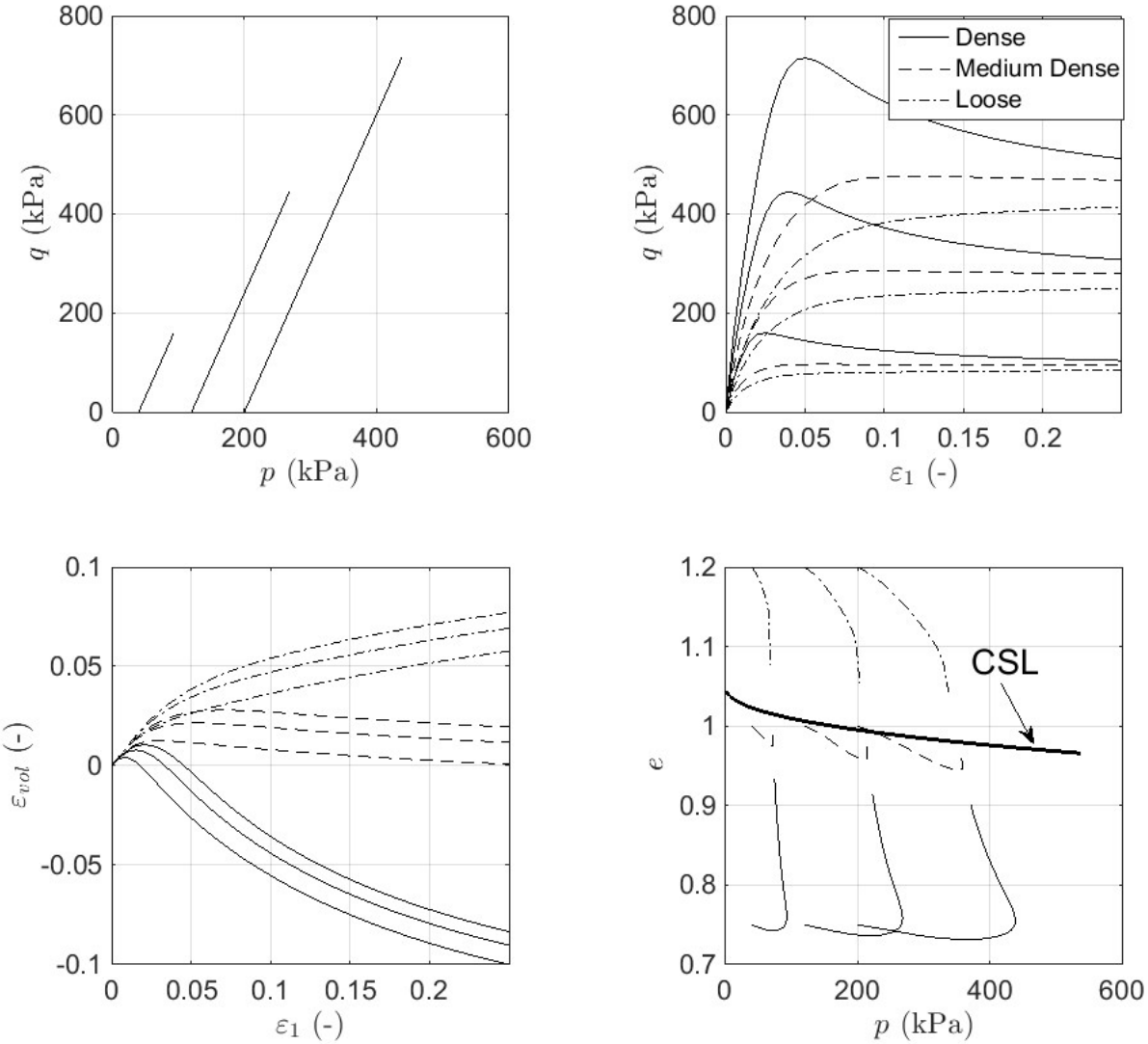


Figure 194: Simulated triaxial compression tests at initial void ratio (0.75, 1.0 and 1.2) with model parameters given in Table 28

5.1.2. DESCRIPTION OF 2D ANALYSIS

To assess the implementation of the model, a number of analyses have been performed and their results scrutinised. These are numerical exercises, comprising the following cases:

1) Monotonic loading

A single backstress with a unique hardening rule is used and the footing is displaced vertically, exploring the effect of different initial void ratios (0.75, 1.0 and 1.2).

2) Numerical perturbation of backstress

This analysis uses the backstress perturbation step described in 4.5.2, which consists of an arbitrary numerical perturbation of the backstress and the enforcement of the consistency condition. This perturbation affects all the Gauss points though the perturbation of the backstress via an internal variable. In this case, given the definition in 4.5.2, the backstress perturbation shares the direction of the goal functions and its magnitude is dependent on the limit function. The analysis uses the same mesh and initial conditions as the monotonic dense simulation described in 1. The perturbation of backstresses is carried out at different loading levels. A comparison with Case 1 enables the assessment of the effect of backstress perturbation.

3) Backstress superposition - Cyclic

In this case the main hardening rule has been duplicated five times and superimposed (Chaboche, 1991). The yield surface contains the total backstress corresponding to the sum of all the active backstresses. A weigth on each of the rules has been introduced, controlling the overall stiffness. The principal direction weights (S_f, S_d) of each of the mapping tensors are also introduced as inputs for each of the rules, controlling only the stiffness in its associated principal direction. The hardening rule in array notation is:

$$\left\{\Delta\alpha^{(k)}\right\} = C^{(k)} f_p f_e \left[\begin{array}{l} S_d^{(k)}\left(\left\{\Delta\varepsilon^p\right\} - f_d\left\|\Delta\varepsilon^p\right\|\tilde{Y}^{(k)}\left\{\Upsilon^{(k)}\right\}\right) + \\ +\dfrac{(S_f^{(k)} - S_d^{(k)})}{3}\left(trace\left\{\Delta\varepsilon^p\right\} - f_d\left\|\Delta\varepsilon^p\right\|\tilde{Y}^{(k)} trace\left\{\Upsilon_{ij}^{(k)}\right\}\right)\underset{\sim}{I} + \\ +(S_f^{(k)} - S_d^{(k)})\left(trace\left\{\Delta\varepsilon^p\right\} - f_d\left\|\Delta\varepsilon^p\right\|\tilde{Y}^{(k)} trace\left\{\Upsilon_{ij}^{(k)}\right\}\right)\dfrac{\left\{\alpha^{*(k)}\right\}}{trace(\alpha^{(k)})} \end{array}\right] \quad (5.1)$$

where $C^{(k)}, S_f^{(k)}, S_d^{(k)} for\ k = [1 \ldots 5]$ are the weights for each of the mapping tensors. The cyclic loading is applied using a load-control boundary conditions with the tied degrees of freedom in the vertical direction along the footing-soil interface, to ensure that the footing remains rigid and displaces uniformly in the vertical direction. Several analyses applying 10 cycles and comparing the response of one, two and up to five backstresses are performed. These analyses are purely to evaluate the compatibility of the superposition and have not been calibrated for any soil in particular.

5.1.3. MONOTONIC LOADING IN DENSE, MEDIUM DENSE AND LOOSE SAND

This set of analyses firstly validates the local integration of the constitutive model and, secondly, explores the asymptotic properties of the model for various initial densities. As discussed in chapter 2, it is a good test to check and verify if the constitutive model has been formulated accounting for a compatible rate of f_d in a boundary value problem.

5.1.3.1. Load displacement curves – failure mechanism

Axy-symmetric conditions are assumed first, simulating a circular footing. Each simulation is carried out over 300 increments, where incremental displacements of 2 mm are applied along the footing-soil interface. Figure 195 shows the displacement versus the reaction at the centre of the footing for loose ($e_0 = 1.2$), medium dense ($e_0 = 1.0$) and dense ($e_0 = 0.75$) initial void ratio.

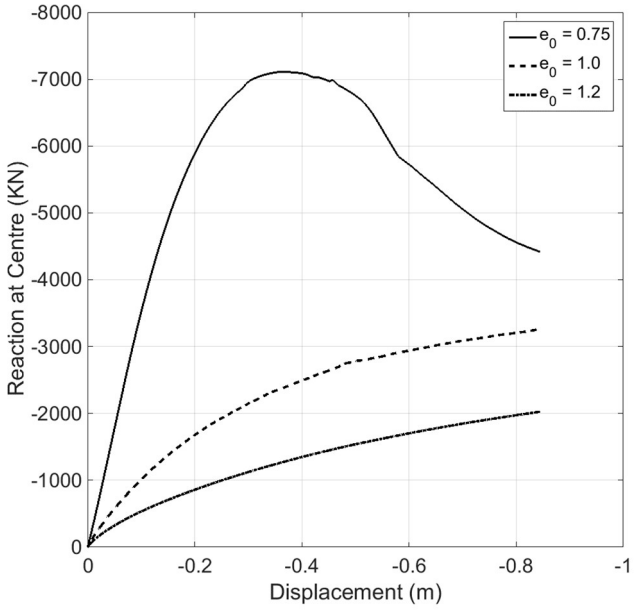


Figure 195: Reaction – displacement curves for three initial void ratios

Figure 195 shows that the model is capable of accounting for the effect of void ratio in sands, which is manifested by the mobilised capacity and initial stiffness. The model also accounts for the shear-volumetric coupling, being contractant for looser states and dilatant for denser states. The consequences of the dilatancy can be identified in the failure mechanisms, plotted in terms of incremental displacement vectors in the soil under the footing in Figure 196 to Figure 198.

For the dense case shown in Figure 196, where the dilatancy governs the problem, the typical logarithmic exponential shape of the failure mechanism can be identified, being shallow under the footing and extending more to the side, beyond the edge of the footing. For looser states (Figure 198) a failure mechanism associated with a contractant response occurs, where the soil under the footing compresses and engages a deeper mechanism. The medium dense case (Figure 197) lies in between the previous two cases, with the soil both under and to the side of the footing being mobilised.

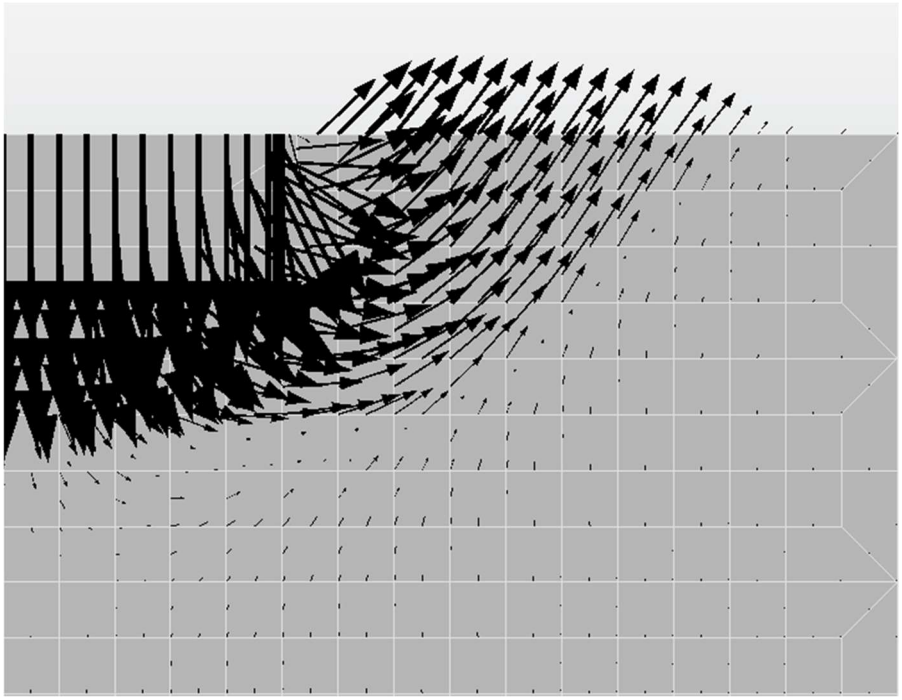


Figure 196: Incremental displacements at failure for very dense case (multiplied by a factor of 150)

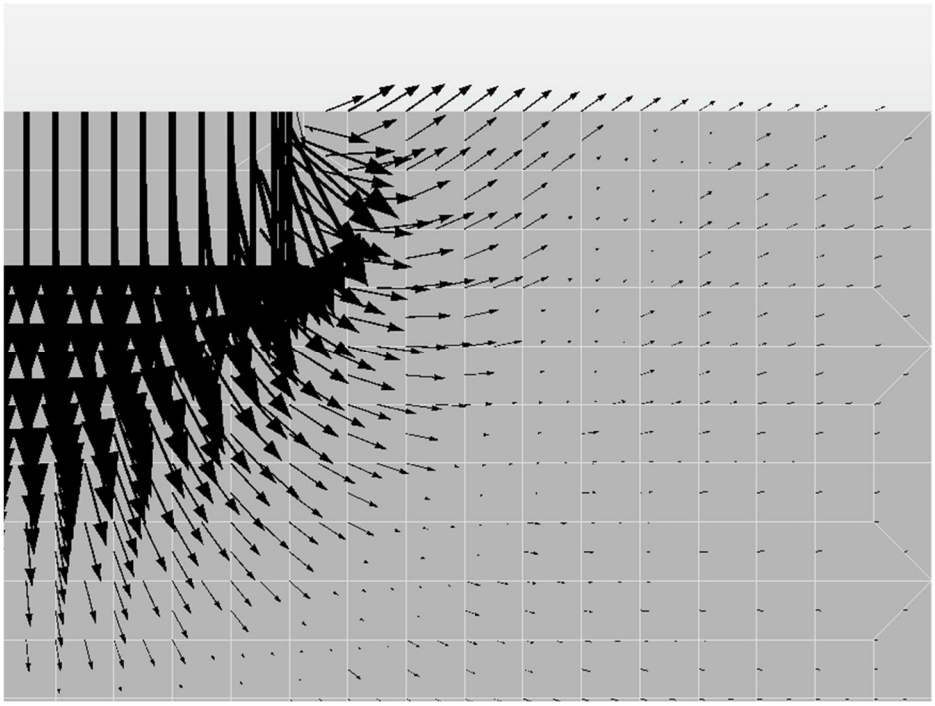


Figure 197: Incremental displacement at failure for medium dense case (multiplied by a factor of 150)

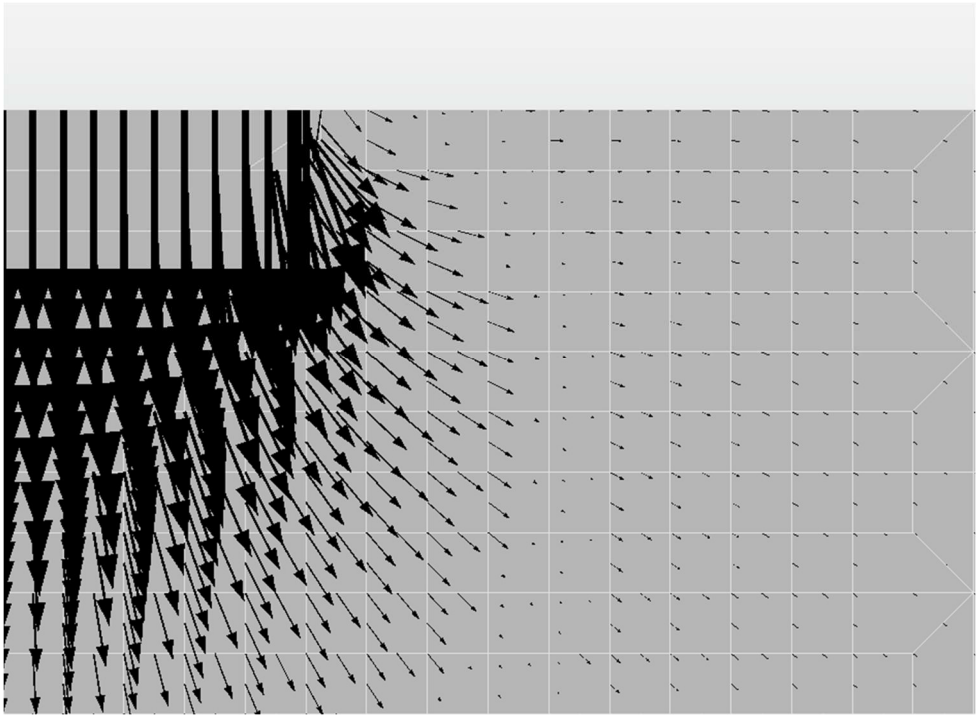


Figure 198: Incremental displacement at failure for very loose case (multiplied by a factor of 150)

5.1.3.2. Local integration

In addition to investigating the general behaviour of the footing, the local integration at integration point level has been investigated for various elements within the mesh. This has been done to evaluate whether possible deficiencies in the constitutive formulation may arise, and whether the deviatoric stress ratio is appropriately bounded for all strain directions Figure 199 shows the positions of some of the elements investigated.

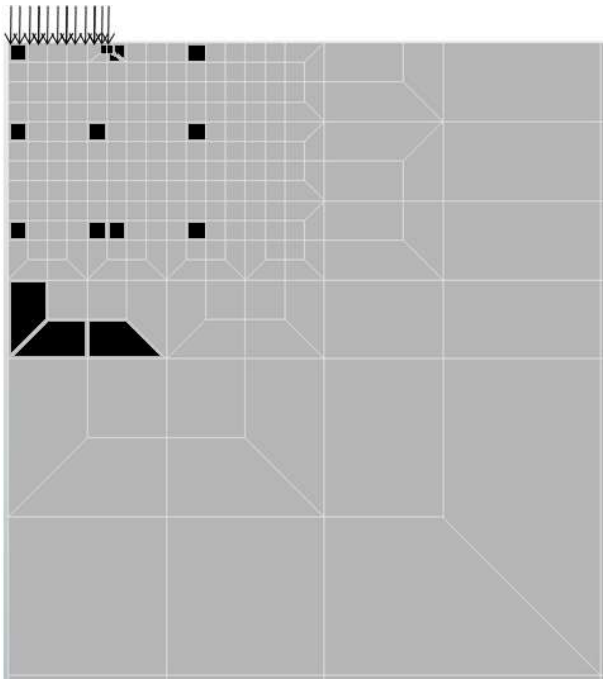


Figure 199: Several of the elements investigated for local integration

The main aspects to be verified are:

1) An asymptotic response of the stress paths towards their associated J/p asymptote and a progressive decrease of the rate of obliquity to zero, defining clearly asymptotic conditions as strain progresses;
2) A natural trend of the soil to travel towards the critical state line when subjected to shear, independently of its initial state, as the CSL is a line of attractors in the void ratio – stress space.

3) Tuning of the stiffness functions to never exhibit $\dot{f}_d < 0$ when $n_{kk} < 0$, regardless of its initial state.

Dense sand case

Figure 200 illustrates the response of the elements within the mesh with an initial void ratio of 0.75 fullfilling the previosu conditions. Firstly, in the top-left graph in Figure 200, it can be verified that the stress path is bounded in the J–p plane, with the mobilized friction angle being a function of the void ratio and the obliquity of the strain rate. Secondly, the model captures adequately the shear-volumetric coupling as a function of the void ratio and its J/p ratio when subjected to shearing (Figure 8 top-centre). The stress path travels to the critical state line as the footing is loaded, respecting the asymptotic behaviour (Figure 8 bottom-left). Finally, in the same figure, it can be appreciated that for all stress paths the undesirable situation $\dot{f}_d < 0$ is never reached and therefore the overestimation the peak strength never occurs.

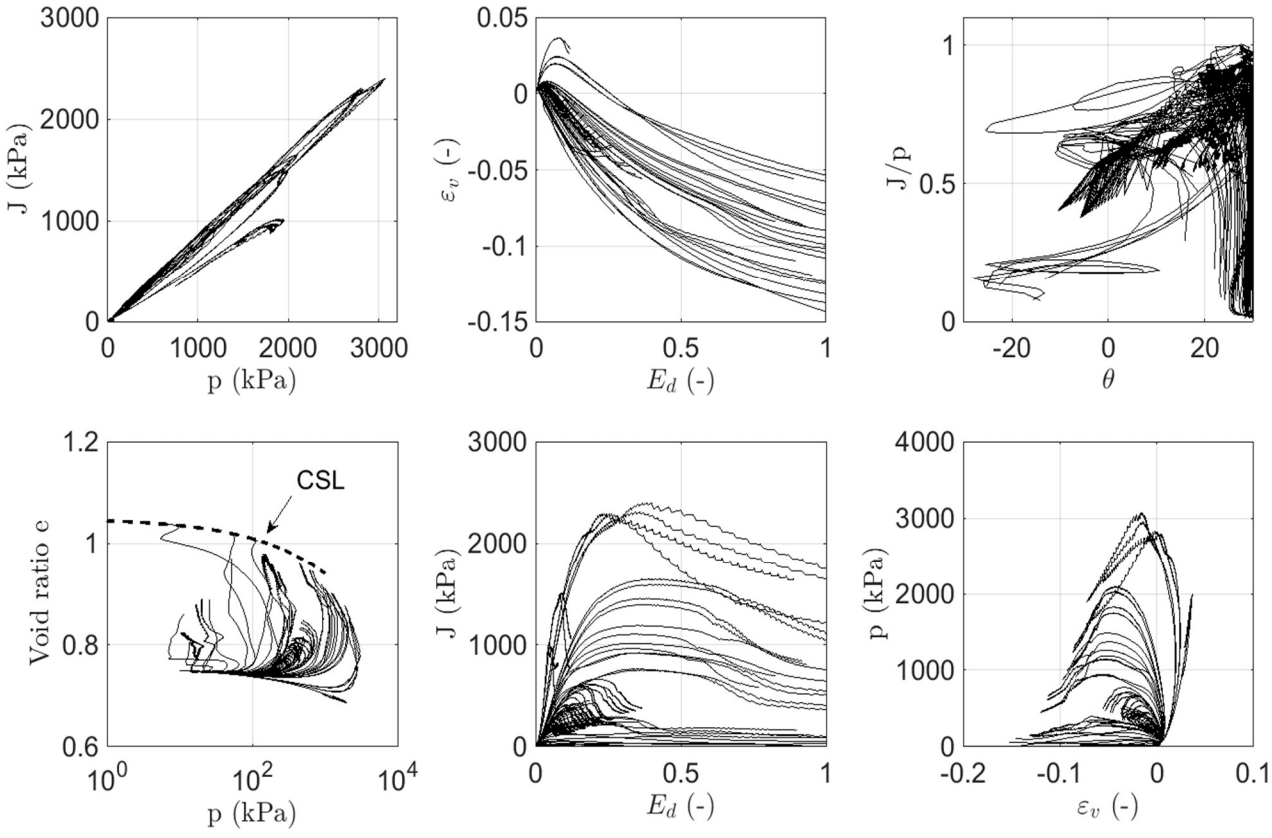


Figure 200: Stress paths for the elements investigated in the mesh, dense case, $e_{in} = 0.75$

Medium dense case

Similar conclusions can be obtained for the medium dense sand, where Figure 201 confirms that conditions for the validity of the model are fulfilled. Perhaps the condition $\dot{f}_d < 0$ is better illustrated for this case (Figure 201 bottom-left), as the endpoints of the stress paths in the e-p' plane follow the CSL slope when subjected to compression. In contrast to the dense case, many of the Gauss points reach critical state conditions when subjected to shearing (Figure 201 up-centre). No clear shear bands where observed in the boundary value problem for this case as softening is small due to the proximity of the CSL.

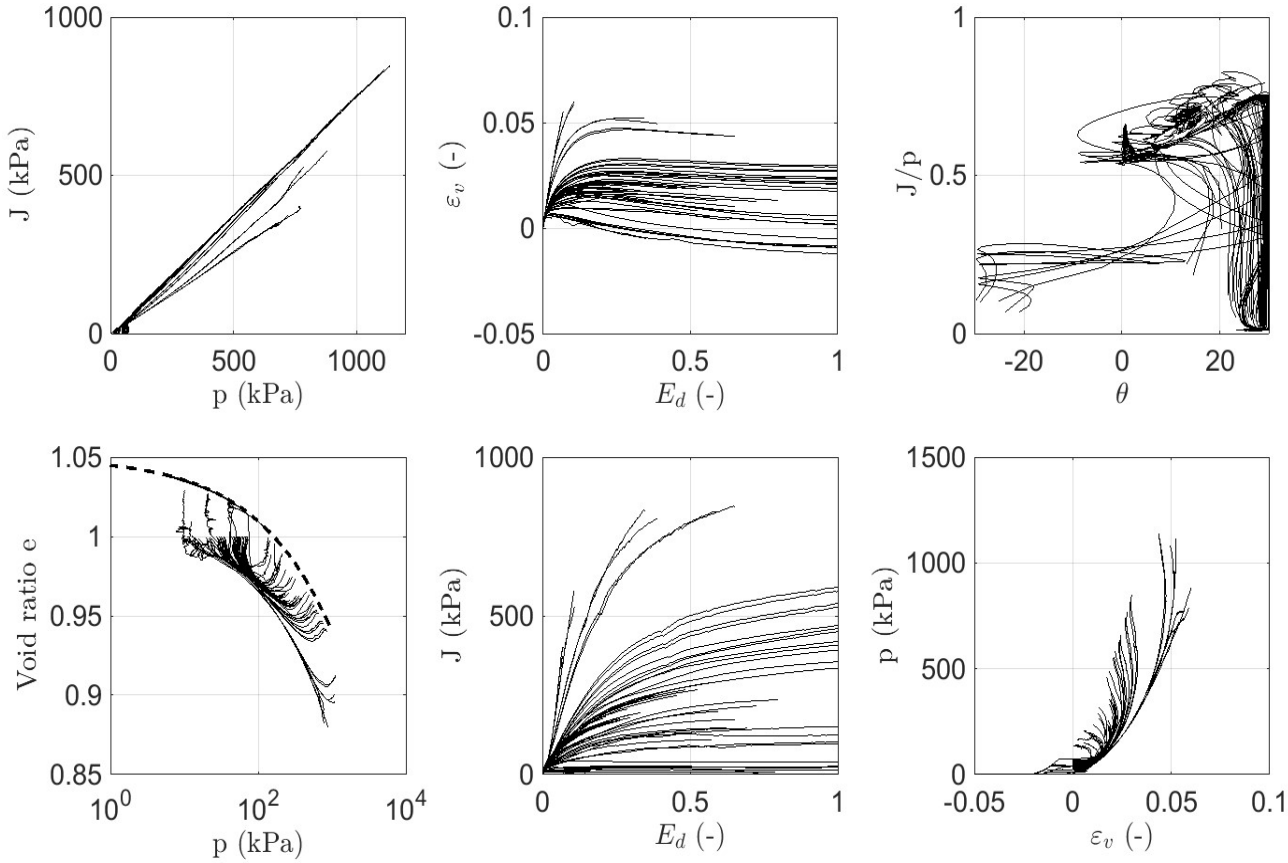


Figure 201: Stress paths for 25 elements in the mesh, slightly dense case

Loose sand case

This case, whose results are shown in Figure 202 corresponds to the case where the initial conditions are above the CSL. In this case the strain path must be contractant until critical state conditions are reached. As can be observed in Figure 202 (bottom-left) all the strain paths are contractant, and travel towards the CSL. At the same time the mobilised friction angle is lower than for the other dense cases.

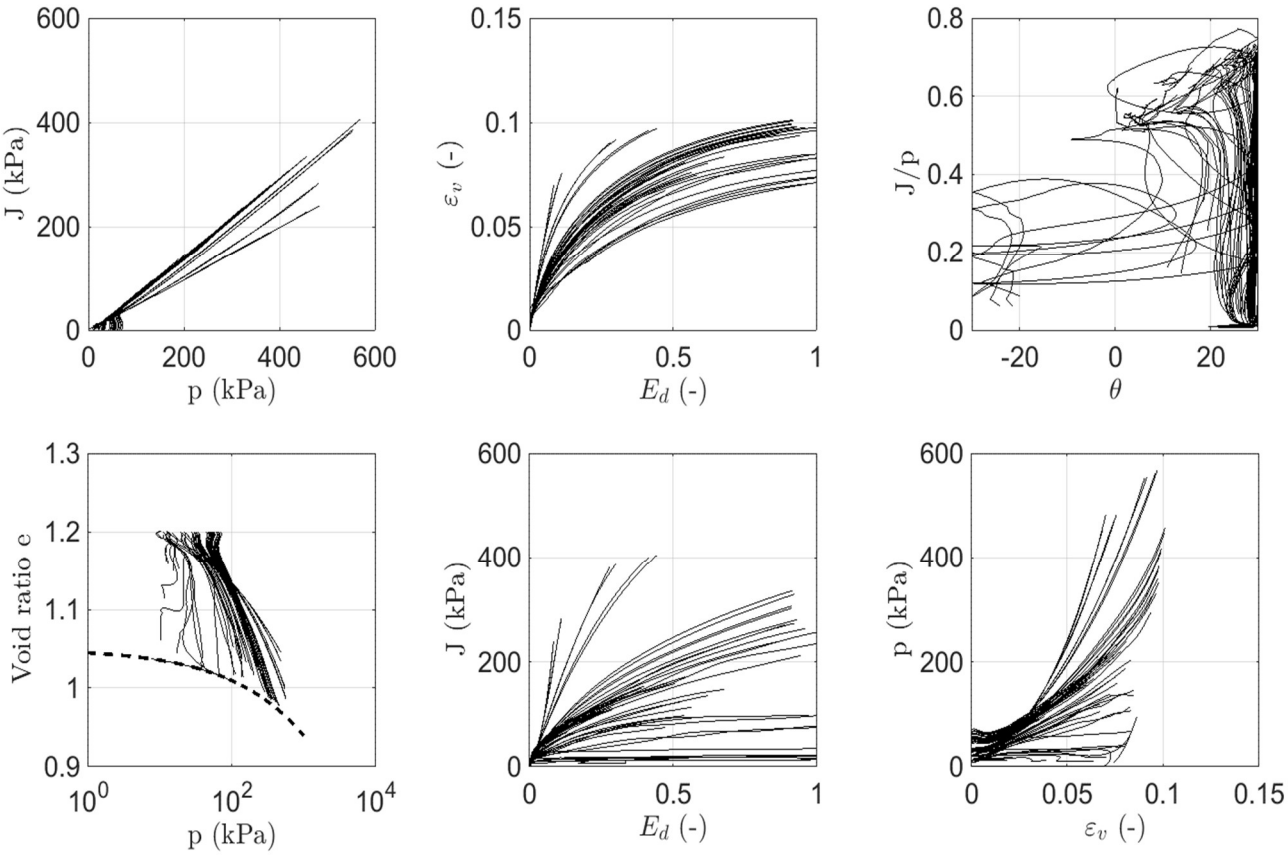


Figure 202: Stress paths for 25 elements in the mesh, loose sand case

Gauss point comparison

To carry out a comparison between all of the analyses, Figure 203 shows a total of 24 stress-strain curves, each corresponding to one of the four Gauss points of two selected elements in the mesh for each of the three analyses. The elements chosen for the comparison correspond to the location under the footing at a depth of 1.0 m and horizontally in the central axis of the footing (element 132, x/R=0.0) and at a distance of 1.3 m (element 188, x/R=1.3). These elements have different stress magnitudes, since confinement (and hence the effect of the developed stress bulb) reduces with the distance to the central axis. Therefore, the element in the centre experiences higher mean effective stresses, while its Lode's angle remains constant due to the symmetry of the model. Conversely, the element located at 1.3 metres from the centre is in the middle of the failure mechanism, though in a less confined state. Overall, it can be seen from Figure 203 that the model captures very well the response of a sand under different initial void ratios and different mean effective stresses, particularly the shear-volumetric response, the mobilised friction angle and the asymptotic behaviour in the e-p' plane.

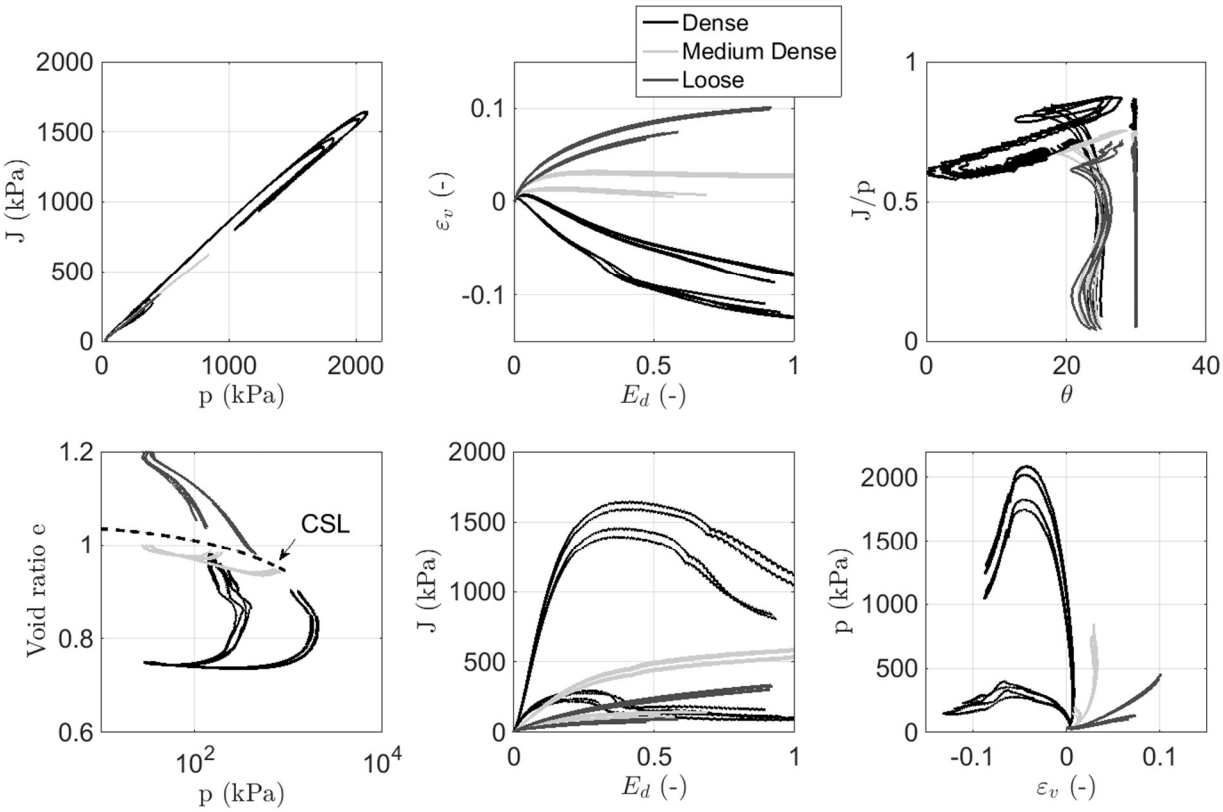


Figure 203: Stress-Strain curves at el. 132 and 188 for dense, medium dense and loose cases (x/R = [0.0 , 1.3], z/R = 1)

Summary

- In this section, the local integration of the model has been verified under monotonic conditions. Tolerances for large excursions of the Euler-forward predictions have been introduced to correct the forward excursions into problematic regions and bounds to stress paths associated with positive obliquities have been introduced as discussed in 2.5.1.
- The features of sand behaviour are appropriately accounted for under monotonic conditions, showing that the mathematical formulation of the constitutive model is robust.
- Analyses were carried out under tight tolerances, showing no global convergence issues. No mesh sensitivity study was carried out for the dense case.

5.1.4. BACKSTRESS PERTURBATION ANALYSIS

The second type of analysis for verification of the model implementation is the investigation of the backstress perturbation step described in Chapter 4. This type of perturbation can be extended to account for batches of cycles or any sort of stress relaxation in a semi-empirical way as discussed in 4.3.3.

The boundary value problem chosen to study the effect of the backstress perturbation is the dense sand case. Similarly, as in the previous analysis, the size of the mesh elements has not been investigated as the principal objective of this analysis is to verify the local integration and the ability of the boundary value problem to recover the global equilibrium after backstress perturbation.

The following section presents a comparison between the monotonic analysis and the backstress perturbation analysis at a Gauss point and at global level. Figure 204 compares the results of the monotonic case and the backstress perturbation case, showing the load displacement curve for both simulations. Three backstress perturbation steps are carried out at different load levels and are indicated in Figure 204 The figure also includes a detail of the vectors of incremental displacement in the soil underneath the footing at points A-A', B-B', C-

C’ and D-D’. In the figure points A’ and C’ show the incremental displacements vectors during backstress perturbation stage while points B’s and D’s during monotonic loading.

The load-displacement curve of the footing in Figure 204 shows the effect of the backstress perturbation, which could be interpreted as creep induced numerically. Under this condition, a perturbation of the backstress forces strains to develop to a new equilibrium state and, as a result, these strains are compliant with the redistribution of the stresses enforced by the backstress perturbation direction. This is clearly seen when comparing stage A’ with A, where the incremental displacement vectors appear in the whole mesh rather than concentrated below the footing, and again between C’ and C. The effect of the backstress perturbation is more pronounced as the soil strength is more mobilised. For example, in state C’ stress state of the soil is characterised by higher values of J/p and therefore has a higher limit surface value, providing a much larger perturbation.

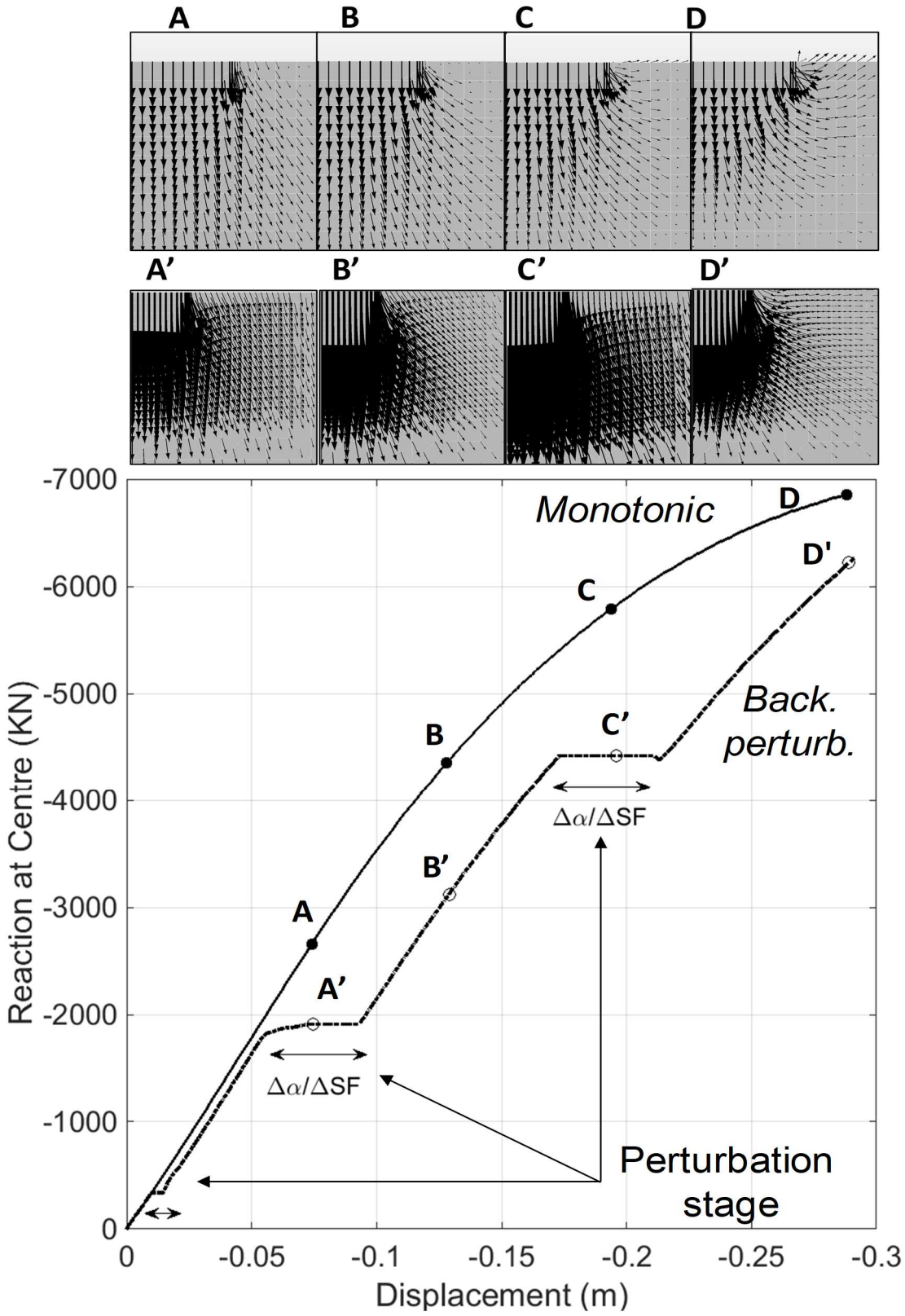


Figure 204: Load-displacement curve for monotonic analysis and backstress perturbation analysis and detail of incremental displacements below the footing

Finally, it can also be appreciated that the stages in which a perturbation of the backstress is carried out do not affect the asymptotic properties of the model. After a backstress perturbation stage the mechanism of failure follows the same trends as the monotonic incremental displacement fields. This is to be expected, as the nature of the model is asymptotic, meaning that regardless of the initial state the stress path will search for its asymptote. Therefore, even if it is perturbated numerically, and hence displaced from its associated asymptote, when monotonical loadeding is resumed the backstress will again travel back to its corresponding asymptote. This is observed when comparing the incremental vectors in C and D' which correspond to similar loading levels. This however, does not mean that the ultimate capacity of both simulations will be the same, as during the backstress perturbation the soil densifies in the whole mesh resulting in higher capacity than the purely monotonic case as the response depends on the void ratio.

5.1.4.1. Comparison between D – D'

In this section a comparison between the monotonic case and the backstress-perturbation case is discussed at the stage where footing settlement reaches 30 cm. To illustrate the effect of the backstress perturbation, a comparison is made at points D and D' (see Figure 204). In particular, in terms of displacement fields, mean stress and void ratio. It should be noted that this comparison does not correspond to the same level of loading.

Figure 205 shows the vertical displacement contours for both cases. It is evident that, in general, the backstress perturbation analysis induces higher magnitudes of displacements, which are also more widely distributed in the soil domain. This is particularly clear in Figure 205 where the vertical displacement is the same at the soil footing interface, but a larger settlement is exhibited away (both laterally and in terms of depth) as a consequence of backstress perturbation.

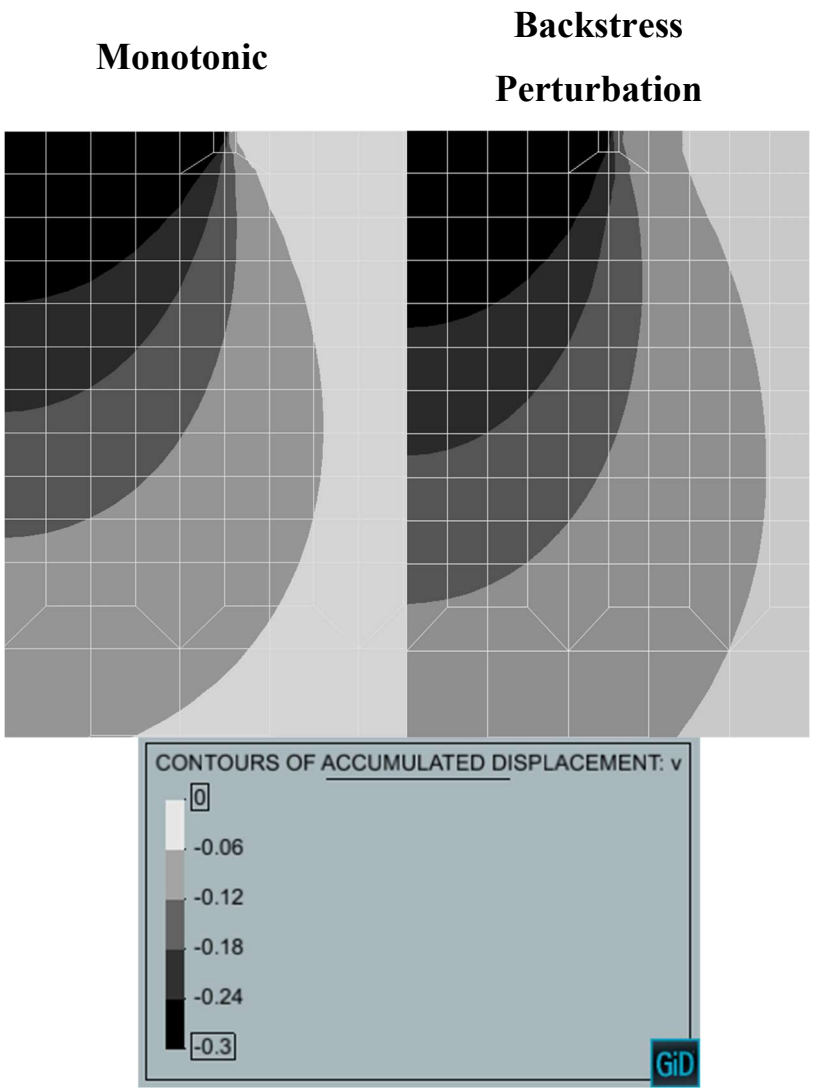


Figure 205: Vertical displacement contours at points D and D' for monotonic and backstress perturbation simulations

In a similar manner, Figure 206 shows contours of the mean effective stress at stages D and D'. However, as the mobilised load is different in both cases, it is acknowledged that limited fair comparisons can be made. A larger concentration of stresses is seen in the monotonic case as the mobilised load is higher. However, it can be expected that, since the problem is not confined, the stress field will be significantly less affected by the backstress perturbation than the displacement field. On the other hand, a different response would be expected in a boundary value problem where the displacement field was constrained, as the stress would then relax in the direction imposed by the backstress perturbation.

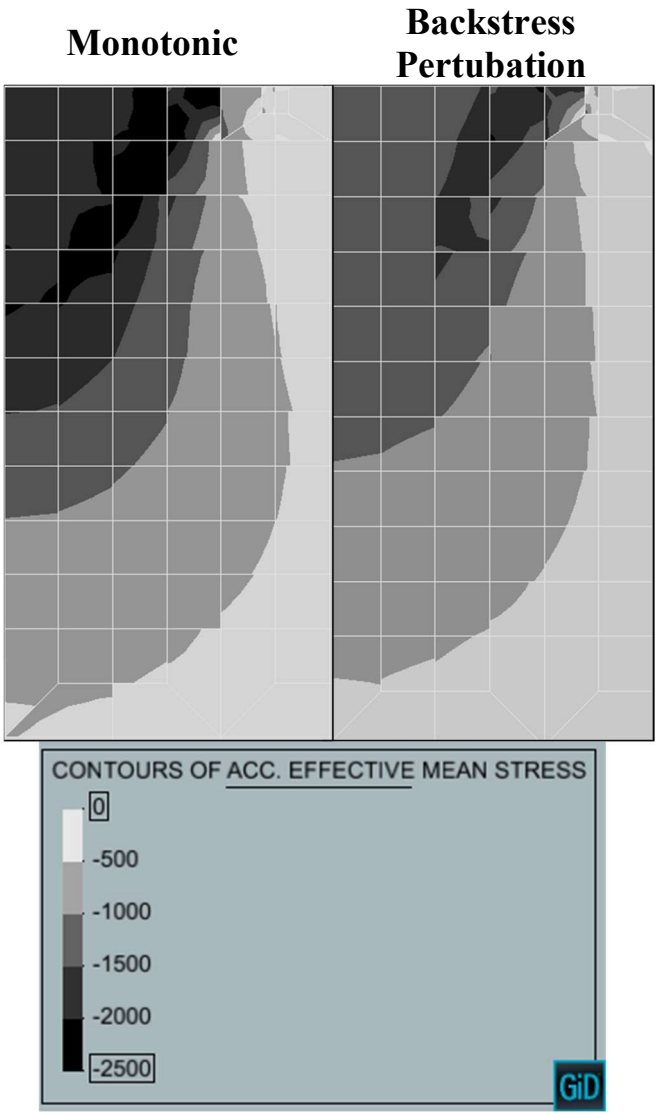


Figure 206: Mean effective stress at points D-D' for monotonic and backstress perturbation simulations

In terms of the void ratio contours at the points D and D', which are represented in Figure 207, it can be observed that the soil becomes denser for the backstress perturbation analysis, in particular because the trace of the goal fucntion is negative which forces densification in a preferential volumetric direction at low J/p' ratios.

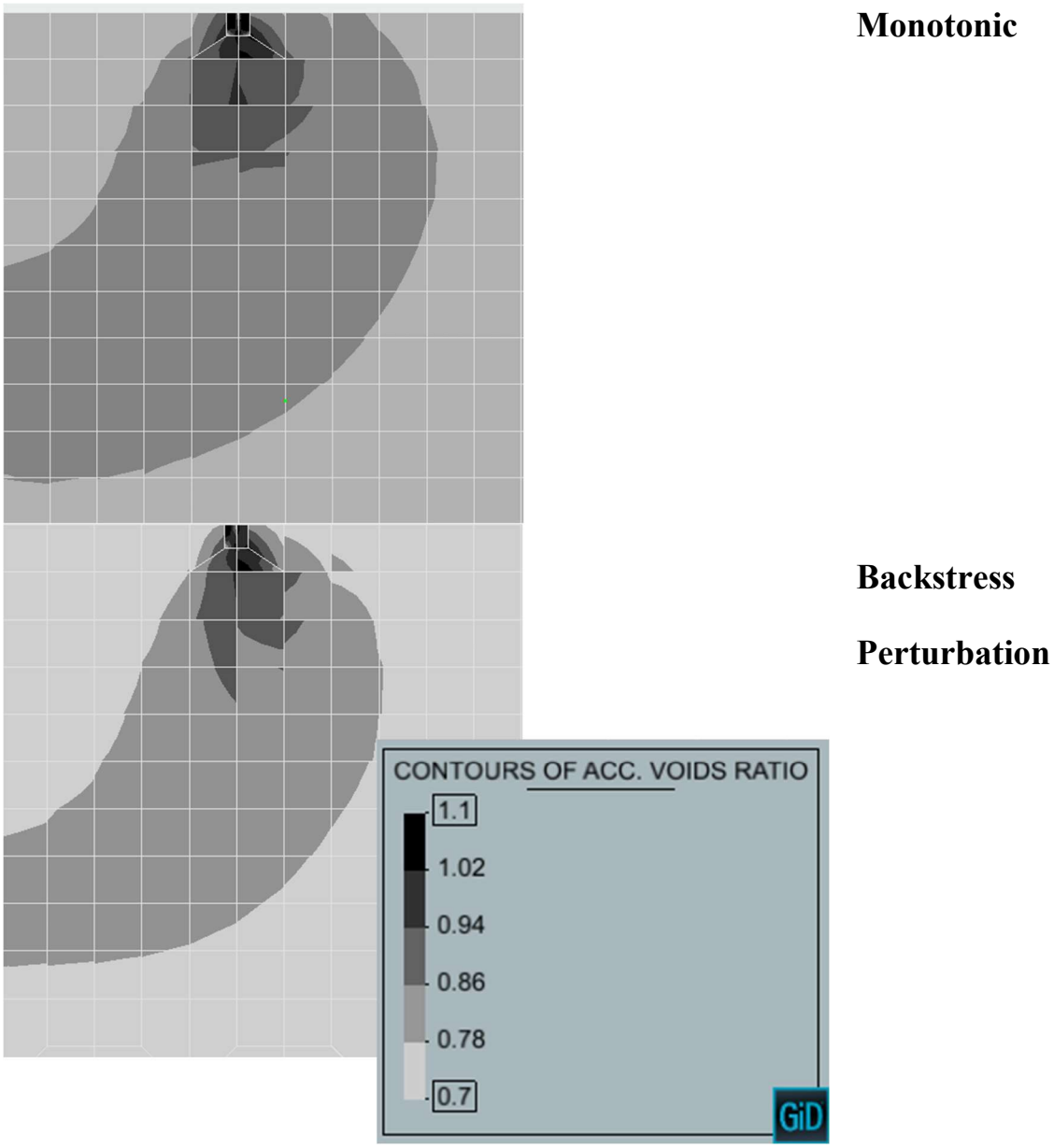


Figure 207: Void ratios at points D and D' for monotonic and backstress perturbation simulations

5.1.4.2. Stress distributions below footing

A challenging region for convergence corresponds to the elements located near the edge of the footing. In that region, a discontinuity in the stress field occurs, and for a vertically displaced footing the soil elements around the edge exhibit distortional strains above 100%. In general, these elements are highly mobilised and upon a backstress perturbation are prone to drift significantly from its previous equilibrium point. These elements impose a major challenge for the global solution system to reach equilibrium. Figure 208 shows the vertical stress distribution along the footing-soil interface at various increments of the monotonic and the backstress perturbation analyses proving that the boundary value problem can reach equilibrium after a backstress perturbation.

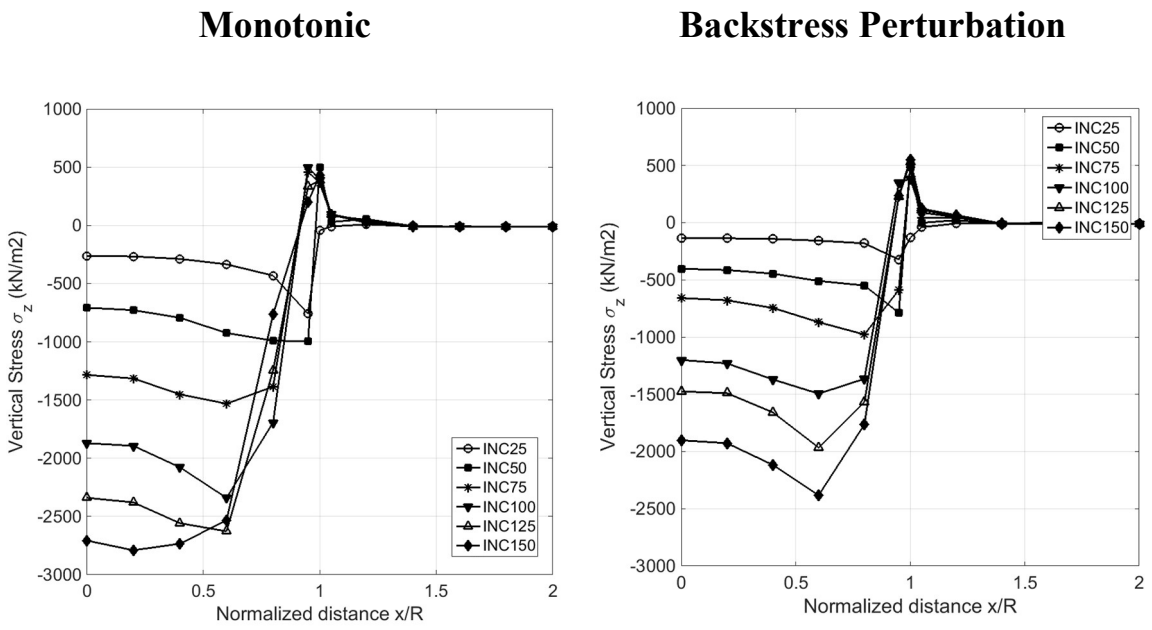


Figure 208: Vertical stress under the footing for monotonic and backstress perturbation analysis

5.1.4.3. Local Integration

In the previous section the effect of a backstress perturbation has been discussed within the context of the global problem. In this section the effect of the backstress perturbation is shown at a Gauss point scale. To do so, the same methodology as shown in the previous section is

followed, where the stress paths at Gauss points is comparted in the general invariant space in Figure 209, showing the comparison between the monotonic and backstress perturbation analyses just for the same two elements below the footing – 132 (z=-1.0 m, x/R=0.0) and 188 (z=-1.0 m, x/R=1.3).

The strain jumps imposed by the backstress perturbation analysis can be identified both in **Error! Reference source not found.** and Figure 209. As mentioned before, this boundary value problem is not confined, so the backstress perturbation shows as a numerical creep where the direction of the creep is controlled by the direction of the goal function. This characteristic is clearly seen in Figure 209, in the E_d - ε_{vol} plot (top-centre), where the strain path is consistent with the direction of the goal function akin to the monotonic case.

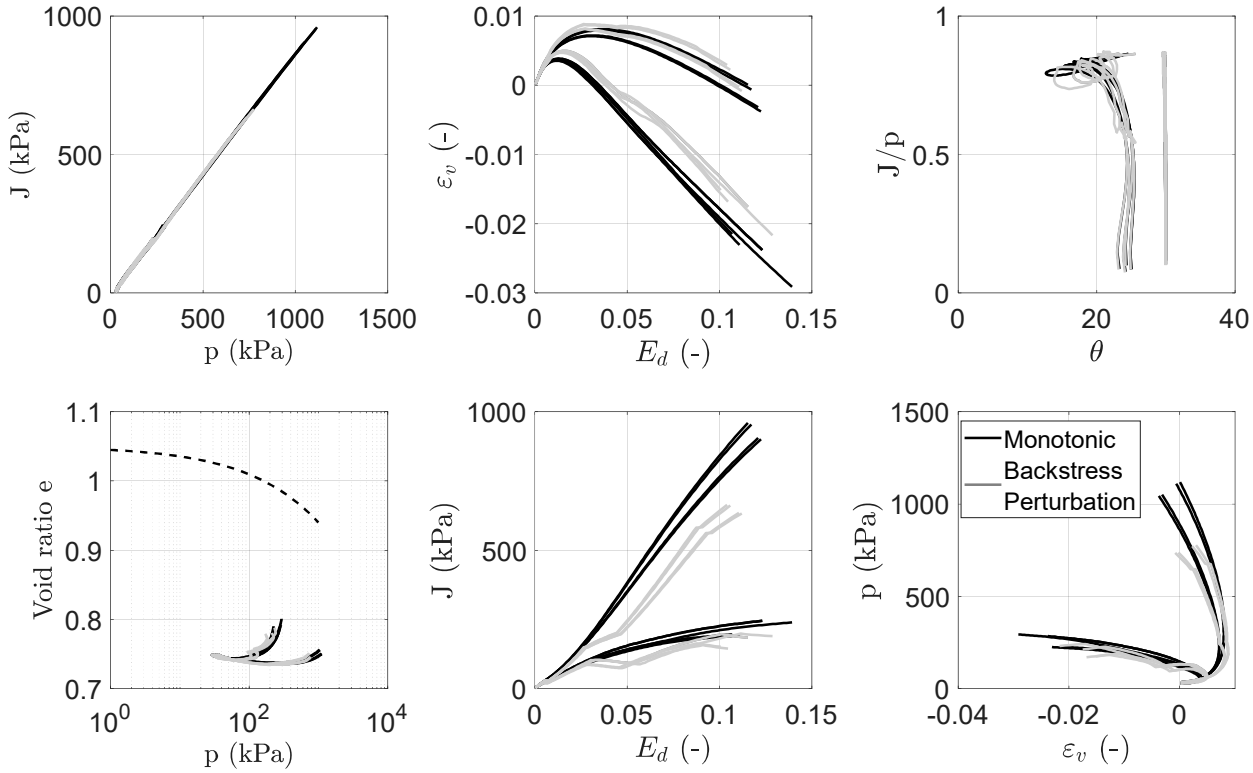


Figure 209: Stress-Strain curves at element 132 and 188(x/R =[0.0 1.0], z/R = 1)

5.1.4.4. Summary

- A numerical backstress perturbation analysis has been carried out to study the possibility of including "numerical creep" though a backstress perturbation step.
- The global and local integration of the model during backstress perturbations has been analysed in detail and its performance has been evaluated and compared with the monotonic response.
- It can be concluded that the numerical procedure can be entirely controlled by the definition of the direction of the goal function, which conveniently enables the modelling of batches of cycles that accumulate strains in preferential directions. In this respect, the response of the model can exhibit characteristics akin to those of the High-Cycle accumulation model of Niemunis et al. (2005) .

5.1.5. CYCLIC LOADING CASES

This section studies the effect of backstress superposition (Chaboche, 1991) in a set of superimposed backstress hardening rules and illustrates some examples of superposition. Five hardening rules have been implemented and four studies are carried out:

- Cyclic case with a single hardening rule
- Cyclic case with a single hardening rule plus a second linear Praguer rule
- Cyclic case with a single hardening rule plus a second non-linear rule
- Cyclic case using the implemented five non-linear backstresses.

The input parameters for the constitutive model are summarised in Table 29 and are chosen to affect the ratcheting response of the model. The inputs of the main hardening rule have been kept the same as in the previous analyses.

Table 29: Input parameters for cyclic benchmark tests

	e_{c0}	e_{d0}	h_s	n	α	β	XF	YF	ZF	ϑ	S_f	ob_{min}	ob_{max}	δ	Sd	C
Basic Sand	1.05	0.55	4E5	0.45	0.15	1.7	0.52	0.77	0.24	0.4	4.0	-1.7	1.0	2.0	1.0	0.5
Linear							1E3	0.0	0.0	4.0	1.0	0.0	0.0	-	1.0	0.5
Non-Linear							1.0	0.0	0.0	4.0	1.0	0.0	0.0	-	1.0	0.5

Figure 210 and Figure 211 show the load reaction curves for the same footing geometry depicted in Figure 193, analysed now as a plane strain case (i.e. a strip footing). Ten cycles of loading are applied, with the footing remaining rigid and with a rough interface. It is clear from Figure 210 that the inclusion of additional hardening rules results in a significant reduction of ratchetting, particularly when the extra hardening rule is linear. Figure 211 compares the curves in the boxed area in Figure 210, which resulted from the model with a superposed linear and non-linear rules. A linear rule always enforces the principal hardening rule to find its stable cycle if it exists, thus forcing the system to shakedown. On the other hand, if a stable cycle does not exist, the system will always travel to a state of minimum ratchetting regardless of the type of hardening rule.

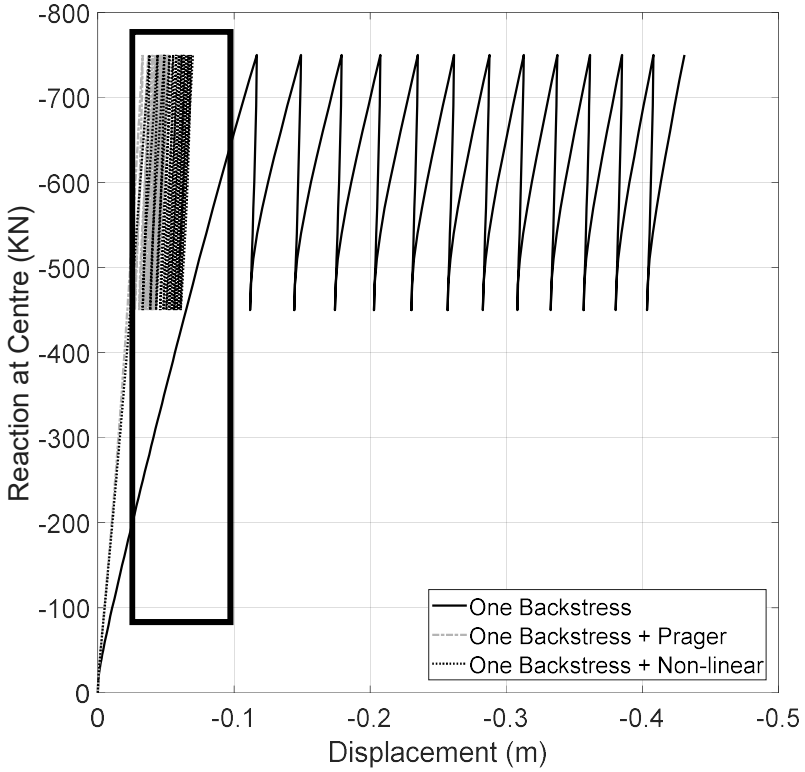


Figure 210: Displacement - Reaction at centre for three cases

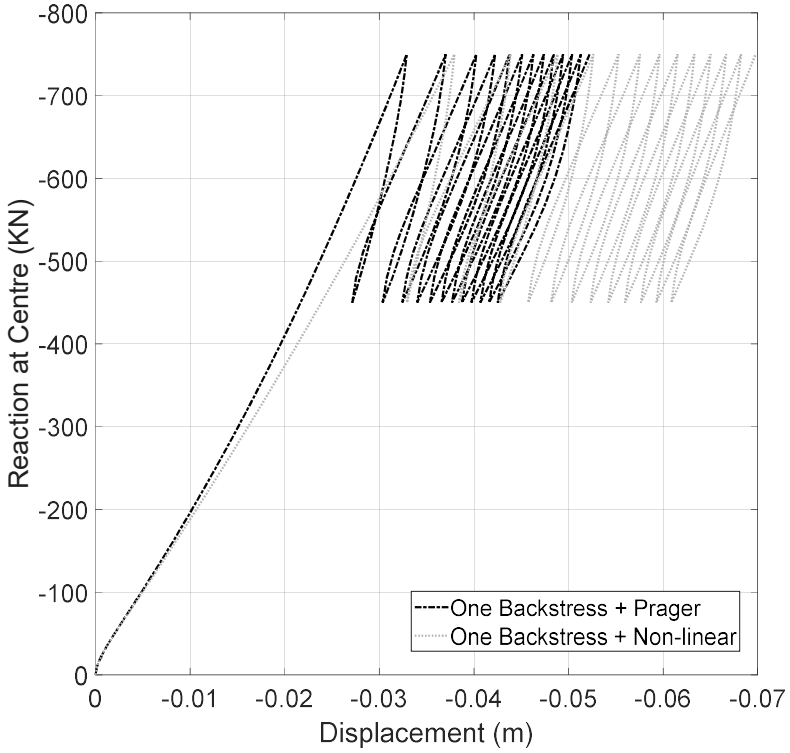


Figure 211: Displacement - Reaction at centre for backstress superposition cases (detail Figure 210).

5.1.5.1. Local integration

As discussed in Chapter 2, the adopted non-linear kinematic hardening rule searches for the minimum possible ratchetting. For each non-linear kinematic rule there exists an orbit in the J/p – z space, where "z" corresponds to the endochronic time, in which the ratcheting in the deviatoric direction is zero. When a non-liner rule is combined with a basic rule, the non-linear rule is "free" to travel to that orbit, reducing drastically the amount of ratchetting (Lemaitre and Chaboche, 1994). Following the same methodology from the previous sections, comparisons of local integration in elements 132 and 188, located 1.0 m below the footing, are shown in Figure 212 and Figure 213. The black line corresponds to the simple case where only one backstress is used, while the grey cases (light grey, dark grey) correspond to the two superposition cases.

As the proposed model admits a bipotential, the plastic shakedown theorem can be applied to the proposed model (Cheng et al., 2015). A stable cycle can be defined as the pairs in the stress-

strain space that are closed, therefore a stable cycle does not produce ratchetting. When using a combination of hardening rules, the stress solution itself becomes a combination of the various hardening rules and the system will search for the combination of strain-stress couples where the ratchetting is minimum. Therefore, ratchetting will be a function of the characteristics of each of the hardening rules. This property is illustrated in Figure 212 where the simple linear-Prager rule is compared with the non-linear rule. Clearly, the linear rule is free to travel anywhere in the stress space as it is not bounded meaning the primary rule is allowed to find its stable cycle producing the minimum ratchetting possible. Conversely, the non-linear kinematic rule is bounded in the stress space, which does not allow the primary rule to find its minimum stable cycle, generally producing more ratchetting.

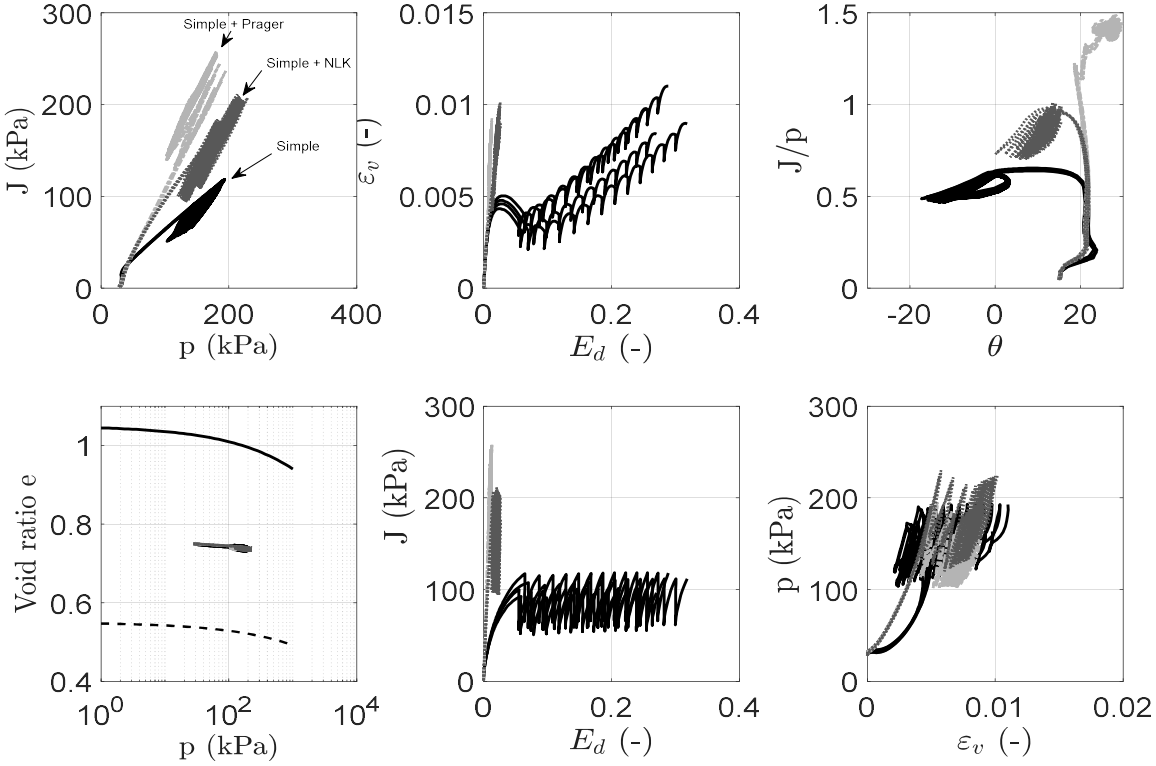


Figure 212: Stress-Strain curves at element 132 (x/R = 1.3, z/R = 1)

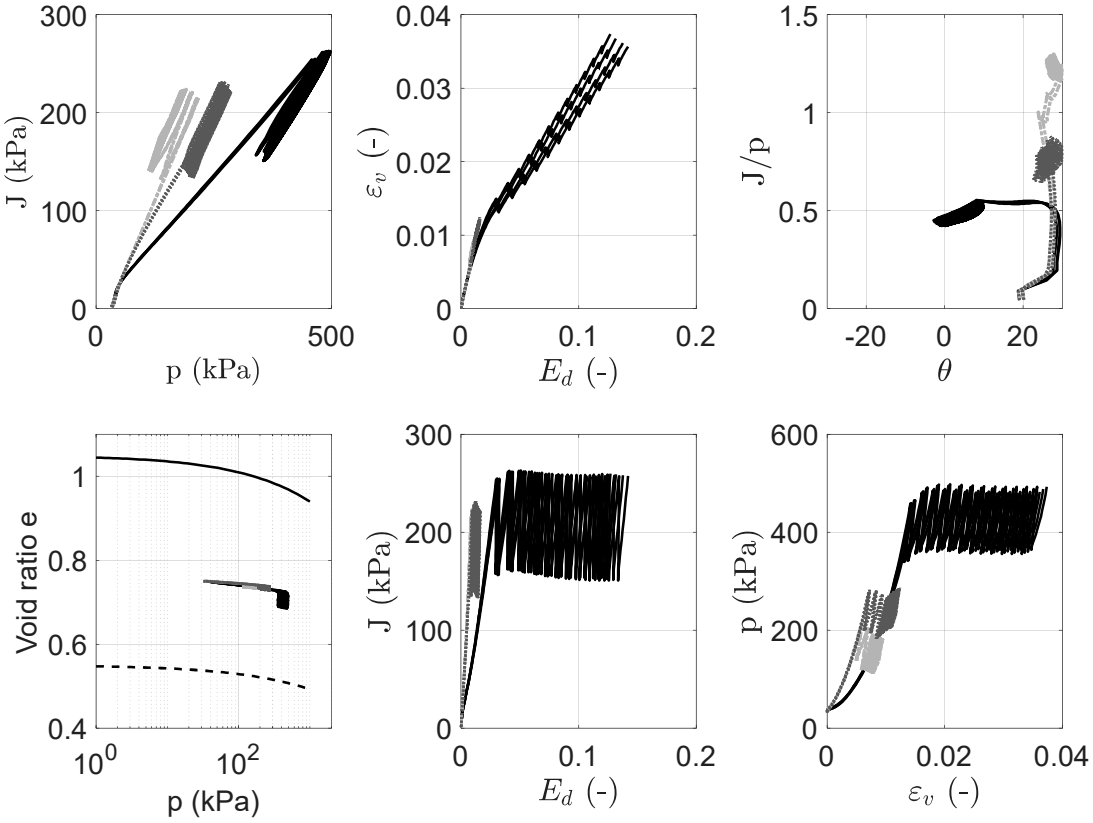


Figure 213: Stress-Strain curves at element 188 (x/R = 0.0, z/R = 1)

5.1.5.2. Superposition of five backstresses

To check for possible errors during their implementation, a test using five backstress hardening rules has been carried out, in this case under axisymmetric conditions (i.e. a circular footing). The model input parameters are given in Table 30.

Table 30: Input parameters for five backstress case

	e_{c0}	e_{d0}	h_s	n	α	β	XV	YF	ZF	$\mathcal{S}$	S_f	ob_{min}	ob_{max}	δ	S_d	C
Rule 1	1.05	0.55	1E6	0.55	0.08	3.0	0.55	0.87	0.1	0.4	3.0	-1.7	0.45	2.25	1.0	0.8
Rule 2							0.5	0	0.1	2.0	1.0	-1.7	-1.7	-	1.0	0.2
Rule 3							0.5	0	0.1	2.0	1.0	-1.0	-1.0	-	1.0	0.2
Rule 4							0.5	0	0.1	2.0	1.0	0.0	0.0	-	1.0	0.2
Rule 5							0.5	0	0.1	2.0	1.0	0.3	0.3	-	1.0	0.2

Figure 214 shows the load – displacement curve of the footing with a single rule and the case including five backstresses. In the latter case a slight reduction of ratchetting must occur as the extra hardening rules have a less strong recall term when compared to the main rule. However as the sum of the weights "C" in is greater than one the predicted response of the case with five backstresses is stiffer.

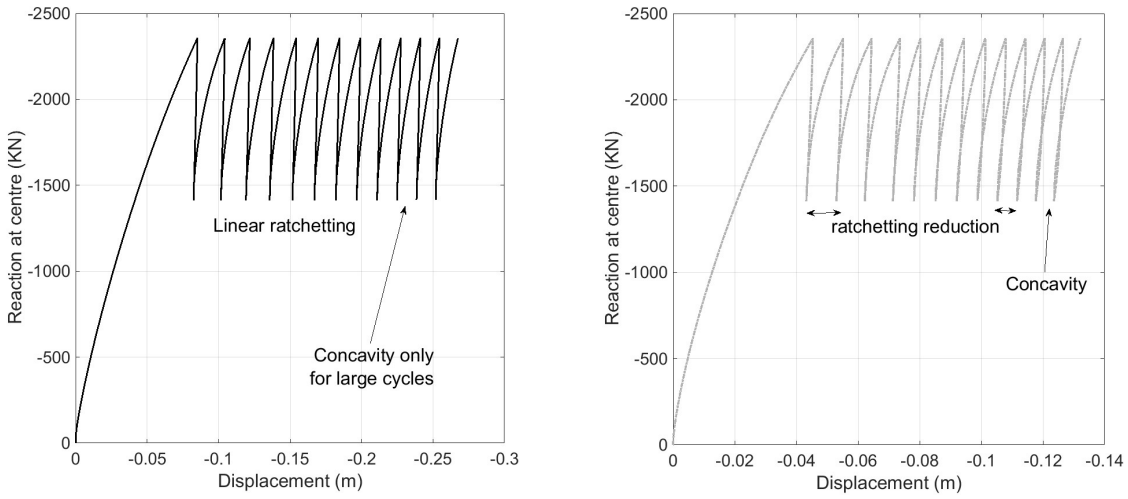


Figure 214: Detail of load-displacement curve for one backstress (a) five backstresses (b)

As expected, when more than one NLKH hardening rule is used, upon cyclic loading, the system tries to reach a combination of strain-backstress cycles compatible with the stress cycles that produce minimum strain accumulation per cycle. As a result, a reduction in the strain accumulation is achieved on every cycle. The inputs in To check for possible errors during their implementation, a test using five backstress hardening rules has been carried out, in this case under axisymmetric conditions (i.e. a circular footing). The model input parameters are given in Table 30.

Table 30 have been chosen to verify the FEA implementation, two of the rules (2, 3) produce a mean backstress relaxation per cycle, travelling to a mean effective stress of zero and becoming inactive after a sufficiently large number of cycles. Conversely, the fifth rule behaves in the opposite manner and is therefore expected to take over and control the ratchetting direction as the number of cycles increases. This is illustrated in Figure 215, where the stress and strain paths are shown for element 132. It should be noted that for the case with five

backstresses the ratchetting direction starts being contractive but ends up exhibiting dilation upon every cycle as the fifth rule takes over. The interpretation of the response when so many hardening rules are present is complex, particularly if the rules are free to move in the volumetric and deviatoric direction. It is recommended to use specialised hardening rules, of the form of those described in Chapter 4.

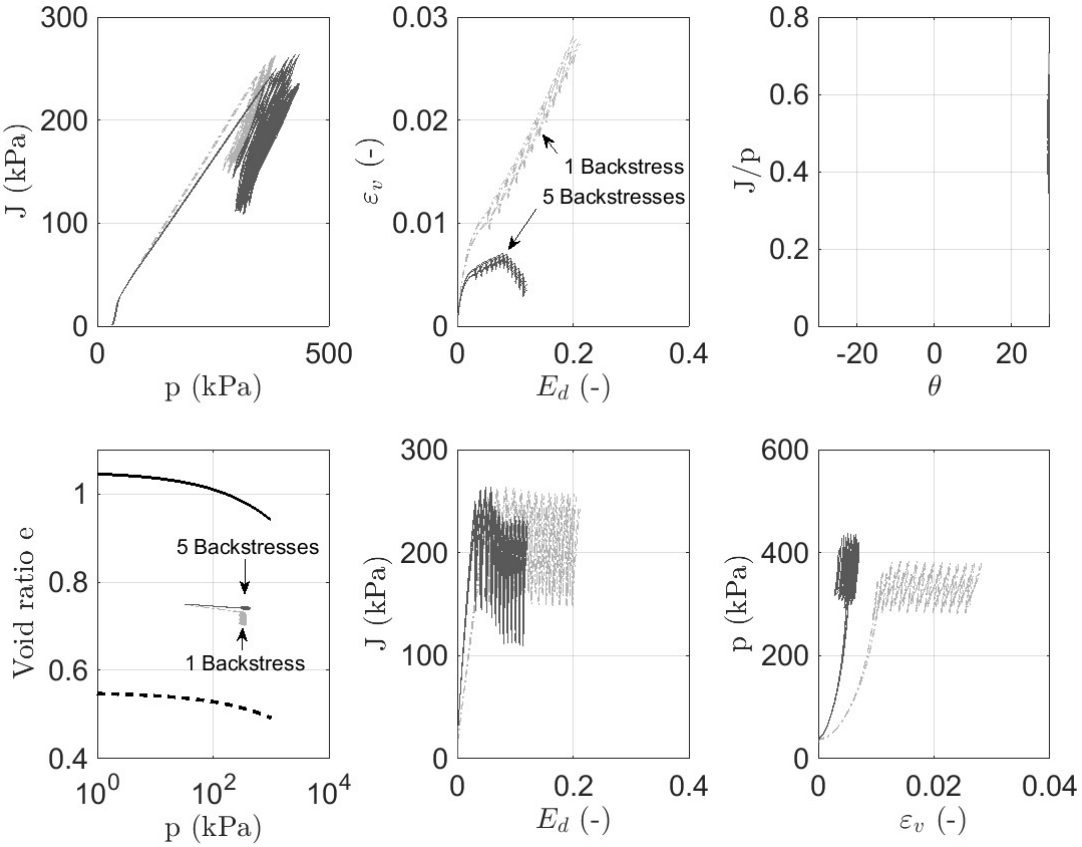


Figure 215: Stress-Strain curves at element 188 (x/R = 0.0, z/R = 1)

5.1.5.3. Summary

- The local integration of the model has been adjusted to accommodate up to four extra backstresses.
- The effect of adding more backstresses allows the calibration of ratchetting, due to the properties of NLKH models (as discussed in Chapter 2)
- The inputs of the model include the weigths of the principal direction of the mapping tensor, as a result it is possible to create hardening rules that move only in the deviatoric or volumetric directions.
- As the sum of backstresses holds and corresponds to the centre of the yield surface, it is always possible to return to a simple hardening rule if monotonic conditions are required after a batch of cycles just turning the weights "C" to zero and enforcing the first backstress to be the sum of all backstreses. The rules can be activated and deactivated at will without complexity.

5.2. APPLICATION TO MONOPILE FOUNDATIONS FOR OFFSHORE WIND TURBINES

The non-linear kinematic hardening framework described in this thesis is applied here to model the large-scale field tests of the Pile Soil Analysis (PISA) project. The project involved a joint academic-industry group to develop new design methods for laterally loaded piles and large-scale pile testing was one aspect of the project. The academic side comprised teams from Imperial College, Oxford University and University College Dublin. The industrial partners comprised 10 major offshore wind developers led by Ørsted (formerly DONG Energy), under the Carbon Trust's Offshore Wind Accelerator programme. The field testing studied the response of laterally loaded piles under monotonic loading, although some of the piles were also subjected to cyclic loading. The emphasis of the project was on the optimization of pile design methods with low slenderness ratio L/D (embedded length/diameter), which are typically found in monopile foundations for offshore wind turbines. This section firstly describes the field tests and ground conditions, followed by the interpretation of the ground model, model calibration and 3D FE modelling. The final section studies the model prediction under cyclic conditions, using some of its advanced features described in previous chapters.

5.2.1. DUNKIRK FIELD TESTING PROGRAMME

The Dunkirk test site is part of an extended beach area, situated on the land owned by the Port Authority of Dunkirk. The soil is characterised as a dense marine Pleistocene sand. The water table at the time of the test programme was at approximately 5.4m depth. This implies the existence of a potentially unsaturated region of sand in the top few metres of soil. This hypothesis is reinforced by a clear gap observed to form on the active pile face during loading and on the passive pile face during unloading (Figure 216). The gaps would typically collapse several days after completion of the tests, which supports the idea that some suction was in the ground during loading. Further description of this effect is given subsequently, when discussing the ground conditions. All the monotonic and cyclic loading tests, including the geometry and loading conditions, are specified in Table 1.

Table 31: Test pile geometries and loading at Dunkirk site

Test	*Type*	D (m)	L (m)	L/D	*t* (mm)	h (m)
DS1	***Monotonic***	0.273	1.43	5.25	7	5.0
DS2	***Rate***	0.273	1.43	5.25	7	5.0
DS3	***Monotonic***	0.273	2.18	8	7	5.0
DS4	***Monotonic***	0.273	2.73	10	7	5.0
DM5	***Monotonic***	0.762	2.27	2.98	9.99	9.99
DM7	***Monotonic***	0.762	2.24	2.94	10.0	10.0
DM9	***Monotonic***	0.762	3.96	5.2	10.0	10.0
DM4	***Monotonic***	0.762	3.98	5.23	9.98	9.98
DM2	***Monotonic / Cyclic***	0.762	3.99	5.24	10.0	10.0
DM1	***Cyclic***	0.762	3.97	5.21	10.02	10.02
DM6	***Monotonic / Rate***	0.762	3.99	5.23	10.0	10.0
DM3	***Monotonic***	0.762	6.02	7.9	10.06	10.06
DL1	***Monotonic / Cyclic***	2.0	10.61	5.3	9.9	9.9
DL2	***Monotonic / Cyclic***	2.0	10.57	5.29	9.89	9.89

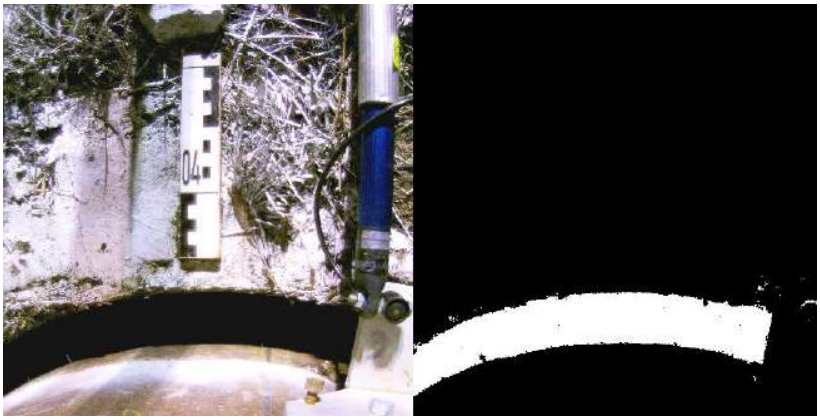


Figure 216: Detail of gap and vertical slope during test loading (AWG, 2015)

Three diameters were tested for L/D ratios between 3 and 10. The arrangement of the site is shown in Figure 217. The smallest diameter piles (DS, D=0.273 m) where tested around the medium diameter DM9 pile which acted as reaction pile. In a similar manner, the medium diameter piles (DM, D=0.762 m) where loaded against a larger diameter reaction pile DR1. Finally, two large diameter piles (DL, D=2.0 m) were loaded against one another. Special loading frames were designed for each of different pile diameters to apply the horizontal load above the ground surface, thus reproducing the position of the load application point typically

observed in wind turbines. For DM and DL this was at a stickup height h=10 m, while for DS piles h=5 m (see Figure 215).

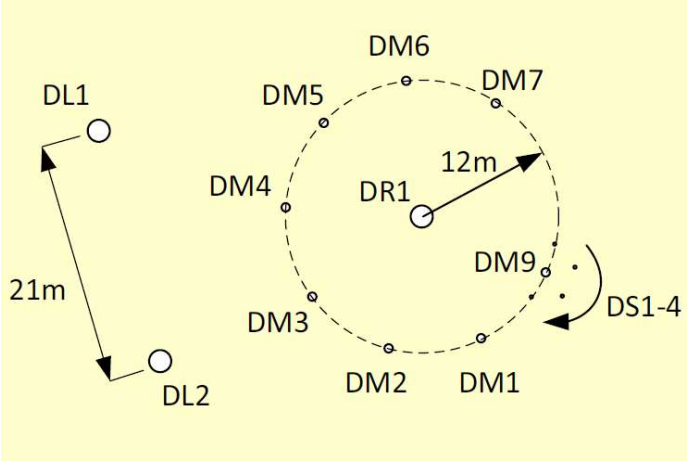


Figure 217: Pile layout at Dunkirk (McAdam, 2018)

Figure 218 shows a sketch of a cross section of the three pile arrangements described above, for each of the pile diameters (0.273 m, 0.762 m, 2.0 m).

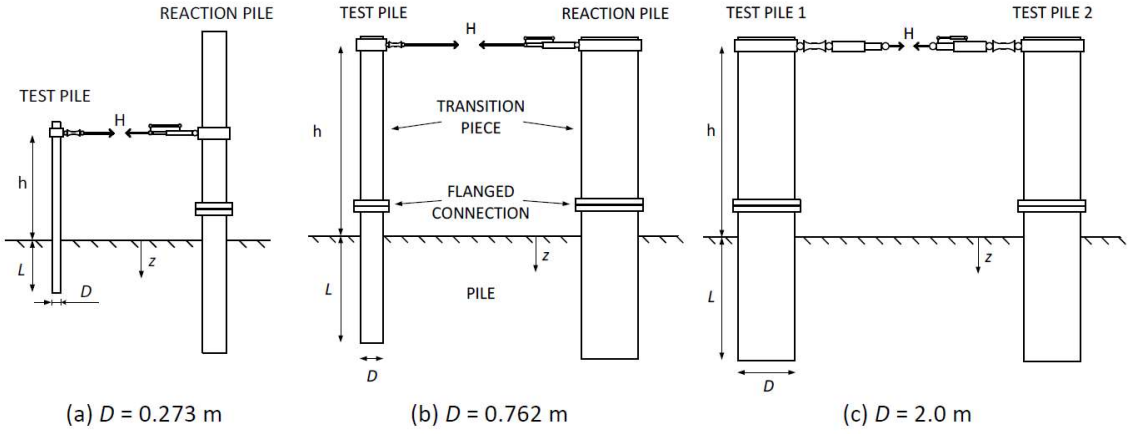


Figure 218: Test configuration for lateral loading for each pile diameter (McAdam, 2018)

5.2.2. SOIL CHARACTERISATION AND MODELLING

The section describes the calibration of the constitutive model and the FE boundary value problem.

5.2.2.1. Geometry and boundary conditions

Four representative piles DM7, DM4, DM3 and DL2 were selected for detailed numerical analyses, with details of the geometries as given in Table 31. Pile geometries are identified in terms of diameter, D, embedded length, L, stickup height, h, and the pile wall thickness, t. The geometry contains a plane of symmetry and only half of the problem is discretised in a finite element mesh. The soil domain is represented with 8484 20-noded displacement-based hexahedral elements, with its bottom boundary at 40 m depth. The vertical cylindrical boundary is at 30 m radial distance for medium diameter piles (D = 0.762 m) and at 40 m distance for large diameter (D = 2.0 m) piles. The pile is discretised with 420 8-noded shell elements (Schroeder et al., 2007), assuming the steel to be linear-elastic, with a Young's modulus E = 200 GPa and a Poisson's ratio ν = 0.30. Special interface elements are introduced around the outside of the pile to allow appropriate constitutive modelling of the pile-soil interface. These are 16 node zero-thickness elements (Day and Potts, 1994), which allow for the separation between the pile and soil to occur, if triggered, they are simulated with an elasto-plastic Mohr-Coulomb model. The elastic parameters of this model are the normal (K_N) and shear (K_s) stiffness values which are both set to 10^5 kN/m^3, ensuring a rough interface and no compression deformation across the element. The plastic part is characterised with zero cohesion (c'= 0) and angle of shearing resistance equal to soil at critical state failure in triaxial compression conditions (ϕ' ~ 32°). Figure 219 shows a picture of the mesh used in one of the analysis.

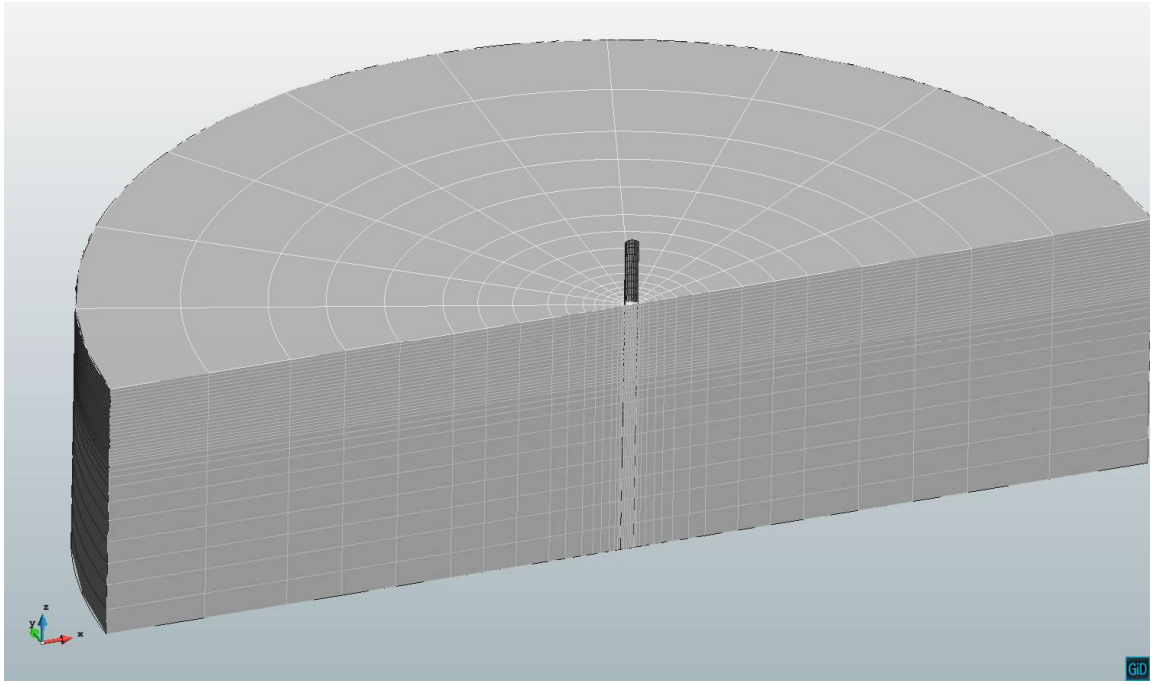


Figure 219: Mesh used for 2m. diameter pile DL2

The applied boundary conditions prevent movements in all coordinate directions (X, Y, Z) at the base of the mesh (at Z = -40m) and in the direction normal to the vertical cylindrical boundary. The plane of symmetry at Y = 0 requires that the displacements in the Y - direction must be set to zero over this plane. Equally, the rotational degrees of freedom about the X and Z axes must be set to zero at the nodes of shell elements contained in the Y = 0 plane. The loading of the pile (at Z = h = 10m) is simulated by applying uniform increments of horizontal displacement in the X-direction around the perimeter of the pile.

5.2.2.2. Ground conditions

The stratigraphy of the Dunkirk site is described in Table 5, the Dunkirk sand deposit consists of a 3.0 m-thick hydraulic fill from the natural sand, overlaying the natural sand deposit. The fill was placed in 1970s to raise the ground level. The pore water pressure profile on site is estimated from the new CPTu tests commissioned as part of the PISA Project shown in Figure 220, indicating the ground water table at 5.4 m depth and a hydrostatic distribution below it. Above the water table the conditions are uncertain, as piezocones are not suited for measuring negative pore water pressures. However, from the work on site it was evident that the ground surface was able to sustain significant effective stresses and subsequent pile testing under lateral load revealed stable gaps occurring around piles. No high-quality sampling was conducted at Dunkirk and no other investigation of the fill material in the top 3.0 m was caried out to characterise the source of its strength and stability. Consequently, the indication of some suction above the ground water table was considered a reasonable option for generating additional strength in the fill in numerical analyses. As shown in Figure 220, the adopted suction profile can be described as: hydrostatic suction from the ground water table to 4.0 m depth, constant suction of 13.5 kPa to 2.0 m depth, then reducing to 10 kPa at the ground surface. The summary data from cone penetration tests (CPT) is shown in Figure 221, which were taken at the position of each pile, the figure shows the maximum and the minimum measurements, indicating a reasonably small variability across the site.

The initial stresses in the ground are obtained using the saturated bulk unit weight γ = 17.1 kN/m^3 above the water table and 19.9 kN/m^3 below it to calculate the total vertical stress. This combined with the pore water pressure in Figure 220 to establish the vertical effective stress, while the horizontal effective stress is then initiated by applying the coefficient of earth pressure at rest, K_0 = 0.4, for a normally consolidated Dunkirk sand.

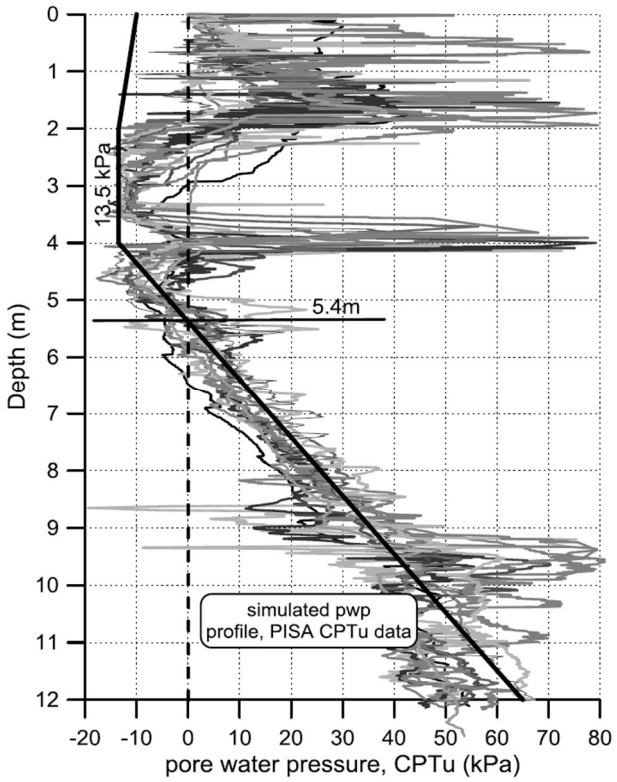


Figure 220: Pore water pressure profile at Dunkirk from CPTu tests (AWG, 2015)

The interpretation of the relative density profiles from the CPT data showed significant dependency of the adopted correlation with the cone resistance. The correlation of Kulhawy and Mayne (1990) resulted in a relative density profile closer to that estimated in Chow (1997): the relative density was considered to be 100 % for the hydraulic fill (top 3 m) and 75 % for the rest of the deposit, which was translated into an initial void ratio of $e_0 = 0.57$ in the hydraulic fill and $e_0 = 0.628$ in the natural sand at 75% relative density (Liu et al. (2017)).

Table 32: Stratigraphy at Dunkirk and CPT measurements

Depth	Material description
0-3 m	Hydraulic fill: Sand fill that was dredged from offshore Flandrian deposits, and placed to raise the ground level. No compaction or surcharge has taken place
3-30	Flandriand sand: Marine sand deposited during three local marine transgressions. These sands are often separated by organic layers. A 600 mm thick organic layer is found at 8 m depth, separating the Flandrian sand into upper and middle units.

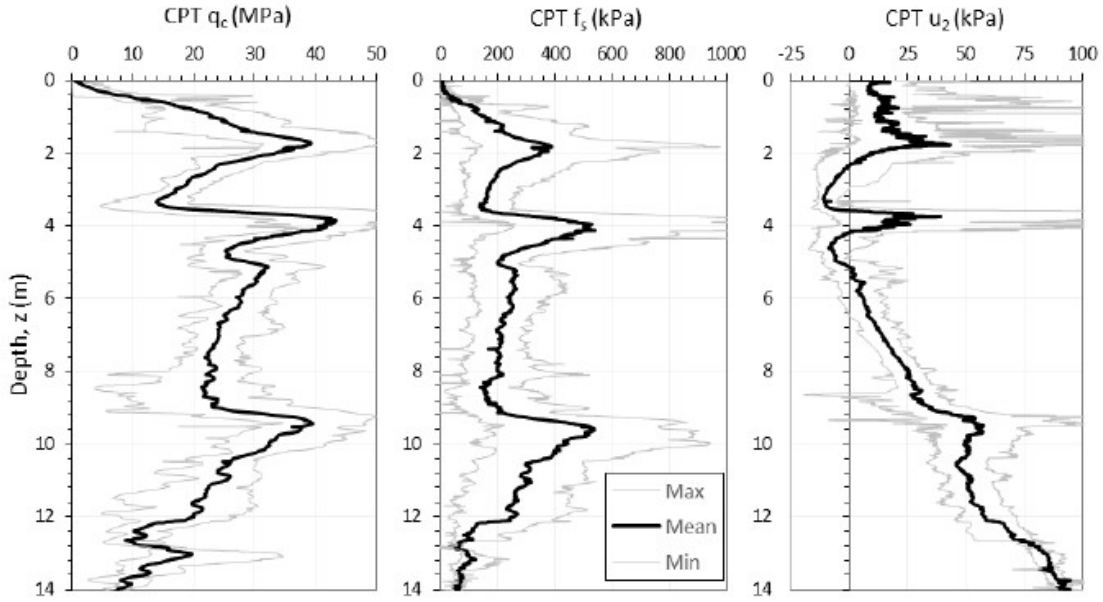


Figure 221: New CPT profiles for Dunkirk site (AWG, 2015)

The same initial pore water pressure profile is prescribed in the interface elements located at the pile-soil interface, with the interface effective normal stress prescribed as equal to the horizontal effective stress in the adjacent soil elements. This ensures the continuity and equilibrium of the stress field at the start of analysis. The pile is modelled as wished in place and therefore installation effects are not considered. All analyses are assumed under drained conditions following the same methodology of the PISA project. Drained conditions are expected for the loading amplitudes and frequencies of the field tests combined with the fact that the first five metres are in unsaturated conditions. No piezometers were installed in Dunkirk site.

5.2.2.3. Methodology for constitutive model calibration

A total of 14 triaxial compression tests in Dunkirk sand model with initial void ratios ranging from 0.57 to 0.72 (Liu et al., 2017) has been used to calibrate the basic sand constitutive model. The stress-strain curves are shown in Figure 222 where it can be seen that, despite its very dense state, the Dunkirk sand does not exhibit a substantial softening after peak strength. Also, it is important to mention that in none of the tests clear critical state conditions after 20% of strain are reached. Nevertheless, the asymptotic tendencies associated with its J/p' - e plane could be clearly identified. The asymptotes have been marked with dashed lines and arrows in Figure 222.

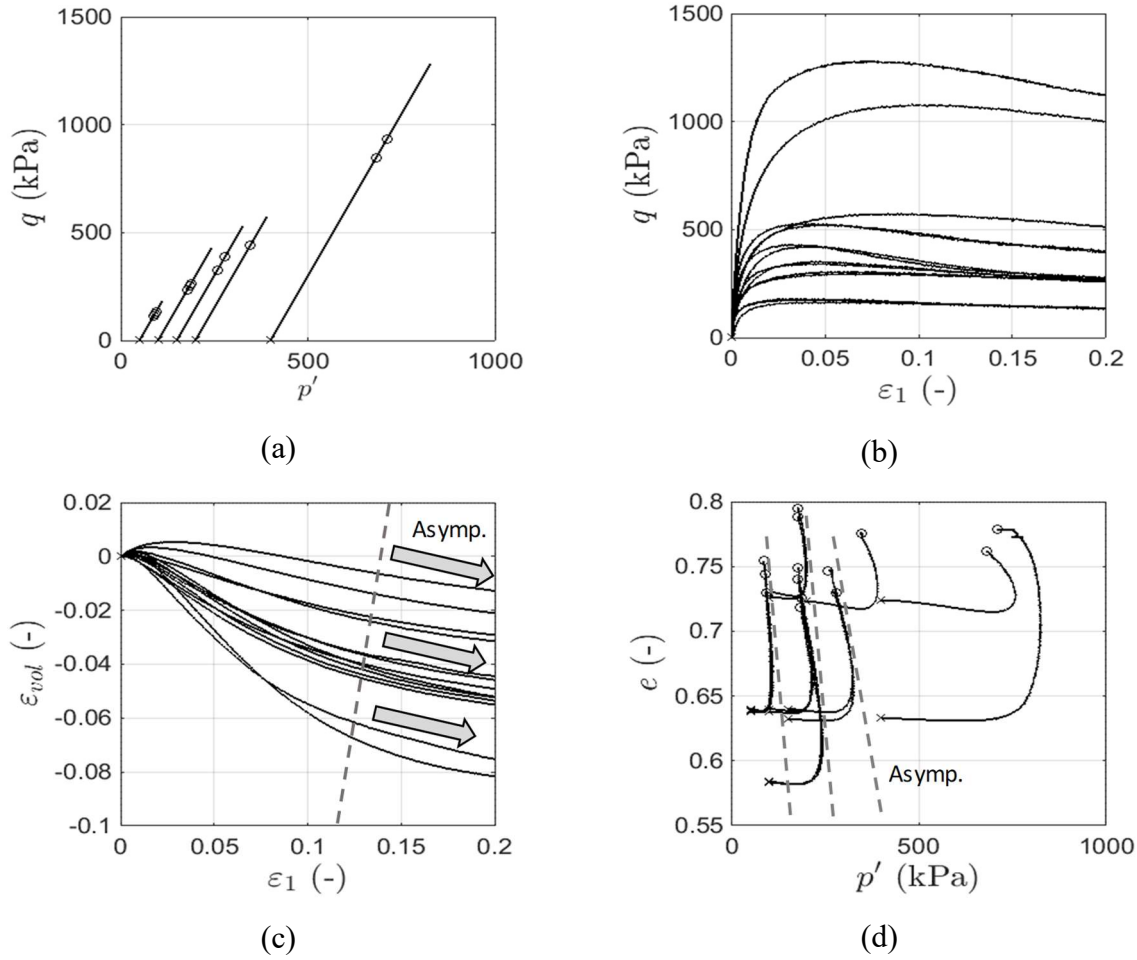


Figure 222: Triaxial tests in Dunkirk sand used for calibration. (Liu et al, 2017)

None of the tests have experienced true critical state conditions and therefore the interpretation of the CSL in Figure 222 must lie above the end points (open circles Figure 222d) of all paths in the e-p' plane. Additionally, due to the absence of other strain-controlled tests (e.g. TXU, isotropic or oedometric), the shape of the CSL (h_s, n) is based only on the drained traixial data, assuming a realistic mapping tensor deviatoric shape factor S_d. Also, this implies that the $J/p' - n_{kk}$ asymptotic envelope (introduced in Chapter 2) cannot be fully defined for low J/p' values.

To mitigate the lack of data with respect to the asymptotic behaviour, two strategies to calibrate the tests have been followed. For the first strategy, the goal functions, which control the position of asymptotic states, have a sharper change as J/p increases, reaching a smaller maximum obliquity at high J/p' values (top-left diagram in Figure 223). For the second strategy the obliquity of the goal function has a gentler transition with respect to J/p' ratio (top-left diagram in Figure 224). Another difference between calibration sets has been the use of different e_{d0} - α values to explore the effect of peak value and post peak behaviour. Figure 223 and Figure 224 present the data of the 14 tests depicted in Figure 222 in the n_{kk} – J/p' space for calibration purposes. The figures include the position of the critical state line, minimum void ratio line, the curvature of the limit surface and the obliquity of the goal functions with respect to the J/p' ratio.

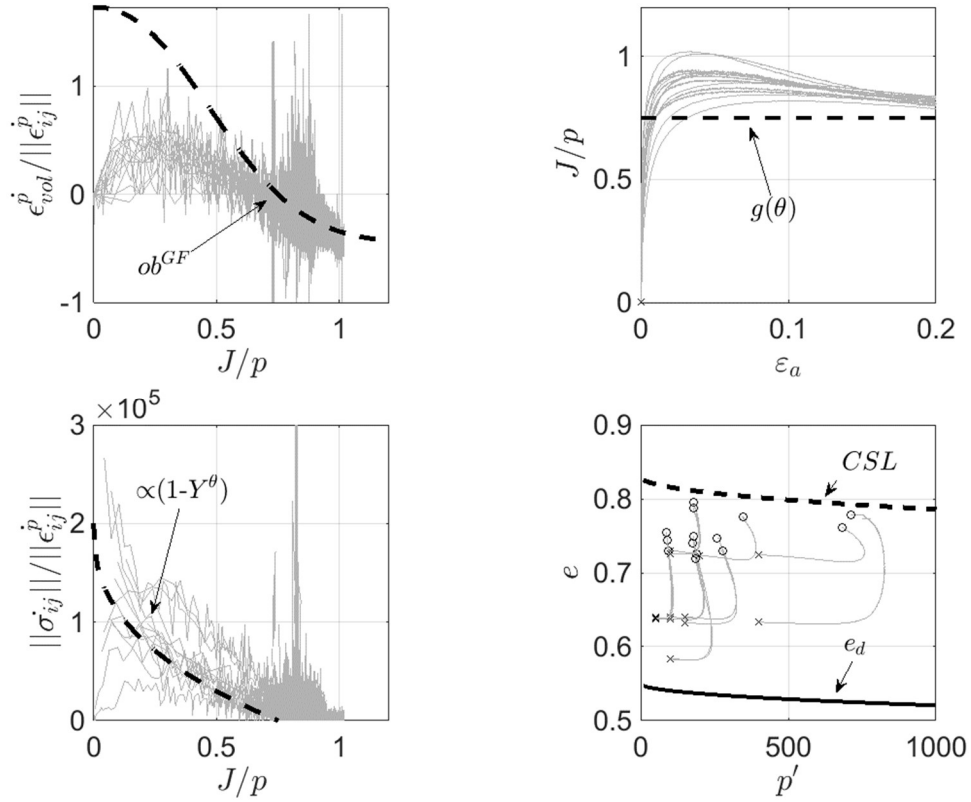


Figure 223: Calibration of strategy 1

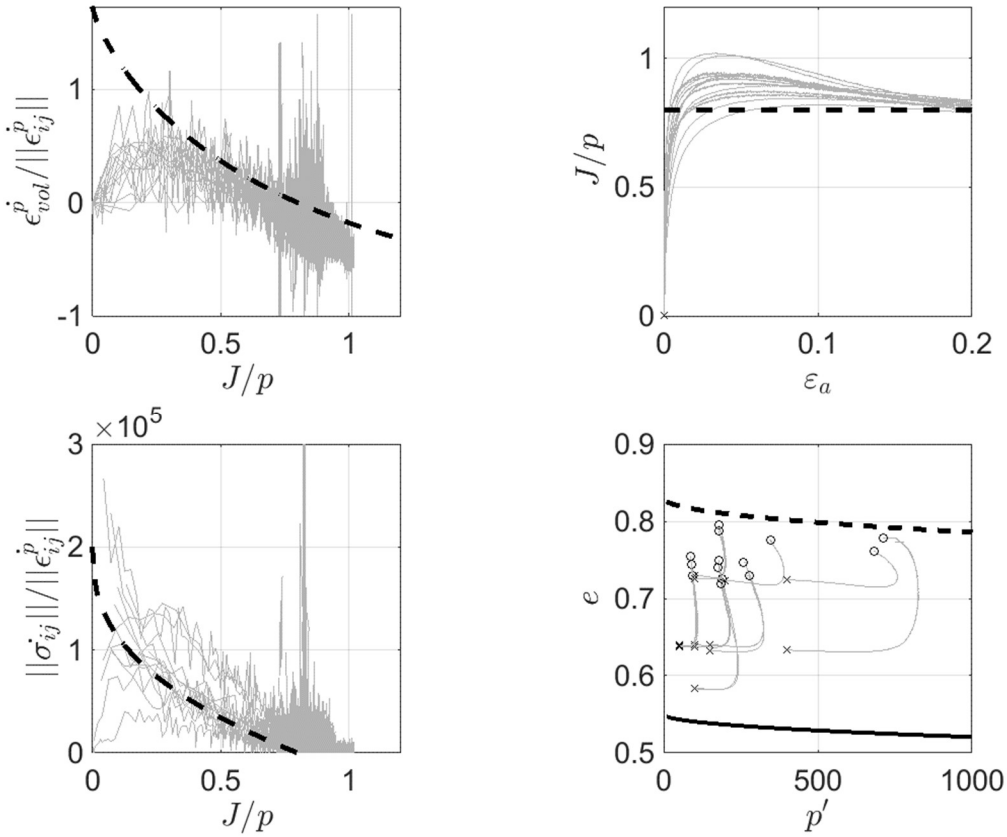


Figure 224: Calibration of strategy 2

The current modelling framework is advantageous in the sense that the model can be adjusted to reproduce quasi-asymptotic states with a quasi-constant obliquity, meaning that it is possible to foresee the maximum associated J/p ratio for any given void ratio and strain direction. Therefore, it is impossible to overestimate the peak strength of the material as it is bounded for all strain directions. An illustration of the former discussion can be observed in the triaxial test used for calibration (Figure 222) where the rate of J/p is nearly zero (quasi-asymptotic) despite the fact that the sand is dilating at a quasi-constant rate.

5.2.2.4. Genetic algorithm optimization

Given the object-oriented programming logic of the constitutive driver, it is possible to include an automatic calibration tool that can use a genetic algorithm (Holland and Goldberg, 1989, Conn et al., 1991) to find the input parameters that best fit the laboratory data using any of the constrained solvers described in chapter 3. This can be done using the inheritance characteristics of modern programming languages, where it is only necessary to define a superclass that includes the laboratory data, and a class constructor of the numerical test class described in 3.1. The logic is relatively simple: the superclass includes a method which, given a set of laboratory data, processes it and constructs the same numerical test for the given set of input objects. The method then runs each of the numerical tests and compares the prediction with the laboratory data and outputs an error or a multi-valued survival function. In summary, the previous object consists of a super-variable that returns an output on how well the set of parameters capture the laboratory data. This process can be done manually, or the object can be fed into a commercial genetic algorithm solver that will explore a range of values and return the optimal of a survival function. The logic of the superclass is shown in Figure 225.

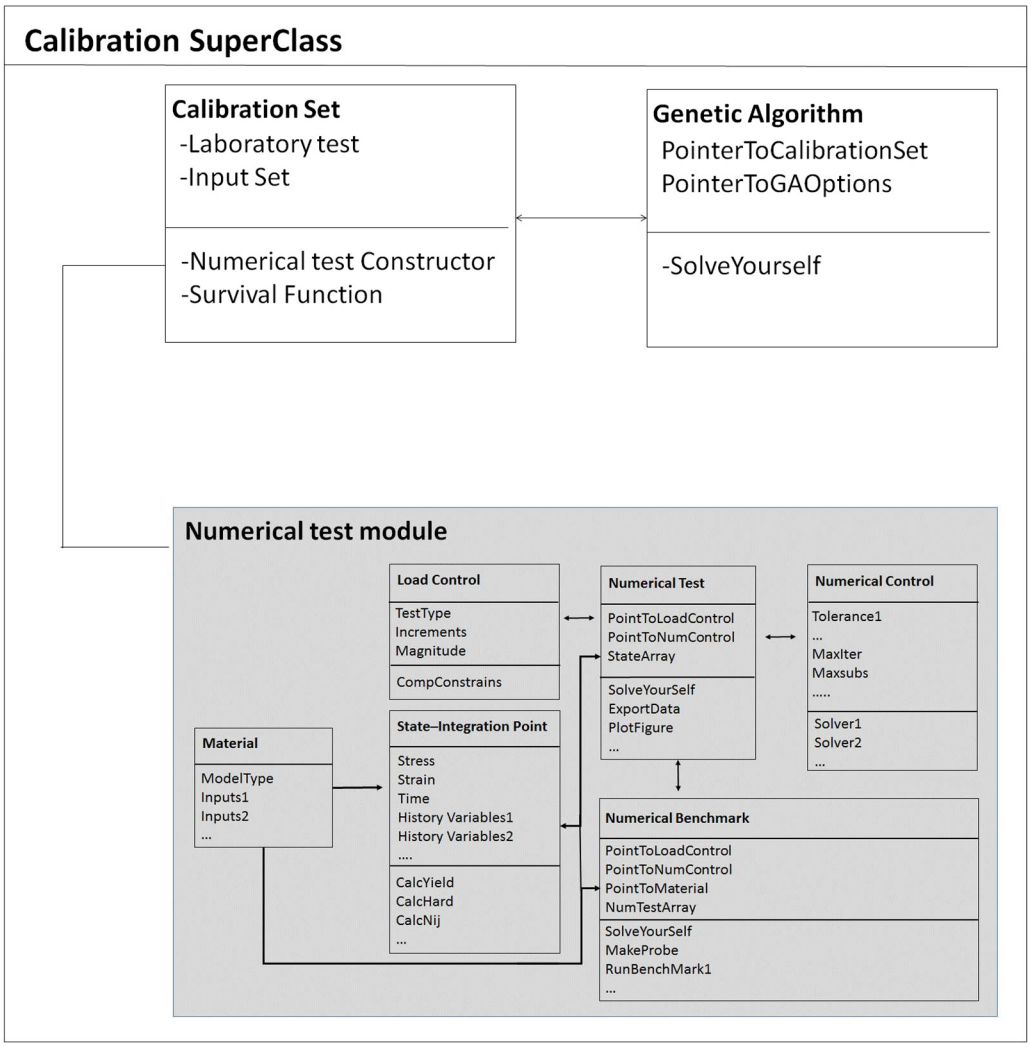


Figure 225: Diagram for calibration class

Given the parameters controlling the goal functions consistent with strategy 1 and strategy 2 act as constrains, the calibration tool can explore an optimal fit of the other parameters, where the results of the calibration are shown in Table 33. A population of 100 individuals or superclass objects with 14 tests each, and a tree of 8 generations were used to perform the analysis. As the number of numerical tests is approximately 5600 and these are independent of each other, the code was parallelised. The calibration procedure roughly takes around 1h with a standard processor of eight logical cores (i7-4770 3.40GHz). The survival function was defined as a weighted average of the relative errors of stress and strain paths with respect to the laboratory data. The obtained set of inputs is shown in Table 6, where the initial manual calibration obtained through trial and error has been included and is compared with the two obtained by the genetic algorithm (GA):

Table 33: Manual versus genetic algorithm calibration

	e_{c0}	e_{d0}	h_s	n	α	β	XV	YF	ZF	θ	S_f	ob_{min}	ob_{max}	δ
Manual	0.84	0.50	1E6	0.55	0.07	2	0.55	0.87	0.1	0.4	3.0	-1.73	0.45	2.25
GA 1	0.84	0.50	1E6	0.55	0.08	2	0.59	0.87	0.1	0.53	4.1	-1.73	0.45	2.25
GA 2	0.84	0.40	1E6	0.55	0.16	2	0.55	0.87	0.1	0.4	4.3	-1.73	1.0	0.8

5.2.2.5. Comparison of parameter sets

To illustrate the differences between the two calibrated sets using genetic algorithms (GA1 and GA2), corresponding to each of the two strategies described above, a set of drained triaxial compression tests and asymptotic numerical tests (tests with constant strain rate direction) have been carried out and are presented in Figure 226 and Figure 227. Figure 226 shows the asymptotic probes, where it can be identified the different different J/p –strain direction envelope for both sets. Conversely, Figure 227 shows the differences of both sets in terms of peak strength and post peak behaviour, which are particularly evident for dense cases where GA2 exhibits slightly higher peaks and quicker post peak degradation than GA1, under triaxial compression.

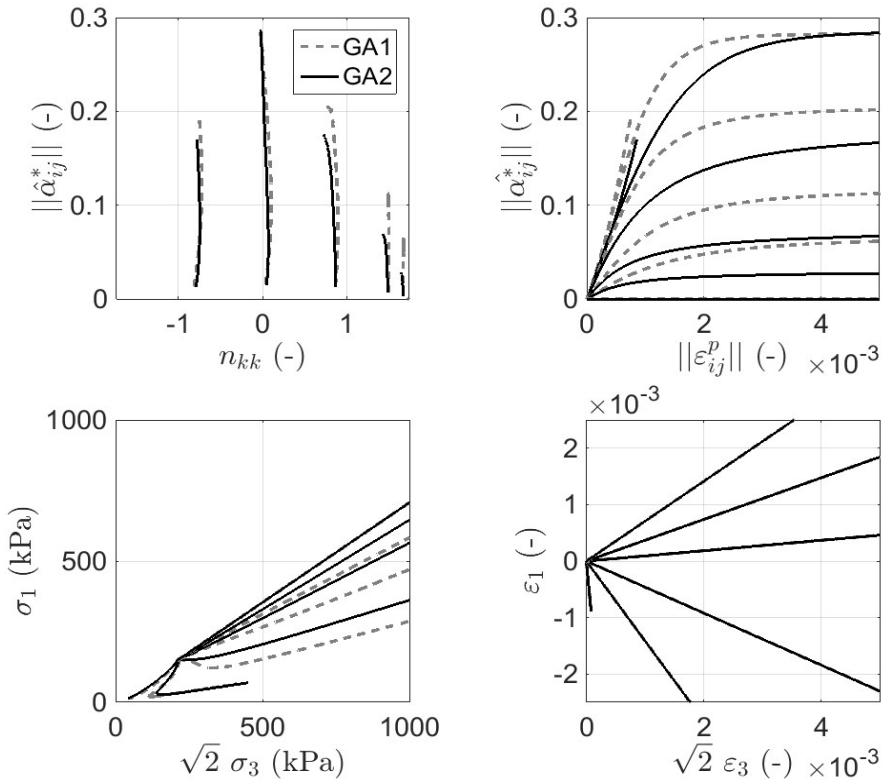


Figure 226: Asymptotic strain tests for GA1 and GA2 calibration

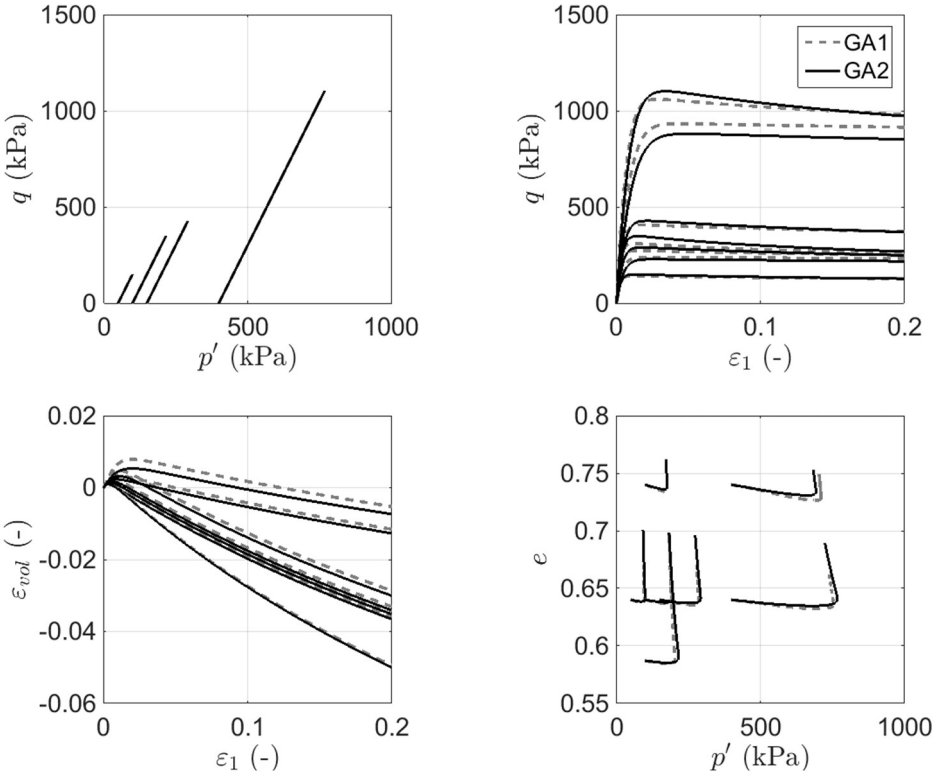


Figure 227: Numerical triaxial tests for GA1 and GA2 calibration

5.3. RESULTS OF 3D ANALYSES

This section discusses the results obtained from the 3D analyses of Dunkirk test piles described in the previous section under static and cyclic conditions. Firstly, the monotonic cases predicted by the FEA analysis are compared with the field data (McAdam et al., 2018) where the behaviour of short rigid piles under lateral loading is assessed. Furthermore, a detailed study for the large diameter pile looking at the structural and soil response is carried out for various mobilised lateral loads. To conclude the study of this type of piles under monotonic conditions, the failure mechanisms and the structural responses of the other medium piles for various L/D ratios are included and the overall response is assessed. The final part of this section covers the response of the model under cyclic conditions, where the effect of backstress superposition is studied in more detail.

5.3.1. LOAD-DISPLACEMENT CURVES

3D numerical analyses have been carried out for the Dunkirk test pile geometries described in 5.2.2.1 (DL2, DM3, DM4 and DM7). Figure 228 shows the load-displacement curves predicted by the set of parameters from calibration GA1, taking the ground-line displacement of $0.1D$ as nominal failure. The figures compare the predicted responses of all four pile tests from the 3D FE analyses and the standard API/DNV p-y method, with those obtained from field testing. Results from the FE simulations show excellent agreement for all the piles, except for the short pile DM7 where the FE predictions overestimate the measured capacity. It must be said that the pile DM7 is completely embedded in the top layer of 3.0 m thick hydraulic fill, which is the material that was not possible to characterise with good certainty.

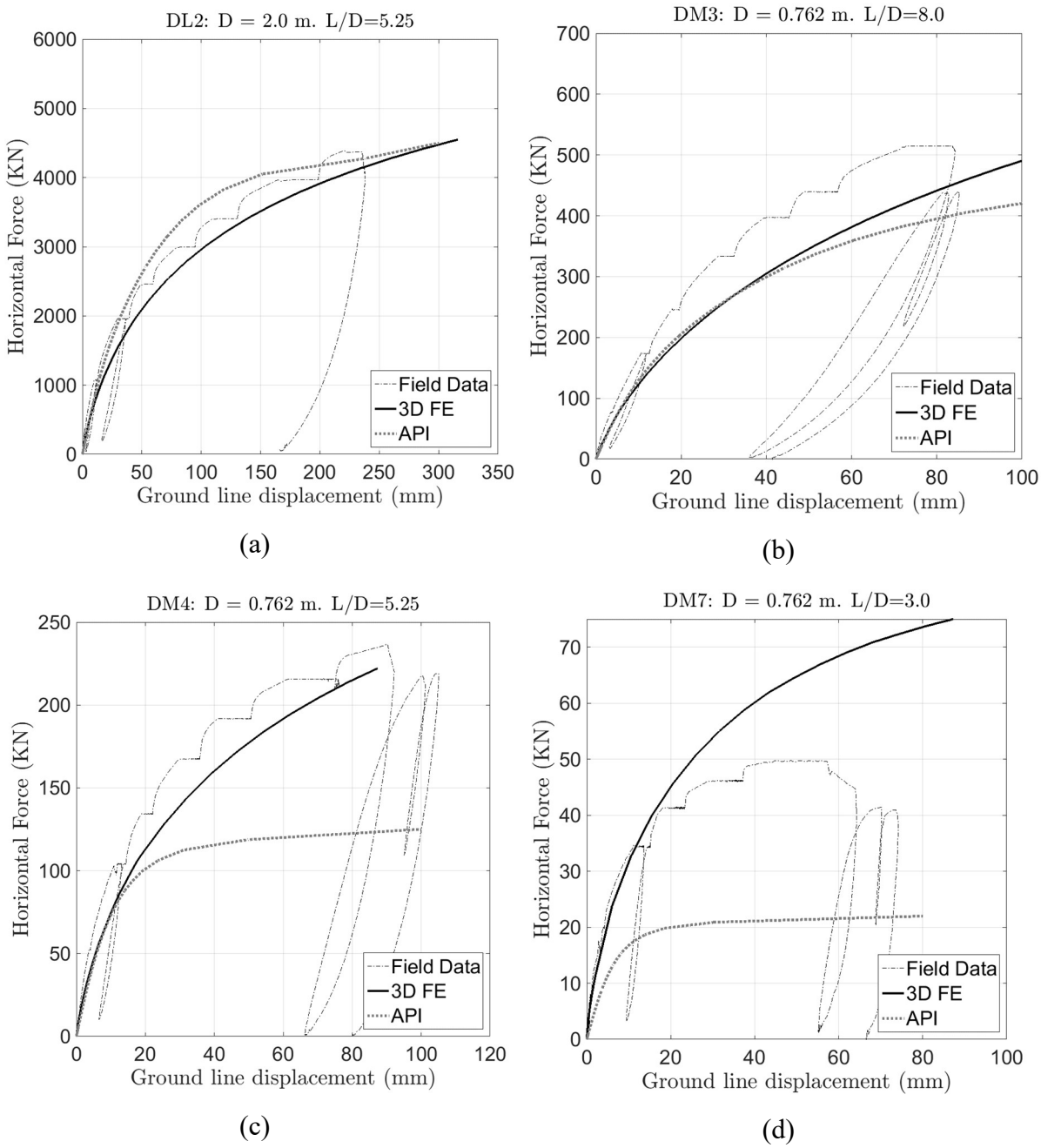


Figure 228: Comparison at ultimate conditions: mudline displacement ~ 0.1D, between measured load – displacement curves, 3D FE analyses and API/DNV methodology, from (McAdam, 2018)

Apart from pile DM7, the FEA analyses capture appropriately the initial response and capacity of the piles for all L/D ratios and diameters studied, producing a better overall prediction than the standard API curves. The API/DNV predictions appear to be inconsistent in this respect,

significantly under-predicting the capacity of short piles DM7 and DM4, while displaying better agreement for longer piles DM3 and DL2. In terms of the initial stiffness, Figure 229 shows a detail of the initial responses of all piles at ground horizontal displacement level of 0.01D, which is more representative for service or operational conditions. The results show good agreement between the field test data and predictions from both 3D FE and API/DNV methodology. In this respect, the initial response of the 3D FE simulations and API/DNV method are practically identical, slightly under-predicting the initial stiffness of the pile.

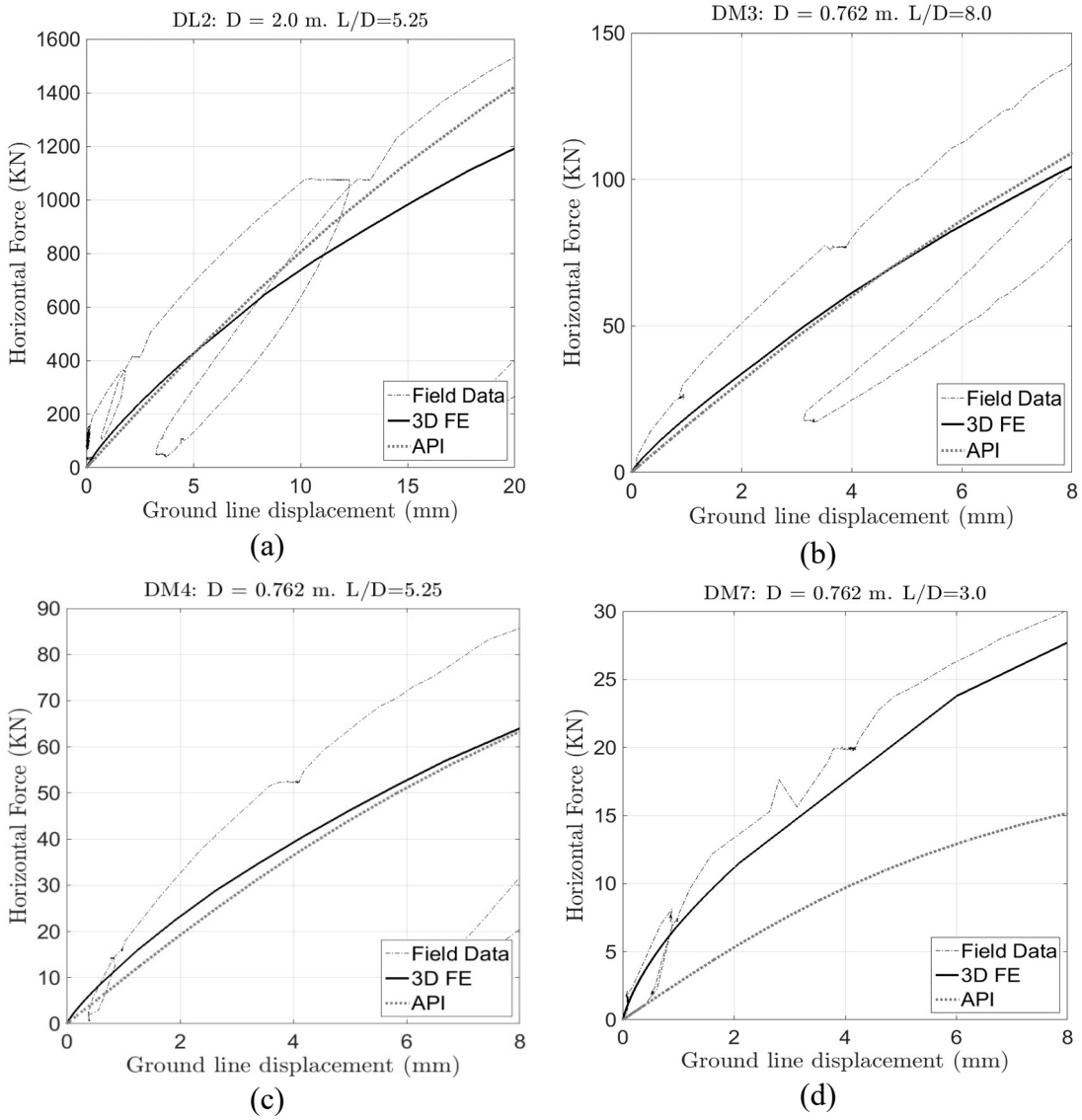


Figure 229: Comparison at operational conditions: mudline displacement ~ 0.01D, between measured load – displacement curves, 3D FE analyses and API/DNV methodology, from (McAdam, 2018)

5.3.2. VERIFICATION OF AUTOMATIC CALIBRATION AND PREDICTED RESPONSE

In this section the predicted 3D FE responses of piles DL2 and DM3 corresponding to the larger diameter and L/D ratio of 8 are compared for the sets summarised in Table 33. The sets were calibrated manually and also using genetic algorithms based on the available laboratory data. The obtained sets using genetic algorithms proved to be accurate for the boundary value problems (see Figure 227. In this sense, the genetic algorithm calibration proved to be useful, being significantly faster than any manual calibration and providing good results for both families of parameters. It should be noted that prior to application of genetic algorithm in the calibration process, some key elements of the model, such as the CSL and trace of the goal functions with the stress ratio, were imposed as a constrain in the optimisation problem.

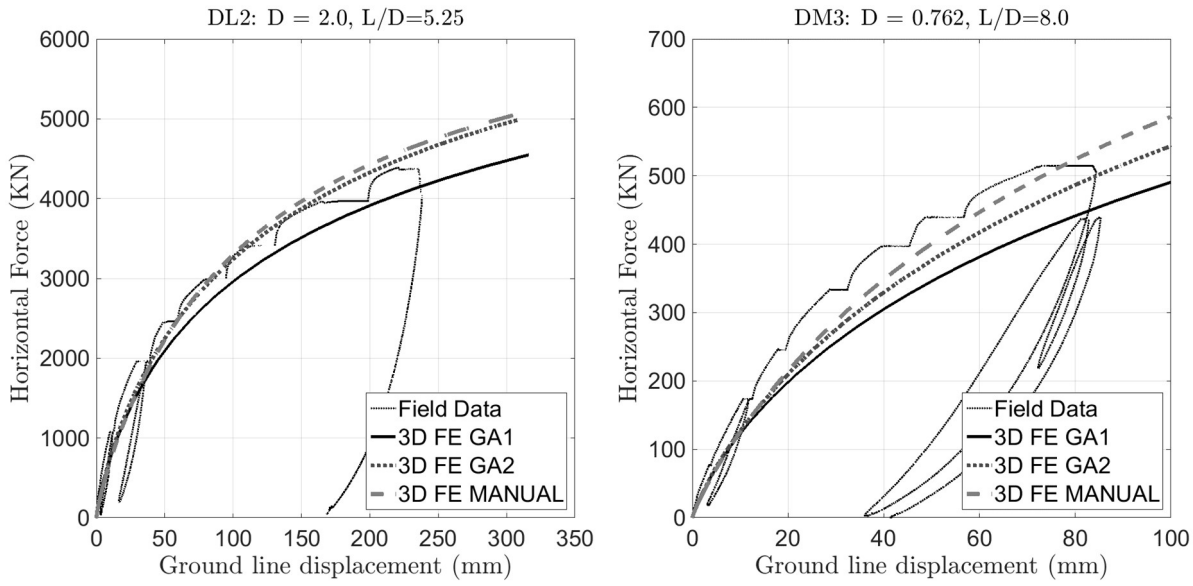


Figure 230: Load – displacement prediction of sets of parameters, manual versus numerical calibration

In general, the response of the pile in terms of load-displacement is satisfactory for all sets, including the manual calibration, being in general better for the "GA1" parameter set (strategy 1) for the large diameter pile. The reason of the differences between calibrations sets are mainly due to the fact that the lateral response is mainly dominated by the peak strength of the material in the hydraulic fill.

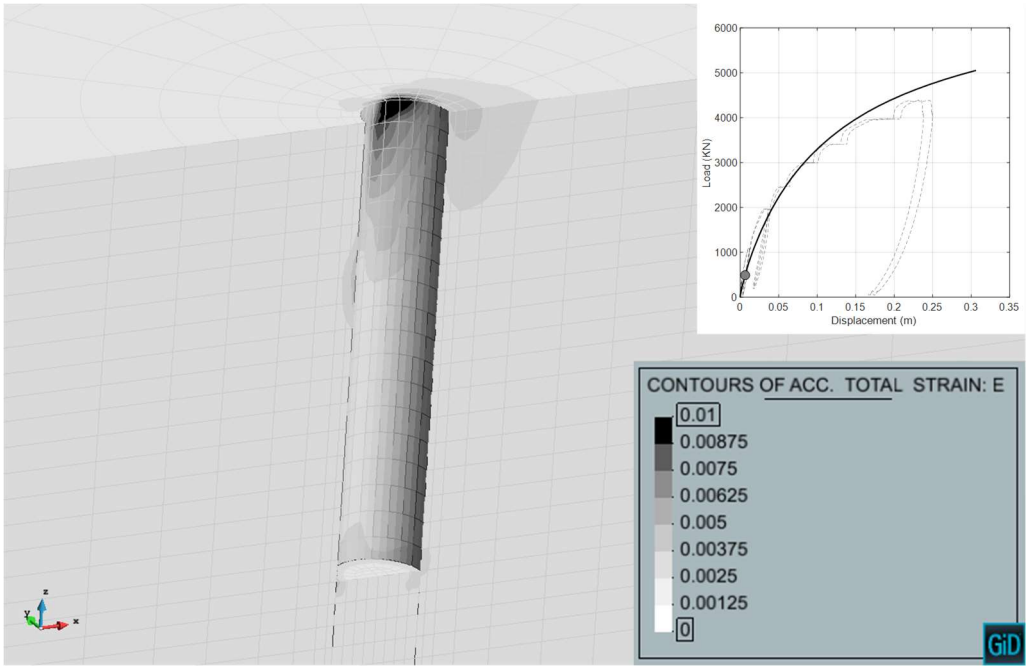
In summary, with respect to the calibration strategies, the main difference between the load-displacement curves obtained with calibrations GA1 and GA2 does not occur due to the distribution of goal functions, but due to the dependence with f_d and consequently the peak strength - void ratio effects. This can be observed comparing the load displacement curves of GA1 versus GA2 and the numerical triaxial tests in Figure 227, where the peak strength is higher for GA2 in denser states, which translates into higher capacity and stiffness in the load displacement curves (Figure 230). In this sense, the fundamental parameters controlling the capacity of the piles are $e_{do,}$ and α, while the stiffness is mostly affected by S_f.

5.3.3. LARGE DIAMETER PILE (DL1, DL2)

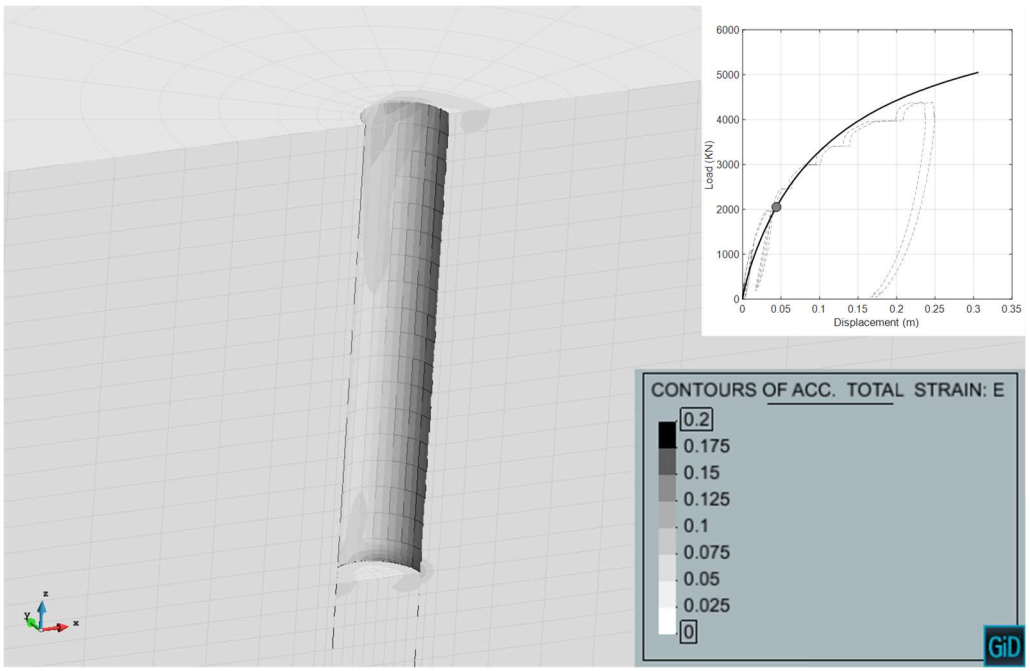
In this section the results from a 3D FE analysis of the large diameter pile DL2 ($D = 2.0m$) are described in detail. A detailed description of the soil response around the pile and its structural response is included, with the last part of the section covering a comparison between the numerical prediction and the interpreted field data.

5.3.3.1. Soil response: Accumulated deviatoric strain

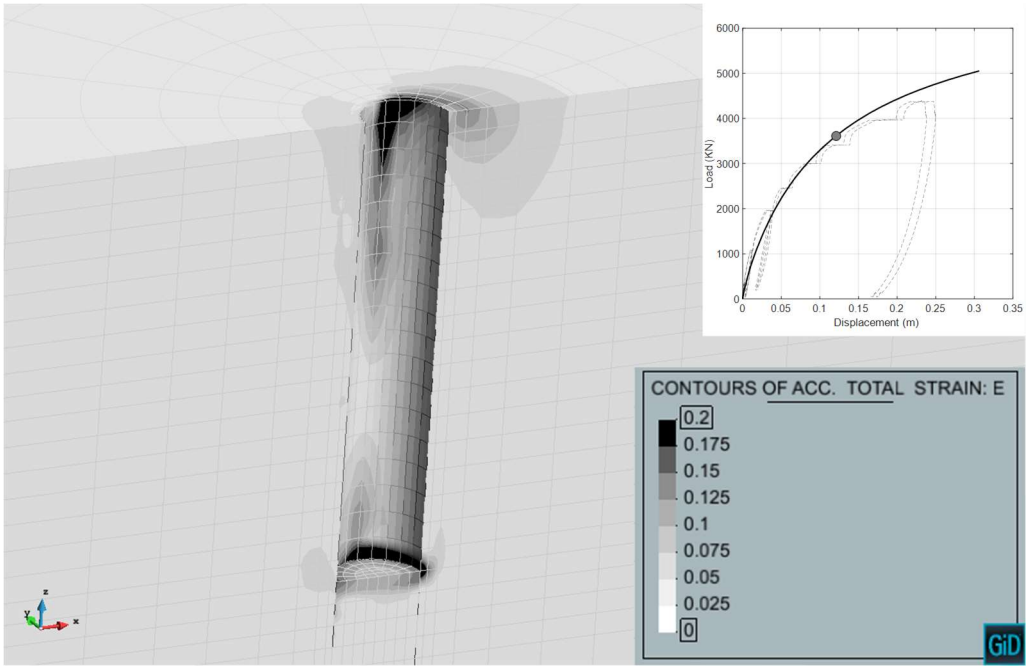
The following set of figures describes the soil response around the pile, showing in the first instance the contours of the accumulated deviatoric strain (E_d). The contour scale is the same, except for the first figure (Figure 231a). A limit of >20 % of deviatoric plastic strain has been used as a limit for the mobilized soil, where beyond that limit the dark colour is maintained. All figures include a detail of the load displacement curve, marking the stage of loading for which the result is shown.


6000
5000
4000
3000
2000
1000
0
Load (KN)
0 0.05 0.1 0.15 0.2 0.25 0.3 0.35
Displacement (m)
CONTOURS OF ACC. TOTAL STRAIN: E
0.01
0.00875
0.0075
0.00625
0.005
0.00375
0.0025
0.00125
0
GiD

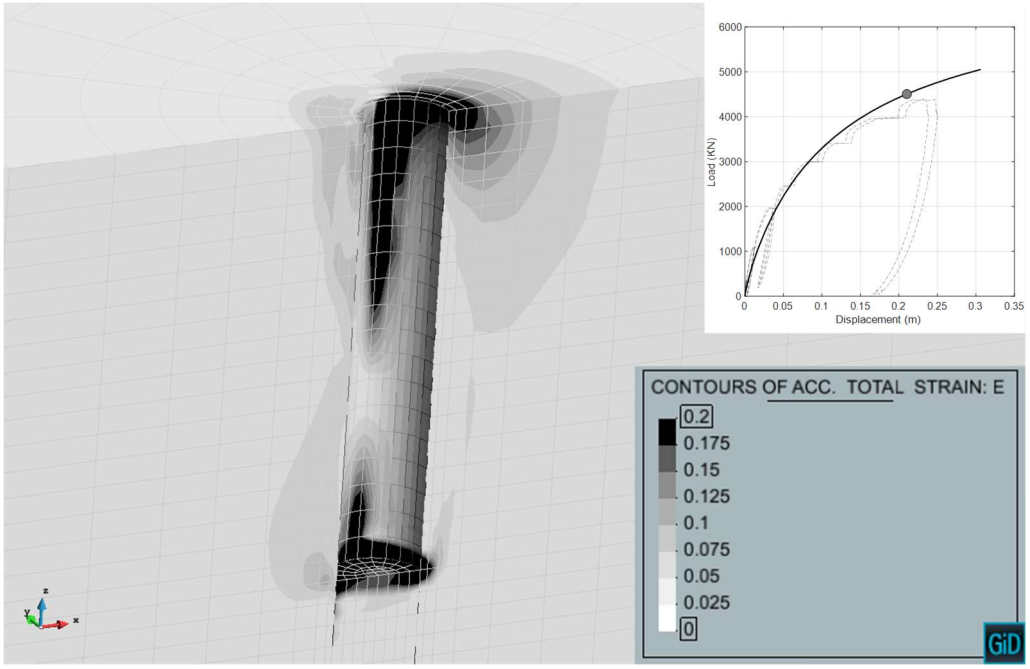
(a)


6000
5000
4000
3000
2000
1000
0
Load (KN)
0 0.05 0.1 0.15 0.2 0.25 0.3 0.35
Displacement (m)
CONTOURS OF ACC. TOTAL STRAIN: E
0.2
0.175
0.15
0.125
0.1
0.075
0.05
0.025
0
GiD

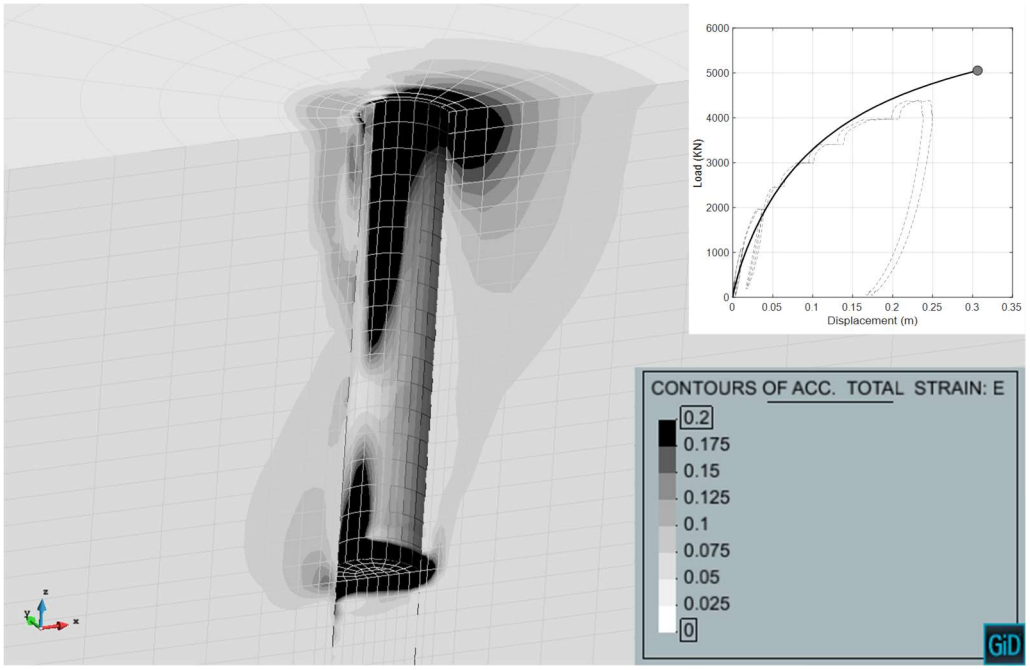
(b)


6000
5000
4000
3000
2000
1000
0
Load (KN)
0
0.05
0.1
0.15
0.2
0.25
0.3
0.35
Displacement (m)
CONTOURS OF ACC. TOTAL STRAIN: E
0.2
0.175
0.15
0.125
0.1
0.075
0.05
0.025
0
GiD

(c)


6000
5000
4000
3000
2000
1000
0
Load (KN)
0
0.05
0.1
0.15
0.2
0.25
0.3
0.35
Displacement (m)
CONTOURS OF ACC. TOTAL STRAIN: E
0.2
0.175
0.15
0.125
0.1
0.075
0.05
0.025
0
GiD

(d)



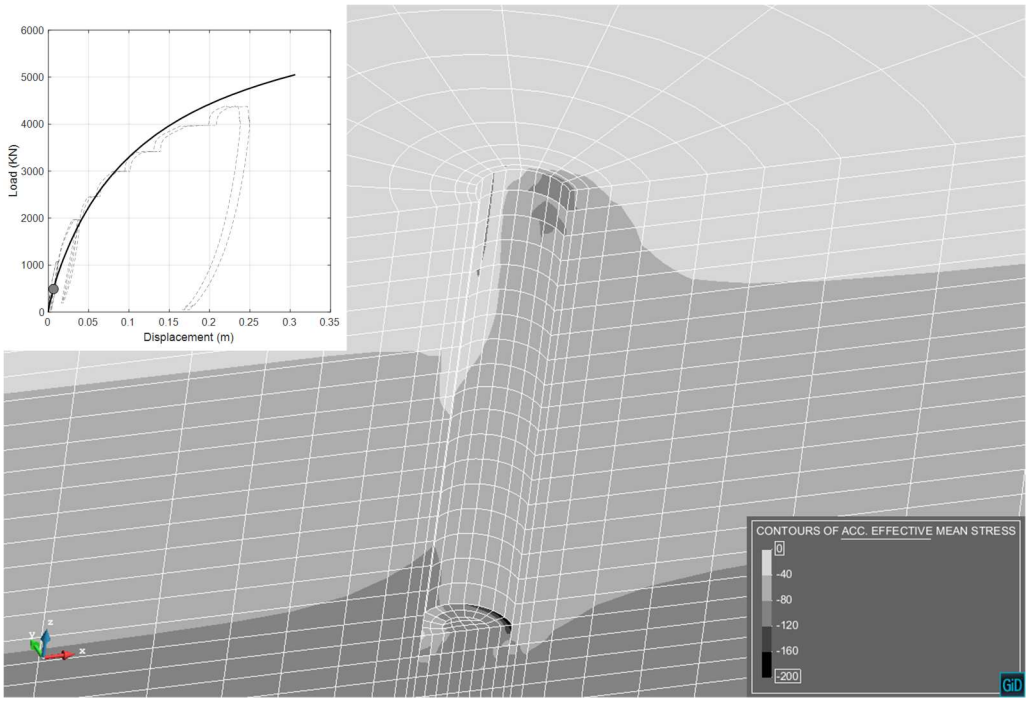
(e)

Figure 231: Accumulated deviatoric strain at various simulation stages

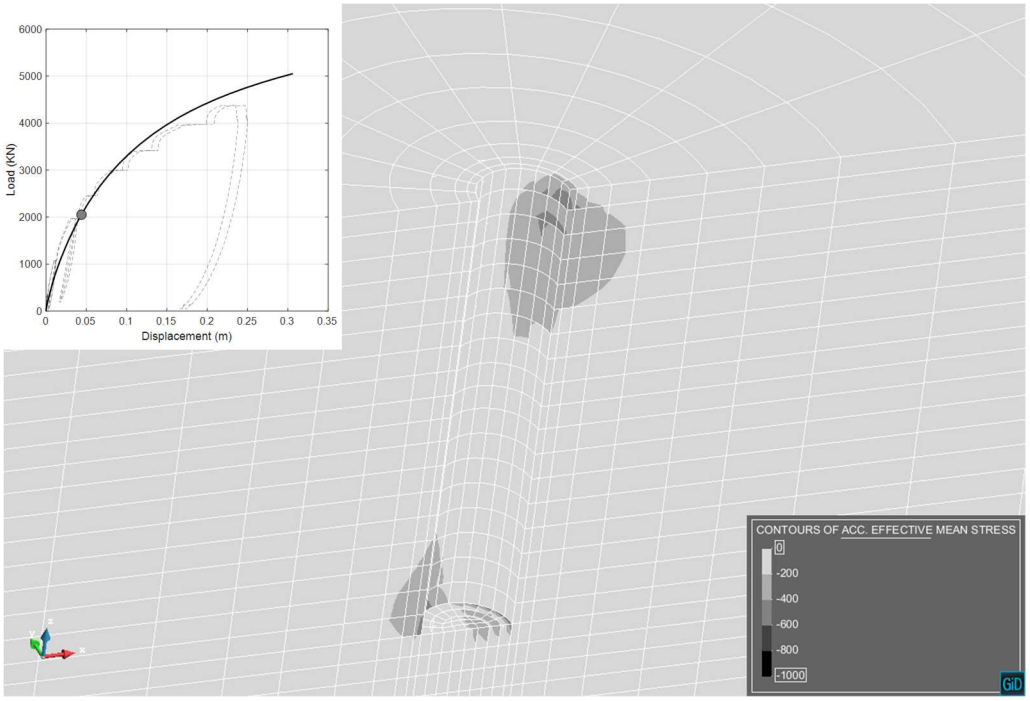
Figure 231 indicates that a rigid mode of monopile rotation appears even at early stages of loading, as deviatoric strains start to develop at the base of the pile caused by the pure distortion imposed by the rigid rotation of the pile. The rigid rotation mechanism progresses as load increases and the centre of rotation corresponds to the position on the pile where there is no shear strain, as can be identified in Figure 231 (c), (d) or (e). Two types of failure mechanism can be identified depending on whether they correspond to the active or passive zone of the pile. In the active zones the soil fails towards the pile, in a mode similar to slope instability, due to the horizontal stress relaxation. On the other hand, in the passive sides the failure mechanism involves the mobilisation of the lower wedge of soil, which is pushed upwards, and of the upper wedge, which is pushed downwards.

5.3.3.2. Soil response: Accumulated mean effective stress

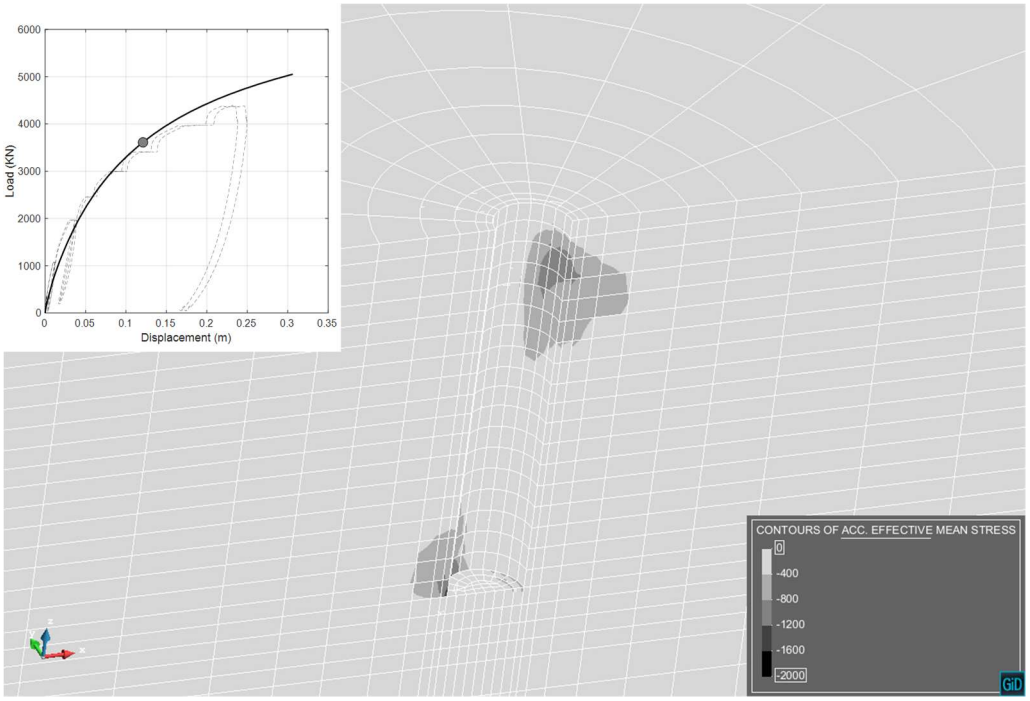
The mobilisation of the effective mean stress, p', for various stages of the simulation is shown in Figure 232. The main pattern of behaviour is the concentration of p' on the passive sides and relaxation on the active sides of the pile. Note that the sign convention is tension positive, so negative stress values indicate compression.



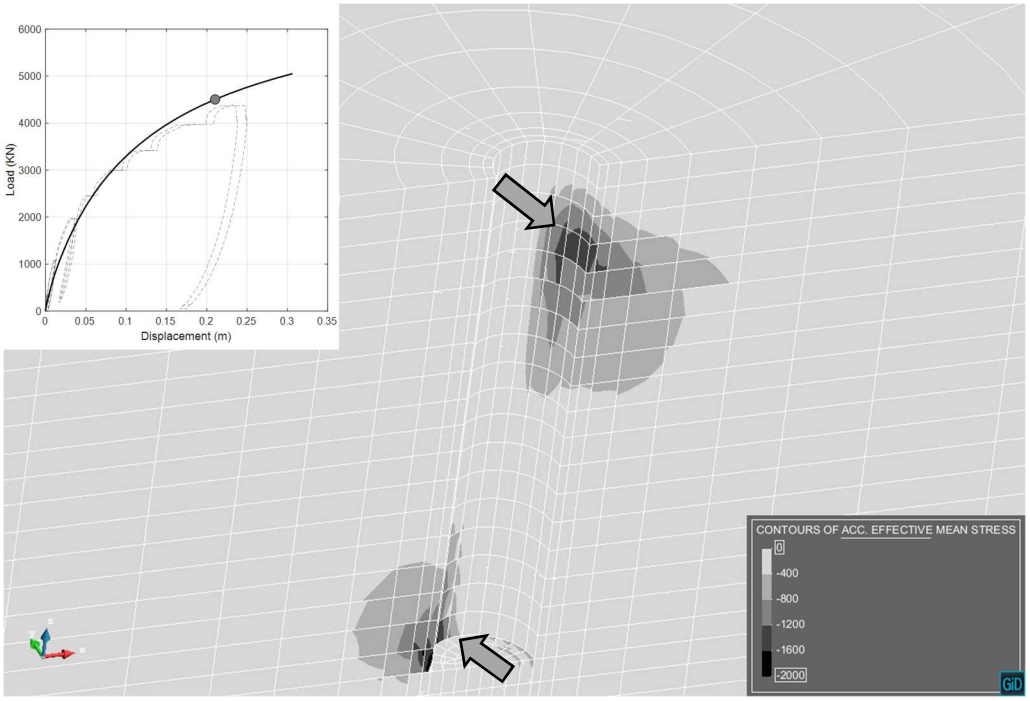
(a)


Load (KN)
Displacement (m)
CONTOURS OF ACC. EFFECTIVE MEAN STRESS
0
-200
-400
-600
-800
-1000
GiD

(b)


Load (KN)
Displacement (m)
CONTOURS OF ACC. EFFECTIVE MEAN STRESS
0
-400
-800
-1200
-1600
-2000
GiD

(c)



(d)

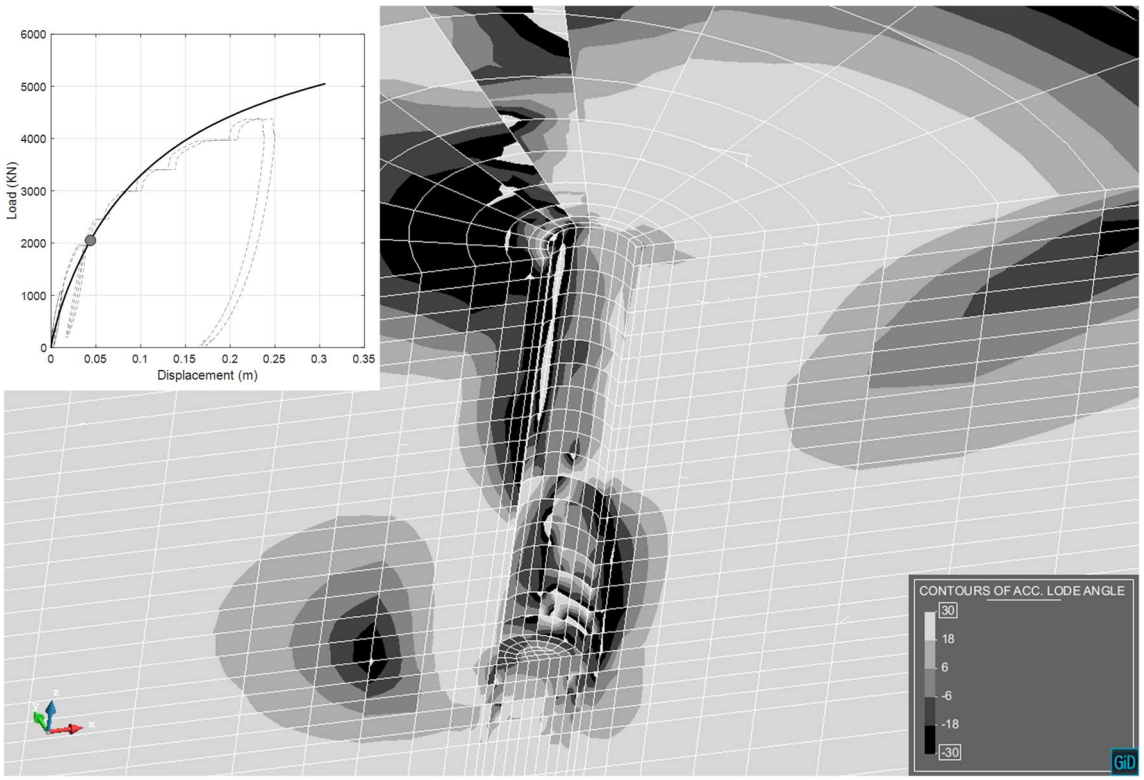
Figure 232: Accumulated mean effective stress

The largest stress concentrations are mobilised at the levering points near the top and base of the pile on the passive sides, which could be considered analogous to an inclined point load. An idealization of the resultant force is depicted in Figure 232(d). The short pile acts akin to a lever, pushing the lower passive wedge upwards and creating a high stress concentration at the levering point. In this analysis it occurs around the transition between the two layers of different density, with obviously more stress being taken by the dense layer as it has higher stiffness and strength.

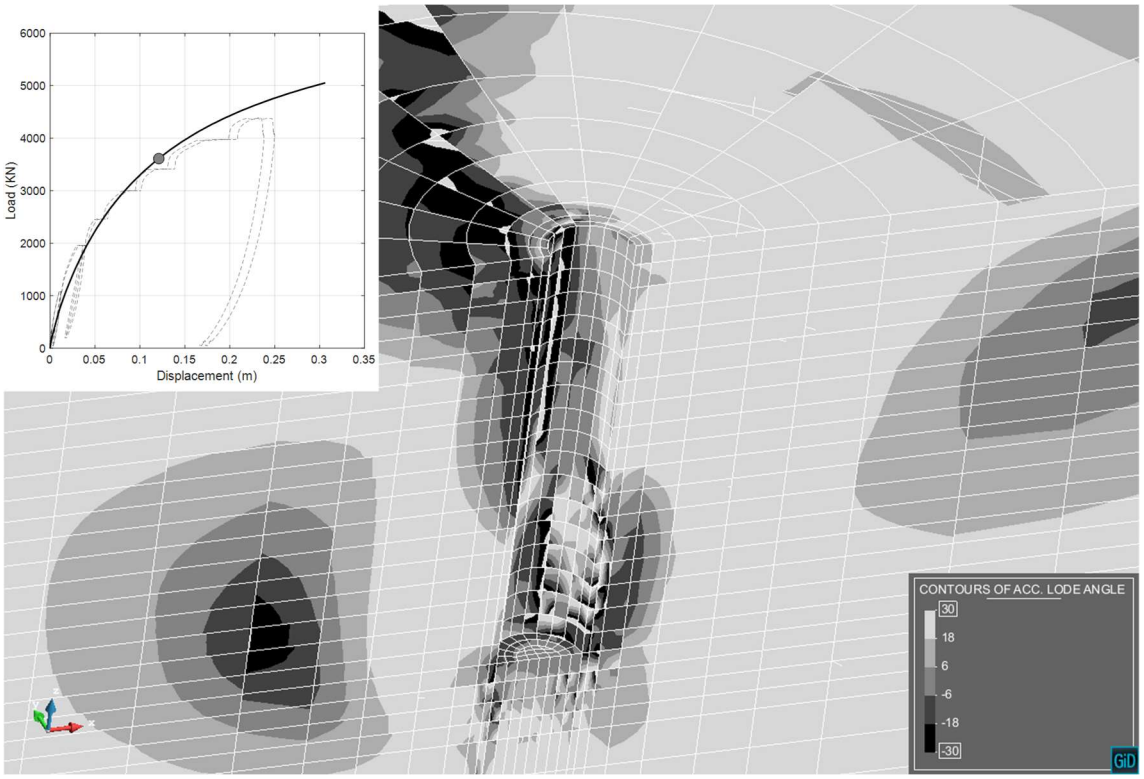
5.3.3.3. Soil response: Lode's angle

The mobilisation of the Lode's angle around the pile is shown in Figure 233, for different stages of pile loading. As the sand is normally consolidated, with $\sigma_v > \sigma_h$, it is initially with the Lode's angle $\theta = +30^o$ akin to triaxial compression (TXC) conditions. During the early loading stages, a gap can be identified in the active faces as a region where the horizontal stress is near zero typically exhibiting a Lode's angle of -30. This behaviour progresses with the pile

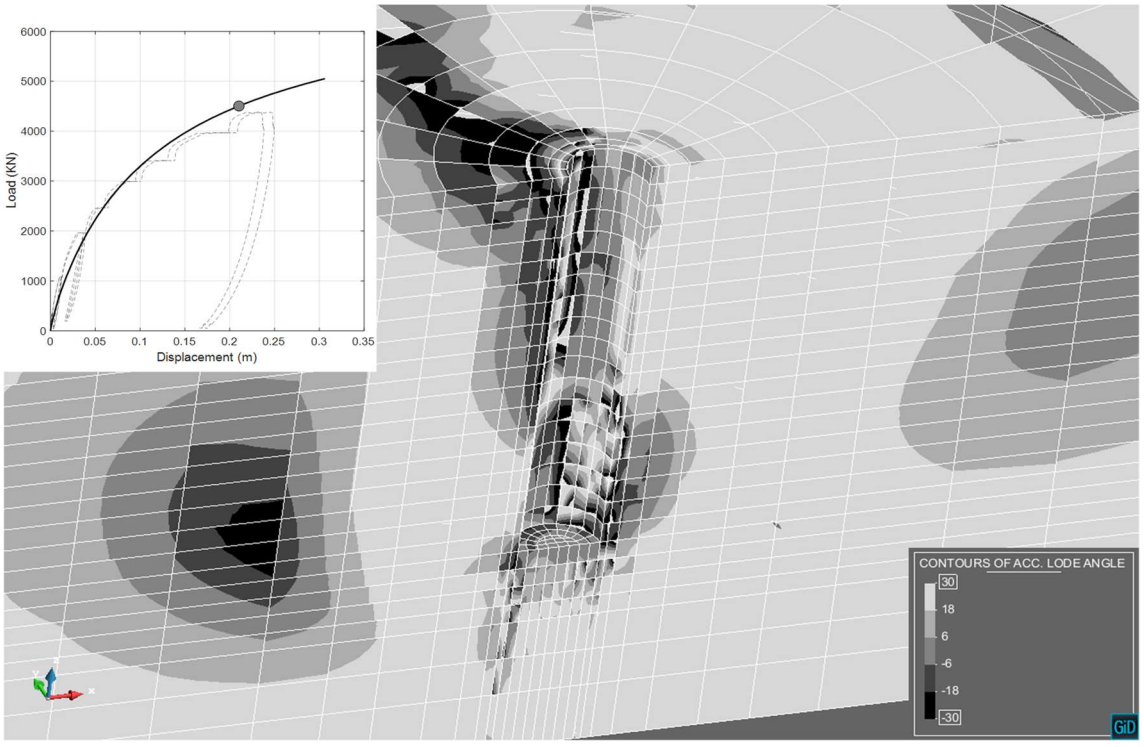
lateral deflection as the mobilisation of the pile capacity increases. Another interesting result from this analysis is the Lode's angle observed in the passive side, which is clearly of about +30 even in the early loading stages (Figure 233(b) and Figure 233(c)). In this sense, the strength is mainly controlled by the soil strength in TXC conditions. On the other hand, for operational conditions with a low mobilization ratio it can be observed how the passive upper side is in extension conditions where the principal stresses have inverted. According to the obtained numerical predictions, triaxial compression tests will be more suitable for the characterisation of the material, however for operational states involving a large number of cycles, a wider range of tests can be more representative of the soil around the upper passive side of the pile, as not all of it is subjected to a stress state corresponding to a Lode's angle of +30.



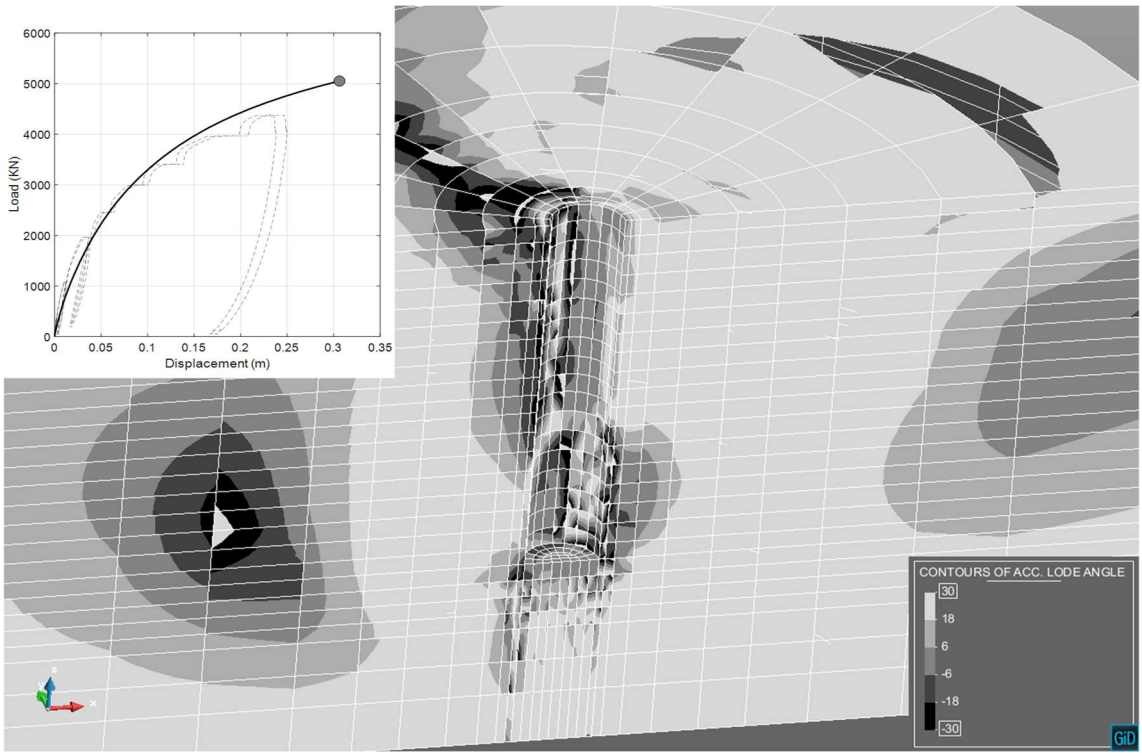
(b)


Load (KN)
Displacement (m)
CONTOURS OF ACC. LODE ANGLE
30
18
6
-6
-18
-30
GiD

(c)


Load (KN)
Displacement (m)
CONTOURS OF ACC. LODE ANGLE
30
18
6
-6
-18
-30
GiD

(d)

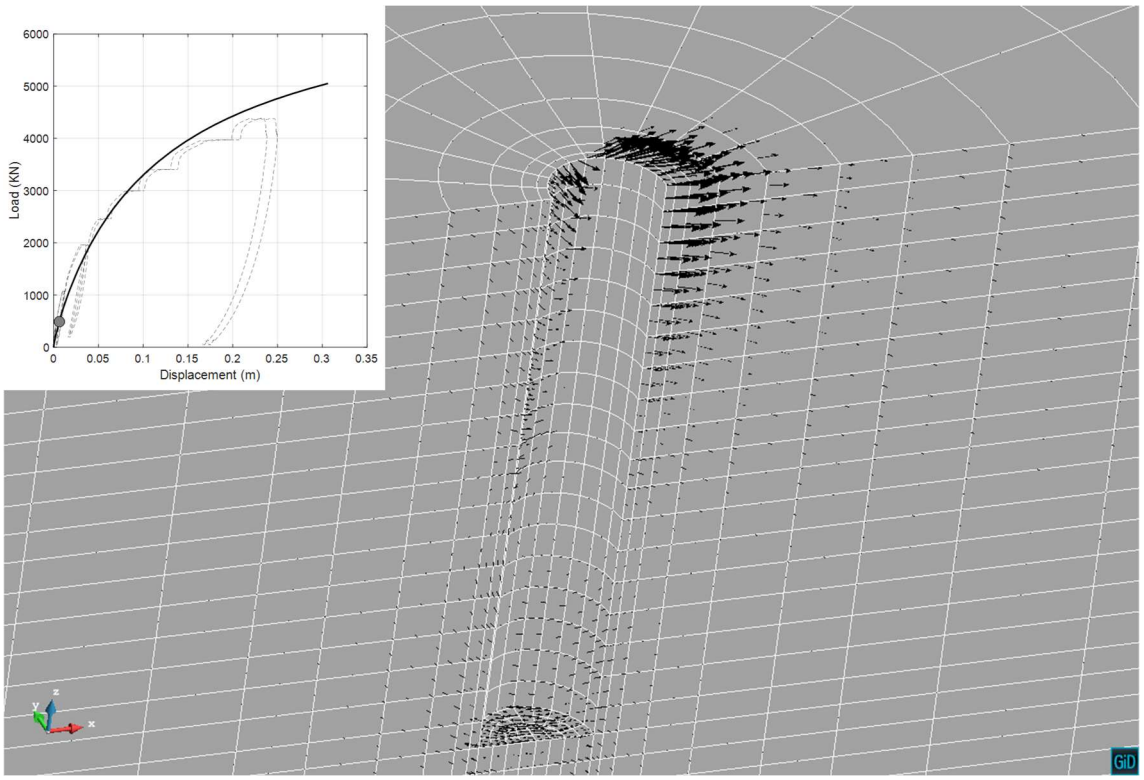


(e)

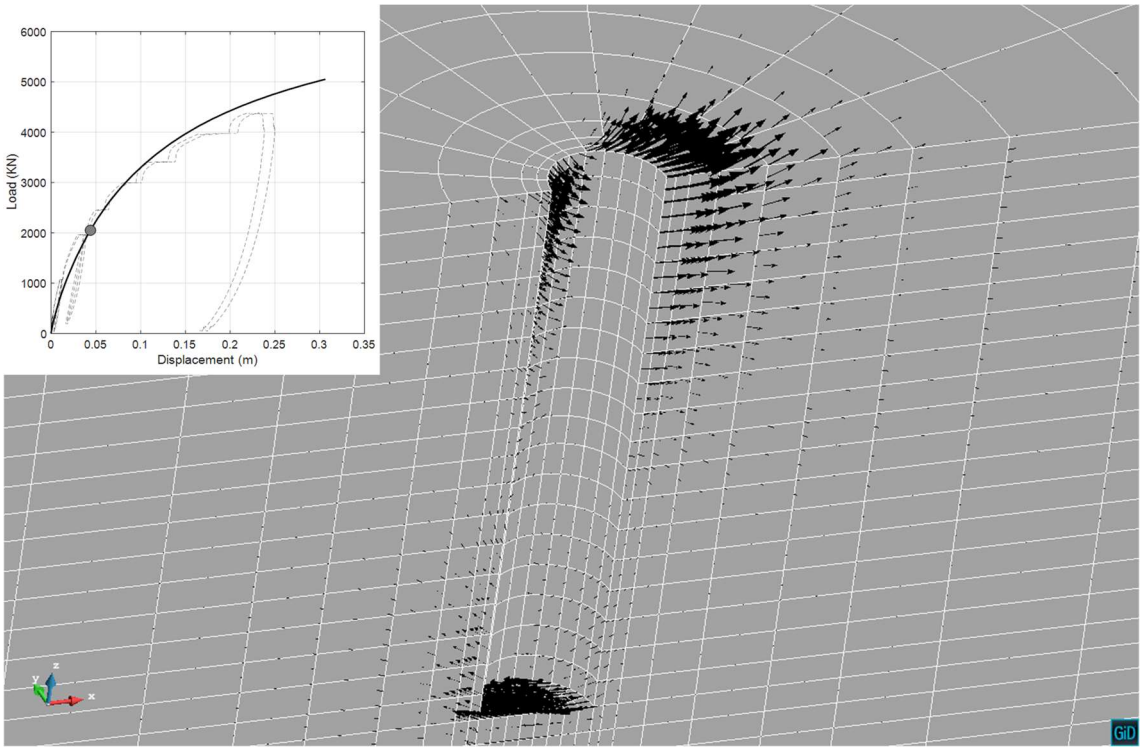
Figure 233: Lode's angle

5.3.3.4. Soil response: Incremental displacement vectors

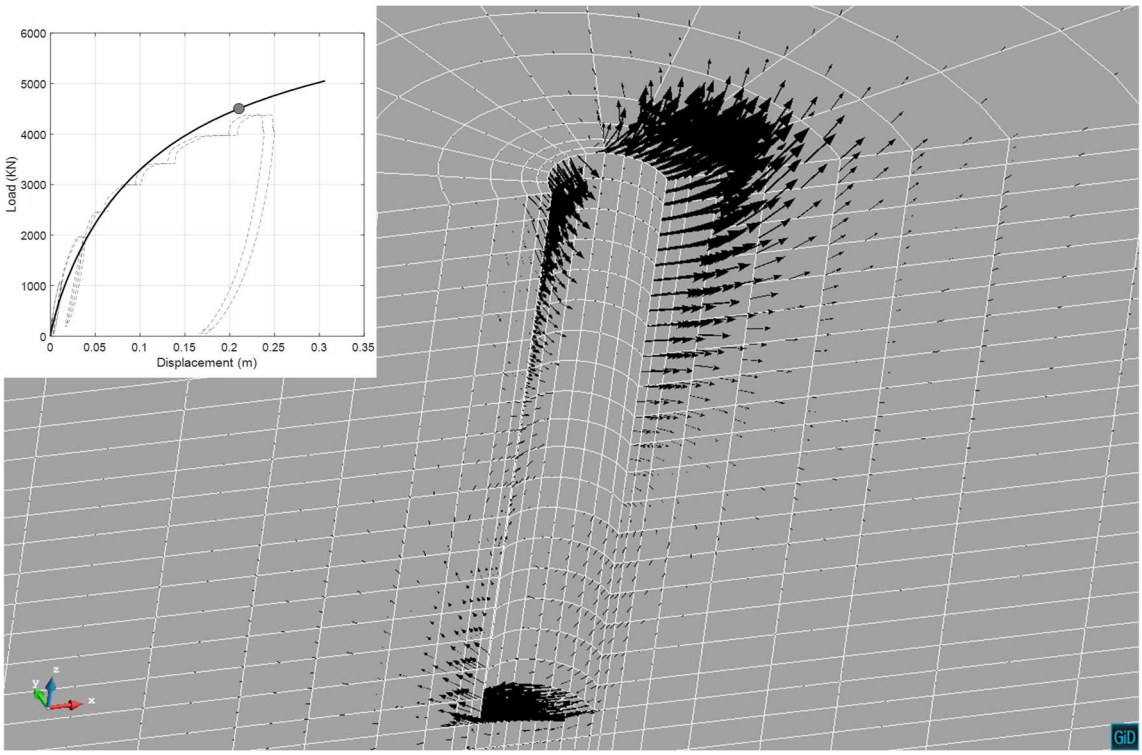
Figure 234 shows the incremental displacement field at various stages of the simulation, illustrating the rigid mechanism of pile behaviour at early loading stages. The initiation of this mechanism can be seen already at the early loading stage depicted in Figure 234(a), with vectors showing the existence of ground movements around the pile base. As discussed previously, due to the levering of the pile against the soil, the failure mechanism on the passive side contains two wedges close to the bottom and top of the pile moving upwards and downwards, respectively. This mechanism is compatible with the pile rotation (Figure 234(c)).


Load (KN)
Displacement (m)
0
1000
2000
3000
4000
5000
6000
0.05
0.1
0.15
0.2
0.25
0.3
0.35
GiD

(a)


Load (KN)
Displacement (m)
0
1000
2000
3000
4000
5000
6000
0.05
0.1
0.15
0.2
0.25
0.3
0.35
GiD

(b)



(c)

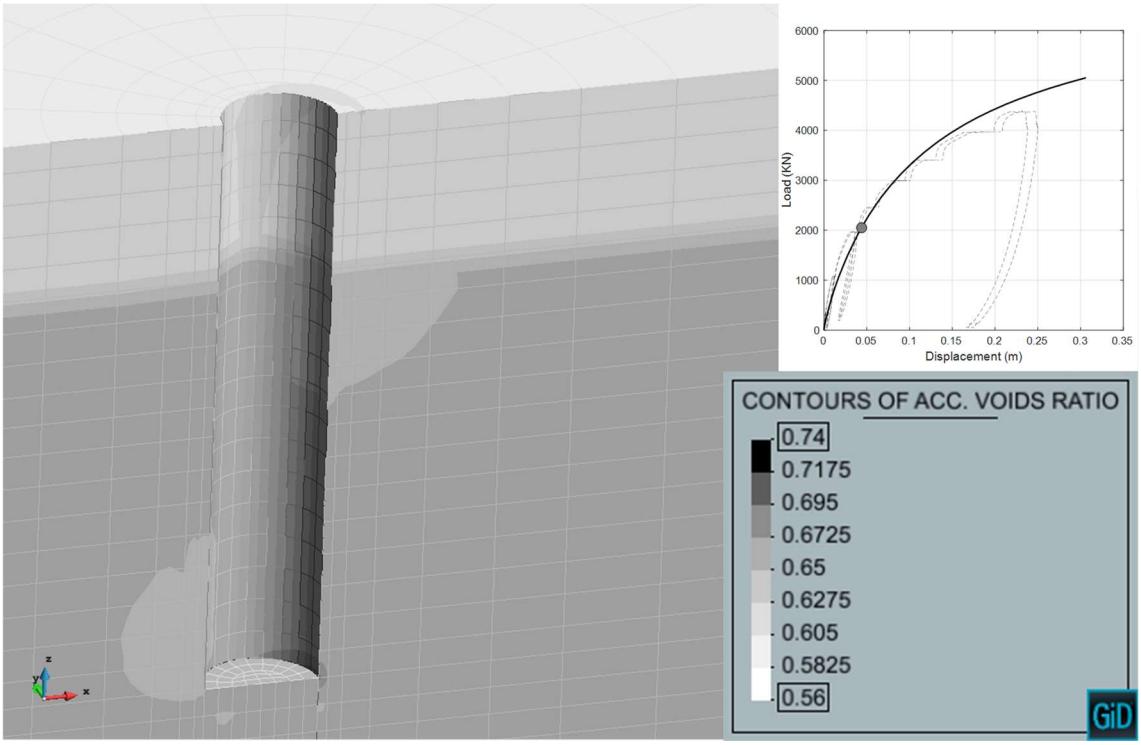
Figure 234: Incremental displacement vectors

5.3.3.5. Soil response: Void ratio

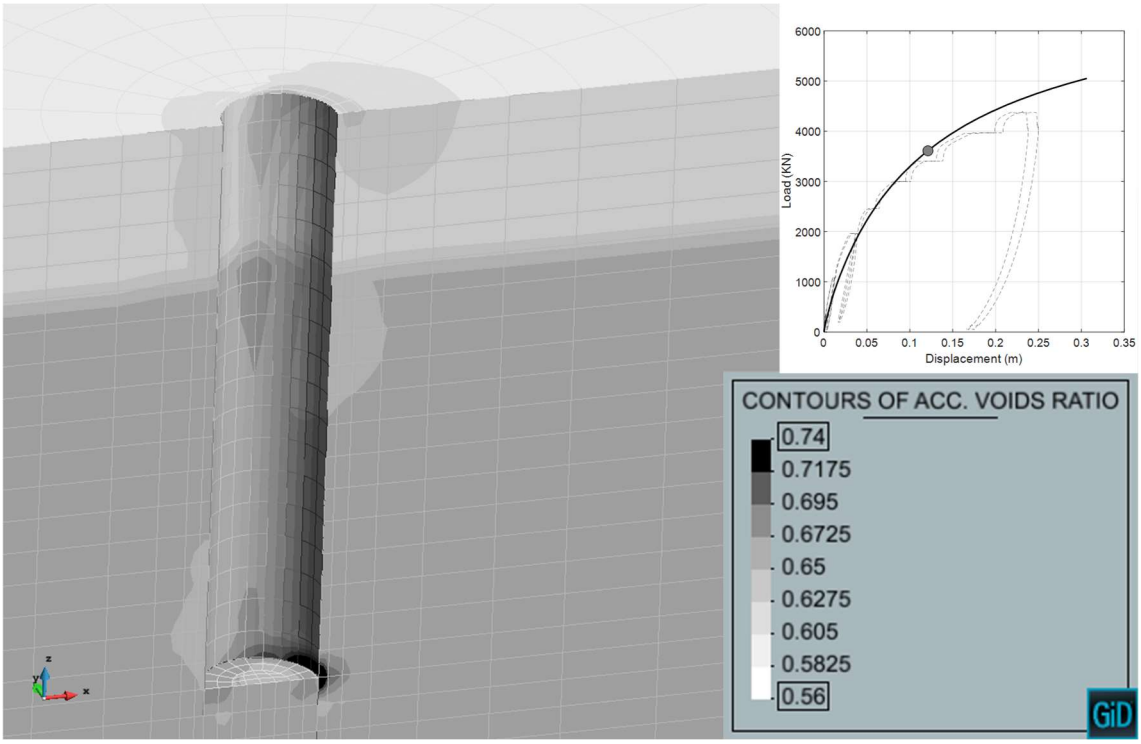
The range of void ratios in the boundary value problem covers a region delimited by the minimum void ratio and that at critical state (see Figure 223). It must be mentioned that few points strictly reach critical state conditions during the 3D simulation due to the low initial void ratio of the soil. At the time the pile reaches failure the soil has exhibited a significant amount of dilation but most of the Gauss points have not reached critical state conditions.

Figure 235 shows the calculated evolution of void ratio during pile loading. It should be noted that the change in void ratio is influenced by two different mechanisms associated with completely different loading conditions. The first mechanism enforces the material to expand through shear-volumetric coupling induced by the goal functions and f_d, while the second mechanism is linked with the overall stress relaxation and is associated swelling. In other words, the void ratio on the active sides of the pile changes mainly due to stress relaxation, while on the passive sides the changes in volume are mainly due to shear-volumetric coupling. Obviously it can happen than both mechanisms occur at the same time, however to understand

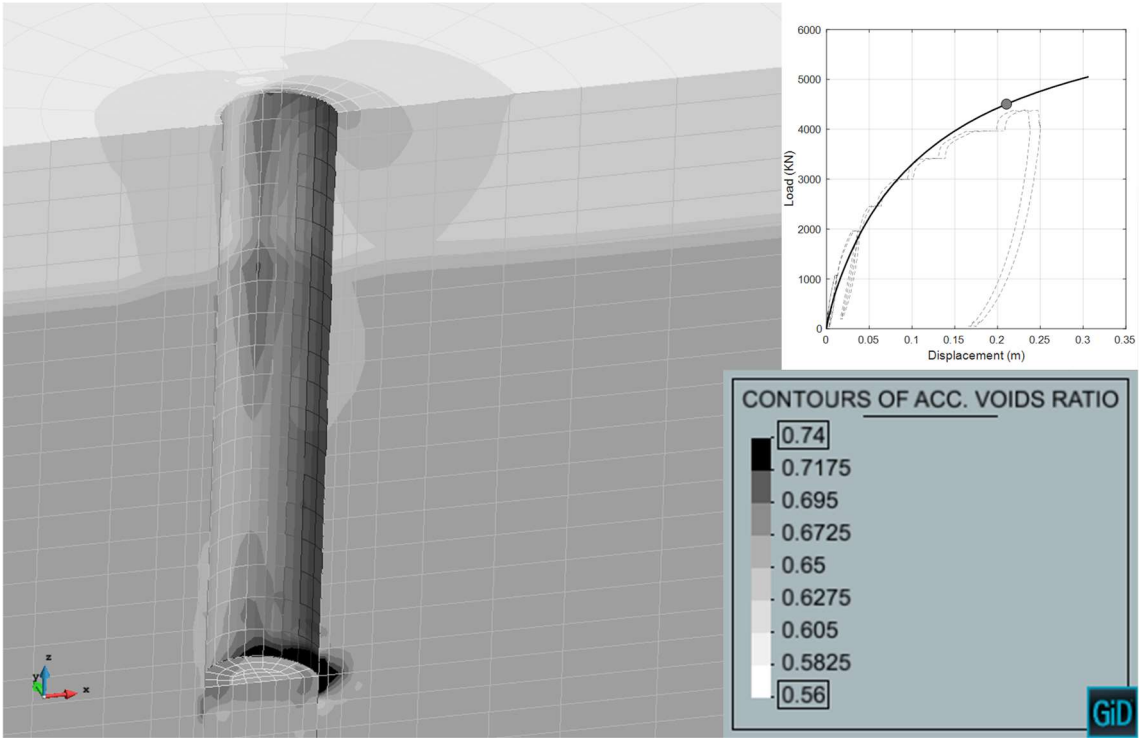
which of the mechanisms dominates requires a comparison of the results in Figure 235 with those in Figure 231. If the void ratio change is similar to the distribution of accumulated deviatoric strain, then shear volumetric coupling governs the behaviour, otherwise the change in void ratio is due to stress relaxation.



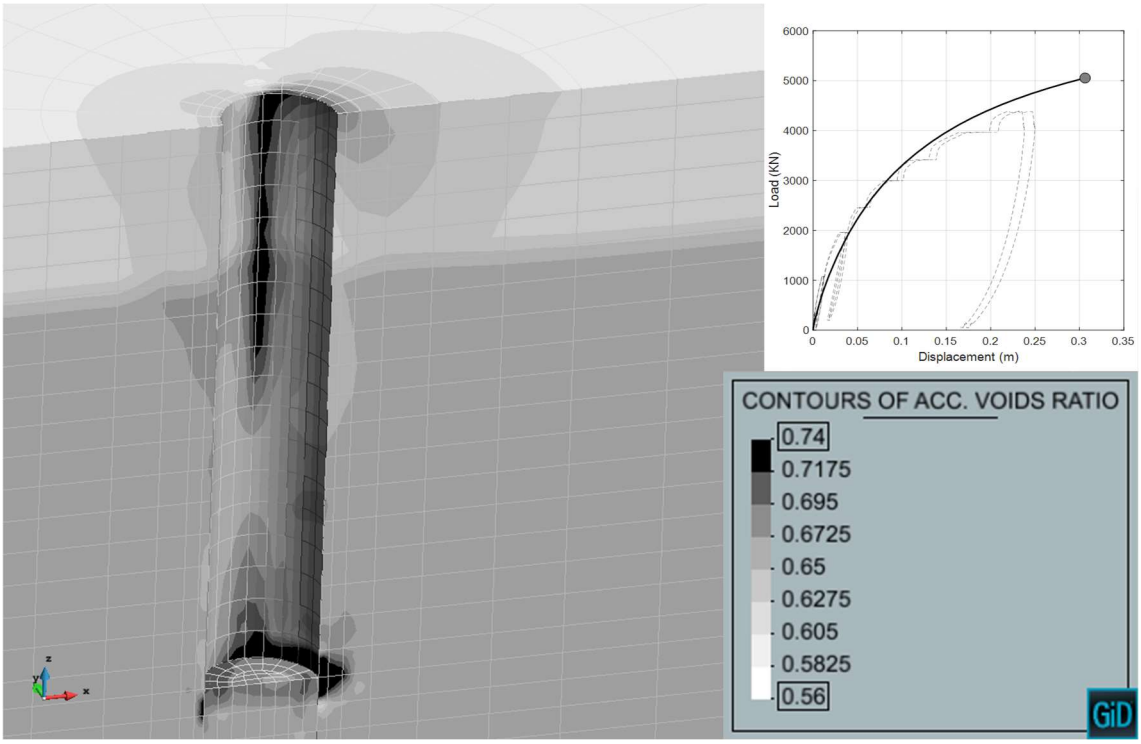
(a)


Load (KN)
Displacement (m)
CONTOURS OF ACC. VOIDS RATIO
0.74
0.7175
0.695
0.6725
0.65
0.6275
0.605
0.5825
0.56
GiD

(b)


Load (KN)
Displacement (m)
CONTOURS OF ACC. VOIDS RATIO
0.74
0.7175
0.695
0.6725
0.65
0.6275
0.605
0.5825
0.56
GiD

(c)



(d)

Figure 235: Void ratio

Apart from a good overall prediction of the field testing results, the model is also able to capture other failure mechanisms in the active zones. For example, in Figure 235(d) a wedge of soil can be identified in the upper active zone falling against the pile, akin to a slope failure. A similar response is predicted in the lower active part, where the material next to the rotation point behaves as a block around it. Also, it can be identified the point of maximum force application of the pile in which the density of the material has not significantly changed from its initial conditions as it moves as a block pushing the soil around it.

5.3.3.6. Structural response

This section covers the structural response of the DL2 pile at various mobilised levels in the analysis. Figure 236 shows the deflected shape of the pile at different current load, expressed as a percentage of the applied maximum load. As discussed previously, the behaviour of the pile is predominantly rigid even at low load-capacity ratios. As the loading increases the depth of the zero rotation point increases slightly and so does the position of the maximum bending moment in Figure 237.

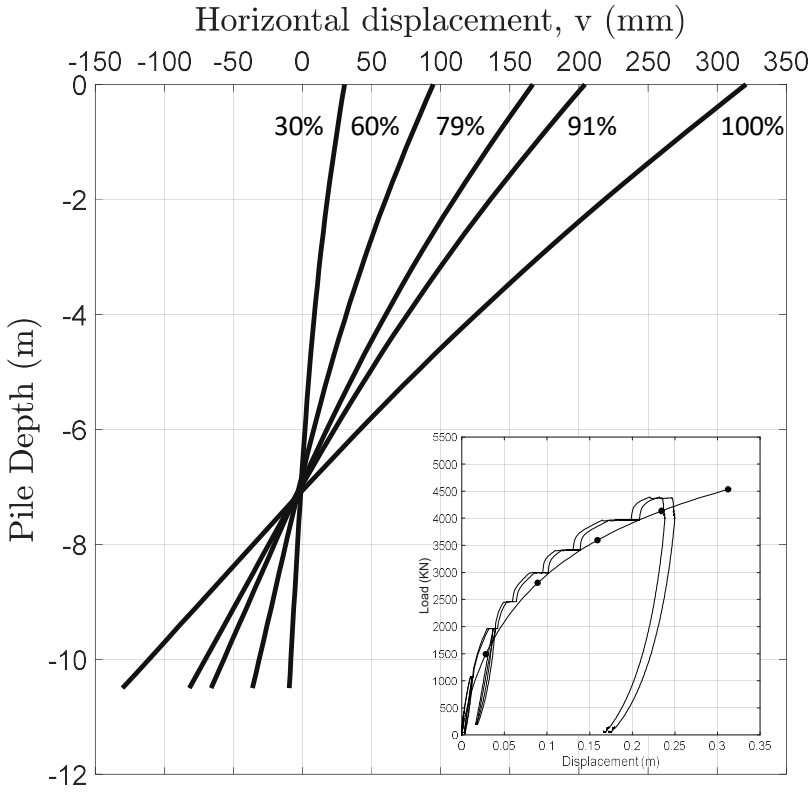


Figure 236: Deflected shape at 30, 60, 79, 91 and 100% of the maximum lateral load

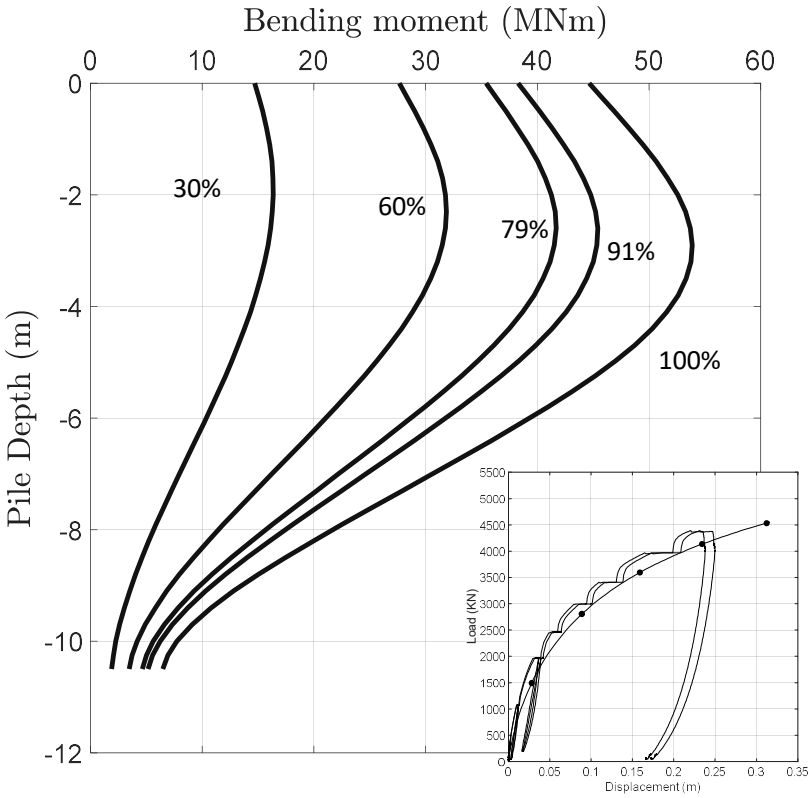


Figure 237: Bending moment distribution at 30, 60, 79, 91 and 100% of the maximum lateral load

Figure 238 shows the normalized deflected shape of the pile, where the transition from flexible to rigid can be identified, although the use of the designation “transition from rigid to very rigid” would be more accurate.

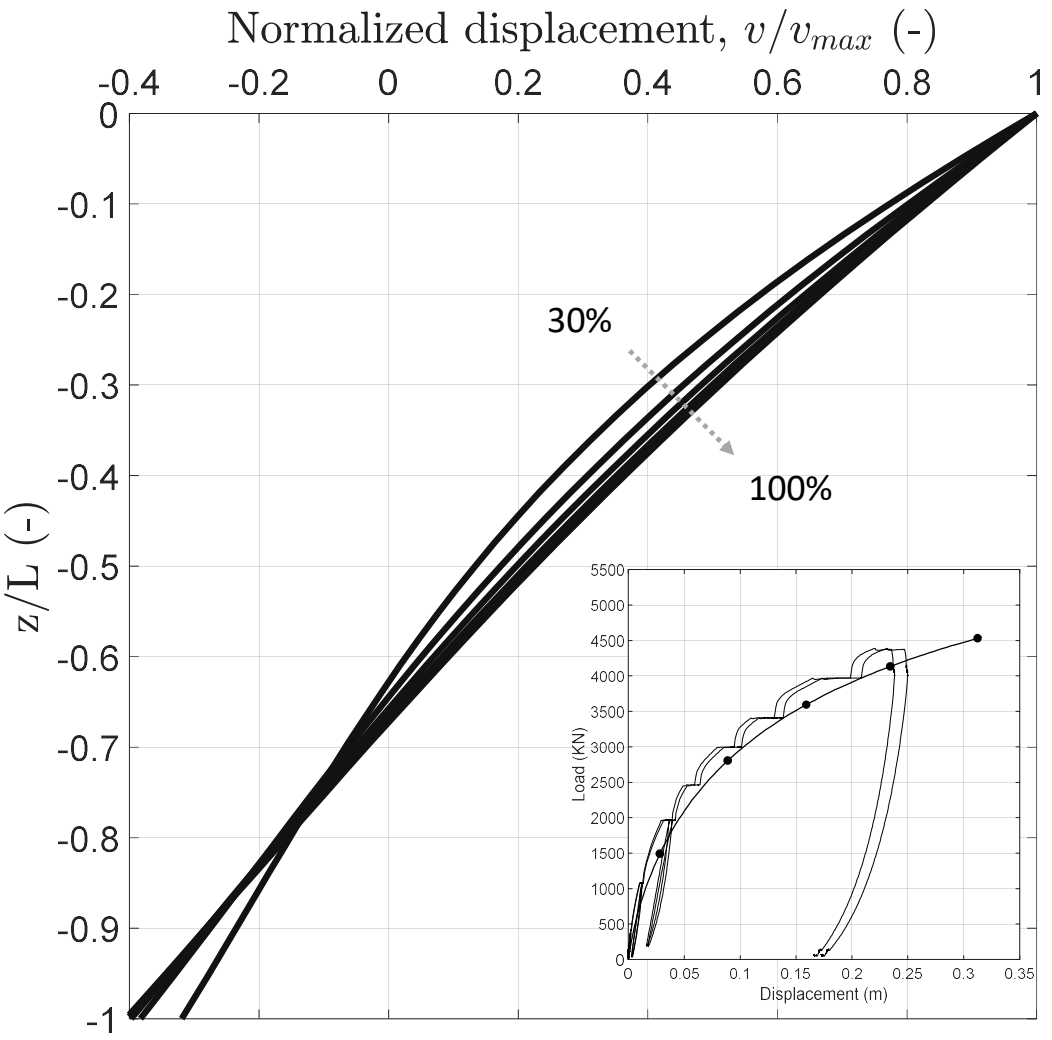


Figure 238: Normalized deflection versus normalized pile length at 30, 60, 79, 91 and 100% of the maximum lateral load

The same conclusions previously obtained from the soil response around the pile can be extracted from the structural response, namely:

- Rigid mode of deflection even at low capacity ratios
- Early and significant toe-kick reaction
- Increase of the depth of maximum bending moment and rotation point as the mobilisation of pile capacity increases.

5.3.3.7. Comparison with field test

Two loading stages have been chosen to compare the field data measurements with the 3D FE predictions. Points A and B, which are indicated in Figure 239, have been chosen for comparison, with point A representative of operational loading level and point B corresponding to failure conditions. The field data are compared with the predicted response using the constitutive model parameters obtained in the calibration GA1.

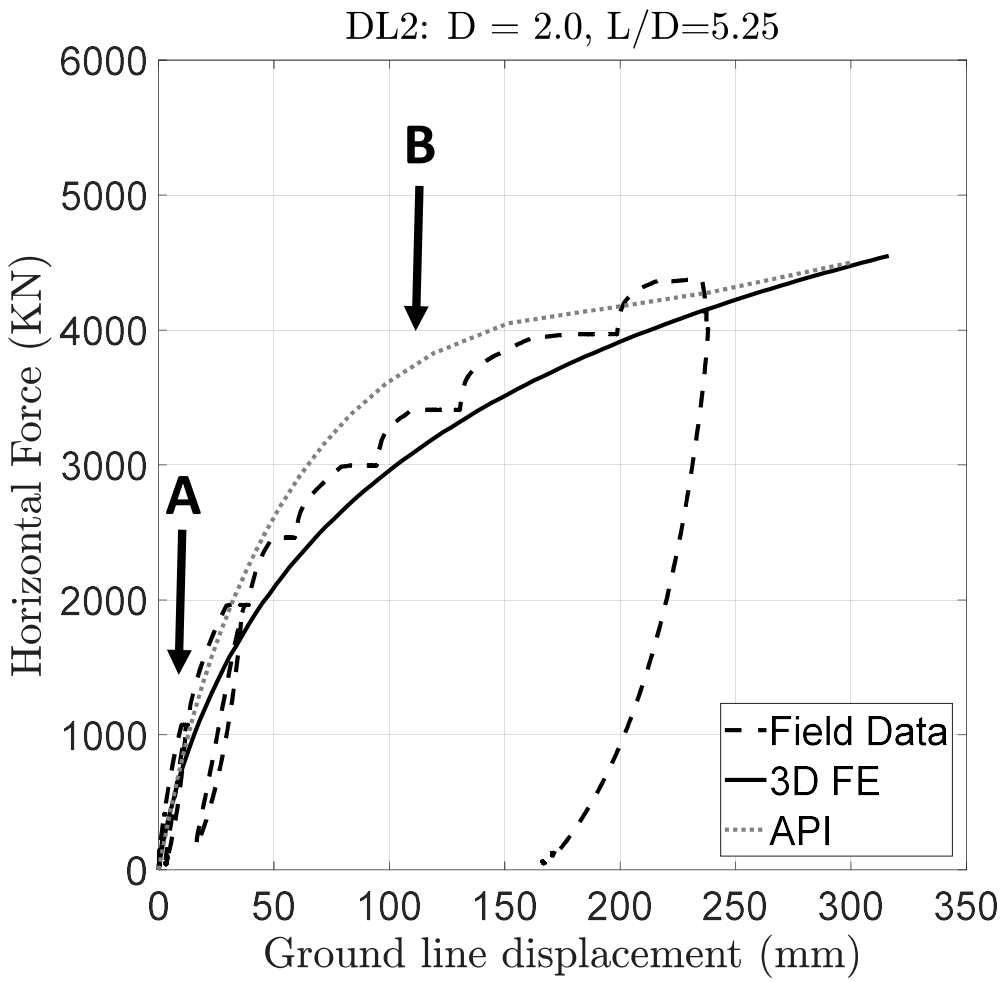
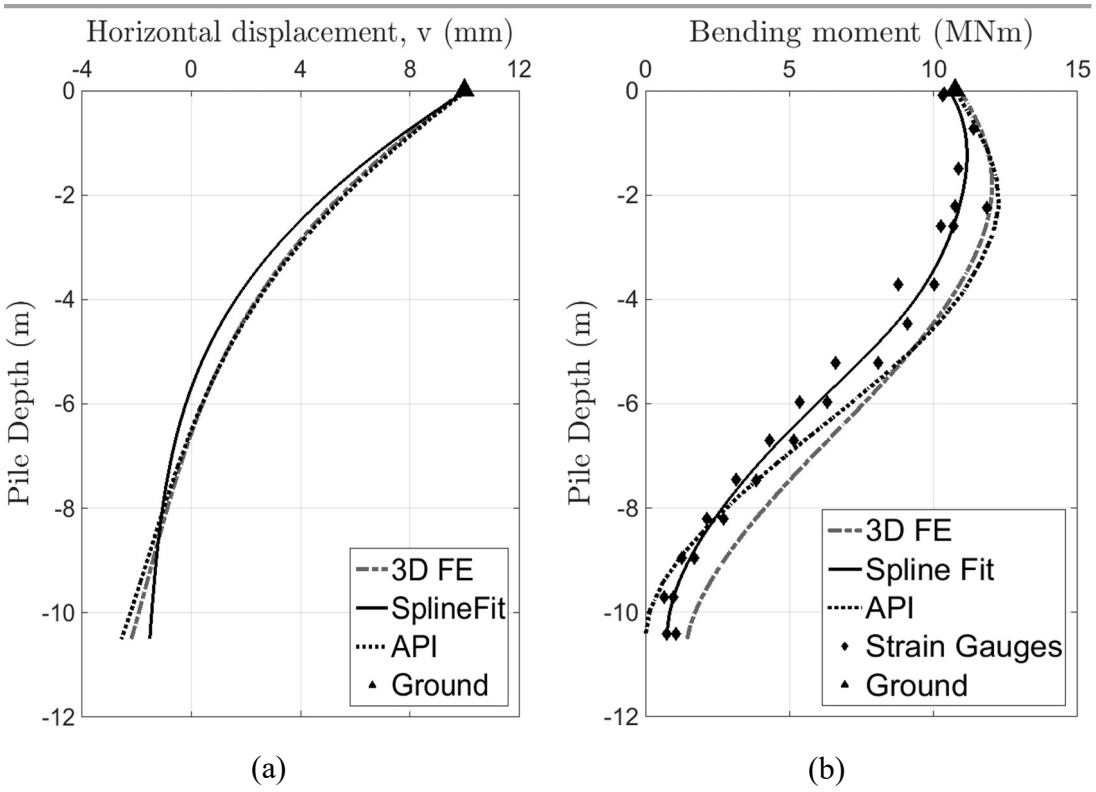


Figure 239: Detail of point A and B for field test comparison – DL1-DL2 load displacement curves, from (McAdam, 2018)

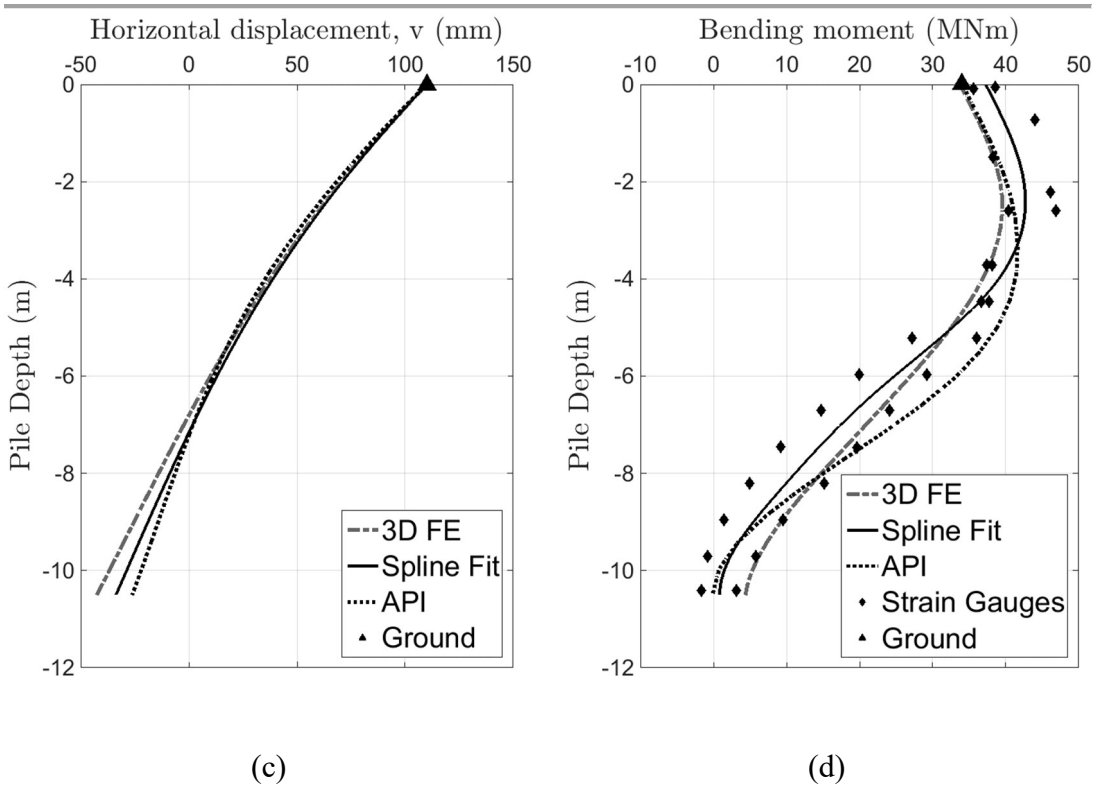
The graphs in Figure 240 are obtained by selecting stages of analysis where either the ground-level displacements or the ground-level moments are the same as those in the field tests.

Point A



(a) (b)

Point B



(c) (d)

Figure 240: Embedded responses of pile DL2: at point A (a) ground-level displacement of 10.1 mm and (b) ground level-moment of 10.8 MNm; and at point B loading (c) ground-level displacement of 110 mm and (d) ground-level moment of 34.1 MNm, from (McAdam et al, 2018)

Both 3D FE and API/DNV analyses are shown to predict with similar accuracy the deflected shape of the pile under operational conditions (Figure 240(a)). On the other hand, the deflected shape determined based on the field test shows a more flexible behaviour than the predicted by both methodologies, indicating that the initial stiffness of the soil around the pile is under-estimated. In terms of moment distribution (Figure 240(b)) both methods predict the same depth for the maximum bending moment. However, the FEA predictions take into account the toe-kick contribution of the base shear while the API/DNV does not. Moreover, both methods slightly overpredict the depths of the maximum moment, which is due to the underestimation of the initial stiffness as seen in Figure 229(a).

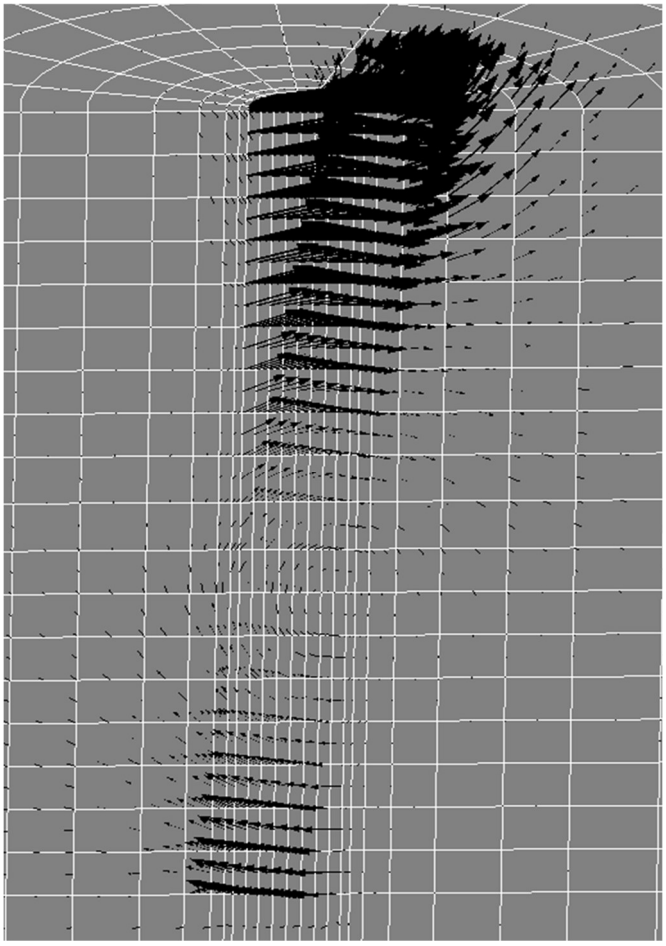
Conversely, under states corresponding to higher load mobilisation (Point B), the deflected shape predicted by the FEA and API/DNV methods diverge, with the API method exhibiting a more flexible behaviour and less mobilization of the toe-kick reaction. Conversely, the FEA prediction is practically rigid. In these conditions, the API method will tend to overestimate the depth of the rotation point, and as a result the maximum bending moment will be located at higher depths than predicted by the FEA analysis. This can be identified in the bending moment profile in Figure 240(d), where the 3D FE agrees better with the depth of the maximum bending moment.

5.3.4. MEDIUM SIZE PILES (DM3, DM4, DM7)

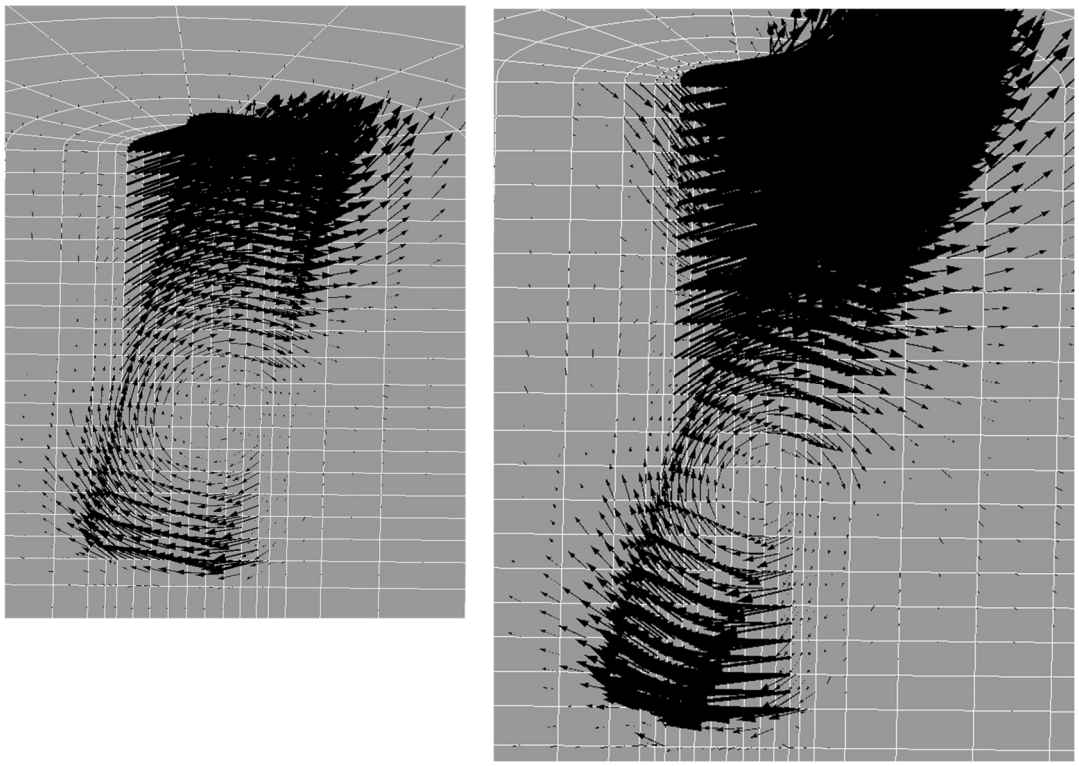
In this section, the effect of the slenderness ratio (L/D) is discussed. To do so, only the medium size piles are compared as the large diameter monopile would see the influence of the hydraulic fill reduced. The piles studied are those labelled DM7, DM4 and DM3, with L/D ratios of 3, 5.25 and 8, respectively. The section shows the failure mechanisms and the structural responses of the piles.

5.3.4.1. Failure mechanism

Figure 241 shows the vectors of incremental displacements at the end of all monotonic analyses presented in 0, clearly identifying the failure mechanisms and rotation points for each pile. Each failure mechanism demonstrates a clear rigid body rotation, even for the largest L/D ratio.



|(a) DM3



(b) DM7 (c) DM4

Figure 241: Failure mechanism of medium diameter piles (a) DM3, (b) DM7 and (c) DM4

As discussed for the large diameter pile (DL2) it can be seen how all the piles lever against the upper passive wedge of the soil, pushing the soil upwards and downwards. This levering point is typically in the region where the upper failure mechanisms and lower failure mechanism will diverge and corresponds to the region of maximum stress concentration. Figure 242 includes a sketch of the typical failure mechanisms observed in all the simulations.

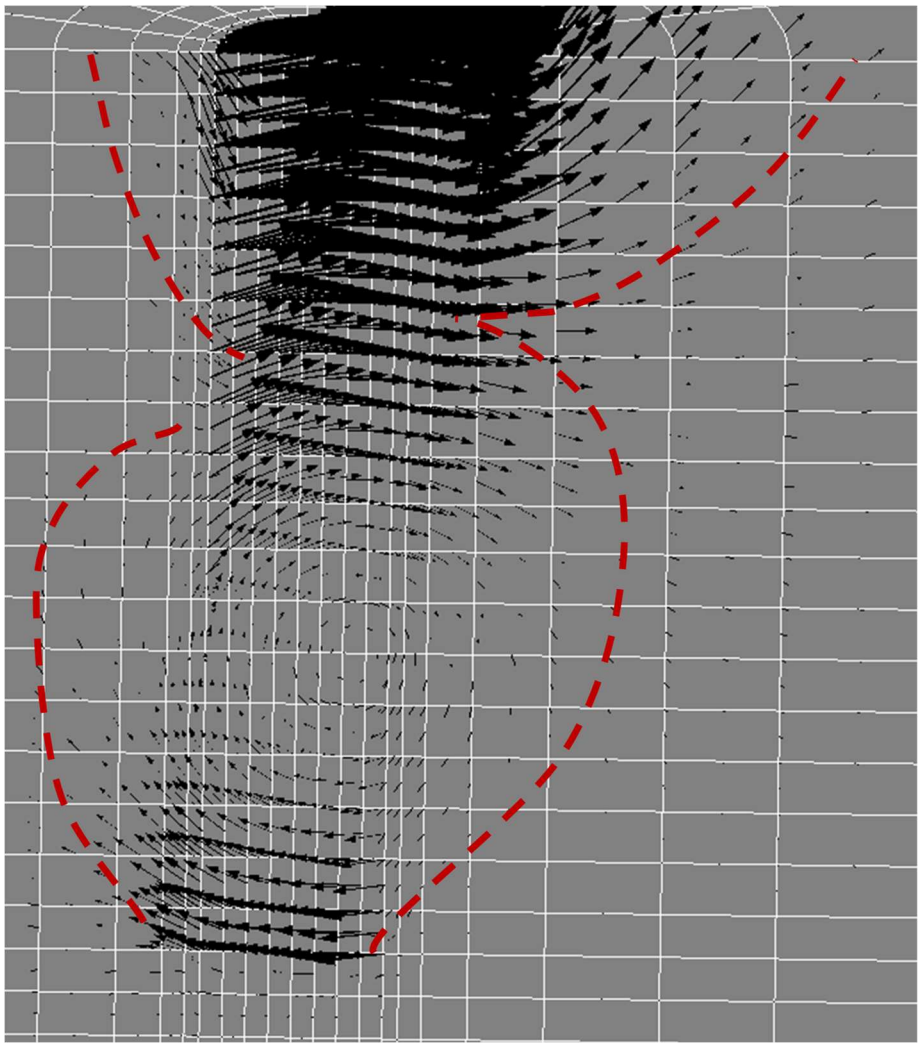
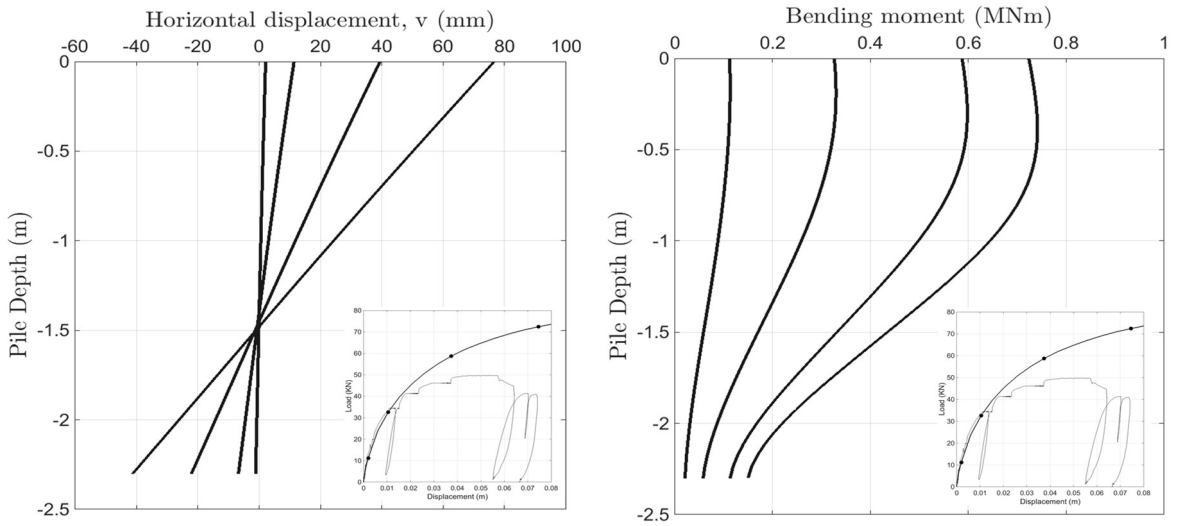


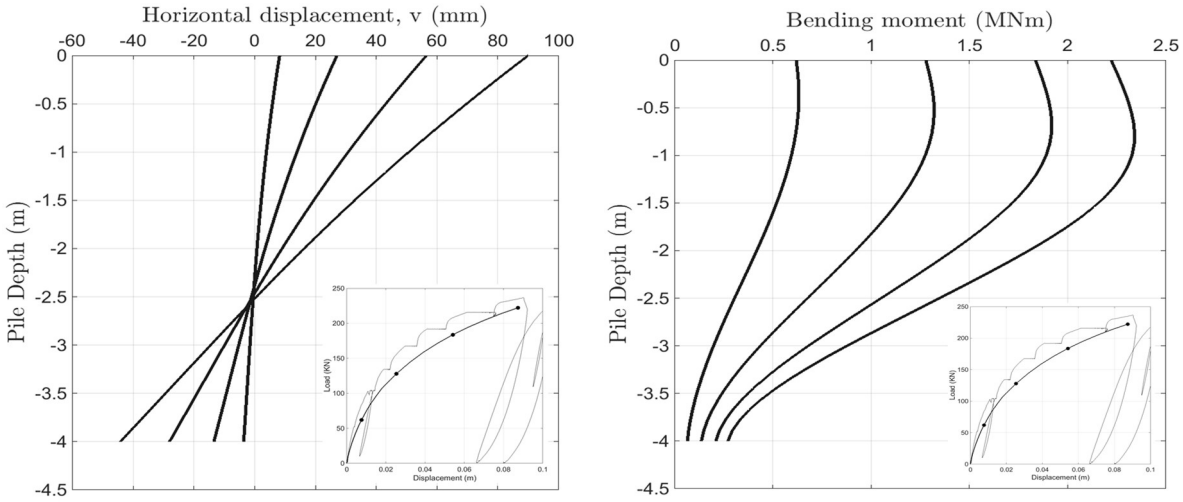
Figure 242: Typical failure mechanism for rigid piles

5.3.4.2. Structural response

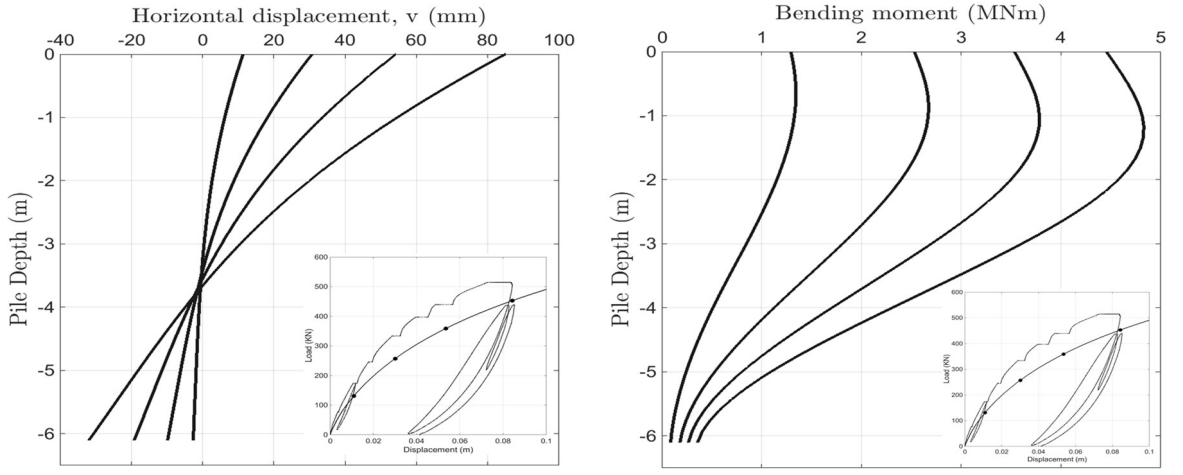
The section presents the predicted structural response of the medium piles following a similar methodology used with the large diameter pile. Similar conclusions can be draw as for the large diameter pile. The predicted deflected shapes and bending moment distributions are illustrated for each of three medium piles in Figure 243. In general, the same trends as in DL2 are found, where DL2 corresponds to an L/D ratio of 5.25, the same as DM4.



(a) DM7



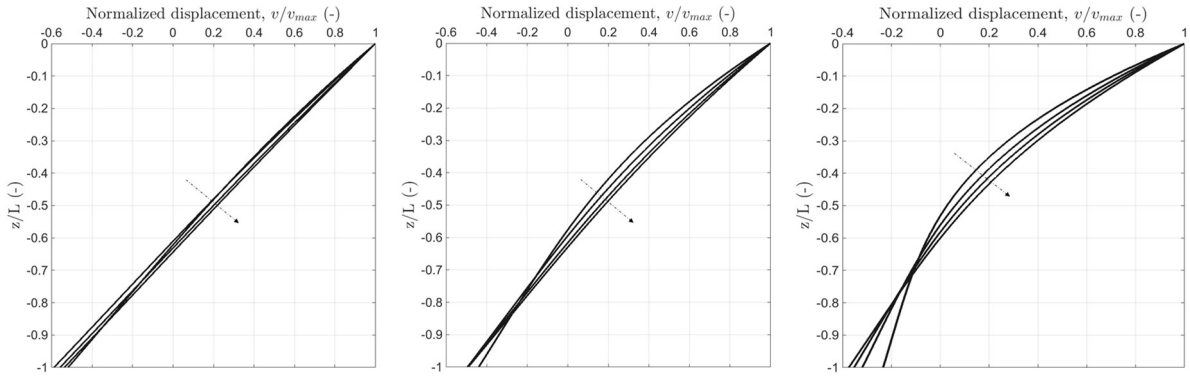
(b) DM4



(c) DM3

Figure 243: Deflected shape and bending moment distribution of DM3, DM4 and DM7 medium diameter piles

Figure 244 shows the normalized deflected shapes (horizontal displacement normalised by the maximum horizontal displacement at the ground surface), indicating a predominantly rigid body rotation mode of deformation for practically all loading levels. The only exception is found in the long pile at around 25% mobilized capacity (DM3 L/D = 8).



(a) L/D = 3 (b) L/D = 5.25 (c) L/D = 8

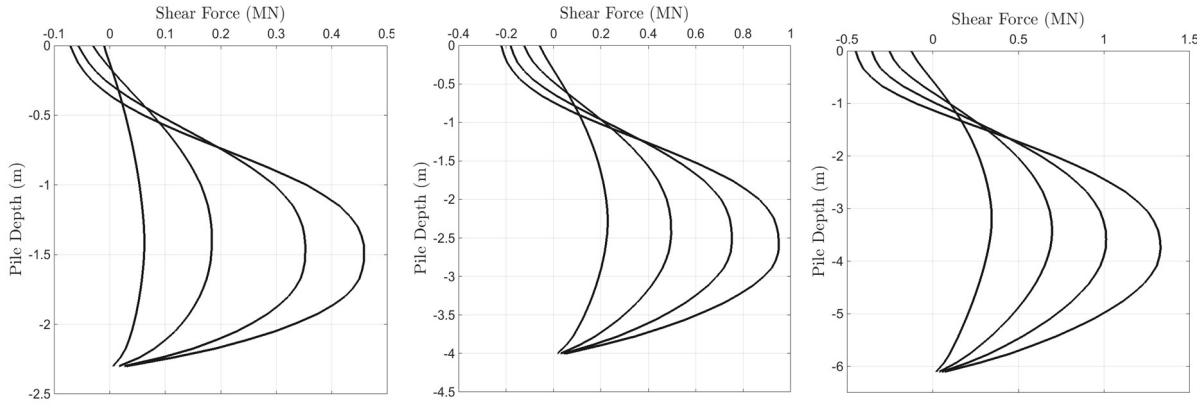
Figure 244: Normalized deflection versus normalized depth of: (a) DM3, (b) DM4 and (c) DM7

5.3.4.3. P-y equivalent curves

One of the objectives of the PISA project is the redevelopment of the standard API/DNV p-y curves through large scale field tests and advanced numerical analysis. In this sense, one of the outcomes of the project is the integration of FEA in wind turbine routine design. To do so the reactions from FEA can be extracted and rationalised in a 1D beam-spring model. The final result of this procedure is a set of distributed pressures and moments that when combined with the deflected shape of the FEA analysis correspond to equivalent p-y curves. The resultant bending moment and shear force can be extracted directly from the shell elements. By enforcing equilibrium in a differential slice of beam the distributed pressure can be extracted as

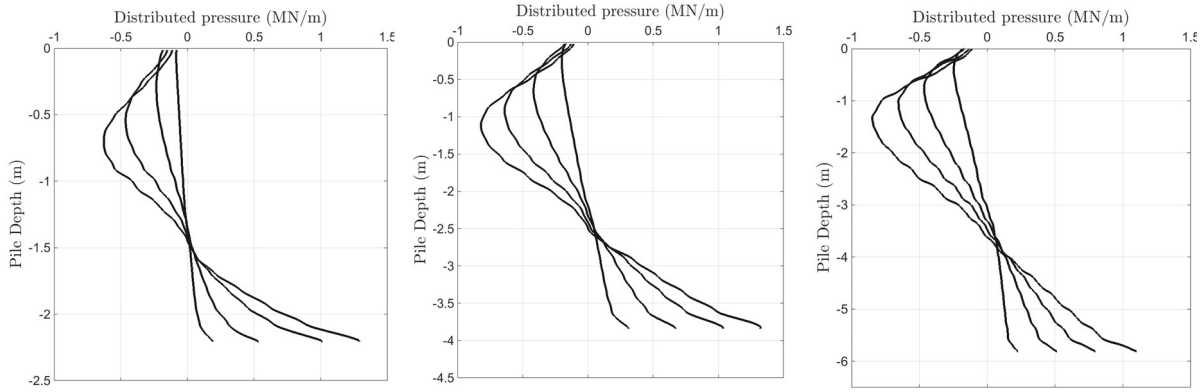
$$\begin{aligned} \frac{\partial V(x)}{\partial x} + p(x) = 0 \\ \frac{\partial M(x)}{\partial x} + V(x) = 0 \end{aligned} \tag{5.2}$$

Figure 245 and Figure 246 show the shear force and the equivalent pressure distributions for all three piles at the loading stages depicted in previous section.



(a) L/D = 3 (b) L/D = 5.25 (c) L/D = 8

Figure 245: Shear force versus depth of: (a) DM3, (b) DM4 and (c) DM7



(a) L/D = 3 (b) L/D = 5.25 (c) L/D = 8

Figure 246: Equivalent pressure versus depth of: (a) DM3, (b) DM4 and (c) DM7

The equivalent p-y curves can be extracted from the deflected shape and the equivalent pressure distribution, Figure 247 presents the extracted p-y reactions for the longest medium pile (6.1 m) at depths of 0.5, 1.5, 2.5, 3.5, 4.5 and 5.5 m.

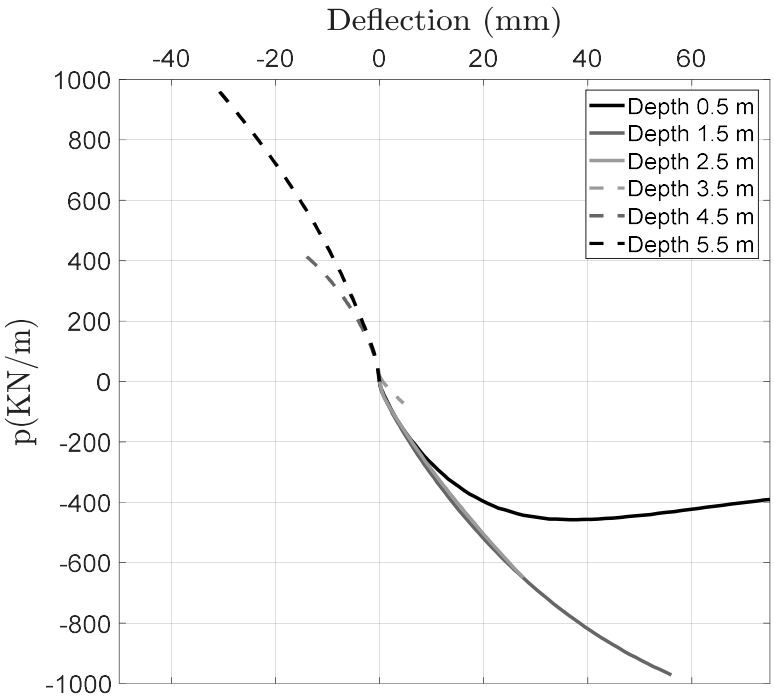


Figure 247: p-y curves DM7

As can be seen from Figure 247, the lateral resistance does not reach complete mobilisation around the pile except in the edges where a significant degree of mobilization has occurred, this is in line with the fact that the soil around the pile has not reached critical state conditions despite the pile has substantial mudline displacement (more than 0.1D).

5.3.5. LARGE DIAMETER PILE (DL1) UNDER CYCLIC LOADING

This section describes briefly the cyclic loading field test carried out for the large diameter piles (DL1) in Dunkirk sand and compares it with the model response under cyclic conditions (AWG, 2015). To do so several 3D FE analyses of the DL1 pile under cyclic loading conditions have been carried out, using the simple version of the sand model with only one hardening rule, as well as the same model with additional hardening rules. The predicted response of both cases is then compared at global, local and structural level, following a similar methodology to that described in the previous sections. Due to the absence of laboratory cyclic tests at this stage, a parametric study has been carried out to evaluate and assess the influence of the additional hardening rules. For all calibrations of the superimposed models, the weights "C" governing

the overall stiffness and linear mapping of the simple model (one backstress) have been kept consistent with the simple rule, to maintain the initial response of the model.

5.3.5.1. Cyclic field tests description

After monotonic loading the large diameter piles (DL1, DL2) where subjected to cyclic loading at 10%, 20%, 40%, 80% and 90% of the ultimate load. The description of the batches of cycles is included in Table 34 and the load-displacement response is shown in Figure 248.

Table 34: Cyclic loading stages for DL1 DL2

	Load Range (kN)	**Number of cycles (N)**
Batch 1	100-420	201
Batch 2	100-840	103
Batch 3	100-1680	50
Batch 4	100-3360	31
Batch 5	100 - 4000	2

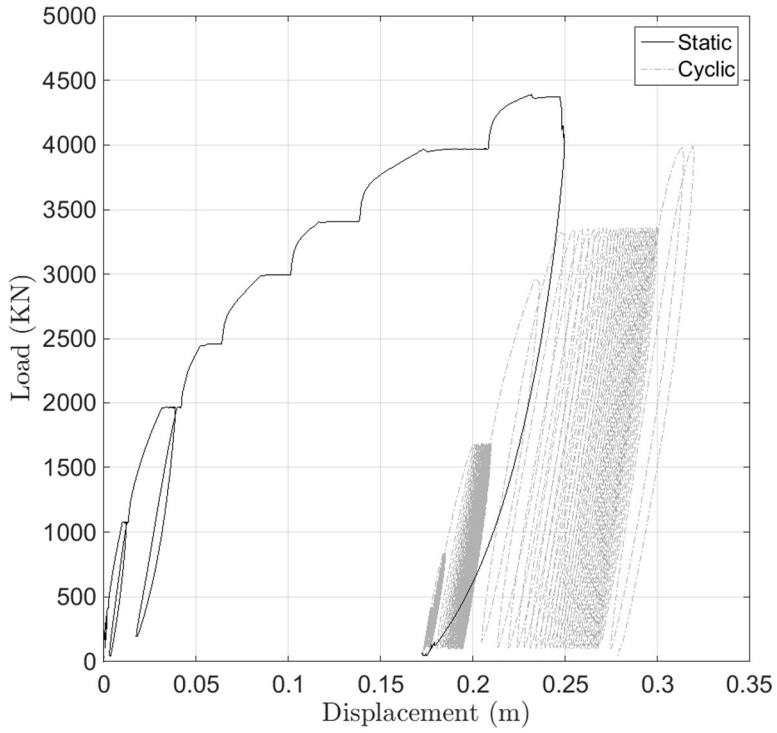


Figure 248: Monotonic and cyclic loading stages for DL1

It can be appreciated from Figure 248 that, regardless of the previous load history, the load-reload stiffness for medium-large amplitudes is not significantly affected by the past cyclic

history, as the loops maintain similar secant stiffness. It is interesting to note that the response tends to find a stable cycle, generally reducing the amount of accumulated displacements over the number of cycles. The amount of accumulated displacements is affected by the amplitude of the cycle: as it can be seen for the cycles below 1900 kN the soil tends to fully shakedown in less than 100 cycles. A detail of the shakedown stable cycles is shown in Figure 249(b), where it can be observed that the load-displacement path travels to a stable cycle which may not always produce displacement accumulation. For example, accumulation of displacements can be produced for the batch at 100-840 kN, while for the batch at 100-420 kN self-healing occurs and the accumulated displacement decreases. This response is in accordance with the concept of cyclic attractors identified by Wichtmann and Triantafyllidis (2015), to which the proposed modelling framework described in this thesis is devoted to.

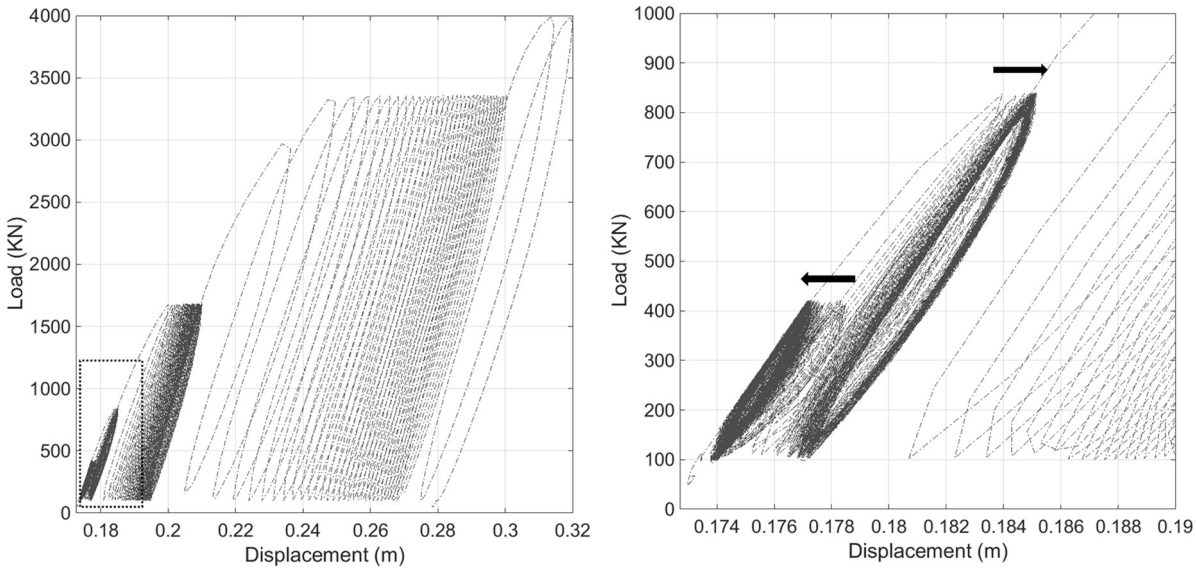


Figure 249: Detail of cyclic tests (a) full test, (b) detail, batches at 10% and 20% of pile capacity, stable cycles

5.3.5.2. Parametric study for various hardening rules

A set of 3D FE cyclic analyses of the large diameter monopile have been carried out to explore the implications of backstress superposition under cyclic loading conditions. Two types of loading cases where carried out. A first set of 3D analyses consists of batches of 5 load-controlled cycles at an amplitude of 840, 1680 and 3360 kN, corresponding respectively to 20%, 40% and 80% of pile capacity. The second type of analysis explores the response under a larger number of cycles at 10% and 20 % ultimate capacity. Table 35 shows the input used for the cyclic simulations; set 1 corresponds to the standard model with a single backstress, while set 2, correspond to cases with one superimposed backstress.

Table 35: Set of input parameters for cyclic simulations

	C	**e_{c0}**	**e_{d0}**	**h_s**	**n**	**α**	**β**	**XV**	**YF**	**ZF**	**θ**	**S_f**	**S_d**	**ob_{min}**	**ob_{max}**	**δ**
Set 1	1.0	0.84	0.50	1E6	0.55	0.08	2	0.59	0.87	0.1	0.53	4.1	1.0	-1.73	0.45	2.25
Set2.1	0.5	0.84	0.50	1E6	0.55	0.08	2	0.59	0.87	0.1	0.53	4.1	1.0	-1.73	0.45	2.25
Set2.2	0.5	-	-	-	-	-	-	0.99	-	-	2.0	4.1	1.0	0.0	0.0	-

All cyclic tests are performend assumming drained conditions as assumed in the PISA project. No piezometers instrumentation was installed in Dunkirk as the first 5 meters of sand where unsaturated, moreover the frequencies at which the loads were applied are sufficiently large to allow drainage in the sand (AWG, 2015).

5.3.5.3. Simple model response

The first set of numerical simulations corresponds to four batches of 5 cycles at 420, 840, 1680 and 3360 kN. Figure 250 shows the predicted response of set 1, corresponding to a case where only the main hardening rule is active. In general, a simple rule is already capable of predicting appropriately the unload-reload behaviour observed in the field tests and the energy dissipation for each load-displacement cycle. However, as would be expected with one hasrdening rule the ratchetting per cycle becomes excessive for all batches, in particular for the batches with larger amplitudes. The second characteristic of the model is the ability to capture cyclic stable or

unstable behaviour as shown in Figure 250. The post peak region of the model is triggered for large amplitudes (80% ultimate capacity), producing dilation which reduces the capacity of the model at a local scale. As a result, the ratchetting per cycle increases as a significant redistribution of stresses occurs and, consequently, the ratchetting of the pile accelerates. Under these conditions the pile will eventually be unable to sustain the load cycle and would fail at a given number of cycles.

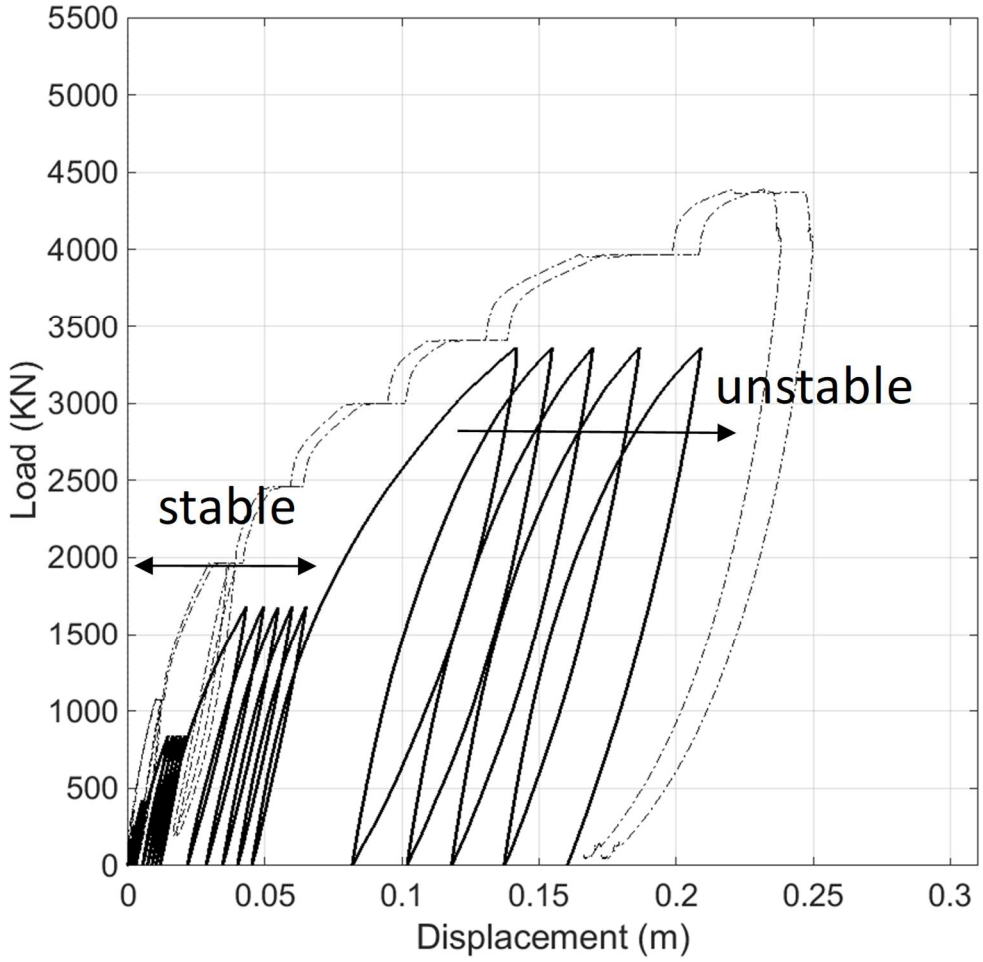


Figure 250: Load displacement curves at mudline for Set1: Comparison with DL1-2

5.3.5.4. Comparison of basic model and superimposed hardening rule model for low-medium amplitude cycles

This section shows the effect of adding the backstress rules and compares in detail, at global, local (Gauss point) and structural levels, the responses obtained using Set 1 and Set 2 parameters given in Table 35. Figure 251 and Figure 252 show four simulations, two consisting of 2 batches of 5 cycles at low-medium load amplitudes of 420, 840 and 1680 kN, and other two corresponding to two batches of 20 cycles at low amplitudes, with the same characteristics of the cyclic tests carried out on pile DL1 (Figure 249b). It can be observed that for set 2 the initial stiffness and energy dissipation along the cycle remains similar to Set1, but the ratchetting per cycle decreases significantly as a function of the load amplitude when compared to set 1 with only one hardening rule. As discussed in the next section, the ratchetting reduction depends on the ability of the combination of backstresses to travel to its stable cyclic attractor (if it exists). In this sense the amount of ratchetting, and the stability of the system upon cyclic loading (Figure 250) depend on the stress amplitude of the cycle and on the admissible stable cycle for each of the hardening rules, mainly governed by the respective recall term.

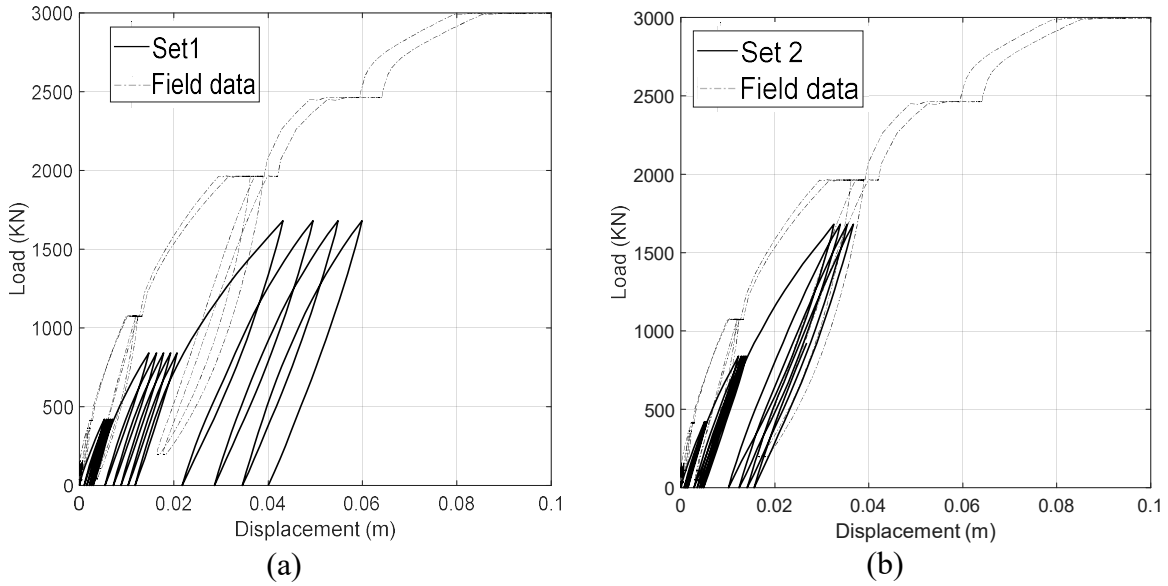


Figure 251:Comparison of load displacement curves at mudline for Set1 and Set4 and field data: (a) One Backstress, (b) Two backstresses; field test – dotted light line, simulation – dark grey line

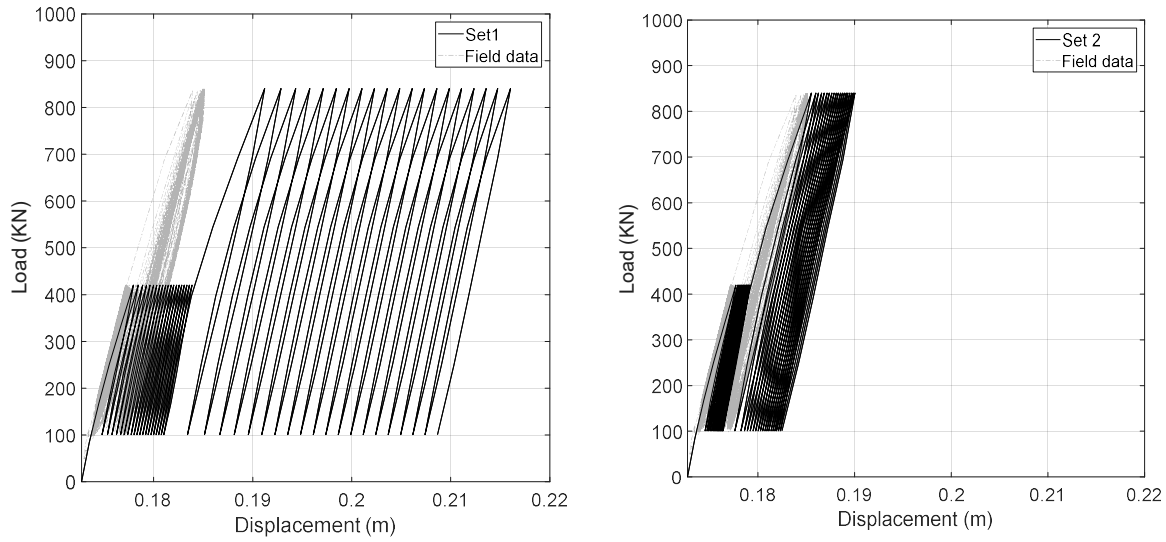


Figure 252: Comparison for N=20 840 KN cycles and cyclic field tests (a) One Backstress, (b) Two backstress

Figure 252 compares the predicted responses with the field tests results (Table 34) for Set 1 and Set 2 of parameters. The effect of adding extra hardening rules is clear, where the ratchetting per cycle decreases significantly. Moreover, it can be seen that, in terms of secant stiffness, both sets of parameters agree very well with the field data as they are calibrated to experience similar stiffness upon loading. Despite the significant reduction of ratchetting in Set 2 analysis, the system cannot shake down for the input parameters selected in Table 35. This is due to the general form of the model, according to which the recall term can never completely cancel out in the volumetric direction, thus never allowing the system to find a stable cycle in the p' space. To illustrate this response a comparison at local level, and also at structural level, is carried out between the numerical predictions obtained with Set 1 and Set 2. The studied points are show in Figure 253, located at 0.5 metres away in the radial direction from the pile, at depths of 2.5, 5.0, 7.5, and 10.0 m. The obtained results at local and structural level are shown in Figure 254 to Figure 260.

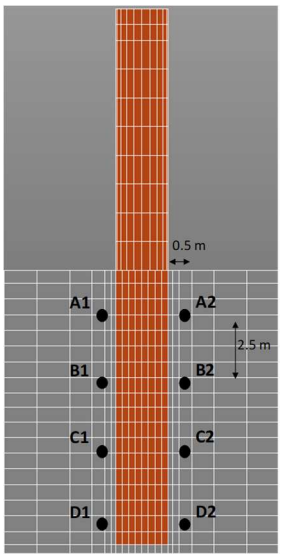


Figure 253: Points of study

Points A2, B2, D1 correspond to the passive sides of the pile, while A1, B1, D2 are on the active side, with the pile rotating clockwise. Although the load amplitude of the cycles is at 10% and 20% of the ultimate load, and therefore far from localising and developing a failure mechanism, it was observed during the monotonic analysis that the pile exhibits an early rigid mode of deflection even for these low-amplitude loading conditions. As a result, points A2 and D1 will exhibit an early increase in the mean effective stress even at small load amplitudes. These regions correspond to the areas where larger stress amplitudes are concentrated, controlling substantially the strain accumulation and in general the pile displacement accumulation per cycle.

Figure 254 to Figure 256 show the stress strain response in the soil on the passive sides of the pile (A2, B2, D1) for both batches of 20 cycles. The dashed line corresponds to the Set1 prediction while the solid line represents the Set 2 (two backstresses) prediction. It can be seen how the Set 2 parameters show a significant reduction of strain accumulation per cycle as a result of the additional backstress. This reduction occurs more significantly in the volumetric direction as the extra hardening rule only produces ratchetting in the deviatoric direction.

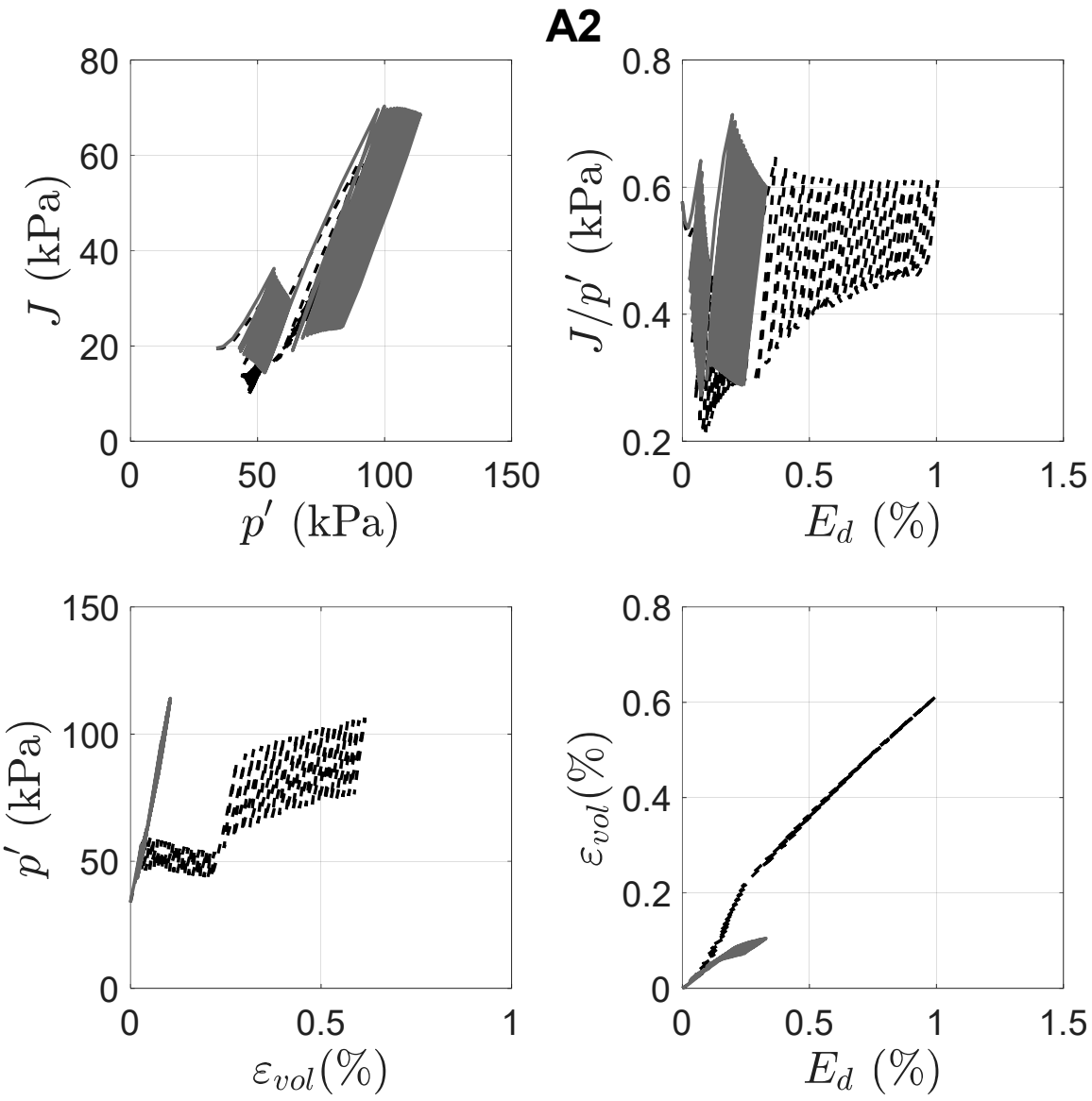


Figure 254: Stress paths for point A2

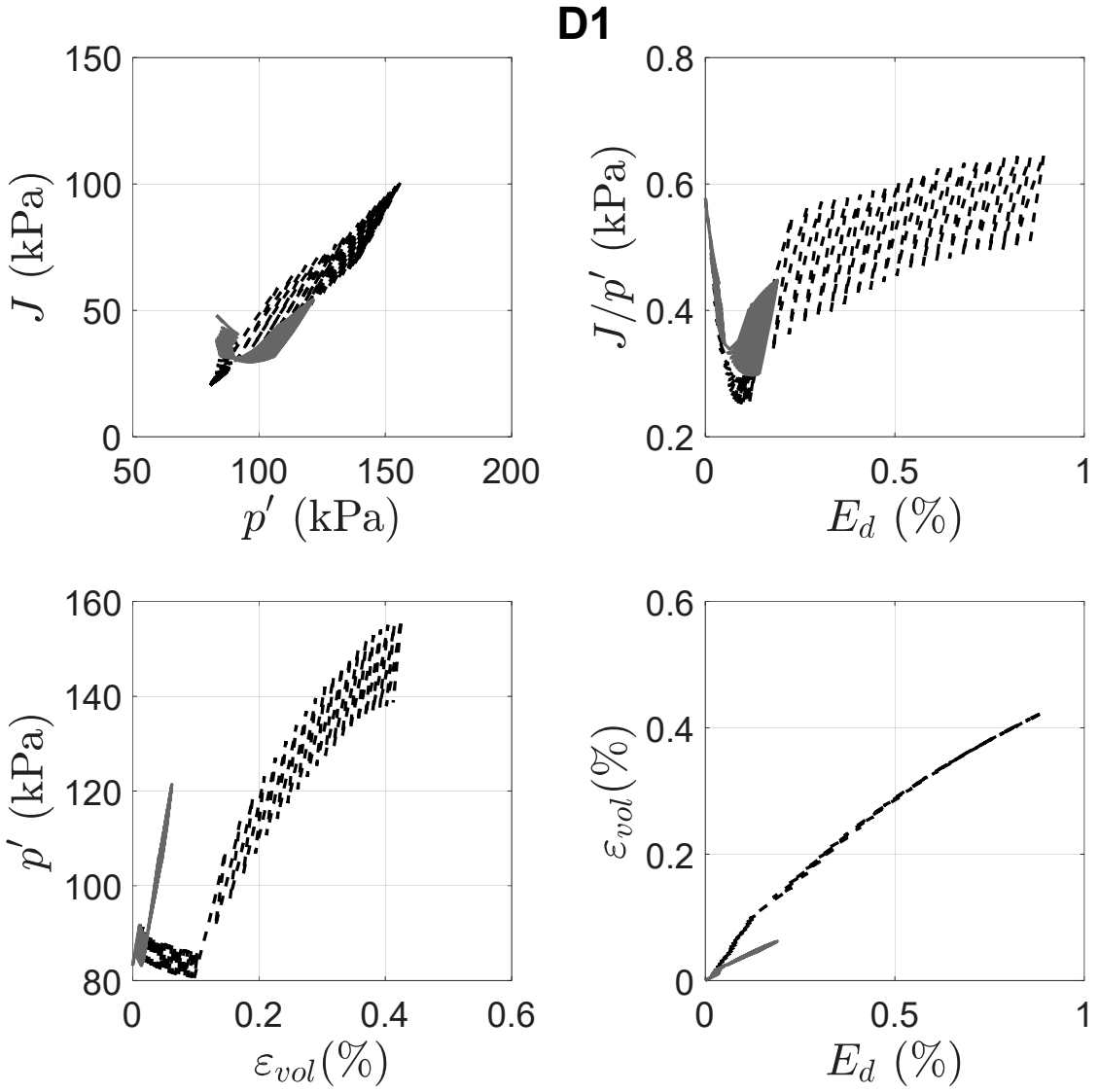


Figure 255: Stress paths for point D1

An interesting result on the effect of extra hardening rule can be observed when comparing point B2 (Figure 256) with point A2 (Figure 254). Point B2 is located near the rotation point of the pile. In these conditions, with one backstress, the pile exhibits a deflected shape in a way that the stress around the pile exhibits stress relaxation, while the response for set 2 will maintain its passive behaviour as the deflection of the pile is smaller.

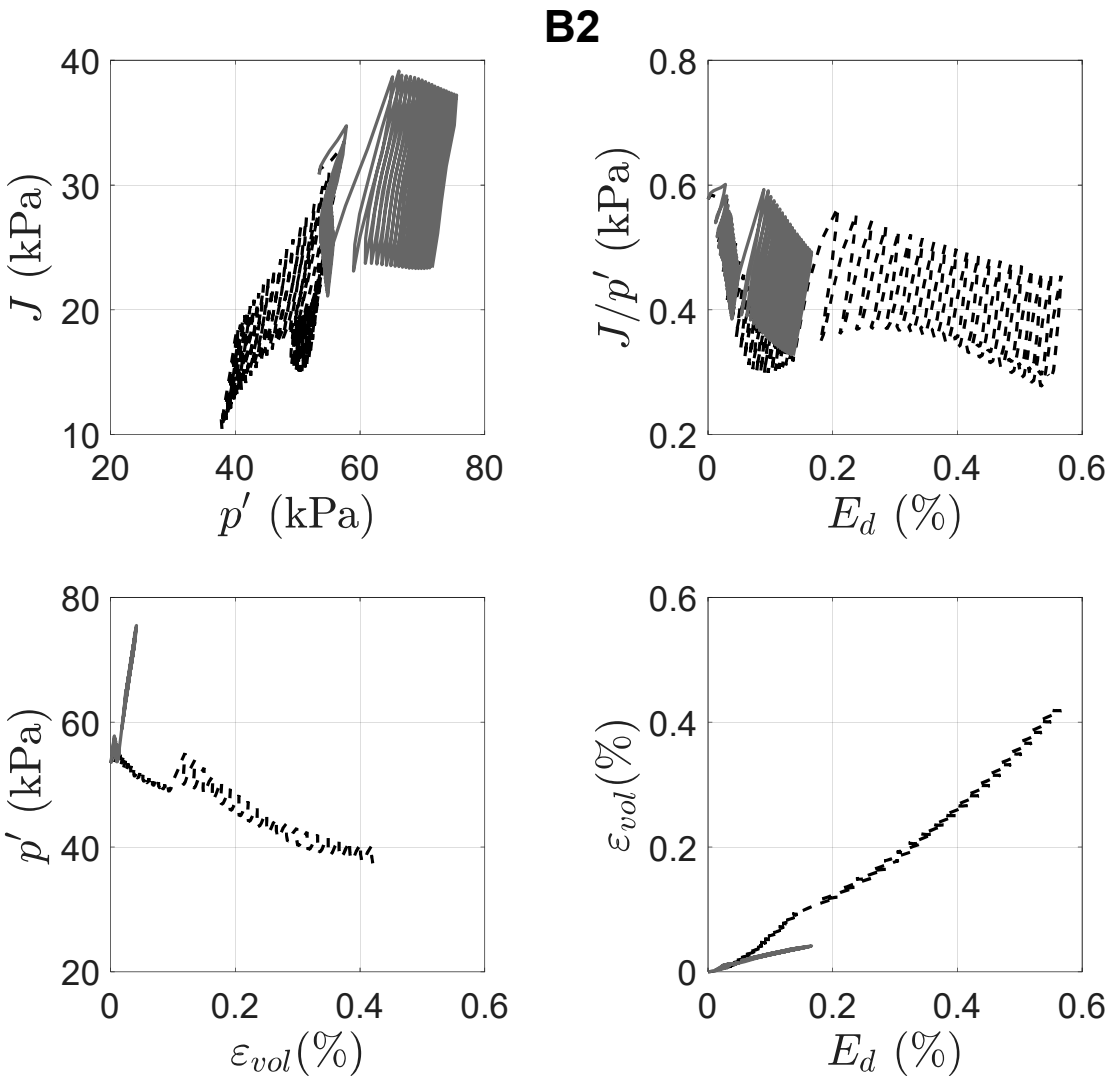


Figure 256: Stress paths for point B2

As mentioned in the previous chapters the reduction of ratchetting is related to the ability of the system of two backstresses to provide a solution for stable cycles that match the stress cycle imposed by the boundary value problem. In this sense, when using various hardening rules, there are more possible solutions of stable cycles and therefore the ratchetting reduces. With one backstress the ratchetting direction is a function of the recall terms. This is clearly observed for set 1 in Figure 254, where the accumulation of strain direction ratchetting is different for each batch of cycles, as their limit functions and goal functions along the cycle are different. Conversely, when various rules are used, the recall term can be evaluated at different regions as the current stress is a sum of the different internal variables (backstresses).

Looking now at the active side of the pile (B1, D2), Figure 257 and Figure 258, it can be observed that the soil is generally subjected to stress relaxation per cycle. Similar to the analysis with ratchetting, when using various hardening rules, the stress relaxation reduces as the sum of the recall terms of all the hardening rules is significantly smaller than with a unique rule. Despite the reduction of magnitude of stress relaxation, the formulation of the model maintains its asymptotic properties in the J/p plane.

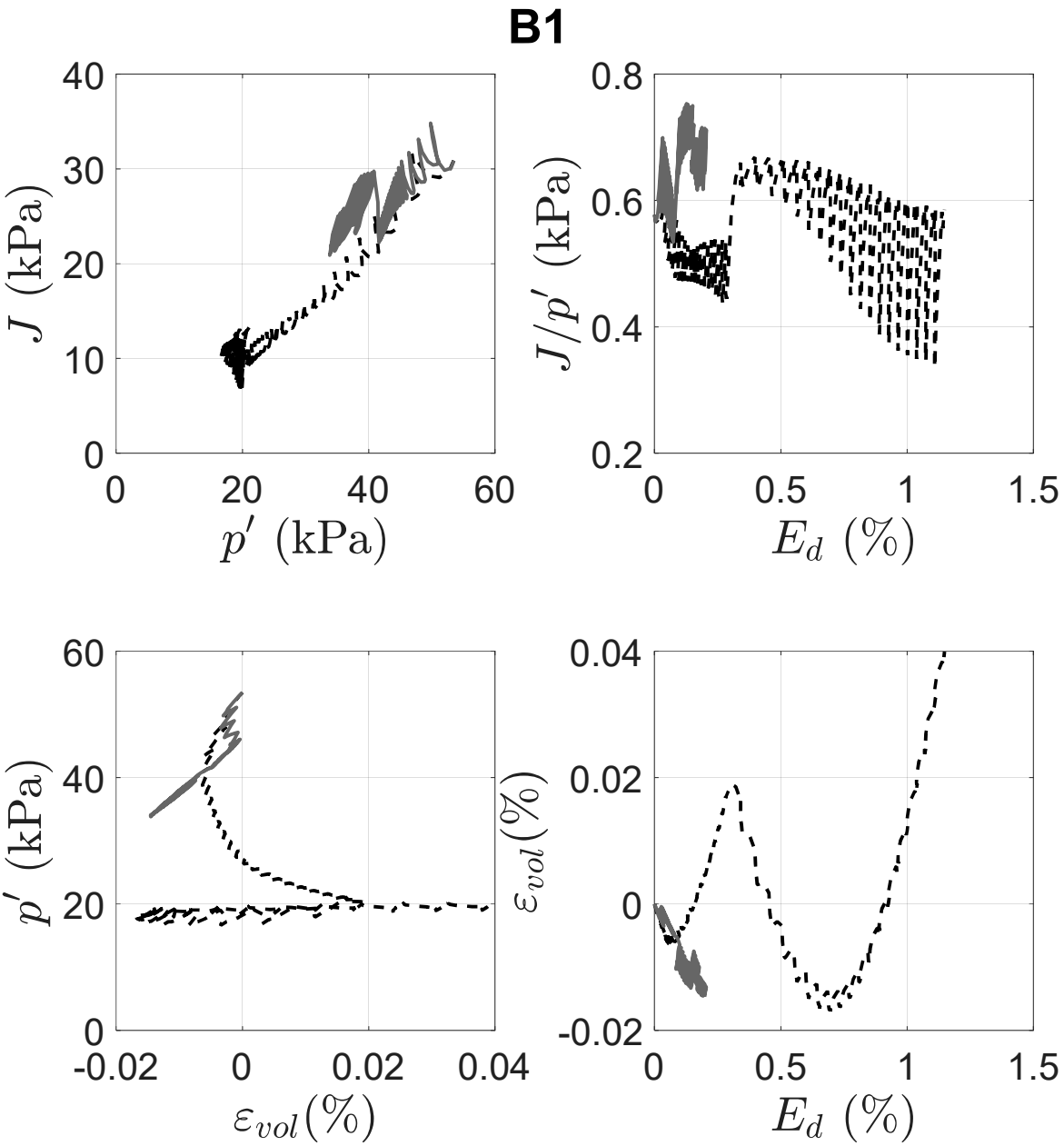


Figure 257: Stress paths for point B1

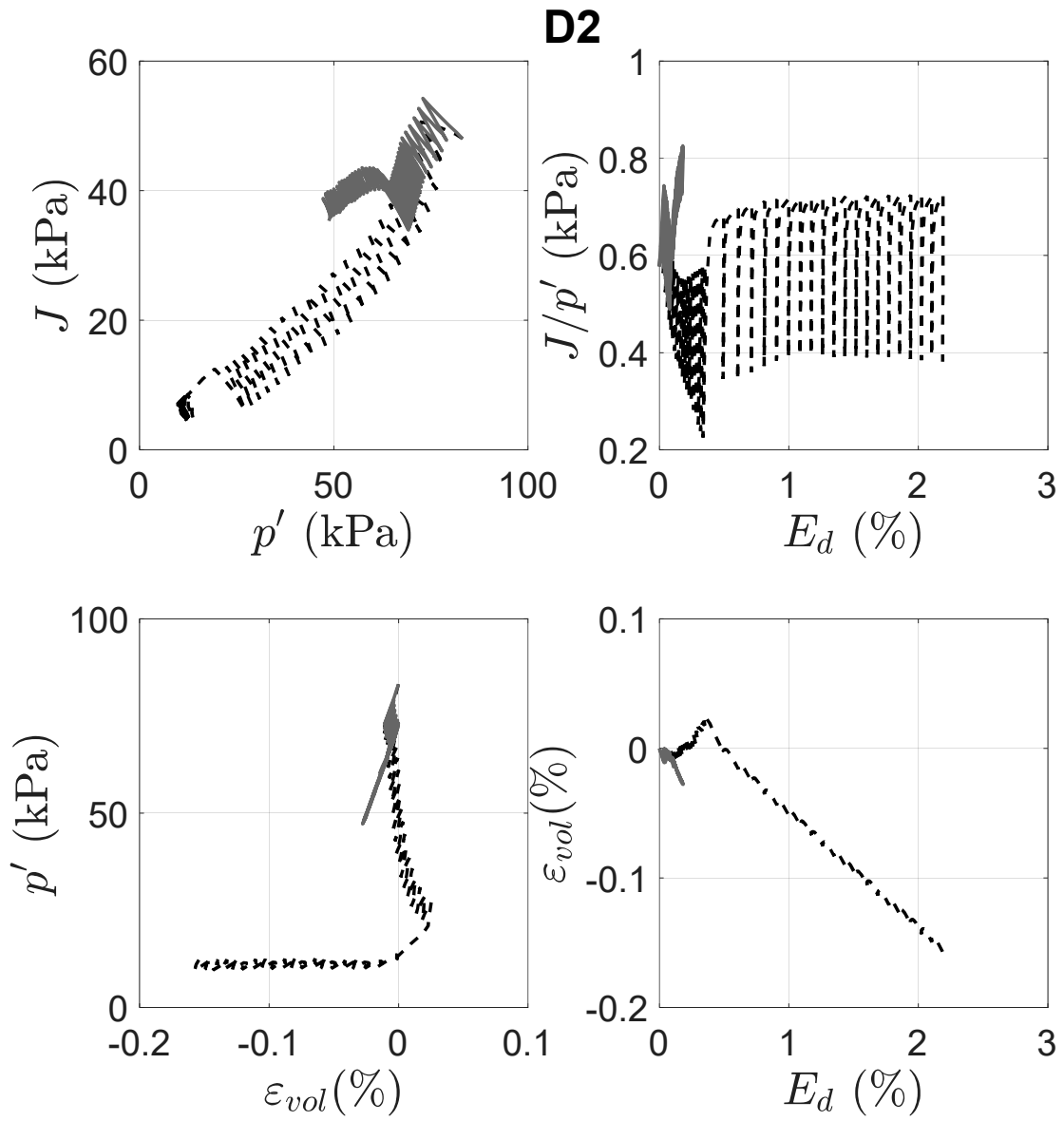


Figure 258: Stress paths for point D2

Overall, it can be concluded that, regardless of the type of loading, when more hardening rules and internal variables are introduced the ratchetting prediction of the model improves, typically reducing the effect of ratchetting and stress relaxation. In the case of a laterally loaded pile, ratchetting reduction occurs more significantly in the passive wedges (points D1, A2 and B2), as a substantial fraction of the deviatoric stress is taken from the second hardening rule which has a less strong non-linear contribution of its recall term. However, it must be noted that, with a superposition of simple hardening rules, there will always be densification in the soil per cycle as the trace of the goal function is never zero. In this sense to improve ratchetting

prediction in preferential directions the specialised hardening rules defined in Chapter 4 are a more convenient choice, which will not require the recalibration of the main hardening rule to achieve full shakedown. Strategies to achieve full shakedown include adding a severe penalisation of curvature of the limit surface, which would force the main rule to maintain its linearity up to relatively high J/p ratios. Under such conditions the ratchetting response would be dominated mostly by the extra hardening rules. The implementation of the specialised rules has not been carried out in a general FE code, only in the local solver. As such, the full deployment of the specialised rules has been left for future study.

5.3.5.5. Structural response

The reduction of accumulated strain produced by the superimposed model will translate in a different structural response. This section describes the implication of ratchetting reduction at structural level. In Figure 259 and Figure 260 the deflected shape and moment distribution at the beginning and end of each batch of 20 cycles are shown. It can be seen that the structural response exhibits a behaviour similar to that observed in the soil, as expected. The basic model with one backstress will exhibit the same accumulation of deflections per cycle, while the version of the model with extra hardening rules will eventually reduce the ratchetting accumulation until a minimum ratchetting per cycle is achieved. As a result, the deflection in the pile is significantly smaller when using the model version with more hardening rules. In terms of redistributions of bending moment, the effect of cycles around the pile does not appear to be significant as the soil around the pile is not confined or constrained. In this sense, there are differences caused only by the deflection of the beam and the compatibility of displacement fields, causing in this case a lower position of the point of maximum curvature with the number of cycles.

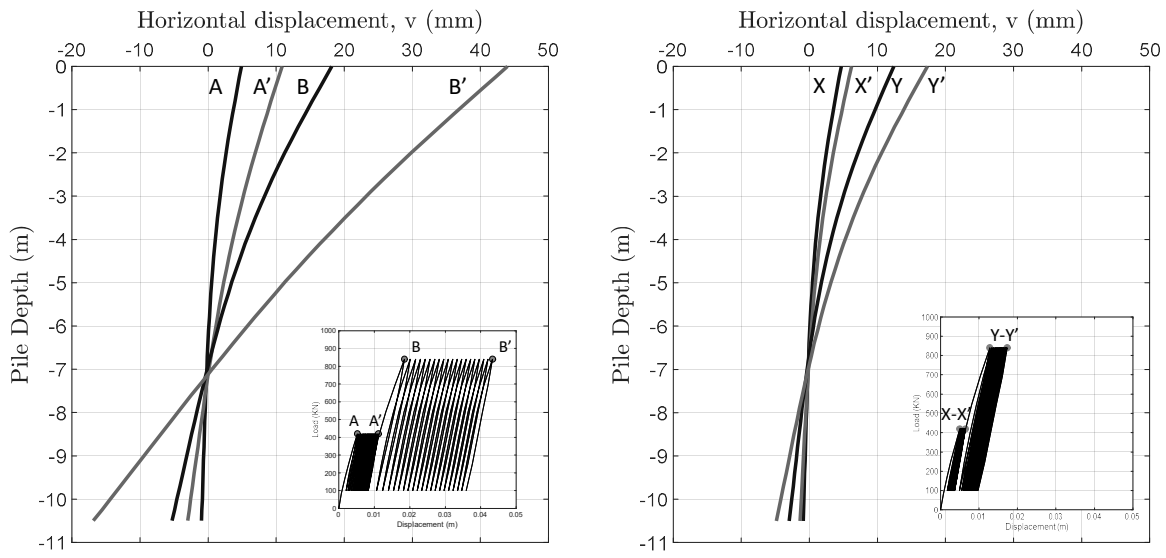


Figure 259: Comparison of deflected shape of Set1 and Set2 predictions at beginning and end of cycle batch

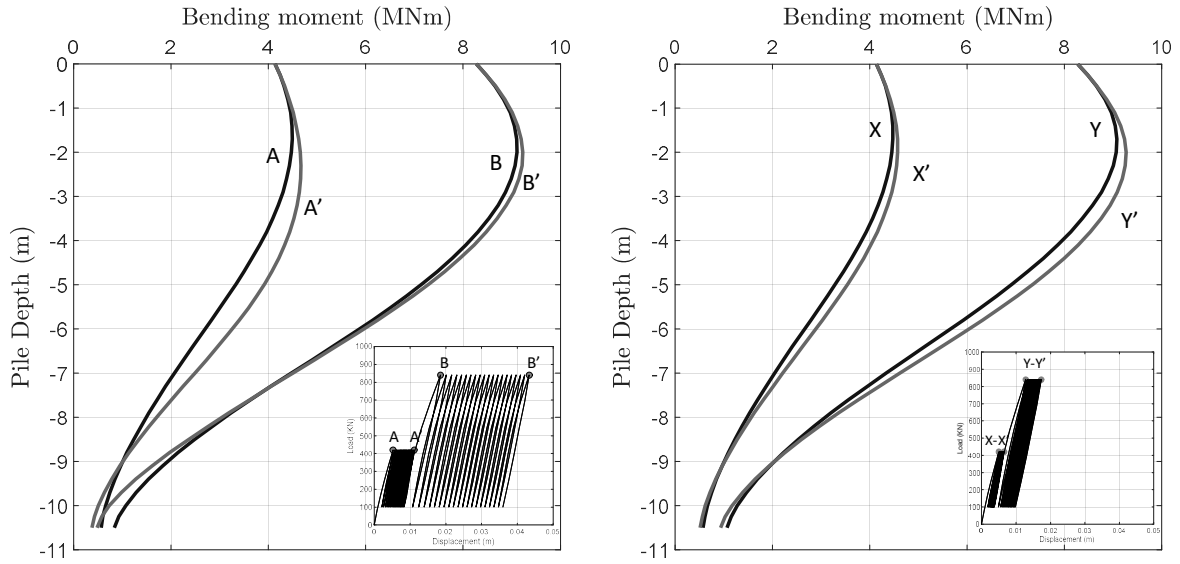
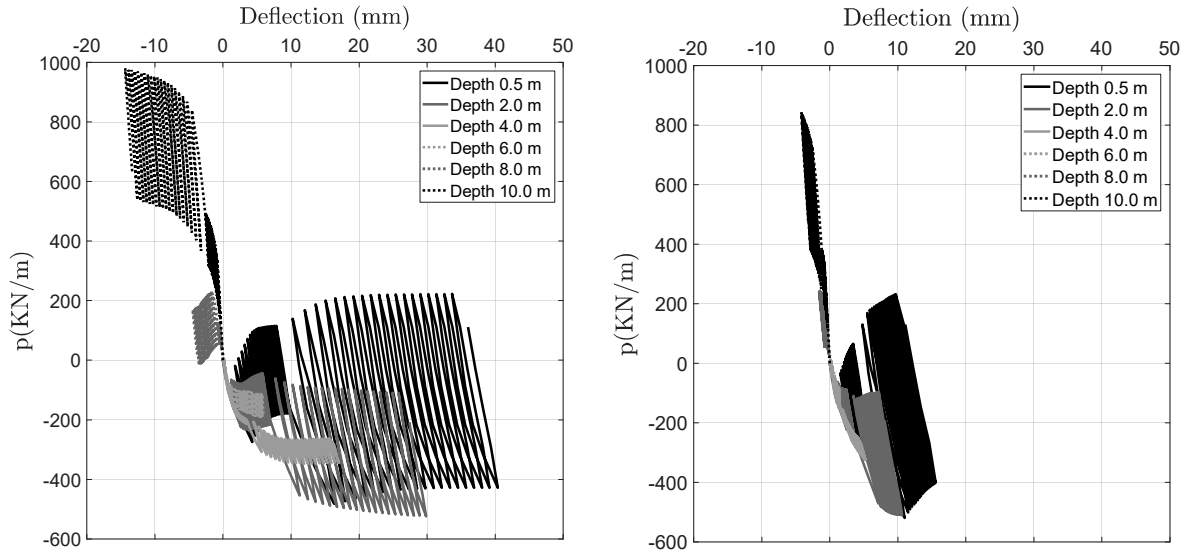


Figure 260: Comparison of bending moments of Set1 and Set2 bending moment predictions at beginning and end of cycle batch

For more structural insight the p-y reactions have been extracted using the same methodology described in the static case. Figure 261 show the obtained p-y reactions at depths of 0.5, 2.0, 4.0, 6.0, 8.0 and 10.0 m and for the simulations carried out using Set 1 and Set 2. The response is similar to the response observed at integration point level where ratchetting is significantly

smaller for the case with variable hardening rules, being for set 1 two times the values obtained for set2.



(Set 1: One hardening rule)

(Set 2: Two hardening rules)

Figure 261: Comparison of equivalent p-y curves for Set1 and Set 2 under operational conditions

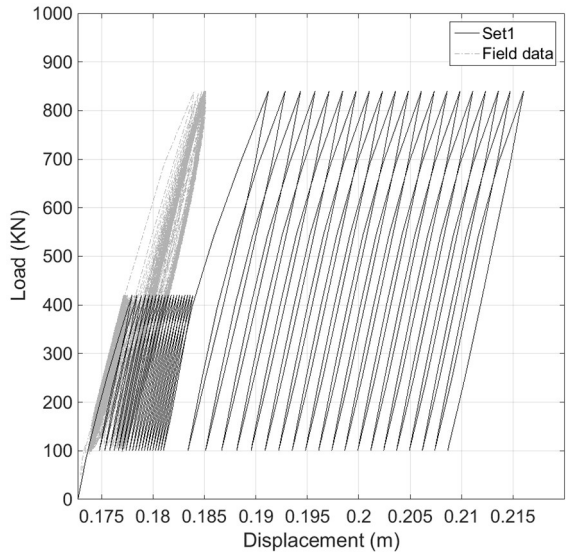
As can be observed in Figure 261, a different type of redistribution of equivalent pressure per cycle occurs. This is because the mode of deflection of the pile is different for each set of parameters (see Figure 259). When only one backstress is used the mode of pile deflection is much more rigid than the mode of deflection predicted by the model with extra hardening rules. This different deflection mode will manifest in a different accumulation of stresses around the pile, where for Set 1 the equivalent pressure at the edges of the pile will increase, while near to the rotation point it will reduce. Conversely for Set 2 the deflection is smaller and the pile is still flexible, in which case the redistribution of stresses around the pile is gentler, with the pressure around the centre of the pile increasing.

5.3.5.6. Parametric study under operational conditions

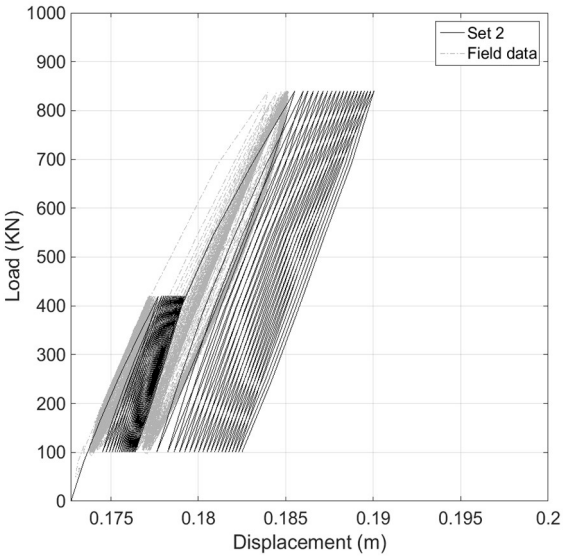
Finally, to study the effect of the input parameters used for backstress superposition, a parametric study employing the same loading conditions as in the field test (Table 34, Stages 1 & 2, 100-420 kN, 100-840 kN) have been carried out for each of the input sets described in Table 36. The results of the simulations are shown in Figure 262(a) to (e). As mentioned in the previous section, it can be seen how the addition of more backstresses reduces the ratchetting and produces a better prediction of the pile under cyclic loading. However, when using the main rule calibrated under static conditions, ratchetting reduces progressively but does not completely shakedown, as the non-linear term of the main hardening rule is not completely cancelled by the other rules. The ratchetting reduction will depend on the amount of stress amplitude that it borrowed from the secondary hardening rule. In this sense, increasing the stiffness or the limit surface of the secondary rule will result in more significant ratchetting reductions. This can be observed in Figure 262 comparing Set 2 and Set 4 predictions. Conversely comparing Set 2 and Set 3 results reveals how the stiffness of the secondary rule also plays a role in the ratchetting reduction, Set 3 being the case with less amount of ratchetting produced, as its overall stiffness with respect to the main rule is higher and its limit surface is very large.

Table 36: Set of input parameters for parametric study of cyclic simulations

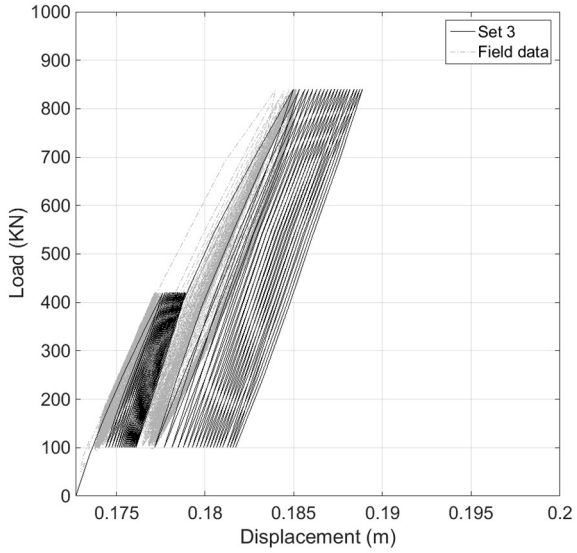
	C	**e_{c0}**	**e_{d0}**	**h_s**	**n**	**α**	**β**	**XV**	**YF**	**ZF**	**θ**	**S_f**	**S_d**	**ob_{min}**	**ob_{max}**	**δ**
Set 1	1.0	0.84	0.50	1E6	0.55	0.08	2	0.59	0.87	0.1	0.53	4.1	1.0	-1.73	0.45	2.25
Set2.1	0.5	0.84	0.50	1E6	0.55	0.08	2	0.59	0.87	0.1	0.53	4.1	1.0	-1.73	0.45	2.25
Set2.2	0.5	-	-	-	-	-	-	0.99	-	-	2.0	4.1	1.0	0.0	0.0	-
Set3.1	0.25	0.84	0.50	1E6	0.55	0.08	2	0.59	0.87	0.1	0.53	4.1	1.0	-1.73	0.45	2.25
Set3.2	0.75	-	-	-	-	-	-	0.99	-	-	2.0	4.1	1.0	0.0	0.0	-
Set4.1	0.5	0.84	0.50	1E6	0.55	0.08	2	0.59	0.87	0.1	0.53	4.1	1.0	-1.73	0.45	2.25
Set4.2	0.5	-	-	-	-	-	-	0.75	-	-	2.0	4.1	1.0	0.0	0.0	-
Set5.1	0.25	0.84	0.50	1E6	0.55	0.08	2	0.59	0.87	0.1	0.53	4.1	1.0	-1.73	0.45	2.25
Set5.2	0.75	-	-	-	-	-	-	0.99	-	-	-	4.1	1.0	0.0	0.0	-
Set5.3	0.2	-	-	-	-	-	-	0.2	-	-	-	12.1	3.0	0.0	0.0	-


Set1
Field data
Load (KN)
Displacement (m)
0
100
200
300
400
500
600
700
800
900
1000
0.175
0.18
0.185
0.19
0.195
0.2
0.205
0.21
0.215

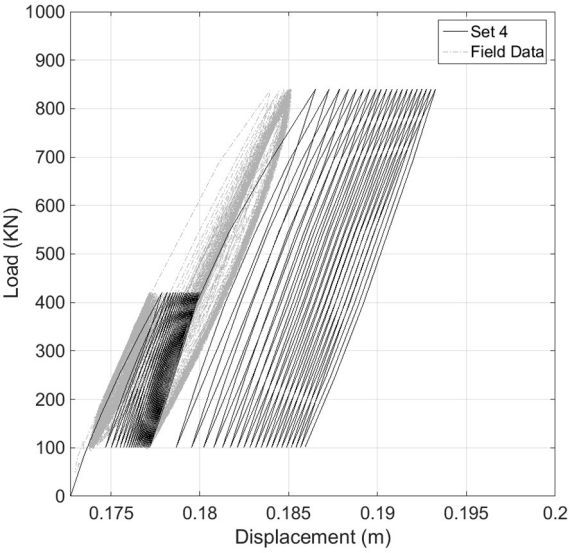
(a)


Set 2
Field data
Load (KN)
Displacement (m)
0
100
200
300
400
500
600
700
800
900
1000
0.175
0.18
0.185
0.19
0.195
0.2

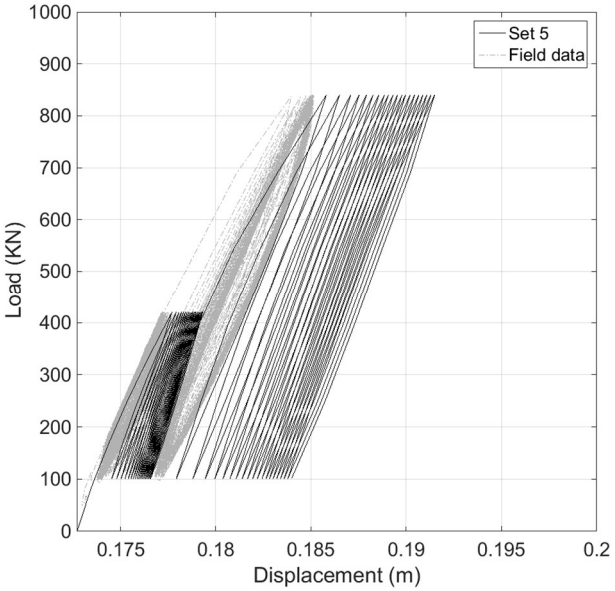
(b)


Set 3
Field data
Load (KN)
Displacement (m)
0
100
200
300
400
500
600
700
800
900
1000
0.175
0.18
0.185
0.19
0.195
0.2

(c)


Set 4
Field Data
Load (KN)
Displacement (m)
0
100
200
300
400
500
600
700
800
900
1000
0.175
0.18
0.185
0.19
0.195
0.2

(d)



(e)

Figure 262: Load displacement curves of parametric 3D FEA analysis, load displacement curve at mudline. (a) Set1, (b) Set 2, (c) Set 3, (d) Set 4, (e) Set 5.

5.4. SUMMARY OF CHAPTER

This chapter has illustrated firstly:

- A simple boundary value problem to benchmark the constitutive model at a local and global level under various initial densities
- A second benchmark using the same mesh and problem to verify the applicability of the advanced features of the basic model described in Chapter 4 (backstress superposition, backstress perturbation)

And secondly:

- The constitutive model developed in this thesis has been used to reproduce with good accuracy the 3D monotonic large-scale PISA field study in Dunkirk dense sand.
- The behaviour of short piles under monotonic and cyclic conditions has been assessed in detail both at soil level and at structural level.

- A method for automatic calibration has been developed and benchmarked for the advanced constitutive model.
- The basic model has been able to capture all features of soil behaviour under monotonic conditions and in terms of energy dissipation and secant stiffness.
- The superposition of backstresses technique has shown to improve ratchetting predictions significantly with respect to the simple model.

CHAPTER 6: CONCLUSIONS AND DISCUSSION

This chapter summarises the conclusions of the thesis and discusses some of the aspects and future possibilities for using NLKH models to reproduce advanced aspects of soil behaviour. The chapter follows a structure akin to that of the thesis, and is divided into three independent blocks, coinciding with the topics covered in this thesis: the theoretical formulation and its extensions, the numerical implementation and computational performance and finally its application to real engineering problems.

From the overall content of the thesis, perhaps the first conclusion that can be drawn is that non-linear kinematic hardening (NLKH) rules framework can be applied generally, to reproduce appropriately the complex aspects of soil behaviour under monotonic and cyclic conditions. This is illustrated throughout the thesis, starting from a general formulation, implementing it in a FE code and applying it to reproduce 3D large-scale field tests carried out during the PISA research project. Secondly, this thesis shows the flexibility of the NLKH formulation, where new and more advanced features are relatively simple to include thanks to its modular formulation (strain metric, limit surface, goal function, mapping tensor, backstress superposition, backstress perturbations). Moreover, an insight on the limit, in the sense of thermodynamic admissibility, has also been studied. In summary, it can be concluded that the proposed formulation opens up new possibilities in terms of constitutive modelling. The study, apart from a formulation standpoint, has also explored numerical integration schemes and computational performance aspects of the problem.

Although literature allegories may perhaps be unsuitable in a scientific document, the author (and perhaps the reader) compares himself to Dante in the 'Divine Comedy', where he begins his trip after *"finding himself within a dark forest, where the straight forward pathway had been lost"* right before entering the gates of the *Inferno* (Chapter 2), then ascending *Mount Purgatory* (Chapters 3 & 4) and finally ending in *Heaven* (Chapter 5), where the framework is finally *redeemed of its sins* and applied to geotechnical problems.

6.1. ON NLKH MODELS FOR SOILS

When starting with the general NLKH formulation, a set of hypotheses were formulated before its final implementation in ICFEP. In this sense no preceding models using a non-linear kinematic Amstrong-Fredrick type formulation applied to soils could be found in the literature. However, hypoplasticity has proven to work in a variety of boundary value problems and, as discussed, several authors point out very similar properties to NLKH. On the other hand, in the context of metals NLKH models are common and have been successfully implemented in general FE models since the 80's.

6.1.1. EARLY DEVELOPMENT

Possibly the cornerstone of this thesis is the fact that the NLKH (Ohno and Wang, 1991) shares formulation aspects of bounding surface plasticity theories share and of stress rate theories such as endochronic models (Bazant, 1978). After all, the non-linear kinematic hardening models proposed here are associated elastoplastic models and it has also been found in the context of geomaterials that hypoplasticity is a limit of elastoplastic models (Einav, 2012). Based on previous findings and owing to the fact that the unification of theories has been carried out successfully in the context of J-plasticity (Erlicher and Point, 2006), nothing indicates that non-linear kinematic rules may not have practical applications for geomaterials.

However, one of the challenges of modelling geomaterials is that, contrary to pressure independent materials, soils exhibit shear-volumetric coupling. Here is where a first challenge appears if traditional approaches such the bounding plasticity theory of Dafalias and Manzari (2004) is used. In this sense the associativity of the yield surface would be sacrificed, losing symmetry and uniqueness of the rate form. This is where the lessons learned from hypoplasticity (Niemunis, 2002) become very handy, in particular, the detailed description of the mathematical form of the pseudo-flow rule (Wu and Niemunis, 1996), which has been reformulated in this thesis (2.3.6) to account for the plastic strain metric. Also, the hypoplastic tensors form (Gudehus, 1996) have been revisited, adopting a more convenient version which employs the general form proposed by Niemunis (2002) (see 2.3.6).

The second doubt that arose about the applicability of the framework was with regard to the size and shape of the yield surface. In this sense hypoplasticity does not have a yield surface and NLKH does. In this respect, the strategy described in Chaboche (2008) was followed, where a yield surface enforcing orthogonality between the relative stress (stress minus backstress) and its rate was a convenient choice thanks to its mathematical implications. The solution for the shape of the yield surface was then clear: a hypersphere. As discussed in section 2.2, thanks to the orthogonality between the relative stress and its rate and the consistency condition, the size of the yield surface does not affect the overall behaviour. In conclusion, the sum of rates of each backstress is the main driver and component of all the models, and the yield surface may be interpreted as a blurred region of valid stress states around the sum of backstresses. Finally, the last doubt to develop the framework was regarding the computational costs of implementing such equations. Therefore, a tool to rapidly benchmark constitutive models was created, with its logic and implementation detailed in section 3.1 to assess the performance before FE implementation. Once well-known advanced models, such as the endochronic models and hypoplastic models such as Masin (2005) or von Wolffersdorff (1996), where implemented and successfully tested as encapsulated models, the framework seemed promising and robust and was further explored in depth.

6.1.2. ON THE GENERAL MATHEMATICAL FORM

Chapter 2 covers in detail the mathematical properties of the general form of NLKH models, with the components divided according to each of its applications similar to Niemunis (2002). In particular, the strain metric has been included in this thesis, akin to the endochronic time, as a gateway for further complex features such as dependencies of the recall term with the plastic strain direction. This general form can be used to include more complex aspects as it shares the structure of the hardening rule which can be recast as a Bouc-Wen model typology (Ismail et al., 2009).

Finally, a difference from hypoplasticity is that instead of using the traditional tensors from von Wolffersdorff (1996) that lead to equivalent goal functions and flow rules, the limit surface and goal functions were formulated in favour of a simpler equivalent expression explicitly which can be easily manipulated. As is shown in Chapter 4, when these tensors and limit surface values are casted in a general stress space, the limit surfaces of hypoplastic models and

the general expressions are practically equivalent. Indeed, the response of standard laboratory tests from the basic models and the encapsulated hypoplastic models are shown to be quite similar, with the most significant differences appearing due to the mapping tensors and the stiffness function f_p, as discussed in 2.3.4.

6.1.3. CONSTITUTIVE MODEL "CONSTRUCTORS"

The term "constructor" is borrowed from the programming language vocabulary, akin to class constructors. Indeed, it can be shown easily that a constitutive model either for sand or clay, using a general form described in Chapter 2, can be formulated completely using a computer-aided program as a constrained optimisation problem. Both versions of basic sand and clay shown in 2.5.1 and 2.5.2 are indeed children of this methodology. To re-illustrate it and assuming coaxiality to be valid between the strain rate, the stress and backstress rate, an ordinary system of equations similar to 2.3.7 can be recast easily as:

$$\Theta(\alpha_i, e) = \frac{\partial \alpha_i}{\partial z} = f_e(e) f_p(\alpha_i) L_{ij}(\alpha_i) \left(\tilde{n}_j^p - f_d(e) Y(\alpha_i) \vec{\Upsilon}_{kl}(\alpha_i) \right) \tag{6.1}$$

Equation 6.1, combined with the void ratio evolution against volumetric strains, becomes a first order ODE with 4 unknowns under monotonic conditions and constant straining. The right hand side of equation 6.1 can be defined as the constructor method of constitutive models and, indeed, it can be coded as such. In this sense, the right hand side of the equation 6.1 can be "constructed" as an object iteratively as part of an optimisation problem. The behaviour of clay, sand or any type of material is then imposed via its constrains and the model is obtained. In this sense, for geomaterials it is only required to impose asymptotic behaviour and critical state conditions when $f_d = 1$. In this sense any choice of asymptotic envelope (such as those shown in Figure 22) is akin to solving:

$$\min \left(\frac{\partial \hat{\alpha}_i}{\partial \alpha_j} \Theta_j(\tilde{n}_j, \alpha_i, e) - f^*(\tilde{n}_j, \alpha_i, e) \right) \quad \textit{subject to} \quad \frac{\partial \hat{\alpha}_i}{\partial \alpha_j} \Theta_j(\alpha_i, e) = 0 \tag{6.2}$$

where f^* is the imposed asymptotic envelope. The second condition corresponds to critical state conditions where:

$$\Theta_j(\tilde{n}_j,\alpha_i,e)=0 \quad subject \quad to \begin{cases} f_d=1 \\ \tilde{n}_1+\tilde{n}_2+\tilde{n}_3=0 \end{cases} \tag{6.3}$$

Equations 6.2 and 6.3 are independent of f_e, and f_p functions, therefore the only term dependent on the void ratio is the f_d function. Given any expression for f_d and a desired asymptotic envelope dependent on the void ratio, the backbone tensors and goal functions of the model can be determined. In this sense the framework adopts a formulation that can use other expressions for f_d such as, for example, the state parameter (Been and Jefferies, 1985). Finally, deriving a model for sand or clay will depend on the extra constrains that are added with respect to equation 6.3 as discussed below and in chapter 2.

6.1.3.1. Clays

This constrains are elegantly detailed in Masin (2013) and no modifications are proposed in this respect. Indeed, the basic clay model uses the idea of Masin for the general formulation. In summary, the constrains to add are: a definition of the Hvorslev pressure, $p_e^*(e)$ and enforcement of

$$\frac{1}{p_e^*}\left(\frac{\partial\dot{\alpha}_i}{\partial z}-\frac{\alpha_i}{p_e^*}\dot{p}_e^*\right)=0 \tag{6.4}$$

plus the hardening rule

$$\dot{p}_e^*=-p_e^*\frac{\dot{\varepsilon}_{kk}^p}{\lambda} \tag{6.5}$$

6.1.3.2. Sands

Compared with clays, to construct models for sands is relatively easier as there are less constrains to enforce. As discussed in 2.5.1, if the expression from Gudehus (1996) for the f_d function is adopted, the value of functions f_b and f_e need to be adjusted to avoid a situation where the rate of f_d is negative for compressive strain paths, as it would produce an unbounded stress path in the deviatoric stress plane. In this sense the constraint for sands is

$$\dot{f}_d > 0 \qquad for \qquad \tilde{n}_1 + \tilde{n}_2 + \tilde{n}_3 < 0 \tag{6.6}$$

As a result, the expressions for f_p and f_e need to be adjusted to comply with 2.5.1. Examples of this can be verified with the formulation proposed in 2.5.1, the solution is non-unique.

6.1.4. COMPARISON WITH CURRENT HYPOPLASTIC MODELS

Section 2.5.2 and 2.5.4 present a comparison of the mathematical structure of encapsulated hypoplastic models against the basic forms of the general hardening rule for sand and clay. Its comparison is carried out for standard monotonic tests and small strain perturbations, following a methodology similar to that outlined in Gudehus and Mašín (2009). The following conclusions have been drawn from this study:

- Both Basic models proposed in this research capture general features of the hypoplastic sand and clay models for conventional monotonic soil tests and asymptotic strain tests;
- Considerable similarities between the limit surfaces and goal functions of basic models and their hypoplastic counterparts exist, although they originate from different mathematical expressions;
- The differences between models occur at a local scale: the mapping tensors induce a different local stiffness response, where the proposed mapping tensor ignores the right mapping of $\hat{\alpha}_{kl}^{*}$ with deviatoric strain directions; additionally, stiffness functions f_p exhibit differences that manifest themselves in a larger size of the mapping upon a strain perturbation for the same CSL;

- The strain metric or the endochronic time “z” of the general form has not been used in this comparative exercise, however it can bring significant improvements as it includes a dependency of the stiffness on the strain direction.

6.1.5. ON THE BIPOTENTIAL

As discussed in 2.4 these plasticity models can be formulated using the bipotential approach. The crux of the bipotential comes from the fact that Fenchel's inequality generalises Hill's maximum power principle, which can lead to an alternative formulation based on a generalisation of Fenchel's inequality and the concept of bipotential (de Saxce and Feng, 1991, de Saxce, 1992). The models originating from this modelling framework are therefore called *implicit standard*, where both sets of thermodynamic forces and flows are formulated implicitly in the same potential named “bipotential”. Let us summarize the idea briefly, because the Fenchel-transform is defined as:

$$\chi(\pi) = \sup\left\{\pi : \dot{\kappa} - \varphi(\dot{\kappa}); \dot{\kappa} \in V\right\} \tag{6.7}$$

which is equivalent to:

$$\forall \dot{\kappa}' \in V \quad \forall \pi' \in F, \quad \varphi(\dot{\kappa}') + \chi(\pi') \geq \dot{\kappa}' : \pi' \tag{6.8}$$

Potentials may not differentiable, but are sub-differentiable, therefore when the couples are extremal, they are related by a *“sub-normality rule”* and are otherwise related by *“sub-differentials”*. This is possibly not the best naming as the adjective to use for this type of models would be “subnormal”, nevertheless they are called *“implicit standard materials”*. To illustrate this with an equation, given the form (6.8) the *standard materials* follow:

$$\varphi(\dot{\kappa}) + \chi(\pi) = \pi : \dot{\kappa} \Leftrightarrow \pi \in \partial\varphi(\dot{\kappa}) \Leftrightarrow \dot{\kappa} \in \partial\chi(\pi) \tag{6.9}$$

Now a bipotential contains the previous both potentials an can be implied that:

$$b(\dot{\kappa}, \pi) = \pi : \dot{\kappa} \Leftrightarrow \pi \in \partial b(\dot{\kappa}, \pi) \Leftrightarrow \dot{\kappa} \in \partial b(\dot{\kappa}, \pi) \tag{6.10}$$

On the other hand. a material formulated by (6.10) is an *implicit standard material*. Thanks to the definition of the bipotential, (1.22) can be recast as:

$$\forall\, \dot{\kappa} \in V \quad \forall\, \pi \in F, \quad b(\dot{\kappa}, \pi) - \dot{\kappa} : \pi \geq 0 \tag{6.11}$$

and as the dissipation is, $\dot{\kappa} : \pi$, and the second principle of thermodynamics (Clausius-Duhem) cannot be violated, $\dot{\kappa} : \pi > 0$, by construction, any proposed bipotential must be greater than zero $b(\dot{\kappa}, \pi) > 0$, as pointed out in 2.4, corresponding therefore to the limit of its thermodynamic admissibility. Finally, the whole constitutive model, relating flows and thermodynamic forces, can be obtained via minimisation, as described in 2.4.

6.2. ON MODEL EVALUATION AND EXTENSIONS

Chapter 4 is the most heterogeneous chapter of the thesis, as it has been split into two topics, including the formulation and implementation. In this sense, the discussion included here covers the former. In particular, its comparison with other hypoplastic models is discussed, together with the proposed extensions of specialised hardening rules and possible improvements based on the Karlsruhe sand calibration benchmark.

6.2.1. ON THE SPECIALISED HARDENING RULES

Using the idea of backstress superposition (Chaboche, 1991) the ratchetting prediction under non-symmetric stress conditions can be improved. In this sense, the effect of adding more backstresses reduces the excessive ratchetting produced by a simple hardening rule and its effects are shown in 2.3.10, in 5.1.4.4 and 5.3.5, applied to various 2D and 3D boundary value problems. However, using fully defined hardening rules makes the calibration process very tedious as all the kinematic hardening rules are inter-related in the deviatoric and isotropic space. The ratchetting is dominated by the non-linear recall term and the asymptotic conditions are well captured by a single hardening rule. Therefore, it is a much more promising strategy to specialise some hardening rules to act as penalties in the principal recall term of the main rule locally, rather than superimposing various main rules. Results shown here illustrate that a main rule is sufficient to capture the monotonic behaviour and large stress amplitudes and thus the improvements are more suitable for enhancing its cyclic performance. Moreover, as ratchetting reduction or shakedown can be achieved when the sum of all recall terms cancel out (see 2.3.9) and this phenomenon typically occurs in soils for small to medium load amplitudes, this is a simpler and more promising approach.

The three hardening rules presented are examples of this type of strategy, showing the framework flexibility in terms of the formulation. Additional backstresses or backstrains can be used as history variables to define stress or strain regions with specialised behaviour. Section 4.3 presented the three examples of specialised hardening rules with the objective of improving the response of the basic models. Section 4.3.3 showed how to include the intergranular strain concept (Niemunis and Herle, 1997) using the formulation of non-hardening strain regions (Ohno, 1982). Section 4.3.1 presents a densification rule to avoid the deficiencies in concavity and excessive ratchetting predicted in compressive tests under cyclic conditions. Finally, a third rule acting in the deviatoric plane is shown in 4.3.2 which acts locally on the goal functions of the main rule, with the objective of improving the response with respect to the amount and direction of ratchetting for small to medium amplitudes.

Each rule can be combined with the main rule and with each other as they vanish in their limit surfaces and the main original rule is recast again. Additionally, these extra rules can be switched on or off, depending on the strain direction or the history variables. The effect of this specialised rules, in particular the “densification rule” and the “intergranular strain”, have been tested in the calibration of the Karlsruhe sand database, improving the predictions obtained using a single hardening rule. However, due to time limitations the whole database has not been validated.

6.2.2. ON THE CALIBRATION FOR KARLSRUHE SAND

The Karlsruhe sand database is available online and comprises a large database of laboratory tests under static and cyclic conditions. This database has been chosen for its large number of tests and its variety of loading conditions. Not all of the tests in the database have been used in the calibration of the constitutive model but have helped in the development of new model features. Nevertheless, all the monotonic and cyclic isotropic, oedometric and strain controlled undrained triaxial tests have been used in the calibration, making a total of 82 tests. Regarding this, the main conclusions obtained are:

- In general, the constitutive model is capable of reproducing complex soil behaviour in monotonic conditions for a wide range of confining stresses and void ratios using only one hardening rule

- The densification rule improves significantly the loading/unloading simulations under isotropic and oedometric conditions, reproducing the cyclic soil behaviour. The cycles exhibit the correct concavity and the ratchetting per cycle reduction and densification is well captured.
- With respect to stiffness in isotropic and oedometric tests, improvements in the definition of the function f_p can be applied to accommodate the stiffness evolution to the asymptotic states in oedometric conditions. However, as the lateral stress in a standard oedometer is unknown, it would become a trial and error process. Nevertheless, the model response is slightly stiffer in oedometric conditions and it could be adjusted by reducing the contribution of the terms that modify equation (2.136)
- The model predicts a good response in general shear conditions for both drained and undrained tests, capturing appropriately the shear-volumetric coupling in dense sands. A possible improvement to the model can be the addition of a dependency on the shape factor of the mapping tensor using the Lode's angle as discussed in 4.2.1.3
- A single hardening rule is capable of reproducing undrained strain cyclic conditions for mid to large amplitudes and also small amplitudes with the intergranular strain specialised rule. It can exhibit the typical butterfly-shaped loops, nevertheless the goal function and limit function were slightly modified as some stress paths seemed to stabilise too early, not reproducing the measured mean effective stress reduction in the tests. In this sense not all calibrations and parameter sets can reproduce this full liquefaction behaviour.
- The intergranular strain rule was used to improve the prediction of the main hardening rule under strain-controlled cycles and under small amplitudes. It can be inferred that the same responses as in Niemunis and Herle (1997) are obtained, and in this sense the idea behind this specialised hardening rule is not new. However, in terms of implementation it shows that hypoplastic advanced features can also be encapsulated and they work accordingly.
- With respect of the intergranular strain it must be said that it reduces ratchetting, creating a severe penalty in the recall term when the backstrain lies inside the strain surface. As a consequence, the correct concavity in the p' space cannot be captured.
- The rest of the cyclic tests have not been used in the current calibrations and have been left for future study. Preliminary analyses have shown good performance but are not included.

6.3. ON THE NUMERICAL INTEGRATION AND IMPLEMENTATION

This section covers the conclusions reached during the numerical study presented in Chapter 3 and also discusses the FE implementation and "numerical artifices" developed during this thesis.

6.3.1. ON THE CONSTITUTIVE DRIVER

Due to the large number of possible combinations of NLKH rules and their future implementation in ICFEP, it was decided to develop a numerical tool to assess the response of this types of models. The logic of an object-oriented constrained constitutive driver (Bardet and Choucair, 1991) was adopted and is described in 3.1. The constitutive driver can deploy a new constitutive model within hours and benchmark it following the original idea described in Kolymbas (1991a).

The modularity of its object-oriented logic has also been used to calibrate parameter sets from laboratory data, providing good results as is detailed in 5.3.2. Many of the numerical analyses shown here have been carried out with this tool, with examples including the Karlsruhe sand database calibration and all the numerical study shown in Chapter 3. Without this tool this thesis would have never been possible. No controllability analysis (Buscarnera et al., 2011) on the constrains imposed have been studied as it was out of the scope of the thesis.

6.3.2. ON THE NUMERICAL INTEGRATION

Chapter 3 is fully devoted to the numerical integration of NLKH rules, studying both strategies for implicit and for explicit integration. With respect to implicit integration, it explores the precision of several discretisations and uses an augmented variational formulation of the CPPM (Armero and Perez-Foguet, 2002) for global convergence and better numerical performance. Two complete numerical studies for two types of NLKH are carried out. The complete numerical pack is carried out for both models: isoerror map, global convergence, convergence rate and computational performance. The numerical stability has not been included and has been left for future study. In summary, the conclusions are:

- A better response in terms of precision and performance is achieved when the normal of the yield surface is evaluated at the end of the step (semi-implicit);
- The consistency condition cannot be fulfilled at the mid and end of the step. In this sense the strategy of Popov is preferable. This does not affect the precision of the overall integration, as discussed in 2.2, as evaluating the plastic strain at the end is closer to the analytical solution. In summary, the order of the approximation depends on where the backstress is evaluated rather than the normal;
- Evaluating the normal at the end of the step leads to a reduced system of equations where the stress unknown can be excluded of the system, which reduces the dimension of the system to solve;
- The implicit discretisation exhibiting higher precision in all isoerror maps and both models tested corresponds to the semi-implicit MID1, in line with Chaboche and Cailletaud (1996);
- The substepping algorithm, despite providing good accuracy and having an easy implementation, becomes computationally costly requiring in addition to the Euler forward evaluations a significant number of drift corrections as the yield surface has high curvature, as discussed in sections 3.4.6 and 3.5.3;
- With respect to the rate of convergence, the standard CPPM algorithm fails to provide global convergence. This is due to the fact that elastic predictors are very far from the solution, not converging or exhibiting a poor rate of convergence when trying to "return" (see 3.3.5 and 3.4.4)

- The aug-CPPM shows global convergence for all models, and its performance depends on the penalty term “c” (see 3.3.5). However, the penalty term seems not to vary from model to model, possibly being dependent on the stiffness of the elastic part. In general, the algorithm exhibits quadratic rate of convergence since the first iteration for all strain directions and strain magnitudes and provided significantly better performance from all the studied solvers (3.5.3).
- Of the three-numerical performance benchmarks carried out, only for small steps and very strict precisions the sub-stepping exhibits better precision than implicit methods.

One of the advantages of explicit over implicit methods is that they do not require second derivatives to integrate the equations and therefore their implementation becomes simpler. Because the derivatives of the goal functions and mapping tensors can be cumbersome (see 3.3.2 and 3.4.2) explicit strategies seem, at first, a more convenient choice. However, section 3.5.2 explores the precision of numerical derivatives versus the analytical ones using the methodology described in Perez-Foguet et al. (2000a), the findings in that respect are:

- The rate of convergence of the aug-CPPM it is not significantly affected if the derivatives are computed numerically with a central scheme or analytically;
- When the integration methods are tested in section 3.5.3 it is found that even with numerical derivatives the numerical efficiency of the semi-implicit MID1 model with aug-CPPM is superior to that of the explicit substep algorithm.
- Considering the previous, the implicit integration strategy with an augmented variational formulation seems the best strategy to integrate this type of rule, owing to the fact that the explicit methods require many small steps and the curvature of the yield surface produces a severe overhead in the drift correction. Additionally, due to the fact that these models admit a bipotential and can be formulated as minimization problems, they open the door to new variational principles and second order programming techniques such as described in Krabbenhøft (2009), this has been left for future study.

6.3.3. ON THE IMPLEMENTATION IN A FE CODE

The finite element implementation of the basic sand model with a set of superimposed rules (five rules) and the safety factor backstress perturbation has been implemented in ICFEP and tested for various boundary value problems, as described in Chapter 5. Amongst these there are boundary value problems involving medium-scale pile tests under cyclic loading performed in the PISA project, which correspond to the last aim of this research.

Regarding ICFEP implementation, contrary to commercial FE packages, the local integration in ICFEP does not use a unique external subroutine with a strain-stress integrator. Instead, it requires several subroutines amongst which the rates of the constitutive relations are required as the local integration is carried out explicitly. In this sense, it was not possible to deploy within ICFEP the constitutive driver and the model was hardcoded again in FORTRAN, ensuring consistency with the architecture of ICFEP. During this process the output of the subroutines and the local integration driver developed for this thesis were compared to assist during its implementation. Nevertheless, the following challenges appeared and were corrected for the explicit integration of this type of models in ICFEP when applied to boundary value problems. The problems encountered were:

- The substepping algorithm uses the forward Euler prediction of the gradients to build the increment. As a result, if the step is not small, this second evaluation will not fulfil the consistency condition (by quite a lot) evaluating the model in forbidden regions, where the rule is undetermined. In this sense during this second evaluations error handling of the forward predictions needed to be handled systematically within the integration subroutines.
- The nature of the model is asymptotic, therefore when the trace of the strain path is positive the zero mean stress corresponds to an attractor. A value of zero mean stress is not computationally acceptable, therefore a small positive backstress cut off was added in the neighbourhood of zero mean effective stress, acting on the hardening rule. In the imposed limit, the hardening rules become deviatoric and can recover their original formulation once the strain path becomes compressive, as discussed in 4.5.1. In this sense this strategy prevents the stress state to reach zero or cross the imposed threshold

marked by the backstress limit and the yield surface, and therefore no extra yield surfaces where required.

6.3.4. ON BACKSTRESS PERTURBATIONS

Sections 4.3.2 and 4.3.3 show two numerical artifices to enforce a perturbation of the backstress while enforcing consistency in the yield surface. Both methods recover the idea presented in Potts and Zdravkovic (2012), which can be integrated in an explicit solver, or more naturally implicitly. The interpretation of the backstress perturbation is similar to creep, in this sense the idea behind the High-Cycle Accumulation model can be recast as a backstress perturbation. As discussed in 2.3.6, a perturbation of the backstress is biunivocaly related to plastic strain. Therefore, the magnitude of numerical creep and its direction resulting from a backstress perturbation will be a function of the non-linear recall term. An example of this type of response can be observed when interrogating the Gauss points in the example shown in 5.1.4.3.

Example 5.1.4 shows that this modelling framework can accommodate a jump-in-cycles method such as that described in the hypoplastic high-cycle accumulation model (Niemunis et al., 2005). After all, in this thesis it has been illustrated that all hypoplastic features can be integrated in NLKH, so this extra capability is not surprising. Finally, instead of enforcing the jump-in-cycles from laboratory data in a semi-empirical way as in the HCA model, the possibility of obtaining a method for real numerical jump-in-cycles is investigated in 4.3.3. This is done using the favourable semi-implicit discretisation and the properties described in 2.3.9 to estimate the backstress perturbation under large number of cycles.

A recursive method using the semi-implicit MID1 discretisation proves to be the most efficient methodology of the tested discretisations to estimate the effect of the cycle batch jump. In particular, the benchmarked tests show that batches of 100 cycles of small amplitude or batches of 10 cycles of medium amplitudes can be captured using the recursion method without inducing excessive error, thus saving computational resources. It must be pointed out that the accuracy of the method is related to the accuracy of the discretisation in which the backstress is evaluated, in this particular case MID1 has second order.

6.4. ON THE APPLICATION OF THE MODEL

This section discusses the model response when applied to boundary value problems.

6.4.1. ON THE VERIFICATION OF THE CONSTITUTIVE MODEL

The basic sand model with five superimposed rules was tested systematically to verify that all its components were properly implemented. Section 5.1 presents a rigid footing, with inputs used in previous numerical benchmarks, as a reference boundary value problem. At this stage many of the issues and corrections described in 4.5.1 where carried out. In general, all the features of the constitutive model where tested and verified, providing the expected results, in particular:

- The asymptotic properties of the model are evaluated where various sand densities of sand can be accounted for realistically under monotonic conditions (see 5.1.2)
- The backstress perturbation works as expected, introducing a gateway for introducing numerical creep and semi-empirical Jump-in-Cycles methods (see 5.1.4)
- The effect of adding new backstresses is shown, where a significant reduction of ratchetting can be observed as a consequence of the new degrees of freedom imposed by the extra hardening rules. This is achieved using a simple superposition of rules without using the specialised hardening rules described in Chapter 4 (see 5.1.4.4)
- The five superimposed rules can work together without producing numerical errors, nevertheless, as discussed in 5.1.5.2, the model calibration can become cumbersome.

6.4.2. ON THE CALIBRATION FOR DUNKIRK SAND

The methodology for Dunkirk sand calibration is detailed in section (5.2.2), where some of the available monotonic laboratory tests were used. Due to the absence of other types of tests such, as undrained triaxial tests or oedometric tests, the shape of the asymptotic envelope was not known with certainty.

A methodology for computer-aided calibration was explored, in addition to manual calibration that was performed and applied to the analysis of laterally loaded piles. The manual calibration of the model produced good predictions of pile tests, however, the shape of the asymptotic envelope was assumed, and a parametric study was required to assess its effect in the overall

response of the pile. Because the constitutive driver was object oriented, it was relatively easy to group the subroutines as described in 3.1 and feed them into a genetic algorithm optimisation solver. In this sense, at the same time that the effect of the asymptotic envelope was studied, an exercise to study the performance of computer-aided calibration of constitutive models was also undertaken. After adding the constrains to the problem and running it in less than an hour the algorithm had provided 10 optimal possible sets, 6 of which looked satisfactory where one was similar to the manual calibration. It must be said that the manual calibration took slightly more than a day. The tool proved extremely practical to obtain calibrated sets of parameters and the new sets where later tested in the boundary value problem improved some of the predictions of the boundary value problem (see 5.3.2), nevertheless it must be said that the manual calibration was already a good estimate for the four piles.

6.4.3. ON THE 3D MODELLING OF THE PISA PILES

The four pile geometries representative of the field tests carried out during the PISA project at Dunkirk site have been simulated with the basic sand model. Model predictions were shown to be in good agreement for three of the four modelled piles, while for the shortest pile the capacity was overpredicted. The shortest pile is completely embedded in the upper dense layer of hydraulic fill, for which less information on soil behaviour was available (see 5.2.2.2). In this sense it is possible that the initial void ratios or initial stress conditions for that layer do not correspond to the real ground conditions, however the ground conditions assumed correspond to the best estimate at this stage.

The soil response, the FE model and the pile behaviour are described in detail in (5.2.2), where the most relevant aspect is the modelling of the pile-soil interface, which are extended below the pile to be compatible with the rigid mode of rotation. All the FE simulations follow the methodology described in Zdravkovic et al. (2015) and details of the soil response around the large diameter monopile (DL2) are presented in 5.3, where the main conclusions are:

- Mode of deflection becomes rigid at early loading stages, shear mobilisation starts to develop around 20 % of pile capacity;
- The pile reaches failure before soil reaches critical state conditions;

- The dominating strength in the deviatoric plane corresponds to a Lode's angle of 30 degrees akin to TXC conditions, except around the base of the pile where a Lode's angle of around zero is observed;
- The pile behaves like a lever, as large stress concentrations are obtained in the levering point and the bottom of the pile is counter-reacting the rotation mechanism, see failure mechanism detailed in 5.3.4.1;
- The void ratio evolution shows an early densification of the sand around the pile in the upper passive side due to the pile pushing the ground, however as the load increases the behaviour becomes dilative and soil expands, indicating a strong shear-volumetric mechanism due to the high relative density of the sand (see 5.3.3.5);
- A gap in the upper active side of the pile starts to develop at around 20 % of pile capacity and subsequently another gap is developed in the lower active wedge as well;
- Section 5.3.3.7 compares the numerical predictions with measured responses of the piles at two stages of field tests, representative of initial and ultimate conditions. The numerical results seem to slightly underpredict the overall stiffness of the soil at the initial stages compared to field measurements, where the measured deflected shape in the field tests is more flexible;
- The rotation points and deflected shapes for mid to high loading stages are well captured.

6.4.4. ON THE STRUCTURAL RESPONSE OF SHORT LATERALLY-LOADED PILES

Sections 5.3.3.6, 5.3.4.2 and 5.3.5.5 describe the overall structural response of all the simulated piles. The normalised deflected shapes show an initial more flexible mode of deformation in all early stages of loading, which rapidly transits to a rigid mode of deformation, as shown in 5.3.4.2. Section 5.3.4.3 illustrates a simple methodology to incorporate the FE reaction as part of a simple 1D structural model, where it can be observed that the p-y reactions in sand do not reach ultimate capacity, supporting what is observed in the soil around the pile, where the soil has not reach critical state condition but the pile is in ultimate design conditions (0.1D displacement at mudline).

6.4.5. ON THE CYCLIC RESPONSE

Section 5.3.5 illustrates the model response when applied to the large diameter monopile (DL2) under cyclic conditions. Two types of numerical analysis are carried out: a first one involving larger amplitudes and a small number of cycles and a second one with small to mid-amplitudes for a larger number of cycles. In both analysis types the effect of adding extra hardening rules is illustrated, which shows how the ratchetting prediction improves significantly when compared to field predictions.

6.4.5.1. Soil response around the pile

In general, a simple hardening rule is capable of reproducing cyclic behaviour for medium to large amplitudes, as can be observed in 5.3.5.3. In this respect the concavity of the loop and the unloading reloading stiffness is well accounted for. Even for large amplitudes in dense conditions a single hardening rule can account for ratchetting acceleration as a result of the large amplitudes, while the dilative nature of the model will reduce the soil strength as a consequence of the void ratio increase, leading to ratchetting acceleration. However, one hardening rule exhibits the drawbacks of any hypoplastic model where for low to mid-amplitude cycles the ratchetting prediction becomes excessive.

The limitation of using only a hardening rule can be corrected using a superposition of hardening rules. Results from this thesis show that through simple superposition, without specialised rules, the cyclic response of the pile can also be improved without the need of severe alterations on the parameters of the main hardening rule. In this sense, the example shows how by adding a second hardening rule with a large linear region reduces significantly the calculated ratchetting (see 5.3.5.2). This can be done as a laterally loaded pile is a problem mainly controlled by the stress and is not strongly constrained (the strain is free and not imposed). In this case the addition of a second rule produces a significant ratchetting reduction, as the main hardening rule can be accommodated in a more stabilised region, reducing the amount of ratchetting it produces (as discussed in 5.1.5.1).

To illustrate this, a detail of the stresses around the pile is shown in 5.3.5.4, where the impact of adding this extra hardening rule can be observed at a local scale in active and passive points of the pile. The addition of extra hardening rules will produce less stress relaxation or less ratchetting. However, as the trace of the goal function of the main hardening is not zero,

complete shakedown conditions cannot be achieved, as discussed in 5.3.5.4 since there is always a term that will enforce densification.

6.4.5.2. Structural response

Section 5.3.5 describes the structural implications of adding extra backstress rules. The response is like what is observed at a local level in the soil, and as a result that ratchetting reduction also manifests itself in the structural behaviour of the monopile. It can be confirmed that a laterally loaded monopile is a stress dominated problem as differences between the two versions of the model appear in the deflected shapes rather than in the moment distributions, as observed in 5.3.5.5. In this sense, the addition of extra hardening rules will have an impact on the displacements and deflections rather than on the forces and pressure distributions around the pile, providing the desired effect as observed in the field tests.

CHAPTER 7: REFERENCES

ANDERSEN, K. H. & LAURITZSEN, R. (1988) Bearing capacity for foundations with cyclic loads. *Journal of Geotechnical Engineering-Asce,* 114, 540-555.

ARMERO, F. & PEREZ-FOGUET, A. (2002) On the formulation of closest-point projection algorithms in elastoplasticity - part I: The variational structure. *International Journal for Numerical Methods in Engineering,* 53, 297-329.

ARMSTRONG, P. J. & FREDERICK, C. (1966) *A mathematical representation of the multiaxial Bauschinger effect*, Central Electricity Generating Board [and] Berkeley Nuclear Laboratories, Research & Development Department Berkeley.

AWG (2015) Field Test Factual Report, Report No. 2260925, PISA AWG

BARDET, J. & CHOUCAIR, W. (1991) A linearized integration technique for incremental constitutive equations. *International Journal for Numerical and Analytical Methods in Geomechanics,* 15, 1-19.

BATISTA, D., ROYIS, P. & DOANH, T. (2003) Time-integration of a hypoplastic constitutive equation in finite element modelling. *Mathematical and Computer Modelling,* 37, 615-621.

BAUER, E. (1996) Calibration of a comprehensive hypoplastic model for granular materials. *Soils and Foundations,* 36, 13-26.

BAZANT, Z. P. (1978) Endochronic inelasticity and incremental plasticity. *International Journal of Solids and Structures,* 14, 691-714.

BAŽANT, Z. P., KRIZEK, R. J. & SHIEH, C. L. (1985) Hysteretic endochronic theory for sand. *Journal of Engineering Mechanics,* 111, 106-108.

BEEN, K. & JEFFERIES, M. G. (1985) A state parameter for sands. *Géotechnique,* 35, 99-112.

BUSCARNERA, G., DATTOLA, G. & DI PRISCO, C. (2011) Controllability, uniqueness and existence of the incremental response: a mathematical criterion for elastoplastic constitutive rules. *International Journal of Solids and Structures,* 48, 1867-1878.

BUTTERFIELD, R. (1979) A natural compression rule for soils (an advance on e-log p'). *Geotechnique,* 29, 469-479.

CHABOCHE, J.-L. (1991) On some modifications of kinematic hardening to improve the description of ratchetting effects. *International journal of plasticity,* 7, 661-678.

CHABOCHE, J. & CAILLETAUD, G. (1996) Integration methods for complex plastic constitutive equations. *Computer methods in applied mechanics and engineering,* 133, 125-155.

CHABOCHE, J., VAN, K. D. & CORDIER, G. Modelization of the strain memory effect on the cyclic hardening of 316 stainless steel. SMiRT 5 1979 Berlin. SMIRT 5.

CHABOCHE, J. L. (2008) A review of some plasticity and viscoplasticity constitutive theories. *International Journal of Plasticity,* 24, 1642-1693.

CHAMBON, R., DESRUES, J., HAMMAD, W. & CHARLIER, R. (1994) CLOE, a new rate-type constitutive model for geomaterials: theoretical basis and implementation. *International Journal for Numerical and Analytical Methods in Geomechanics,* 18, 253-278.

CHANG, C. S. & WHITMAN, R. V. (1988) Drained permanent deformation of sand due to cyclic loading. *Journal of geotechnical engineering,* 114, 1164-1180.

CHENG, L., JIA, Y., OUESLATI, A., DE SAXCÉ, G. & KONDO, D. (2015) A bipotential-based limit analysis and homogenization of ductile porous materials with non-associated Drucker–Prager matrix. *Journal of the Mechanics and Physics of Solids,* 77, 1-26.

CHU, J. & LO, S. C. R. (1994) Asymptotic behaviour of a granular soil in strain path testing. *Geotechnique,* 44, 65-82.

COLLINS, I. & HOULSBY, G. (1997) Application of thermomechanical principles to the modelling of geotechnical materials. *Proceedings of the Royal Society of London. Series A: Mathematical, Physical and Engineering Sciences,* 453, 1975-2001.

CONN, A. R., GOULD, N. I. & TOINT, P. (1991) A globally convergent augmented Lagrangian algorithm for optimization with general constraints and simple bounds. *SIAM Journal on Numerical Analysis,* 28, 545-572.

CONN, A. R., GOULD, N. I. M., ORBAN, D. & TOINT, P. L. (2000) A primal-dual trust-region algorithm for non-convex nonlinear programming. *Mathematical Programming,* 87, 215-249.

CORCIULO, S., ZANOLI, O. & PISANÒ, F. (2017) Transient response of offshore wind turbines on monopiles in sand: role of cyclic hydro–mechanical soil behaviour. *Computers and Geotechnics,* 83, 221-238.

DAFALIAS, Y. & POPOV, E. (1976) Plastic internal variables formalism of cyclic plasticity. *Journal of applied mechanics,* 43, 645-651.

DAFALIAS, Y. F. (1986) Bounding surface plasticity 1: Mathematical foundation and hypoplasticity. *Journal of Engineering Mechanics-Asce,* 112, 966-987.

DAFALIAS, Y. F. & MANZARI, M. T. (2004) Simple plasticity sand model accounting for fabric change effects. *Journal of Engineering Mechanics-Asce,* 130, 622-634.

DAY, R. A. & POTTS, D. M. (1994) Zero thickness interface elements - numerical stability and application. *International Journal for Numerical and Analytical Methods in Geomechanics,* 18, 689-708.

DE SAXCE, G. (1992) A generalization of fenchels inequality and its application to constitutive rules. *Comptes rendus de l'Académie des sciences. Série 2, Mécanique, Physique, Chimie, Sciences de l'univers, Sciences de la Terre,* 314, 125-129.

DE SAXCE, G. & BOUSSHINE, L. (2002) Implicit standard materials. *In:* WEICHERT, D. & MAIER, G. (eds.) *Inelastic Behaviour of Structures under Variable Repeated Loads: Direct Analysis Methods.*

DE SAXCE, G. & FENG, Z. Q. (1991) New inequality and functional for contact with friction - the implicit standard material approach. *Mechanics of Structures and Machines,* 19, 301-325.

DE SOUZA NETO, E. A. (2004) On general isotropic tensor functions of one tensor. *International Journal for Numerical Methods in Engineering,* 61, 880-895.

DE SOUZA NETO, E. A., PERIC, D. & OWEN, D. R. J. (2008) *Computational methods for plasticity: theory and applications,* Chichester, John Wiley & Sons.

DELOBELLE, P., ROBINET, P. & BOCHER, L. (1995) Experimental study and phenomenological modelization of ratchet under uniaxial and biaxial loading on an austenitic stainless-steel. *International Journal of Plasticity,* 11, 295-330.

EINAV, I. (2012) The unification of hypo-plastic and elasto-plastic theories. *International Journal of Solids and Structures,* 49, 1305-1315.

EINAV, I., PUZRIN, A. & HOULSBY, G. (2003a) Continuous hyperplastic models for overconsolidated clays. *Mathematical and Computer Modelling,* 37, 515-523.

EINAV, I., PUZRIN, A. M. & HOULSBY, G. T. (2003b) Numerical studies of hyperplasticity with single, multiple and a continuous field of yield surfaces. *International journal for numerical and analytical methods in geomechanics,* 27, 837-858.

ERLICHER, S. & POINT, N. (2006) Endochronic theory, non-linear kinematic hardening rule and generalized plasticity: a new interpretation based on generalized normality assumption. *International Journal of Solids and Structures,* 43, 4175-4200.

FELLIN, W., MITTENDORFER, M. & OSTERMANN, A. (2009) Adaptive integration of constitutive rate equations. *Computers and Geotechnics,* 36, 698-708.

GOLDSCHEIDER, M. (1982) Workshop on Constitutive Relations for Soils *In:* G. GUDEHUS, F. D. A. I. V. (eds.) *True triaxial tests on dense sand* Balkerna

GUDEHUS, G. (1996) Comprehensive constitutive equation for granular materials. *Soils and Foundations,* 36, 1-12.

GUDEHUS, G. & MAŠÍN, D. (2009) Graphical representation of constitutive equations. *Géotechnique,* 59, 147-151.

HEINS, E. & GRABE, J. (2017) Class-A-prediction of lateral pile deformation with respect to vibratory and impact pile driving. *Computers and Geotechnics,* 86, 108-119.

HERLE, I. & KOLYMBAS, D. (2004) Hypoplasticity for soils with low friction angles. *Computers and Geotechnics,* 31, 365-373.

HOLLAND, J. & GOLDBERG, D. (1989) *Genetic algorithms in search, optimization and machine learning,* Massachusetts, Addison-Wesley.

HONG, Y., HE, B., WANG, L. Z., WANG, Z., NG, C. W. W. & MASIN, D. (2017) Cyclic lateral response and failure mechanisms of semi-rigid pile in soft clay: centrifuge tests and numerical modelling. *Canadian Geotechnical Journal,* 54, 806-824.

HOULSBY, G. T. & PUZRIN, A. M. (2007) *Principles of hyperplasticity: an approach to plasticity theory based on thermodynamic principles,* London, Springer.

ISMAIL, M., IKHOUANE, F. & RODELLAR, J. (2009) The Hysteresis Bouc-Wen Model, a Survey. *Archives of Computational Methods in Engineering,* 16, 161-188.

JARDINE, R. J., POTTS, D. M., BURLAND, J. B. & FOURIE, A. B. (1986) Studies of the influence of non-linear stress–strain characteristics in soil–structure interaction. *Geotechnique,* 36, 377-396.

JIANG, Y. & KURATH, P. (1996) Characteristics of the Armstrong-Frederick type plasticity models. *International Journal of Plasticity,* 12, 387-415.

JOSTAD, H., GRIMSTAD, G., ANDERSEN, K. & SIVASITHAMPARAM, N. A FE procedure for calculation of cyclic behaviour of offshore foundations under partly drained conditions. Frontiers in Offshore Geotechnics III, 2015. 153.

JOSTAD, H. P., GRIMSTAD, G., ANDERSEN, K. H., SAUE, M., SHIN, Y. & YOU, D. (2014) A FE procedure for foundation design of offshore structures - Applied to study a potential OWT monopile foundation in the Korean Western Sea. *Geotechnical Engineering,* 45, 63-72.

KOBAYASHI, M. & OHNO, N. (2002) Implementation of cyclic plasticity models based on a general form of kinematic hardening. *International Journal for Numerical Methods in Engineering,* 53, 2217-2238.

KOLYMBAS, D. (1991a) Computer-aided design of constitutive rules. *International Journal for Numerical and Analytical Methods in Geomechanics,* 15, 593-604.

KOLYMBAS, D. (1991b) An outline of hypoplasticity. *Archive of Applied Mechanics,* 61, 143-151.

KOLYMBAS, D. (2000) *Introduction to Hypoplasticity,* Rotterdam, Balkerna.

KRABBENHØFT, K. (2009) A variational principle of elastoplasticity and its application to the modeling of frictional materials. *International Journal of Solids and Structures,* 46, 464-479.

KULHAWY, F. H. & MAYNE, P. W. (1990) Manual on estimating soil properties for foundation design Electric Power Research Inst., Palo Alto, CA (USA); Cornell Univ., Ithaca, NY (USA). Geotechnical Engineering Group

LEMAITRE, J. & CHABOCHE, J.-L. (1994) *Mechanics of solid materials,* Cambridge, Cambridge university press.

LIU, T., AGHAKOUCHAK, A., TABORDA, D. M. G. & JARDINE, R. J. Advanced laboratory characterization of a fine marine sand from Dunkirk, France. ICSMGE 2017 - 19th International Conference on Soil Mechanics and Geotechnical Engineering, 2017. 439-442.

LUBARDA, V. A. & BENSON, D. J. (2002) On the numerical algorithm for isotropic-kinematic hardening with the Armstrong-Frederick evolution of the back stress. *Computer Methods in Applied Mechanics and Engineering,* 191, 3583-3596.

LUBLINER, J., TAYLOR, R. & AURICCHIO, F. (1993) A new model of generalized plasticity and its numerical implementation. *International Journal of Solids and Structures,* 30, 3171-3184.

MACHACEK, J., WICHTMANN, T., ZACHERT, H. & TRIANTAFYLLIDIS, T. (2018) Long-term settlements of a ship lock: Measurements vs. FE-prediction using a high cycle accumulation model. *Computers and Geotechnics,* 97, 222-232.

MASIN, D. (2005) A hypoplastic constitutive model for clays. *International Journal for Numerical and Analytical Methods in Geomechanics,* 29, 311-336.

MASIN, D. (2012a) Asymptotic behaviour of granular materials. *Granular Matter,* 14, 759-774.

MASIN, D. (2012b) Hypoplastic Cam-clay model. *Geotechnique,* 62, 549-553.

MASIN, D. (2013) Clay hypoplasticity with explicitly defined asymptotic states. *Acta Geotechnica,* 8, 481-496.

MCADAM, R. A., BYRNE, B. W., HOULSBY, G. T., BEUCKELAERS, W. J. A. P., BURD, H. J., GAVIN, K., IGOE, D., JARDINE, R. J., MARTIN, C. M., MUIR WOOD, A., POTTS, D. M., SKOV GRETLUND, J., TABORDA, D. M. G. & ZDRAVKOVIC, L. 2018. Monotonic lateral loaded pile testing in a dense marine sand at Dunkirk. *submitted to Géotechnique*.

MOREAU, J.-J. (1970) Sur les lois de frottement, de plasticité et de viscosité. *Comptes Rendus de l'Académie des Sciences,* 271, 608-611.

NIEMUNIS, A. (2002) *Extended hypoplastic models for soils*. Habilitation Thesis, Ruhr-University.

NIEMUNIS, A. & HERLE, I. (1997) Hypoplastic model for cohesionless soils with elastic strain range. *Mechanics of Cohesive-Frictional Materials,* 2, 279-299.

NIEMUNIS, A. & WICHTMANN, T. (2014) Separation of time scales in the HCA model for sand. *Acta Geophysica,* 62, 1127-1145.

NIEMUNIS, A., WICHTMANN, T. & TRIANTAFYLLIDIS, T. (2005) A high-cycle accumulation model for sand. *Computers and Geotechnics,* 32, 245-263.

OHNO, N. (1982) A constitutive model of cyclic plasticity with a nonhardening strain region. *Journal of Applied Mechanics,* 49, 721-727.

OHNO, N. (1990) Recent topics in constitutive modeling of cyclic plasticity and viscoplasticity. *Applied Mechanics Reviews,* 43, 283-295.

OHNO, N. & WANG, J. D. (1991) Transformation of a nonlinear kinematic hardening rule to a multisurface form under isothermal and nonisothermal conditions. *International Journal of Plasticity,* 7, 879-891.

OHNO, N. & WANG, J. D. (1993a) Kinematic hardening rules with critical state of dynamic recovery, part I: formulation and basic features for ratchetting behavior. *International Journal of Plasticity,* 9, 375-390.

OHNO, N. & WANG, J. D. (1993b) Kinematic hardening rules with critical state of dynamic recovery, part II: Application to experiments of ratchetting behavior. *International Journal of Plasticity,* 9, 391-403.

ORTIZ, M. & POPOV, E. P. (1985) Accuracy and stability of integration algorithms for elastoplastic constitutive relations. *International journal for numerical methods in engineering,* 21, 1561-1576.

PASTOR, M., ZIENKIEWICZ, O. C. & CHAN, A. H. C. (1990) Generalized plasticity and the modelling of soil behaviour. *International Journal for Numerical and Analytical Methods in Geomechanics,* 14, 151-190.

PATZAK, B. & BITTNAR, Z. (2001) Design of object oriented finite element code. *Advances in Engineering Software,* 32, 759-767.

PEREZ-FOGUET, A. & ARMERO, F. (2002) On the formulation of closest-point projection algorithms in elastoplasticity - part II: Globally convergent schemes. *International Journal for Numerical Methods in Engineering,* 53, 331-374.

PEREZ-FOGUET, A., RODRIGUEZ-FERRAN, A. & HUERTA, A. (2000a) Numerical differentiation for local and global tangent operators in computational plasticity. *Computer Methods in Applied Mechanics and Engineering,* 189, 277-296.

PEREZ-FOGUET, A., RODRIQUEZ-FERRAN, A. & HUERTA, A. (2000b) Numerical differentiation for non-trivial consistent tangent matrices: an application to the MRS-Lade model. *International Journal for Numerical Methods in Engineering,* 48, 159-184.

POTTS, D. M. & GENS, A. (1985) A critical assesment of methods of correcting for drift from the yield surface in elasto-plastic finite element analysis. *International Journal for Numerical and Analytical Methods in Geomechanics,* 9, 149-159.

POTTS, D. M. & ZDRAVKOVIC, L. (1999) *Finite element analysis in geotechnical engineering: theory,* London, Thomas Telford.

POTTS, D. M. & ZDRAVKOVIC, L. (2012) Accounting for partial material factors in numerical analysis. *Geotechnique,* 62, 1053-1065.

PUZRIN, A. & KIRSCHENBOIM, E. (2001) Kinematic hardening model for overconsolidated clays. *Computers and Geotechnics,* 28, 1-36.

PYKE, R. (1986) The use of linear elastic and piecewise linear models in finite element analyses. *Geomechanics Modeling in Engineering Practice,* 167, 188.

ROSCOE, K. H. & BURLAND, J. (1968) Engineering Plasticity *In:* J. HEYMAN, F. L. (eds.) *On the generalized stress-strain behaviour of wet clay* Cambridge Cambridge University Press

SCALET , G. & AURICCHIO, F. (2017) Computational Methods for Elastoplasticity: An Overview of Conventional and Less-Conventional Approaches. *Archives of Computational Methods in Engineering*.

SCHOFIELD, A. & WROTH, P. (1968) *Critical state soil mechanics*, McGraw-Hill London.

SCHROEDER, F. C., DAY, R. A., POTTS, D. M. & ADDENBROOKE, T. I. (2007) Quadrilateral isoparametric shear deformable shell element for use in soil-structure interaction problems. *International Journal of Geomechanics,* 7, 44-52.

SLOAN, S. W. (1987) Substepping schemes for the numerical integration of elastoplastic stress-strain relations. *International Journal for Numerical Methods in Engineering,* 24, 893-911.

TABORDA, D. M. G. & ZDRAVKOVIC, L. (2012) Application of a Hill-Climbing technique to the formulation of a new cyclic nonlinear elastic constitutive model. *Computers and Geotechnics,* 43, 80-91.

TABORDA, D. M. G., ZDRAVKOVIC, L., KONTOE, S. & POTTS, D. M. (2014) Computational study on the modification of a bounding surface plasticity model for sands. *Computers and Geotechnics,* 59, 145-160.

TAMAGNINI, C., VIGGIANI, G., CHAMBON, R. & DESRUES, J. (2000) Evaluation of different strategies for the integration of hypoplastic constitutive equations: Application to the CLoE model. *Mechanics of Cohesive-Frictional Materials,* 5, 263-289.

TOPOLNICKI, M., GUDEHUS, G. & MAZURKIEWICZ, B. (1990) Observed stress–strain behaviour of remoulded saturated clay under plane strain conditions. *Géotechnique,* 40, 155-187.

VALANIS, K. (1971) A theory of viscoplasticity without a yield surface. *Arch. Mech. Stos.,* 23, 515-553.

VALANIS, K. C. (1980) Fundamental consequences of a new intrinsic time measure. Plasticity as a limit of the endochronic theory. *Arch. Mech. Stos.,* 32.

VALANIS, K. C. & PETERS, J. F. (1991) An endochronic plasticity theory with shear-volumetric coupling. *International Journal for Numerical and Analytical Methods in Geomechanics,* 15, 77-102.

VAN EEKELEN, H. A. M. (1980) Isotropic yield surfaces in 3 dimensions for use in soil mechanics. *International Journal for Numerical and Analytical Methods in Geomechanics,* 4, 89-101.

VON WOLFFERSDORFF, P. A. (1996) Hypoplastic relation for granular materials with a predefined limit state surface. *Mechanics of Cohesive-Frictional Materials,* 1, 251-271.

WATANABE, O. & ATLURI, S. (1986a) Constitutive modeling of cyclic plasticity and creep, using an internal time concept. *International Journal of Plasticity,* 2, 107-134.

WATANABE, O. & ATLURI, S. N. (1986b) Internal time, general internal variable, and multi-yield-surface theories of plasticity and creep: A unification of concepts. *International Journal of Plasticity,* 2, 37-57.

WICHTMANN, T., ANDERSEN, K. H., SJURSEN, M. A. & BERRE, T. (2013) Cyclic tests on high-quality undisturbed block samples of soft marine Norwegian clay. *Canadian Geotechnical Journal,* 50, 400-412.

WICHTMANN, T., NIEMUNIS, A. & TRIANTAFYLLIDIS, T. (2009) Validation and calibration of a high-cycle accumulation model based on cyclic triaxial tests on eigth sands. *Soils and Foundations,* 49, 711-728.

WICHTMANN, T., NIEMUNIS, A. & TRIANTAFYLLIDIS, T. (2010) On the determination of a set of material constants for a high-cycle accumulation model for non-cohesive soils. *International Journal for Numerical and Analytical Methods in Geomechanics,* 34, 409-440.

WICHTMANN, T., NIEMUNIS, A. & TRIANTAFYLLIDIS, T. (2014) Flow rule in a high-cycle accumulation model backed by cyclic test data of 22 sands. *Acta Geotechnica,* 9, 695-709.

WICHTMANN, T., NIEMUNIS, A. & TRIANTAFYLLIDIS, T. (2015) Improved simplified calibration procedure for a high-cycle accumulation model. *Soil Dynamics and Earthquake Engineering,* 70, 118-132.

WICHTMANN, T. & TRIANTAFYLLIDIS, T. (2015) Stress attractors predicted by a high-cycle accumulation model confirmed by undrained cyclic triaxial tests. *Soil Dynamics and Earthquake Engineering,* 69, 125-137.

WICHTMANN, T. & TRIANTAFYLLIDIS, T. (2016a) An experimental database for the development, calibration and verification of constitutive models for sand with focus to cyclic loading: part I—tests with monotonic loading and stress cycles. *Acta Geotechnica,* 11, 739-761.

WICHTMANN, T. & TRIANTAFYLLIDIS, T. (2016b) An experimental database for the development, calibration and verification of constitutive models for sand with focus to cyclic loading: part II—tests with strain cycles and combined loading. *Acta Geotechnica,* 11, 763-774.

WU, H. C. & KOMARAKULNANAKORN, C. (1992) On the limit case of endochronic theory. *International Journal of Solids and Structures,* 29, 135-143.

WU, W. (1992) *Hypoplastizitat als mathematisches Modell zum mechanischen Verhalten granularer Stoffe*. PhD, Universitat Karlsruhe.

WU, W. & NIEMUNIS, A. (1996) Failure criterion, flow rule and dissipation function derived from hypoplasticity. *Mechanics of Cohesive-frictional Materials,* 1, 145-163.

ZDRAVKOVIC, L., TABORDA, D. M. G., POTTS, D. M., JARDINE, R. J., SIDERI, M., SCHROEDER, F. C., BYRNE, B. W., MCADAM, R., BURD, H. J., HOULSBY, G. T., MARTIN, C. M., GAVIN, K., DOHERTY, P., IGOE, D., MUIRWOOD, A., KALLEHAVE, D. & SKOV GRETLUND, J. Numerical modelling of large diameter piles under lateral loading for offshore wind applications. Frontiers in Offshore Geotechnics III - Proceedings of the 3rd International Symposium on Frontiers in Offshore Geotechnics, ISFOG 2015, 2015. 759-764.

ZIEGLER, H. (1977) *An introduction to thermomechanics,* Amsterdam, North-Holland.

APPENDIX I APLICATION OF NON-SMOOTH MECHANICS TO PLASTICITY THEORY

In this section some definitions as transcribed in de Saxce and Bousshine (2002) are included that are recalled when discussing the thermodynamic admissibility of the proposed framework. The general form of NLKH can be classified as *implicit standard materials* (de Saxce and Bousshine, 2002) and the thermodynamic admissibility is provided by the non-smooth mechanics theory using tools of convex analysis. The definitions shown in the next section have been extracted from de Saxce and Bousshine (2002).

A. SUBGRADIENT

de Saxce (2002) presented the definition of subgradient as follows: Let **V** be a topological vector space of velocities $\dot{\kappa}$, and **F** be its dual space collecting the associated variables π with the scalar product being: $(\dot{\kappa}, \pi) \rightarrow \dot{\kappa} : \pi$. Let $\bar{R} \rightarrow R \cap \{-\infty\}$ be the set of extended real numbers equipped with the natural operations and ordering it inherits from the set **R** with particular rules concerning to $+\infty$ $\bar{R} \rightarrow R \cap \{-\infty\}$ then the existence of a lower semi-continuous and convex (but not necessarily differentiable) function is postulated: $\varphi : V \rightarrow \bar{R}$. Then for any $\pi \in F$ a **subgradient** of φ at $\dot{\kappa}$ is defined as:

$$\forall \dot{\kappa} \in V, \quad \varphi(\dot{\kappa}') - \varphi(\dot{\kappa}) \geq \pi : (\dot{\kappa}' - \dot{\kappa}) \tag{7.1}$$

Therefore, it is clear that the subgradient is a generalized gradient which is not necessarily unique, i.e. it can be a set. This set (all the subgradients at $\dot{\kappa}$) is designated the ***subdifferential*** of φ at $\dot{\kappa}$ and is denoted by $\partial\varphi(\dot{\kappa})$. For notation purposes it is symbolised by the *differential inclusion:*

$$\pi \in \partial\varphi(\dot{\kappa}) \tag{7.2}$$

B. POLAR FUNCTION

The concept of *polar (or conjugate) function* is useful when combined with semi-continuous and convex (but not necessarily differentiable) function, which is defined by a Legendre-Fenchel transform (de Saxce, 2002):

$$\chi(\pi) = \sup\left\{\pi : \dot{\kappa} - \varphi(\dot{\kappa}); \dot{\kappa} \in V\right\} \tag{7.3}$$

Given that φ is convex, it follows that χ is also convex. A straightforward consequence of polar function of any convex fucntions is the relationship:

$$\forall \dot{\kappa}' \in V \quad \forall \pi' \in F, \quad \varphi(\dot{\kappa}') + \chi(\pi') \geq \dot{\kappa}' : \pi' \tag{7.4}$$

Secondly, it can be shown that taking any of the couples π or $\dot{\kappa}$ in (7.4) and subtracting member by member from (7.4) the couples π or $\dot{\kappa}$ are related by a subdifferential By de

$$\pi \in \partial\varphi(\dot{\kappa}) \qquad \dot{\kappa} \in \partial\chi(\pi) \tag{7.5}$$

C. EXTREMAL COUPLES

Given any set of couples $(\dot{\kappa}, \pi)$, a constitutive multi-valued rule can be achieved by obtaining the couples $(\dot{\kappa}, \pi)$ that are ***extremal*** with regard to the inequality (7.4). In other words the couples $(\dot{\kappa}, \pi)$ for which the following relation holds:

$$\forall \dot{\kappa} \in V \quad \forall \pi \in F, \quad \varphi(\dot{\kappa}) + \chi(\pi) = \dot{\kappa} : \pi \tag{7.6}$$

It can be concluded that the double equivalence exists:

$$\varphi(\dot{\kappa}) + \chi(\pi) = \pi : \dot{\kappa} \Leftrightarrow \pi \in \partial\varphi(\dot{\kappa}) \Leftrightarrow \dot{\kappa} \in \partial\chi(\pi) \tag{7.7}$$

Firstly it is obvious that (7.5) is recovered by substracting a extremal couple $(\dot{\kappa},\pi)$ of a non extremal couple $(\dot{\kappa}',\pi)$ member by member from (7.4), secondly due to the fact that $(\dot{\kappa},\pi)$ are extremal the following conditions is always true

$$\varphi(\dot{\kappa}) - \pi : \dot{\kappa} \leq \varphi(\dot{\kappa}') - \pi : \dot{\kappa}' \tag{7.8}$$

By looking at (7.8) the equality must be reached at its infimun of the right hand side, in other words

$$\varphi(\dot{\kappa}) - \pi : \dot{\kappa} = \inf\left\{\varphi(\dot{\kappa}') - \pi : \dot{\kappa}', \dot{\kappa}' \in V\right\} \tag{7.9}$$

which after some manipulations is equivalent to the polar function

$$\inf\left\{\varphi(\dot{\kappa}') - \pi : \dot{\kappa}', \dot{\kappa}' \in V\right\} = -\sup\left\{\pi : \dot{\kappa}' - \varphi(\dot{\kappa}'), \dot{\kappa}' \in V\right\} = -\chi(\pi) \tag{7.10}$$

Therefore, it can be concluded that the double equivalence exists for extremal couples:

$$\varphi(\dot{\kappa}) + \chi(\pi) = \pi : \dot{\kappa} \Leftrightarrow \pi \in \partial\varphi(\dot{\kappa}) \Leftrightarrow \dot{\kappa} \in \partial\chi(\pi) \tag{7.11}$$

This proces is analogous for π

In other words, for extremal couples $(\pi,\dot{\kappa})$ the variables are related by differential inclusions of pseudo-potentials which are $\varphi(\dot{\kappa})$ and its polar function $\chi(\pi)$. These differential inclusions in (7.11) can be interpreted as the inverse constitutive rules relating strain velocities with thermodynamic stresses which is the fundamental idea to derive the constitutive models.

D. BIPOTENTIAL

Borrowing the idea of convex non-differentiable fucntiona and its polar fucntion the bipotential goes one step further. Again, the formal definitions states (de Saxce & Bousshine, 2002): Let **V** be a topological vector of velocities $\dot{\kappa}$, and **F** be its dual space collecting the associated variables π (or thermodynamic forces), the scalar product can be defined as: $(\dot{\kappa},\pi) \rightarrow \dot{\kappa} : \pi$

. The definition of a **bipotential** comes from a function $b : V \times F \to \overline{R}$, separately convex, which satisfies the fundamental inequality:

$$\forall (\dot{\kappa}', \pi') \in V \times F, \quad b(\dot{\kappa}', \pi') \geq \dot{\kappa}' : \pi' \tag{7.12}$$

Clearly, the couples $(\dot{\kappa}, \pi)$ are related by the dissipative constitutive rule. They are qualified as extremal since the equality in (7.11) is verified:

$$b(\dot{\kappa}, \pi) = \dot{\kappa} : \pi \tag{7.13}$$

Therefore, as carried out in the previous section, taking the value of the extreme couples and subtracting member by member (7.13) from (2.88), the following two relations can be established:

$$\forall \pi' \in F, \quad b(\dot{\kappa}, \pi') - b(\dot{\kappa}, \pi) \geq (\pi' - \pi) : \dot{\kappa} \tag{7.14}$$

and

$$\forall \dot{\kappa}' \in V, \quad b(\dot{\kappa}', \pi) - b(\dot{\kappa}, \pi) \geq \pi : (\dot{\kappa}' - \dot{\kappa}) \tag{7.15}$$

Again, expressions (7.14) and (7.15) are subdifferentials. Based on the fact that when a couple is extremal as defined in (7.13), the double equivalence (7.16) also exists for the bipotentials, where the vector flows and its conjugate variables belong to the differential inclusion of the bipotential. Moreover, considering (7.11) it follows that

$$b(\dot{\kappa}, \pi) = \varphi(\dot{\kappa}) + \chi(\pi) = \pi : \dot{\kappa} \Leftrightarrow \pi \in \partial_{\dot{\kappa}} b \Leftrightarrow \dot{\kappa} \in \partial_{\pi} b \tag{7.16}$$

is also true. This type of relationship is designated as **implicit normality rules,** since the unknown $\dot{\kappa}$ belongs to both left and right hand members of the constitutive relation. As a result, the dissipation potential plus its thermodynamic conjugate are not defined separately, but rather implicitly.

APPENDIX II OTHER RESPONSES OF CALIBRATION SETS FOR KARLSRUHE SAND: PITFALLS

The nature of NLKH is to find for a state of minimum ratchetting, thus is achieved as under strain controlled conditions the backstress perturbation travels on every cycle to a region that enforces a stable cycle where shakedown would occur. This type of response is against the nature of some soil responses, for example, in sands under undrained cyclic conditions (ergo strain controlled conditions) the stress path does not stabilize and the soil liquefies. To achieve the desired response with a NLKH the calibration parameters enforce in a way that the stable cycle is only reached in the neightbourhoog of a small mean effective stress value or not reached at all. This can be achieved penalizing the dilatancy induced by the goal functions providing more strength to the contractant part that the dilatatant. This appendix ilusstrates this using the two sets calibrated for Karlsruhe sand and comparing their predictions with cyclic undrained tests and monotonic drained tests. Table 37 presents both sets for cylic and monotonic conditions calibrated in 4.4.2 and 4.4.5.

Table 37: Parameter sets for static and cyclic tests for Karlsruhe sand calibration

Mono. set	Main rule	e_{c0}	e_{d0}	h_s	n	α	β	XV	YF	ZF	θ	S_f	ob_{min}	ob_{max}	δ
		1.0	0.55	4E5	0.45	0.15	2.5	0.53	0.77	0.24	0.4	3.5	-1.73	1.0	2.5
Cylclic set	Main rule	e_{c0}	e_{d0}	h_s	n	α	β	XV	YF	ZF	θ	S_f	ob_{min}	ob_{max}	δ
		1.0	0.55	4E5	0.45	0.15	2.5	0.53	0.77	0.24	0.7	4	-1.73	0.1	1.6
	Inter	R	βr	$Mv^{)}$	Md	X									
		3E-4	0.5	2.0	2.0	4.0									

A. MONOTONIC RESPONSE FOR CYCLIC SET

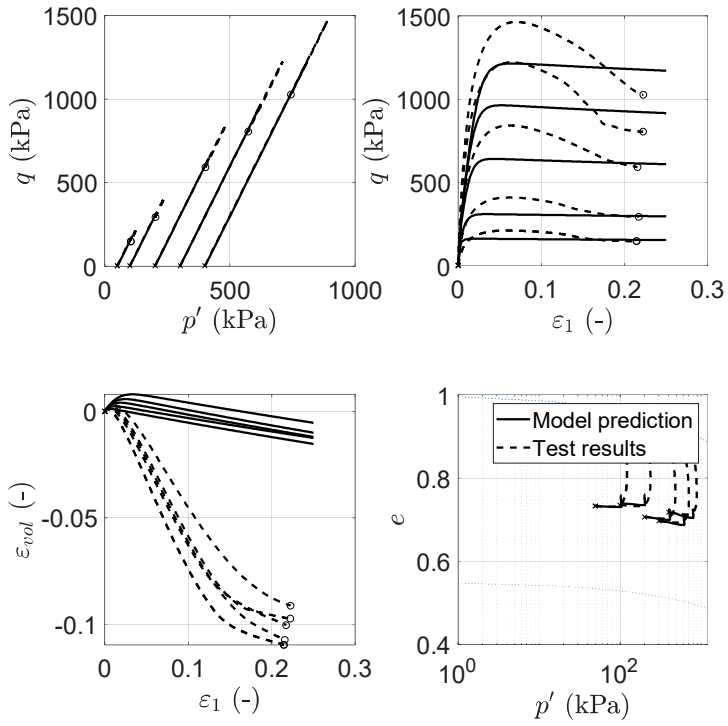


Figure 263: Triaxial test for very dense sand

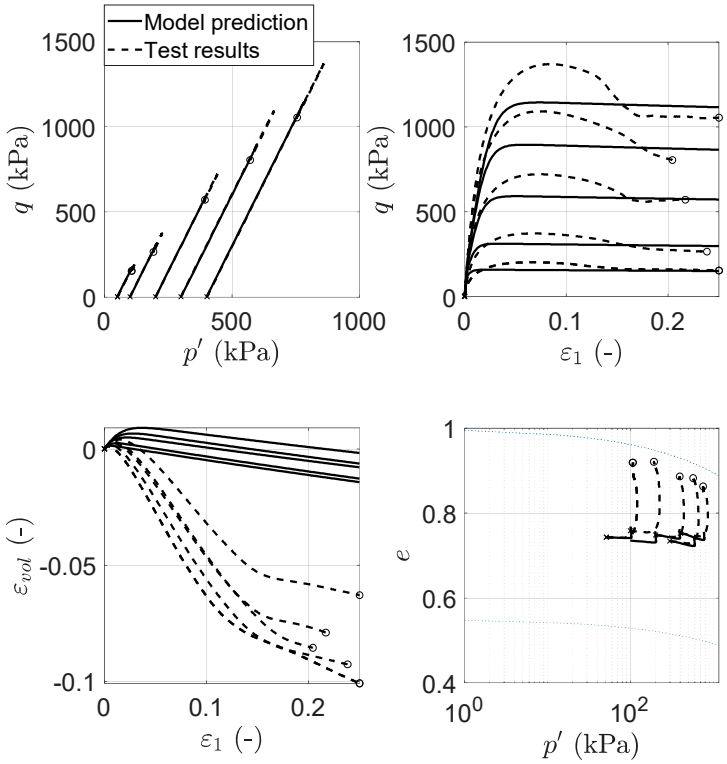


Figure 264: Triaxial test for dense sand

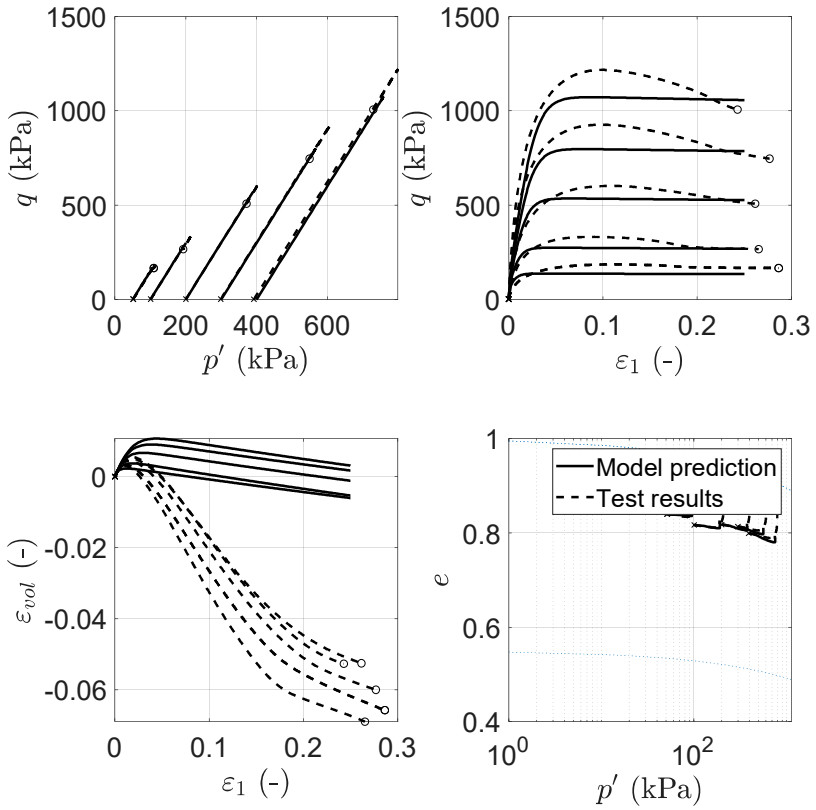


Figure 265: Traiaxila test for medium sand

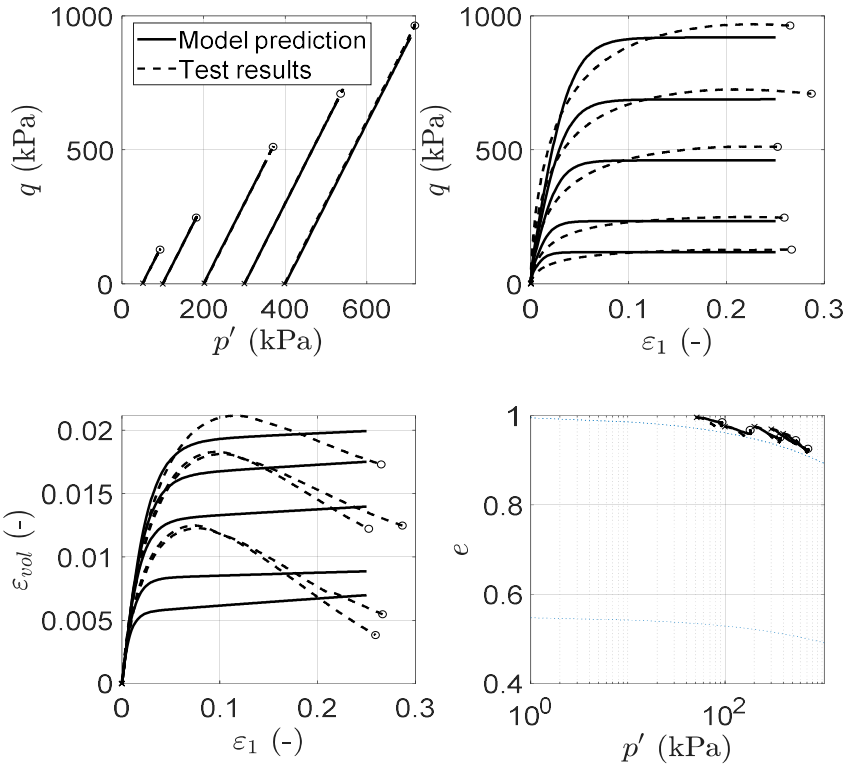
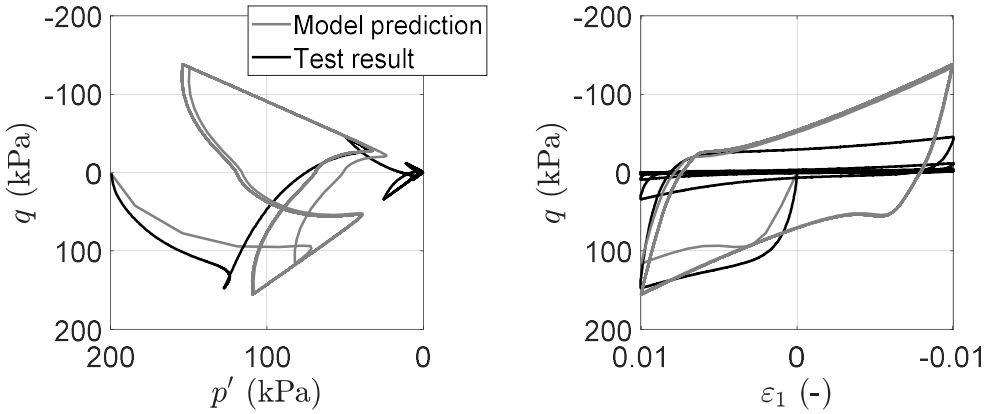
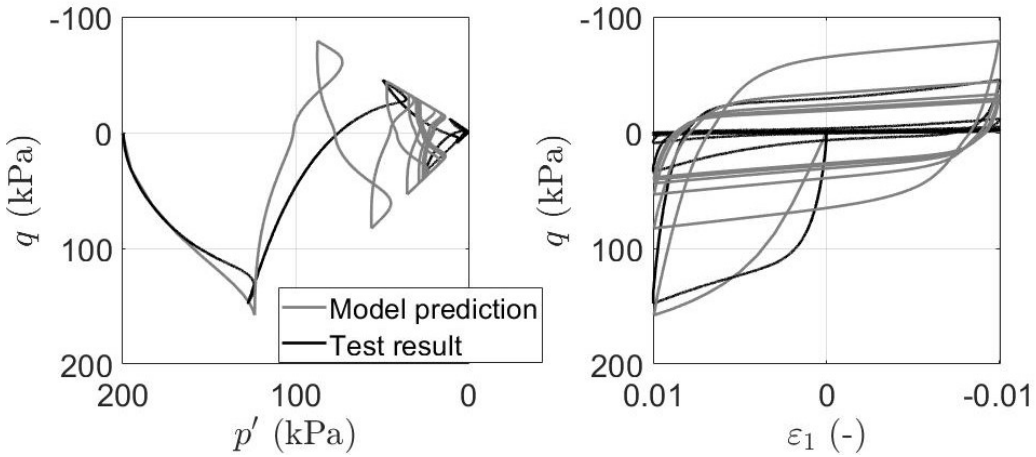


Figure 266: Triaxial test for loose sand

B. CYCLIC RESPONSE – LARGE AMPLITUDES FOR MONOTONIC SET



(a)



(b)

Figure 267: Large amplitude undrained strain controlled triaxial test 16 against numerical prediction: (a) monotonic set (b) cylic set